sustainability

Topical Collection Reprint

Sustainable Development of Coal Based Energy

Technology, Environment, Humanities, Economy, and Education: Green and Sustainable Coal Mining

Edited by
Cun Zhang, Fangtian Wang, Shiqi Liu and Erhu Bai

mdpi.com/journal/sustainability

MDPI

Sustainable Development of Coal Based Energy: Technology, Environment, Humanities, Economy, and Education

Sustainable Development of Coal Based Energy: Technology, Environment, Humanities, Economy, and Education

Green and Sustainable Coal Mining

Collection Editors

Cun Zhang
Fangtian Wang
Shiqi Liu
Erhu Bai

MDPI

Basel • Beijing • Wuhan • Barcelona • Belgrade • Novi Sad • Cluj • Manchester

Collection Editors

Cun Zhang
School of Energy and Mining Engineering
China University of Mining and Technology (Beijing)
Beijing
China

Erhu Bai
School of Energy Science and Engineering
Henan Polytechnic University
Jiaozuo
China

Fangtian Wang
School of Mines
China University of Mining and Technology
Xuzhou
China

Shiqi Liu
School of Energy and Mining Engineering
China University of Mining & Technology (Beijing)
Beijing
China

Editorial Office
MDPI AG
Grosspeteranlage 5
4052 Basel, Switzerland

This is a reprint of the Topical Collection, published open access by the journal *Sustainability* (ISSN 2071-1050), freely accessible at: https://www.mdpi.com/journal/sustainability/topical_collections/mining_tech_envir_energy.

For citation purposes, cite each article independently as indicated on the article page online and as indicated below:

Lastname, A.A.; Lastname, B.B. Article Title. *Journal Name* **Year**, *Volume Number*, Page Range.

Volume II
ISBN 978-3-7258-6494-2 (Hbk)
ISBN 978-3-7258-6495-9 (PDF)
https://doi.org/10.3390/books978-3-7258-6495-9

Set
ISBN 978-3-7258-6828-5 (Hbk)
ISBN 978-3-7258-6829-2 (PDF)

Contents

About the Editors

Cun Zhang

Cun Zhang is a Professor affiliated with the School of Energy and Mining Engineering at China University of Mining and Technology, Beijing. His research interests primarily include mine pressure and strata control, mine water resource utilization, coal and gas co-mining, and the reuse of abandoned mines. He has presided over more than 10 national and provincial-level vertical projects. His notable achievements include being a recipient of the Excellent Doctoral Dissertation Award from the Chinese Society of Rock Mechanics and Engineering, being accepted to the Young Talent Promotion Project of the China Association for Science and Technology, and being elected as a Fellow of the International Association of Advanced Materials (IAAM Fellow). Furthermore, he has been continuously listed in the Stanford University's Top 2% of the World's Most-Cited Scientists since 2022. In terms of academic contributions, he has received one first prize award for provincial-level teaching and five first prize awards for provincial-level scientific and technological progress, among other awards. He has produced over 200 publications, including more than 50 JCR Q1 papers as first or corresponding author, and 8 ESI highly cited papers, and has published 4 monographs and holds more than 10 invention patents as the first inventor. In addition to this, he serves as an Associate Editor for the SCI *Journal of Geophysics and Engineering* and is an Editorial Board Member for *Rock Mechanics Bulletin* and *Sustainability*.

Fangtian Wang

Fangtian Wang is a Professor at the School of Mines, China University of Mining and Technology. He has led more than 10 national and provincial-level research projects. Among his key honors, he is a recipient of the Jiangsu Outstanding Youth Fund and has been recognized as a young academic leader in the national key discipline of mining engineering. He has also been awarded the Sun Yueqi Youth Science and Technology Award and was selected as a young and middle-aged academic leader under the Jiangsu Provincial "Qinglan Project". In addition, he serves as a member of the International Society for Mine Surveying and on the Editorial Board of the *Journal of Mining and Strata Control Engineering*. His research and teaching activities are centered on mining rock mechanics and the intelligent, green mining of coal-related resources. To date, he has published over 60 high-quality papers, 8 of which have been recognized as ESI Highly Cited Papers or selected for the F5000 program. He has authored 3 books, secured 31 invention patents, and registered 13 software copyrights. His academic contributions have earned him several prestigious awards, including three first prizes for scientific and technological progress at the provincial and ministerial level. Furthermore, under his mentorship, students have achieved top honors such as the Gold Award in the China International College Students' Innovation Competition and the Grand Prize in the National "Challenge Cup" Competition.

Shiqi Liu

Shiqi Liu, born in Hengshui, Hebei Province, is currently an Associate Professor and Doctoral Supervisor at the School of Energy and Mining, China University of Mining and Technology, Beijing. Dr. Liu earned his Bachelor's, Master's, and Ph.D. degrees in Mining Engineering from China University of Mining and Technology, Beijing, between 2006 and 2016, after which he began his teaching career at the university. His research focuses on mine water utilization and prevention, shaft damage control, and comprehensive utilization of abandoned mines. In the past three years, he has

led over 20 research projects, published 3 industry standards, authored 2 monographs, and produced more than 40 academic papers. His achievements include 3 provincial/ministerial first-class and 7 second-class scientific awards, 11 authorized national invention patents, and 5 registered software copyrights. Dr. Liu serves as a Youth Editorial Board Member of *Coal Science and Technology* and Guest Associate Editor of *Sustainability* (SCI). He has been recognized with honors such as the "National Huang Danian-style Teacher Team", "Senior Expert of Shanxi Coal Society Thousand-Person Think Tank", and "Outstanding Young Teacher Teaching Award".

Erhu Bai

Erhu Bai, Ph.D., born in July 1989, is a Professor currently serving as Deputy Director of the Intelligent Mining Department at Henan Polytechnic University's School of Energy Science and Engineering, and holds the position of Youth Editorial Board Member for the *Journal of Mining and Safety Engineering*. His research focuses on green coal mining; "three-under" mining (extraction under structures, water bodies, and railways); and mining damage and protection. He has led two National Natural Science Foundation projects, one sub-project of an NSFC joint key program, one national major project sub-task, and six provincial/ministerial-level projects, while participating in four NSFC joint key projects and four general projects. His honors include 16 provincial/ministerial scientific awards (with 5 government awards, 1 ranked first), the National Coal Industry Teaching Achievement Special Prize, and Henan Higher Education Teaching Achievement First Prize. He has published nearly 30 SCI/EI papers as first/corresponding author, as well as 6 monographs and textbooks, with 1 textbook winning the Henan Textbook Construction First Prize and National Coal Industry Outstanding Textbook Special Prize. His course "Mining Damage and Environmental Protection" is recognized as a National First-Class Undergraduate Course. He holds over 10 invention patents, a Silver Medal at the Geneva International Exhibition of Inventions, and has contributed to 1 national energy industry standard. Additional accolades include Zhongyuan Young Talents, Henan Higher Education Institutions Innovation Talent, and Green Mining Youth Science and Technology Award.

Preface

Coal has long been a cornerstone of global energy supply, powering economic growth and industrialization for centuries. As the world's largest producer and consumer of coal, China and many other countries rely heavily on coal-based energy to meet their burgeoning energy demands. However, traditional coal mining practices have often come at a significant environmental cost, including land subsidence, water contamination, air pollution, greenhouse gas emissions, and ecosystem degradation. These challenges underscore the urgent need for a transition towards green and sustainable coal mining practices that balance energy security with environmental stewardship.

In response to these challenges, governments and industries worldwide are adopting innovative policies and technologies to promote sustainable coal mining. Initiatives such as China's "Green Mine" construction, the European Union's emissions trading system (EU ETS), and various national strategies for carbon peak and carbon neutrality are driving the shift towards cleaner practices. Key advancements include the development of paste backfilling technologies, which utilize coal gangue and fly ash to fill underground goafs, reducing surface subsidence and waste accumulation; reuse technology for abandoned mines based on pumped storage, thermal storage, and CO2 sequestration; the integration of renewable energy sources; and the implementation of carbon capture, utilization, and storage (CCUS) systems. These approaches not only mitigate environmental impacts but also enhance resource efficiency and economic viability.

This Reprint, "Sustainable Development of Coal-Based Energy: Green and Sustainable Coal Mining", comprises 14 seminal research papers that explore these critical issues from multiple perspectives. These papers provide a comprehensive analysis of both theoretical frameworks and practical applications, offering valuable insights for achieving sustainable coal mining. Together, they highlight the importance of interdisciplinary approaches, combining geology, engineering, economics, and environmental science to address complex challenges.

This Reprint is designed for a diverse audience, including undergraduate and graduate students of mining engineering, environmental science, and energy policy; researchers seeking cutting-edge knowledge in sustainable resource management; and practitioners and policymakers involved in the coal industry. By presenting evidence-based solutions and innovative technologies, we aim to inspire further research and action towards a greener and more sustainable future for coal-based energy.

We extend our gratitude to all the authors and researchers whose work is featured in this volume. Their contributions are essential for advancing our understanding and implementation of sustainable practices in coal mining. As the world strives to meet the dual goals of energy security and environmental protection, this Reprint serves as a timely resource, fostering dialog and driving progress.

Cun Zhang, Fangtian Wang, Shiqi Liu, and Erhu Bai
Collection Editors

sustainability

MDPI

Article

The Re-Crushing Spatiotemporal Evolution Law of Broken Coal in the Goaf for Sustainable Utilization of Abandoned Mines

Yanhong Chen [1], Cun Zhang [1,2,*], Juhao Cheng [1] and Xiangyu Zhao [1]

[1] School of Energy and Mining Engineering, China University of Mining and Technology, Beijing 100083, China; cumtbck16@163.com (Y.C.); 17795584778@163.com (X.Z.)
[2] Engineering Research Center of Green and Intelligent Mining for Thick Coal Seam, Ministry of Education, China University of Mining and Technology, Beijing 100083, China
* Correspondence: cumt-zc@cumtb.edu.cn

Abstract: The broken coal samples' (BCS) re-crushing characteristics in the goaf during roof compaction directly affect the mechanics and seepage characteristics of the caving zone. This will further affect the safety of coal mining and the sustainable utilization of abandoned mines. Thus, the experiment of BCS compaction is carried out with the help of an acoustic emission (AE) monitoring system. The Hurst exponent changes of the AE counts at different stages were obtained using the R/S analysis method. The results indicate that the compaction and re-crushing of the BCS at the laboratory scale have long-term memory. When providing sufficient stress, the AE activity of BCS will continue to develop according to the current trend. Based on the AE breakage location technology, the spatial distribution re-crushing characteristics of the BCS are obtained. Re-crushing of the BCS demonstrates uniform breakage in the horizontal direction and layered breakage in the vertical direction. In the horizontal direction, the boundary area first began to break, and the damage gradually spread evenly to the central area. In the vertical direction, the upper layer was the first to be broken, and then the damage began to shift to the middle and lower layers.

Keywords: goaf; broken coal samples; acoustic emission; layered re-crushing; sustainable utilization

1. Introduction

After coal seam mining, the overlying rock layer gradually sinks and collapses due to the impact of mining. The caving zone, fractured zone, and subsidence zones are formed above the coal seam [1–5]. The goaf caving zone is a porous medium composed of broken rock and coal masses (BRCM), which contains a large amount of porous structure, and its porosity can reach levels of 30% to 45% [6,7]. When it is subjected to external forces, the natural gradation defects in BRCM in the goaf areas result in significant fragmentation, expansion, and compressibility characteristics, especially under high-stress conditions. Previous research has shown that particle crushing and compaction can effectively improve the initial gradation defects of natural particles [8,9]. And it has a significant impact on their macroscopic mechanical properties [10]. Long-term loading and compaction of BRCM in the goaf will cause changes in density, porosity, permeability, etc. [11,12]. The BRCM re-crushing characteristics in the goaf during roof compaction directly affect the mechanics and seepage characteristics of the caving zone. This will further affect the safety of coal mining and the sustainable utilization of abandoned mines [10]. As shown in Figure 1, utilizing the goaf of abandoned mines for thermal and energy storage is an important method for the sustainable utilization of abandoned mines. But the mechanics and seepage characteristics of BRCM in the goaf directly affect the stability and water storage and heat storage capacity of the goaf. Therefore, accurately understanding the compaction re-crushing mechanism of BRCM in the goaf under long-term compaction is of great significance.

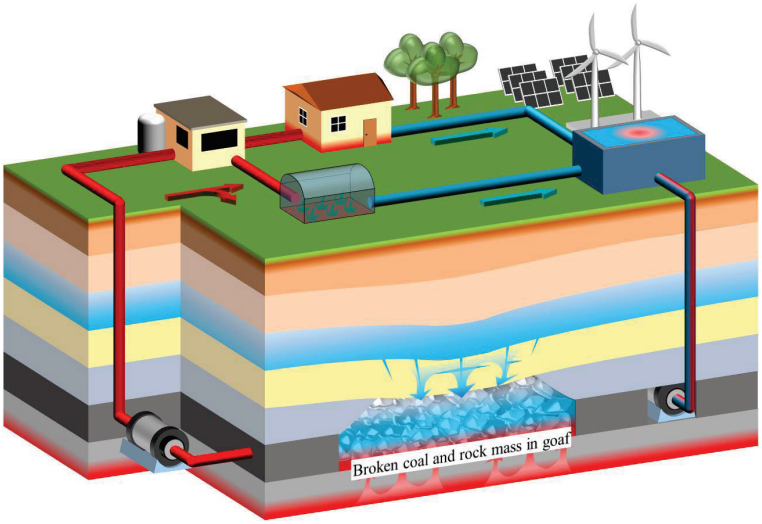

Figure 1. Sustainable utilization of abandoned mines based on multi energy complementarity.

Previous researchers have conducted studies on the re-crushing characteristics and their effect on the mechanical behavior and flow characteristics of BCS from the perspectives of particle size, strength, and loading method [13–16]. The results indicate that the strength and particle size of BCS are important factors affecting the mechanical behaviors of BCS. The deformation ability of BCS increases with the increase in particle size, and particles with higher size and lower strength are more prone to break. The deformation of BCS is also affected by temperature, moisture, and environmental humidity [17–20]. Temperature rising will alter the stress distribution of the BCS, accelerating the re-crushing of particles. The softening and lubricating effects of water molecules cause a significant reduction in the frictional force between BCS. The ability to resist deformation is significantly reduced, making it more prone to deformation. Thus, under the same axial stress, the bearing capacity of BCS decreases with increasing temperature, moisture, and environmental humidity.

However, due to the fact that the goaf is a closed space and most of the experiments on BSC are conducted in closed chambers, it is hard to obtain the characteristics of re-crushing directly during the compaction of BCS. With the development of acoustic emission (AE) technology, some scholars have begun to try using AE technology on granular materials such as BCS. By monitoring the AE signals generated during the experimental process (ringing count, energy count, etc.), the relationship between stress–strain of BCS and parameters such as AE count and AE energy has been established [21–24]. An AE localization method suitable for gangue material was proposed by Feng et al. [25] and Li et al. [26]. The characteristic of layered crushing of broken anthracite has been discovered. However, it is difficult for laboratory-scale BCS to achieve a closed state of long-term high-stress loading in the goaf due to limitations in experimental equipment and loading stress.

Thus, this article first introduces the experimental equipment and methods. And the experiment of BCS compaction is carried out with the help of an acoustic emission (AE) monitoring system. Combining the R/S analysis method and AE positioning technology, the long-term memory effect and spatial broken characteristics during the compaction process were revealed. Finally, the impact of the compacting and re-crushing of BCS on coal mine safety and the sustainable utilization of abandoned mines was summarized. This article also discusses the potential applications of our research findings.

2. Experiment Sample and Equipment

2.1. Experimental Sample

The experimental BCS was selected from the goaf of the 08 longwall face of Caojiatan Coal Mine. The 08 longwall face adopts a top-coal caving mining method. The longwall face mining height is 4 m, and the caving height is 6 m. The top-coal caving mining method

caused a large amount of residual coal to be left in the goaf. This can easily lead to the spontaneous combustion of the residual coal in the goaf after long-term accumulation. It can also cause the release of toxic and harmful gases. This poses a serious threat to the safe production of the working face. In addition, after the mining of the longwall face is completed, a large amount of mine water flows into the goaf, and the compaction and seepage characteristics of the BCS also affect the water storage and seepage capacity of the goaf. Thus, the mechanics and pore permeability evolution of BCS in the goaf directly affect the safety of coal mining and the sustainable utilization of abandoned mines. Considering the size of the experimental chamber, the sample size selected for this experiment is 0–5 mm. The average density of the BCS was 1.30 g/cm^3.

2.2. Experimental Equipment

Lateral compression experiments were used to conduct compression experiments on BCS. The diameter of the compression chamber is 100 mm, and the height of the cylinder is 150 mm. The experiments were loaded by an MTS universal servo tester, and the displacement loading method was used. The acoustic emission device is a Micro-Express Transmitter test monitoring device with eight channels, and the probe sampling frequency is 20–200 KHz. It is possible to monitor the entire compression stage in real time and perform three-dimensional localization of AE signals to obtain the re-crushing locations of the BCS within the chamber.

In this test, six channels were selected to monitor the AE information, and the arrangement was shown in Figure 2. Six AE probes are arranged at the intersection of the lower, middle, and upper layers. During the experiment, the sampling frequency is set to 1 MSPS, and the threshold of the AE signal receiver is set to 40 dB to minimize the impact of noise during the experiment. After the cavity is filled with materials, we use the AE device to emit pulses. We conduct material acoustic characteristic matrix testing on the entire device to obtain the AE wave velocity during the experimental process. The weight of BCS is 540 g, and the initial stacking height is 100 mm. We place the uniformly mixed dispersion into the chamber and shake it thoroughly. The experiment uses a displacement-controlled loading method, with a loading rate of 2 mm/min. The entire experiment is monitored using an AE device. The test is stopped when the maximum loading range of 300 kN is reached.

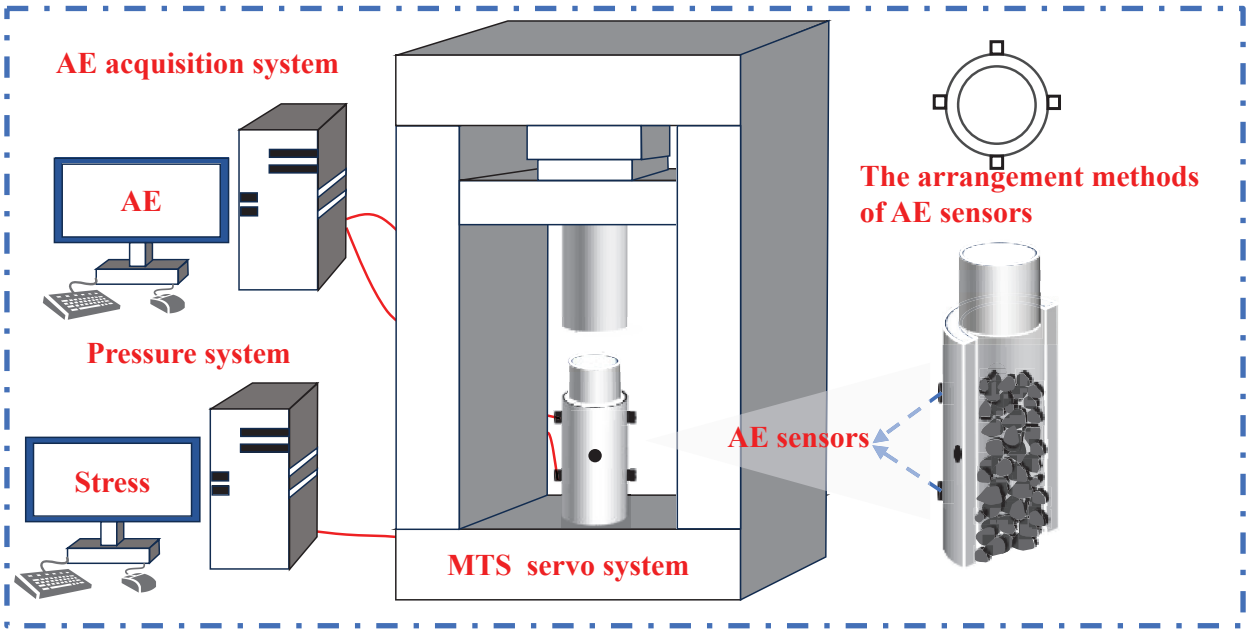

Figure 2. Main equipment and AE probe arrangement for lateral compression of BCS experiment.

3. Results and Discussions

3.1. Compaction Evolution Stage of BCS

Research has shown that the compaction of BCS can be divided into three stages; these are the self-adjustment stage, the broken stage, and the elastic stage [3,4,12,20,27–29]. Figure 3 shows the stress, void ratio, and pore structure at different stages during the compaction process of BCS.

In the self-adjustment stage, granular materials are in a loose state of natural accumulation. Under the action of their own gravity and the stress from the compaction device, the particles undergo structural adjustment and rearrangement by overcoming frictional resistance. The gap between the blocks acquires a small filling, and particle breakage only occurs at the edges and corners. The porosity loss primarily comes from the particle rearrangement, including particle rotation and displacement [30–33]. In this stage, the re-crushing and porosity changes of the BCS are limited due to the small degree of stress. Moreover, when the granular materials have a higher strength, larger particles, and larger initial porosity, the self-adjustment stage takes longer [12].

As the loading stress increases, particle re-crushing is also gradually increasing. In the broken stage, the large particles gradually start to break, forming a new pore structure and gradually becoming filled by small particles [20]. Thus, particle breaking is the major deformation mechanism at this stage. The degree and frequency of BCS breakage increase significantly with the increase in stress. Strain exhibits a concave upward rapid growth pattern as stress increases, and the secant modulus gradually increases with increasing stress [1,34].

After the model strain reaches a certain value, BCS compaction begins to progress to the elastic stage. In this stage, larger particles are surrounded by many smaller particles, forming a good, graded distribution. Due to the high coordination number, BCS particles are subjected to uniform stress. Thus, little re-crushing of BCS occurs. The secant modulus in the elastic stage is basically unchanged as the stress increases. It is suggested that the compaction of BCS is a process of improving the initial grading defects via repeated particle re-crushing and rearrangement [2,32].

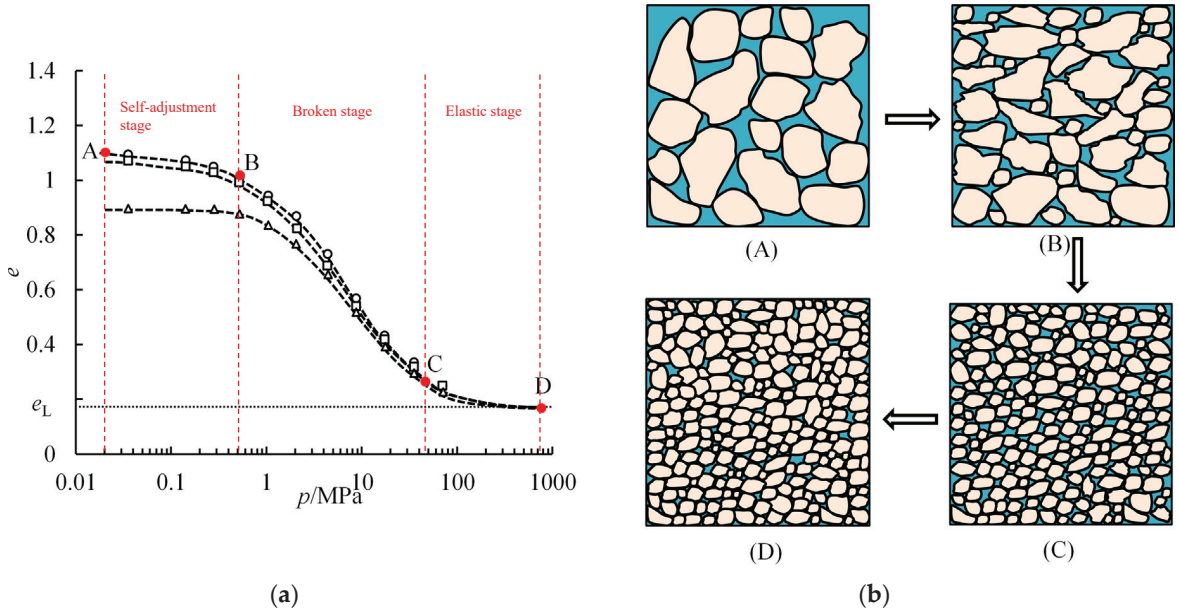

Figure 3. Lateral compression of broken particles: (**a**) loading stress (*p*)–void ratio (*e*); (**b**) pore structure and re-crushing ((**b**) shows the pore structure and re-crushing in different stages of (**a**)). Where A is the initial state. B is the self-adjustment stage. C is the broken stage. D is the Elastic stage. modified after Liu et al. [35] and Hagerty et al. [36]).

Figure 4 shows the strain and stress changes of BCS during lateral compression. Due to the BCS having been sufficient shaken in the cavity before loading in this experiment, the load pressure head has a certain initial stress (gravity). Moreover, the measuring range of the test servo device is 300 kN, which cannot reach the load required for the compaction elastic stage of the BCS. Therefore, the curve mainly consists of a broken stage and a small section in the self-adjustment stage. The secant modulus of the BCS gradually increases during the loading process. The compaction stress increases exponentially with strain, and as the loading progresses, the axial strain changes more slowly.

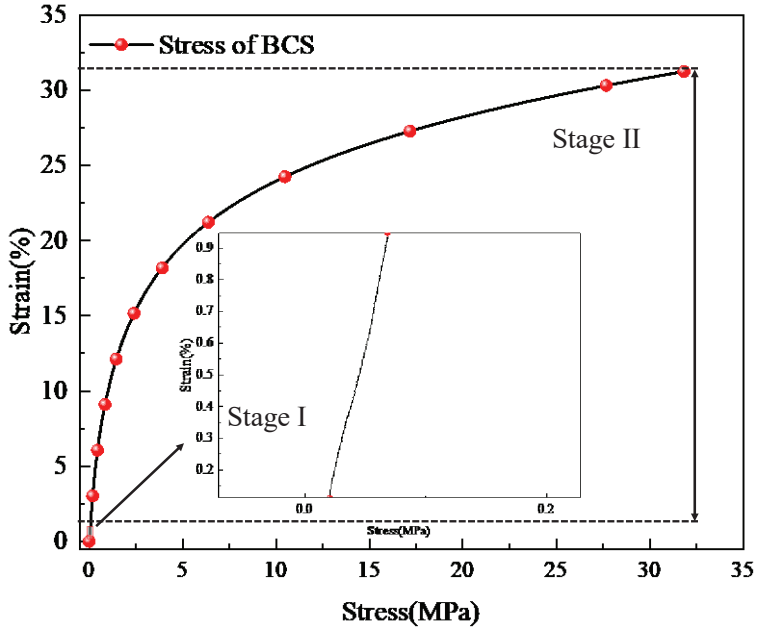

Figure 4. Stress–strain curve during compaction of BCS.

The AE count and energy of BCS are shown in Figure 5. The AE count and energy show a continuous increase as the axial stress increases. The cumulative count and the cumulative energy rise exponentially. The slope of the cumulative AE energy and count curve keeps increasing in the BCS compaction. This indicates that the re-crushing of particles becomes more pronounced as the stress increases.

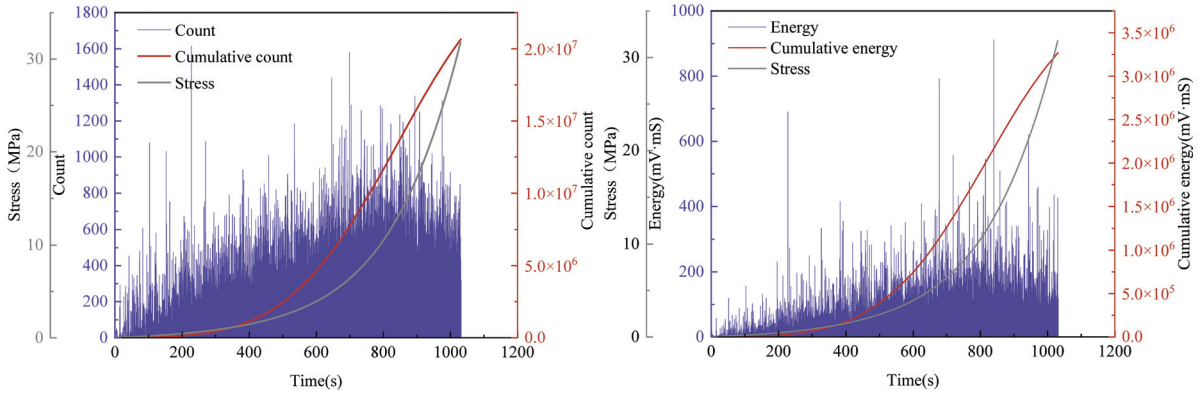

(**a**) AE count (**b**) AE energy

Figure 5. AE and stress evolution during the compaction of BCS.

3.2. Spatiotemporal Evolution of Compaction and Re-Crushing of BCS

The long-term trends and short-term fluctuations of the time series (TS) data can be revealed via the Hurst exponent (*H*) [37,38], which is widely used in fields such as rock

mechanics. To investigate the evolution law of the TS after re-crushing the BCS, H was determined via the rescaled range (R/S) method [39].

The TS of AE counting is taken as the research object and recorded as a TS of length N: $(x = \{x(t)\}, t = 1, 2, ..., N)$. It is divided into M consecutive subsequences of length n (n = 3). For any integer $x_{i,m}$ = 1, 2, 3, . . ., n, the mean sequence is defined as

$$\overline{X_{n,m}} = \frac{1}{n}\sum_{i=1}^{n} x_{i,m}. \tag{1}$$

The standard deviation of the subsequence is

$$S_{n,m} = \sqrt{\frac{1}{n}\sum_{t=1}^{n}\left(x_{t,m} - \frac{1}{n}\sum_{i=1}^{n} x_{i,m}\right)^2}. \tag{2}$$

Defining the cumulative deviation of a single subsequence,

$$Y_{n,m} = \sum_{k=1}^{n}\left(x_{k,m} - \frac{1}{n}\sum_{i=1}^{n} x_{i,m}\right). \tag{3}$$

The range of the subsequence is

$$R_{n,m} = \max Y_{n,m} - \min Y_{n,m}. \tag{4}$$

Rescaling the range on each subsequence,

$$(R/S)_{n,m} = \frac{R_{n,m}}{S_{n,m}}. \tag{5}$$

After rescaling the subsequence of length n, we obtain

$$(R/S)_n = \frac{1}{M}\sum_{m}^{M}(R/S)_{n,m}. \tag{6}$$

The scaling relationship between the rescaling price difference value of AE counts and the length of the AE counts TS is

$$(R/S)_n = c \times n^H. \tag{7}$$

Double logarithmic regression was performed on the obtained range value $(R/S)_n$ to obtain the expression for H:

$$\log(R/S)n = \log(C) + H\log(n). \tag{8}$$

Previous studies have shown that the TS data exhibit a characteristic of anti-persistence when $0 \leq H < 0.5$. This means that the trend of change in the next stage is the opposite to that of the current stage. While TS data have a certain degree of randomness when H = 0.5, they have a certain degree of long-term memory, with $0.5 < H < 1$. This means that the future trend of change is consistent with the current situation. When H = 1, TS data are fluctuating at $1/f$. When $H > 1$, TS data denote a non-stationary signal with volatility [29,38,40].

The entire compaction process was divided into 10 stages based on peak stresses of 0.1, 0.2, 0.3, 0.4, 0.5, 0.6, 0.7, 0.8, 0.9, and 1.0 times. Hurst exponent changes of BCS were obtained at different compression stages according to the above steps using MATLAB 2019, as shown in Figure 6. Before the stress reaches 0.2 times the peak stress, the H index of BCS exceeds 1. At this point, the AE signal is non-stationary. This is because the AE activity of BCS during the initial loading stage is relatively scattered and complex. There are both tensile fracture signals

and shear fracture signals caused by particle slip, rotation, and filling. Thus, some of the BCS have not yet begun to cause damage. When the stress exceeds 0.2 times the peak stress, the internal damage of the BCS gradually transitions from a disordered state to an ordered state. At this point, the Hurst exponent remains stable between 0.5 and 1.0. This indicates that the AE counts have long-term memory. When providing sufficient stress, the AE activity of BCS will continue to develop according to the current trend. The BCS will remain in the broken stage and have not entered the elastic stage.

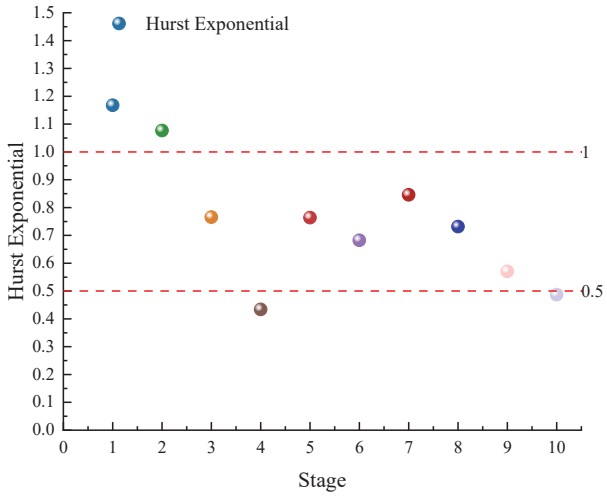

Figure 6. Hurst exponent evolution diagram (different color symbols represent the H of different stages).

There is a linear relationship between the Hurst exponent and fractal dimension D [41]:

$$D = 2 - H. \tag{9}$$

The fractal dimension D value was obtained based on the obtained Hurst exponent. Figure 7 shows the fractal dimension compression stage curve of AE counts. The fractal dimension of BCS fluctuates between 0.8 and 1.6. The continuous decrease in D indicates an orderly reduction in the number of microcracks during this stage. The continuous increase in D indicates an orderly increase in the number of microcracks during this stage. Overall, the compaction and re-crushing of BCS is a disordered process of microcracks continuously generating, closing, and fluctuating.

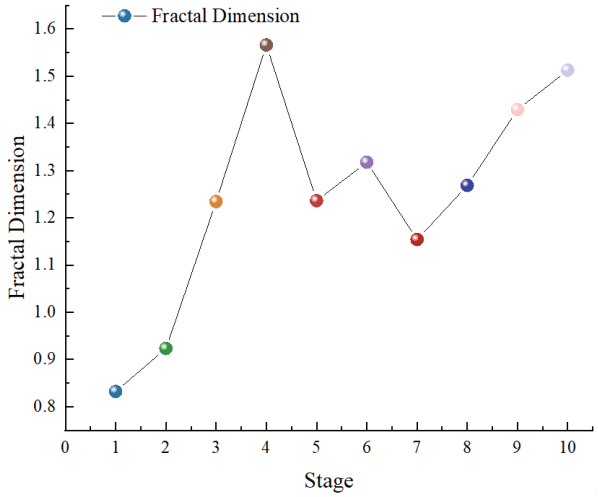

Figure 7. Fractal dimension variation of AE parameter (different color symbols represent fractal dimension of different stages).

3.3. Spatial Distribution of Particle Re-Crushing

To distinguish the location of particle re-crushing, each compression stage was defined as a 10 mm downward compression, and the compaction process was roughly divided into five stages. Figure 8 shows a 3D localization map of AE for the five stages in the compaction test. The red circles in the figure represent the contact positions between the loading head and the BCS. Unlike intact coal samples that exhibit complete macroscopic fracture surfaces during compression, BCS belong to granular media, and the locations of re-crushing are dispersed. Therefore, the AE activities exhibit a dispersed and random distribution characteristic. The number of AE localization points gradually increases, and the coverage is also gradually expanding during the loading. Overall, the AE localization points are randomly scattered throughout various positions inside the cavity, without any apparent distribution pattern.

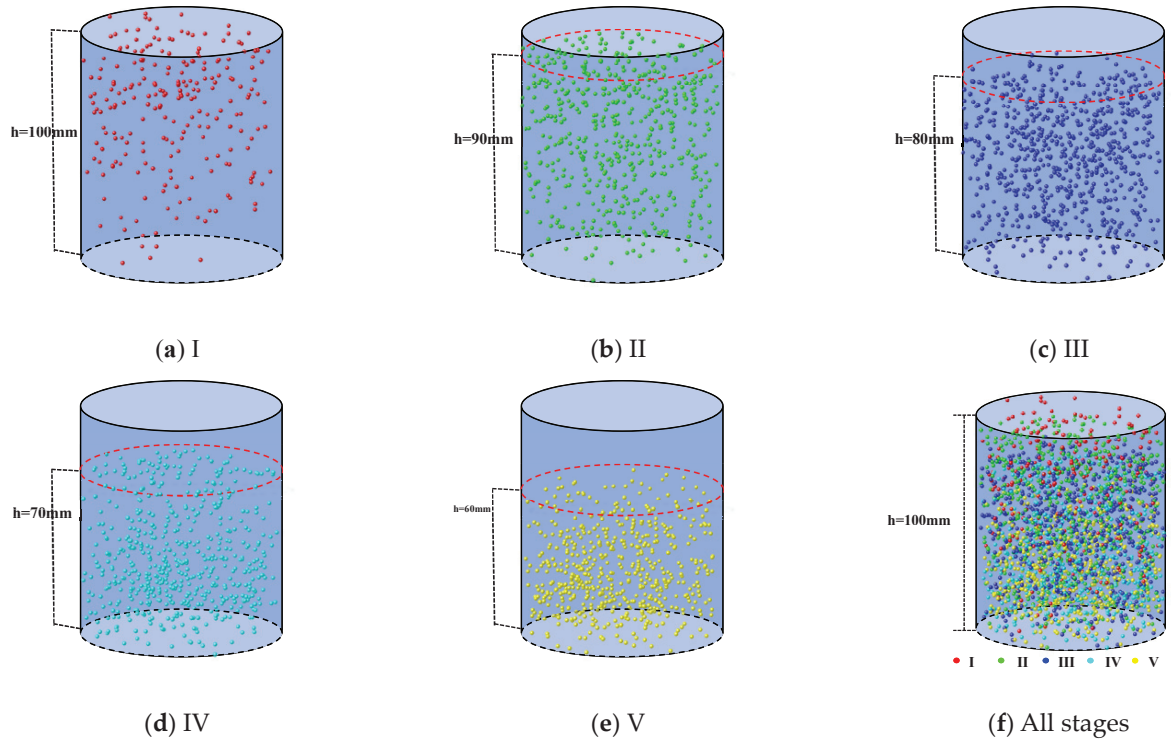

(**a**) I (**b**) II (**c**) III

(**d**) IV (**e**) V (**f**) All stages

Figure 8. Evolution of three-dimensional localization map of AE signals.

To better perform layered statistics on the AE localization in the horizontal and vertical directions of the BCS, we further divided the cavity space. In the vertical direction, the BCS accumulated inside the cavity are divided into three layers with equal divisions from top to bottom. In the horizontal direction, the BCS are divided into four annular regions (regions II, III, IV, and V) based on ring widths of 10mm, as well as a central circular region (region I), as shown in Figure 9. The distribution of AE signals in different regions during different loading stages is shown in Figure 10.

By comparing the *XY*-axis and *YZ*-axis profile diagrams at different stages, it can be observed that there is a certain pattern in the spatial distribution of particle re-crushing characteristics during the compaction process of BCS. Figure 10a shows that the AE localization points are uniformly dispersed across different areas from a horizontal perspective. However, due to the high stiffness and strength of the cavity wall, there are significantly more AE localization points in the outer regions compared to the ones closer to the center. In vertical direction, the AE localization points are primarily concentrated in the upper layers, especially near the pressure head, and there are sporadic localization points in the middle and lower layers. As the load goes on, BCS located in the upper part gradually shift towards the middle and lower parts due to the pressure head descent. This causes a

continuous decrease in BCS in the upper layers. The frequency of AE localization points in the lower and middle layers exceeds that of the upper layer, indicating a gradual shift of AE phenomenon towards the middle and lower parts.

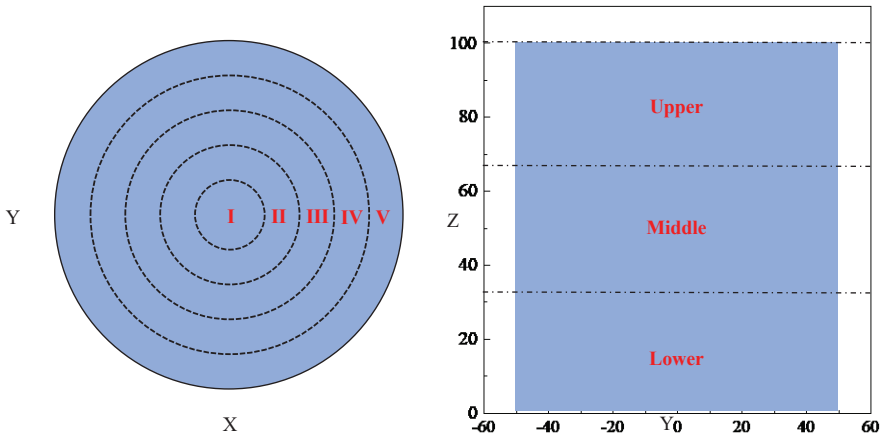

Figure 9. Schematic diagram of cavity space zoning (The Roman numerals in the diagram represent the five areas of the XY profile, and Upper, Middle, and Lower represent the three areas of the YZ profile).

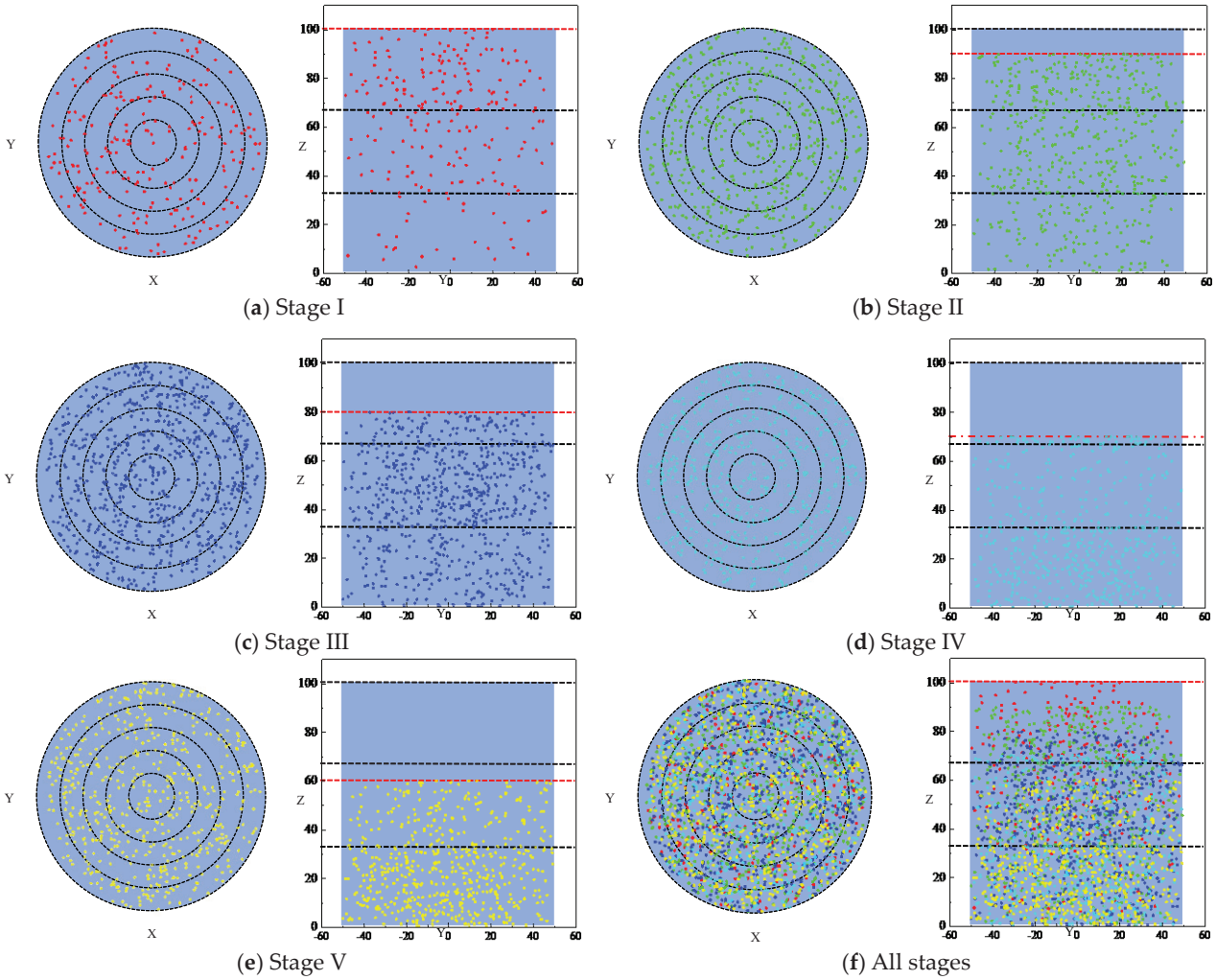

Figure 10. Layered evolution of AE localization at different stages (The black dotted line in the figure is the auxiliary line divided by the area, the red dotted line represents the position of the indenter, and dots represents the location of the AE signal).

An AE layer density was defined by Li et al. [42], which is equal to the ratio of AE localization points within the layer to the total AE localization points. However, different layer space sizes are not considered. Therefore, the AE intensity in this paper is redefined as the product of the percentage of AE localization points in the same areas (Equation (10)). In the vertical and horizontal directions, the area ratio between the different layers, respectively, is 1:1:1 and 1:3:5:7:9. Figure 11 shows the intensity of the AE localization points in the horizontal and vertical regions, respectively.

$$I_A = \frac{S_i}{S} \times \frac{N_i}{N}, \tag{10}$$

where S_i and N_i are the area of the region and the AE location numbers in the corresponding stage, S is the total area, and N is the entire AE location numbers in the stage.

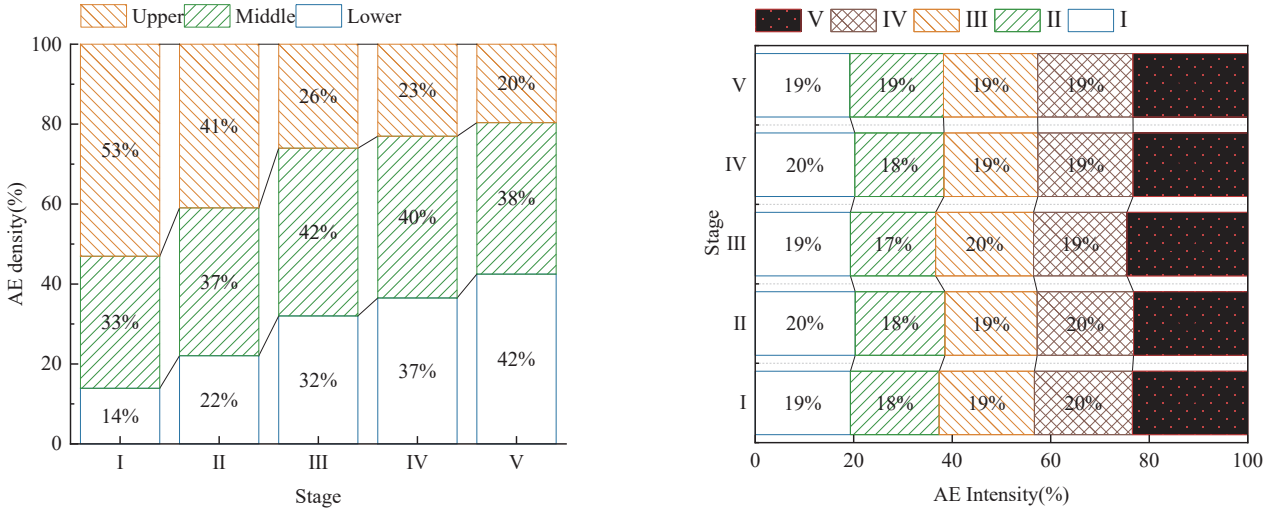

(**a**) Vertical AE density (**b**) Horizontal AE density

Figure 11. The AE intensity of the BCS in different regions and stages.

Figure 11 shows that the AE signal of the BCS is in the dynamic change stage of constant updating. There is no obvious difference in AE signal intensity among the four internal regions in the horizontal direction; the average intensities of the AE signals are 19.68%, 18.15%, 19.22%, and 19.42%, respectively. Only the outermost region (region V) exhibits a slightly higher level compared to the other four regions because of the squeezing between the two walls of the cavity. The maximum intensity difference in the same stage reached 7.21% in the horizontal direction. The fundamental reason is due to the high stiffness of the cavity. There is no lateral displacement, resulting in the cavity boundary BCS being easy to break. In the vertical direction, the AE signal is first concentrated in the upper part, especially close to the pressure head position; there are a few AE localization points in the lower and middle layers, and the AE localization point in the lower layer is less than that in the middle layer; respectively, they account for 14% and 33% of the total signals. The one reason for the high breakage rate near the pressure head is that the stiffness of the pressure head is large. Moreover, the stress is transferred from top to bottom, also causing priority re-crushing of the upper samples. As the loading continues, the density of the upper layer begins to decrease, gradually shifting to the middle and lower layers. This is largely due to the BCS in the upper layer being gradually transferred to the lower layer after being squeezed by the pressure head. The accumulation height of the BCS gradually decreases; thus, the volume of the upper layer of the BCS is gradually reduced. Until the particles in the upper position are completely compressed to the lower layer, the upper layer no longer exhibits the particle breakage phenomenon; the intensity of AE in that area has been decreasing continuously. The intensity of the lower and middle

layers is increasing due to the continuous axial stress and the extrusion of the upper BCS. And in the early stage of loading, the AE intensity of the middle layer is greater than that of the lower layer. However, the difference between these two layers is gradually decreasing, from 19% in stage I to 3% in stage IV. In stage V, the upper layer particles were gradually compacted, the void is filled, and the number of particles broken is gradually reduced. And the AE intensity in the lower layer is the largest (up to 43%). This further shows that the compaction process of BCS has the characteristics of layered failure in the vertical direction. Specifically, as the loading progresses, the breaking process starts from the upper portion and gradually transitions towards the middle and lower portions. Eventually, the breaking process becomes more uniform throughout the BCS.

4. Discussion

The compaction and seepage properties of the BCRM are crucial for safe mining and resource recovery and utilization in coal mines. However, due to the often-closed state of the BCRM in coal mines, the physical and mechanical properties and seepage characteristics are difficult to detect directly [6,43]. Thus, in order to obtain the compaction and seepage characteristics of the BCRM during coal mining and their influencing factors, laboratory tests on the BCRM are the main research methods employed. In this paper, with the help of AE localization technology and the Hurst exponent, the spatiotemporal distribution characteristics of the BCS during the compaction process were revealed. The long-term memory effect of compaction and re-crushing was verified; it provides a valuable reference for understanding the permeability and mechanical stability of the goaf in the 08 longwall face of Caojiatan Coal Mine. However, although the top coal caving mining method was used in the studied coal mines, the main medium in the goaf caving zone is still broken rock mass. This is mainly due to the height of the caving zone in the longwall face of the studied mine having reached 50m. Thus, further research is needed to focus on the compaction and re-crushing characteristics of broken rock samples and broken coal and rock samples.

In our test, we conducted compaction experiments on BCS with particle sizes ranging from 0 to 5 mm. This is mainly due to the fact that the maximum particle size of the BCS should be less than 1/5 of the diameter of the experimental chamber [44]. However, the sample size in this paper was smaller than the actual size of the BCRM on site. Moreover, existing research indicates that particle size is also a major factor affecting the compaction and re-crushing characteristics of BCS [5]. This means that the research results obtained in this article cannot be directly applied to the field. But the main purpose of this study is to reveal the re-crushing characteristics of BCS after compaction. This can provide a theoretical basis for mechanical models and safety assessments in real goafs. In future work, we will consider the cavity size (Φ100) in experiments and employ six particle sizes: 0–5 mm, 5–10 mm, 10–15 mm, 15–20 mm, 20–25 mm, and 25–30 mm. On this basis, we will obtain the compaction characteristics of BCS, considering particle size. In addition, we will also design laboratory-scale particle sizes based on fractal theory according to the measured particle size distribution on site [3]. The experimental results obtained in the laboratory can provide the basic parameters for numerical simulation and theoretical models.

5. Conclusions

(1) In the broken stage, compaction stress increases exponentially with strain. The evolution law of the compaction process of BCS is characterized by the AE device. The AE signal increases continuously with the increase in loading stress. The cumulative counts and the cumulative energy rise exponentially.

(2) The Hurst exponent can predict the evolution of compaction and re-crushing of the BCS. It indicates that the AE counts in this paper have long-term memory. When providing sufficient stress, the AE activity of the BCS will continue to develop according to the current trend. This further indicates that the BCS in this experiment have been in the broken stage all along.

(3) The three-dimensional AE localization indicated that the compaction of the BCS exhibited a relatively uniform breakage in the horizontal direction. But it has the characteristics of a layered breakage in the vertical direction. The AE signals are similar in the four internal regions in the horizontal direction; the region near the outer wall is slightly higher than that in the other four regions. In the vertical direction, the AE signals start from the upper portion and gradually transition towards the middle and lower portions. At the end of the loading process, the AE signals become more uniform throughout the entire BCS.

Author Contributions: Methodology, C.Z.; software, Y.C.; data curation, J.C. and X.Z.; writing—original draft preparation, Y.C.; writing—review and editing, C.Z. All authors have read and agreed to the published version of the manuscript.

Funding: The National Natural Science Foundation of China (52474161, 52104155), the Postdoctoral Research Foundation of China (2023M733778), the China Association for Science and Technology Youth Talent Recruitment Project (YESS20220514), and the Fundamental Research Funds for Central Universities (2024ZKPYNY01).

Institutional Review Board Statement: Not applicable.

Informed Consent Statement: Not applicable.

Data Availability Statement: All data, models, or codes that support the findings of this study are available from the corresponding author upon reasonable request.

Conflicts of Interest: The authors declare no conflicts of interest regarding the publication of this article.

References

1. Feng, G.; Li, Z.; Hu, S.; Zhang, Y.; Zhang, A.; Gao, Q.; Jiang, H.; Guo, X.; Li, C.; Cui, J. Distribution of gob empty space for methane drainage during the longwall mining: A case study. *J. Nat. Gas Sci. Eng.* **2018**, *60*, 112–124. [CrossRef]
2. Wang, C.X.; Shen, B.T.; Chen, J.T.; Tong, W.X.; Jiang, Z.; Liu, Y.; Li, Y.Y. Compression characteristics of filling gangue and simulation of mining with gangue backfilling: An experimental investigation. *Geomech. Eng.* **2020**, *20*, 485–495. [CrossRef]
3. Zhang, C.; Chen, Y.; Ren, Z.; Wang, F. Compaction and seepage characteristics of broken coal and rock masses in coal mining: A review in laboratory tests. *Rock Mech. Bull.* **2024**, *3*, 100102. [CrossRef]
4. Zhang, C.; Chen, Y.; Wang, Y.; Bai, Q. Discrete element method simulation of granular materials considering particle breakage in geotechnical and mining engineering: A short review. *Green Smart Min. Eng.* **2024**, *1*, 190–207. [CrossRef]
5. Zhang, C.; Zhang, L. Permeability characteristics of broken coal and rock under cyclic loading and unloading. *Nat. Resour. Res.* **2019**, *28*, 1055–1069. [CrossRef]
6. Zhang, C.; Tu, S.; Zhang, L.; Bai, Q.; Yuan, Y.; Wang, F. A methodology for determining the evolution law of gob permeability and its distributions in longwall coal mines. *J. Geophys. Eng.* **2016**, *13*, 181–193. [CrossRef]
7. Zhang, C.; Tu, S.H.; Zhao, Y.X. Compaction characteristics of the caving zone in a longwall goaf: A review. *Environ. Earth Sci.* **2019**, *78*, 1–20. [CrossRef]
8. Wang, B.; Zhang, J.; Qi, X.H.; Li, T.; Gao, S.S.; Wang, L. Experimental research on the instability characteristics of the overlying strata structure that characterizes shallow interval goaf mining. *J. Geophys. Eng.* **2023**, *20*, 816–829. [CrossRef]
9. Zhu, D.; Yu, B.; Wang, D.; Zhang, Y. Fusion of finite element and machine learning methods to predict rock shear strength parameters. *J. Geophys. Eng.* **2024**, *21*, 1183–1193. [CrossRef]
10. Zhang, C.; Zhao, Y.X.; Tu, S.H.; Hao, X.J.; Hao, D.Y.; Liu, J.B.; Ren, Z.P. Influence mechanism of particle size on the compaction and breakage characteristics of broken coal mass in goaf. *China Coal Soc.* **2020**, *45*, 660–670. [CrossRef]
11. Li, B.; Yang, X.; Yuan, Y.; Liang, Y.; Li, S.; Zhu, C.; Peng, W. Experimental research on the influence of different factors on the behaviour of broken coal and rock particles during compaction. *Constr. Build. Mater.* **2023**, *367*, 130127. [CrossRef]
12. Zhang, C.; Zhao, Y.X.; Bai, Q.S. 3D DEM method for compaction and breakage characteristics simulation of broken rock mass in goaf. *Acta Geotech.* **2022**, *17*, 2765–2781. [CrossRef]
13. Feng, M.; Wu, J.; Ma, D.; Ni, X.; Yu, B.; Chen, Z. Experimental investigation on the seepage property of saturated broken red sandstone of continuous gradation. *Bull. Eng. Geol. Environ.* **2018**, *77*, 1167–1178. [CrossRef]
14. Pang, M.; Zhang, T.; Guo, Y.; Zhang, L. Re-crushing process and non-Darcian seepage characteristics of broken coal medium in coal mine water inrush. *Sci. Rep.* **2021**, *11*, 11380. [CrossRef] [PubMed]
15. Wu, D.T.; Luo, F.; Li, M.; Diao, Y.L.; Guo, Y.J.; Xu, P.D. Macroscopic and microscopic study on the compression bearing characteristics and deformation failure mechanism of gangue with different particle sizes. *Powder Technol.* **2021**, *383*, 198–211. [CrossRef]

16. Zhang, B.; He, Q.; Lin, Z.; Li, Z. Experimental study on the flow behaviour of water-sand mixtures in fractured rock specimens. *Int. J. Min. Sci. Technol.* **2021**, *31*, 377–385. [CrossRef]
17. Chao, J.; Chu, T.; Yu, M.; Han, X.; Hu, D.; Liu, W.; Yang, X. An experimental study on the oxidation kinetics characterization of broken coal under stress loading. *Fuel* **2020**, *287*, 119515. [CrossRef]
18. Chao, J.; Yu, M.; Chu, T.; Han, X.; Teng, F.; Li, P. Evolution of broken coal permeability under the condition of stress, temperature, moisture content, and pore pressure. *Rock Mech. Rock Eng.* **2019**, *52*, 2803–2814. [CrossRef]
19. Chen, J.; Zeng, B.; Hu, S.; Xu, W.; Wang, S.; Liu, Z. Mechanical behaviour and instability mechanism of sandstones with impact tendency under different loading paths. *Int. J. Min. Reclam. Environ.* **2024**, *38*, 1–20. [CrossRef]
20. Yang, X.; Chu, T.; Yu, M.; Wang, L.; Chao, J.; Han, X. Evolution characteristics of bulking factor in the multi-field loading of broken coal: An experimental study. *Rock Mech. Rock Eng.* **2021**, *54*, 1481–1499. [CrossRef]
21. Li, J.; Huang, Y.; Zhai, W.; Li, Y.; Ouyang, S.; Gao, H.; Li, W.; Ma, K.; Wu, L. Experimental study on acoustic emission of confined compression of crushed gangue under different loading rates: Disposal of gangue solid waste. *Sustainability* **2020**, *12*, 3911. [CrossRef]
22. Luo, X.L.; He, X.; Yang, K. Study on Bearing Characteristics and Acoustic Emission Response Characteristics of Gangue Aggregate under Talbol Grading. *Coal Technol.* **2023**, *42*, 27–31. [CrossRef]
23. Wen, P.; Guo, W.B.; Bai, E.H.; Wu, D.T.; Wang, B.B.; Ma, Z.B.; Yang, W.Q. Compaction deformation and acoustic emission characteristics if fractured rock with different lithology in goaf. *J. Min. Saf. Eng.* **2024**, *41*, 384–394. [CrossRef]
24. Xin, H.Q.; Huang, Y.L.; Zhang, W.Q.; Wu, L.W.; Ouyang, S.Y.; Guo, Y.C.; Li, J.M. Research on deformation and crushing rules and acoustic emission characteristics of gangue bulk under the condition of confined compression. *J. Min. Saf. Eng.* **2020**, *37*, 162. [CrossRef]
25. Feng, G.; Zhao, J.; Wang, H.; Li, Z.; Fang, Z.; Fan, W.; Yang, P.; Yang, X. Study of the internal re-breaking characteristics of broken limestone during compression. *Powder Technol.* **2022**, *396*, 449–455. [CrossRef]
26. Li, Z.; Yang, X.; Yang, P.; Feng, G.; Liu, J.; Zhu, C.; Cheng, X. Layered re-breaking behavior of gangue backfilling materials and inspirations for protecting mined ecological environments. *Constr. Build. Mater.* **2023**, *368*, 130477. [CrossRef]
27. Li, J.; Huang, Y.; Gao, H.; Ouyang, S.; Guo, Y. Transparent characterization of spatial-temporal evolution of gangue solid wastes' void structures during compression based on CT scanning. *Powder Technol.* **2020**, *376*, 477–485. [CrossRef]
28. Li, M.; Zhang, J.; Huang, P.; Sun, Q.; Yan, H. Deformation behaviour of crushed waste rock under lateral cyclic loading. *Rock Mech. Rock Eng.* **2021**, *54*, 6665–6672. [CrossRef]
29. Sun, C.; Yan, S.H.; Xu, N.Z.; Yin, X.W.; Tian, G.S. Experimental study on the stiffness of waste rock of gob of fully mechanized mining with large mining height. *J. China Coal Soc.* **2020**, *45*, 38–48. [CrossRef]
30. Li, M.; Zhang, J.X.; Huang, Y.L.; Zhang, Q. Research on compression ratio design based on compaction properties of solid backfill materials. *J. Min. Saf. Eng.* **2017**, *34*, 1110. [CrossRef]
31. Liu, A.; Liu, S.; Wang, G.; Elsworth, D. Continuous compaction and permeability evolution in longwall gob materials. *Rock Mech. Rock Eng.* **2020**, *53*, 5489–5510. [CrossRef]
32. Su, C.D.; Gu, M.; Tang, X.; Guo, W.B. Experiment study of compaction characteristics of crushed stones from coal seam roof. *Chin. J. Rock Mech. Eng.* **2012**, *31*, 18–26. [CrossRef]
33. Zhang, J.W.; Wang, H.L.; Chen, S.J.; Li, Y.L. Bearing deformation characteristics of large-size broken rock. *J. China Coal Soc.* **2018**, *43*, 1000–1007. [CrossRef]
34. Zhang, Z.D.; Li, G.Y. Experimental study on particle breakage behaviors of rockfill under cyclic loadings. *Chin. J. Geotech. Eng.* **2017**, *39*, 1510–1516. [CrossRef]
35. Liu, L.; Yao, Y.; Luo, T.; Zhou, A. A constitutive model for granular materials subjected to a large stress range. *Comput. Geotech.* **2020**, *120*, 103408. [CrossRef]
36. Hagerty, M.M.; Hite, D.R.; Ullrich, C.R.; Hagerty, D.J. One-dimensional high-pressure compression of granular media. *J. Geotech. Eng.* **1993**, *119*, 1–18. [CrossRef]
37. Liu, X.; Zhang, Z.; Wang, E.; Wang, X.; Yang, B.; Wang, H. Characteristics of electromagnetic radiation signal of coal and rock under uniaxial compression and its field application. *J. Earth Syst. Sci.* **2020**, *129*, 1–11. [CrossRef]
38. Sun, L.F.; Feng, G.C.; Ming, W. Analysis of coal's character based on HURST index method. In Proceedings of the 2009 International Conference on Future BioMedical Information Engineering (FBIE), Sanya, China, 13–14 December 2009; pp. 168–171. [CrossRef]
39. Song, Y.; Yang, S.; Hu, X.; Song, W.; Sang, N.; Cai, J.; Xu, Q. Prediction of gas and coal spontaneous combustion coexisting disaster through the chaotic characteristic analysis of gas indexes in goaf gas extraction. *Process Saf. Environ. Prot.* **2019**, *129*, 8–16. [CrossRef]
40. Nannan, L.; Jiansheng, Q.; Zhikai, Z.; Liqin, Z.; Jin, L. Self-similarity analysis of Coal or Rock Electromagnetic Emission signal. In Proceedings of the Chinese Control and Decision Conference, Guilin, China, 17–19 June 2009; pp. 2895–2899. [CrossRef]
41. Wei, Y.; Li, Z.H.; Zhang, Z.B.; Kong, Y.H.; Yin, S.; Liu, S.J.; Cheng, F.Q. Research on acoustic emission characteristics of loaded sandstone based on R/S analysis. *J. Mine Autom.* **2017**, *43*, 37–42. [CrossRef]
42. Li, Z.; Fang, Z.; Feng, G.; Zhao, J. Three dimensional acoustic emission location method for crushed coal and rock and its layered fracture characteristics. *J. Taiyuan Univ. Technol.* **2022**, *53*, 507–514. (In Chinese) [CrossRef]

43. Esterhuizen, G.; Karacan, C. A methodology for determining gob permeability distributions and its application to reservoir modelling of coal mine longwalls. In Proceedings of the SME Annual Meeting, Salt Lake City, UT, USA, 25–28 February 2007.
44. *AASHTO T 307-99*; Standard Test Method for Determining the Resilient Modulus of Soils and Aggregate Materials. AASHTO: Washington, DC, USA, 2003.

sustainability

MDPI

Article

Pumped Storage Hydropower in Abandoned Mine Shafts: Key Concerns and Research Directions

Xin Lyu [1,2,3,*], Tong Zhang [2,*], Liang Yuan [1,2,3], Ke Yang [1,2,3], Juejing Fang [1], Shanshan Li [1] and Shuai Liu [1]

[1] State Key Laboratory of Mining Response and Disaster Prevention and Control in Deep Coal Mines, Anhui University of Science and Technology, Huainan 232001, China
[2] Institute of Energy, Hefei Comprehensive National Science Center, Hefei 230031, China
[3] Coal Mine Safety Mining Equipment Innovation Center of Anhui Province, Anhui University of Science and Technology, Huainan 232001, China
* Correspondence: xin_lyu2020@163.com (X.L.); zhangt_1990@sina.com (T.Z.)

Abstract: The quest for carbon neutrality raises challenges in most sectors. In coal mining, overcapacity cutting is the major concern at this time, and the increase in the number of abandoned mine shafts is a pervasive issue. Pumped storage hydropower (PSH) plants built in abandoned mine shafts can convert intermittent electricity into useful energy. However, studies on basic theories and key technologies are a pressing issue. Six key scientific problems have been identified in PSH development in abandoned mine shafts that are relevant to China's national conditions, current resource structure, and relative status of energy storage technologies in China and other countries. It is proposed that the research on pumped storage should move closer to the direction of intelligence, stabilization, and greening, and the construction and development should gradually realize integration, completion, and coordination. The goal is to realize integrated, complete, and coordinated development of PSH in abandoned mine shafts, streamline national policies concerning PSH, drive the co-development of industry, education and research, and achieve the carbon neutrality targets set by China.

Keywords: abandoned mine shafts; pumped storage hydropower; underground reservoir; carbon neutrality targets; energy storage technology

1. Introduction

China is currently undergoing a transition from a fossil-dominated energy structure to one dominated by clean, low-carbon, new energy technologies. China has committed to peak carbon dioxide emissions by 2030 and achieve carbon neutralization by 2060, which are both fast-approaching deadlines [1–3]. According to the predictions by the International Energy Agency, China needs to cut the proportion of fossil fuel to approximately 20% while raising the proportion of renewable energy to approximately 70% [4–6].

By the end of 2021, China's total energy consumption reached up to 5240 million tons of standard coal equivalent [7–9]. The consumption of non-fossil energies, including natural gas, hydropower, and wind power, accounted for 25.5% this year, which represents an increase of 1.2% compared with the previous year [10,11]. Besides, China's exploitable land-based wind energy is estimated to be 7.2 billion kW [12]. The total annual insolation in regions that are extremely abundant and abundant in solar energy, such as Qinghai-Tibet Plateau, Gansu, Xinjiang, and Inner Mongolia, is equivalent to about 4 thousand trillion kW·h. The installed capacity of exploitable hydropower reaches 540 million kW. The environmental protection requirements for the energy sector are expected to become stricter in the future, accompanied by a sharp decrease in coal consumption and a growing number of abandoned mine shafts.

In the 12th Five-Year Period alone, China had 7100 abandoned coal mines [13–15]. According to the key consulting project of the Chinese Academy of Engineering, titled

Strategies of High-Efficiency Recovery and Energy Saving for Coal Resources in China, it is estimated that by 2030, China will have about 15,000 abandoned mine shafts [16].

However, a one-size-fits-all strategy is usually adopted for handling abandoned mine shafts [17]. This is contrary to the guiding principles specified in the *Implementation Scheme for Promoting the High-Quality Development of New Energy in the New Era*, namely, the general principles of construction before destruction and the prioritization of overall planning. Considerable resources can be tapped from abandoned mine shafts to reap economic benefits. They offer new pathways for innovation in energy exploitation and utilization and developing new types of power systems. In a word, abandoned mine shafts can be used to solve the "construction" problem as opposed to the "destruction" problem mentioned above. Besides, exploiting these "abandoned" resources may help overcome the drawbacks of existing power systems, such as poor adaptability to connecting large-scale, high-proportion new energy to the grid, consumption of new energy, and limited land resources [18]. Based on this, research on the construction of pumped storage power stations in abandoned mines is carried out, the existing policies are analyzed, the existing problems are determined, and the direction of follow-up research and development are proposed. Provide a theoretical basis for the implementation of the project.

2. Current Development of Energy Storage Technologies

In the context of carbon neutrality, the amount of electricity produced by wind and solar energy will increase from 210 GW and 205 GW, respectively, in 2019 to 480 GW and 570 GW in 2030, and further to 1440 GW and 2160 GW in 2050. In the meantime, by 2035, the peak-valley load difference in China will exceed 1 billion kW [19]. The power system must also cope with the intermittence and fluctuation of electricity generated from new energy sources [20]. Energy storage technologies are regarded as important means to redress the changeability of new energy sources. They also lie at the core of achieving the carbon neutrality commitments by China. However, current electrochemical energy storage technologies are limited either geographically or in terms of scale, economical efficiency, and safety. Little breakthrough has been made in new technologies or techniques in this respect. The cross-regional, large-scale, centralized consumption of new energy can hardly be realized in the present or the foreseeable future. From 2007 to 2017, China's total full-caliber power generation had already exceeded the power consumption [21] (Figure 1a). After 2018, the adjustment of the energy structure has led to an increase in the installed capacity of new energy power generation. However, electricity cannot be efficiently stored during the off-peak period during the low period, and the wastage rates of wind and solar energy are surprisingly high (Figure 1b). The increasing peak-valley load difference indicates the contradictions between electricity demand and allocation. In this context, energy storage systems offer an efficient method for new energy development and grid connection [22].

At present, energy storage technologies can be roughly divided into three categories depending on the storage method (Figure 2a). Electrochemical energy storage is the most widely used, though its short service life is a defect that cannot be overlooked. Energy storage can be divided into two types based on scale (Figure 2b). Centralized energy storage has a scale that varies between several megawatts and hundreds of megawatts, with a longer discharge time [23]. By contrast, the scale of distributed energy storage is much smaller than that of centralized energy storage and varies between a few kilowatts to several megawatts.

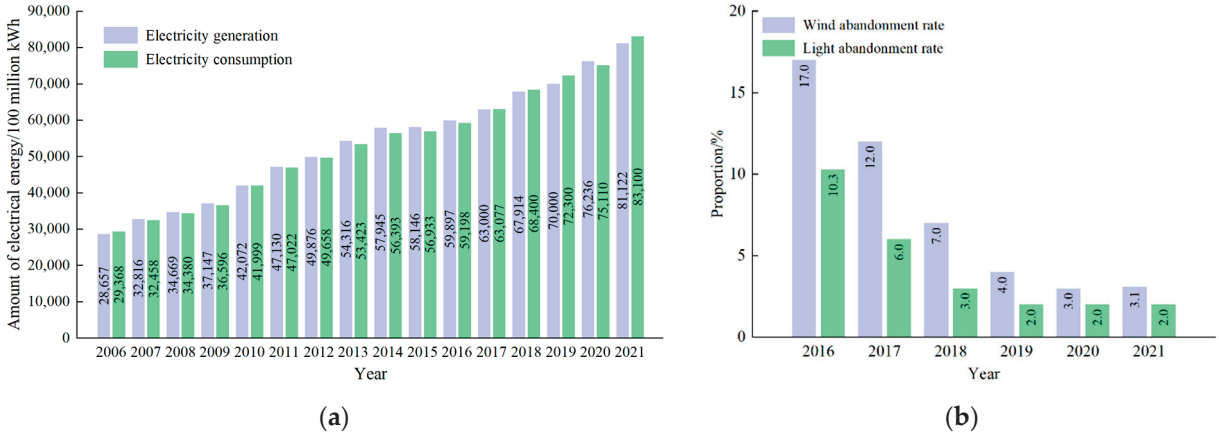

Figure 1. Electrical energy wastage. (**a**) Full-caliber total power generation and power consumption; (**b**) Average wind and light wastage rate in China.

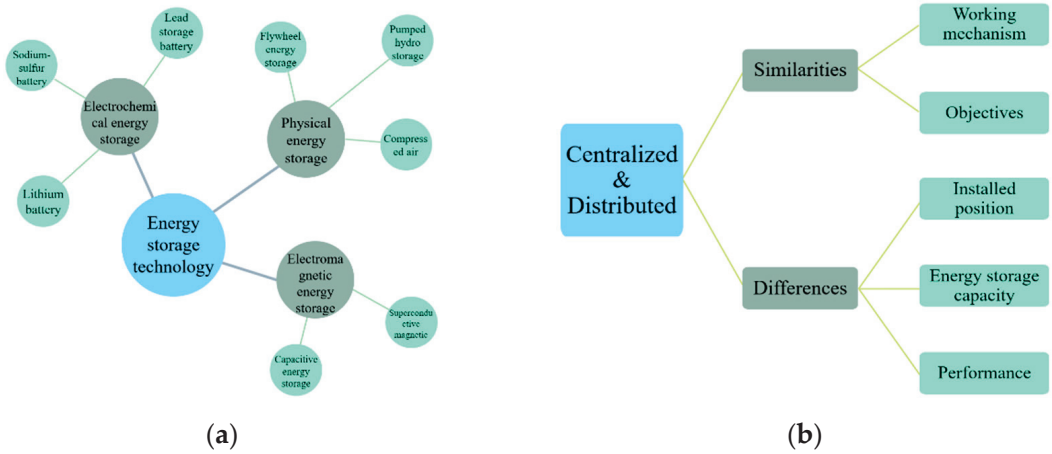

Figure 2. Energy storage technologies. (**a**) Energy storage methods; (**b**) Scale of energy storage.

In 2019, the total global energy storage capacity was 184.6 GW, with PSH capacity reaching 170.9 GW and accounting for 92.6% [24]. The electrochemical energy storage capacity was 9.6 GW, accounting for 5.2%. According to the statistics of China Energy Storage Alliance (CNESA) in 2021, PSH accounted for 86.3% of China's total energy storage capacity, new energy storage capacity accounted for 12.5%, and the rest accounted for 1.2% (Figure 3). Different types of energy storage are different in response speed, energy density, efficiency, life, and economic cost (Table 1). However, in the actual selection process, the environment required for construction and the scale of power storage that can be achieved is often considered. Although the new energy storage method has the advantages of fast response and high efficiency, its scale is limited, and the environmental requirements are high. PSH is the dominant energy storage technology globally. Technically mature large-scale PSH is the most practicable and reliable new energy source for large-scale, concentrated consumption in the present and the future. At the same time, the underground space contained in abandoned mines can save the initial investment in the construction of PSH, and the deep space is more conducive to the preservation of water sources.

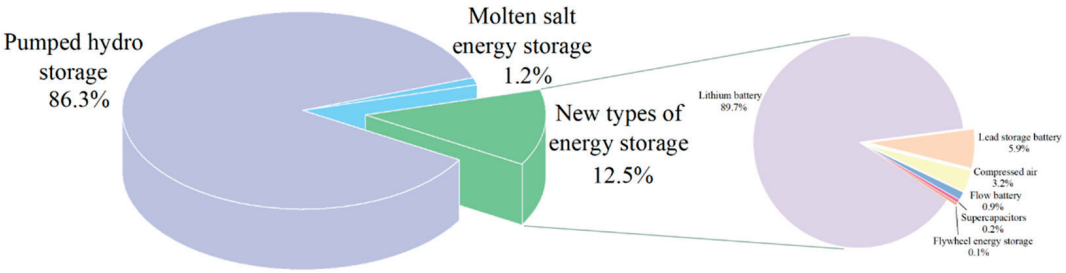

Figure 3. Proportions of installed capacity of different energy storage methods in China in 2021.

Table 1. Comparison of different energy storage technologies.

Energy Storage Technology	Response Rate	Efficiency/%	Cycle Life/Times	Cost/(Yuan·kW^{-1})	Intended Use
PSH	Second to minute scale	75–85	>10,000	1000–6000	Large-scale energy restoration to improve the reliability of power supply
Electrochemical energy storage	Millisecond scale	60–95	2500–3000	2000–3000	As a backup and for frequency modulation to improve the reliability of power supply
Compressed-air energy storage	Second to minute scale	80	>10,000	3000–4000	Using the peak load shifting strategy to improve the reliability of power supply
Thermal energy storage	Second to minute scale	50–90	>10,000	500–4000	Consuming the renewable energy and using the peak load shifting strategy
Hydrogen energy storage	Second scale	25–85	1000	2000–50,000	Consuming the renewable energy and achieving seasonal energy storage

3. Development of Pumped Hydro Energy Storage at Home and Abroad

3.1. Advantages of a PSH Plant

PSH plant is a special type of hydropower plant that can store electric energy. It is composed of an upper water reservoir, water transport system, generator set, water pump, and lower water reservoir. There are three types of reservoirs depending on the position, namely, entirely above the ground, semi-underground, and entirely underground [25].

The PSH plant uses water for energy conversion between the turbine and the pump. The water is pumped using surplus electric energy so that the water in the lower reservoir gains potential energy during the off-peak period by being transported and stored in the upper reservoir. When the load demand increases sharply, water will be released from the upper reservoir to the lower reservoir and flows down through a turbine that generates electricity (Figure 4). Thus, the peaks and valleys are reduced, and the power consumption profile is flattened, while the water can be used repeatedly in the PSH plant [26].

The National Energy Administration has explicitly pointed out in the *Pumped Storage Medium and Long-Term Development Plan 2021–2035* that "PSH plants fulfill multiple functions, including peak regulation, valley filling, frequency regulation, phase regulation, energy storage, backup for accidents, and black start. PSH plants are an integral part of the power system that is clean, low-carbon, safe, reliable, smart, flexible, economical, and highly efficient" [27].

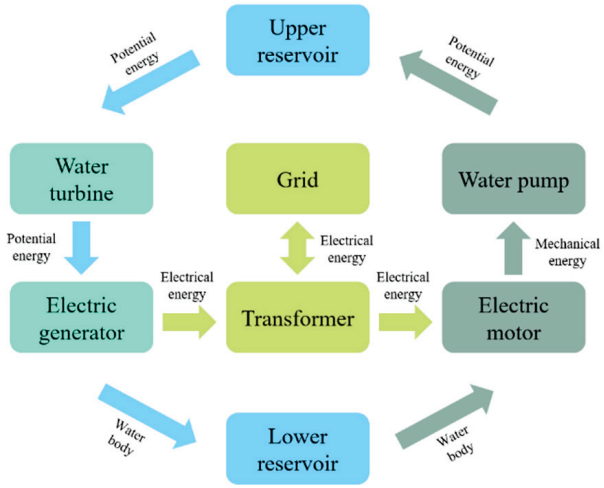

Figure 4. Schematic diagram of energy conversion.

The PSH plant reallocates the electric generation capacity of the power system temporally and reconciles the contradictions between power generation and power consumption. However, energy loss seems inevitable during the energy conversion process. The power generation efficiency of a PSH plant can reach 75–80% [28,29]. Relative economic efficiency is the practical consideration when the entire PSH system is concerned. Considering this, a PSH plant can be built in the abandoned mine shaft to dramatically reduce the construction and investment and simplify the water pipeline layout.

A PSH plant in an abandoned mine shaft utilizes the difference in elevation between the upper and lower reservoirs (Figure 5) to store and convert energy. It operates basically as a conventional PSH plant, except that the water storage facilities and the reservoir lie underground. The abandoned mine shaft provides the space required for water storage, and there is no need to do the rebuilding. Moreover, building a PSH plant in an abandoned mine shaft does not require surface land resources or damage the surface environment. It is estimated that the total installed capacity of conventional PSH plants in China will be 110 GW in 2030. Meanwhile, there will be about 15,000 sites suitable for building mineshaft-based PSH plants, with an installed capacity of approximately 1800 GW. These statistics suggest a huge market potential [30–32].

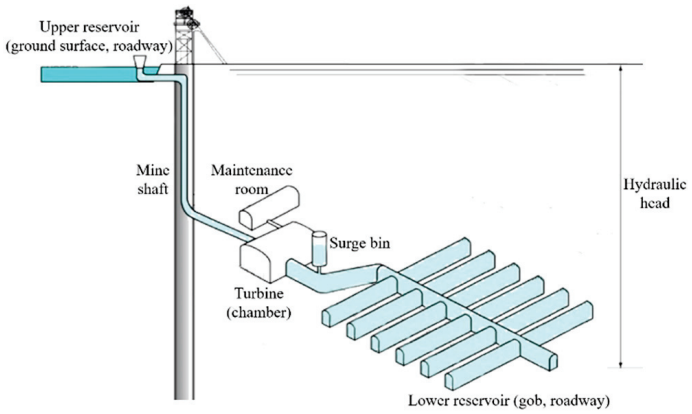

Figure 5. Schematic diagram of PSH in an abandoned mine shaft.

3.2. Current Status of PSH in Abandoned Mine Shafts at Home and Abroad

The world's first PSH plant that utilizes an abandoned mine shaft was built in the Prosper-Haniel hard coal mine in Germany [33]. This coal mine has a horizontal underground roadway that extends for approximately 25 km. The roadway depth is 1.2 km, and the water storage capacity reaches 1 million m^3. Germany also plans to build a fully

underground PSH plant in Upper Harz, where an abandoned metal mine with a roadway with a diameter of 3.5 m and depth of 760 m is used as an underground reservoir. The reservoir capacity is estimated to be 250,000 m^3, and the installed capacity is 100 MW.

In New Jersey, US, a semi-underground PSH plant of 1000-MW capacity has been built in an abandoned iron-ore mine 760 m deep. The Eagle Mountain PSH project in California has been built by utilizing two abandoned mine pits, one upper and one lower, with an installed capacity of 1300 MW. The mine water inrush in the Asturian coal mine in Spain is exploited as the water source to build a semi-underground PSH plant. South Africa has converted an abandoned gold mine into a cascade PSH plant (Table 2).

Table 2. Design parameters of PSH plants constructed in abandoned mine shafts in the world.

Name	Type	Hydraulic Head/m	Capacity of Water Reservoir/km^3	Power/MW	Reservoir Capacity/MWh
Asturian coal mine in Spain	Semi-underground	300–600	170	23.52	141
FWR in South Africa	Fully underground	1200–1500	1000	1000	6800
Prosper-Haniel coal mine in Germany	Semi-underground	560	600	200	820
Grund ore mine in Germany	Semi-underground	700	260	100	400

In China, a demonstration project commenced in the Shenhua Daliuta coal mine in 2010. Thirty-two underground reservoirs have been completed so far, with a total capacity reaching 31 million m^3, making it the only underground reservoir group built in coal mines. In 2022, Shandong Province plans to invest a total of 3.3 billion RMB in building a 0.3 million-kW agro-optical complementary power station and a 0.2-million-kW PSH plant in the abandoned mine pits in Zichuan [34,35].

At present, the design of a PSH plant in coal mines is influenced by several factors, including geological conditions and mine structure. However, the PSH plant may adapt poorly to varying mine conditions, and the technical bottleneck for the large-scale application of PSH plants in coal mines still exists.

3.3. Domestic Policies for the Development of PSH

Several favorable policies have been issued by governments and relative authorities at various levels as the importance of energy storage technologies, especially PSH has been growing (Table 3). *The 14th Five-Year Plan for Scientific and Technological Innovation in the Energy Sector* lists PSH technology as the primary field of innovation in energy storage technologies. It also points out that by 2025, these energy storage technologies will enter the stage of large-scale commercialization.

In the meantime, reforms of the grid market are also underway. The National Development and Reform Commission has released a *Notice on Intensifying the Action Plan for Tariff Mechanism Reform During the 14th Five-Year Period* to accelerate the implementation of the tariff mechanism for PSH. The document titled *Opinions on Further Improving the Price Formation Mechanism of Pumped Storage* proposes competition-oriented electricity price formation and specifies the electricity price allocation mechanism for PSH.

So far, 23 provinces in China have released policies that urge the construction of energy storage facilities suitable for new energy generation. There is also a mandate for distributed energy distribution and storage. Building PSH plants in abandoned mine shafts are high on the agenda [36].

Table 3. Summary of policies related to PSH.

Time	Institution	Policy	Contents
31 May 2022	State Council	*A package of policy measures to stabilize the economy*	To construct a series of PSH plants that will considerably promote power system security and large-scale development of new energies
10 Aug 2021	State Development and Reform Commission, National Energy Administration	*Notice on encouraging renewable electricity generation enterprises to self-build or purchase peak shaving capacity to increase the grid-connected scale*	To encourage electricity generation enterprises to self-build or purchase peak shaving capacity
23 Jul 2021	State Development and Reform Commission	*Notice on tasks for coping with the summer peak season of energy consumption in 2021*	To greatly boost the accelerated PSH development and new types of energy storage
11 Jul 2021	National Energy Administration	*Notice on the development and construction of wind and PV power in 2021*	To connect to grid the flexible regulation capacity for the newly generated PSH, new types of stored energy, and adjustable load
13 Mar 2021	State Council	*Outline of the 14th Five-Year Plan for National Economic and Social Development and Vision 2035 of the People's Republic of China*	To speed up the construction of PSH plants and the large-scale application of new energy storage technologies
28 Jul 2020	State Council	*Outline of the Integrated Regional Development of the Yangtze River Delta*	To study and establish the cost allocation mechanism for the market-oriented operation of PSH in East China Power Grid
18 Jun 2020	State Development and Reform Commission, National Energy Administration	*Guiding opinions on guaranteeing energy security in 2020*	To proactively promote the construction of power sources with peak-shaving capacity, such as PSH plants and leading hydropower stations
23 Mar 2018	State Development and Reform Commission, National Energy Administration	*Guiding opinions on upgrading the regulation capacity of the electric power system*	To speed up the construction of the PSH plants that have been approved and for which the sites have been planned and recommended and conduct a new round of site-selection planning
30 Jun 2017	State Development and Reform Commission, Ministry of Commerce	*Negative List for Foreign Investment Access*	To continue encouraging the construction of large-scale PSH generators with a rated power of 350 MW and above

4. Key Scientific Issues in PSH Development in Abandoned Mine Shafts

To achieve carbon neutrality targets, China needs to speed up infrastructure construction for PSH exploitation in abandoned mine shafts. Concerted efforts will be made to initiate supply-side energy reformation, with a prioritization of energy regulation and a shift of focus from cutting down emissions alone to popularizing clean energy. The above measures are not only conducive to solving the existing ills in China's energy sector but will also revolutionize China's energy structure, energy planning, grid operation, and clean energy consumption. Several scientific problems need to be tackled during the implementation of PSH projects in abandoned mine shafts.

4.1. Evaluation Model for Site Selection of PSH Plants in Abandoned Mine Shafts

There is considerable variability in the construction of abandoned mine shafts across the mining areas due to historical reasons. We need to study the factors specific to abandoned mine shafts and summarize the conditions for PSH exploitation in abandoned mine shafts that have distinct geographical, sectoral, and technical features. It is necessary to build a mature evaluation system for PSH exploitation and utilization and propose a set of criteria for site selection in such PSH projects.

4.2. Purifying Minewater That Has Complex Components

The hydrodynamic and chemical profiles in the region change dramatically after the mines are closed. This will cause pollution of reservoir water sources, threatening normal operation and shortening the service life of the equipment. Purification technologies for water sources in abandoned mine shafts should be developed extensively; samples from mine water sources in the five major regions should be collected and analyzed for the chemical composition of mine water; the key purification parameters for each ingredient should be determined, and the influence of these components on PSH facilities should be analyzed. It is necessary to investigate the impact of mine water on the environment and soil in the upper reservoir and to determine the changes in composition during the cycle of the upper and lower reservoirs. New types of purification reagents must be developed to improve the water quality and timeliness of purification while decreasing the operating cost.

4.3. Clarifying the Evolutionary Mechanism of Groundwater Storage Coefficient for Transparent Mines

Data-driven health status evaluation and prewarning technology and suitable platforms should be proposed for the mining group, along with key equipment for the specific working environment (deep water and deep land, water-air alternation, and difficulty in manual operation) based on the precise detection and smart monitoring technology for underground spaces. We should analyze the structure and characteristics of underground water reservoirs to determine the spatial variation pattern of underground water reservoirs in abandoned mine shafts as space and time evolve and achieve dynamic feedback and regulation of the operation of PSH plants in abandoned mine shafts.

4.4. Assessing the Stability of Water Reservoirs under the Action of Long-Term Infiltration and Surging

Underground water reservoirs of PSH plants in abandoned mine shafts should satisfy the dual requirements of impermeability and stability. PSH plant reservoirs are subjected to long-term infiltration and cycling. It is necessary to reveal the mechanism of corrosion-induced weakening of the coal pillar dam body during water-rock ion exchange, analyze the influence of hydraulic shock on the mechanical parameters of the reservoir dam body, investigate the mechanism of fissure development under high surrounding rock stress, and build the multi-field coupled mechanical model for the reservoir dam body in abandoned mine shafts.

4.5. Proposing the Dispatching and Operating Model for PSH Plant Group in the Abandoned Mine Shaft

Although the total underground spaces of abandoned mine shafts are massive, the spaces in roadways and chambers are limited, which entails the use of distributed mode at both the planning and operational stages. We should study grid operation in both the peak and off-peak periods corresponding to varying availability of wind and solar energies, specifically, the conditions for electricity generation and consumption based on one day, ten days, and three months. The coupled factors that influence the operating environment of distributed underground water reservoirs should be considered, and the dispatching and operating mode for the PSH plant group in abandoned coal mines should be established.

4.6. Establishing Grid-Level Energy Transmission Mode for PSH Plant in Abandoned Mine Shafts

When the PSH plant is connected to the grid, the diesel generators and gas turbine generator set will be used as the backup power. PSH can be used to lower the peak and raise the valley to smooth out the fluctuations in power production by the photovoltaic system. Therefore, the entire renewable energy system will become more stable and efficient. When the PSH plant is disconnected from the grid, the PSH and light energy will complement each other, balance the electricity demand and supply and guarantee the maximum consumption of electricity generated by the photovoltaic system. The above-described design is crucial

to sustaining the stable operation and development of the microgrid. We should also push ahead with the grid access management system for PSH in abandoned mine shafts and carry out the demonstration project for cluster PSH plants in abandoned mineshafts. The grid-level construction of PSH plants in abandoned mine shafts should be optimized based on the grid constraint conditions, real-time electricity pricing strategy, and instructions from dispatching institutions.

5. Potential Research Fields and Development Directions of PSH in Abandoned Mine Shafts

In order to realize carbon neutrality targets and resource reuse in abandoned mine shafts, studies on PSH development should be oriented toward intelligence, stabilization, and greening. Moreover, PSH development in abandoned mine shafts should also be aimed at integration, completion, and coordination (Figure 6).

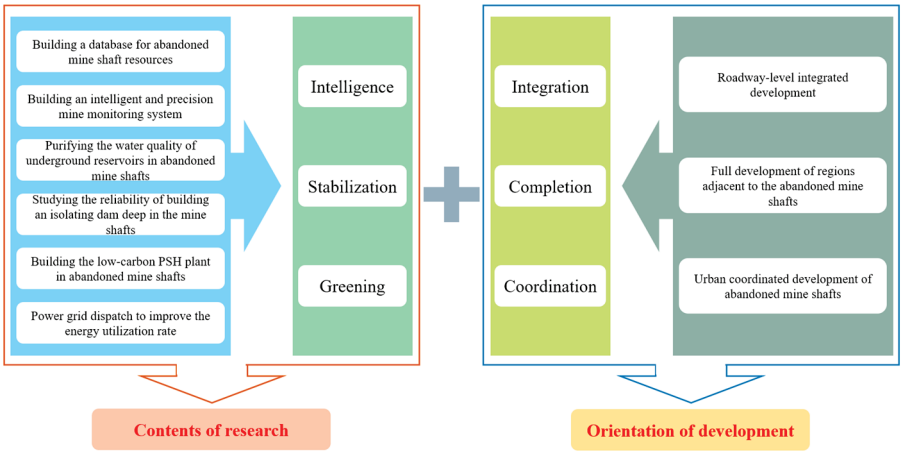

Figure 6. Framework of the contents of research and orientation of the development of PSH in abandoned mine shafts.

5.1. Thrust Areas of Research

5.1.1. Building a Database of Abandoned Mine Shaft Resources

Government authorities should take the lead, and industry should offer assistance for exhaustive research into the distribution, residual resources, and historical development of abandoned mine shafts in China. Enterprises in this industry should cooperate with government authorities and relevant parties in the above study. A database should be built regarding China's abandoned mine shafts to facilitate easy availability and exchange of information, which can lay a solid foundation for the regional, diversified planning and development of energy storage technologies and facilities.

5.1.2. Building an Intelligent and Precision Mine Monitoring System

Five major regions will be considered in the research. A survey will be conducted underground after the mine shafts stop operation, with full consideration of the regional geological features and the differences in the mining system. Real-time prospecting will be combined with numerical simulation to build a 3D visualization model for the abandoned mine shaft.

IOT-based monitoring equipment specific for underground water reservoirs in abandoned mine shafts should be developed for real-time capture-feedback-response. A health status evaluation method for PSH electromechanical equipment will be needed to provide data support for the maintenance and operation of the PSH plant in the abandoned mine shaft.

5.1.3. Improving the Water Quality of Underground Reservoirs in Abandoned Mine Shafts

We should analyze the water quality of typical water sources in mine shafts and determine the influence of underground water reservoirs on water sources. Deep purification technology for mine water with complex compositions must be investigated, and a comparative analysis of the influence of chemical reagents on the reservoirs and power generation equipment must also be carried out. The variation law of key purification parameters of underground water reservoirs in abandoned mine shafts must be determined.

We should push forward the research and development of water purification products to address water quality-related problems discovered on site; study the mechanism of ionic corrosion in mine water; establish grading indicators for mine water in abandoned mine shafts; summarize the advantages and disadvantages of each purification technology; analyze the key influence factors of the timeliness of water purification, and propose a composite influence model for mine water purification.

5.1.4. Improving the Reliability of Dam Construction Deep in the Mine Shafts

In underground dam construction, we should fully consider the effects of the underground stress environment, long-term water infiltration, and periodic shock. It is also necessary to analyze the mechanism of the hinged joint between the coal pillar and artificial dam body and optimize the reservoir dam body structure; investigate the mechanism of periodic water infiltration to induce the weakening of the reservoir dam body and develop an anti-seepage construction process for the dam body; determine the mechanical performance of underground coal pillar-artificial dam body, and build a mathematical model for underground reservoir stability.

We can perform indoor laboratory tests, theoretical analyses, and numerical simulations to reveal the damage mechanism of the dam body under different hydraulic pressures, classify the working conditions of the PSH plant, consider the impact caused by a surge to underground reservoirs, and determine the reliability indicators of the coal pillar dam body.

5.1.5. Building a Low-Carbon PSH Plant in Abandoned Mine Shafts

The construction of PSH plants in abandoned mine shafts can improve the comprehensive utilization rate of resources and promote social and economic development. During the construction process, we should give full consideration to the following aspects: regional water and soil loss, water quality degradation, balancing the contraindications of social development and ecological protection, constructing demonstration low-carbon projects, and adhering to the operating principles of precise management and sufficient implementation; practicing the water liability system, with the local government as the main actor to construct a management system that clearly defines the responsibility of each party and facilitates coordination and supervision. Such a liability system is highly important for the orderly construction of PSH plants in abandoned mine shafts.

5.1.6. Improving the Utilization Rate of Energy Generated by the Cluster Generator Set

Stand-alone medium- to small-sized power stations will serve as basic units in abandoned mine shafts. A clustered layout will be used if necessary. The PSH generator sets should be coordinated efficiently to fully utilize small reservoirs, such as distributed loads and ease of monitoring. The regulation ability of reservoir capacity can be increased through clustered reservoirs.

We should optimize the regional grid, prevent the wastage of solar energy and wind, improve load dispatch of regional grids, enhance information collection for electricity generated from new energy sources, optimize dispatch efficiency, build and improve multi-energy coordination optimization control technology, and reasonably allocate the power generation from wind, solar, and hydraulic energies across time periods in the grid and determine the proportion of energy storage and amount of energy transmission for each renewable energy source.

5.2. Main Orientations of Development

5.2.1. Roadway-Level Integrated Development of Abandoned Mine Shafts

Based on existing shafts and roadway spaces in abandoned mine shafts, we should estimate the underground water capacity and choose the mode of construction for the upper and lower reservoirs, depending on the geological and hydrological conditions of the mine shafts, take measures to ensure the stability and impermeability of the reservoirs, overcome problems associated with basic science in PSH exploitation in abandoned mine shafts, accomplish the PSH demonstration projects in several abandoned mine shafts, and release supportive regulations on PSH development in abandoned mine shafts. Form a pumped storage power station as the core, and build an integrated base for diesel power generation, gas power generation, and photovoltaic power generation in abandoned mines to provide power protection for production and life (Figure 7).

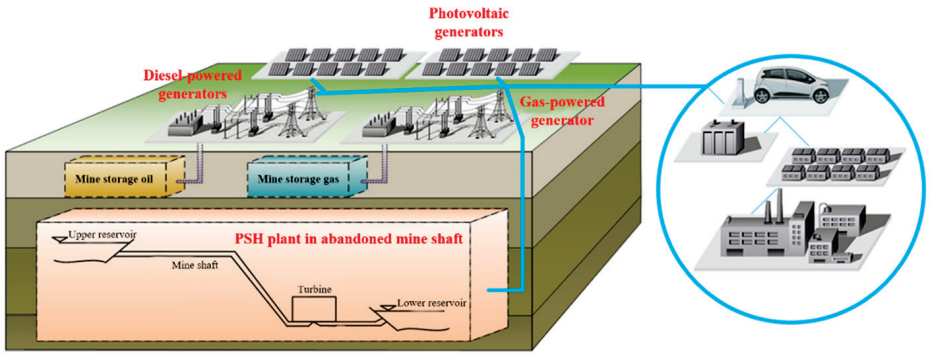

Figure 7. Integrated development.

5.2.2. Full Development of Regions Adjacent to Abandoned Mine Shafts

PSH plant trial projects can be launched in several abandoned mine shafts with stable geological conditions and favorable downhole transformation conditions (Figure 8). The transformation projects for PSH development in abandoned mine shafts lie at the core, while ecological restoration, new energy construction, and grid service facilities may be built near the abandoned mine shafts. One goal is to complete a series of engineering projects for large-scale energy storage to create a profitability system centered around the mining area. The main aim is to peak carbon dioxide emissions by 2030.

Figure 8. Full development.

5.2.3. City-Level Coordinated Development of Abandoned Mine Shafts

Based on abandoned mine shaft groups around China's resource-depleted cities, a series of underground energy storage projects will be built. Thus, several regionally distributed smart energy systems where renewable (light, hydraulic, wind, gas) and conventional energy sources and thermal energy that complement each other will be formed (Figure 9). Resource-depleted cities may thus be transformed, driven by the regional industrial chain and accompanied by the resettlement of mining-related populations. A national-level underground energy storage cloud based on PSH plants in abandoned mine shafts will be built, thereby laying the foundation for large-scale energy storage to meet China's carbon neutrality targets in 2060.

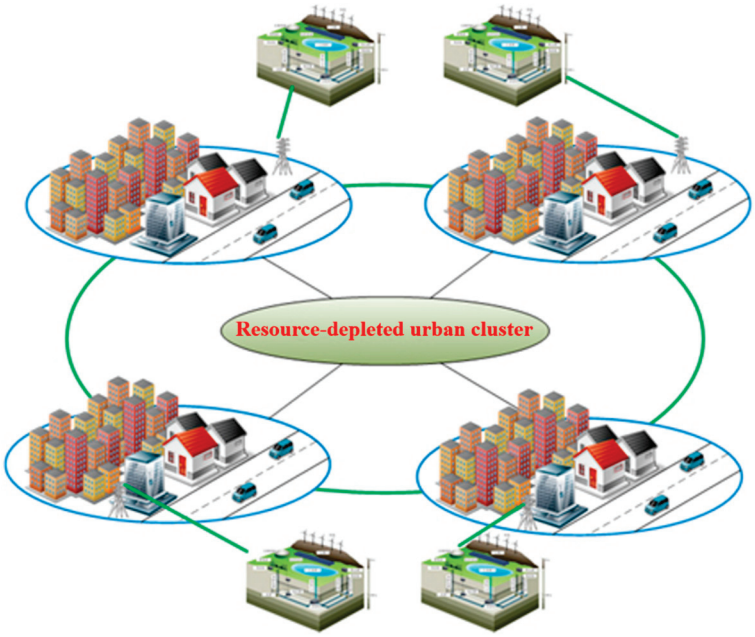

Figure 9. Coordinated development.

6. Outlook

China is riding a new wave of scientific and technological innovation and industrial transformation. The coal sector is facing the greatest period of change in a hundred years. To achieve carbon peaking and carbon neutrality targets, China needs to establish the full life cycle of coal mines and formulate and implement technological strategies for the transformational development of abandoned mine shafts. In the meantime, China should fully encourage new energy development, plan and construct a series of demonstration PSH plants, and push forward studies in relevant fields.

China should also step up efforts in the following aspects as resource development in abandoned mine shafts proceed: carry out a census of abandoned mine shafts; develop standards for resource development and utilization in abandoned mine shafts; enhance top-level design and policy guidance; promote safe, low-carbon development and utilization of PSH resources in abandoned mine shafts and the innovation of relevant technologies to upgrade the scientific and technological support capabilities; prioritize energy exploitation and utilization in abandoned mine shafts; focus on constructing abandoned mine shaft exploitation and utilization platform and talent cultivation; and achieve international leadership in relevant technologies through research, thereby making China a strong presence in cutting-edge energy science.

Author Contributions: Conceptualization, X.L.; validation, J.F.; formal analysis, T.Z.; resources, S.L. (Shanshan Li); data curation, S.L. (Shuai Liu); writing—original draft preparation, X.L. and T.Z.; writing—review and editing, X.L. and J.F.; supervision, L.Y.; project administration, K.Y. All authors have read and agreed to the published version of the manuscript.

Funding: This research was funded by Anhui Provincial University Scientific Research Project (No.YJS20210391), the Key Research Development Plan of Anhui Province (No.202104a07020009) and the Chinese Academy of Engineering-Academic Cooperation Project (No.2020SX5) and China National Scholarship Fund Project (No.202208340045).

Institutional Review Board Statement: Not applicable.

Informed Consent Statement: Not applicable.

Data Availability Statement: The data used for conducting classifications are available from the corresponding author upon request.

Acknowledgments: Thanks to the Energy Research Institute of Hefei Comprehensive National Science Center for supporting this project.

Conflicts of Interest: The authors declare no conflict of interest.

References

1. Yuan, L.; Yang, K. Further discussion on the scientific problems and countermeasures in the utilization of abandoned mines. *J. China Coal Soc.* **2021**, *46*, 16–24. [CrossRef]
2. Lyu, X.; Yang, K.; Fang, J. Utilization of resources in abandoned coal mines for carbon neutrality. *Sci. Total Environ.* **2022**, *822*, 153646. [CrossRef]
3. Ma, D.; Duan, H.Y.; Zhang, J.X. Solid grain migration on hydraulic properties of fault rocks in underground mining tunnel: Radial seepage experiments and verification of permeability prediction. *Tunn. Undergr. Space Technol.* **2020**, *126*, 104525. [CrossRef]
4. Chen, D.; Chen, A.; Hu, X.; Li, B.; Li, X.; Guo, L.; Feng, R.; Yang, Y.; Fang, X. Substantial methane emissions from abandoned coal mines in China. *Environ. Res.* **2022**, *214*, 113944. [CrossRef]
5. Bian, Z.; Zhou, Y.; Zeng, C.; Huang, J.; Pu, H.; Axel, P.; Zhang, B.; Habil, C.B.; Bai, H.; Meng, Q.; et al. Discussion of the basic problems for the construction of underground pumped storage reservoir in abandoned coal mines. *J. China Coal Soc.* **2021**, *46*, 3308–3318. [CrossRef]
6. Ma, D.; Duan, H.Y.; Zhang, J.X.; Bai, H. A state-of-the-art review on rock seepage mechanism of water inrush disaster in coal mines. *Int. J. Coal Sci. Technol.* **2022**, *9*, 50. [CrossRef]
7. Chen, J.; Liu, N.; Ma, X. Energy eco-efficiency measurement and driving factors of China's eight comprehensive economic zones. *China Environ. Sci.* **2021**, *41*, 2471–2480. [CrossRef]
8. Dong, F.; Hua, Y.; Yu, B. Peak carbon emissions in China: Status, key factors and countermeasures-A literature review. *Sustainability* **2018**, *10*, 2895. [CrossRef]
9. Ma, D.; Duan, H.Y.; Zhang, J.X.; Liu, X.W.; Li, Z.H. Numerical simulation of water-silt inrush hazard of fault rock: A three-phase flow model. *Rock Mech. Rock Eng.* **2022**, *55*, 5163–5182. [CrossRef]
10. Hao, J.; Gao, F.; Fang, X.; Nong, X.; Zhang, Y.; Hong, F. Multi-factor decomposition and multi-scenario prediction decoupling analysis of China's carbon emission under dual carbon goal. *Sci. Total Environ.* **2022**, *841*, 156788. [CrossRef]
11. Liu, Y.; Lu, F.; Xian, C.; Ouyang, Z. Urban development and resource endowments shape natural resource utilization efficiency in Chinese cities. *J. Environ. Sci.* **2022**, *26*, 806–816. [CrossRef]
12. Pan, Y.; Yin, X.; Hu, J.; He, J. Centralized exploitation and large-scale delivery of wind and solar energies in west China based on flexible DC grid. *Power Syst. Technol.* **2016**, *40*, 3621–3629. [CrossRef]
13. Yuan, L. Promote the precise development and utilization of closed/abandoned mine resources in China. *Coal Econ. Res.* **2019**, *39*, 1. [CrossRef]
14. Wang, Q.; Peng, S. Review of research on recreational utilization of abandoned mining areas and construction of research framework system. *J. China Coal Soc.* **2022**, *47*, 2150–2160. [CrossRef]
15. Koudelkova, J.; Urbanec, V.; Korandova, B.; Hummel, M. Geomontaneous tourism and the possibilities of utilizing abandoned mine workings in the Czech Republic. *Geoheritage* **2022**, *14*, 29. [CrossRef]
16. Yuan, L.; Jiang, Y.; Wang, K.; Zhao, Y.; Hao, X.; Xu, C. Precision exploitation and utilization of closed/abandoned mine resources in China. *J. China Coal Soc.* **2018**, *43*, 14–20. [CrossRef]
17. Tian, Y.; Qiao, Y.; Zhang, Y. Construction of green emission reduction system under the constraint of carbon neutrality. *Chem. Ind. Eng. Prog.* **2022**, *41*, 1078–1084. [CrossRef]
18. Fambri, G.; Diaz-Londono, C.; Mazza, A.; Badami, M.; Sihvonen, T.; Weiss, R. Techno-economic analysis of Power-to-Gas plants in a gas and electricity distribution network system with high renewable energy penetration. *Appl. Energy* **2022**, *312*, 118743. [CrossRef]

19. Wang, X.; Bamisile, O.; Chen, S.; Hu, W.; Luo, S.; Huang, Q.; Hu, W. Decarbonization of China's electricity systems with hydropower penetration and pumped-hydro storage: Comparing the policies with a techno-economic analysis. *Renew. Energy* **2022**, *196*, 65–83. [CrossRef]
20. Liu, J.; Sun, X.; Bo, R.; Wang, S.; Ou, M. Economic dispatch for electricity merchant with energy storage and wind plant: State of charge based decision making considering market impact and uncertainties. *J. Energy Storage* **2022**, *53*, 104816. [CrossRef]
21. Shang, D.; Pei, P. Analysis of influencing factors of modification potential of abandoned coal mine into pumped storage power station. *J. Energy Resour. Technol.* **2021**, *143*, 112003. [CrossRef]
22. Pujades, E.; Poulain, A.; Orban, P.; Goderniaux, P.; Dassargues, A. The impact of hydrogeological features on the performance of underground pumped-storage hydropower (UPSH). *Appl. Sci.* **2021**, *11*, 1760. [CrossRef]
23. Luo, Y.; Yuan, H.; Wang, X.; Li, Y.; Jing, J.; Da, T. A new distributed collaborative control for double-layer dynamic optimal scheduling of energy network. *Energy Rep.* **2022**, *8*, 847–856. [CrossRef]
24. Li, T.; Li, A.; Song, Y. Development and utilization of renewable energy based on carbon emission reduction-evaluation of multiple MCDM methods. *Sustainability* **2021**, *13*, 9822. [CrossRef]
25. Guo, Z.; Ye, R.; Liu, R.; Liu, J. Optimal scheduling strategy for renewable energy system with pumped storage station. *Electr. Power Autom. Equip.* **2018**, *38*, 7–15. [CrossRef]
26. Han, Y.; Zhang, X.; Wang, S.; Xie, Y.; Yang, L. Feasibility and techno-economic research on multi-scenario utilization of pumped storage in abandoned mine. *Mod. Bus. Trade Ind.* **2020**, *41*, 210–213. [CrossRef]
27. Hong, Y.; Apolinario, G.F.D.G.; Lu, T.; Chu, C. Chance-constrained unit commitment with energy storage systems in electric power systems. *Energy Rep.* **2022**, *8*, 1067–1090. [CrossRef]
28. Kitsikoudis, V.; Archambeau, P.; Dewals, B.; Pujades, E.; Orban, P.; Dassargues, A.; Pirotton, M.; Erpicum, S. Underground pumped-storage hydropower (UPSH) at the martelange mine (Belgium): Underground reservoir hydraulics. *Energies* **2020**, *13*, 3512. [CrossRef]
29. Zhang, Y.; Wang, S.; Shao, W.; Hao, J. Feasible distributed energy supply options for household energy use in China from a carbon neutral perspective. *Int. J. Environ. Res. Public Health* **2022**, *18*, 12992. [CrossRef]
30. Kushwaha, A.; Tewari, S.; Mandal, P.K.; Bhattacharjee, R.; Das, A.J.; Singh, K.K.K. Stability evaluation of old and unapproachable underground mine workings below surface structures. *J. Geol. Soc. India* **2019**, *93*, 351–359. [CrossRef]
31. Kozlowska-Woszczycka, A.; Pactwa, K. Social license for closure-A participatory approach to the management of the mine closure process. *Sustainability* **2022**, *14*, 6610. [CrossRef]
32. Gao, R.; Wu, F.; Zou, Q.; Chen, J. Optimal dispatching of wind-PV-mine pumped storage power station: A case study in Lingxin coal mine in Ningxia Province, China. *Energy* **2022**, *243*, 123061. [CrossRef]
33. Niemann, A.; Perau, E.; Schreiber, U.; Koch, M.K. Opportunities and risks of underground pumped storage plants in coal mines of the Ruhr Area. *Wasserwirtschaft* **2014**, *104*, 66–69. [CrossRef]
34. Lv, H.; Chen, Y.; Wu, J.; Zhu, Z. Performance of isobaric adiabatic compressed humid air energy storage system with shared equipment and road-return scheme. *Appl. Therm. Eng.* **2022**, *211*, 118440. [CrossRef]
35. Liu, F.Y.; Yang, K.; Yang, T.H.; Gao, Y.; Li, J.D.; Liu, Q.; Fu, Q. Pumped storage hydropower in an abandoned open-pit coal mine: Slope stability analysis under different water levels. *Front. Earth Sci.* **2022**, *10*, 941119. [CrossRef]
36. Shang, D.C.; Pei, P.; Zuo, Y.J. Techno-Economic feasibility analysis of pumped storage hydroelectricity in abandoned underground coal mines. *J. Energy Resour. Technol.* **2020**, *142*, 122001. [CrossRef]

sustainability

MDPI

Article

Characteristics and Formation Mechanism of Surface Residual Deformation above Longwall Abandoned Goaf

Erhu Bai [1,2,3,4], Xueyi Li [2], Wenbing Guo [1,2,3,4], Yi Tan [1,2,3,4,*], Mingjie Guo [2], Peng Wen [2] and Zhibao Ma [2]

[1] Shaanxi Provincial Key Laboratory of Geological Support for Coal Green Exploitation, Xi'an University of Science and Technology, Xi'an 710054, China
[2] School of Energy Science and Engineering, Henan Polytechnic University, Jiaozuo 454003, China
[3] State Key Laboratory of Coal Resources in Western China, Xi'an University of Science and Technology, Xi'an 710054, China
[4] State Collaborative Innovative Centre of Coal Work Safety and Clean-Efficiency Utilization, Jiaozuo 454003, China
* Correspondence: tanyi@hpu.edu.cn; Tel.: +86-13453177787

Abstract: With the rapid development of social economy in China, the contradiction between the wide distribution of abandoned goaf and the shortage of land for engineering construction is becoming increasingly prominent. The effective utilization of coal mining subsidence areas has become an effective measure to alleviate the poverty of construction land in mining areas and promote the green transformation of mining cities. The key to the scientific utilization of abandoned goaf is the prevention and control of surface residual deformation, which depends on the formation mechanism of surface residual deformation. Based on the regularity of mining-induced surface movement and deformation under different mining sizes, it is concluded that the full mining degree of working face is the primary condition for entering the surface recession period. The trapezoidal and periodic forward movement characteristics of mining-induced overburden destruction are analyzed. The regularity of upward transmission of mining-induced fissures with overburden destruction is clarified. The influencing factors of surface residual deformation are equivalent to the influencing factors of overburden structure and caved zone. The deformation characteristics of broken rock in the caved zone under different conditions (particle size, gradation, and water content) are analyzed. It is concluded that the surface residual subsidence near the boundary of the goaf is more significant than that in the middle of the goaf. It is revealed that the overburden structure at the boundary of the goaf and the re-compaction of the caved zone is the mechanism of surface residual deformation. The characteristics of surface residual deformation in abandoned goaf have been verified by field measurement, and it is pointed out that the surface residual deformation in abandoned goaf has long-term characteristics, which provides a theoretical basis for accurate prediction of surface residual deformation and rational utilization of abandoned goaf.

Keywords: abandoned goaf; surface residual deformation; formation mechanism; overburden structure

1. Introduction

As an essential fundamental energy source in China, coal occupies a dominant position in China's primary energy structure, accounting for about 60% of said energy structure, and plays an irreplaceable role in developing the national economy [1–3]. According to IHS Markit forecasts, coal will remain the world's most influential power generation energy in the coming decades. When the coal is mined underground, the relative equilibrium strata are disturbed by mining and cause movement, deformation and destruction. As the coal mining continues, the influence range will be expanded continuously, and transmitted upward to the surface, forming a much larger subsidence basin than the goaf. Due to the hysteresis of surface subsidence, the surface subsidence will continue for a period of

time after the working face completed, thus forming the final surface movement basin. Therefore, the geological and environmental problems have been caused by large-scale coal mining, such as surface subsidence, landslide, groundwater loss, land desertification, and vegetation destruction [4–9], have seriously restricted the regional economic development, social stability, and sustainable development of the ecological environment, which has attracted great attention from all countries in the world [10–12].

At present, the area of land affected by mining in China is about 30,300 km^2, and is increasing at about 700 km^2/a. The subsidence area of some mining cities exceeds 10% of the total urban area. With the proposal of the carbon neutral and carbon peak strategy, and the acceleration of urbanization process, the contradiction between the increasing subsidence area and the tension of construction land has become increasingly prominent, which has become one of the main problems limiting the integrated development of urban and rural. Due to the tight land supply, it is inevitable to carry out ecological restoration or engineering construction in the subsidence area [13–15], and even to build subways, high-speed railways, which indicating that subsidence area are no longer abandoned land, but a valuable resource to be developed [16]. However, abandoned goaf may be activated under additional stress and induce secondary damage [17–20], such as the collapse of the Fengfeng Group Machinery Plant, which was built above the abandoned area after 20 years. Therefore, whether the subsidence area can be used as construction land depends on the control of surface residual deformation, and the effectiveness of surface residual deformation control depends on its formation mechanism.

In terms of surface residual deformation characteristics and prediction, Goulty concluded that surface subsidence has different mechanical mechanisms during the active and residual deformation stages, and is not possible to predict the residual subsidence time according to the active stage [21]. Guéguen analyzed the average surface residual deformation of abandoned goaf in northern France as 10 mm/a within 7 years after stopping mining [22]. Statham analyzed the collapse accidents of 400 abandoned goaf in South Wales, and 16% were caused by the buildings stress [23]. Meanwhile, Graniczny [24], Blachowski [25], and André [26] et al. have continuously monitored the surface residual deformation of the abandoned goaf and obtained the residual subsidence in the corresponding time period. In terms of the prediction of surface residual deformation, Cui established a model to calculate the duration of residual subsidence and the annual residual surface subsidence factor caused by abandoned longwall coal mining [27]. Li proposed a novel mathematical model calculating surface progressive residual subsidence based on the logistic time function [28]. Meanwhile, many scholars [29–32] have established prediction models for surface residual deformation under the different mining conditions based on the probability integral method, and have successfully carried out field. Due to the difference geological conditions leads to different degrees of surface residual deformation, based on the overburden failure degree and regional division of mining fracture, this paper analyzes the generation mechanism of surface residual deformation from the source of underground mining, providing a theoretical basis for effective control of surface residual deformation and rational use of abandoned goaf land.

2. Surface Subsidence Characteristics under the Mining Influence

2.1. Overview of the Study Area

Xinlong Mining Co., Ltd. is located 6.0 km southwest of Yuzhou City, China, the coalmine is delineated by 28 coordinated inflection points, which is 8.5~13.4 km long from east to west, 4.5 km wide from south to north, and covers an area of 43.8 km^2. The north and east are slightly inclined plains in front of mountains, with flat terrain, densely distributed villages, and ground elevation of +105~+120 m. The west and south are hills, and the ground elevation gradually decreases from west (+325 m) to east (+105 m). The designed production is 0.9 Mt/a, the mining thickness of No. 21 coal seam is about 4.5 m, the mining depth is 424~634 m, and the dip angle is 5~18°. At present, the 11 mining

area has been completed, the panel distribution and its mining time in the west wing of 11 mining area are shown in Figure 1.

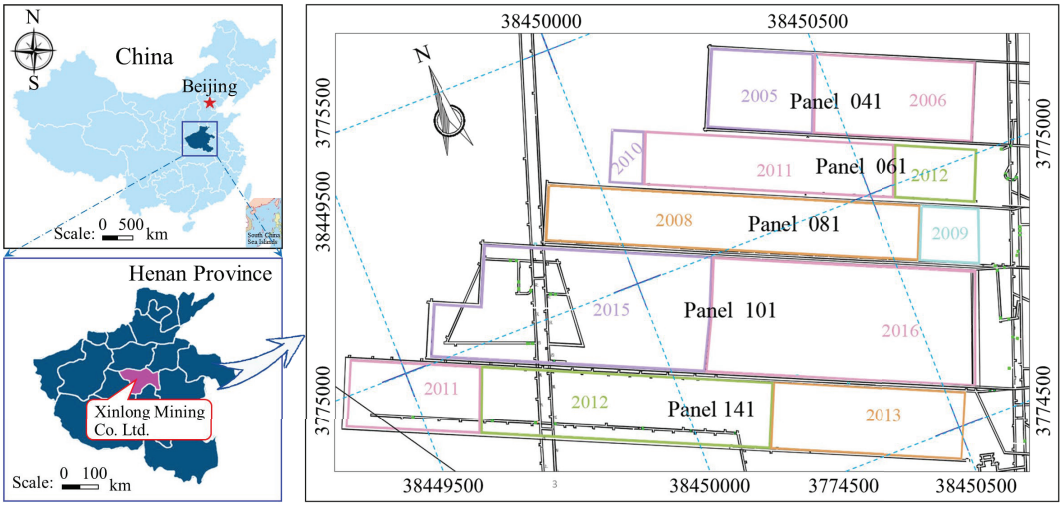

Figure 1. The panel distribution and its mining time of the west wing in the 11 mining area.

As can be seen from Figure 1, the mining time of panel 141 and 061 are basically same, but the boundary conditions are different, where the panel 141 has coal pillars. The strike is 1263 m and the dip is 136 m. The average mining depth is 580 m, with an average of 12°. In general, the coal seam in the middle and west of the coalfield are relatively thick and slightly thin on both sides. The proctor hardness f = 0.15~0.25, which is an extremely soft coal seam. Both sides of the panel 061 are goaf, with strike length of 747.8 m and average dip length of 112.3 m. The coal thickness is 2.6~5.3 m, and 8~12° of dip, and the whole working face is typically thicker in the middle and west, and slightly thinner on both sides. The roof of the working face is relatively hard, and full caved management is adopted.

2.2. Surface Response Characteristics under the Mining Influence

In combination with the mining time of each working face, an observation line with a spacing of 30 m is arranged on the strike and dip of panel 141 and 061, respectively. The observation time of 141 working faces is from November 2011 to March 2014, nine leveling surveys and four comprehensive observations were carried out. The observation time of panel 061 is from September 2011 to October 2012, during which eight leveling surveys were conducted. The strike subsidence curve is shown in Figure 2 based on the monitoring data.

It can be seen from Figure 2 that the maximum subsidence of the two panels are 153 mm and 1632 mm, respectively, which is mainly because the strike and dip of the 061 working face have reached critical mining under the influence of adjacent goaf. The overburden separation and fractures have been fully developed, broken rock in the caved zone has been compacted, and the overburden void is relatively small. The cracks and subsidence occurred on the surface during the mining process, which continued to extend forward with the mining progress. Meanwhile, the structure cracks were caused at the upper corner of the window (as shown in Figure 3). It indicates that when the working face is sub-critical mining, the surface still has large subsidence under the mining influence of the adjacent panel, which will cause serious damage to the surface.

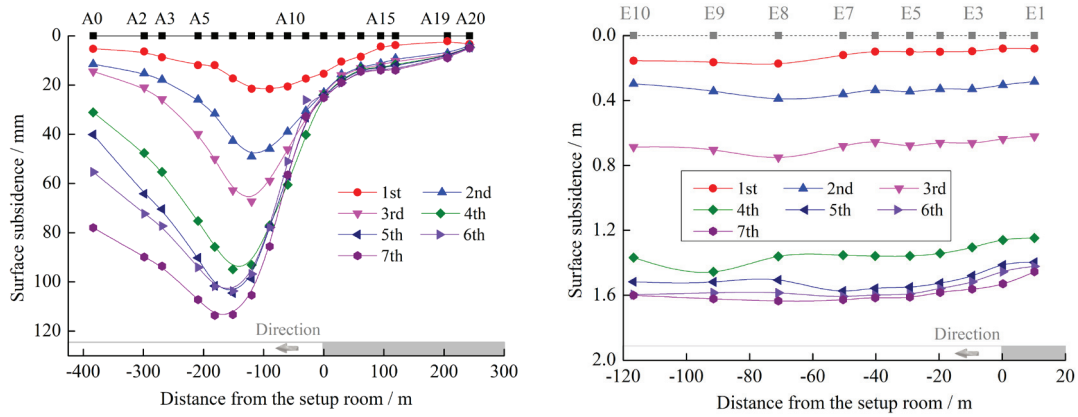

(**a**) (**b**)

Figure 2. The surface subsidence of the working face in the 11 mining area: (**a**) surface subsidence of panel 141, and (**b**) surface subsidence of panel 061.

(**a**) (**b**)

Figure 3. The response of surface and structure under the mining influence: (**a**) surface subsidence and (**b**) surface and structure damage.

3. Overburden Failure Characteristics

The overburden structure is an important basis for maintaining the overburden stability. During the mining process, the overlying strata collapses. When the roof is pressed periodically, the stress and fracture of the collapsed rock will change again. The final manifestation is that there are significant differences in the overburden structure at the open cut, middle area and stopping line of the goaf. Therefore, it is necessary to analyze the distribution characteristics of the stress and overburden fractures after mining.

3.1. Numerical Simulation

Based on geological and mining conditions and borehole histogram of 11,061 working face, 3DEC is adopted to establish the length, width, and height of a 230 m × 210 m × 120 m three-dimensional numerical model, the overburden thickness of the simulated working face is 94.11 m and applied the unstimulated 380 m rock stratum load 9.38 MPa above the model. The Mohr-Coulomb criterion is selected as the constitutive model, and the area contact elastoplastic model is selected as the joint constitutive model. The physical and mechanical parameters of partial strata are shown in Table 1, and the stress distribution of mining overburden at different advanced distances is shown in Figure 4.

Table 1. The physical and mechanical parameters of partial overburden above the working face.

No.	Lithology	Thickness (m)	Elastic Modulus (GPa)	Tensile (MPa)	Poisson's Ratio	Cohesion (MPa)	Friction Angle (°)
1	Sandstone	10.3	10.9	1.68	0.23	1.05	30
2	Sandy mudstone	3.0	14.5	3.05	0.27	1.18	32
3	Medium sandstone	0.9	36.1	5.13	0.26	4.40	36
4	Mudstone	7.7	14.5	3.05	0.27	1.18	32
5	Medium sandstone	3.2	36.1	5.13	0.26	4.40	36
6	Sandy mudstone	2.5	14.5	3.05	0.27	1.18	32
7	Mudstone	1.3	6.9	1.68	0.23	1.05	30
8	Siltstone	1.3	21.6	3.84	0.20	2.75	38
9	Mudstone	2.9	6.9	1.68	0.23	1.05	30
10	Sandy mudstone	1.3	14.5	3.05	0.27	1.18	32
11	Mudstone	8.7	6.9	1.68	0.23	1.05	30
12	Siltstone	1.1	21.6	3.84	0.20	2.75	38
13	Mudstone	8.9	6.9	1.68	0.23	1.05	30
14	Medium sandstone	5.7	36.1	5.13	0.26	4.40	36
15	Sandy mudstone	6.9	14.5	3.05	0.27	1.18	32
16	Mudstone	4.5	6.9	1.68	0.23	1.05	30
17	Siltstone	4.8	21.6	3.84	0.20	2.75	38
18	Mudstone	1.7	6.9	1.68	0.23	1.05	30
19	Sandy mudstone	6.2	14.5	3.05	0.27	1.18	32
20	Fine sandstone	7.6	38.4	6.75	0.18	3.80	37
21	Sandy mudstone	4.7	14.5	3.05	0.27	1.18	32
22	Coal seam	4.5	2.3	1.03	0.31	0.50	24
23	Mudstone	3.8	6.9	1.68	0.23	1.05	30

It can be seen from Figure 4 that with the working face advancing forward, the abutment pressure at the working face boundary is 15.8~29.8 MPa, which is about 2~3 times the original rock stress. The pressure relief area with an arch shape appears in the rock above the working face, and the normal stress phenomenon appears in some overburden near the coal seam, indicating that there is a local tensile stress area in the overburden. When the working face advances 80 m, the pressure relief area reaches the maximum, under the old roof pressure, the local rock strata gradually compact and a compacted area appears. In the process of advancing to 120 m, the pressure relief area is no longer developed upward, while the compacted area continues to expand to the top of the pressure relief area. As the working face continues to advance, there is no obvious change in the range of the relief area at the open cut side, the width of the relief area at the working face side is basically stable and moves with the working face, and the range of compacted area in the middle continues to expand, and the width of the relief area at the open cut side is always smaller than that at the stopping line, which also verifies that the overburden breaking angle at the open cut is greater than that at the stopping line [33]. It can be seen that the overburden in the middle of the goaf is in a compacted state, while the overburden structure exists at the boundary of the working face, indicating that the boundary of the working face is the main area where the overburden voids exist.

In order to further analyze the overburden failure and structural characteristics, combined with the numerical models, the distribution of overburden cracks with different advancing distances was obtained as shown in Figure 5.

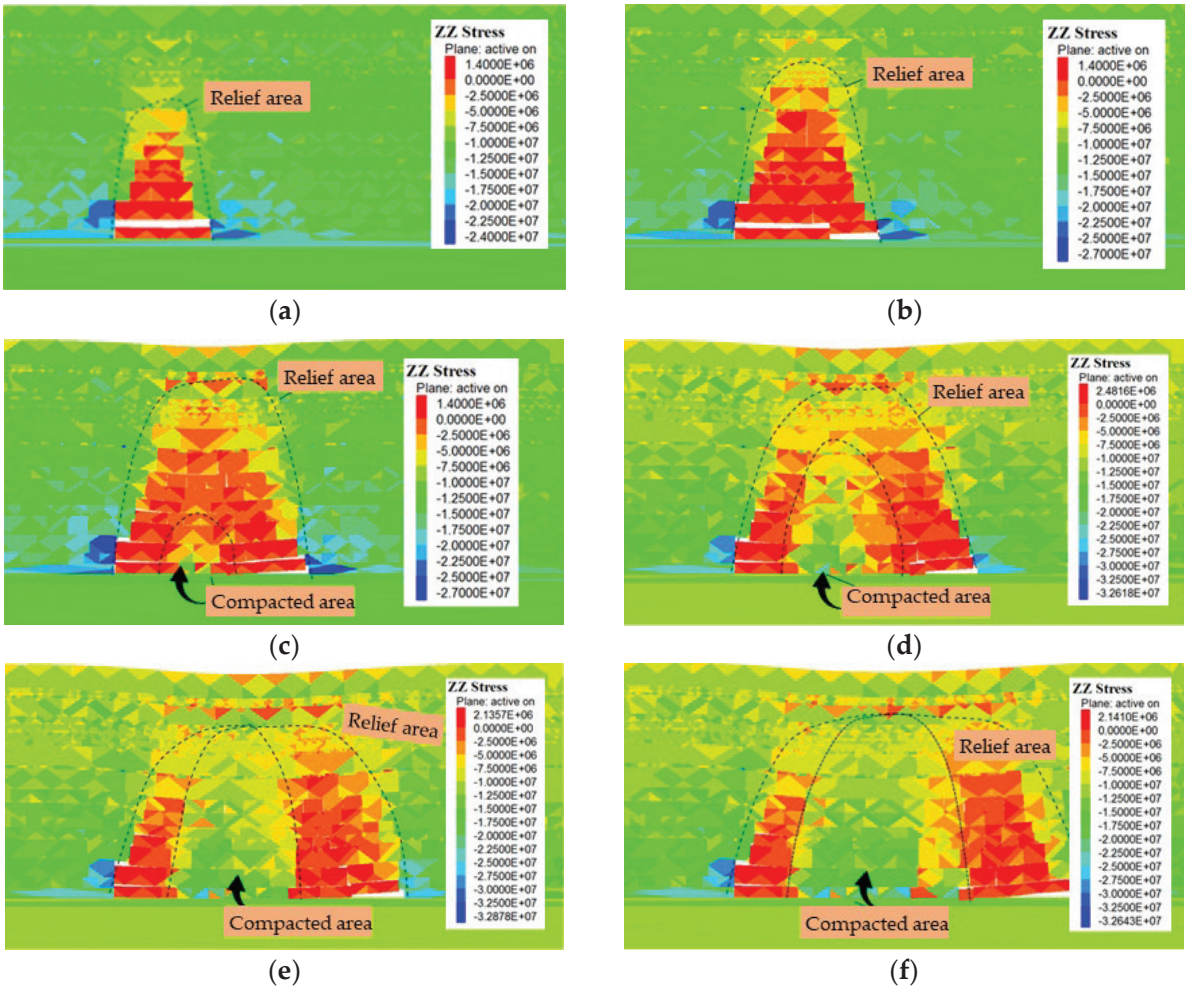

Figure 4. The overburden stress distribution at different advanced distances: (**a**) advance 40 m, (**b**) advance 60 m, (**c**) advance 80 m, (**d**) advance 100 m, (**e**) advance 120 m, and (**f**) advance 140 m.

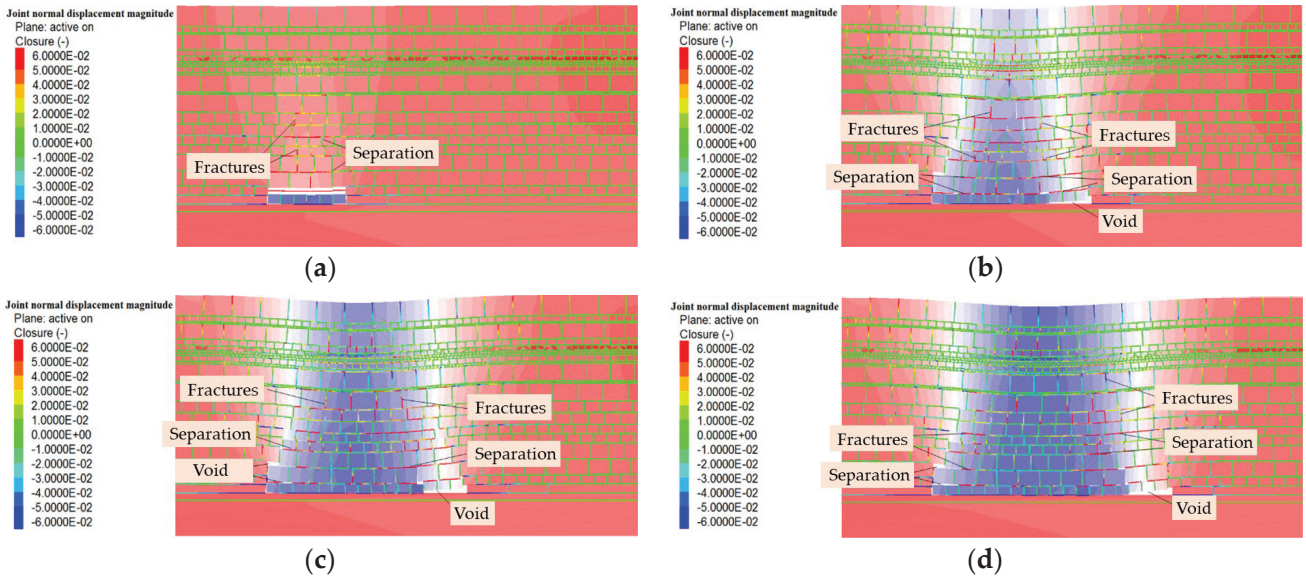

Figure 5. The distribution of overburden cracks with different advancing distances: (**a**) advance 40 m, (**b**) advance 80 m, (**c**) advance 100 m, and (**d**) advance 120 m.

As shown in Figure 5, when the working face advances 40 m, the development height of mining fractures and separation layers is about 18 m, the separation layers are mainly formed due to the asynchronous movement of the rock stratum, and the mining fractures are formed by the fracture of the rock stratum. When advancing 80 m, the separation layer and fractures develop upward, and the fractures develop to 36.4 m, while the separation layer is about 63 m, the cracks in the overburden rock under mining develop upward in a trapezoidal manner, the separation layer develops upward in an inverted trapezoidal manner, and the cracks closure phenomenon appears in the middle goaf. When advancing 100 m, the height of fracture development remains unchanged, indicating that the height of the fracture zone reaches the maximum, while the separation layer continues to develop upward to 74 m. Due to the existence of overburden structure, the side cracks of the open cut are basically unchanged, and the side cracks of the working face move forward continuously. When the panel advances 120 m, the compaction area in the middle goaf increases continuously, and the range of fracture development area on the working face side is larger than that on the open cut side.

From the evolution of mining cracks, it can be seen that the cracks in the middle of the extraction area gradually close after compaction and the area range keeps expanding; due to the existence of a masonry beam structure at the boundary, the cracks are well-developed and stable, which also indicates that the movement space after the reactivation of overburden is mainly concentrated in the fractured zone and caved zone.

3.2. Physical Simulation

Based on the geological and mining conditions of the working face, a 1:50 similar model is established using river sand, calcium carbonate, gypsum, and other materials. According to the key strata theory, there are four key strata that were calculated to exist within the overburden rock. Due to the limited size of the test stand, in order to more accurately analyze the migration and fracture evolution of mining overburden, a 1:50 similarity ratio was selected based on the test-bed size (2500 × 200 × 1300 mm), and the similarity scale coefficient of the physical model as shown in Table 2 [34].

Table 2. Similarity scale coefficient of physical model.

Category	Geometric Ratio	Time Ratio	Density Ratio	Strength Ratio	External Force Ratio	Elastic Modulus Ratio	Poisson's Ratio
Coefficient	1/50	1/10	0.6	0.012	1.2×10^{-6}	0.012	1

Due to the burial depth of coal seam is too large, the model was not simulated to the surface, and the remaining overburden was applied to the top of the model with an equivalent load of 0.18 MPa. Therefore, this overburden has only three inferior key strata in the model, nine equidistant measuring lines are laid on the model, all measuring points are 10 cm apart, and 225 non-coding points are arranged. Combined with the actual mining speed of the panel (6.7 m/d) and the similarity scale coefficient of physical model, the model is advanced at a speed of 10 cm/1.8 h from the right side. The overburden failure characteristics and its structural evolution are shown in Figure 6.

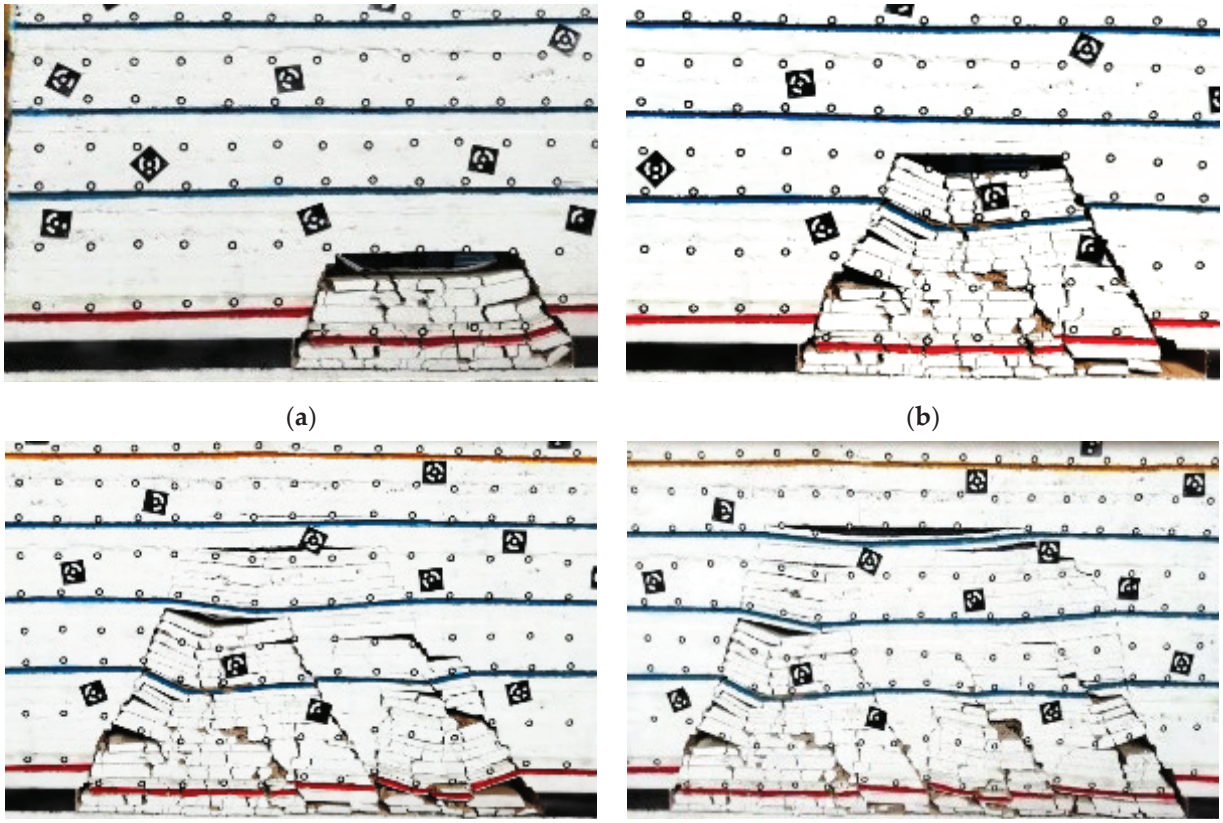

Figure 6. The failure characteristics and evolution of the overburden structure: (**a**) advance 30 m, (**b**) advance 45 m, (**c**) advance 61 m, and (**d**) advance 78.5 m.

From Figure 6, it can be seen that when the face has advanced 30 m, the height of the caved zone of the overburden rock reaches the maximum, at the meantime, the rock strata in the goaf have no bearing effect and only accumulate in the goaf to form a pressure relief area. When advancing 45 m, the masonry beam structure appears in the overburden at the side of the open cut, at which time the overburden failure enters the crack zone range, and the contact state between the middle of the caved zone and the rock strata above gradually changes from no contact to point-surface, line-surface, and surface-surface contact. When advanced 61 m, a temporary masonry beam structure is formed again at the working face, the separation space of the lower rock strata is compacted, and the separation between the upper rock strata is intensified, meanwhile, the overburden structure on the mining side only shows dynamic evolution, and the change of gap distribution mainly occurs on the fracture side of the panel. When it is advanced to 78.5 m, the mining fractures develop below the sub-key stratum, the overburden failure height reaches the maximum, and the breaking angle of the rock stratum at the mining side is smaller than that at the open cut side with distributed asymmetrically. The rock stratum in the middle goaf forms a compacted area due to the closure of the gap, while the two ends of the goaf present a pressure relief area due to the overburden structure. Therefore, when the working face reaches critical mining, the overburden failure height reaches the maximum. The rock stratum gap in the middle of the fracture zone is gradually compacted, and the overburden failure height at goaf boundary and the caved zone in the middle is the main areas where the overburden gaps exist.

4. Mechanism and Discussion of Surface Residual Deformation in Abandoned Goaf

4.1. Influence Factors

The formation of surface residual deformation mainly lies in the overburden gaps, and the distribution of overburden gaps mainly lies in the overburden failure and its structure [35]. Thus, the influencing factors of surface residual deformation are equivalent to that of overburden structure and caved zone, which also is the influence factors of overburden failure height.

1. Overburden lithology: When the overburden is of hard lithology, it is easy to produce fracture and break under the influence of mining, and the overburden failure height is large. Conversely, when it is a soft lithology, the rock stratum is not easy to break and the failure height of the overburden formed by it is small. In addition, it is known from the empirical formula in the Specification that the calculation of the height of the caved zone and fracture zone under the same mining conditions is based on the overburden lithology as an indicator.
2. Coal seam occurrence state: It primarily includes coal seam dip angle, buried depth, etc. The larger the coal seam dip angle is, the saddle shape of overburden failure will gradually change into a parabola shape, which is mainly due to the gradual increase of the tangential sliding force of the overburden along the bedding plane, while the pressure acting on its level becomes smaller, and the broken rock block in the goaf moves downward results in the space above is larger than that below. The influence of coal seam burial depth on overburden failure is mainly reflected in the severity of overburden failure.
3. Roof control methods: It is equivalent to the mining method and determines the overburden failure height, mainly including four types: full collapse, full filling, partial filling, and coal pillar support. When the full caving method is used to manage the roof, the overburden caving is the most sufficient and the failure height is the largest; while for roof management with the full filling method, based on the principle of equivalent replacement, the limited collapse space of the rock stratum results in a small overburden failure height, which is an effective measure to reduce the failure height of overburden, and also a technology to restrain mining disturbance from the source.
4. Mining thickness: It is the main factor affecting the maximum height of overburden failure in high-strength mining. In general, the greater the mining thickness of the coal seam, the larger the space for the collapse of the overlying strata, the higher the height of the water-conducting fracture zone of the rock stratum, and the larger the range of the overburden gaps and mining fractures, thus the potential for the residual deformation of the goaf surface is also increased.
5. Working face size: The smaller values of strike and dip length determine the overburden failure height. When the dip of the working face does not reach full mining, the overburden failure height will increase with the increase of the dip length, and will not be affected by the mining size when it reaches the maximum; only when the size of the working face meets the requirements of full mining, the overburden failure height reaches the maximum value under the geological conditions, and the residual deformation of the goaf surface will also reach the maximum.
6. Advancing speed: The fast-advancing speed of the working face is one of the factors inducing roof disaster. Since the overburden cannot be fully depressurized in a short time, the integrity of the rock stratum after destruction is strong and the gap formed after accumulation in goaf is small. The range of the overburden pressure relief area and adjacent failure area decreases with the increase in work speed. On the contrary, when the advancing speed is low, the scope of overburden failure will increase, thus forming more overburden gaps. For the residual deformation of abandoned goaf, it is also equivalent to the influence of mining time.

In summary, the main factors affecting the residual deformation of goaf are overburden lithology, coal seam occurrence, mining method, mining thickness, working face size, and advancing speed. The influencing factors all affect the residual deformation of the goaf through the height of the fracture zone or the overburden structure, while the residual deformation of the goaf is closely related to the overburden gaps. Since the overburden gaps are mainly concentrated in the fracture zone on both sides of the goaf and the caved zone in the middle, it is necessary to study the compaction deformation characteristics of the broken rock in the caved zone.

4.2. Compaction Characteristics and Discussion of Broken Rock

Combined with the geological conditions of the mine, the sandstone of the caved zone was selected to carry out the compaction deformation test of the broken rock. The test mainly analyzes the influence of particle size, gradation combination, and saturated state on the deformation of broken rock from the perspective of stress-strain, providing a theoretical basis for the formation mechanism and prevention and control ideas of surface residual deformation in abandoned goaf.

4.2.1. Experiment Scheme

The physical and mechanical parameters are tested by processing the test rock sample into a standard sample, and the mechanical parameters are shown in Table 3.

Table 3. Standard physical parameters of sandstone.

Density (g·cm^{-3})	Elastic Modulus (GPa)	Tensile (MPa)	Poisson's Ratio	Friction Angle (°)
2.49	24.9	5.68	0.25	32.4

Crushed stone with a particle size of 0~10 cm is used in the test, and five groups of particle size samples with the particle size of 0~2 cm, 2~4 cm, 4~6 cm, 6~8 cm, and 8~10 cm are sieved, respectively. Crushed rock deformation seepage test system is used to conduct crushed rock compression test. The inner diameter of the test cylinder is 400 mm, the cylinder height is 680 mm, the material is 45 # steel, and the displacement and stress dual control servo loading system is used to achieve dual control of displacement and stress. The test is divided into four groups, with a loading rate of 0.5 kN/s and a load application range of 0~450 kN. The specific scheme is as follows:

(1) The first group mainly studies the pressure-bearing deformation of five groups of broken rock with different particle sizes (0~2 cm, 2~4 cm, 4~6 cm, 6~8 cm, 8~10 cm) under dry and continuous loading.
(2) The second group mainly studies the pressure-bearing deformation of seven groups of broken rock with different grading indexes (n = 0.2~0.8) under dry and continuous loading.
(3) The third group mainly studies the influence of saturated water on the pressure-bearing deformation of broken rock when the gradation index n = 0.2.

Place each group of crushed stones in the test cylinder one by one, so that their natural stacking height is close to 32 cm, and the error between each group is not more than 0.5 cm. The natural stacking height and amount of each group of crushed stones in the test are shown in Table 4.

Table 4. The accumulation parameters of broken rocks with different particle sizes.

No.	Particle Size (cm)	Stacking Height (cm)	Mass (g)	Volume (cm^3)	Density ($g \cdot cm^{-3}$)
1	0~2	32.28	56,338	40,539.92	1.389692
2	2~4	32.11	51,246	40,317.83	1.271051
3	4~6	32.07	47,775	40,277.54	1.186145
4	6~8	32.26	46,387	40,508.67	1.145113
5	8~10	31.91	45,568	40,068.75	1.137245

4.2.2. Results and Discussion

1. Different particle sizes

Using the displacement-stress dual control servo system, the dry crushed stone in the test cylinder is loaded step by step, and the application of axial load and the change of crushed stone displacement with time is recorded in real-time. The stress-strain relationships for the five groups of grain-size crushed stones are shown in Figure 7.

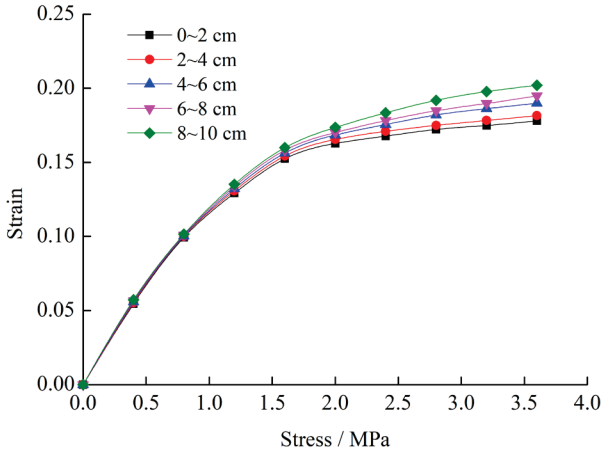

Figure 7. The stress-strain for sandstone with different particle sizes.

It can be seen from Figure 7 that the strain increase rate of the five groups of particle-size crushed stone in the low-stress stage is greater than that in the high-stress stage. At the initial stage, the contact mode between crushed stone particles is mainly point-point, which makes up a very loose skeleton with a large gap size, and connectivity between gravel particles is good, and the deformation develops rapidly. With the increase of stress, a part of crushed stone is compressed and deformed or even broken, small particles fill the gaps to form a more compact structure, and the contact gradually transits from point-point contact to point-face and face-face contact. Meanwhile, the ability of a crushed stone to resist deformation gradually increases, so the strain increases rate in the low-stress stage is greater than that in the high-stress stage.

2. Different gradations

Using the Talbol grading theory was used for the particle size proportioning of different graded crushed stones, and the mass of each group of graded aggregates was specified to be 50 kg, and the continuous loading test of 0~450 kN is carried out for 4 groups of graded crushed stones under different grading indexes. The stress-strain curve of each group of graded crushed stones is shown in Figure 8.

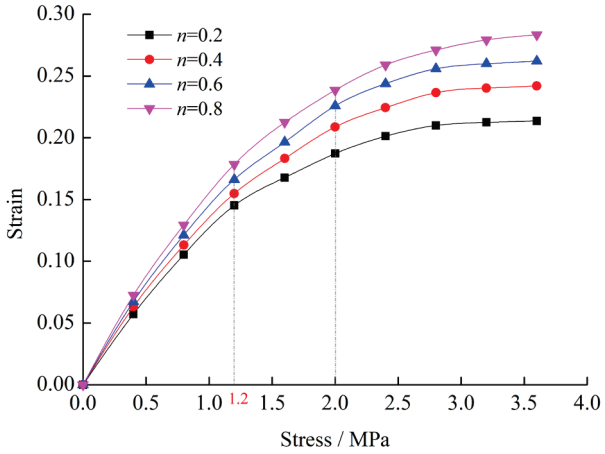

Figure 8. The stress-strain for sandstone with different grading indexes.

It can be seen from Figure 8 that at the initial stage of stress application, the strain of broken rocks in each group of graded increases rapidly under different gradation indexes. When the stress exceeds 1.2 MPa, the strain of crushed stone rises slowly, and the strain gap between each group of crushed stone becomes larger, mainly due to a large number of gaps between different particle sizes of crushed stone, which is easy to deform under stress, and the crushed stone gap is compressed to form. When the stress is greater than 2.0 MPa, the strain gap of each group of the crushed stone changes obviously, mainly because the proportion of large-size crushed stone increases with the increase of grading index, and the porosity is easier to compact with the rise of gradation index, the edges of large-size broken rocks grind each other and become smooth, and the generated small size rock blocks fill the gaps of the rock blocks. Therefore, the crushed stone group with index n has a relatively sizable final strain value.

3. Water-saturated graded broken sandstone

Put the crushed sandstone (50 kg) with n = 0.2 into the test cylinder for a water-saturated compaction test, so that the internal pores of the crushed stone are filled with water. By comparing with the stress-strain relationship of dry broken rock under continuous loading, the results are shown in Figure 9.

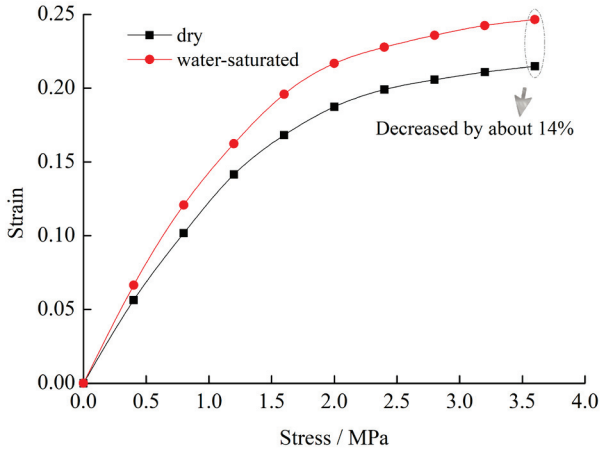

Figure 9. The stress-strain of dry and water-saturated sandstone samples.

As shown in Figure 9, the strain of water-saturated crushed stone under the same stress is obviously greater than that under the dry state. It is mainly because the water weakens the cohesion between the rock particles, water molecules reduce the connection between the internal particles of the rock sample so that the energy required for rock fracture is

reduced, the strength of the crushed stone is diminished, and deformation is more likely to occur under load. Meanwhile, large size crushed stone will be broken into smooth particles again and fill the gap again so that the rock strain increases. In addition, the bearing capacity of broken sandstone is reduced by nearly 14% under the water-saturated influence, which indicates that the water content has a significant impact on the compaction of broken sandstone.

In summary, the compaction of broken rocks in the caved zone is the main factor that causes residual surface deformation in the middle of the goaf, and it is also one of the factors that affect the stability of the overburden structure on both sides of the goaf. It can be seen that the formation mechanism of the surface residual deformation is mainly due to the overburden structure on both sides of the goaf and the compaction of the broken rocks in the caved zone, and the surface shows that the residual subsidence on both sides of the goaf is slightly greater than that in the middle of the goaf.

5. Engineering Applications

Due to the mining time of the west wing of 11 mining area is from 2005 to 2016, the surface will enter a recession period within 2.5–3 years after mining. Therefore, the goaf has entered the stage of surface residual deformation. By setting up a control monitoring network with a spacing of 50 × 100 m above the abandoned goaf, a total of 3 (6 sections) observation lines are arranged in a grid-like, and named line A, line B, and line C, respectively. There are 127 measuring points for Line A, 72 measuring points for Line B and 153 measuring points for Line C. By using RTK monitoring technology of the level D horizontal control network, the surface residual deformation of each measuring point from February 2019 to August 2022 were obtained. The measuring points in the west wing of 11 mining area and its residual subsidence are shown in Figure 10.

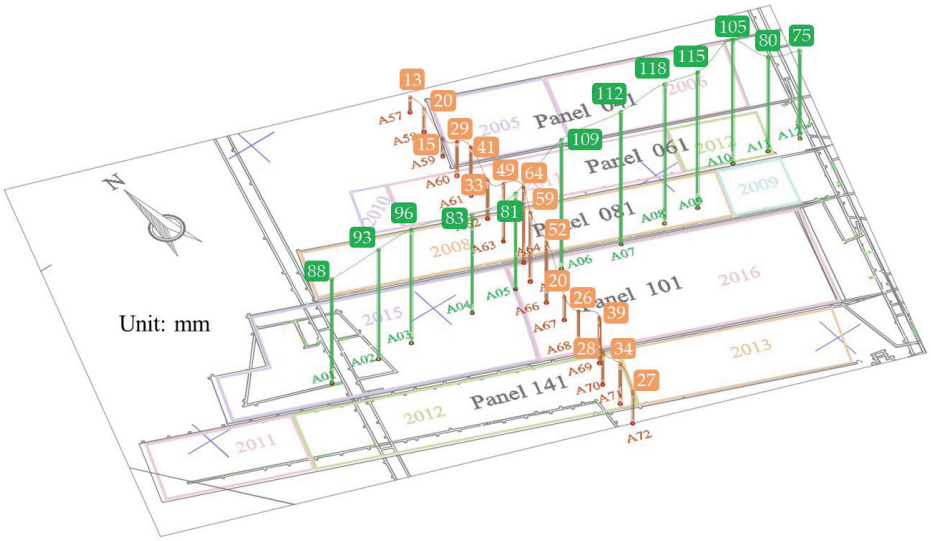

Figure 10. The measuring points and its residual subsidence in the 11 mining area.

As shown in Figure 10, the maximum residual deformation value of A8 is 118 mm, which is located between 101 and 081 working faces. This is mainly due to the late mining time of the 101 working face and the secondary activation of mining overburden rock caused by repeated mining. It also verifies the accuracy that the overburden gaps are mostly concentrated at the overburden structure. In addition, the measuring subsidence at the boundary of the goaf is basically greater than that in the middle goaf, which also further verifies that the gaps on goaf boundary are more than that in the middle goaf. Based on the subsidence curve on the dip, the cumulative subsidence of the measuring point generally shows a change law of first increasing and then decreasing, which is mainly caused by the different mining time. The subsidence curve presents a wave state after passing through

A68, mainly caused by the different positions of measuring points and goaf. It shows that the gap compression at the overburden structure is greater than that at the middle goaf, which again verifies the previous conclusion above. In conclusion, the surface residual deformation above the goaf is closely related to the mining time. The later the mining is completed, the greater the cumulative subsidence of surface residual. For the old goaf (such as the panel 041) that has been mined for more than 15 years, the surface residual deformation is basically 15~20 mm/a, which indicates that surface residual deformation has a long-term characteristic, and the measures should be taken to reduce the generation of residual deformation during the surface utilization above the abandoned goaf.

6. Conclusions

1. Based on the surface response characteristics under the influence of mining, the characteristics of trapezoidal and periodic forward movement of overburden failure during mining were analyzed, and the transmission law of mining fracture up layer by layer with the overburden failure was studied, and the overburden structure was formed at the steep subsidence curve was clarified.
2. The main influencing factors of surface residual deformation in abandoned goaf were analyzed, and the characteristics of broken rock in the caved zone under different conditions (particle size, grading, and water content) were studied and the overburden structure on both sides of the goaf and the compaction of the caved zone where the formation mechanisms of surface residual deformation was revealed.
3. The field-measured data show that the surface subsidence near the goaf boundary was greater than that in the middle goaf, the correctness of the overburden voids distribution and the source of residual deformation in goaf was verified. Meanwhile, the surface residual deformation has long-term and dangerous characteristics were analyzed, which provides a theoretical basis for scientific prevention of the surface residual deformation and the effective utilization of the mining subsidence area.

Author Contributions: Conceptualization, E.B., W.G. and Y.T.; methodology, E.B., W.G. and Y.T.; software, E.B., P.W. and M.G.; formal analysis, E.B., X.L., P.W. and Z.M.; investigation, X.L., P.W. and Z.M.; data curation, E.B. and Y.T.; writing—original draft preparation, E.B. and X.L.; writing—review and editing, W.G. and Y.T.; funding acquisition, E.B., W.G. and Y.T. All authors have read and agreed to the published version of the manuscript.

Funding: This research was funded by the Open Fund of Shaanxi Key Laboratory of Geological Support for Coal Green Exploitation (DZBZ2020-04), the National Natural Science Foundation of China (52104127, 51974105 and 52174108), the Key Project of the National Natural Science Foundation of China (U21A20108), Leading talents in scientific and technological innovation in Central Plains (224200510012), the Key Scientific Research Projects of Colleges and Universities in Henan Province (21A440003), the Henan Science and Technology Research Project (222102320058), and the Open fund of State Key Laboratory of Coal Resources in Western China (SKLCRKF20-01), Program for Outstanding Young Talent Projects of Henan Province (222300420045), Program for Science and Technology Innovation Talents in Universities of Henan Province (21HASTIT024).

Data Availability Statement: Relevant data are listed in the paper.

Conflicts of Interest: The authors declare no conflict of interest.

References

1. Bloch, H.; Rafiq, S.; Salim, R. Coal consumption, CO_2 emission and economic growth in China: Empirical evidence and policy responses. *Energy Econ.* **2012**, *34*, 518–528. [CrossRef]
2. Lin, B.Q.; Liu, J.H. Estimating coal production peak and trends of coal imports in China. *Energy Policy* **2010**, *38*, 512–519. [CrossRef]
3. Bai, E.H.; Guo, W.B.; Tan, Y. Negative externalities of high-intensity mining and disaster prevention technology in China. *Bull. Eng. Geol. Environ.* **2019**, *78*, 5219–5235. [CrossRef]
4. Bell, F.G.; Stacey, T.R.; Genske, D.D. Mining subsidence and its effect on the environment: Some differing examples. *Environ Geol.* **2020**, *40*, 135–152. [CrossRef]

5. Sun, Q.; Zhang, J.X.; Li, M.; Zhou, N. Experimental evaluation of physical, mechanical, and permeability parameters of key aquiclude strata in a typical mining area of China. *J. Clean. Prod.* **2020**, *267*, 122109. [CrossRef]
6. Karakus, M.; Tutmez, B. Fuzzy and multiple regression modelling for evaluation of intact rock strength based on point load, schmidt hammer and sonic velocity. *Rock Mech. Rock Eng.* **2006**, *39*, 45–57. [CrossRef]
7. Jing, Z.R.; Wang, J.M.; Zhu, Y.C.; Feng, Y. Effects of land subsidence resulted from coal mining on soil nutrient distributions in a loess area of China. *J. Clean. Prod.* **2018**, *177*, 350–361. [CrossRef]
8. Booth, C. Groundwater as an environmental constraint of longwall coal mining. *Environ. Geol.* **2006**, *49*, 796–803. [CrossRef]
9. Salmi, E.F.; Nazem, M.; Karakus, M. Numerical analysis of a large landslide induced by coal mining subsidence. *Eng. Geol.* **2017**, *217*, 141–152. [CrossRef]
10. Liu, J.G.; Diamond, J. China's environment in a globalizing world. *Nature* **2005**, *435*, 1179–1186. [CrossRef]
11. Shahbaz, M.; Nasir, M.A.; Hille, E.; Mahalik, M.K. UK's net-zero carbon emissions target: Investigating the potential role of economic growth, financial development, and R&D expenditures based on historical data (1870-2017). *Technol. Forecast. Soc. Chang.* **2020**, *161*, 120255. [CrossRef]
12. Tajdu's, K.; Sroka, A.; Misa, R.; Hager, S.; Rusek, J.; Dudek, M.; Wollnik, F. Analysis of mining-induced delayed surface subsidence. *Minerals* **2021**, *11*, 1187. [CrossRef]
13. Cui, C.Q.; Wang, B.; Zhao, Y.X.; Xue, L.M. Waste mine to emerging wealth: Innovative solutions for abandoned underground coal mine reutilization on a waste management level. *J. Clean. Prod.* **2020**, *252*, 119748. [CrossRef]
14. Li, L.; Wu, K.; Zhou, D.W. Evaluation theory and application of foundation stability of new buildings over an old goaf using longwall mining technology. *Environ. Earth Sci.* **2016**, *75*, 763. [CrossRef]
15. Yuan, L.; Jiang, Y.D.; Wang, K.; Zhao, Y.X.; Hao, X.J.; Xu, C. Precision exploitation and utilization of closed/abandoned mine resources in China. *J. China Coal Soc.* **2018**, *43*, 14–20. [CrossRef]
16. Lyu, X.; Yang, K.; Fang, J.J. Utilization of resources in abandoned coal mines for carbon neutrality. *Sci. Total Environ.* **2022**, *822*, 153646. [CrossRef]
17. Wang, C.H.; Lu, Y.; Qin, C.R.; Li, Y.Y.; Sun, Q.C.; Wang, D.J. Ground disturbance of different building locations in old goaf area: A case study in China. *Geotech. Geol. Eng.* **2019**, *37*, 4311–4325. [CrossRef]
18. Han, C.P.; Zu, F.J.; Du, C.; Shi, L. Analysis of excavation stability and reinforcement treatment of the cutting slope under the influence of old goaf. *Appl. Sci.* **2022**, *12*, 8698. [CrossRef]
19. Li, P.X.; Yan, L.L.; Yao, D.H. Study of tunnel damage caused by underground mining deformation: Calculation, analysis, and reinforcement. *Adv. Civ. Eng.* **2019**, *2019*, 4865161. [CrossRef]
20. Mhlongo, S.E.; Amponsah-Dacosta, F. A review of problems and solutions of abandoned mines in South Africa. *Int. J. Min. Reclam. Environ.* **2016**, *30*, 279–294. [CrossRef]
21. Goulty, N.R.; Al-Rawahy, S.Y.S. Reappraisal of time-dependent subsidence due to longwall coal mining. *Q. J. Eng. Geol.* **1996**, *29*, 83–91. [CrossRef]
22. Guéguen, Y.; Deffontaines, B.; Fruneau, B.; AlHeib, M.; Michele, M.; Raucoules, D.; Guise, Y.; Planchenault, J. Monitoring residual mining subsidence of Nord/Pas-de-Calais coal basin from differential and Persistent Scatterer Interferometry (Northern France). *J. Appl. Geophys.* **2009**, *69*, 24–34. [CrossRef]
23. Statham, I.; Trehame, G. Subsidence due to abandoned mining in the South Wales coalfield, UK: Causes, mechanisms and environmental risk assessment. In Proceedings of the 4th International Conference on Land Subsidence, Houston, TX, USA, 12–17 May 1991.
24. Graniczny, M.; Colombo, D.; Kowalski, Z.; Przyucka, M.; Zdanowski, A. New results on ground deformation in the upper silesian Coal Basin (southern Poland) obtained during the DORIS Project (EU-FP 7). *Pure Appl. Geophys.* **2015**, *172*, 3029–3042. [CrossRef]
25. Blachowski, J.; Kopeć, A.; Milczarek, W.; Owczarz, K. Evolution of secondary deformations captured by satellite radar interferometry: Case study of an abandoned Coal Basin in SW Poland. *Sustainability* **2019**, *11*, 913. [CrossRef]
26. André, V. Surface movement above an underground coal longwall mine after closure. *Nat. Hazards Earth Syst.* **2016**, *16*, 2107–2121. [CrossRef]
27. Cui, X.M.; Zhao, Y.L.; Wang, G.R.; Zhang, B.; Li, C.Y. Calculation of residual surface subsidence above abandoned longwall coal mining. *Sustainability* **2020**, *12*, 1528. [CrossRef]
28. Li, C.Y.; Ding, L.Z.; Cui, X.M.; Zhao, Y.L.; He, Y.H.; Zhang, W.Z.; Bai, Z.H. Calculation model for progressive residual surface subsidence above mined-out areas based on logistic time function. *Energies* **2022**, *15*, 5024. [CrossRef]
29. Guo, Q.B.; Meng, X.R.; Li, Y.M.; Lv, X.; Liu, C. A prediction model for the surface residual subsidence in an abandoned goaf for sustainable development of resource-exhausted cities. *J. Clean. Prod.* **2021**, *279*, 123803. [CrossRef]
30. Fan, H.D.; Lu, L.; Yao, Y.H. Method combining probability integration model and a small baseline subset for time series monitoring of mining subsidence. *Remote Sens.* **2018**, *10*, 1444. [CrossRef]
31. Sun, Q.; Zhou, N.; Song, W.J.; Zhao, X. Risk assessment and prevention of surface subsidence under buildings by cemented paste filling and strip mining methods: A case study. *Adv. Civ. Eng.* **2021**, *2021*, 9965279. [CrossRef]
32. Vervoort, A. The time duration of the effects of total extraction mining methods on surface movement. *Energies* **2020**, *13*, 4107. [CrossRef]
33. Yu, Q.G.; Zhang, H.X.; Deng, W.N.; Zou, Y.P. Analysis of influencing factors of surface skewed subsidence based on key strata theory. *J. China Coal Soc.* **2018**, *43*, 1322–1327. [CrossRef]

34. Li, H.C. *Similar Simulation Test of Ground Pressure*; China University of Mining and Technology Press: Xuzhou, China, 2017.
35. Bai, E.H.; Guo, W.B.; Tan, Y.; Guo, M.J.; Wen, P.; Liu, Z.Q.; Ma, Z.B.; Yang, W.Q. Regional division and its criteria of mining fractures based on overburden critical failure. *Sustainability* **2022**, *14*, 5161. [CrossRef]

sustainability

MDPI

Article

Which Provincial Regions in China Should Give Priority to the Redevelopment of Abandoned Coal Mines? A Redevelopment Potential Evaluation Based Analysis

Yuliang Yang [1,2] and Chaoqun Cui [2,3,*]

[1] School of Coal Engingeering, Shanxi Datong University, Datong 037003, China
[2] School of Energy and Mining Engineering, China University of Mining and Technology (Beijing), Beijing 100083, China
[3] School of Mining and Geomatics Engineering, Hebei University of Engineering, Handan 056038, China
* Correspondence: chaoquncui@126.com

Abstract: Abandoned mines have a double nature consisting of resources and assets, and their rational redevelopment is one of the most important practices of the recycling economy. To direct the layout of the regional abandoned mine redevelopment, this paper constructs a comprehensive assessment framework for abandoned mine redevelopment potential based on the driving force–state–response (DSR) model. It is quantitatively evaluated by three-dimensional cloud models, and the results are coupled using a four-quadrant approach. From the perspective of space control, this paper proposes classification principles of redevelopment potential and redevelopment sequence and summarizes the important policy implementations for each category. The paper studies the redevelopment potential of abandoned mines from the provincial perspective in 25 coal-producing provinces of China. The results indicate that not all areas with high resource potential are suitable for redevelopment. In the northern and western regions, the regional abandoned mines have high resource potential and strong redevelopment drivers. However, the spatial pattern of the suitability of the development conditions is not distributed in the same way as the resources. The distribution of the abandoned mine redevelopment potential reveals that the eastern and east-central regions should give priority to the construction of demonstration projects. Different driving force scenarios confirm that most provinces have no obvious driving factor preference, with a few exceptions. This evaluation model is established from a more comprehensive perspective and is a valuable aid for decision makers when arranging abandoned mine regeneration projects.

Keywords: abandoned coal mine; redevelopment potential; cloud model; DSR model; redevelopment sequence

1. Introduction

An abandoned mine, also known as a mine closure or a closed mine, refers to the mine being closed permanently due to the depletion of its reserves or because of other premature closure reasons, such as the failure to meet safe mining conditions, community pressures, no standard regulations or policies, etc. [1] (Amirshenava and Osanloo, 2018). Along with the circular economy gaining popularity in China, people have paid more and more attention to the redevelopment of abandoned mines, not only because they contain a large number of reusable energy resources, such as residual coal and coal-bed methane, but also because they have abundant mine drainage, geothermal energy, underground space, tourism resources, etc. [2]. The inappropriate and irrational use of abandoned mines brought not only a huge waste of coal but also serious deterioration. Such severe influences on-site and off-site are outstandingly shown in the sharp economic recession, unemployment, ecological environment pollution, and so on [3–5]. Therefore, from the perspective of China's energy policy, environmental policy, and governance in general, the

redevelopment of abandoned mines is imperative to mitigate the unintended consequences of the energy structure adjustment policies [6].

Abandoned mine redevelopment (AMR) refers to the reconfiguration of its functions by engineering, biological, and other measures to maximize the resource value. For example, the old underground tunnels can be reused as energy storage peaking power stations or heating centers [7], and the mining subsidence area can be reconstructed as a new energy base [8]. To improve the efficiency and quality of AMR and avoid the situation which is blossoming everywhere, it is urgent to make a quantitative assessment of the abandoned mine redevelopment potential (AMRP).

The AMRP means the potential ability that can be brought into play to promote the sustainable development of the AMR industry in competition with other regions under the comprehensive action of resource endowment, economic, social, and environmental demand, and social support capacity [9]. Consequently, as the basic work of AMR sequence planning, the assessment of AMRP has an important influence on maximizing the value of projects and reducing the investment risk [10].

As the world's largest producer and consumer of coal, China still maintains high-intensity coal mining. With the gradual implementation of the policy on reducing the coal capacity, the coal mines with poor reserves (reserves–production ratio of less than 5 years) or with backward productivity are being closed, which is leading to a drastic increase in the number of closed mines [11]. In 2016–2017 alone, the number of closed coal mines in China was about 3000. The number of coal mines in China began to decrease from more than 14,000 in the early stage of the 12th five-year plan to about 5800 by the end of 2018. Despite China having a relatively large number of abandoned mines, the resourceful reutilization effect of the abandoned mines is unsatisfactory. AMR is faced with many challenges. The most prominent manifestation is that the assessment system of the AMRP is not perfect and lacks the necessary data for supporting the layout of the redevelopment industry, which directly affects the redevelopment quality. The absence of a quantitative evaluation framework of the abandoned mines' values in China seriously hinders the redevelopment advancement.

According to the search conducted in Scopus, Google Scholar, and Crossref, there are few references for the assessment of AMRP. Currently, the scattered but valuable research is mainly concentrated on the aspects of value identification, management measures, and the development sequence of single resources such as mined land, industrial heritage, mining waste, and underground space. Bakhtavar et al. [12] studied the reuse of mined land and pointed out that the reuse model must be decided reasonably according to the effective evaluation of the economic factors and regional conditions. Sutherland [13] emphasized the industrial tourism value of abandoned mines and concluded that the development of industrial heritage should be combined with regional transformation to ensure the coordinated development of the economy and the environment. Lèbre et al. [14] revealed the recycling value of mining waste from three critical aspects: time, the extractive strategy, and the economic context. Kubit [15] comprehensively considered the influence of the regional economic development level, the labor force level, local employment, market demand, energy consumption, and the environmental conditions on the utilization of abandoned mining land after reclamation. Li et al. [16] proposed a driving force–state–response (DSR) model of abandoned coal mine industry square redevelopment, which integrates planning, land rehabilitation, and ecology, and analyzed the factors influencing the DSR framework. It can be seen that the current research is not comprehensive and in-depth with regard to the basic strategic issues, such as the study of regional abandoned mine redevelopment potential and redevelopment sequence. To our knowledge, no study has explored AMRP from the perspective of a provincial scale, and there is no quantitative assessment framework for AMRP, which presents an opportunity for the contributions of this paper.

Through analyzing the current research status and problems, this paper proposes a comprehensive indicator system for AMRP, including resource potential, driving force,

and the suitability of development conditions based on the DSR mode. A complete index system is essential for assessing the comprehensive performance of AMRP. To reflect the contributions of the indicators, this paper calculates the indicators' weights by the improved analytic hierarchy process (IAHP) method to avoid the coincidence examination and the adjustment of the judgment matrix. Then, the cloud model is employed to calculate the potential level of the resource potential, the driving force, and the suitability of the development conditions to take into account, respectively, the randomness and fuzziness of the indicators. The level of AMRP is determined by these three dimensions, and this paper therefore uses the four-quadrant method with a bubbles map to couple the results of the driving force (D), the resource potential (state), and the suitability of the development conditions (response) and, finally, to comprehensively classify the redevelopment potential and redevelopment sequence of regional abandoned mine development. Then, ArcGIS is used to discuss the spatial patterns of the three dimensions and to analyze the regional differences, respectively.

2. Components of Abandoned Mine Redevelopment Potential

Based on the PSR model developed by the United Nations Commission on Sustainable Development (UNCSD), the driving force–state–response (DSR) model was constructed for sustainable assessment [17]. According to the DSR framework, this paper proposed the assessment system of the AMRP from three dimensions. The interactions of the dimensions are demonstrated in Figure 1, where "driving force" is the fundamental factor that causes the changes of the "state", "State" is the constraint condition for the realization of "Driving force" and the basic basis for the formulation of "Response", and the "Response" is an important way to promote the change of the "State".

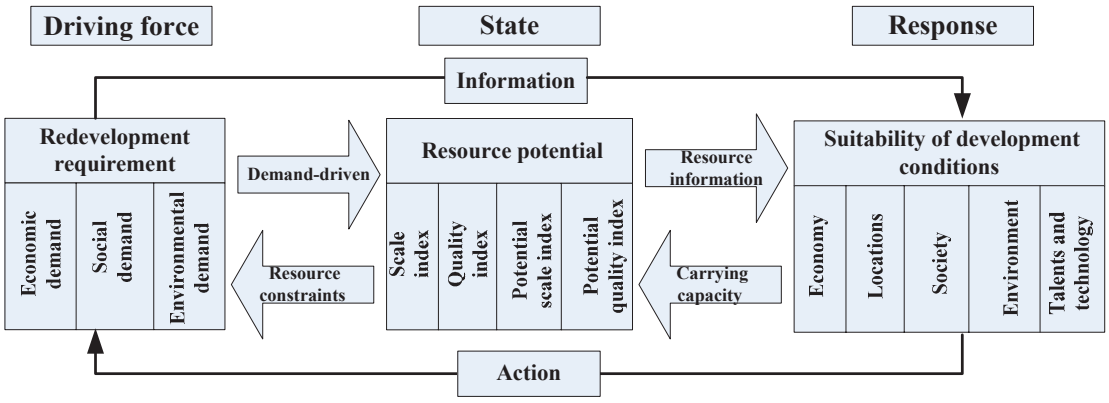

Figure 1. DSR model of abandoned mine redevelopment potential.

2.1. Driving Force

As AMR can contribute to the region socially, economically, and ecologically, the driving force is oriented to the performance of AMR [18]. Due to the performance being difficult to express quantitatively, this paper adopts the requirements of the regional sustainable development of mining and society to reflect the driving force indirectly. The more in demand it is in the region, the better the benefit and the stronger the driving force. According to the triple bottom line principle of sustainability, the demands of AMR are mainly identified from the economic, social, and environmental aspects [19,20]. The economic demand indicators are selected from the impacts of mine closure on the regional economy and financial revenue. Due to the absence of added value data on the coal mining industry, this paper replaces this indicator with mining investment. The social demand indicators stem from two aspects: the influences of mine closure on society and the resource constraints of social development. The environmental demand indicators come from the environmental carrying capacity. As the emissions data of wastes in the provincial area are unavailable, this paper uses the "Per unit GDP energy consumption" to indirectly reflect

the environmental pollution. All the detailed indicators of driving force are listed in Table 1.

Table 1. Summary of driving force indicators.

Principle	Criteria	Indicators	Measure	Reference
Driving force	Economic demand	Share of mining investment D_1 (‰)	Investment of mining/Total investment	Cui et al. [21]; Cao [22]
		Share of resource tax D_2 (%)	Resources tax/Tax revenue	Batterham [23]; Groth and Schou, [24]
	Social demand	Share of the average wage of mining staff D_3	The wage of mining employees/Average annualwage	Unger et al. [25]; Nehring and Cheng [26]
		Share of mining staff D_4 (‰)	Mining employees/Total employees	Amirshenava and Osanloo, [1]; Laurence [19]
		Population density D_5 (people/km^2)	Total population/Total area	Wang et al. [27]; Volk et al. [28]
		Urbanization rate D_6 (%)	Urban population/Total population	Ruan et al. [29]; Zhang et al. [30]
	Environmental demand	Per unit GDP energy consumption D_7 (tons/CNY 10,000)	Unit GDP energy consumption	Gorman and Dzombak [3]; Mishra et al. [31]
		Vegetation coverage D_8 (%)	Coverage space of green areas/Total area	Laurence [19]; Amirshenava and Osanloo [20]

2.2. State

The "State" refers to the basic conditions of the abandoned mines, which reflects the resource potential available for redevelopment. Due to a large number of abandoned mines, various types of residual resources, and the shortage of value classification standards for the various resources, it is difficult to recognize the value of the abandoned mine and evaluate the resource potential of the regional abandoned mines. Therefore, from the perspective of data availability and quantitative analysis, this paper adopts the scale index and quality index to measure the resource ontology characteristics of the abandoned mines [32]. The scaled index refers to the number of abandoned mines in a region, and a large number of abandoned mines is certain to bring out industry-scale effects [33]. The quality index is explained as the average capacity of the regional closed mines. The fact is that most of the small-scale mines operated using poor mining technology, which resulted in serious damage to the underground space. Moreover, the incomplete mine information causes the low redevelopment value of these mines. Therefore, the larger the capacity, the easier the abandoned mines will be to redevelop. The quantity and quality of the "potential resources" of the abandoned mines are the important basic foundation for future redevelopment. These indicators are the final determinants of whether the regional abandoned mines have the development possibility in the future. To facilitate quantitative analysis, the number of existing mines and the average capacity of these mines are adopted to reflect the value characteristics of the potential resources. The indicators of resource potential are presented in Table 2.

Table 2. Summary of resource potential indicators.

Principle	Criteria	Indicators	Measure	Reference
Resource potential	Resources status index	Scale index R_1 (a)	Number of closed mines	Chang et al. [34]; Caulk et al. [35]
		Quality index R_2 (Mt/a)	The average capacity of closed mines	Bakhtavar et al. [12]; Naidu et al. [36]
	Potential resources index	Potential scale index R_3 (a)	Number of existing mines	Mishra et al. [26]; Zhang et al. [37]
		Potential quality index R_4 (Mt/a)	The average capacity of existing mines	Nehring and Cheng [26]; Wang et al. [38]

2.3. Response

The evaluation of AMRP cannot exist away from the regional conditions [25]. The "response" mainly considers the support degree of the local development conditions in the economy, infrastructure, technology, governmental ability, and so on. This paper uses the suitability of development conditions to reflect the response of a region. It should be pointed out that the locational conditions directly affect the redevelopment potential [39]. If the locational conditions are extremely good, the mail addressed to the area will get sent elsewhere. The better the support, the stronger the support degree became. Based on the works of the literature reviews, this paper classified the suitability of the external conditions into economy, locational conditions, talent science and technology, environmental support, and social support. The indicators of the response are shown in Table 3.

Table 3. Summary of the suitability of redevelopment condition indicators.

Principle	Criteria	Indicators	Measure	Reference
Suitability	Economic support	GDP S_1 (CNY 100 million)	–	Unger et al. [25]; Bangian et al. [40]
		Disposable income S_2 (per capita)	–	Gorman and Dzombak [3]; Bangian et al. [40]
	Locational conditions	Road area ratio S_3 (%)	Road area/Total area	Kubit [15]; Cui et al. [21]
		Degree of openness S_4 (%)	Foreign investment/GDP	Song et al. [41]; Lee and Chou [42]
		Share of tertiary industry S_5 (%)	The GDP of tertiary industry/GDP	Chang et al. [34]; Zhu et al. [43]
	Talents and technology	Research investment level S_6 (%)	The funds of R&D/GDP	Song et al. [41]; Miremadi et al. [44]
		Share of talents S_7 (people)	University and College student enrollmentper 100,000 persons	Wang et al. [27]; Zhou et al. [45]
	Environmental support	Industrial pollution control investment level S_8 (‰)	Investment in industrial pollution control/GDP	Cui et al. [21]; Chang et al. [34]
		Share of environmental protection charge S_9 (%)	Environmental protection charge/Financial expenditure	Naidu et al. [36]; Bangian et al. [40]
	Social support	Social security and employment S_{10} (%)	Social security and employment expenditure/Financial expenditure	Chang et al. [34]; Knierzinger and Sopelle [46]
		Expenditure for S. E. C. H S_{11} (%)	Science–education–culture–health expenditure/Financial expenditure	Cui et al. [21]; Wang et al. [47];
		Share infrastructure investment S_{12} (%)	Investment in electricity, gas, water, traffic, transport, storage, post/Fixed assets	Wang et al. [27]; Zhang et al. [30]

3. Methodologies

3.1. Cloud Model for Abandoned Mine Redevelopment Potential

3.1.1. The Basic Theory of the Cloud Model

The evaluation of potential is a multi-dimensional decision-making process, and the evaluation method should take into account the randomness and fuzziness of uncertain concepts to obtain more scientific results. The cloud model is a powerful tool to realize the transformation between the quantitative concepts and the qualitative data by cloud generators. The forward cloud generator is used to convert the cloud model to the specific value. The algorithm is described in Table A1. The one-dimensional normal cloud, constructed based on the normal distribution and Gaussian membership function, is a

very important cloud model with general applicability. It has been widely applied in environmental assessment [48], risk assessment [49], artificial intelligence [50], and so on. The normal cloud model discards the traditional membership function but uses three numerical features, namely expected (*Ex*), entropy (*En*), and super entropy (*He*), to describe the fuzziness and randomness of the indicators. The description of each parameter and the calculation formulas are shown in Table 4 by referring to [21]. To illustrate the cloud model more clearly, we present a cloud figure corresponding to the cloud parameters (0.5, 0.1, 0.02). It can be seen in Figure 2 that the expectation value is 0.5 with a variation range (0.2–0.8) based on the "3En criterion". The span of the cloud image reflects the fuzziness, and the cloud image thickness interprets the randomness of the concept.

Table 4. Descriptions of parameters.

Parameters	Original Descriptions	Algorithm of Cloud Parameter
Ex	The best sample point of concept quantization	$Ex_{ij} = \left({x_{ij}}^{\min} + {x_{ij}}^{\max}\right)/2$
En	Fuzzy degree of a qualitative concept	$En_{ij} = \left({x_{ij}}^{\max} - {x_{ij}}^{\min}\right)/2.355$
He	Uncertain degree of entropy	Determined by testing results

Note: the ${x_{ij}}^{\min}$ and ${x_{ij}}^{\max}$ represent the minimum and maximum values of one indicator with a bilateral constraint.

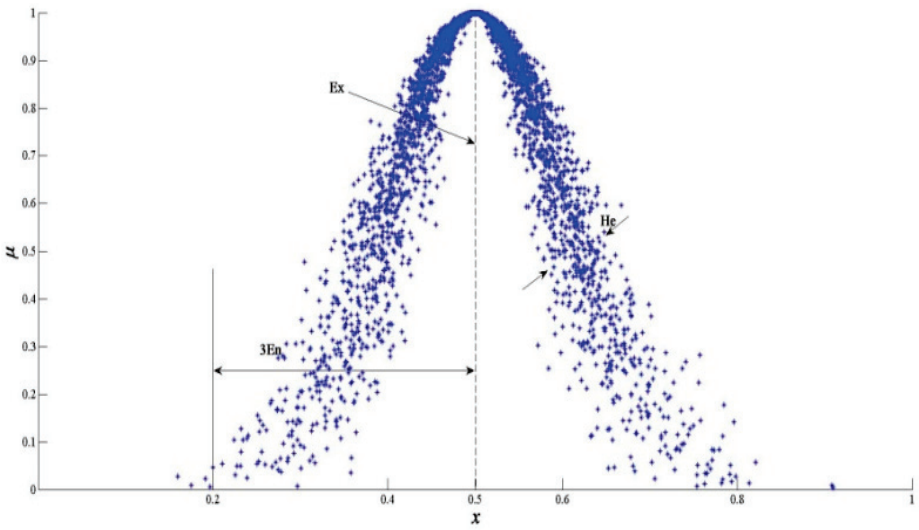

Figure 2. Normal cloud model corresponding to an indicator.

3.1.2. Evaluation Process for AMRP Based on Cloud Model

The assessment processes by the normal cloud method are shown as follows:

Step 1: Set the indicator sets, weight sets, and estimation sets

Based on the multidimensional decision theory, the paper proposed three indicator sets, $U_1 = \{D_1, D_2, \ldots, D_8\}$, $U_2 = \{R_1, R_2, R_3, R_4\}$, and $U_3 = \{S_1, S_2, \ldots, S_{12}\}$, where the elements of these sets are derived from the driving force, the resource potential, and suitability of the development condition, respectively. Accordingly, there are three weight sets $W_1 = \{WD_1, WD_2, \ldots, WD_8\}$, $W_2 = \{WR_1, WR_2, WR_3, WR_4\}$, and $W_3 = \{WS_1, WS_2, \ldots, WS_{12}\}$ to respond to the three indicator sets. The estimation set can be described as V = $\{V_1, V_2, \ldots, V_5\}$ = {Lower, Lower, Moderate, High, Higher}, where the number 5 represents 5 assessment grades.

Step 2: Grade the cloud model

The indicators' intervals are first determined by the mean variance classification method. Then, the cloud parameters of all the indicators can be calculated by the computation formula given in Table 4. The cloud parameters of the indicators used in this paper are shown in Table A2.

Step 3: Obtain the certainty degrees of the indicators

Inputting the collected basic data of the 24 indicators into the forward cloud generator and calculating the average membership value by repeating 100 times, we can obtain the subordinate degrees of the evaluated indicators that belong to different grades. The three membership matrixes U_i (i = 1, 2, 3) are obtained by Equation (1):

$$U_i = \begin{vmatrix} \mu_{11} & \cdots & \mu_{15} \\ \vdots & & \vdots \\ \mu_{n1} & \cdots & \mu_{n5} \end{vmatrix} \quad (1)$$

where n refers to the indicator number of each dimension, and 5 represents the assessment grades.

Step 4: Determine the level of the three dimensions

Combining the weight matrices W_i (i = 1, 2, 3) calculated in Section 3.2, the grade memberships of the different dimensions are acquired by Equation (2):

$$R = W \times U \quad (2)$$

where $R = (r_1, r_2, \cdots, r_5)$, and r_j indicates the degree of membership that belongs to C_j (j = 1, 2, 3, 4, 5). The unfitness of the maximum membership principle could be overcome by the feature value of grades (FVG) for the results quantification, and the calculation formula is given in Equation (3). The final assessment results are demonstrated in Table A3.

$$R = \sum_{k=1}^{5} kR_k / \sum_{k=1}^{5} R_k \quad (3)$$

3.2. Indicators Weights by Improved AHP

The analytic hierarchy process (AHP) is the most common method for determining the weight [51]. However, with the relatively complex indicator system of AMRP (three dimensions with 24 indexes), there are some problems in the AHP. The major problem in the practical application is how to examine and correct the consistency of the judgment matrix, which greatly limits its application. For the sake of the efficient determination of the indicators' weights, this paper adopts the scale-extending method to improve the traditional AHP (IAHP). The construction processes of the judgment matrix by the IAHP are as follows. Firstly, all the criteria layer indicators are to be ranked according to the order of their importance. The importance value as judged by the individual expert's opinion is referred to the nine-point scale proposed by Saaty (see Table A4). The obtained importance sequence of the indicators is set as $x_1 > x_2 > x_3 > \cdots > x_n$. Then, the judgment matrix R which has a satisfactory consistency is shown in Equation (4). The indicators' weights can be calculated by Equation (5).

When the criteria layer indicators' weights are determined, we can determine the index layer indicators' weights by the same algorithm. The global weights of all the indicators are calculated by multiplying the criteria layer indicators' weights by the corresponding index layer indicators' weights. The improved AHP method avoids the coincidence examination and the adjustment of the judgment matrix, which simplifies the calculation and defines the weighing more scientifically and more properly.

$$R = \begin{vmatrix} 1 & t_1 & t_1t_2 & t_1t_2t_3 & \cdots & t_1t_2\cdots t_{n-1} \\ 1/t_1 & 1 & t_2 & t_2t_3 & \cdots & t_2t_3\cdots t_{n-1} \\ 1/t_1t_2 & 1/t_2 & 1 & t_3 & \cdots & t_3t_4\cdots t_{n-1} \\ 1/t_1t_2t_3 & 1/t_2t_3 & 1/t_3 & 1 & \cdots & t_4t_5\cdots t_{n-1} \\ \vdots & \vdots & \vdots & \vdots & \vdots & \vdots \\ 1/t_1t_2\cdots t_{n-2} & 1/t_2t_3\cdots t_{n-2} & 1/t_3t_4\cdots t_{n-2} & 1/t_4t_5\cdots t_{n-2} & \cdots & t_{n-1} \\ 1/t_1t_2\cdots t_{n-1} & 1/t_2t_3\cdots t_{n-1} & 1/t_3t_4\cdots t_{n-1} & 1/t_4t_5\cdots t_{n-1} & \cdots & 1 \end{vmatrix} \quad (4)$$

$$w_i = \sqrt[n]{\prod_{j=1}^{n} r_{ij}} \Big/ \sum_{i=1}^{n} \sqrt[n]{\prod_{j=1}^{n} r_{ij}} \quad (5)$$

where w_i is the weight value of the i-th indicator given by an individual expert; r_{ij} is the value of the preference of the i-th compared to the j-th element.

Due to the weights being determined by a group of experts, the experts' preferences expressed by the IAHP judgment matrix in group decision making should be effectively integrated. The most common way is to fuse all the experts' judgment matrices into one judgment matrix by the weighted geometric average (WGA) method [51]. The judgment matrix elements are calculated according to Equation (6):

$$a_{ij} = (a_{ij}, 1)^{2_1} \times (a_{ij}, 2)^{2_2} \cdots (a_{ij}, m)^{2_k} \quad (6)$$

In Equation (6), k represents the number of experts, (a_{ij}, k) is the matrix element of the k-th expert, and λ_k indicates the weight of each expert. As the weight of the experts is difficult to determine, this article assumes that the importance of each expert is of equal weight; so, Equation (6) can be simplified as Equation (7). The final weights results are listed in Table 5.

$$a_{ij} = \sqrt[k]{(a_{ij}, 1) \times (a_{ij}, 2) \cdots (a_{ij}, m)} \quad (7)$$

Table 5. Weights of indexes for AMRP.

Indicator	D_1	D_2	D_3	D_4	D_5	D_6	D_7	D_8	R_1
Weight	0.2952	0.1148	0.0495	0.0627	0.1221	0.0957	0.0962	0.1638	0.1190
Indicator	R_2	R_3	R_4	S_1	S_2	S_3	S_4	S_5	S_6
Weight	0.2210	0.2904	0.3696	0.2665	0.1435	0.1696	0.1120	0.0384	0.0434
Indicator	S_7	S_8	S_9	S_{10}	S_{11}	S_{12}			
Weight	0.0266	0.0512	0.0288	0.0156	0.0156	0.0228			

Note: *D*, *R*, and *S* correspond to 3 criteria in Tables 1–3, and each criterion has its representative indexes. For example, D_1, D_2; R_1, R_2.

4. Results and Discussion

4.1. Spatial Patterns of AMRP

Because a coal mine that has been closed for many years is hard to reuse (except for the land and part of the facilities), this paper mainly focuses on the mine's closed redevelopment since the implementation of the coal capacity cut policy in 2016. Based on the basic data collected in Tables 1–3 in 2017, this article adopts the normal cloud model to assess the grades of abandoned mine resource potential, the driving force, and the development condition suitability, respectively. The feature value of the grade results is shown in Table 6. The potential evaluation results of the three dimensions are divided into 5 grades by the Jenks method in ArcGIS 10.2, and the grade distribution diagrams are obtained through the technology of spatial visualization. As can be seen in Figure 3a–c, the darker the color, the higher the grade. To support the demonstration and analysis of the results, this paper also presents a spatial distribution diagram that reflects the information on the total coal consumption, the economic aggregate, and the basic reserves of coal in 2017 in Figure 3d. Furthermore, the per capita water resources and the number of mines and the coal production capacity by region in China are given in Figure 3e,f, respectively, to compare the evaluation results.

Table 6. The results of FVG by cloud model-based assessment approach.

Provinces	FVG_D	FVG_R	FVG_S
BJ	2.2847	2.9734	3.2224
HE	2.6134	2.4853	2.6675
SN	3.2856	4.2241	2.4914
IM	4.1816	3.8994	2.1749
LN	2.8181	2.7182	2.9173
JL	2.1992	1.5017	1.7978
HL	3.1129	2.5864	1.7260
JS	2.6535	2.8650	4.0202
AH	2.3694	3.3482	2.5481
FU	1.6831	1.2059	3.1962
JX	1.5874	1.9861	2.0699
SD	2.7071	2.8110	3.7028
HA	2.3323	2.4206	2.8950
HB	1.8728	1.4041	2.8215
HN	1.7588	2.4293	2.6578
GX	1.4890	1.6063	1.7661
CQ	2.1834	1.4982	2.4834
SC	1.9476	2.4475	2.4940
GZ	2.5363	2.5652	1.4699
YN	1.8492	1.4198	1.5801
SX	2.9681	3.4581	2.1046
GS	2.6743	2.0523	1.7637
QH	3.4969	1.2526	1.6723
NX	3.8297	3.2973	2.3382
XJ	4.0099	2.9757	1.5724

Note: Table A5 lists the 25 provincial administrative units used for this study, with their abbreviations. FVG_D, FVG_R, and FVG_S are the feature values of the grades of the driving force, resource potential, and the suitability of development conditions, respectively.

The driving force score is shown in Figure 3a; the provinces with a high driving force ($FVG_D \geq 2.96$) are Inner Mongolia, Xinjiang, Ningxia, Shanxi, and Shaanxi, which belong to the northwest region. Combined with Figure 3d, it can be seen that the richer the province in terms of natural resources, the stronger its driving force ranking. However, these provinces' economies rely heavily on coal production. Such a phenomenon is outstandingly shown in three aspects: the high proportion of the added value of the coal industry, the huge coal consumption, and the high proportion of mining workers. With the changing international environment and market environment, the traditional industrial strategy of resource exploitation and simple economic structure would suffer more. As can be seen in Figure 3e, the distribution of water resource reserves is the reverse of that of the coal resources. As the carriers of ecological benefits, the water resources have been seriously damaged by the processes of coal exploitation. If the water resources are not effectively protected in the process of mine closure, the pollution and destruction will be further aggravated. With the continuous implementation of the policy of cutting the coal capacity, the development of these provinces with severe overcapacity will face more sustainable development problems, which could lead to a strong endogenous impetus for abandoned mine redevelopment [6]. The driving force of the southern provinces is relatively weak. The reason can be explained by two factors: the relatively optimized industrial structure and the low dependence on resource exploitation [43]. It should be noted that the driving force of some of the eastern provinces which have satisfactory economic situation, such as Shandong, Jiangsu, and Hebei, is stronger than that of the southern provinces, which may be caused by overpopulation density, lack of water resources, and strong resource constraints [52].

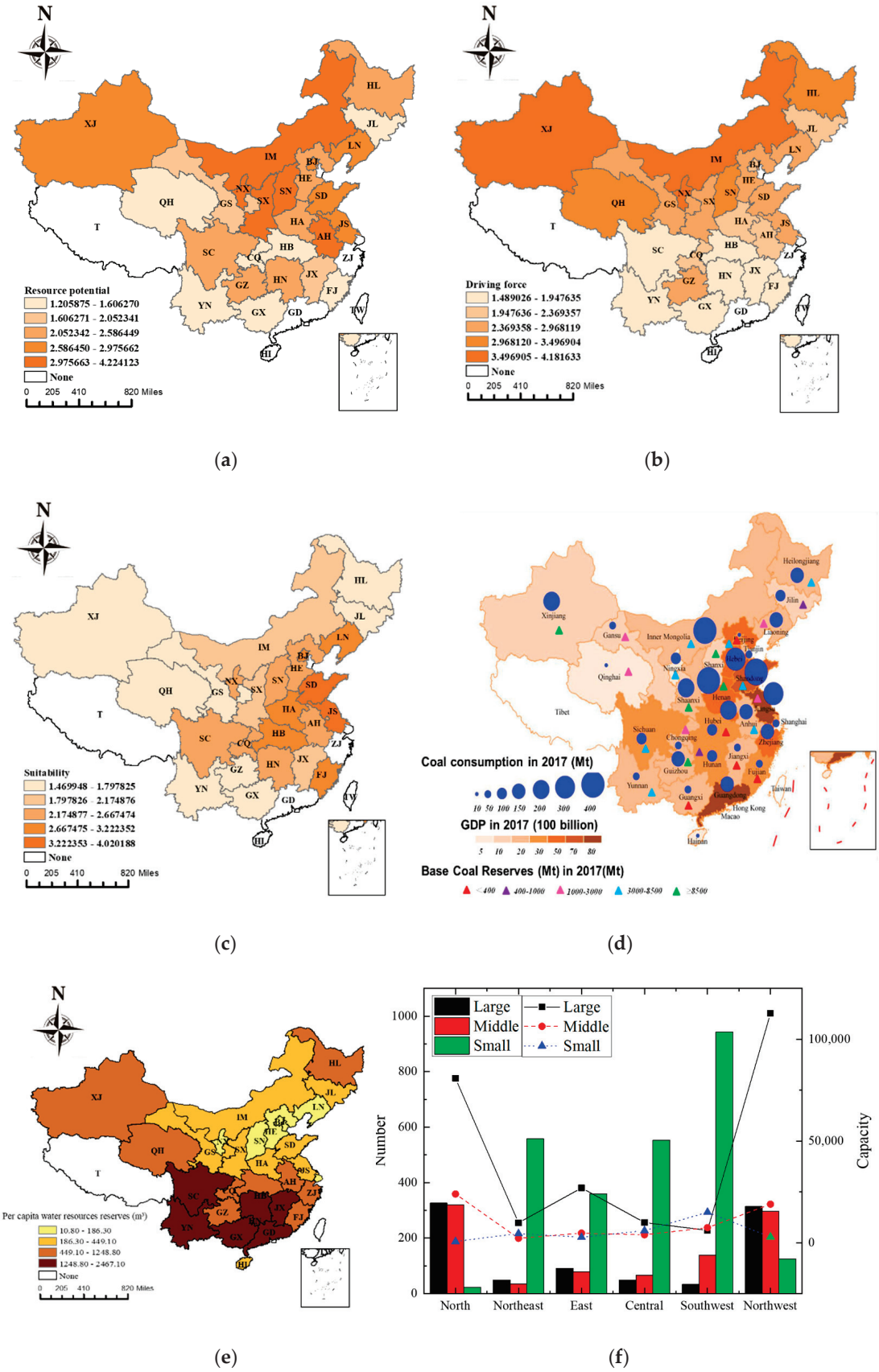

Figure 3. Spatial distribution in three dimensions of AMRP.

In terms of the resource potential demonstrated in Figure 3b, the areas with high resource potential ($FVG_R \geq 2.97$) include Shanxi, Inner Mongolia, Shaanxi, Ningxia, Xinjiang, Anhui, and Beijing. On the whole, the distribution of the abandoned mines' resource potential corresponds to the reserve distribution of the coal resources, as shown in Figure 3d. It can be seen in Figure 3f that in north and northwest areas, the medium and large mines occupy the dominant position, while in the southwest, central, and northeast regions, the coal mines are driven mainly by small-scale operations. According to the 13th five-year plan of the coal industry [53], the central and eastern provinces such as Beijing and Anhui should compress the scale of coal production, and the northern and western provinces need to harmonize the environmental protection and coal mining due to the fragile ecological environment. Therefore, with the background that the country is devoted to reducing excess coal capacity and strengthening ecological protection, the resource potential of these provinces, which have a long history of coal mining and many backward mines, is high. As for the southern provinces, such as Fujian, Jiangxi, Guangxi, Sichuan, and Yunnan (southwest in Figure 3f), it is necessary to speed up the closure of coal mines because of the sporadic distribution of resources and backward production capacity. However, even though the numbers of abandoned mines look great, the vast majority of them belong to small mines. That is why the southern provinces have a low resource potential.

The suitability of the development conditions in China has greater diversity among various regions, as shown in Figure 3c. The reasons could be described by the fact that the differences in regional economic development, geographical location, and traffic conditions directly affect the level of suitability. The distribution pattern of this indicator can be described as follows: the east region is the best, followed by the middle, and the west and southwest are the weakest [21]. As can be seen in Figure 3d, relative to the western regions, the middle and east regions, including Beijing, Shandong, Jiangsu, Fujian, and Liaoning, have a good economic development basis and regional advantage. Therefore, according to the theory of the grades development, the abandoned mine redevelopment industry should give priority to the mining areas of the eastern and central regions because these are the regions with high resource potential and strong driving forces.

4.2. Category Classification of Redevelopment Potential and Redevelopment Sequence

Considering that the AMRP is influenced by three dimensions, this paper adopted the four-quadrant method combined with a bubbles map (Figure 4) to comprehensively position the AMRP level into specific categories, and finally, it sorted the four quadrants according to different goal orientations. Based on the comprehensive consideration of the basic conditions of the abandoned mines and the suitability of the development conditions, this article proposed the classification principles of "resource advance and coordinate development" and divided the AMRP into five classes: higher, high, moderate, low, and lower. Figure 5 is the scatter diagram with the values of the three dimensions of the 25 provinces. It is divided into four quadrants according to the feature value of the grade medians of the driving force and the suitability of the development conditions. The resource potential is displayed as a bubble map, with the various colors representing different grades of resource potential, where the colored bubbles indicate that the resource potential feature value of the grades is above the median, while the black bubbles represent the values below the median. In Figure 5, the first quadrant represents "High Driving Force-High Suitability (HDFHS)", and the colored bubbles in this quadrant denote the higher redevelopment potential areas. The second quadrant is expressed as "Low Driving Force-High Suitability (LDFHS)", and the colored bubbles in this quadrant indicate the high redevelopment potential areas, while the black bubbles are the low potential areas. The third quadrant signifies "Low Driving Force-Low Suitability ((LDFLS)", and the black bubbles in this quadrant indicate the lower redevelopment potential areas. The fourth quadrant is depicted as "High Driving Force-Low Suitability (HDFLS)", and the colored bubbles in this quadrant indicate the high redevelopment potential areas, while the black bubbles are the low potential areas. According to the planning principles of "progressive order, progressive

development, long-term planning, and timely development", the redevelopment sequence is classified into four broad categories: "Urgent action, Recent planning, Medium-term planning, and Long-term planning". The "Recent planning" and "Medium-term planning" phases are further divided into three stages, respectively, according to the combined relationship between the three dimensions. The specific grades of redevelopment potential, redevelopment sequence, and the combination relationship between the conditions are shown in Table 7. According to the different redevelopment stages, the action and emphasis of policy implementation for each redevelopment stage are put forward, respectively.

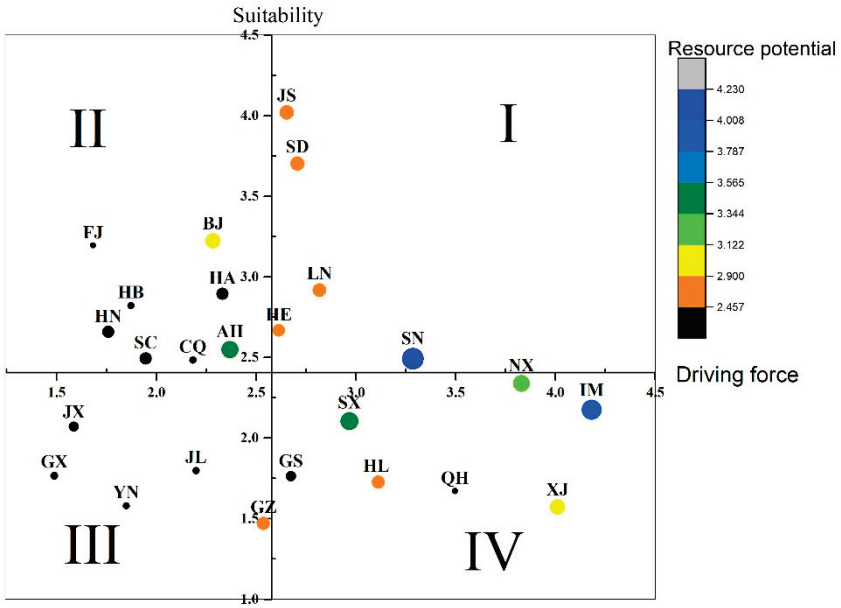

Figure 4. Scatter plot of the resource potential, driving force, and development conditions suitability.

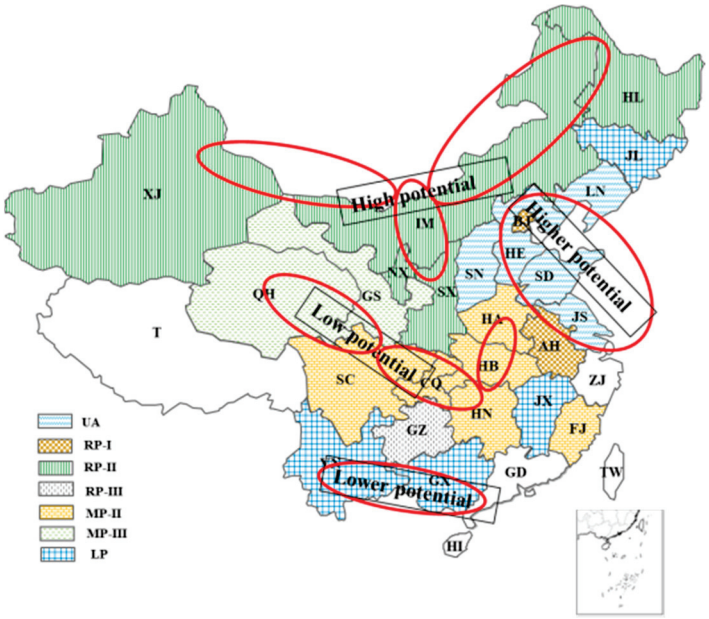

Figure 5. Province classification of redevelopment potential and redevelopment sequence.

Table 7. Ranking of abandoned mine redevelopment potential and redevelopment sequence planning.

Conditions			Redevelopment Potential	Redevelopment Sequence	Action and Emphasis
D	S	R			
●	●	●	Higher potential	Urgent action (UA)	➢ Compile urgent strategic planning ➢ Correct improper development ➢ Set standards and policies
○	●	●		Recent planning-I (RP-I)	➢ Detailed development plan ➢ Expand tactics and market benefit ➢ Major project investment argument
●	●	○	High potential	Recent planning-II (RP-II)	➢ Detailed development plan ➢ Necessary project implementation guarantee ➢ Extraterritorial capital and technical cooperation
○	●	○	Moderate	Recent planning-III (RP-III)	➢ Resource protection and enhancement measures ➢ Cost-effectiveness argument ➢ Major project implementation argument ➢ Necessary project implementation guarantee
●	○	●	Low potential	Medium-term planning-I (MP-I)	➢ Re-identify the resource potential ➢ Extraterritorial deployment of capital technology
○	○	●	Lower potential	Medium-term planning-II (MP-II)	➢ Re-identify the resource potential ➢ Expand tactics and market benefit ➢ Extraterritorial deployment of capital technology
●	○	○		Medium-term planning-III (MP-III)	➢ Re-identify the resource potential ➢ Major project implementation argument ➢ Extraterritorial capital and technical cooperation
○	○	○		Long-term planning (LP)	without considering

Note: D = driving force, S = resource potential, R = suitability of development conditions. The black dot ● indicates that the value is equal to or greater than the median, and a white dot ○ indicates that the value is less than the median.

Following the combination of Figure 5 and Table 7, the spatial pattern of the redevelopment potential and the redevelopment sequence of China's provinces are shown in Figure 6. It can be observed that Jiangsu, Shandong, Liaoning, Hebei, Shanxi, Anhui, and Beijing are "higher potential" provinces. Among these provinces, the first five provinces with the higher resource potential, driving force, and suitability of development conditions values are suggested to be the first abandoned mine redevelopment project demonstration zones. Beijing and Anhui are at the "Recent planning-I (RP-I)" stage. Shaanxi, Ningxia, Inner Mongolia, Heilongjiang, and Xinjiang are regarded as the "Recent planning-I (RP-II)" stage. The regions with better performance in only one dimension, such as Guizhou, Fujian, Hubei, Hunan, Sichuan, Chongqing, Henan, Gansu, Qinghai, etc., can be evaluated as "potential development zones" for the abandoned mine resources redevelopment. Yunnan, Jiangxi, Guangxi, and Jilin performed the worst in all three dimensions; therefore, the abandoned mines in these areas were suggested only for ecological rehabilitation but not redevelopment.

4.3. Key Indicators for AMRP

Owing to the various types of abandoned mines, China's AMRP level varies according to the region, with differences in the regional advantage and the basis of the regional economy. The radar chart method was adopted to reflect the indicators' difference of objects (Figure 6) in order to reveal the key indicators restricting the AMRP.

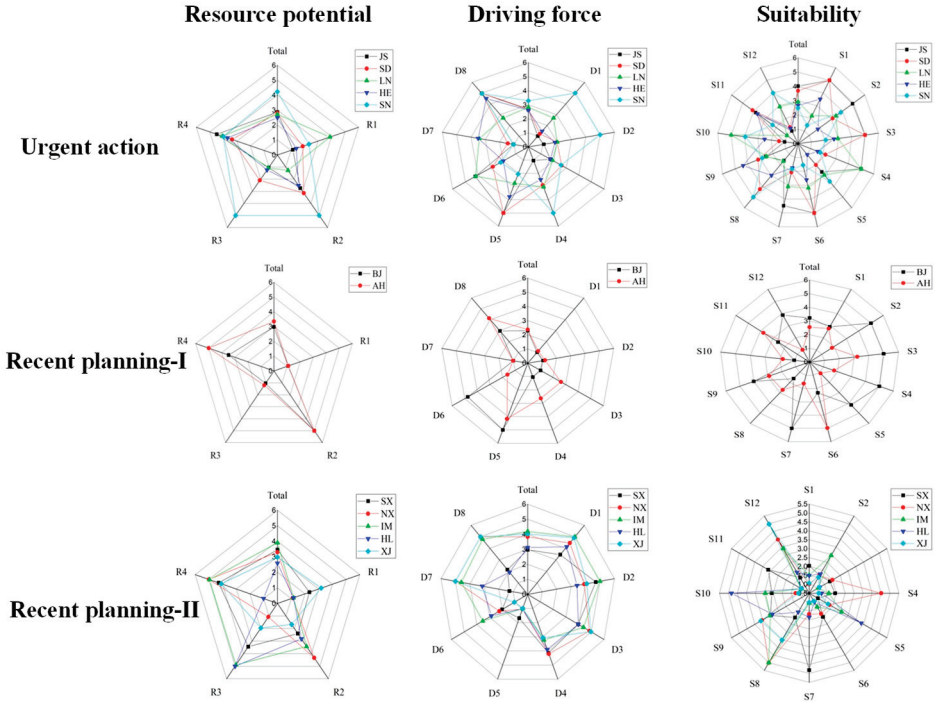

Figure 6. Inter-domain comparison in the same redevelopment stage.

For the provinces in the "Urgent action" phase, although the three dimensions performed relatively better than in the other areas, they still need to improve the relatively weak indicators to enhance the redevelopment potential. Take Shanxi as an example; as the key coal producer in China, Shanxi has lots of abandoned mines with large sizes; so, the resource potential grade is high. Many typical phenomena of a resource-based economy, such as the simplification of a leading industry, unreasonable economic structure, and high dependence on resources, lead to the strong driving force in Shanxi. However, the suitability of the development conditions is lower than that of Jiangsu and Shandong, which is prominently manifested in the economic scale (S_1), the traffic conditions (S_3), the opening level (S_4), the intensity of the input into science and technology (S_6), and the investment in environmental protection (S_9). Therefore, Shanxi should continue to strengthen investment in infrastructure construction, science and technology, and environmental protection and should actively introduce foreign capital to enhance the suitability of the external conditions [22].

For the provinces in the "Recent planning-I" phase, Anhui's resource potential is higher than that of Beijing, but its development conditions are far behind those of Beijing. It should be pointed out that Beijing's investment intensity in scientific research (S_6), industrial pollution control (S_8), and science, education, culture, and health (S_{11}) is insufficient. As for the driving force, due to the high population density (D_5) and strong environmental and resource constraints (D_6 and D_8), Beijing urgently needs to develop mined land and underground space to release more urban development space, while Anhui's driving force mainly comes from the social and environmental impact caused by mine closure (D_3 and D_4).

For the provinces in the "Recent planning-II" phase, although the resource potential and driving force of these areas are strong, the suitability of the development conditions limits their redevelopment. It can be seen that the driving forces of Xinjiang and Inner Mongolia are significantly higher than those of Shaanxi, Ningxia, and Heilongjiang, but the resource potential of Xinjiang and Heilongjiang is not as good as that of Inner Mongolia. As for the indicators of the suitability for development conditions, except for the proportion of infrastructure investment, Xinjiang is at a disadvantage in terms of the economy, location, talent science and technology, social security, and other indicators. Ningxia has the best

performance in capital opening and industrial pollution investment, while the other indicators need to be improved. However, driven by the development policy in western China, the infrastructure and economic scale of the western region will be greatly improved, and the suitability of the development conditions will change qualitatively [53].

4.4. Different Driving Force Scenarios

It can be seen in Table 4 that the weights of economic demand account for 41% of the total driving force weights, while the weights of social demand and environmental demand account for 33% and 26%, respectively. Therefore, under the distribution of the existing weights, the redevelopment priority is given to meeting economic demand. This scenario was regarded as the economic priority scenario. However, different provinces may have various redevelopment preferences. Therefore, this article gives two other driving force scenarios to illustrate the performances of all the provinces under different demand priorities. The first one is the social priority scenario, which was devoted to increasing re-employment, reducing the impact on miners' lives, and solving the resource constraints of sustainable development. In this scenario, the weights for social demand were set as 0.5, while the weights of economic demand and environmental demand were 0.25, respectively. The results in this scenario are shown in Figure 7. The second scenario is the environmental priority scenario, which emphasizes environmental protection and energy savings. In this scenario, the weight of environmental demand was set as 0.5, while the weights of economic demand and social demand were 0.25, respectively. The results are presented in Figure 8.

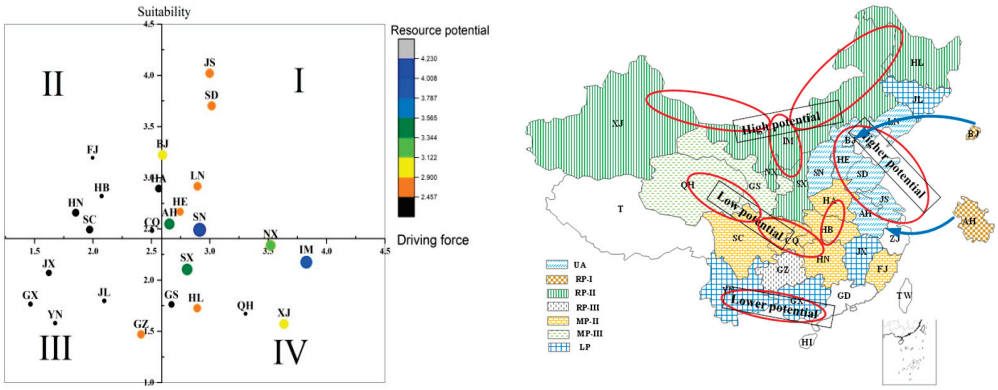

Figure 7. Results under social priority scenario.

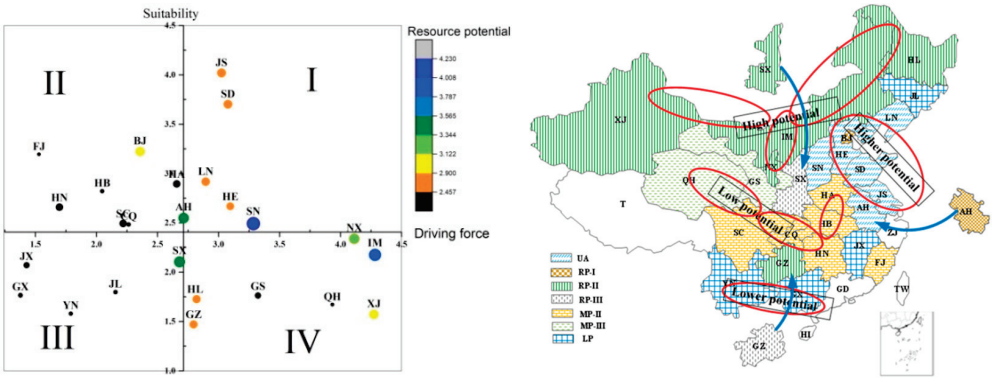

Figure 8. Results under environmental priority scenario.

By comparing with the results of the economic priority scenario, it can be found that, although the indicators values were changed under different scenarios, the redevelopment potential and redevelopment sequence classification of most provinces remain unchanged, which proves that most provinces have no obvious preference for the benefits of abandoned

mine redevelopment. However, under the social priority scenario (Figure 7), the redevelopment sequence of Beijing and Anhui moved from "Recent planning-I" up to "Urgency action", which indicates that the redevelopment of abandoned mines in these two provinces should pay more attention to the social requirements compared to the economic needs. This conclusion has been verified in Section 4.3; that is, Anhui province should mainly address the problem of unemployment, while Beijing should focus on solving the resource and environmental constraints faced by urban development. In the environmental priority scenario, the redevelopment sequence of Anhui, Guizhou, and Shaanxi is changed (in Figure 8). Specifically, the redevelopment sequence of Anhui was changed from "Recent planning-I" up to "Urgency action". The redevelopment sequence of Shaanxi was changed from "Recent planning-II" to "Recent planning-I"; however, Guizhou's redevelopment sequence was just the opposite.

5. Conclusions and Policy Implications

This paper is the first study to provide a quantitative assessment of the basic information on the abandoned mine resource potential, the driving force, and the suitability of the redevelopment conditions and to put forward a priority list of abandoned mine redevelopment from the provincial perspective; this provides scientific foundation references for rational abandoned mine redevelopment industry distribution and regional eco-environment protection in the future.

5.1. Conclusions

(1) As for the theoretical contribution, this paper first constructs a comprehensive evaluation index system with the outstanding characteristics of the abandoned coal mines and the moderate scope. Secondly, the normal cloud model used in this paper, which discarded the traditional concept of membership but integrated the fuzziness and randomness of the indicators, provides a simple and reliable method for quantitative evaluation. This study evaluates the redevelopment potential of provincial abandoned mines from a more comprehensive perspective, which makes up for the deficiency of the current research in this field.

(2) For the problem of scientific decision making with regard to abandoned mine redevelopment, this article proposes the classification principles as "resource advance and coordinate development" and gives five types of potential levels and eight categories of redevelopment sequences. On this basis, it proposes policy emphasis suggestions for different redevelopment sequences; these suggestions have important value for practical redevelopment planning.

(3) The provinces with high potential for the redevelopment of abandoned mines in China are concentrated in the middle and eastern regions. The abandoned mines in most southwest provinces are not recommended for reuse, and the main focus should be on simple ecological restoration. The multi-driving force scenario simulation analysis shows that there is no obvious preference for abandoned mine development in most provinces of China, but Beijing, Anhui, Shaanxi, and Guizhou provinces should make further argumentation and analysis according to the demand preference.

(4) This paper provides a clear image of each province's AMRP in China from the macrolevel of regional demand and the economic development stage, which will guide the government to introduce effective strategic plans. However, the evaluation of the abandoned mine resource potential is still rough, and the redevelopment modes selection of abandoned mines needs to be further studied.

5.2. Policy Implications

A correct regional policy of abandoned mine redevelopment is derived from the accurate judgment of the stage and the level of development, or it would be blind or negative. Based on the above evaluation and the conclusions on the abandoned mine redevelopment potential, this paper provides the following policy implications and recommendations:

(1) For the "Urgent action" provinces, it is suggested that they conduct unprecedented experiments with AMR and establish the first comprehensive experimental areas. Considering that these provinces bear the burden of formulating the industrial policies and relevant standards for the other provinces, the government would need to carry out a "carrot and stick" policy in dealing with abandoned mine redevelopment. On the one side, penalties should be adopted to force these provinces to redevelop abandoned mines. On the other side, the government could provide some rewarding policies, such as financial subsidies, tax reductions or exemptions, special funds, etc., to encourage enterprises to try to reuse abandoned mine resources.

(2) For the "Recent planning" provinces, considering that the difficulty and cost of abandoned mine reutilization will increase if it is not planned earlier, the government is advised to provide strong supporting policies and incentive policies, such as increasing the input of the soft- and hardware in these areas, providing more subsidies, and building more relevant research institutes to support these provinces in participating in the redevelopment of the abandoned mines.

(3) For the "Medium-term planning" provinces, the provinces with better development conditions are encouraged to invest capital and technology in the provinces with higher resource potential. The government also can provide specific funds to support the research on the resource identification and value evaluation of the abandoned mines and further demonstrate the feasibility of abandoned mine redevelopment.

Author Contributions: Conceptualization, Y.Y. and C.C.; methodology, C.C.; software, Y.Y.; validation, Y.Y. and C.C.; formal analysis, C.C.; investigation, Y.Y.; resources, C.C.; data curation, Y.Y.; writing—original draft preparation, C.C.; writing—review and editing, Y.Y.; visualization, Y.Y.; supervision, C.C.; project administration, C.C.; funding acquisition, Y.Y. All authors have read and agreed to the published version of the manuscript.

Funding: This research was funded by the National Natural Science Foundation of China (No. 71704178) and the Natural Science Foundation of Shanxi Province, (No. 20210302123336).

Institutional Review Board Statement: Not applicable.

Informed Consent Statement: Not applicable.

Data Availability Statement: Not applicable.

Acknowledgments: We gratefully acknowledge the National Natural Science Foundation of China (No. 71704178) and the Natural Science Foundation of Shanxi Province, (No. 20210302123336). The authors also appreciate the experts for giving helpful suggestions that improved the content.

Conflicts of Interest: The authors declare no conflict of interest.

Appendix A Appendix A

Table A1. Algorithm of forward normal cloud.

Given the Three Numerical Descriptors of One Factor (*Ex*, *En*, *He*) and the Specific Value x_i	
Step 1	Initially generate normal random E_{ni}' with expectation *Ex* and variance *En*;
Step 2	Generate again normal random X_i with expectation *En* and variance *He*. The normal distribution function is expressed as *NORM*;
Step 3	Calculate $\mu_i = \exp\left[-(x_i - Ex)^2/2(E_{ni}')^2\right]$;
Step 4	The cloud drops drop(x, μ(x));
Step 5	Repeat steps 1–4 until n cloud drops are generated.

Table A2. The cloud parameters of indicators.

	I	II	III	IV	V
R_1	21.5; 18.2; 0.02	76.8; 28.8; 0.02	144.6; 28.8; 0.02	212.3; 28.8; 0.02	381.7; 115.1; 0.02
R_2	8.8; 7.5; 0.02	29.3; 9.9; 0.02	52.7; 9.9; 0.02	76.1; 9.9; 0.02	134.6; 39.7; 0.02
R_3	34.9; 29.7; 0.02	113.5; 37; 0.02	200.6; 37; 0.02	287.8; 37; 0.02	505.7; 148.1; 0.02
R_4	29.2; 24.8; 0.02	81.1; 19.3; 0.02	126.7; 19.3; 0.02	172.2; 19.3; 0.02	286.1; 77.4; 0.02
D_1	6; 5.1; 0.02	16.7; 4; 0.02	26.2; 4; 0.02	35.6; 4; 0.02	59.3; 16.1; 0.02
D_2	0.8; 0.7; 0.02	2.9; 1.1; 0.02	5.4; 1.1; 0.02	7.9; 1.1; 0.02	14.1; 4.3; 0.02
D_3	0.46; 0.39; 0.02	0.97; 0.05; 0.02	1.08; 0.05; 0.02	1.19; 0.05; 0.02	1.47; 0.19; 0.02
D_4	9.5; 8.1; 0.02	29.2; 8.6; 0.02	49.6; 8.6; 0.02	69.9; 8.6; 0.02	120.9; 34.6; 0.02
D_5	86.6; 73.5; 0.02	229.1; 47.5; 0.02	341.1; 47.5; 0.02	453.1; 47.5; 0.02	733.0; 190.2; 0.02
D_6	25.8; 21.9; 0.02	54.0; 2.0; 0.02	58.6; 2.0; 0.02	63.2; 2.0; 0.02	74.8; 7.9; 0.02
D_7	0.3; 0.2; 0.02	0.6; 0.1; 0.02	0.8; 01; 0.02	1.1; 0.1; 0.02	1.6; 0.4; 0.02
D_8	66.1; 14.4; 0.02	44.9; 3.6; 0.02	36.4; 3.6; 0.02	28.0; 3.6; 0.02	11.9; 10.1; 0.02
S_1	8186.6; 6952.5; 0.02	21,200.8; 4099.9; 0.02	30,856.1; 4099.9; 0.02	40,511.4; 4099.9; 0.02	64,649.7; 16399.7; 0.02
S_2	10,022.0; 8511.3; 0.02	22,087.4; 1735.3; 0.02	26,174.1; 1735.3; 0.02	30,260.8; 1735.3; 0.02	40,477.5; 6941.3; 0.02
S_3	0.4; 0.3; 0.02	1.3; 0.5; 0.02	2.4; 0.5; 0.02	3.5; 0.5; 0.02	6.3; 1.9; 0.02
S_4	1; 0.9; 0.02	2.7; 0.6; 0.02	4.1; 0.6; 0.02	5.6; 0.6; 0.02	9.1; 2.4; 0.02
S_5	22.5; 19.1; 0.02	46.8; 1.6; 0.02	50.6; 1.6; 0.02	54.5; 1.6; 0.02	64.0; 6.5; 0.02
S_6	0.4; 0.3; 0.02	0.9; 0.1; 0.02	1.1; 0.1; 0.02	1.4; 0.1; 0.02	2.0; 0.4; 0.02
S_7	1106.6; 939.8; 0.02	2399.4; 158.1; 0.02	2771.7; 158.1; 0.02	3144.0; 158.1; 0.02	4074.7; 632.3; 0.02
S_8	0.3; 0.2; 0.02	0.7; 0.2; 0.02	1.1; 0.2; 0.02	1.5; 0.2; 0.02	2.5; 0.7; 0.02
S_9	1.3; 1.1; 0.02	2.9; 0.2; 0.02	3.4; 0.2; 0.02	4.0; 0.2; 0.02	5.4; 1.0; 0.02
S_{10}	6.3; 5.3; 0.02	13.5; 0.8; 0.02	15.3; 0.8; 0.02	17.2; 0.8; 0.02	21.8; 3.2; 0.02
S_{11}	13.2; 11.2; 0.02	27.3; 0.8; 0.02	29.1; 0.8; 0.02	30.9; 0.8; 0.02	35.5; 3.1; 0.02
S_{12}	6.6; 5.6; 0.02	14.5; 1.1; 0.02	17.2; 1.1; 0.02	19.9; 1.1; 0.02	26.5; 4.5; 0.02

Table A3. Results by cloud model assessment approach.

Province	Dimension	I	II	III	IV	V
BJ	Resource potential	0.2300	0.0110	0.2915	0.0921	0.1788
	Driving force	0.4256	0.0113	0.1611	0.0153	0.1504
	Suitability	0.0556	0.1372	0.2652	0.0281	0.1847
HE	Resource potential	0.3381	0.2500	0.2957	0.1615	0.0901
	Driving force	0.2546	0.3754	0.1833	0.1674	0.1417
	Suitability	0.1932	0.3565	0.4016	0.1229	0.1127
SN	Resource potential	0.0000	0.0976	0.1242	0.2851	0.5582
	Driving force	0.1491	0.1895	0.1046	0.0046	0.3563
	Suitability	0.2992	0.4622	0.0999	0.2296	0.1101
IM	Resource potential	0.1189	0.0223	0.1844	0.0801	0.4951
	Driving force	0.1132	0.0031	0.0848	0.1477	0.6035
	Suitability	0.4856	0.2673	0.2545	0.0517	0.1108
LN	Resource potential	0.4620	0.0753	0.1134	0.3986	0.1336
	Driving force	0.0723	0.3580	0.5393	0.0536	0.1205
	Suitability	0.1296	0.3503	0.4500	0.1039	0.2016
JL	Resource potential	0.6169	0.4181	0.0310	0.0000	0.0157
	Driving force	0.3332	0.3398	0.4190	0.0058	0.0433
	Suitability	0.4925	0.5158	0.0554	0.0527	0.0331
HL	Resource potential	0.4541	0.0990	0.1467	0.0010	0.2968
	Driving force	0.2103	0.1512	0.3562	0.3833	0.1658
	Suitability	0.6231	0.4154	0.0360	0.0602	0.0476
JS	Resource potential	0.3032	0.1120	0.1303	0.1926	0.1997
	Driving force	0.4682	0.0547	0.0000	0.0078	0.3406
	Suitability	0.1138	0.0652	0.0698	0.0492	0.5590
AH	Resource potential	0.3651	0.0627	0.0001	0.0000	0.5702
	Driving force	0.5300	0.1441	0.0709	0.2835	0.1034
	Suitability	0.2045	0.4509	0.4251	0.0612	0.1154

Table A3. *Cont.*

Province	Dimension	I	II	III	IV	V
FJ	Resource potential	0.8383	0.1643	0.0076	0.0000	0.0075
	Driving force	0.7424	0.0422	0.1062	0.0718	0.0566
	Suitability	0.1372	0.2405	0.3931	0.3886	0.1961
JX	Resource potential	0.4678	0.2408	0.0975	0.1052	0.0488
	Driving force	0.5715	0.3079	0.0996	0.0003	0.0197
	Suitability	0.2575	0.8131	0.1364	0.0382	0.0449
SD	Resource potential	0.0321	0.4051	0.5738	0.0675	0.0904
	Driving force	0.3356	0.2060	0.1885	0.0126	0.2821
	Suitability	0.0872	0.2086	0.2079	0.1072	0.5436
HA	Resource potential	0.0857	0.6501	0.3366	0.0303	0.0590
	Driving force	0.3976	0.2468	0.0221	0.0378	0.2001
	Suitability	0.2345	0.2630	0.2807	0.2292	0.1887
HB	Resource potential	0.7609	0.0584	0.1190	0.0071	0.0179
	Driving force	0.5855	0.1201	0.3400	0.0082	0.0304
	Suitability	0.1611	0.3802	0.3655	0.2302	0.1236
HN	Resource potential	0.4824	0.0942	0.0789	0.2784	0.0963
	Driving force	0.4692	0.4624	0.1305	0.0031	0.0233
	Suitability	0.1705	0.4573	0.3990	0.1532	0.1030
GX	Resource potential	0.4755	0.3111	0.0767	0.0001	0.0173
	Driving force	0.5085	0.3900	0.0041	0.0013	0.0114
	Suitability	0.4335	0.6302	0.0374	0.0269	0.0243
CQ	Resource potential	0.8465	0.0832	0.0000	0.0001	0.1084
	Driving force	0.5614	0.1172	0.1811	0.1766	0.0771
	Suitability	0.2138	0.4849	0.4004	0.0759	0.0913
SC	Resource potential	0.5463	0.0467	0.0795	0.2324	0.1594
	Driving force	0.3903	0.3557	0.2034	0.0222	0.0300
	Suitability	0.3520	0.4013	0.1763	0.2614	0.0962
GZ	Resource potential	0.5063	0.1045	0.0002	0.0150	0.3408
	Driving force	0.1624	0.3979	0.3664	0.0983	0.0605
	Suitability	0.7527	0.2033	0.0457	0.0391	0.0219
YN	Resource potential	0.6190	0.2821	0.0041	0.0000	0.0251
	Driving force	0.3336	0.4213	0.0943	0.0162	0.0242
	Suitability	0.6765	0.3078	0.0571	0.0317	0.0308
SX	Resource potential	0.0002	0.2657	0.3346	0.4000	0.2104
	Driving force	0.1610	0.2595	0.3355	0.2072	0.1691
	Suitability	0.2668	0.7768	0.0987	0.0385	0.0741
GS	Resource potential	0.4463	0.2817	0.3526	0.0098	0.0445
	Driving force	0.2492	0.4297	0.0335	0.1375	0.2209
	Suitability	0.7095	0.1722	0.0930	0.0709	0.0703
QH	Resource potential	0.7219	0.2033	0.0004	0.0000	0.0079
	Driving force	0.1193	0.0800	0.3509	0.0312	0.3835
	Suitability	0.5804	0.2369	0.0342	0.0308	0.0587
NX	Resource potential	0.3842	0.0279	0.0027	0.1821	0.4649
	Driving force	0.1572	0.0500	0.0942	0.3049	0.4808
	Suitability	0.3847	0.3974	0.0396	0.1133	0.1633
XJ	Resource potential	0.1189	0.3967	0.1828	0.3452	0.1303
	Driving force	0.1325	0.0094	0.0797	0.1214	0.5045
	Suitability	0.6822	0.1450	0.0677	0.0153	0.0568

Table A4. Comparison scale of analytic hierarchy process.

Factor of Preference	Importance Definition
1	Equal importance
3	Moderate importance of one over another
5	The strong or essential importance of one over another
7	Very strong or demonstrated importance of one over another
9	The extreme importance of one over another
2, 4, 6, 8	Intermediate values

Table A5. Listing and abbreviations of the provincial-level administrative units.

Provinces	Abbreviation	Provinces	Abbreviation
Beijing	BJ	Hunan	HN
Tianjin	TJ	Guangdong	GD
Heibei	HE	Guangxi	GX
Shaanxi	SX	Hainan	HI
Inner Mongolia	IM	Chongqing	CQ
Liaoning	LN	Sichuan	SC
Jilin	JL	Guizhou	GZ
Heilongjiang	HL	Yunnan	YN
Henan	HA	Shanxi	SN
Jiangsu	JS	Gansu	GS
Zhejiang	ZJ	Qinghai	QH
Anhui	AH	Ningxia	NX
Fujian	FJ	Xinjiang	XJ
Jiangxi	JX		
Shandong	SD		
Hubei	HB		

References

1. Amirshenava, S.; Osanloo, M. Mine closure risk management: An integration of 3D risk model and MCDM techniques. *J. Clean. Prod.* **2018**, *184*, 389–401. [CrossRef]
2. Yuan, L.; Jing, Y.; Wang, K.; Zhao, Y.; Hao, X.; Xu, C. Precision exploitation and utilization of closed/abandoned mine resources in China. *J. China Coal Soc.* **2018**, *43*, 14–20. (In Chinese) [CrossRef]
3. Gorman, M.R.; Dzombak, D.A. A review of sustainable mining and resource management: Transitioning from the life cycle of the mine to the life cycle of the mineral. *Resour. Conserv. Recycl.* **2018**, *137*, 281–291. [CrossRef]
4. Zhang, C.; Li, B.; Song, Z.; Liu, J.; Zhou, J. Breakage mechanism and pore evolution characteristics of gangue materials under compression. *Acta Geotech.* **2022**, *17*, 4823–4835. [CrossRef]
5. Zhang, C.; Zhao, Y.; Bai, Q. 3D DEM method for compaction and breakage characteristics simulation of broken rock mass in goaf. *Acta Geotech.* **2022**, *17*, 2765–2781. [CrossRef]
6. Shi, X.; Rioux, B.; Galkin, P. Unintended consequences of China's coal capacity cut policy. *Energy Policy* **2018**, *113*, 478–486. [CrossRef]
7. Luo, P.; Chen, N. Abandoned coal mine tunnels: Future heating/power supply centers. *Min. Sci. Technol.* **2011**, *21*, 637–640. [CrossRef]
8. Pouran, H.M. From collapsed coal mines to floating solar farms, why China's new power stations matter. *Energy Policy* **2018**, *123*, 414–420. [CrossRef]
9. Ahmad, N.; Zhu, Y.; Shafait, Z.; Sahibzada, U.F.; Waheed, A. Critical barriers to brown field redevelopment in developing countries: The case of Pakistan. *J. Clean. Prod.* **2019**, *212*, 1193–1209. [CrossRef]
10. Doyle, M.R. From hydro/geology to the streetscape: Evaluating urban underground resource potential. *Tunn. Undergr. Sp. Technol.* **2016**, *55*, 83–95. [CrossRef]
11. Lin, J.; Fridley, D.; Lu, H.; Price, L.; Zhou, N. Has coal use peaked in China: Near-term trends in China's coal consumption. *Energy Policy* **2018**, *123*, 208–214. [CrossRef]
12. Bakhtavar, E.; Aghayarloo, R.; Youse, S.; Hewage, K.; Sadiq, R. Renewable energy based mine reclamation strategy: A hybrid fuzzy-based network analysis. *J. Clean. Prod.* **2019**, *230*, 253–263. [CrossRef]
13. Sutherland, F. Community-driven mining heritage in the Cuyuna Iron Mining District: Past, present, and future projects. *Extr. Ind. Soc.* **2015**, *2*, 519–530. [CrossRef]
14. Lèbre, É.; Corder, G.D.; Golev, A. Sustainable practices in the management of mining waste: A focus on the mineral resource. *Miner. Eng.* **2017**, *107*, 34–42. [CrossRef]

15. Kubit, O.E.; Pluhar, C.J.; De Graff, J.V. A model for prioritizing sites and reclamation methods at abandoned mines. *Environ. Earth Sci.* **2015**, *73*, 7915–7931. [CrossRef]
16. Li, X.; Yang, H.; Chen, Z.; Wang, Z.; Guo, L.; Song, Y.; Liu, L. Evaluation system for prioritization tool to redevelop abandoned coal mine industry square based on DSR model. *Trans. Chin. Soc. Agric. Eng.* **2018**, *34*, 224–231. (In Chinese) [CrossRef]
17. Lu, W.; Xu, C.; Wu, J.; Cheng, S. Ecological effect assessment based on the DPSIR model of a polluted urban river during restoration: A case study of the Nanfei River, China. *Ecol. Indic.* **2019**, *96*, 146–152. [CrossRef]
18. Han, S.; Chen, H.; Long, R.; Cui, X. Peak coal in China: A literature review. Resources. *Conserv. Recycl.* **2018**, *129*, 293–306. [CrossRef]
19. Laurence, D. Establishing a sustainable mining operation: An overview. *J. Clean. Prod.* **2011**, *19*, 278–284. [CrossRef]
20. Amirshenava, S.; Osanloo, M. A hybrid semi-quantitative approach for impact assessment of mining activities on sustainable development indexes. *J. Clean. Prod.* **2019**, *218*, 823–834. [CrossRef]
21. Cui, C.; Wang, B.; Zhao, Y.; Wang, Q.; Sun, Z. China's regional sustainability assessment on mineral resources: Results from an improved analytic hierarchy process-based normal cloud model. *J. Clean. Prod.* **2019**, *210*, 105–120. [CrossRef]
22. Cao, X. Policy and regulatory responses to coal mine closure and coal resources consolidation for sustainability in Shanxi, China. *J. Clean. Prod.* **2017**, *145*, 199–208. [CrossRef]
23. Batterham, R.J. The mine of the future—Even more sustainable. *Miner. Eng.* **2017**, *107*, 2–7. [CrossRef]
24. Groth, C.; Schou, P. Growth and non-renewable resources: The different roles of capital and resource taxes. *J. Environ. Econ. Manag.* **2007**, *53*, 80–98. [CrossRef]
25. Unger, C.J.; Lechner, A.M.; Kenway, J.; Glenn, V.; Walton, A. A jurisdictional maturity model for risk management, accountability and continual improvement of abandoned mine remediation programs. *Resour. Policy* **2015**, *43*, 1–10. [CrossRef]
26. Nehring, M.; Cheng, X. An investigation into the impact of mine closure and its associated cost on life of mine planning and resource recovery. *J. Clean. Prod.* **2016**, *127*, 228–239. [CrossRef]
27. Wang, B.; Mi, Z.; Nistor, I.; Yuan, X.-C. How does hydrogen-based renewable energy change with economic development? Empirical evidence from 32 countries. *Int. J. Hydrogen Energy* **2018**, *43*, 11629–11638. [CrossRef]
28. Volk, R.; Müller, R.; Reinhardt, J.; Schultmann, F. An Integrated Material Flows, Stakeholders and Policies Approach to Identify and Exploit Regional Resource Potentials. *Ecol. Econ.* **2019**, *161*, 292–320. [CrossRef]
29. Ruan, W.; Li, Y.; Zhang, S.; Liu, C. Evaluation and drive mechanism of tourism ecological security based on the DPSIR-DEA model. *Tour. Manag.* **2019**, *75*, 609–625. [CrossRef]
30. Zhang, M.; Liu, Y.; Wu, J.; Wang, T. Index system of urban resource and environment carrying capacity based on ecological civilization. *Environ. Impact Assess. Rev.* **2018**, *68*, 90–97. [CrossRef]
31. Mishra, S.K.; Hitzhusen, F.J.; Sohngen, B.L.; Guldmann, J. Costs of abandoned coal mine reclamation and associated recreation bene fits in Ohio. *J. Environ. Manag.* **2012**, *100*, 52–58. [CrossRef] [PubMed]
32. Mhlongo, S.E.; Amponsah-dacosta, F. A review of problems and solutions of abandoned mines in South Africa. *Int. J. Min. Reclam. Environ.* **2016**, *30*, 279–294. [CrossRef]
33. Yi, S. Resource recovery potentials by landfill mining and reclamation in South Korea. *J. Environ. Manag.* **2019**, *242*, 178–185. [CrossRef] [PubMed]
34. Chang, J.; Chen, Y.; Li, Z.; Wang, H.; Feng, S. The characteristics and dynamic mechanism of regional development and evolution of Pan'an Lake. *Coal Geol. Explor.* **2022**, *50*, 25–34.
35. Caulk, R.A.; Graduate, M.S.; Tomac, I. Reuse of abandoned oil and gas wells for geothermal energy production. *Renew. Energy* **2017**, *112*, 388–397. [CrossRef]
36. Naidu, G.; Ryu, S.; Thiruvenkatachari, R.; Choi, Y.; Jeong, S.; Vigneswaran, S. A critical review on remediation, reuse, and resource recovery from acid mine drainage. *Environ. Pollut.* **2019**, *247*, 1110–1124. [CrossRef]
37. Zhang, X.; Winchester, N.; Zhang, X. The future of coal in China. *Energy Policy* **2017**, *110*, 644–652. [CrossRef]
38. Wang, D.; Wan, K.; Song, X. Quota allocation of coal overcapacity reduction among provinces in China. *Energy Policy* **2018**, *116*, 170–181. [CrossRef]
39. Ramírez-alesón, M.; Fleta-asín, J. Is the Importance of Location Factors Different Depending on the Degree of Development of the Country? *J. Int. Manag.* **2016**, *22*, 29–43. [CrossRef]
40. Bangian, A.H.; Ataei, M.; Sayadi, A.; Gholinejad, A. Optimizing post-mining land use for pit area in open-pit mining using fuzzy decision making method. *Int. J. Environ. Sci. Technol.* **2012**, *9*, 613–628. [CrossRef]
41. Song, X.; Zhou, Y.; Jia, W. How do Economic Openness and R&D Investment Affect Green Economic Growth?—Evidence from China. *Resour. Conserv. Recycl.* **2019**, *146*, 405–415. [CrossRef]
42. Lee, C.; Chou, P. Financial openness and market liquidity in emerging markets. *Financ. Res. Lett.* **2018**, *25*, 124–130. [CrossRef]
43. Zhu, B.; Zhang, M.; Zhou, Y.; Wang, P.; Sheng, J.; He, K.; Wei, Y.; Xie, R. Exploring the effect of industrial structure adjustment on interprovincial green development efficiency in China: A novel integrated approach. *Energy Policy* **2019**, *134*, 110946. [CrossRef]
44. Miremadi, I.; Saboohi, Y.; Arasti, M. The influence of public R&D and knowledge spillovers on the development of renewable energy sources: The case of the Nordic countries. *Technol. Forecast. Soc. Chang.* **2019**, *146*, 450–463. [CrossRef]
45. Zhou, Y.; Guo, Y.; Liu, Y. High-level talent flow and its influence on regional unbalanced development in China. *Appl. Geogr.* **2018**, *91*, 89–98. [CrossRef]

46. Knierzinger, J.; Sopelle, I.T. Mine closure from below: Transformative movements in two shrinking West African mining towns. *Extr. Ind. Soc.* **2019**, *6*, 145–153. [CrossRef]
47. Wang, D.; Shi, Y.; Wan, K. Integrated evaluation of the carrying capacities of mineral resource-based cities considering synergy between subsystems. *Ecol. Indic.* **2020**, *108*, 105701. [CrossRef]
48. Wang, D.; Liu, D.; Ding, H.; Singh, V.P.; Wang, Y.; Zeng, X.; Wu, J.; Wang, L. A cloud model-based approach for water quality assessment. *Environ. Res.* **2016**, *148*, 24–35. [CrossRef]
49. Guo, Y.; Meng, X.; Meng, T.; Wang, D.; Liu, S. A novel method of risk assessment based on cloud inference for natural gas pipelines. *J. Nat. Gas Sci. Eng.* **2016**, *30*, 421–429. [CrossRef]
50. Lü, X.; Chen, C.; Wang, P.; Meng, L. Status evaluation of mobile welding robot driven by fuel cell hybrid power system based on cloud model. *Energy Convers. Manag.* **2019**, *198*, 111904. [CrossRef]
51. Senapati, T.; Yager, R.R. Fermatean fuzzy weighted averaging/geometric operators and its application in multi-criteria decision-making methods. *Eng. Appl. Artif. Intell.* **2019**, *85*, 112–121. [CrossRef]
52. Wang, R.; Cheng, J.; Zhu, Y.; Lu, P. Evaluation on the coupling coordination of resources and environment carrying capacity in Chinese mining economic zones. *Resour. Policy* **2017**, *53*, 20–25. [CrossRef]
53. Yang, F.; Yang, M.; Xue, B.; Luo, Q. The effects of China's western development strategy implementation on local ecological economic performance. *J. Clean. Prod.* **2018**, *202*, 925–933. [CrossRef]

sustainability

MDPI

Article

Soil Reinforcement with Geocells and Vegetation for Ecological Mitigation of Shallow Slope Failure

Gaofeng Song [1,*], Xiaoruan Song [1], Shiqin He [1], Dezhong Kong [2] and Shuai Zhang [3]

[1] School of Civil Engineering, North China University of Technology, Beijing 100144, China
[2] Mining College, Guizhou University, Guiyang 550025, China
[3] School of Architecture and Design, Beijing Jiaotong University, Beijing 100044, China
* Correspondence: song.gaofeng@ncut.edu.cn

Abstract: Soil reinforcement using geocells and vegetation is one of the best forms of soil protection for shallow slope failure control. The geocell supports the vegetation growth and the vegetation cover provides protection against the surface erosion. This work proposed a soil treatment method using geocells for supporting the vegetation growth and stabilizing the shallow slope. A step-by-step installation of the geocells in the field and the development of vegetation growth were also described. The authors developed nine physical models that were reinforced with different sized geocell structures (no reinforcement and small and large geocell reinforcement). The models were placed under three rainfall intensities (50, 75, and 100 mm/h). The stability of the slope under the rainfall and the performance of the geocell reinforcement were assessed from the the development of slope failures, the soil erosion and the slope displacement. The results showed that the stability of geocell reinforced slopes were better off than the unsupported slope. The small geocell-reinforced slopes showed less measured soil erosion and also smaller slope displacement. In general, small geocells outperformed large geocells in terms of the erosion control and slope stabilization. The rainfall intensity dramatically increased the soil erosion on slopes. The geocell- and vegetation-treated slope in the field showed good resistance against the surface erosion.

Keywords: soil reinforcement; slope stabilization; erosion control; vegetation growth; geocell

1. Introduction

Shallow slope failure is the superficial removal of the small-scale topsoil and vegetation cover from the slopes [1,2], which can be classified into the shallow landslide and the shallow erosion [3]. Shallow landslides may occur when the forces acting on the downslope exceed the mechanical resistance of the slope soil [4–6]. Shallow soil erosion, on the other hand, mostly occurs under a heavy rainfall as the rainwater dislodges soil particles and carries them off a lope [7]. Shallow slope failure is commonly observed in areas of hilly or mountainous terrain, engineered roads and embankments [8,9]. Shallow slope failure is a worldwide serious geologic hazard and causes severe problems in both the natural environment and human properties [10–14].

Soil erosion treatment with vegetation is one of the most effective methods for controlling the surface erosion and improving the slope stability [15–17]. The new vegetation cover on slopes provides protection against the surface erosion both mechanically and hydrologically [2,18,19]. The vegetation root structures penetrated into the topsoil provide strength to the soil by holding it in place to resist movement. The cover of the vegetation on the top also protects the slope against the wind and rain. Other benefits such as slowing down the water velocity, removing moisture from the soil, and maintaining soil porosity are also identified. Properly designed and planted vegetation on steep slopes plays an important role in preventing the long-term erosion and the subsequent movement of the shallow slope mass [20–22]. Most of the vegetative measures are also inexpensive, cover a

large area on the slope, and look harmonious with the natural landscape for the esthetic consideration [23].

As one of the best forms of soil protection, vegetation often requires a stronger engineered product such as the geocell to support it. This is because in some cases, when not supported, the vegetation cover on slopes can slough off on mass before it starts to stabilize the soil [24,25]. The stability of the new vegetation in the early stage should be ensured. In areas unlikely to establish natural vegetation, engineered erosion products (geocells) may be used to support vegetation growth and protect embankments and infrastructure. For more challenging conditions such as extremely steep slopes and high runoff flow, more effective and robust products are necessary. The product should be fixed securely and provide protection for vegetation. A geocell can be used to hold slope soil within its profile, maintain the integrity of the soil surface, and support vegetation growth. A number of advantages are identified [26–28]. The flat and collapsible geocell allows easy and low-cost transportation. The cost-effective structure provides rapid installation with the use of the local available material. The installation only requires minimal use of machinery, low manpower, and unskilled labor to allow the vegetation growth on slopes.

In this work, a composite soil reinforcement method using the geocell structures and the wheat straws was proposed for vegetation support and slope stabilization [29,30]. The geocell structures were first placed on the prepared bare slope; the local soil was utilized to fill the geocell sections. A thin layer of the soil–straw mixture was placed on top of the treated slope to retard the water runoff. They may also increase the biological activities in the soil, modify the level of available nutrients, and help to maintain or increase the level of soil organic matter [21,22,31,32]. Seeding was then performed after the slope treatment to establish vegetation. This composite reinforcement method modified the soil surface and topography of the bare slope to control the runoff and support vegetation growth. This work attempted to study the soil reinforcement and slope stabilization using geocells and wheat straws from physical models and field practice. The work had three main goals: (1) to develop a number of physical models with different sized geocell reinforcement and rainfall intensities; (2) obtain the progressive development of slope failures by assessing the soil erosion characteristics, the amount of soil erosion, and the slope displacement; (3) perform the soil treatment and vegetation growth in the field for slope stabilization.

2. Physical Modeling Study

2.1. Model Development

2.1.1. Model Description

The authors designed nine physical models in this research (Table 1). The models were set up at a slope ratio of 1:1.5 (rise/run). The three models in Group A were constructed using the bare soil with no extra reinforcement. The slopes in Group B were reinforced using the wheat straw and small geocells. The small geocell was 370 mm long, 370 mm wide, and 150 mm high. In Group C, the large geocells (445 × 445 × 200 mm) were utilized. The models were placed under three different rainfall intensities at 50 mm/h, 75 mm/h, and 100 mm/h, which were determined from the rainfall condition at the studied site in Yinchuan city.

Table 1. Soil reinforcement and rainfall intensity for different models.

Models	Soil Reinforcement	Geocell Size	Rainfall Intensity (mm/h)
A_1	Bare soil	-	50
A_2			75
A_3			100
B_1	Geocell and wheat straw reinforcement	Small	50
B_2			75
B_3			100
C_1	Geocell and wheat straw reinforcement	Large	50
C_2			75
C_3			100

2.1.2. Modeling Rig and Model Construction

A physical modeling rig with the dimensions of 3000 mm long, 1200 mm wide, and 500 mm high was used in this research to investigate the performance of the soil slopes under the impact of rainfall. A thin steel plate was forged in the middle of the rig to include two physical models. Local soil was used to infill the modeling rig for model construction. Wheat straws from the current season with good resilience were collected and mixed with the soil before infilling. The diameter of the straws is about 5 mm. These straws were cut to 3–5 mm long and fully mixed with the collected soil. To ensure the best reinforcement, the ratio of straw reinforcement (the ratio between the weight of wheat straws and the weight of the soil–straw mixture) was determined as 0.5%.

The physical models in Group A contained the bare soil with no extra reinforcement. For the geocell and straw reinforced slopes, the geocells were placed on the compacted soil layer at the bottom, and were infilled with the mixture of soil and straw. The infilled soil was properly compacted until the designed height was reached. The rear side of the rig can be lifted to adjust the slope steepness. The finished model is shown in Figure 1.

Figure 1. The constructed physical model at a slope ratio of 1:1.5.

The scaling law is important to the physical study for obtaining accurate and meaningful results. The similarity principles were followed when performing the physical modeling test. Since the full-size geocells were used in the experiment, the geometry coefficient was selected as 1. The density and strength similarity coefficients were also determined as 1. The soils were compacted properly when constructing the physical models so that the density and strength of the modeling slopes were close to the real case.

Five sprayers were fixed evenly above the modeling rig to simulate the rainfall [33,34]. The whole area of the slopes was covered by the artificial rainwater. The average annual precipitation in Guyuan is around 500–600 mm. Intense individual downpours for a relatively short time are not unusual in July and August. Sometimes, the rainfall intensity of the individual downpours can be extremely high. The measured heaviest rainfalls to occur in 24 h and 1 h were more than 110 mm and 50 mm, respectively. According to the rainfall condition on the studied site, the three rainfall intensities in this experiment were selected as 50, 75, and 100 mm/h. Each rainfall continued for 30 min. The high levels of rainfall intensities were selected in this study for considering the worst-case scenario. The rainwater was collected and measured from the runoff ports forged at the front edge of the rig. The amount of soil erosion and the slope displacement were also measured in this work. The amount of soil erosion was determined from the collected water and soil at the runoff ports. The displacement of the slope at the top section was measured using the ruler fixed on the modeling rig.

2.2. Experimental Results

2.2.1. Slope Failures

Figure 2 shows the failure characteristics of the bare slopes under different rainfall intensities after 30 min of rainfall. A number of cracks were observed on the bare slope in Model A_1 at the rainfall intensity of 50 mm/h (Figure 2a). However, the inverse impact of the raindrop to the slope was not significant, and the slope surface still remained smooth and flat. By contrast, an increase in the rainfall intensity contributed to the soil degradation in Models A_2 and A_3. Under the rainfall intensity of 75 mm/h, the soil erosion was insignificant at the top section of the slope, but the soil deterioration was clearly observed at the bottom (Figure 2b). As the rainfall intensity increased to 100 mm/h, rill erosion was found over the majority part of the slope surface (Figure 2c).

(**a**) Model A_1: 50 mm/h (**b**) Model A_2: 75 mm/h (**c**) Model A_3: 100 mm/h

Figure 2. Failure characteristics of the bare slopes after the rainfall.

The stability and surface erosion of the geocell reinforced slopes were better off as compared with the bare slope. Figure 3 shows the final appearance of the small geocell-reinforced slopes under the three rainfall intensities. The overall integrity of the geocell-reinforced slopes was maintained. No cracks or any gully and rill erosion were observed on the slope surfaces reinforced by geocells. The geocell structures played an important role in improving the slope stability by holding the soil in place. On the other hand, the soil degradation increased with the rainfall intensity, which was observed from the depth of the re-appeared geocell section.

Model B_1: 50 mm/h Model B_2: 75 mm/h Model B_3: 100 mm/h

Figure 3. Failure characteristics of the small geocell-reinforced slopes after the rainfall.

The large geocell-reinforced slopes after 30 min of rainfall are shown in Figure 4. Again, the rainfall reduced the slope stability significantly, and an increase in the rainfall intensity resulted in more soil deterioration. The soil erosion and the stability of slopes were also compared to those reinforced with small geocells in Figure 3. It was noted that, in Figure 4, a larger depth of the re-appeared geocell sections was observed, indicating an increased amount of soil erosion. Hence, the small geocells outperformed the large geocells in terms of the soil erosion control.

Model C_1: 50 mm/h Model C_2: 75 mm/h Model C_3: 100 mm/h

Figure 4. Failure characteristics of the large geocell-reinforced slopes after the rainfall.

2.2.2. Soil Erosion

Figure 5 shows the growth of soil erosion with the rainfall process for different slopes. The amount of soil erosion was almost unnoticeable under the rainfall intensity of 50 mm/h. However, the soil erosion increased with the rainfall intensity at an even faster rate. The bare slope saw 550 g of soil erosion at the end of the 50 mm/h rainfall, which was significantly raised to about 9000 g and 22,000 g at the rainfall intensities of 75 mm/h and 100 mm/h, respectively (Figure 5a). The soil erosion was decreased when the slope was reinforced with the small geocells and the wheat straw. The amounts of soil erosion for the three slopes were observed as 40 g, 1400 g, and 3900 g at the cease of the rainfall. The large geocells also decreased the soil erosion; the amounts of soil erosion were 30 g, 1500 g and 5000 g under the three rainfall intensities. However, the small geocell-reinforced models showed less soil erosion; therefore, the small geocells outperformed the large ones.

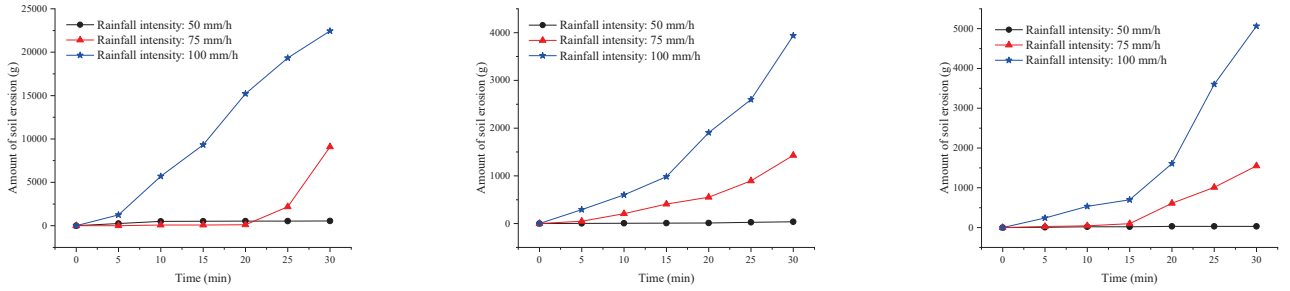

(**a**) Bare slope (**b**) Small geocell reinforcement (**c**) Large geocell reinforcement

Figure 5. Amount of soil erosion for different reinforced slopes under the three rainfall intensities.

2.2.3. Slope Displacement

The displacement at the top section of the slope was recorded during the test until 30 min after the rainfall (see Figure 6). The slope displacement increased at the first 30 min as the rainfall continued. The increase in slope displacement slowed down and started to stabilize after the rainfall ceased. The increase in the rainfall intensity increased the slope displacement. For the bare slope, the final slope displacement grew from 4 mm to 7.6 mm and 12 mm as the rainfall intensity increased (Figure 6a). The geocells improved the slope stability with decreased slope displacement. Particularly, the slope displacement was better controlled with the small geocells. This was seen from the fact that, after the rainfall ceased for 30 min, the small geocell-reinforced slopes found the displacement stabilizing at 1 mm, 2 mm, and 2.6 mm under the three rainfall intensities, respectively (Figure 6b). By comparison, the slope displacement with the large geocells stood at 2 mm, 4.4 mm, and 5.3 mm (Figure 6c).

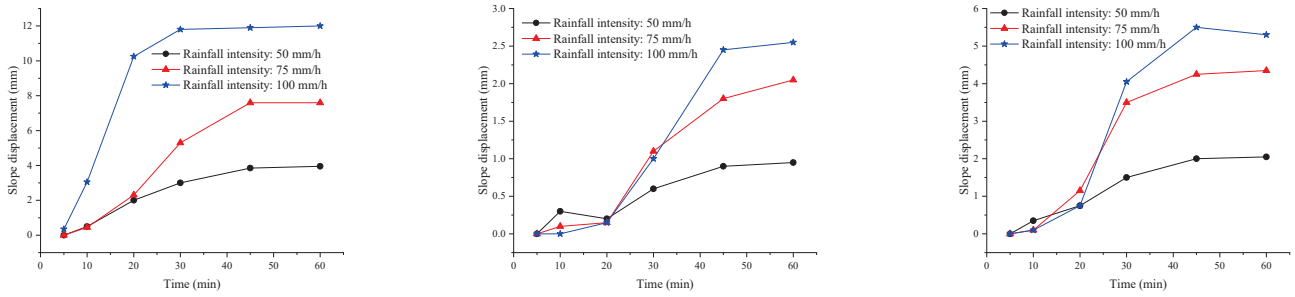

(**a**) Bare slope (**b**) Small geocell reinforcement (**c**) Large geocell reinforcement

Figure 6. Amount of soil erosion for different reinforced slopes under the three rainfall intensities.

3. Filed Practice

3.1. Geocell Installation

3.1.1. Site Preparation

The first step for the slope stabilization with geocells and vegetation was the site preparation. An area of 10 m × 10 m was first selected on the subgrade at the studied area (Figure 7a). The selected area was then properly prepared by removing all the debris, rocks, sticks, weeds, vegetation and gullies before installing the geocell structures (Figure 7b). Voids or channels were filled so that uncontrolled water flow was not allowed under the geocells. The surface was properly leveled and compacted to ensure a smooth and fine graded slope surface. The finished slope after preparation is shown in Figure 7b.

(**a**) (**b**)

Figure 7. Site preparation: (**a**) slope preparation; (**b**) the slope after preparation.

3.1.2. Geocell Installation and Infilling

The next step was the installation of the geocells over the slope and infilling. The geocell was held in place at the crest of the slope with anchors, and fully expanded down the slope and secured at the toe of the slope (Figure 8a). The geocells were opened to a fixed width using separator bars and fixed to the ground using U-shaped nails at a proper interval. A full contact between the cell and the slope surface was properly maintained. After the geocell sections were secured on the prepared surface, infills were placed into the cells. The infills for this study were the local topsoil with appropriate nutrients. The bottom 10 cm of infill placed into the cells was the sufficient bare soil extracted from the neighbouring site (Figure 8a), while the top 10 cm infill was the mixture of the bare soil and wheat straws. Infilling was performed from the crest to the toe (Figure 8b). The topsoil was spread uniformly and evenly over the entire surface. The soil materials were overfilled 25 mm and compacted to the designed height. Excess soil was scraped off from the surface. The treated slope surface is shown in Figure 8c.

(**a**) (**b**) (**c**)

Figure 8. Infilling of the top soil: (**a**) bottom 10 cm of bare soil; (**b**) infilling from the crest to the toe; (**c**) the finished slope after treatment.

3.1.3. Seeding

The third step in the ecological restoration process of the slope was to seed the studied area to be vegetated. The seed is suitable to the soil condition at the studied site. It can also be easily adapted to the local climate and geographical area. The vegetation also has a fast growth rate. The fertilizer is rich in nitrogen, phosphorus, and potassium. The fertilizer was mixed with the topsoil before infilling. In this work, the seed was placed by hand

over the entire surface on 18 July 2019. Once infilled with all the soil materials, an erosion control blanket was used to cover the treated slope face (Figure 9).

Figure 9. Slope surface covered with blanket after seeding.

3.2. Development of Vegetation

The vegetation growth 13 days after seeding is shown in Figure 10. The fast-growing vegetation was well developed beneath the erosion control blanket on the geocell- and wheat straw-treated slope (Figure 10a). The slope was covered with the vegetation over the entire slope surface within the selected area. This was compared to the neighboring untreated bare slope with only few plants on the sandy ground (Figure 10b). As compared with the treated slope soil in the studied area, the sandy soil on the bare slope was unable to provide sufficient and proper nutrients for the vegetation growth. The poor water conditions on the bare slope were also unfavorable to the growth of new vegetation. Vegetation can hardly be planted on the bare slope unless properly treated.

(**a**) (**b**)

Figure 10. Vegetation growth at the 13rd day after seeding: (**a**) vegetation growth within the selected area; (**b**) comparison of the vegetation growth on the treated and bare slopes.

A rainstorm event occurred at the studied site on 4 August 2019, the 17th day after seeding. The slope condition after the impact of the rainstorm is shown in Figure 11. The vegetation was observed on most of the area above the erosion control blanket (Figure 11a). The treated slope in the selected area was neat and clean, with only limited rock and wood debris found at the edge of the selected site, which might be shifted from the neighboring

untreated area by the rainwater. This indicates that the slope in the area covered with the erosion control blanket was barely influenced by the rainstorm. By contrast, no protection against erosion was provided to the neighboring untreated slope. As a result, the bare slope saw a large amount of rock debris scoured around by the rainwater (Figure 11).

(**a**) (**b**)

Figure 11. The condition of the slope under the impact of the rainfall on the 17th day after seeding. (**a**) vegetation observed above the blanket; (**b**) comparison of conditions of the treated and bare slopes.

The establishment of the vegetation after 75 days and 120 days of seeding is shown in Figure 12a,b respectively. A picture of the vegetation was taken from the other side of the river on 1 October 2019 (Figure 12a). It was observed that that the vegetation was well developed on the selected slope surface, in strike contrast to the neighboring untreated slope area with only few plants observed. The new vegetation provided protection against the surface erosion. Four months after seeding, another visit was paid to the studied site on 15 November 2019. The grass in the studied area turned brown in the winter time (Figure 12b). As compared with the bare slope, however, the vegetation cover still protected the slope against the wind, rain and snow. The root system of the vegetation and the geocell structures also provided strength to the soil by holding it in place.

(**a**) (**b**)

Figure 12. Establishment of vegetation after (**a**) 75 days and (**b**) 120 days.

4. Summary and Conclusions

This work proposed a vegetative and soil treatment measure for soil erosion control and slope stabilization. The geocells were used to support the vegetation growth. The vegetation protected the slope against the surface erosion and provided strong root strength to resist movement. The filled soil–straw mixture enhanced nutrients in soil after decomposition. A total of nine physical slopes were prepared in this work; the models were reinforced with different-sized geocells and were placed under different rainfall intensities.

The development of slope failures, soil erosion, and surface displacement were recorded and analyzed. The geocell installation and seeding were also performed at the selected area in the field. Important findings are listed below.

The slope stability was largely improved by the geocell and wheat straw reinforcement. Horizontal cracks and rill erosion were clearly observed on the bare slopes. By contrast, the reinforced models maintained a good integrity and overall stability. The stability improvement by geocells and wheat straws were also verified from the soil erosion and slope displacement. The amount of soil erosion for the bare slope reached 22,000 g under a heavy rainfall, which was compared with below 5000 g for the reinforced slopes. Similarly, the largest displacement of the bare slope was observed at 12 mm, compared with 3–5 mm for the reinforced models.

The small geocells outperformed the large geocells in terms of the soil erosion control. More loss of soil was clearly seen from the large geocell-reinforced slopes, which was also validated from the measured amount of soil erosion with 3900 g of soil loss for the small geocell-reinforced slopes and 5000 g for the large geocell-reinforced slopes. The slope displacement further confirmed this trend, as the largest slope displacement for the large geocell slopes was 5.3 mm, compared with only 2.6 mm for the slopes reinforced with small geocells.

The rainfall had a significant adverse influence on the slope stability. The soil condition and slope stability deteriorated with the rainfall process. On the other hand, the amount of soil erosion and the slope displacement were dramatically increased with an increase in the rainfall intensity. The soil erosion was unnoticeable at the low rainfall intensity. It rose rapidly with the rainfall intensity. Likewise, the slope displacement tripled as the rainfall intensity increased from 50 to 100 mm/h.

The installation of the geocells in the field included the site preparation, geocell installation, infilling, and seeding. The geocells were secured at the crest and toe of the slope, and were expanded down over the slope surface. U-shaped nails were used to fix the geocells to the slope at a proper interval, so that an intimate contact with the soil was ensured. The treated slope face was covered with an erosion control blanket after seeding. The vegetation was well developed after 13 days of seeding. Compared with the untreated slope, the geocell-reinforced and vegetation-treated slope in the studied area showed good resistance to the impacts of the rainstorm on the 17th day after seeding. The fully-developed vegetation started to provide protection to the slope against wind and rainfall; the root system worked as integrated with the geocell structures to provide mechanical reinforcement to the slope.

Author Contributions: All authors contributed to the study conception and design. Material preparation, data collection and analysis were performed by G.S., X.S., S.H., D.K. and S.Z. The first draft of the manuscript was written by G.S. and all authors commented on previous versions of the manuscript. All authors have read and agreed to the published version of the manuscript.

Funding: The paper was supported by National Natural Science Foundation of China (52004010), R&D Program of Beijing Municipal Education Commission (KM202010009001) and the Excellent Research Team of North China University of Technology (107051360021XN083/019).

Institutional Review Board Statement: Not applicable.

Informed Consent Statement: Not applicable.

Data Availability Statement: Data is contained within the article.

Conflicts of Interest: The authors have no relevant financial or non-financial interests to disclose.

References

1. Hess, D.M.; Leshchinsky, B.A.; Bunn, M.; Benjamin Mason, H.; Olsen, M.J. A simplified three-dimensional shallow landslide susceptibility framework considering topography and seismicity. *Landslides* **2017**, *14*, 1677–1697. [CrossRef]
2. Meusburger, K.; Alewell, C. Impacts of anthropogenic and environmental factors on the occurrence of shallow landslides in an alpine catchment (Urseren Valley, Switzerland). *Nat. Hazards Earth Syst. Sci.* **2008**, *8*, 509–520. [CrossRef]
3. Löbmann, M.T.; Geitner, C.; Wellstein, C.; Zerbe, S. The influence of herbaceous vegetation on slope stability—A review. *Earth-Sci. Rev.* **2020**, *209*, 1–17. [CrossRef]
4. Caviezel, C.; Hunziker, M.; Schaffner, M.; Kuhn, N. Soil-vegetation interaction on slopes with bush encroachment in the central Alps–adapting slope stability measurements to shifting process domains. *Earth Surf. Process. Landforms* **2013**, *39*, 509–521. [CrossRef]
5. Sidle, R.C.; Ochiai, H. Landslides: Processes, prediction, and land use. In *Water Resources Monograph 18*; American Geophysical Union: Washington, DC, USA, 2006.
6. Walker, L.R.; Shiels, A.B. *Landslide Ecology*; Cambridge University Press: Cambridge, UK, 2013.
7. Wiegand, C.; Geitner, C. Investigations into the distribution and diversity of shallow eroded areas on steep grasslands in Tyrol (Austria). *Erdkunde* **2013**, *67*, 325–343. [CrossRef]
8. Boardman, J.; Poesen, J. *Soil Erosion in Europe*; Wiley: Chichester, UK, 2006; p. 855.
9. Stokes, A.; Douglas, G.B.; Fourcaud, T.; Giadrossich, F.; Gillies, C.; Hubble, T.; Kim, J.H.; Loades, K.W.; Mao, Z.; McIvor, I.R.; et al. Ecological mitigation of hillslope instability: Ten key issues facing researchers and practitioners. *Plant Soil* **2014**, *377*, 1–23. [CrossRef]
10. Arca, D.; Kutoğlu, H.Ş.; Becek, K. Landslide susceptibility mapping in an area of underground mining using the multicriteria decision analysis method. *Environ. Monit. Assess.* **2018**, *190*, 725. [CrossRef]
11. Brown, W.J. Landslide control on North Island, New Zealand. *Geogr. Rev.* **1991**, *81*, 457–472. [CrossRef]
12. Kainthola, A.; Singh, P.K.; Singh, T.N. Stability investigation of road cut slope in basaltic rockmass. *Geosci. Front.* **2015**, *6*, 837–845. [CrossRef]
13. Rahardjo, H.; Satyanaga, A.; Leong, E.C.; Santoso, V.A.; Ng, Y.S. Performance of an instrumented slope covered with shrubs and deep-rooted grass. *Soils Found.* **2014**, *54*, 417–425. [CrossRef]
14. Zieher, T.; Perzl, F.; Rossel, M.; Rutzinger, M.; Meisl, G.; Markart, G.; Geitner, C. A multi-annual landslide inventory for the assessment of shallow landslide susceptibility–two test cases in Vorarlberg, Austria. *Geomorphology* **2016**, *259*, 40–54. [CrossRef]
15. Stokes, A.; Atger, C.; Bengough, A.G.; Fourcaud, T.; Sidle, R.C. Desirable plant root traits for protecting natural and engineered slopes against landslides. *Plant Soil* **2009**, *324*, 1–30. [CrossRef]
16. Stokes, A.; Sotir, R.; Chen, W.; Ghestem, M. Soil bio- and eco-engineering in China: Past experience and future priorities. *Ecol. Eng.* **2010**, *36*, 247–257. [CrossRef]
17. Rickson, R.J. Evaluating the effectiveness of geotextiles for slope erosion control in mine restoration. In *Proceedings of the 7th International Conference on Mine Closure, Brisbane, Australia, 25–27 September 2012*; Australian Centre for Geomechanics: Perth, Australia, 2012; pp. 101–113.
18. Osman, N.; Barakbah, S. Parameters to predict slope stability—Soil water and root profiles. *Ecol. Eng.* **2006**, *28*, 90–95. [CrossRef]
19. Wu, T.H. Root reinforcement of soil: Review of analytical models, test results, and applications to design. *Can. Geotech. J.* **2013**, *50*, 259–274. [CrossRef]
20. Jastrow, J.D.; Miller, R.M.; Lussenhop, J. Contributions of interacting biological mechanisms to soil aggregate stabilization in restored prairie. *Soil Biol. Biochem.* **1998**, *30*, 905–916. [CrossRef]
21. Gyssels, G.; Poesen, J.; Bochet, E.; Li, Y. Impact of plant roots on the resistance of soils to erosion by water: A review. *Prog. Phys. Geogr.* **2005**, *29*, 189–217. [CrossRef]
22. Fattet, M.; Fu, Y.; Ghestem, M.; Ma, W.; Foulonneau, M.; Nespoulous, J.; Bissonnais, Y.L.; Stokes, A. Effects of vegetation type on soil resistance to erosion: Relationship between aggregate stability and shear strength. *Catena* **2011**, *87*, 60–69. [CrossRef]
23. Rivas, T. *Erosion Control Treatment Selection Guide*; National Technology and Development Program; U.S. Department of Agriculture, Forest Service: Washington, DC, USA, 2006.
24. Acharya, M.S. Bamboo Crib Wall: A sustainable soil bioengineering method to stabilize slopes in Nepal. *J. Dev. Innov.* **2020**, *4*, 99–118.
25. Song, X.R.; Huang, M.S.; He, S.Q.; Song, G.F.; Shen, R.Z.; Huang, P.Z.; Zhang, G.F. Erosion control treatment using geocell and wheat straw for slope protection. *Adv. Civ. Eng.* **2021**. [CrossRef]
26. Wang, G.Y.; Han, Y.; Wang, X.H. Stability analysis of geocell flexible slope protection in rainfall. *Rock Soil Mech.* **2012**, *33*, 3020–3024. (In Chinese)
27. Yan, C.G.; Yang, X.H.; Xie, Y.L.; Li, J.C. Experimental research on anti-eroding effect of geocells in loess embankment. *Rock Soil Mech.* **2005**, *26*, 1342–1348. (In Chinese)
28. Bouhicha, M.; Aouissi, F.; Kenai, S. Performance of composite soil reinforced with barley straw. *Cem. Concr. Compos.* **2005**, *27*, 617–621. [CrossRef]
29. Sato, T.; Kojma, K. Development of slope protection work using geocell and soil nailing. *Jpn. Railw. Eng.* **2018**, *202*, 1–3.
30. Arvin, M.R.; Zakeri, A.; Shoorijeh, M.B. Using finite element strength reduction method for stability analysis of geocell-reinforced slopes. *Geotech. Geol. Eng.* **2019**, *37*, 1453–1467. [CrossRef]

31. Barré, P.; Hallett, P.D. Rheological stabilization of wet soils bymodel root and fungal exudates depends on clay mineralogy. *Eur. J. Soil Sci.* **2009**, *60*, 525–538. [CrossRef]
32. Zhang, C.; Zhao, Y.X.; Han, P.H.; Bai, Q.S. Coal pillar failure analysis and instability evaluation methods: A short review and prospect. *Eng. Fail. Anal.* **2022**, *138*, 106344. [CrossRef]
33. Liu, S.Y.; Han, Q.Z.; Nie, Z.G.; Jia, T.H. Study on characteristic and application of SB-YZCP artificial rainfall simulator. *J. Soil Water Conserv.* **1998**, *4*, 48–54. (In Chinese)
34. Zhou, Y.; Wang, J.; Hu, S.W. Designing and calibration of Kust 03-1 rainfall simulating system. *J. Kunming Univ. Sci. Technol.* **2008**, *2*, 81–85. (In Chinese)

sustainability

MDPI

Article

Spatial Pattern Reconstruction of Water and Land Resources in Coal Mining Subsidence Areas within Urban Regions

Xiaojun Zhu [1,2,*], Feng Zha [1], Hua Cheng [1], Liugen Zheng [1], Hui Liu [1], Wenshan Huang [2], Yu Yan [2], Liangjun Dai [3], Shenzhu Fang [3] and Xiaoyu Yang [4]

[1] Anhui Province Engineering Laboratory for Mine Ecological Remediation, Anhui University, Hefei 230601, China
[2] Huaibei Bureau of Natural Resources and Planning, Huaibei 235000, China
[3] Anhui Construction Engineering Group Corporation Limited, Hefei 230031, China
[4] Department of Engineering Management, Hefei College of Finance and Economics, Hefei 231299, China
* Correspondence: zhuxiaojunahu@126.com; Tel.: +86-1890-5657-910

Abstract: Water and land resources are important material bases of economic and social development, and their spatial patterns determine the pattern of the urban development. The development and expansion of coal-resource-based cities have introduced new societal problems, such as the overlapping of new city construction areas and underground coal resources. Underground coal mining also leads to surface subsidence, which destroys water and land resources and seriously affects the sustainable development of coal-resource-based cities. The surface subsidence area takes a long time to stabilize, and may form a large waterlogging area due to the high groundwater level, thereby increasing the difficulty of reconstructing mining subsidence areas. In this context, a scientific and complete method for reconstructing the spatial pattern of water and land resources in unstable coal mining subsidence areas within urban is proposed in this paper. This method initially predicts the surface subsidence value and then divides the subsidence area within the urban region into the waterlogging area and the non-waterlogging area according to the surface subsidence value. The waterlogging area will be renovated into a landscape lake district in the city by a series of transformation measures. Afterwards, goaf rock mass activation and surface stability evaluation analyses are performed in the non-waterlogging area. According to the evaluation results, land resources can be divided into unaffected, restricted and prohibited building areas, with each area being transformed differently. The Lv Jin Lake in Huaibei is selected as a case study, and the proposed method is applied to reconstruct its water and land resources. The original spatial pattern of the large-scale waterlogging area and abandoned land due to mining subsidence in urban areas is then reconstructed into a spatial pattern that integrates the urban landscape, scenario living and eco-tourism. Compared with traditional subsidence area management, the proposed method greatly increases the utilization value of water and land resources, improves the urban ecological environment, enhances the urban quality and effectively alleviates the problems of land shortage and human–land conflict in coal-resource-based cities.

Keywords: surface subsidence; subsidence waterlogging; urban sustainability; water and land resources; spatial pattern reconstruction

1. Introduction

Coal is a main energy resource in the world that supports sustained and stable economic development. However, the dependence on this resource has also introduced a series of environmental problems [1,2]. After underground coal is excavated, the surrounding rock mass loses its original stress balance state, and stress redistribution creates stress concentration [3,4]. When the concentrated stress on the roof of the roadway exceeds the strength limit, the roof rock produces deformation, cracks and falls, and causes the

overburden stratum to produce compaction and consolidation subsidence. This eventually leads to the movement and deformation of the entire overlying strata, and subsidence basin formed on the surface [5–10]. Many negative environmental impacts are caused by long-term high intensity and large-scale coal mining activities, including surface subsidence, ground fissures, landslides and land encroachment [11–14]. Statistics show that every 1000 tons of coal mining in China causes approximately 0.2 to 0.33 hectares of land subsidence and expands the subsidence area by approximately 7×10^4 hectares every year [15]. Coal mining subsidence areas have been recorded in 151 counties of 23 provinces across China [16]. The total coal mining subsidence area in the country has exceeded 2.0×10^6 hectares, whilst that of some coal-resource-based cities has already exceeded 10% of the total urban area [17].

Subsidence areas with high groundwater levels can easily suffer from waterlogging [18]. When the subsidence basin exceeds the height of groundwater to form a waterlogging area, the groundwater begins to flow into the subsidence basin, and the subsidence basin begins to accumulate water [19]. The subsidence waterlogging expands along with the subsidence basin [20]. When the input and output water volumes reach a balanced state, the range of the waterlogging area remains unchanged in the subsidence basin as shown in Figure 1. The Huainan and Huaibei mining areas in Anhui Province are amongst the 14 largest coal bases in China, characterized by deep burial, thick coal seams and high groundwater levels [21]. On the one hand, these mining areas are located in temperate and humid climates, with annual precipitations ranging between 800 mm and 900 mm [16]. On the other hand, the underground water depths in these areas are less than 5 m [22]. Groundwater porous flow forms the waterlogging area when the surface subsidence exceeds the height of underground water and the high groundwater level and abundant precipitation altogether lead to large-scale waterlogging in the subsidence basin [23]. Statistics show that the subsidence area in Huainan had reached 3.5×10^4 hectares in 2020, of which the waterlogging area accounted for 2.6×10^4 hectares. The total subsidence area will reach 6.78×10^4 hectares, and the waterlogging area will reach 5.0×10^4 hectares [16]. Many instances of subsidence waterlogging due to underground coal mining have also been reported around the world. For instance, the Berkeley Pit Lake in Montana, US [24], the Pontes in Spain [25] and the Raigarh District in India [26] are all affected by coal mining subsidence, hence reaffirming the status of coal mining subsidence as a global geological disaster [16].

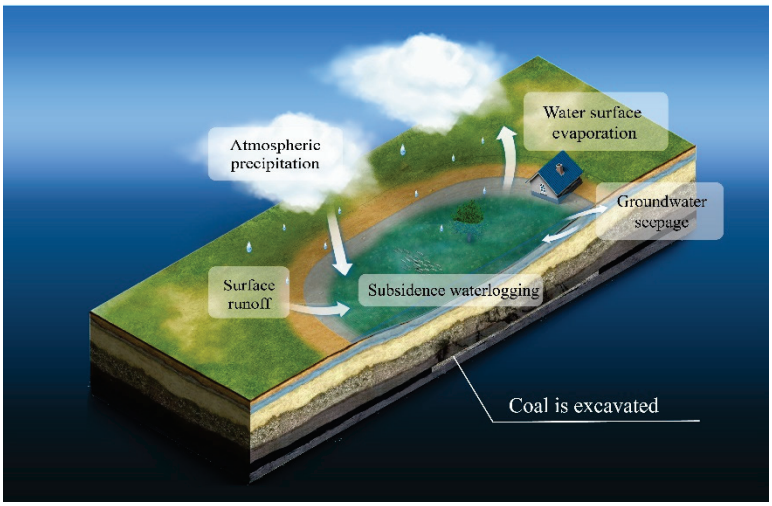

Figure 1. Schematic diagram of the formation of waterlogging in the subsidence area.

Large-scale subsidence areas are caused by coal mining activities and form waterlogging areas [18]. A large amount of subsidence water can destroy land resources and consequently hinder farming activities [27] (Figure 2). Scientific studies have proposed

comprehensive technologies for treating coal mining subsidence areas [28,29]. The Pan'an Lake in Xuzhou City, Jiangsu Province in China presents a successful case of coal mining subsidence area treatment [30,31]. The traditional method for coal mining subsidence treatment mainly aims towards reconstructing these areas into cultivated lands, but the land reclamation rate only ranges from 15% to 25% [32]. In addition, these methods consume much time and have a mediocre governance effect. Hu proposed the concurrent mining and reclamation method, which realizes concurrent mining and reclamation through reasonable reclamation measures to reduce land damage, and preferred reclamation opportunities and schemes before or during the subsidence [28,33]. This method leverages a full combination of mining and reclamation technologies, ensures synchronization with the mining program, improves the land restoration rate, shortens the reclamation cycle and increases the reclamation benefits [34,35]. After a series of treatment measures, the damaged land resources can be used again. However, the broken spatial patterns of coal-resource-based cities cannot be solved properly using the traditional subsidence area treatment methods.

Figure 2. Photo of the coal mining subsidence waterlogging with high groundwater level.

Underground coal mining has a very significant impact on coal-resource-based cities [36]. With the continuous development and expansion of cities, their construction areas begin to overlap with underground coal resources [37]. Coal-resource-based cities have a complex and changeable spatial pattern with certain regional particularity [38]. The urban spatial pattern is a direct representation of urban development and serves as the carrier of economic activities. Therefore, any change in the urban spatial pattern affects the process of urban development [39]. Coal mining brings a series of environmental and social problems, including water pollution, environmental degradation, land shortage, population loss and human–land conflict, in coal-resource-based cities. This activity can also lead to a fragmented and patchy urban spatial pattern and affects the sustainable development of coal-resource-based cities [40–42]. Many coal-resource-based cities are affected by coal mining subsidence in China [36]. For instance, Xintai in Shandong Province is a typical coal-resource-exhausted city whose land and water resources have been completely destroyed due to long-term intensive mining activities. Therefore, the spatial pattern of water and land resources has become a bottleneck that restricts urban development [43–45].

Large land subsidence and waterlogging areas can transform the original terrestrial ecosystem into an aquatic–terrestrial complex ecosystem [16]. The spatial pattern of coal-resource-based cities has changed significantly. In addition, the traditional methods for treating coal mining subsidence, such as the reclamation of subsidence areas into farmlands,

woodlands and fishponds, cannot address the human–land conflict [36,44,45]. Reducing the time of land abandonment and rationally planning the spatial pattern based on the cross-complexity in the space of unstable coal mining subsidence areas within urban areas and the high added-value of land have become crucial issues that need to be addressed to achieve successful reclamation in coal-resource-based cities. To address these problems, this paper proposes a set of methods for the spatial pattern reconstruction of water and land resources in unstable coal mining subsidence areas within urban regions. The Lv Jin Lake mining subsidence area in Huaibei, Anhui Province is selected as a case study. The following research questions are proposed: (1) how can the changed water and land resources be reasonably planned according to the needs of urban development and the stability of the non-waterlogging and waterlogging areas caused by underground mining? (2) How can the reconstruction of water and land resources in coal mining subsidence areas within urban spaces greatly shorten the abandonment time of these resources?

The rest of this paper is organized as follows. Section 2 briefly describes the proposed spatial pattern reconstruction method and the reconstruction of water and land resources in waterlogging and non-waterlogging areas. Section 3 presents an engineering case of the spatial pattern reconstruction method. Section 4 highlights the benefits of coal mining subsidence area treatment to the economy, ecology and society. Section 5 concludes the paper.

2. Spatial Pattern Reconstruction Method of Water and Land Resources in Unstable Coal Mining Subsidence Area within Urban Regions

2.1. A Brief Description of the Spatial Pattern Reconstruction Method

The development and expansion of coal-resource-based cities can lead to an overlap between new city construction areas and underground coal resources. Underground coal mining results in surface subsidence, which in turn leads to houses collapsing, road subsidence, bridge fractures and the deterioration of cultivated land and water. Surface subsidence in urban areas destroys water and land resources, thereby seriously affecting urban sustainable development and the stability of the urban ecosystem. The abandonment of land and water resources, disturbance of the ecological system and deterioration of human settlements in coal mining subsidence areas within urban spaces are the three major factors that restrict the construction of coal-resource-based cities. Figure 3 illustrates the proposed method for reconstructing the spatial pattern of water and land resources in unstable coal mining subsidence areas within urban regions. Specifically, this method aims to reconstruct the waterlogging and abandoned land in urban areas into a spatial pattern that integrates the urban landscape, scenario living and eco-tourism. In this way, human–land conflicts can be effectively addressed, and a coordinated development amongst the society, economy and nature can be promoted. This method also effectively improves the ecological environment and promotes the rapid and sustainable development of regional economies in coal mining subsidence areas within urban areas. The flow of this method is described as follows:

(1) Data on the geological and mining conditions of the subsidence areas are initially collected, including their strata composition, geological structure, hydrogeological data and coal mining data. The final subsidence values are then predicted based on the collected data, the probability integration method and the subsidence prediction parameters. The subsidence values, groundwater level elevation and precipitation are combined to analyze the distribution of subsidence waterlogging. Afterwards, the subsidence areas within urban regions are divided into waterlogging and non-waterlogging areas.

(2) The scope of subsidence waterlogging and the underwater bottom topography of the waterlogging area are predicted. This area will be renovated into a landscape lake district in the city by a series of transformation measures, including deep-excavation and shallow-filling governance, slope revetment reconstruction and ecological environment management.

(3) The stability of the overlying strata in the goaf of the non-waterlogging area is analyzed based on the structure and damage of the overlying strata above the goaf. The ground areas above the goaf are divided into stable and unstable areas. The unstable area is transformed into an urban green space, whereas the stable area is further analyzed as a construction area.

(4) The surface residual subsidence values at the stable area above the goaf are predicted. If the surface subsidence is large and exceeds the subsidence limit, then this area will be designated as the prohibited building area or restricted construction area until the surface subsidence becomes stabilized after a few years. The remaining area within the subsidence limit needs to be further evaluated for the foundation stability of the construction buildings so as to determine the allowable height of buildings. The sum of the height of the fracture zone and caving zone and the influence depth of the building load are then calculated. If the calculated value is less than the coal mining depth, then the building height has no restriction. Otherwise, the design height of the building is reduced until the foundation stability requirements of the construction buildings are met. This area will also be designated as the restricted construction area. If the foundation stability requirements cannot be met, then this area will be designated as the prohibited building area.

(5) According to the foundation stability of the surface buildings, the land resources of the non-waterlogging area are divided into unaffected, restricted and prohibited building areas, which are transformed differently as follows:

a. The unaffected building areas are reasonably planned as the residential and commercial areas to solve the contradiction between the expansion of the subsidence area and the rapid growth of residential land resources for construction and to improve the value of land use.

b. Although the buildings in the restricted construction area are affected by mining subsidence, the impact is relatively small, and residential areas and large shopping malls with low floors can be built.

c. The prohibited building area can be designed as part of a wetland park to maintain and improve the surrounding ecological environment. In this area, urban green spaces can be built, and sports and entertainment facilities can be constructed to provide recreational places for the surrounding residents.

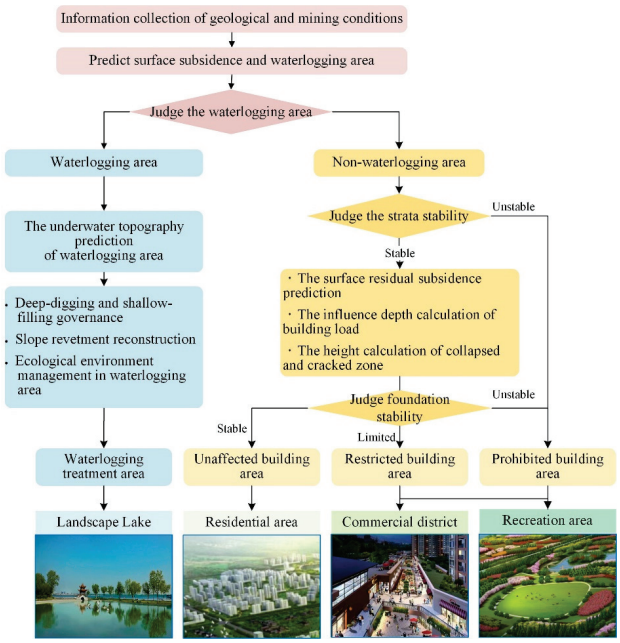

Figure 3. Reconstruction method of the spatial pattern of water and land resources.

2.2. Reconstruction of Water and Land Resources in the Waterlogging Area

2.2.1. Surface Subsidence Prediction

Surface subsidence prediction is one of the most important steps in the proposed spatial pattern reconstruction method, and its accuracy directly affects the area of water and land resources reconstruction and the early-stage stability assessment of building construction.

The probability integral method (PIM) is a mining subsidence prediction method based on stochastic medium theory. This theory was introduced to strata movement research by J. Litwiniszyn in the 1950s [46], and it was later developed by Chinese scholars Liu Baochen and Liao Guohua et al. into the probability integral method [47]. In China, the PIM is the most used function for coal mine subsidence prediction and plays an important role in reducing the loss of mining subsidence. The strata are regarded as continuous media in the PIM, the movement of the strata and surface is regarded as granular media for the stochastic medium and the granular media move down randomly under the action of gravity (Figure 4). The most important step in the PIM is to obtain the prediction parameters accurately; as this method has been in use in China for a long time, scholars have already summarized the prediction parameters for most coal mines in the country, and these parameters are stated in regulations for easy reference [48]. In engineering applications, apart from accuracy, the convenience and implementability of the prediction method also need to be considered. The PIM is a mature method with only a few prediction parameters. According to the principles of mining subsidence prediction for the PIM, the surface subsidence caused by a small unit can be computed as:

$$W_e(x,y) = \frac{1}{r} e^{-\pi \frac{x^2+y^2}{r^2}}, \tag{1}$$

where $W_e(x,y)$ is the surface subsidence caused by small unit mining, (x, y) are the coordinates of the surface point, r is the major influence radius given by $r = H/tan\beta$, H is the mining depth and $tan\beta$ is the tangent of the major influence angle.

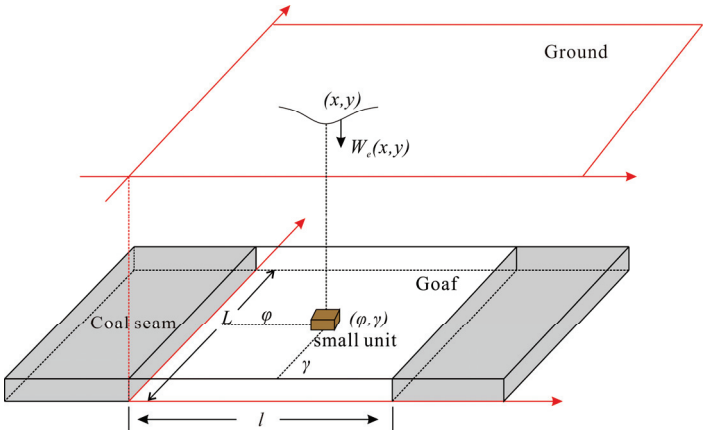

Figure 4. Schematic of surface subsidence calculation by PIM.

The integral is carried out on the whole working face, and the subsidence value of any point caused by the mining of the working face can be calculated as:

$$W(x,y) = \iint_D W_0 W_e(x,y) dsdt = \iint_D \frac{W_0}{r^2} e^{-\pi \frac{(x-s)^2+(y-t)^2}{r^2}} dsdt, \tag{2}$$

where $W(x,y)$ is the subsidence of working face mining; W_0 is the maximum ground subsidence, $W_0 = mq\cos\alpha$; m is the mining thickness; q is the subsidence factor; α is the dip angle of the coal seam; D is the calculation mining area of the working face; the length of the area along the strike is D_3; l is the calculated length of the working face along the strike, which can be calculated by $l = D_3 - 2S$; S is the inflection point offset; the length

of the area D along inclination is D_1; L is the calculated length of the working face along the dip, which can be calculated by $L = (D_1 - 2S)\frac{\sin(\theta+\alpha)}{\sin(\theta)}$; θ is the main propagation angle; *dsdt* is the integration variable of the double integral of area D.

The scope change of the subsidence area caused by underground coal mining is a dynamic process with the advancement of the working face. The surface subsidence gradually develops to the strike direction of the working face. A large-scale waterlogging area forms in the mining area with a high groundwater level, and the subsidence accumulation of water is also a dynamic process. The waterlogging area gradually expands with the advancement of the working face. Therefore, to utilize water and land resources in unstable coal mining subsidence areas comprehensively, predicting the waterlogging area's scope is important. As shown in Figure 5, when the working face is advanced to different positions (T_1, T_2, T_3, … T_n), the range of the subsidence basin and the position of the waterlogging area boundary are different (B_1, B_2, B_3, … B_n).

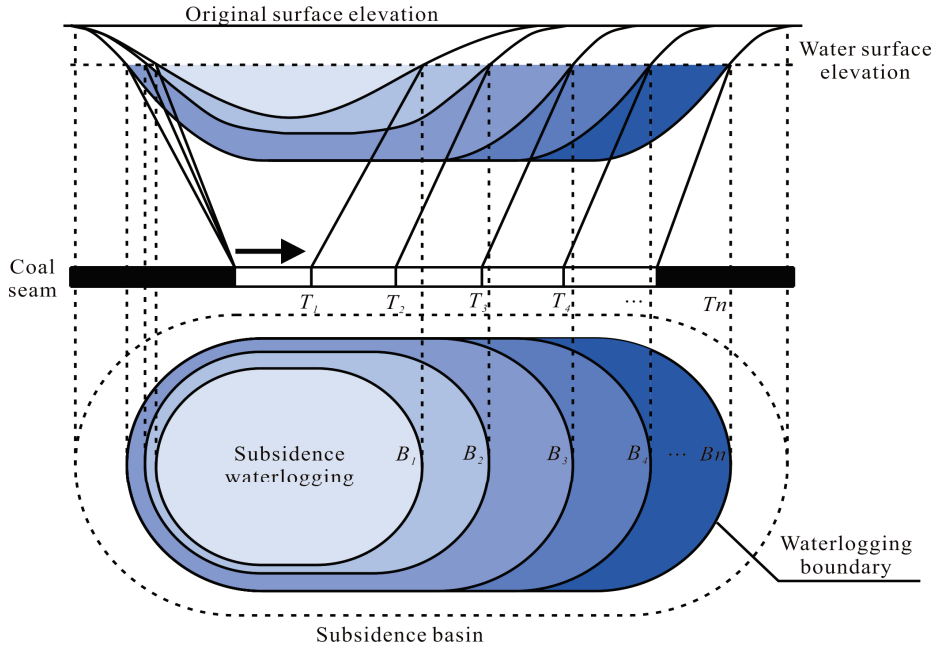

Figure 5. Change of subsidence and waterlogging area with the advance of the coal mining panel.

The Knothe time function is introduced to dynamically predict the subsidence of the working face advancing to different positions [49]. This function was introduced by Polish scholar Knothe [50], who proposed that the sinking speed of a point on the surface at time t is proportional to the difference between the final subsidence of this point and the subsidence at time t. By combining the Knothe time function with the PIM, the progressive surface subsidence can be computed as [51]:

$$W(x,t) = \begin{cases} w_0 \cdot v \int_0^1 \frac{1}{r} e^{-\pi \frac{(x-v\tau)^2}{r^2}} [1-e^{-c(t-\tau)}] d\tau, t \le \frac{L}{v} \\ w_0 \cdot v \int_0^{\frac{L}{v}} \frac{1}{r} e^{-\pi \frac{(x-v\tau)^2}{r^2}} [1-e^{-c(t-\tau)}] d\tau, t \ge \frac{L}{v} \end{cases} \quad (3)$$

where v is the advance rate, and L is the mining length of the working face.

2.2.2. Waterlogging Area Prediction

The predicted surface subsidence, groundwater level and precipitation are used to predict the waterlogging area. A high groundwater level area can easily produce a large waterlogging area. After a coal mining activity is completed, the surface gradually becomes relatively stable. Despite not reaching a stable state of subsidence, the range of the waterlogging area does not significantly fluctuate. This range can be determined based

on the precipitation and topographic contours of subsidence areas (Figure 6). The area of subsidence waterlogging can be computed as:

$$A^w = \frac{1}{2}\sum_{i=1}^{n}(x_i^w y_{i+1}^w - x_{i+1}^w y_i^w), \tag{4}$$

where A^w is the area of waterlogging, and (x_i^w, y_i^w) are the coordinates of any point in the waterlogging area.

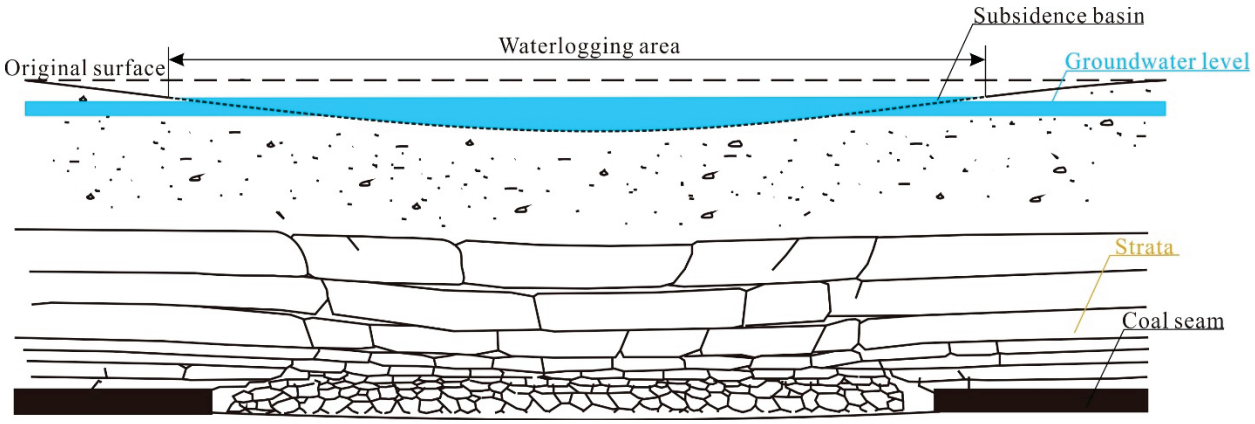

Figure 6. Schematic of the formation of the waterlogging area.

Waterlogging in coal mining subsidence areas is a type of abundant water resource. However, the shape of the waterlogging area is irregular, and the underwater bottom topography is complex, thereby introducing problems in planning and utilizing subsidence waterlogging in advance. Therefore, the underwater bottom topography is predicted based on the predicted surface subsidence. The elevation of the subsidence basin is calculated by subtracting the surface subsidence from the original surface elevation. The underwater bottom topography of the subsidence waterlogging area can then be drawn as:

$$h = H_w - H(x, y) \tag{5}$$

where h is the water depth at any position, $H(x, y)$ is the elevation in this point after mining and H_w is the elevation of the water surface.

2.2.3. Terrain Modification and Reconstruction of the Subsidence Waterlogging Area

On the basis of the obtained underwater bottom topography of the subsidence waterlogging area, the waterlogging area will be renovated into a landscape lake district in the city by a series of transformation measures, including deep-excavation and shallow-filling governance, slope revetment reconstruction and ecological environment management.

The basic rules of earthwork balance and ecological benefit maximization are followed according to the surface subsidence value and the designed terrain of the waterlogging area for designing the terrain of the future subsidence waterlogging area. Terrain modification and reconstruction are carried out before the mining of the working face or the stable subsidence of the surface [16]. The deep-excavation and shallow-filling method excavates the middle of the surface subsidence basin and fills in the edge of the surface subsidence basin after the excavation of the underground coal working face is completed or when the surface becomes stable. This method turns the waterlogging area into a landscape lake. The surface terrain is then transformed into the final terrain design as shown in Figure 7. The deep-excavation and shallow-filling area is divided into four parts. Area I is located near the boundary of the surface subsidence basin from the subsidence boundary ($W(x) = 0$, $H_1(x) = H_0(x)$) to the upper boundary of the surface slope after treatment ($H_2(x) = H_0(x)$). Area II is situated in the slope area subjected to tensile deformation from

the upper boundary of the surface slope after treatment to the boundary of 'deep-excavation and shallow-filling' ($H_1(x) = 0$). Area III is located in the slope area subjected to compression deformation from the boundary line of 'deep-excavation and shallow-filling' to the lower boundary of the surface slope after treatment (where $W(x)$ is the maximum subsidence value). After the coal mining subsidence surface stabilizes, the terrains of Areas II and III become a design slope, and slope revetment reconstruction is then carried out. Area IV is located at the bottom of the subsidence basin after treatment. The mathematical model of the terrain reconstruction partition reconstruction is shown in Table 1. The terrain modification of the subsidence waterlogging area serves as the basis for the subsequent ecological environment reconstruction.

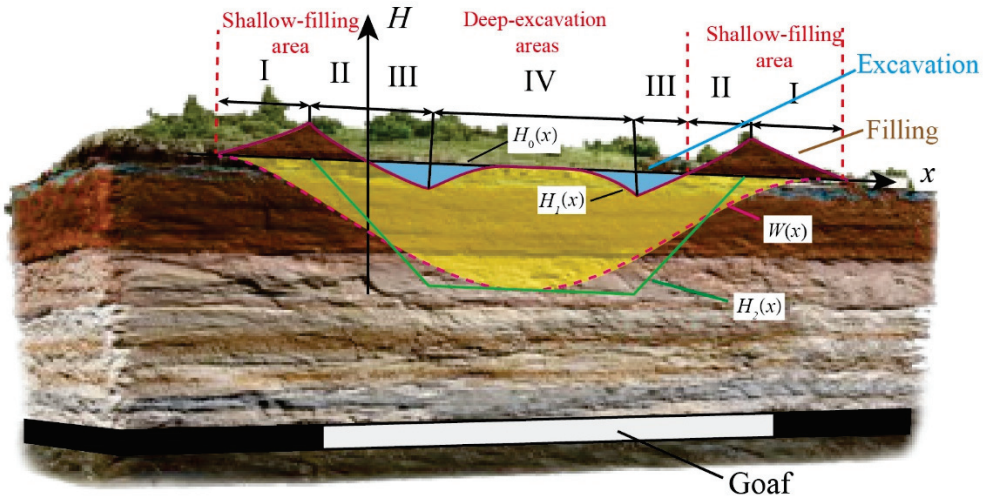

Figure 7. Schematic of deep-excavation and shallow-filling method.

Table 1. Mathematical model of terrain reconstruction in subsidence area.

Area	x Range of Coordinates		Design Elevation of Filling
I	$-r - s_1 < x < -b/k$	$l + b/k < x < l + s_2 + r$	$H_0 + W(x)$
II	$-b/k < x < x_0$	$L - x_0 < x < l + b/k$	$H_0 + W(x) - H_2(x)$
III	$x_0 < x < (W_{max} - b)/k$	$L - (W_{max} - b)/k < x < l - x_0$	$H_0 + W(x) - H_2(x)$
IV	$(W_{max} - b)/k < x < l/2$	$L/2 < x < l - (W_{max} - b)/k$	$H_0 + W(x) - W_{max}$

Where r is the major influence radius; s_1 and s_2 are the inflection point offsets; l is the calculated length of the working face along the strike; L is the calculated length of the working face along the dip; W_{max} is the maximum subsidence value; k is the slope of the design slope equation; b is the intercept of the designed slope equation; $H_0(x)$ is the original surface elevation; $H_1(x)$ is the fill design elevation; and $H_2(x)$ is the treated surface elevation.

The terrain after different transformations is divided into several areas. The flat land is used to plant flowers and plants to beautify the environment, the slope land is used to fix the soil by vegetation and the subsidence waterlogging area is planted with aquatic plants to purify the aquatic environment.

2.3. Reconstruction of Land Resources in the Non-Waterlogging Area

The traditional method of land reclamation is to reclaim the land in the non-waterlogging subsidence area and then plant crops. However, land resources are very precious due to the coal mining subsidence area in the city. If these land resources are abandoned, then much usable value will be lost. To improve the land use value, this paper proposes the construction of buildings in the subsidence area in the city, and a stability assessment must be carried out before construction to ensure the safety of the buildings during use.

The stability assessment of the non-waterlogging subsidence area involves an activation analysis of the rock mass in goaf, a surface residual subsidence analysis and an influence depth analysis of the ground building load. The activation of the goaf has a great influence on the rock mass deformation process, which increases the subsidence of the terrain surface. The rock mass activation analysis determines whether the strata are stable after the mining and confirms whether the subsidence of the terrain surface will increase again so as to prevent building-related disasters in the future. The surface may retain a small residual deformation for a long time after the coal seam mining is completed, and the negative effects of these small deformations on the ground buildings should be evaluated. Given that the coal mining subsidence area is located in the city, new buildings may be built. When new buildings are built on the ground, their self-weight stress acts on the top of the goaf. The gravity will be transferred to the underground soil, sand and rock in the formation, thereby affecting the underground rock mass that tends to stabilize, destroying the stable structure and increasing subsidence on the surface. The feasibility of building and the allowable building height are determined by analyzing the influence depth of additional loads and the height of the collapsed zone and cracked zone. Therefore, the stability assessment should be based on the activation analysis of the rock mass in goaf, the surface residual subsidence analysis and the influence depth analysis of the ground building load. The surface areas above the goaf are divided into stable and unstable areas. The unstable area above the goaf is transformed into an urban green space, whereas the stable area is further analyzed as a construction area.

2.3.1. Activation Analysis of the Rock Mass in Goaf

After mining, some cavities at the edge of the goaf are not completely filled by the collapsed rock. As long as no new mining activities are conducted in and nearby the goaf, the activation deformation of the goaf is small, and the subsidence process on the ground surface is slow. A limited uneven subsidence can also be observed, and no severe structural instability type of subsidence failure is expected.

2.3.2. The Surface Residual Subsidence Prediction

Residual subsidence in the coal mining subsidence area affects the safety of surface buildings. New buildings in the area without subsidence waterlogging need to predict the surface residual subsidence. The PIM is mainly used to predict the subsidence and calculate the residual subsidence of coal mining subsidence, combining subsidence prediction parameters of the PIM. The regression analysis of subsidence parameters and time establishes the relationship model between the residual subsidence coefficient and the subsidence coefficient and time. The residual subsidence coefficient q_r is as follows:

$$q_r = (1 - q)k\left[1 - e^{-(1-\frac{t}{50})}\right], \tag{6}$$

where q is the subsidence coefficient; k is the adjustment coefficient; the value is 0.5–1.0; and t is the time from the end of mining. The unit is by year.

The measured data and the calculated residual subsidence coefficient are used to predict residual subsidence. According to the regulation [48], determining the damage (protection) grade standard for brick-concrete buildings, whose length or length in the joint deformation section is less than 20 m is possible. A building's Grade I damage standard is: inclination deformation less than 3.0 mm/m, horizontal deformation less than 2.0 mm/m and curvature deformation less than 0.2 mm/m^2.

2.3.3. The Influence Depth Calculation of Ground Building Load

The stability of the subsidence area is evaluated based on whether the residual deformation of the surface is singular, and the residual deformation is predicted by solely considering the degree of deformation of the surface over time without additional stress. When a new building is built on the ground, the gravity of this building acts above the goaf,

and the compression of the surface by gravity will be transmitted to the ground through the soil, sand and rock in the strata. The gravity of the building affects the original stable strata. The stable structure is broken down again, and the surface has a new deformation. The load size and position of surface buildings are the main factors that disturb the stability of the foundation. Therefore, the influence depth of the building load on the foundation and height of the crack zone and the caving zone formed above the goaf should be calculated. A comprehensive analysis of the relationship between the height of the belt and the foundation stability of the subsidence area must also be performed.

According to the evaluation method of foundation stability in the subsidence area in the regulation [48], the influence depth of the ground building load is mainly determined by the additional stress generated by the building load and the foundation's self-weight stress. For the coal mining subsidence area, generally, when the additional stress in the foundation is equal to 10% of the self-weight stress of the corresponding position, the influence of the building load at this depth can be ignored. To consider the complexity of the activation of the damaged rock foundation in the goaf and the self-compacting effect of the deep-excavation and shallow-filling soil for safety reasons, the additional stress in the foundation is equal to 5% of the self-weight stress as the criterion for the negligible influence of the additional stress on the activated deformation of the rock mass caused by mining.

The calculation formula for the self-weight stress in the foundation is the following:

$$\sigma_c = \sum_{i=1}^{n} r_i h_i, \tag{7}$$

where σ_c is the self-weight stress, kPa; n is the number of soil layers from the ground to the depth z; r_i is the soil bulk density, kN/m^3; and h_i is the thickness of soil layer, m.

The formula for calculating the additional stress at the depth z under the center point of the rectangular vertical uniform load is as follows:

$$\sigma_z = \frac{2p}{\pi}\left[\frac{2mn\left(1+n^2+8m^2\right)}{\sqrt{1+n^2+4m^2(1+4m^2)(n^2+4m^2)}} + \arctan\frac{n}{2m\sqrt{1+n^2+4m^2}}\right] = \alpha_0 pm = \frac{l}{b}.....m = \frac{l}{b} \tag{8}$$

where α_0 is the distribution coefficient of vertical stress below the center point under rectangular vertical uniform load; P is the uniform load, kPa; b is the width of the rectangular base, m; l is the length of the rectangular base, m; and z is the calculation point depth, m.

2.3.4. The Height Calculation of Collapsed Zone and Cracked Zone

The height of the collapsed zone and cracked zone can be calculated according to the lithology of the rock mass by calculating the depth of the building under the condition of $\sigma_z = 0.05\sigma_c$, as the influence depth of buildings. At the same time, the influence depth of building H_{dz}, the height of the collapsed zone and cracked zone above the goaf H_k and H_l and the minimum mining depth of coal seam $H_{\min}$ are calculated. Then, the relationship between them is determined. When the condition $H_{\min} \geq H_k + H_l + H_{dz}$ is met, the influence depth of the building will not touch the collapsed zone and cracked zone above the goaf. The maximum height of the collapsed zone and cracked zone can be determined based on geological data.

2.3.5. The Height Calculation of Buildings

New buildings in the coal mining subsidence area need to determine the height of buildings. The building height is the main factor affecting the influence depth of the building load. The uniform load P is positively related to the height of the building, which according to $H_{\min} \geq H_k + H_l + H_{dz}$ and Formulas (7) and (8), can determine the allowable height of ground buildings.

3. Case Study

3.1. Overview of the Study Area

The Lv Jin Lake mining subsidence treatment area is located east of Huaibei City, Anhui Province. With the development and expansion of Huaibei City, the scope of its urban construction starts overlapping with that of underground coal mining. The coal mining study area was surrounded by an urban trunk road during the development of the city and is located only 2.8 km away from the city center. The surface subsidence and subsidence waterlogging due to underground mining in urban areas destroy water and land resources and seriously affect the sustainable development of the city. The geographical location of the study area is within urban limits as shown in Figure 8.

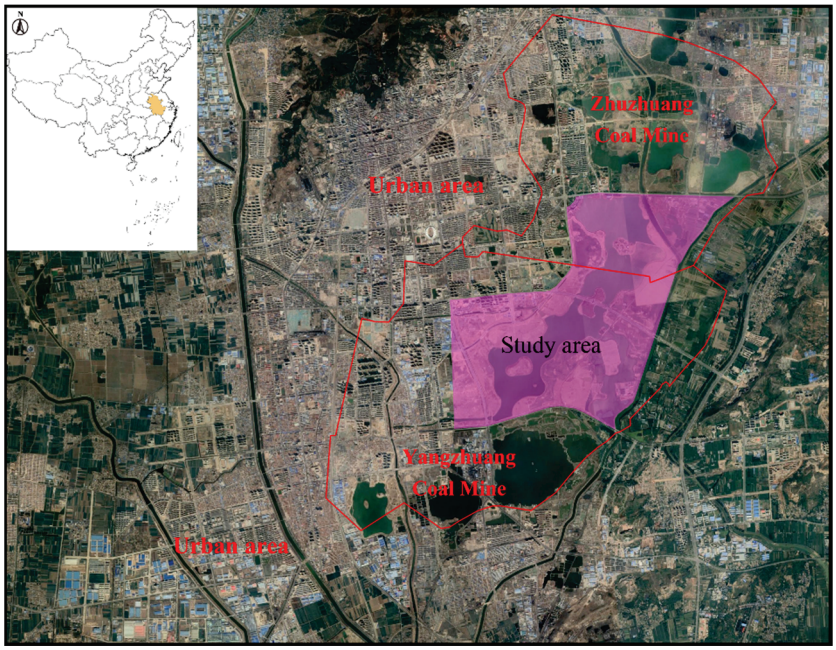

Figure 8. Schematic of the geographical location of the study area (the remote sensing image is Sentinel-2 satellite image).

The study area is located above the Zhuzhuang and Yangzhuang coal mines. The Zhuzhuang coal mine lies northeast of the Lv Jin Lake, the Yangzhuang coal mine is located southwest and the total treatment area is 24.1 km^2. The study area has flat topography with farmland and buildings. The inclination angle of the coal seam generally ranges between 7° and 15°, and the total thickness of the mineable coal seam is approximately 7.57 m. The coal mining method applied in this area is longwall mining, and the caving method is adopted to manage the roof. A graphic log of the simplified strata structure is presented in Figure 9.

The coal mining in this area has brought many negative environmental impacts as shown in Figure 10. Specifically, due to the years-long coal mining activities in the Zhuzhuang and Yangzhuang coal mines, a large area of goaf has been formed, different degrees of subsidence can be observed and a large-scale subsidence basin has been developed. The study area also has high groundwater levels and an abundant precipitation area, thereby forming a large permanent and seasonal waterlogging area.

System	Series	Formation	Thickness	Drill log (1: 300)	Note
Q	Holocene Series		200		Mainly composed of clay, sand and gravel
	Pleistocene Series				
N	Pliocene Series		28		Mainly composed of clay, sandy gravel, sand and sandy clay
	Miocene Series	Upper Member	55		
		Lower Member	65		
E		Upper Member	15		Mainly composed of gray-purple, brown-red mudstone, argillaceous sandstone and conglomerate
		Middle Member	27		
		Lower Member	30		
P	Upper Permian Series	Upper Shihezi Formation	67		Coal seam group 3 is well developed, while 1 and 2 coal seam groups have many layers and poor coal quality
	Lower Permian Series	Lower Shihezi Formation	65		Containing 5, 6, 7, and 8 coal seam groups, the coal quality is good and the coal seam is thick, which is the main mineable coal seam
		Shanxi Formation Upper Member	30		Contains 11 and 10 coal seam groups, which are locally recoverable
		Shanxi Formation Lower Member	21		

Figure 9. Schematic of drill hole columnar section in the study area.

Figure 10. Photo of environmental damage caused by coal mining in study area.

3.2. The Waterlogging Area Prediction

The scope of the waterlogging area is predicted to reconstruct the terrain by the 'deep-excavation and shallow-filling' method in advance. The PIM is used to predict the final surface subsidence value, the subsidence area is mainly located above the working face shown in Figure 11 and the big waterlogging area will be formed in here finally. As shown in Figure 12a, part of the waterlogging area is observed in the northern part of the study area, and the coal mining subsidence area is in an unstable subsidence state. In the future, this waterlogging area may subside sequentially, thereby resulting in the formation of a wider waterlogging area, and abundant water and land resources will be abandoned for a long time. The human–land conflict is intensified, and the development of coal-resource-based cities is restricted. Therefore, the 'deep-excavation and shallow-filling' method is used for treating the coal subsidence area shown in Figure 12b. The middle

of the study area is then excavated, and the edge is filled. Given that the study area is surrounded by roads, the deep-excavation and shallow-filling method is not applied in the marginal partial area of the predicted waterlogging area. However, slope revetment reconstruction is performed to ensure that the partial area is non-waterlogging. The study area terrain is transformed into the final terrain design shown in Figure 12c.

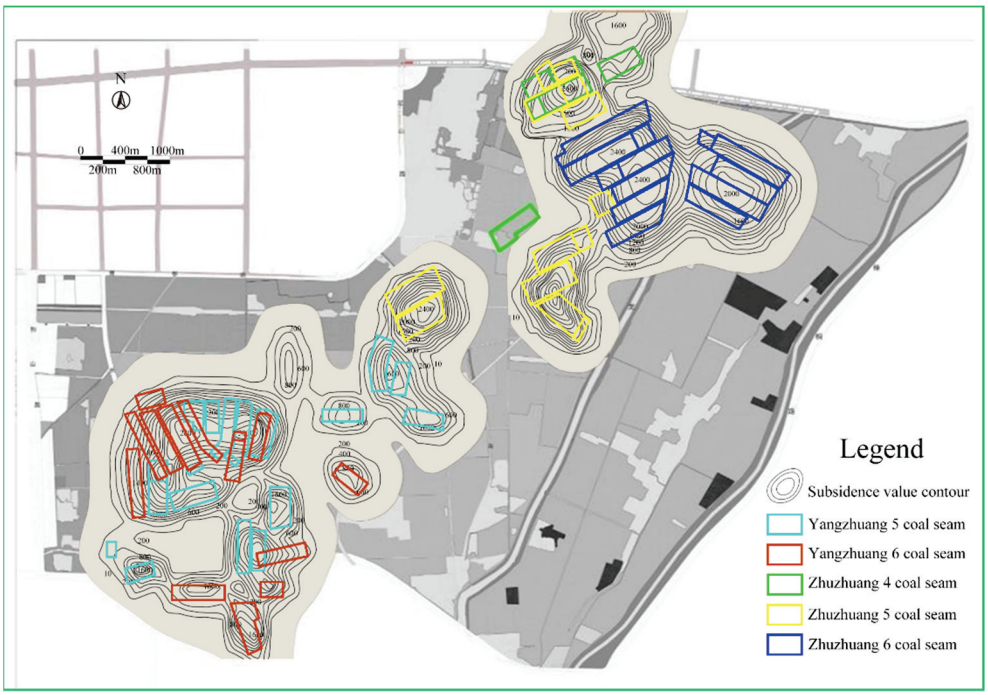

Figure 11. Schematic of the predicted waterlogging area.

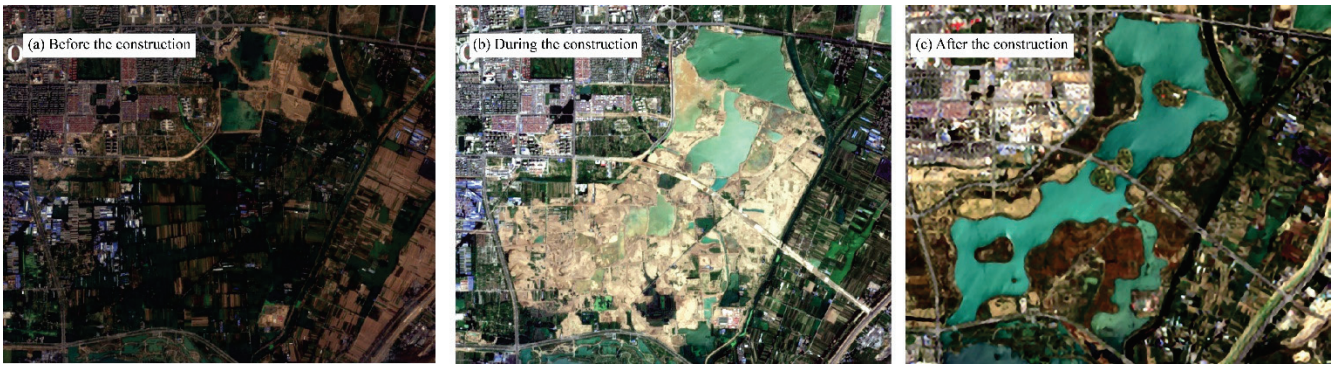

Figure 12. Changes in the treatment process of waterlogging area (the remote sensing images are Sentinel-2 satellite image).

3.3. The Residual Subsidence Prediction

Aiming at the non-waterlogging area, the goaf rock mass activation analysis and surface stability evaluation analysis are carried out. The coal mining subsidence in the Lv Jin Lake mining area has changed strata and rock soil's engineering geological characteristics and properties. It has formed complex foundation conditions with bad engineering geology, which has brought difficulties and hidden dangers to the development and utilization of the land above the abandoned goaf for building. After the mining is over and the surface subsidence is stable, the mining rock system forms a new relative balance and stability. Under the action of factors such as in-situ stress, external force, rock mass strength attenuation or their combination, the balance of the rock mass system will be broken again, resulting in stress redistribution, the strata and surface movement and deformation,

activating the goaf. The activation of the goaf in Lv Jin Lake is the key issue that affects the utilization of the surface buildings in the treatment area and causes the destruction of the new buildings above the area. Therefore, the residual subsidence of the area must be predicted before the land use planning. The residual subsidence model has been introduced in Chapter 2 Section 3 Part 2. The PIM parameters for predicting residual subsidence are shown in Table 2. The extreme values of residual subsidence deformation are shown in Table 3.

Table 2. Prediction parameters of probability integral method.

Prediction Parameters	Subsidence q/m	Tangent of Major Influence Angle tanβ	Deviation of Influence Point S/m	Propagation Angle s/°	Displacement Factor b
Subsidence	1.18	1.6	0	86	0.36
Residual subsidence	0.056	1.6	0	86	0.36

Table 3. The extreme value of residual subsidence deformation.

Subsidence (mm)	Inclination (mm/m)	Curvature (mm/m^2)	Horizontal Movement (mm)	Horizontal Deformation (mm/m)
364	1.3	0.01	93	−0.9,0.6

According to the prediction parameters of residual subsidence, the residual subsidence contour can be predicted as shown in Figure 13. Based on the analysis of Figure 13 and Table 3, the maximum residual subsidence value is 364 mm, the maximum residual inclination value is 1.3 mm/m, the maximum residual curvature deformation value is 0.01 mm/m^2, the maximum residual horizontal movement value is 93 mm, the maximum residual compression deformation is 0.9 mm/m and the maximum residual tensile deformation is 0.6 mm/m. The residual horizontal deformation, curvature and inclination that occurred in the study area are within the Grade I building damage level range in the reference standard. Thus, from the perspective of surface residual deformation, new buildings in the study area are less affected by the surface residual deformation. In theory, buildings can be carried out anywhere in the area.

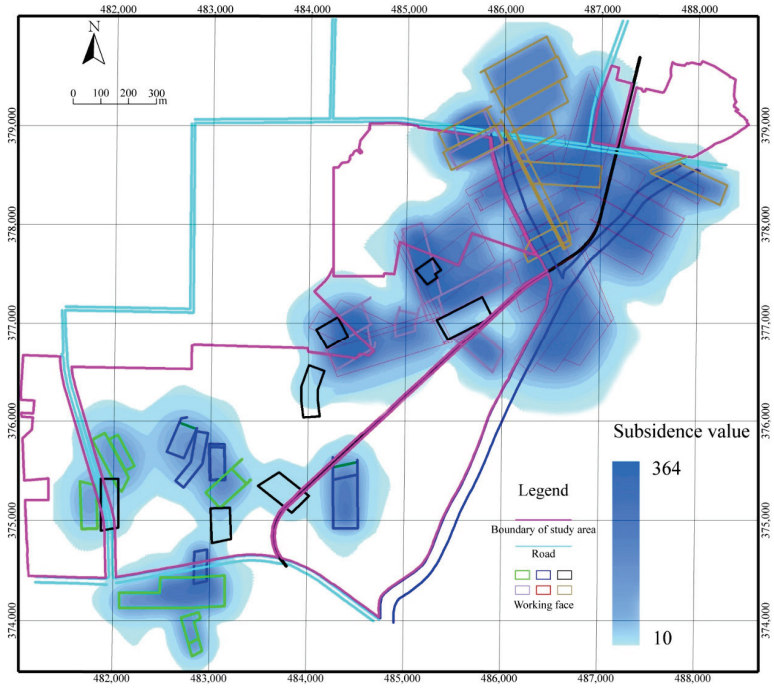

Figure 13. Nephogram of residual subsidence in the study area.

3.4. The Building Feasibility Analysis of the Study Area

3.4.1. The Height Calculation of Collapsed Zone and Cracked Zone

The overlying strata of the coal seam roof in the study area are medium-hard rock. The inclination angle of the Yangzhuang coal mine seam is 7–25°, and the inclination angle of the Zhuzhuang coal mine seam is 7–15°. Mainly mining the fourth, fifth and sixth coal seams, the thickness of each coal seam is 2.37, 2.90 and 3.00 m, respectively. According to the regulation [48], combining the geological data, the height calculation formulas of the collapsed zone and cracked zone are as follows:

$$H_k = \frac{100M}{4.7M + 19} \pm 2.2, \tag{9}$$

$$H_l = 20\sqrt{M} + 10, \tag{10}$$

where M is the coal seam mining thickness, caused by the complexity of interaction between working faces, and the maximum thickness of the coal seam is taken in the calculation.

The height calculation of the collapsed zone and cracked zone above the working face of the fourth, fifth and sixed coal seams is shown in Table 4.

Table 4. Maximum height of collapsed zone and cracked zone in coal seams.

Coal Seam	The Fourth	The Fifth	The Sixth
H_k (m)	10.06	12.65	11.26
H_l (m)	40.79	49.50	44.64
H_k + H_l (m)	50.85	62.15	55.90

3.4.2. The Allowable Height Calculation of Buildings

According to the most common architectural design at present, the length of new buildings in the study area is 40 m, and the width is 10 m. The surface load P under a single layer action is 20 kPa. Combining with the thickness measured by drilling and the self-weight stress parameter of the soil layer, the quaternary system is 62.5 m below the ground surface, bulk density is 19 kN/m^3, sandstone is below 62.5 m and shale and argillaceous sandstone have an average bulk density of 22 kN/m^3. The additional stress coefficient α_0 can be found by using Boussinesq's formula. The number of building floors can be obtained according to the additional stress α_0.

The minimum mining depth of the fourth coal seam III426 working face is 112 m. The height sum of the collapsed zone and cracked zone is 50.85 m. The distance to the ground surface is 61.15 m. According to $z/b = 6.115$, 6.0 is taken, and the additional stress coefficient α_0 is 0.1161. According to formulas (7) and (8), the maximum number of building floors is 25 floors. The theoretical design of the building floors of each working face of the fourth coal seam is shown in Table 5. By drawing the curve between the distance from the surface to the collapsed zone and cracked zone and building floors, shown in Figure 14, as the distance from the surface to the collapsed zone and cracked zone increases, the allowable value of the building floors increases with the exponential relationship. The reason is that the additional stress coefficient gradually decreases with depth, and the deeper the depth, the faster the decrease. The mining depth of the fifth and sixth coal seams' working face is 300–680 m, the maximum height sum of the collapsed zone and cracked zone is 62.15 m; the analysis shows that the disturbance depth of the buildings is far from affecting the collapsed zone and cracked zone. Theoretically, the number of building floors has no limit.

Table 5. The building floors above the fourth coal seam.

Name	The Distance from Surface to Collapsed Zone and Cracked Zone/m	Building Floors
III4420	132	183
III4418	127	150
III4416	120	125
III4417	111	99
III4415	106	84
III4423	76	39
III428	65	29
III426	61	25

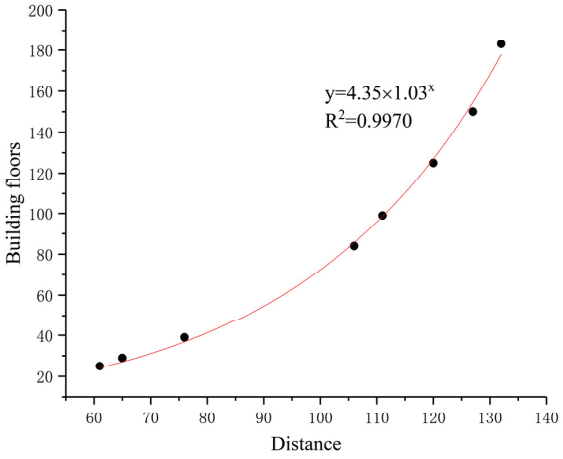

Figure 14. Curve relationship between the distance from surface to collapsed zone and cracked and building floors.

3.5. Spatial Pattern Reconstruction of Water and Land Resources in the Study Area

According to the above design rules, the land in the study area is rationally planned. The study area is divided into unaffected building area, building area affected by residual subsidence, restricted building area, water area and green land, as shown in Figure 15.

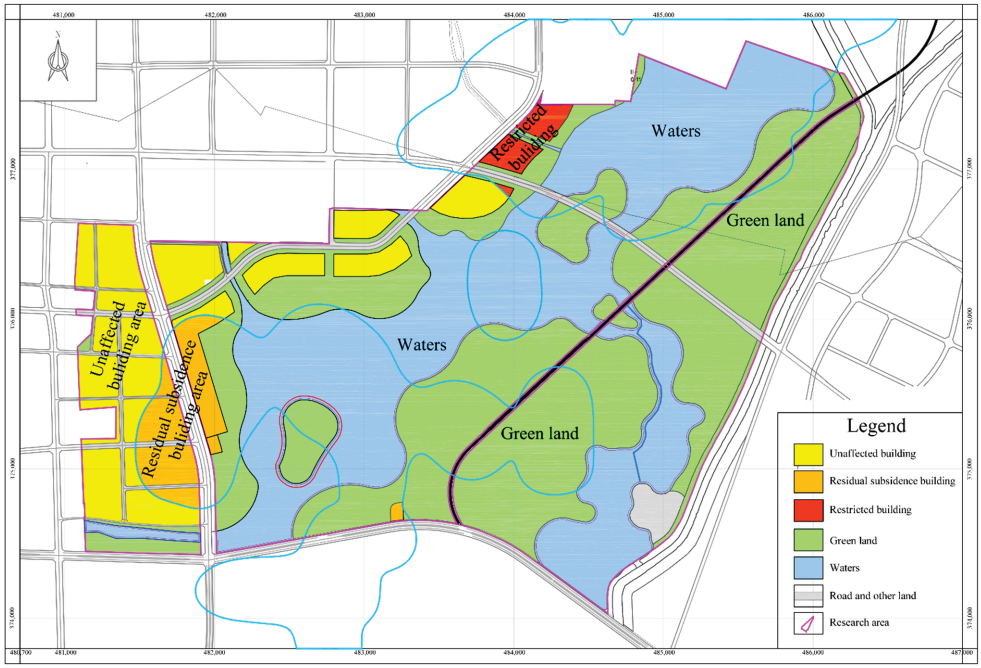

Figure 15. Treatment planning of coal mining subsidence area.

The utilization of water and land resources is described as follows:

(1) Unaffected building area is the yellow area in Figure 15. The surface deformation and the disturbing depth of the building foundation are within the safe value in this area. New buildings affected by the residual deformation are small. According to construction needs, residential houses and large shopping malls can be built in this area to solve the contradiction between the expansion of the subsidence area and the rapid growth of residential land. For several central islands in the lake, considering the complexity of the foundation and the rationality of the landscape ecology, the islands should be planned as wildlife habitats, which increases the ecological value of Lv Jin Lake Central Park. The island that the road crosses is located in the central area and can build low-level floor public health facilities.

(2) Building area affected by residual subsidence is the orange area in Figure 15. The building in this area is affected by residual subsidence. The damage value is less than the Grade I building damage level. The building will not be damaged theoretically. When calculating the additional stress, the number of building floors has no limit. Therefore, although the building in this area is affected by mining, the impact is relatively small, and residential houses and large shopping malls can be built.

(3) Restricted building area is the red area in Figure 15, mainly distributed in the northeast of the treatment area. It is mainly affected by the height of the collapsed zone and cracked zone in the III 426 working face of the fourth coal seam. Therefore, building structures with more than 25 floors in the nearby area is not advisable. Hotels and resorts can be built in this area, to serve the tourism industry in the Lv Jin Lake.

(4) Green land is the green area in Figure 15. A small part of the building area is planned as a greening area to reduce soil erosion in the boundary area of deep-excavation and shallow-filling. The surface has deformations, but the surface movement and deformation are small, and the surface fluctuation does not change significantly.

(5) Water area is the blue area in Figure 15. It is a combination of the waterlogging area and the terrain change caused by the implementation of deep-excavation and shallow-filling projects in the coal mining subsidence. The area is planned as a water area and an important part of the plan. Given the impact of coal mining subsidence in the early stage, a large waterlogging area is formed in the Lv Jin Lake research area, which is planned as part of the water area. On the one hand, to increase the integrity of the lake, water bodies with large areas and abundant biomass and plants and their landscape environment are restored, and a new tourism route is built, which integrates sightseeing and ecological leisure. On the other hand, large areas of water are utilized to develop cage culture. This method has higher requirements on the water body. If feasible, it can significantly alleviate the tension of farmland loss caused by subsidence.

By the spatial pattern reconstruction of water and land resources, the coal mining subsidence area can be transformed into sustainable green urban zones, as shown in Figure 16. Sufficient residential houses have been constructed in the buildable area, which alleviate the human–land conflict. Furthermore, abundant water and land resources have been utilized. A large area of landscape lake and green land is reconstructed, forming the aquatic-terrestrial complex ecosystem and promoting the succession in biological communities. Meanwhile, the transportation system around the reconstruction area is built, people's travel is facilitated and the life quality is improved. After a series of reconstruction, the environment becomes beautiful and pleasant (Figure 17).

Figure 16. Prospects of sustainable development in coal mining subsidence area.

(**a**)

(**b**)

Figure 17. Planning and design status of Lv Jin Lake coal mining subsidence area, (**a**) conceptual graph of Lv Jin Lake, (**b**) live photo of Lv Jin Lake.

4. Discussion

The successful treatment of the Lv Jin Lake coal mining subsidence area has promoted the development of Huaibei City. The waterlogging area in the coal mining subsidence area is taken as the core, integrating cityscape, scene life, culture creativity and eco-tourism to realize the integrated planning concept of living environment improvement and ecological restoration in the coal mining subsidence area. Furthermore, the spatial pattern of the coal mining subsidence area within urban areas is constructed. The coordinated development of people and the environment is promoted. Thus, the urban region has greatly benefited areas including economics, ecology and social humanities (Table 6).

Table 6. Benefits of coal mining subsidence area after treatment.

Type	Benefits
Economy	It provides 1634 hectares of usable land and 774 hectares of usable water areas. The utilization rate of water and land resources reached 100%. The revenue exceeded 30 billion yuan.
Ecology	The structure and function of the regional ecosystem have changed significantly. They have many functions, such as water supply, conditioning, biodiversity conservation and leisure.
Society	A total of 498 villages affected by coal mining subsidence have been relocated, and more than 2×10^5 people have been successfully resettled, easing human–land conflicts.

4.1. Economic Benefits

Construction and operation and maintenance costs of approximately 75.178 million yuan are saved in engineering applications. Thirty percent of Zhuzhuang and Yangzhuang coal mine subsidence areas are restored to usable land. The total area of the wetland park in the reconstruction subsidence area is 2408 hectares, with 1634 hectares of usable land, including 534 hectares of construction land and 774 hectares of usable water areas and a storage capacity of 36.8 million m^3. In the subsidence area, 54.69% of the land was transformed into flat land; 31.55% of the slope land was planted with trees, shrubs and grass; and 13.76% of the water area was used as a breeding area. The utilization rate of water and land resources reached 100%, and the direct revenue exceeded 30 billion yuan. According to the future urban land use plan, the prices of 66.7 and 12.7 hectares of commercial land sales rise after development. In terms of indirect economic benefits, the development income of construction land is expected to reach 2.5 billion yuan in the near future. The evaluation results of the ecosystem service function of Lv Jin Lake show that the economic benefits in water purification and water supply are approximately 63.72 million yuan per year.

4.2. Ecological Benefits

The Lv Jin Lake coal mining subsidence area has been transformed from a farmland ecosystem to a large-scale aquatic ecosystem before coal mining. The structure and function of the regional ecosystem have changed significantly. The ecological islands provide habitats for more than 100 species of animals and nearly 100 species of plants. It uses many abandoned lands, and has many functions such as water supply, conditioning, biodiversity conservation, leisure and entertainment. Furthermore, the landscape ecology in subsidence areas promotes ecological succession. Ecosystem services' functions have huge potential and allow further development of eco-tourism and other ecological civilization construction industries. Meanwhile, through scientific and reasonable planning, the water system structure formed in the Lv Jin Lake subsidence area has caused important changes in the urban ecological spatial pattern. It undertakes crucial functions, such as industrial and agricultural water supply and water source protection areas. The total ecological benefits will be approximately 72.9 million yuan per year in terms of the ecosystem.

4.3. Social Benefits

The formation of the subsidence wetland park after treatment will produce good social benefits. More than 6670 hectares of cultivated land and more than 2000 hectares of construction land have been added, effectively alleviating the shortage of urban construction land. A total of 498 villages were affected by coal mining subsidence and have been relocated, and more than 2×10^5 people have been successfully resettled. Employment opportunities and foundation stability are provided. The original subsidence abandoned land is built in a commercial area to promote the development of all walks of life. The subsidence waterlogging area within urban regions is planned under the concept of the

human dwelling environment and eco-integration, reconstructing the urban integrate landscape environment, culture and eco-tourism. Lv Jin Lake Wetland Park improves the environmental appearance of the coal mining subsidence area; eases the human–land conflicts in mining areas; and promotes the coordinated development of society, economy and nature.

4.4. Comparison Analysis

The coal mining subsidence area is reconstructed in the following types. Firstly, the dredging and draining method [52] is applied for coal mining subsidence areas with a small surface subsidence and a small waterlogging area scope. Reasonable drainage measures are used to drain the stagnant water, and then the surface is repaired to restore its land use function. This method has a huge workload of drainage and soil filling, and the original topography changes greatly, so the renovation cost is huge. However, the method in this paper is based on the existing terrain to transform according to local conditions. The water resources are transformed into the landscape lake, and land resources are transformed into green land and building land. Secondly, the backfill reclamation method is applied [53], where coal gangue, fly ash and river mud are used to fill the coal mining subsidence area. This method has great economic benefits but may lead to secondary pollution. Thirdly, the direct use method is applied [54], where cage fish, duck, lotus root or wet-resistant crops are scattered across the large coal mining subsidence and waterlogging areas, depending on the local conditions. However, this method cannot adapt to the coal mining subsidence area within urban regions and cannot create more land use value. Fourthly, the ecological engineering reclamation method is applied [55], where land reclamation and ecological engineering technologies are combined to treat the coal mining subsidence area. This method only restores the local ecological environment and does not assess whether the land can be used for construction. Compared with the above reconstruction methods described in the literature, the spatial pattern reconstruction method proposed in this paper has a high utilization rate of water and land resources and is suitable for coal mining subsidence areas within urban areas.

In summary, the spatial pattern reconstruction of water and land resources in Lv Jin Lake subsidence promotes the sustainable development of the urban area and transforms resource-based urban areas based on coal mining into sustainable urban areas. It also provides an example for comprehensive ecological environment management in similar areas.

5. Conclusions

(1) This study introduces a set of scientific and complete methods for reconstructing the spatial pattern of water and land resources in unstable coal mining subsidence areas within urban areas. The shortage of land resources in coal mining subsidence areas is addressed, the stability of the coal mining subsidence area is analyzed, the unstable subsidence area is reasonably planned and utilized and an ecologically livable green urban area is built to achieve a sustainable development of coal-resource-based cities.

(2) The Lv Jin Lake in Huaibei is selected as a case study, on the basis of surface subsidence and groundwater level; the coal mining subsidence is divided into waterlogging and non-waterlogging areas. Terrain modification and reconstruction are carried out in the waterlogging area by using the deep-excavation and shallow-filling method and by reconstructing the slope. New buildings are constructed in the non-waterlogging area. The allowable height of buildings on the ground is calculated by analyzing the superposition of surface residual subsidence, the height of the collapsed zone and cracked zone and the additional stress of surface buildings. The fourth coal seam III426 working face has the minimum mining depth, and the allowable building height above is not more than 25 floors. The height of buildings in other areas theoretically has no limit.

(3) Scientific and rational planning ensures that the abundant water and land resources are fully utilized. Residential houses and large shopping malls are built in the un-

affected building area, and the building area is influenced by residual subsidence. Buildings with no more than 25 floors, hotels and resorts are built in the restricted building area. The green land can reduce soil erosion, and the large area of water increases the integrity of the study area. Abundant biomass and plants are restored, and cage culture is developed.

(4) In the case study, a coal-resource-based city is transformed into a sustainable development city with huge economic, ecologic and social benefits. In this area, the water and land resources utilization rate reaches 100%, and the direct revenues exceed 30 billion yuan. A habitat for plants and animals is provided, and the available ecosystem services have huge potential. The shortage of urban construction land is alleviated, more than 2×10^5 people have been successfully resettled and employment opportunities are abundant. The human–land conflict in mining areas is eased, and a coordinated development of society, economy and nature is promoted. The work presented in this paper may serve as a reference for similar mining subsidence area treatment projects in the future.

Author Contributions: Conceptualization, X.Z., H.C., L.D. and S.F.; methodology, X.Z., H.L. and L.Z.; software, X.Z. and F.Z.; writing—original draft preparation, X.Z. and F.Z.; writing—review and editing, X.Z., W.H., Y.Y. and X.Y.; visualization, X.Z. and F.Z.; supervision, H.C. and L.Z. All authors have read and agreed to the published version of the manuscript.

Funding: This research was funded by the National Natural Science Foundation of China (51804001), the Key University Science Research Project of Anhui Province (KJ2021A0080) and Open Project Program of Anhui Province Engineering Laboratory for Mine Ecological Remediation (KS-2021-005).

Institutional Review Board Statement: Not applicable.

Informed Consent Statement: Not applicable.

Data Availability Statement: Not applicable.

Acknowledgments: Financial support for this work, provided by the National Natural Science Foundation of China (51804001), the Key University Science Research Project of Anhui Province (KJ2021A0080) and Open Project Program of Anhui Province Engineering Laboratory for Mine Ecological Remediation (KS-2021-005) are gratefully acknowledged.

Conflicts of Interest: The authors declare no conflict of interest.

References

1. Huang, J.; Tian, C.Y.; Xing, L.F.; Bian, Z.F.; Miao, X.X. Green and sustainable mining: Underground coal mine fully mechanized solid dense stowing-mining method. *Sustainability* **2017**, *9*, 1418. [CrossRef]
2. Qian, D.Y.; Zhang, N.; Pan, D.J.; Xie, Z.Z.; Shimada, H.; Wang, Y.; Zhang, C.H.; Zhang, N.C. Stability of deep underground openings through large fault zones in argillaceous rock. *Sustainability* **2017**, *9*, 2153. [CrossRef]
3. Zhang, M.W.; Shimada, H.; Sasaoka, T.; Matsui, K.; Dou, L.M. Evolution and effect of the stress concentration and rock failure in the deep multi-seam coal mining. *Environ. Earth Sci.* **2014**, *72*, 629–643. [CrossRef]
4. Bai, E.H.; Guo, W.B.; Zhang, H.B.; Tan, Y.; Guo, M.J. In situ groundwater protection technology based on mining-conservation coordination in the middle and upper reaches of Yellow River Basin. *J. China Coal Soc.* **2021**, *46*, 907–914.
5. Zhu, X.J.; Zha, F.; Guo, G.L.; Zhang, P.F.; Cheng, H.; Liu, H.; Yang, X.Y. Subsidence control design method and application to backfill-strip mining technology. *Adv. Civ. Eng.* **2021**, *2021*, 5177174. [CrossRef]
6. Jiang, N.; Wang, C.X.; Pan, H.Y.; Yin, D.W.; Ma, J.B. Modeling study on the influence of the strip filling mining sequence on mining-induced failure. *Energy Sci. Eng.* **2020**, *8*, 2239–2255. [CrossRef]
7. Marschalko, M.; Yilmaz, I.; Křístková, V.; Fuka, M.; Kubečka, K.; Bouchal, T.; Bednarik, M. Optimization of building site category determination in an undermined area prior to and after exhausting coal seams. *Int. J. Rock Mech. Min. Sci.* **2012**, *54*, 9–18. [CrossRef]
8. Wang, C.L.; Zhang, C.S.; Zhao, X.D.; Liao, L.; Zhang, S.L. Dynamic structural evolution of overlying strata during shallow coal seam longwall mining. *Int. J. Rock Mech. Min. Sci.* **2018**, *103*, 20–32. [CrossRef]
9. He, M.C.; Wang, Q.; Wu, Q.Y. Innovation and future of mining rock mechanics. *J. Rock Mech. Geotech. Eng.* **2021**, *13*, 1–21. [CrossRef]
10. Xie, Z.Z.; Zhang, N.; Yuan, Y.X.; Xu, G.; Wei, Q. Study on safety control of composite roof in deep roadway based on energy balance theory. *Sustainability* **2019**, *11*, 3688. [CrossRef]

11. Wang, F.; Jiang, B.Y.; Chen, S.J.; Ren, M.Z. Surface collapse control under thick unconsolidated layers by backfilling strip mining in coal mines. *Int. J. Rock Mech. Min. Sci.* **2019**, *113*, 268–277. [CrossRef]
12. Zhang, Y.; Cao, S.G.; Zhang, N.; Zhao, C.Z. The application of short-wall block backfill mining to preserve surface water resources in northwest China. *J. Clean. Prod.* **2020**, *261*, 121232. [CrossRef]
13. Huang, Y.L.; Li, J.M.; Ma, D.; Gao, H.D.; Guo, Y.C.; Ouyang, S.Y. Triaxial compression behaviour of gangue solid wastes under effects of particle size and confining pressure. *Sci. Total Environ.* **2019**, *693*, 133607. [CrossRef] [PubMed]
14. Nie, L.; Wang, H.; Xu, Y.; Li, Z. A new prediction model for mining subsidence deformation: The arc tangent function model. *Nat. Hazards* **2014**, *75*, 2185–2198. [CrossRef]
15. Hu, Z.Q.; Duo, L.H.; Shao, F. Optimal Thickness of Soil Cover for Reclaiming Subsided Land with Yellow River Sediments. *Sustainability* **2018**, *10*, 3853. [CrossRef]
16. Liu, H.; Zhang, M.; Su, L.J.; Chen, X.X.; Liu, C.F.; Sun, A.G. A boundary model of terrain reconstruction in a coal-mining subsidence waterlogged area. *Environ. Earth Sci.* **2021**, *80*, 187. [CrossRef]
17. Hu, B.N.; Guo, W.Y. Mining subsidence area status, syntheses governance model and governance recommendation. *Coal Min. Technol.* **2018**, *23*, 1–4.
18. Zhao, J.H.; Jiang, N.; Yin, L.M.; Bai, L.Y. The effects of mining subsidence and drainage improvements on a waterlogged area. *Bull. Eng. Geol. Environ.* **2018**, *78*, 3815–3831.
19. Faunt, C.C.; Sneed, M.; Traum, J.; Brandt, J.T. Water availability and land subsidence in the Central Valley, California, USA. *Hydrogeol. J.* **2015**, *24*, 675–684. [CrossRef]
20. Wu, Q.Y.; Pang, J.W.; Qi, S.Z.; Li, Y.P.; Han, C.C.; Liu, T.X.; Huang, L.M. Impacts of coal mining subsidence on the surface landscape in Longkou city, Shandong Province of China. *Environ. Earth Sci.* **2009**, *59*, 783–791.
21. Shang, Y.Z.; Lu, S.B.; Li, X.F.; Hei, P.F.; Lei, X.H.; Gong, J.G.; Liu, J.H.; Zhai, J.Q.; Wang, H. Balancing development of major coal bases with available water resources in China through 2020. *Appl. Energy* **2017**, *194*, 735–750. [CrossRef]
22. Liu, H.; Zhu, X.J.; Cheng, H.; Su, L.J.; Dai, L.J.; Zheng, L.G.; Fang, S.Z.; Jiang, C.L.; Zhang, Q.; Sun, Q.Y.; et al. Key technology of human environment and ecological reconstruction in high submersible level coal mining subsidence area: A case study from Lüjin Lake, Huaibei. *J. China Coal Soc.* **2021**, *46*, 4021–4032.
23. Singh, S.K.; Pandey, A.C. Geomorphology and the controls of geohydrology on waterlogging in Gangetic Plains, North Bihar, India. *Environ. Earth Sci.* **2013**, *71*, 1561–1579. [CrossRef]
24. Blanchette, M.L.; Lund, M.A. Pit lakes are a global legacy of mining: An integrated approach to achieving sustainable ecosystems and value for communities. *Curr. Opin. Environ. Sustain.* **2016**, *23*, 28–34. [CrossRef]
25. Pérez-Sindín, X.; Blanchette, M.L. Correction to: Understanding public perceptions of a new Pit Lake in as pontes, Spain. *Mine Water Environ.* **2020**, *39*, 657. [CrossRef]
26. Dhakate, R.; Modi, D.; Rao, V.V.S.G. Impact assessment of coal mining on river water and groundwater and its interaction through hydrological, isotopic characteristics, and simulation flow modeling. *Arab. J. Geosci.* **2018**, *12*, 8. [CrossRef]
27. Zhu, X.J.; Ning, Z.Y.; Cheng, H.; Zhang, P.F.; Sun, R.; Yang, X.Y.; Liu, H. A novel calculation method of subsidence waterlogging spatial information based on remote sensing techniques and surface subsidence prediction. *J. Clean. Prod.* **2022**, *335*, 130366. [CrossRef]
28. Hu, Z.Q.; Xiao, W.; Zhao, Y.L. Re-discussion on coal mine eco-environment concurrent mining and reclamation. *J. China Coal Soc.* **2020**, *45*, 351–359.
29. Li, F.M. Discussion on several technical problems in comprehensive treatment of surface ground subsidence caused by coal mining operation. *Coal Sci. Technol.* **2003**, *33*, 59–60.
30. Tan, X.H.; Peng, Y.L.; Liu, S.L.; Liu, P. Landscape pattern and ecotourism carrying capacity of Pan'an Lake wetland park in Xuzhou City, China. *Desalination Water Treat.* **2020**, *188*, 288–296. [CrossRef]
31. Xu, J.X.; Yin, P.C.; Hu, W.M.; Fu, L.L.; Zhao, H. Assessing the ecological regime and spatial spillover effects of a reclaimed mining subsided lake: A case study of the Pan'an Lake wetland in Xuzhou. *PLoS ONE* **2020**, *15*, e0238243. [CrossRef] [PubMed]
32. Hu, Z.Q. The 30 years' land reclamation and ecological restoration in China: Review, rethinking and prospect. *Coal Sci. Technol.* **2019**, *47*, 25–36. [CrossRef]
33. Hu, Z.Q.; Xiao, W. Optimization of concurrent mining and reclamation plans for single coal seam: A case study in northern Anhui, China. *Environ. Earth Sci.* **2012**, *68*, 1247–1254. [CrossRef]
34. Chugh, Y.P. Concurrent mining and reclamation for underground coal mining subsidence impacts in China. In Proceedings of the 2nd International Symposium on Land Reclamation and Ecological Restoration (LRER), Xian, China, 20–23 October 2017; pp. 315–332.
35. Hu, Z.; Xiao, W.; Fu, Y. Innovations of concurrent mining and reclamation for underground coal mines in China. In Proceedings of the 16th International Symposium on Environmental Issues and Waste Management in Energy and Mineral Production (SWEMP)/International Symposium on Computer Applications (CAMI), Istanbul, Turkey, 5–7 October 2016.
36. Guan, J.; Yu, P. Does coal mining have effects on land use changes in a coal resource-based city? Evidence from Huaibei City on the North China Plain. *Int. J. Environ. Res. Public Health* **2021**, *18*, 11616. [CrossRef] [PubMed]
37. Li, G.S.; Hu, Z.Q.; Li, P.Y.; Yuan, D.Z.; Wang, W.J.; Han, J.Z.; Yang, K. Optimal layout of underground coal mining with ground development or protection: A case study of Jining, China. *Res. Policy* **2022**, *76*, 102639. [CrossRef]

38. Wu, J.; Bai, Z.K. Spatial and temporal changes of the ecological footprint of China's resource-based cities in the process of urbanization. *Res. Policy* **2022**, *75*, 102491. [CrossRef]
39. He, Y.; Lin, Y.; Zhou, G.; Zhu, Y.; Tang, K. Spatial pattern and drivers of urbanization in China's mid-level developing urban agglomeration: A case study of Chang-Zhu-Tan. *Reg. Sustain.* **2021**, *2*, 83–97. [CrossRef]
40. Ge, X.J.; Liu, X.X. Urban land use efficiency under resource-based economic transformation—A case study of Shanxi Province. *Land* **2021**, *10*, 850. [CrossRef]
41. Wu, Z.H.; Lei, S.G.; Yan, Q.W.; Bian, Z.F.; Lu, Q.Q. Landscape ecological network construction controlling surface coal mining effect on landscape ecology: A case study of a mining city in semi-arid steppe. *Ecol. Indic.* **2021**, *133*, 108403. [CrossRef]
42. Yang, D.W.; Gao, X.L.; Xu, L.X.; Guo, Q.H. Constraint-adaptation challenges and resilience transitions of the industry–environmental system in a resource-dependent city. *Res. Conserv. Recycl.* **2018**, *134*, 196–205. [CrossRef]
43. Xiang, Z.; Liu, X.Y. Coal-based transformation of cities in Shandong Province, China. *Chin. J. Popul. Res. Environ.* **2015**, *13*, 358–364. [CrossRef]
44. Lin, C.C.; Zheng, L.G.; Wei, X.P.; Dong, X.L.; Chen, X. Study on landscape pattern changes before and after the governance in zhonghu coal mining subsidence area in Huaibei. *Adm. Tech. Environ. Monit.* **2021**, *33*, 14–19.
45. Liu, Y.; Zhu, J.R.; Gao, W.H.; Guo, Z.H.; Xue, C.; Pang, J.Y.; Shu, L.Z. Effects of biochar amendment on bacterial and fungal communities in the reclaimed soil from a mining subsidence area. *Environ. Sci. Pollut. Res. Int.* **2019**, *26*, 34368–34376. [CrossRef]
46. Litwiniszyn, J. Application of the equation of stochastic processes to mechanics of loose bodies. *Arch. Mech. Stos.* **1956**, *8*, 393–411.
47. Liu, B.C. Stochastic medium theory and its application in surface subsidence caused by excavation. *Chin. J. Nonferrous Met.* **1992**, *2*, 8–14.
48. China Coal Research Institute. Buildings, water bodies, railways and main shafts and coal pillars and coal mining regulations. *China Coal Ind. Press* **2017**, *in press*.
49. Hu, Q.F.; Deng, X.B.; Feng, R.M.; Li, C.Y.; Wang, X.J.; Jiang, T. Model for calculating the parameter of the Knothe time function based on angle of full subsidence. *Int. J. Rock Mech. Min. Sci.* **2015**, *78*, 19–26. [CrossRef]
50. Cui, X.M.; Wang, J.C.; Liu, Y.S. Prediction of progressive surface subsidence above longwall coal mining using a time function. *Int. J. Rock Mech. Min. Sci.* **2001**, *38*, 1057–1063. [CrossRef]
51. Zhu, X.J.; Guo, G.L.; Zha, J.F.; Chen, T.; Fang, Q.; Yang, X.Y. Surface dynamic subsidence prediction model of solid backfill mining. *Environ. Earth Sci.* **2016**, *75*, 1007. [CrossRef]
52. Bian, Z.F.; Zhang, G.L. Principle of dredging and draining method of subsided land reclamation for coal mining and its application. *J. China Univ. Min. Technol.* **1996**, *25*, 84–88.
53. Bernadette, U.U.; Ogbonnaya, L.; Oyem, E.U. Modeling and characterization of mine pit backflling/reclamation materials around Gyel'A' and Kantoma areas of Plateau state using integrated method. *Modeling Earth Syst. Environ.* **2021**, *2022*, 3385–3398.
54. Pan, H.Y.; Cheng, A.G. Comparative study on comprehensive control policies for mining subsidence at home and abroad. *Energy Technol. Manag.* **2020**, *45*, 25–28 + 32.
55. Li, Q.T.; Peng, T.; Yang, J.; He, J.Q.; Wang, J.W. Investigate ecological restoration project of abandoned mines in Beijing-Tianjin-Hebei area. *World Nonferrous Met.* **2020**, *6*, 259–260.

sustainability

MDPI

Article

CO_2 Flow Characteristics in Macro-Scale Coal Sample: Effect of CO_2 Injection Pressure and Buried Depth

Huping Wang [1,2], Zhao Wang [3,*], Haikui Yin [4], Chao Jin [5], Xiaogang Zhang [5] and Langtao Liu [5]

[1] School of Public Policy and Management, China University of Mining and Technology, Xuzhou 221116, China
[2] School of Marxism, Hebei University of Engineering, Handan 056038, China
[3] School of Management Engineering and Business, Hebei University of Engineering, Handan 056038, China
[4] School of Water Conservancy and Hydroelectric Power, Hebei University of Engineering, Handan 056038, China
[5] School of Earth Science and Engineering, Hebei University of Engineering, Handan 056038, China
* Correspondence: wangzhao@hebeu.edu.cn

Abstract: Experimental studies have confirmed the permeability reduction of coal samples upon the adsorption of CO_2. However, these studies were carried out under limited experimental conditions. In this study, CO_2 flow behaviors in a macro-scale coal sample were numerically simulated using a coupled gas flow, mechanical deformation, and sorption-induced deformation finite element model. The simulation results show that the effect of the reduction of effective stress on the enhancement of permeability is greater than the negative effect of permeability reduction due to CO_2 adsorption for low injection pressures. CO_2 pressure development in the sample increases with increasing injection pressure due to the enhanced advection flux for sub-critical CO_2 injections, while for super-critical CO_2 injections, CO_2 pressure development, as well as concentrations in the sample, decreases compared to sub-critical CO_2 injections because of greater density and viscosity of super-critical CO_2 as well as coal matrix swelling induced by the adsorption of super-critical CO_2. Increasing axial stress (buried depth) obstructs CO_2 migration in the sample due to the increased effective stress, and this effect is more influential for low injection pressures, which indicates that high CO_2 injection pressures are preferred for CO_2 sequestration in deep coal seams.

Keywords: CO_2 sequestration; numerical simulation; CO_2 flow characteristics; permeability variation; coal matrix swelling

1. Introduction

Recent years have witnessed a wave of severe natural disasters linked to climate change [1–4]. Scientists have long been able to prove that global warming, which is mainly driven by excessive consumption of fossil fuels, significantly contributes to global climate change [5]. Anthropogenic carbon dioxide emissions from fossil fuels have hit a historic new peak of 33.90 gigatons in 2021 [6]. Therefore, sustainable development goals have called for actions by all countries to take urgent responses to combat climate change [7]. In light of this, the Paris Agreement has set the goal of containing the mean global temperature rise well below 2 °C above the pre-industrial levels by the end of this century and striving to limit global warming to 1.5 °C above pre-industrial levels [8]. This requires significant carbon emission reductions to achieve the target, and carbon dioxide storage in deep underground formations has been proposed and validated as an effective strategy to mitigate carbon emissions. Among various geologic sinks, CO_2 injection into deep-buried coal seams for sequestration is a viable method to mitigate carbon emissions, with the potential benefit of enhancing methane recovery for energy purposes [9–11]. The first field trial was conducted in the San Juan Basin of the Fruitland Formation in Colorado, USA, in 1993 [12], and since then, a number of field demonstrations have been conducted in different regions of the world [13]. However, many field projects

have experienced reductions in CO_2 injectivity due to reduced coal seam permeability. This reduced permeability of coal seams is believed to be the result of coal matrix swelling caused by the adsorption of CO_2. The cleat system of coal provides flow paths for gas molecules, and the swelling of the coal matrix narrows or even shuts down the cleats in coal, resulting in reduced permeability. Many experimental studies to date have confirmed the swelling phenomenon of coal upon interaction with CO_2 [14–20], and there are a number of factors contributing to the alteration of the permeability of coal. These factors can be categorized into two main groups: injecting gas properties and coal mass properties. According to the literature, the permeability of coal decreases with the adsorption of CO_2, and this reduction is significantly enhanced for super-critical CO_2 injections as the adsorption capacity of CO_2 increases with increasing injection pressure [21,22]. Temperature has an intricate effect on permeability variation. Gas molecules tend to desorb from coal pore walls under high-temperature conditions as gas adsorption is an exothermic process; coal matrix swelling due to the adsorption of CO_2, therefore, can be recovered to some extent which, in turn, facilitates gas transportation and adsorption in coal. Perera et al. performed a series of CO_2 injections on coal under different temperature conditions; they found that temperature has an insignificant influence on permeability variations for gas injection pressure less than 9 MPa, while permeability of coal increases with increasing temperature for CO_2 injection pressure greater than 10 MPa [23]. Increasing effective stress acting on coal results in a reduction of coal permeability as gas flow paths are cramped or even closed under high-stress conditions [24,25]. High-rank coals are more likely to be affected by the adsorption of CO_2 than low-rank coals due to their highly-developed cleat systems which facilitate gas movement in coal [26]. However, these studies were all conducted on mesoscale samples with lengths usually less than 100 mm, and gas flow behaviors in coal cannot be directly observed due to the limited sample length. De Silva and Ranjith developed an advanced large-scale core flooding apparatus that can accommodate coal samples with diameters of 203 mm and lengths up to 1 m [27]. They have performed a series of CO_2 injections under sub-critical conditions to investigate CO_2 flow behaviors in coal. Ranathunga et al. extended their study by performing super-critical CO_2 injections up to 14 MPa to study the effect of the CO_2 phase on gas flow behaviors along low-rank coal samples [28]. The effect of CO_2 injection pressures and effective stress on gas flow behaviors and CO_2 storage variations on high-rank coal samples was also studied using the same apparatus [14,29]. However, the above studies were carried out under limited experimental conditions, as for such large-scale tests, extensive time and labor are required to complete the associated tests. Numerical modeling approaches can eliminate such limitations [30,31], and the aim of this study was to develop a large-scale laboratory model to investigate the effect of CO_2 injection properties and stress conditions on gas flow behaviors in coal. This study can provide new insights into CO_2 flow behaviors in large-scale samples under various test conditions.

The mathematical model was represented by partial differential equations (PDEs), and the governing equations were written in the COMSOL Multiphysics simulator to solve the model. COMSOL Multiphysics is a commercially developed cross-platform finite element simulation tool. This software provides conventional physics-based user interfaces, user-defined interfaces, and user-developed PDEs. A model with uncertain structure or parameters can significantly limit its applicability. Using the experimental data to validate the model is to guarantee that the developed model can be used to make engineering predictions with a high degree of confidence. By validating the developed model using the experimental results, the model can be extended to conditions that are difficult to achieve in the laboratory. In this case, CO_2 flow behaviors in coal under high CO_2 injection pressures and stress conditions were simulated using the developed model to represent conditions deep underground.

2. Model Development

Darcy's equation is the fundamental theory that describes gas migration in the cleat system of coal. Previous studies have concluded that the permeability evolution of coal during CO_2 injection is controlled by the response of the cleat system, which is affected by both effective stress and adsorption-induced strains [32–34]. The increased reservoir pressure after CO_2 injection reduces the effective stress, which causes cleats to expand, leading to the enhancement of coal seam permeability, while the adsorption of CO_2-induced coal matrix swelling shrinks the cleats, thereby reducing permeability. Both of these processes need to be taken into consideration during model development.

2.1. Coal Deformation

As stated previously, coal deformation during CO_2 injection is attributed to effective stress-induced deformation and adsorption-induced deformation. In turn, this deformation of coal influences gas migration behavior in coal. The Navier equation for linear poroelastic materials can be used to describe the stress and strain relation. Assuming the model system is isothermal, and the coal materials modeled in this study are a homogeneous, isotropic, and elastic continuum, the equilibrium equation for coal can be written using Equation (1) without consideration of inertia force:

$$\sigma_{ij,j} + F_i = 0 \tag{1}$$

where, $\sigma_{ij,j}$ is a component of the total stress tensor, i and j are the space coordinates, and F_i denotes the component of the body force in the i-direction.

The relation between strain and displacement can then be defined using Equation (2):

$$\varepsilon_{ij} = \frac{(\mu_{i,j} + \mu_{j,i})}{2} \tag{2}$$

where, ε_{ij} is a component of the total strain tensor, and $\mu_{i,j}$ and $\mu_{j,i}$ are components of the displacement.

2.2. Stress–Strain Relation

The stress and strain response of coal mass under force can be expressed using Equation (3):

$$\varepsilon_{ij} = \frac{1}{2G}\sigma_{ij} - \left(\frac{1}{6G} - \frac{1}{9K}\right)\sigma_{kk}\delta_{ij} \tag{3}$$

$$G = \frac{E}{2(1+\gamma)} \tag{4}$$

$$K = \frac{E}{3(1-2\gamma)} \tag{5}$$

where G is the shear modulus of coal, K is the bulk modulus of coal, E and γ are Young's modulus and Poisson's ratio of coal, respectively, σ_{kk} is the total stress of the coal matrix, and $\sigma_{kk} = \sigma_{11} + \sigma_{22} + \sigma_{33}$, δ_{ij} is the Kronecker delta, which is equal to 1 when i = j; otherwise, it is equal to 0.

For CO_2 transportation in coal, the gas pressure in the cleat system created by the free CO_2 causes additional stress to the coal matrix. Therefore, Equation (3) can be written as Equation (6):

$$\varepsilon_{ij} = \frac{1}{2G}\sigma_{ij} - \left(\frac{1}{6G} - \frac{1}{9K}\right)\sigma_{kk}\delta_{ij} + \frac{1}{3K}\alpha_b P_f \delta_{ij} \tag{6}$$

where, α_b is Biot's coefficient and $\alpha_b = 1 - K/K_s$, K_s is the bulk modulus of the coal matrix and P_f is the CO_2 pressure in coal cleats.

Considering the combined effects of CO_2 pore pressure and CO_2 adsorption-induced strain, Equation (6) can be rewritten as Equation (7):

$$\varepsilon_{ij} = \frac{1}{2G}\sigma_{ij} - \left(\frac{1}{6G} - \frac{1}{9K}\right)\sigma_{kk}\delta_{ij} + \frac{1}{3K}\alpha_b P_f \delta_{ij} + \frac{\varepsilon_s \delta_{ij}}{3} \tag{7}$$

where ε_s is the matrix strain induced by the adsorption of CO_2.

By combining Equations (1), (2) and (7), the governing equation for coal deformation can be expressed using the improved displacement-based Navier equation, as indicated in Equation (8):

$$G\mu_{i,jj} + \frac{G}{1-2\gamma}\mu_{j,ji} - \alpha_b P_f - K\varepsilon_{si} + F_i = 0 \tag{8}$$

2.3. Permeability Model with Porosity

The cubic law defines the relation between the permeability and porosity of a material, as indicated in Equation (9):

$$k = k_0\left(\frac{\varphi}{\varphi_0}\right)^3 \tag{9}$$

where k is the permeability, k_0 is the original permeability, φ is the porosity of coal and φ_0 is the original porosity of coal.

The general porosity model is given in Equation (10) [35]:

$$d\varphi = \frac{1}{K}(\alpha - \varphi)(d\overline{\sigma} + dp) \tag{10}$$

Given that the initial mean compressive stress within the coal seam is $\overline{\sigma_0}$ and the initial pore pressure of p_0, the integration of Equation (10) gives Equation (11):

$$\int_{\varphi_0}^{\varphi} \frac{d\varphi}{\alpha - \varphi} = \frac{1}{K}\left(\int_{\overline{\sigma_0}}^{\overline{\sigma}} d\overline{\sigma} + \int_{p_0}^{p} dp\right) \tag{11}$$

According to Equation (7), the volumetric strain of coal can be expressed by Equation (12):

$$\varepsilon_v = \frac{1}{K}(\overline{\sigma} + \alpha p) + \varepsilon_s \tag{12}$$

where $\varepsilon_v = \varepsilon_1 + \varepsilon_2 + \varepsilon_3$ is the volumetric strain of coal, and $\overline{\sigma} = \frac{1}{3}(\sigma_1 + \sigma_2 + \sigma_3)$ is the mean stress.

Based on Equations (11) and (12), the porosity evolution of coal with the variation of stress condition and adsorption-induced strain can be written as Equation (13):

$$\varphi = \alpha - (\alpha - \varphi_0)\exp\left\{\left[\left(\varepsilon_v + \frac{p}{K_s} - \varepsilon_s\right) - \left(\varepsilon_{v0} + \frac{p_0}{K_s} - \varepsilon_{s0}\right)\right]\right\} \tag{13}$$

The adsorption-induced volumetric strain ε_s is related to the CO_2 adsorption amount and can be quantified using a Langmuir-like equation, as indicated in Equation (14):

$$\varepsilon_s = \frac{\varepsilon_L p}{p + P_L} \tag{14}$$

where ε_L is the Langmuir sorption strain constant of CO_2 for coal, and P_L is the Langmuir pressure of CO_2 for coal.

2.4. Gas Migration in Coal

The governing equation for gas flow in a porous medium is defined by the mass balance equation indicated in Equation (15):

$$\frac{\partial m}{\partial t}\varepsilon_s + \nabla(\rho_g q) = Q_s \tag{15}$$

where m represents the mass of CO_2 per volume of coal, t is time, ρ_g is the density of free CO_2 in cleats, q is the Darcy velocity of the free CO_2 in cleats, and Q_s is the source term related to the injection.

The CO_2 content in coal (m) mainly consists of the free gas in cleats (m_f) and the adsorbed gas on the coal surface (m_a), which is represented by Equation (16):

$$m = m_f + m_a \tag{16}$$

The amount of free gas in cleats can be calculated if the porosity of the coal is known, as shown in Equation (17):

$$m_f = \varphi\rho_g \tag{17}$$

Based on the Langmuir adsorption theory [36], the amount of CO_2 adsorbed in coal can be expressed using Equation (18):

$$m_a = \rho_{ga}\rho_c\frac{pV_L}{p+P_L} \tag{18}$$

where ρ_{ga} is the density of CO_2 under standard conditions, and ρ_c is the density of coal.

The relation between gas density and the associated gas pressure and temperature can be described using the ideal gas law as $\rho_{ga} = Mp_a/RT_a$ and $\rho_g = Mp/RT$, where p_a and T_a are the standard pressure and temperature, respectively, and M is the molecular weight of the CO_2.

CO_2 flow in the cleat system is driven by pressure differences, and compared to the pressure gradient, the effect of gravity is negligible. Therefore, Darcy's law of flow is given by:

$$q = -\frac{k}{\mu}\nabla p \tag{19}$$

where k is the permeability of CO_2 in coal, μ is the dynamic viscosity of CO_2 at a given temperature and pressure, and p is the gas pressure in the cleat system.

Equation (15) can be rewritten as Equation (20) by substituting Equations (16)–(19) into Equation (15).

$$\rho_g\frac{\partial\varphi}{\partial t} + \left[\frac{\varphi M}{RT} + \frac{\rho_{ga}\,\rho_c P_L V_L}{(p+P_L)^2}\right]\frac{\partial p}{\partial t} + \nabla\left(-\rho_g\frac{k}{\mu}\nabla p\right) \tag{20}$$

The partial derivative of porosity (φ) of coal with respect to time (t) from Equation (13) is given by Equation (21):

$$\begin{aligned}\tfrac{\partial\varphi}{\partial t} &= -(\alpha-\varphi_0)\exp\left\{-\left[\left(\varepsilon_v + \tfrac{p}{K_s} - \varepsilon_s\right) - \left(\varepsilon_{v0} + \tfrac{p_0}{K_s} - \varepsilon_{s0}\right)\right]\right\} \\ &\times\left[-\left(\tfrac{\partial\varepsilon_v}{\partial t} + \tfrac{1}{K}\tfrac{\partial p}{\partial t} - \tfrac{\partial\varepsilon_s}{\partial t}\right)\right] = (\alpha-\varphi)\left[\left(\tfrac{\partial\varepsilon_v}{\partial t} + \tfrac{1}{K_s}\tfrac{\partial p}{\partial t} - \tfrac{\partial\varepsilon_s}{\partial t}\right)\right]\end{aligned} \tag{21}$$

while the term $\partial\varepsilon_s/\partial t$ can be expressed by Equation (22):

$$\frac{\partial\varepsilon_s}{\partial t} = \frac{\varepsilon_L p}{(p+P_L)^2}\frac{\partial p}{\partial t} \tag{22}$$

By substituting Equations (21) and (22) into Equation (20), Equation (23) is obtained:

$$\left[\frac{\varphi}{t}+\frac{P_a\rho_c P_L V_L}{T_a(p+P_L)^2}+\frac{p(\alpha-\varphi)}{TK_s}-\frac{p(\alpha-\varphi)P_L\varepsilon_L}{T(p+P_L)^2}\right]\frac{M}{R}\frac{\partial p}{\partial t}+\nabla\left(-\rho_g\frac{k}{\mu}\nabla p\right)=Q_s-\rho_g(\alpha-\varphi)\frac{\partial\varepsilon_v}{\partial t} \tag{23}$$

By substituting Equations (9) and (13), the governing equation for gas flow in coal is derived by coupling the effect of CO_2 adsorption-induced strain and the variation of stress conditions, as indicated in Equation (24):

$$\begin{gathered}\left(\begin{array}{c}\frac{\alpha-(\alpha-\varphi_0)\exp\left\{\left[\left(\varepsilon_v+\frac{p}{K_s}-\varepsilon_s\right)-\left(\varepsilon_{v0}+\frac{p_0}{K_s}-\varepsilon_{s0}\right)\right]\right\}}{t}+\frac{P_a\rho_c P_L V_L}{T_a(p+P_L)^2}+\\ \frac{p\left(-(\alpha-\varphi_0)\exp\left\{\left[\left(\varepsilon_v+\frac{p}{K_s}-\varepsilon_s\right)-\left(\varepsilon_{v0}+\frac{p_0}{K_s}-\varepsilon_{s0}\right)\right]\right\}\right)}{TK_s}-\\ \frac{p\left(-(\alpha-\varphi_0)\exp\left\{\left[\left(\varepsilon_v+\frac{p}{K_s}-\varepsilon_s\right)-\left(\varepsilon_{v0}+\frac{p_0}{K_s}-\varepsilon_{s0}\right)\right]\right\}\right)P_L\varepsilon_L}{T(p+P_L)^2}\end{array}\right)\frac{M}{R}\frac{\partial p}{\partial t}+\\ \nabla\left(-\rho_g\frac{kk_0\left(\alpha-(\alpha-\varphi_0)\exp\left\{\left[\left(\varepsilon_v+\frac{p}{K_s}-\varepsilon_s\right)-\left(\varepsilon_{v0}+\frac{p_0}{K_s}-\varepsilon_{s0}\right)\right]\right\}\right)^3}{\mu{\varphi_0}^3}\nabla p\right)=\\ Q_s-\rho_g\left(\alpha-\alpha-(\alpha-\varphi_0)\exp\left\{\left[\left(\varepsilon_v+\frac{p}{K_s}-\varepsilon_s\right)-\left(\varepsilon_{v0}+\frac{p_0}{K_s}-\varepsilon_{s0}\right)\right]\right\}\right)\frac{\partial\varepsilon_v}{\partial t}\end{gathered} \tag{24}$$

Equation (24) defines a mathematical model for coupled CO_2 migration in coal under stress conditions. The first term on the left-hand side includes all the effective factors that contribute to the variation of coal's porosity, including the volume taken by the free gas, the volume occupied by the adsorbed gas, the volume changes due to the variation of stress condition and the volume changes due to gas adsorption-induced strain. The second term on the left-hand side is related to the attributes of gas movement in coal. The first term on the right-hand side is the source term which is related to injection, the second term on the right-hand side is the coupled term which involves the rate of variation of coal's volumetric strain due to deformation, and it can be considered as a source or sink due to mechanical deformation. Equation (24) is a partial differential equation with p as the dependent variable. It was implemented in COMSOL Multiphysics 5.3 and solved by the finite element method (FEM).

3. Finite Element Simulation

A two-dimensional laboratory-scale numerical model was built using COMSOL Multiphysics, and the governing equation for coupled gas migration in coal was written and solved by the Coefficient Form PDE module under the PDE interfaces of Mathematics in COMSOL.

3.1. Model Definition and Boundary Conditions

The dimensions of the model are based on the coal sample used in the experimental study [29], as indicated in Figure 1. In the experimental study, the macro-reconstituted coal sample is a core cylinder with a diameter of 203 mm and a length of 1000 mm. Therefore, the 2D numerical model is 203 mm in height and 1000 mm in length.

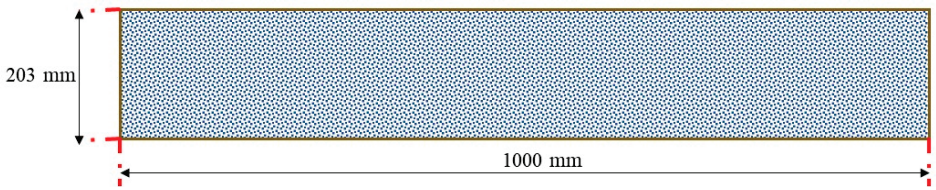

Figure 1. Dimensions of sample model.

The boundary conditions adopted for this model are illustrated in Figure 2. From the perspective of solid mechanics, as the sample is enclosed in a steel cylinder, the circumference of the sample is subjected to the restriction of the apparatus in an axial direction.

Therefore, both the top and bottom of the model are assigned as roller boundaries. The right end of the sample is subjected to the cell cap and hence is assumed to be a fixed boundary, and the left end of the sample is subjected to a constant axial load boundary. From the perspective of gas migration in coal, CO_2 injection is introduced from the left end of the sample at constant gas pressure. The top boundary, bottom boundary, and right end of the model are set as zero flux conditions.

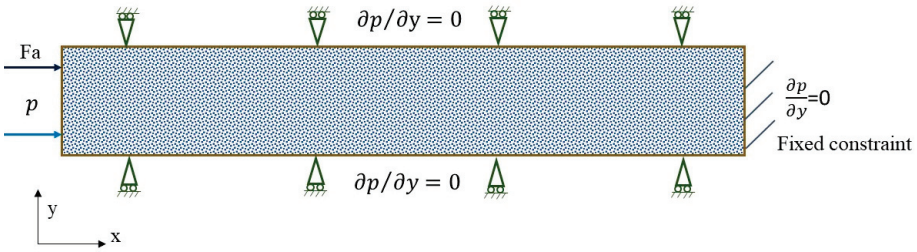

Figure 2. Boundary conditions of model.

3.2. Model Parameters

The model input parameters are listed in Table 1, most of the parameters being derived from the associated experimental results. The density and dynamic viscosity of CO_2 under different pressure conditions were calculated from the REFPROP database [37].

Table 1. Model input parameters.

Model Parameter	Value
CO_2 properties	
Langmuir pressure of CO_2 on coal (P_L)	2.32 MPa
Langmuir volume of CO_2 on coal (V_L)	0.0513 m^3/kg
Injection pressure (p)	From 6 MPa to 25 MPa
Coal properties	
Density (ρ_c)	1450 kg/m^3
Young's modulus (E)	3.37 GPa
Poisson's ratio (γ)	0.263

3.3. Model Meshing

As the model domain is bounded by four boundary segments and there are no isolated or embedded vertices or boundary segments, a 2D-mapped quadrilateral mesh was adopted to mesh the model. The extremely fine element size was selected for the meshing. The completed mesh of the model consists of 2100 domain elements and 242 boundary elements.

4. Results and Discussion

4.1. Effect of Injection Time on Gas Flow Behaviour in Coal

First, gas transportation in the coal sample with time was examined by comparing the CO_2 pressure development along the coal sample for various injection durations. Based on the experimental results, CO_2 pressure development in the coal sample becomes stable after around eight days of injection for 6 MPa injection. Therefore, a time-dependent study was applied to the calculation with times ranging from 1 to 10 days, with 1 day for each step. Figure 3 shows the CO_2 pressure development in the coal sample after 1-day, 3-day, 5-day, 7-day, 9-day, and 11-day CO_2 injection at 6 MPa injection pressure under 10 MPa axial load.

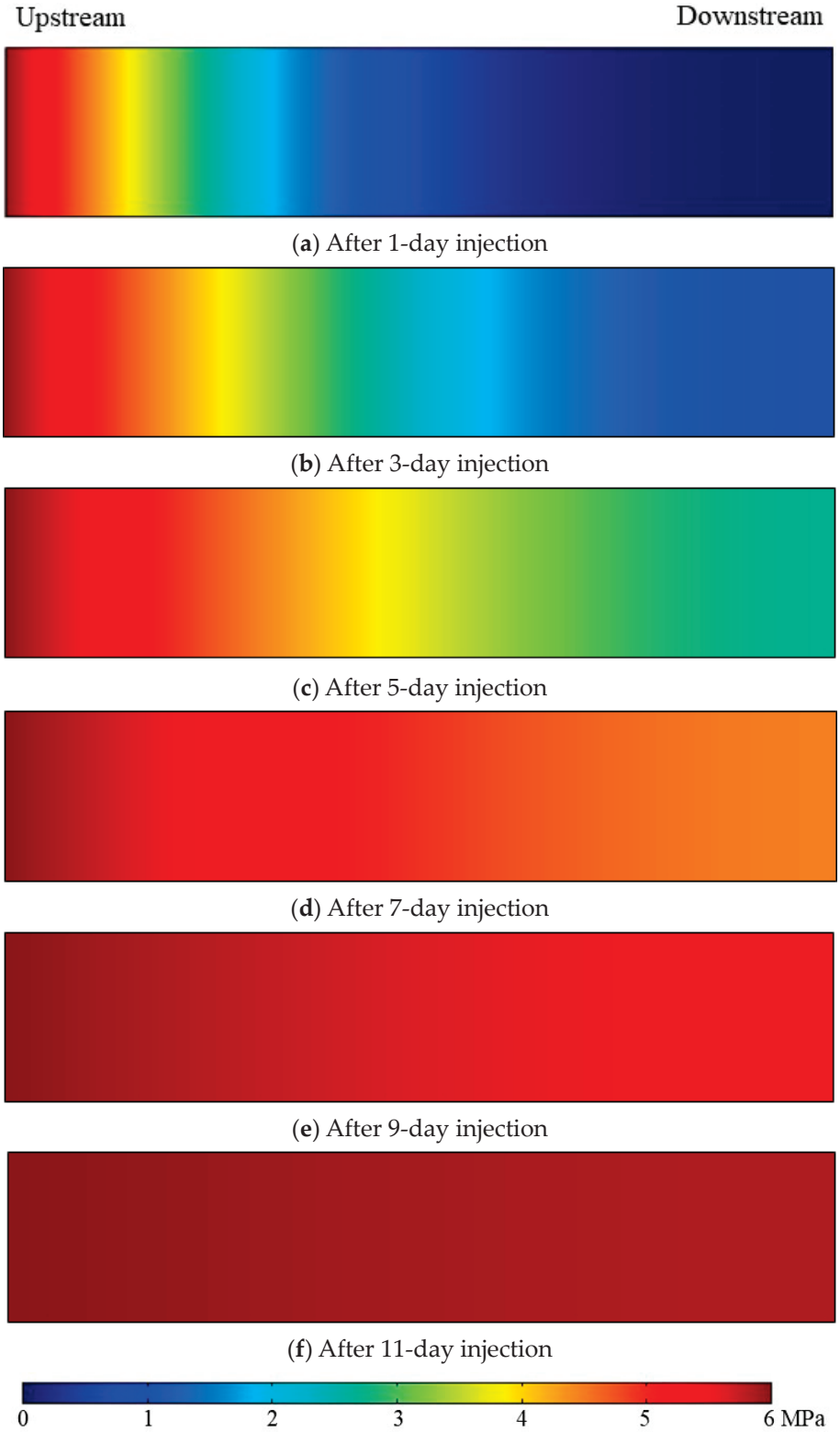

Figure 3. CO_2 pressure development in coal for 6 MPa injection pressure at 10 MPa axial load.

As indicated in Figure 3, CO_2 pressure develops from the upstream to the downstream with time due to the pressure difference (advection) along the sample, and after around 11 days, the downstream reaches a steady state with a uniform pressure present throughout the sample. However, the pressure development rate varies with time, as indicated in Figure 3. In order to study the rate of CO_2 pressure development along the sample with

time, a sample length for which the CO_2 pressure was greater than 5 MPa was selected. Figure 4 illustrates the sample length (where CO_2 pressure is greater than 5 MPa) variation with injection duration.

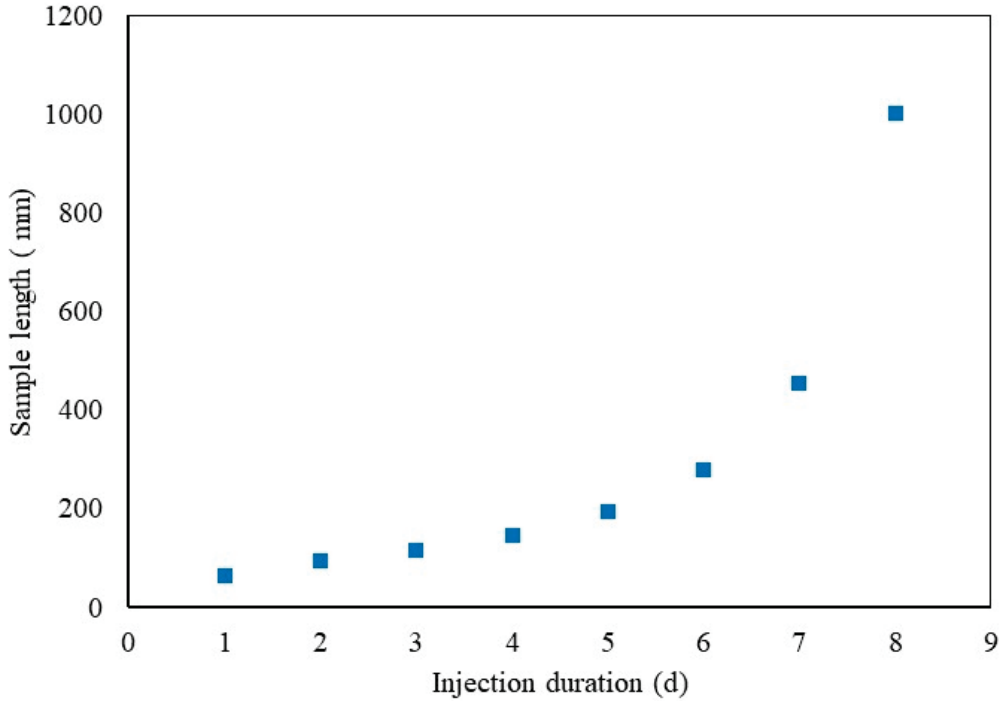

Figure 4. Variation of sample length (inside CO_2 pressure is greater than 5 MPa) with injection duration.

Based on the information provided by Figures 3 and 4, CO_2 migrates in coal at a relatively slow and steady rate in the first few days after injection. The sample length for which the inside CO_2 pressure is greater than 5 MPa is around 65 mm, 93 mm, 115 mm, 145 mm, and 193 mm after 1-day, 2-day, 3-day, 4-day, and 5-day injections, respectively. However, this length significantly increases to 455 mm after a seven-day CO_2 injection, which demonstrates that the sample becomes more permeable with the development of CO_2 pressure along it. As indicated in Figure 3, CO_2 pressure development accelerates after the CO_2 migrates downstream, which means the effect of the reduction of effective stress on the enhancement of sample permeability dominates the permeability variation of coal over the negative effect of permeability reduction induced by the adsorption of CO_2-induced coal matrix swelling.

Figure 5 shows the modeling results of CO_2 concentration along the sample after 1-day, 3-day, 5-day, 7-day, 9-day, and 11-day injections, respectively. Similar to the CO_2 pressure development with time, the amount of CO_2 injected into the sample increases with injection duration at a slow rate in the first few days of injection, followed by a much more rapid concentration development after a five-day CO_2 injection. The increased permeability of coal at the later stage of injection significantly improves CO_2 transportation in coal, which contributes to the considerable increment of CO_2 concentration in coal.

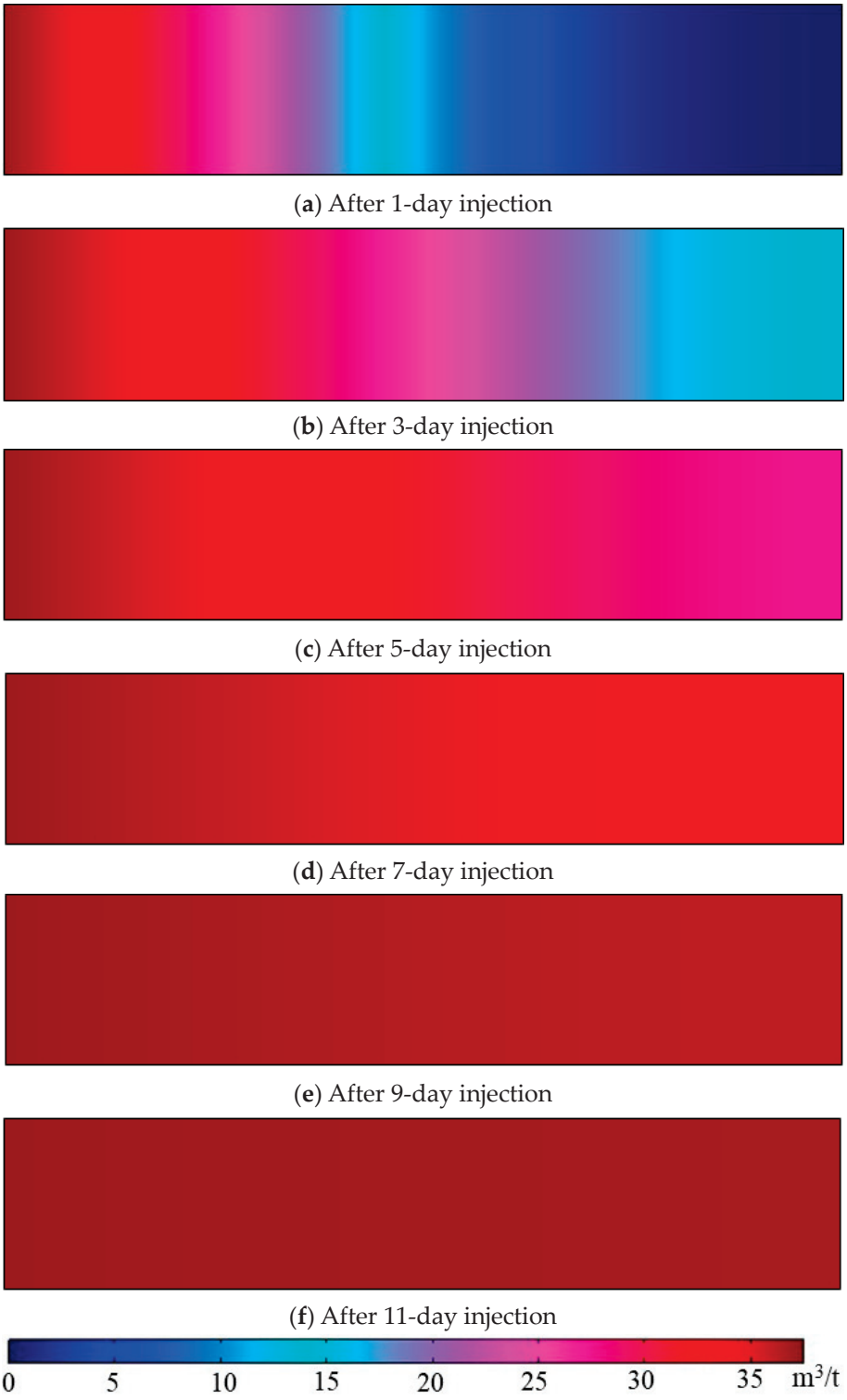

Figure 5. Variation of CO_2 concentration along a sample with injection durations for 6 MPa injection pressure at 10 MPa axial load.

4.2. Effect of CO_2 Injection Pressure on Gas Flow Behaviour in Coal

Increasing injection pressure raises pore pressure in coal, which results in cleat openings or fractures as the effective stress applied to coal is consequently reduced. Hence, the permeability of coal is increased with enhanced gas flow, and this effect intensifies with the increase of injection pressure. However, this is applicable for non-sorption gases such

as N_2 injection. Carbon dioxide has great adsorption affinity to coal for its more linear structure endowed with a high quadrupole moment [38]; the adsorbed CO_2 molecules in coal cause strain to be induced between the gas layer and coal pore walls, which can narrow or even close the cleats for gas flow, resulting in reduced gas flow and consequently, reduced permeability. This reduction of permeability due to the adsorption of CO_2 increases with increasing CO_2 injection pressure since studies have demonstrated that the amount of gas adsorbed in coal increases with increasing pressure to some extent [39,40]. CO_2 injection pressure is an important parameter for field applications and should be high enough to deliver sufficient CO_2 into the coal seam while maintaining the integrity of the seam. However, coal swelling induced by the adsorption of CO_2 increases to some extent with increasing CO_2 pressure [41–43], which causes permeability reduction and further complicates CO_2 migration in coal. Therefore, this part of the study was to investigate the effect of CO_2 injection pressure on CO_2 transportation behavior in coal.

Figure 6 shows the pressure development of CO_2 along the sample at 6 MPa, 7 MPa, 8 MPa, and 9 MPa injection pressures under 10 MPa axial stress. In order to compare the CO_2 migration behaviors for different injection pressures, the same injection duration (six days in this case) was selected to ensure that the injection pressure was the only variable for the different injection scenarios.

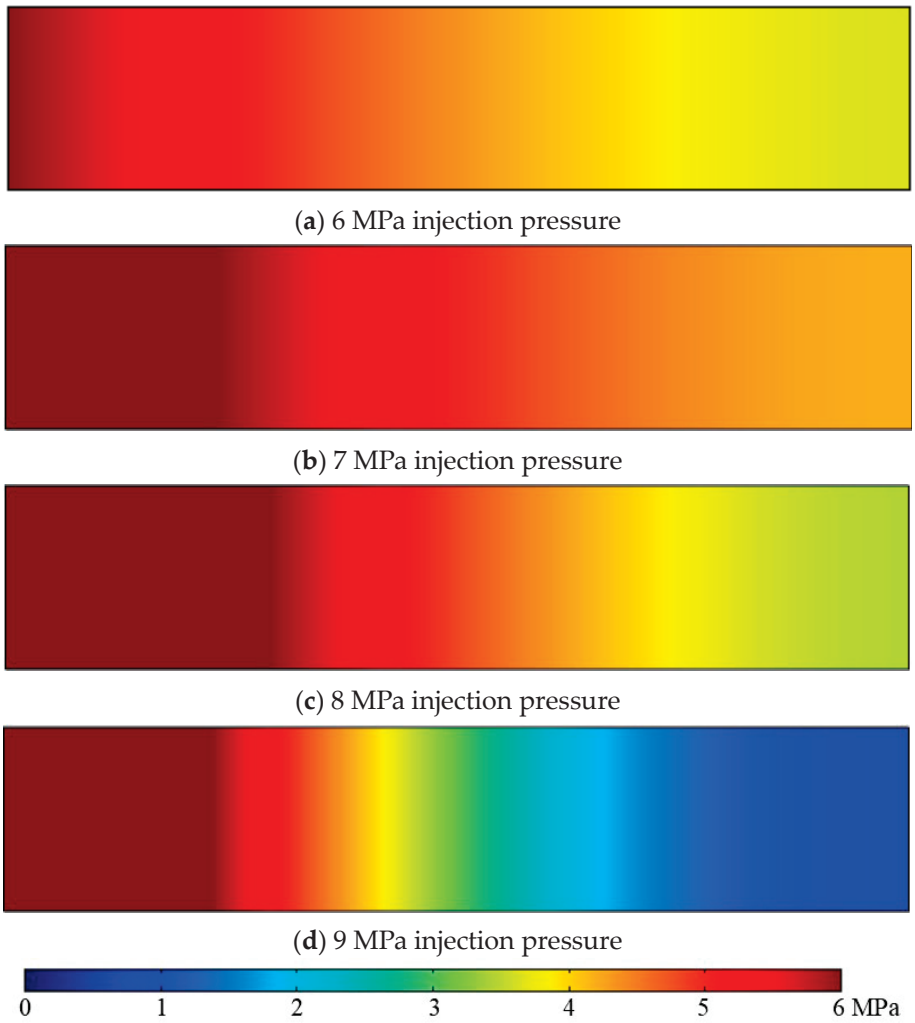

Figure 6. CO_2 pressure development in coal for different CO_2 injection pressures at 10 MPa axial stress after six-day injection.

As demonstrated in Figure 6, increasing the injection pressure from 6 MPa to 7 MPa causes greater pressure development in the sample as the downstream pressure develops

to around 3.64 MPa and 4.19 MPa, respectively. Although it is believed that higher CO_2 injection pressure favors greater coal matrix swelling and the associated permeability reduction, the improved gas pressure development along the sample for 7 MPa CO_2 injection indicates that the permeability reduction caused by CO_2 adsorption-induced strain is insignificant compared with the enhanced advection flux under higher CO_2 injection pressures. However, the CO_2 migration pattern in the sample exhibits different behaviors when the injection pressure increases to 8 MPa and 9 MPa, as shown in Figure 6. Lower pressure development was observed from the simulation results for 8 MPa CO_2 injection pressure than for 7 MPa, as the downstream pressure reached around 3.45 MPa for 8 MPa injection pressure. As the model condition is maintained at 37 °C and 8 MPa, the CO_2 is in a super-critical state in which the hydrodynamic properties of CO_2 significantly change. Both the density and dynamic viscosity of 8 MPa super-critical CO_2 is relatively higher than those of 7 MPa sub-critical CO_2. Therefore, the increased advection flow due to the increasing pressure difference for 8 MPa injection is overshadowed by the obstruction of CO_2 flows with greater density and viscosity. This effect is significantly enhanced for 9 MPa injection pressure, as the downstream pressure developed only to around 0.83 MPa after a six-day injection. Both the density and viscosity of 9 MPa CO_2 are considerably higher than those of sub-critical CO_2, and this highly dense and viscous super-critical CO_2 faces greater obstacles when traveling through the sample.

Further, Table 2 shows the minimum porosity of the sample under different injection pressures. The areas where the minimum porosity of the sample is found are at the injection site, where the greatest CO_2 pressure is present. As indicated in Table 2, the value of the minimum porosity of the sample decreases with increasing CO_2 injection pressure, which indicates that the increment of porosity due to reduced effective stress is less than the reduction of porosity due to CO_2 adsorption-induced strain. Therefore, the overall variation of sample porosity decreases with increasing injection pressure, which leads to greater permeability reduction for higher CO_2 injection pressure. In addition, the time required for the downstream to achieve a stable state (when the downstream pressure is greater than 95% of its corresponding injection pressure, it is considered as the stable state) is around 10 days, 10 days, 13 days, and 20 days for 6 MPa, 7 MPa, 8 MPa, and 9 MPa injection pressure, respectively, which is consistent with the above analysis that super-critical CO_2 injection faces greater obstacles traveling in the coal sample. Most CO_2 sequestration demonstrations are preferred to be implemented in deep-buried coal seams where the pressure and temperature of the environment are beyond the critical point, and the above simulation results suggest that migration of super-critical CO_2 in deep-buried coal seams is the main challenge for CO_2 sequestration projects.

Table 2. Minimum sample porosity for different CO_2 injection pressures under 10 MPa axial stress after six-day injection.

Injection Pressure	Minimum Porosity
6 MPa	6.94%
7 MPa	6.87%
8 MPa	6.81%
9 MPa	6.76%

Figure 7 shows the distribution of CO_2 concentration along the sample for different CO_2 injection pressures under 10 MPa axial stress after a three-day injection. Similarly, increasing injection pressure from 6 MPa to 7 MPa is accompanied by a slight enhancement of CO_2 concentration, which can be attributed to the greater advection flow for higher injection pressure. However, when the injection pressure further increases to the super-critical phase, evident reductions in CO_2 concentration development are observed, especially for 9 MPa super-critical injection. Permeability reduction with the increase of injection pressure for super-critical CO_2 injection impedes CO_2 traveling through the sample. Additionally, the much higher density and dynamic viscosity of super-critical CO_2 further obstruct the

passage of CO_2 within the sample. For example, the density of CO_2 at 37 °C is 209.94 kg/m^3, 324.02 kg/m^{3,} and 610.30 kg/m^3 for 7 MPa, 8 MPa, and 9 MPa pressures, respectively, and dynamic viscosity of CO_2 at 37 °C is 19.28 μPa*s, 23.85 μPa*s, and 45.52 μPa*s, for 7 MPa, 8 MPa, and 9 MPa pressures, respectively.

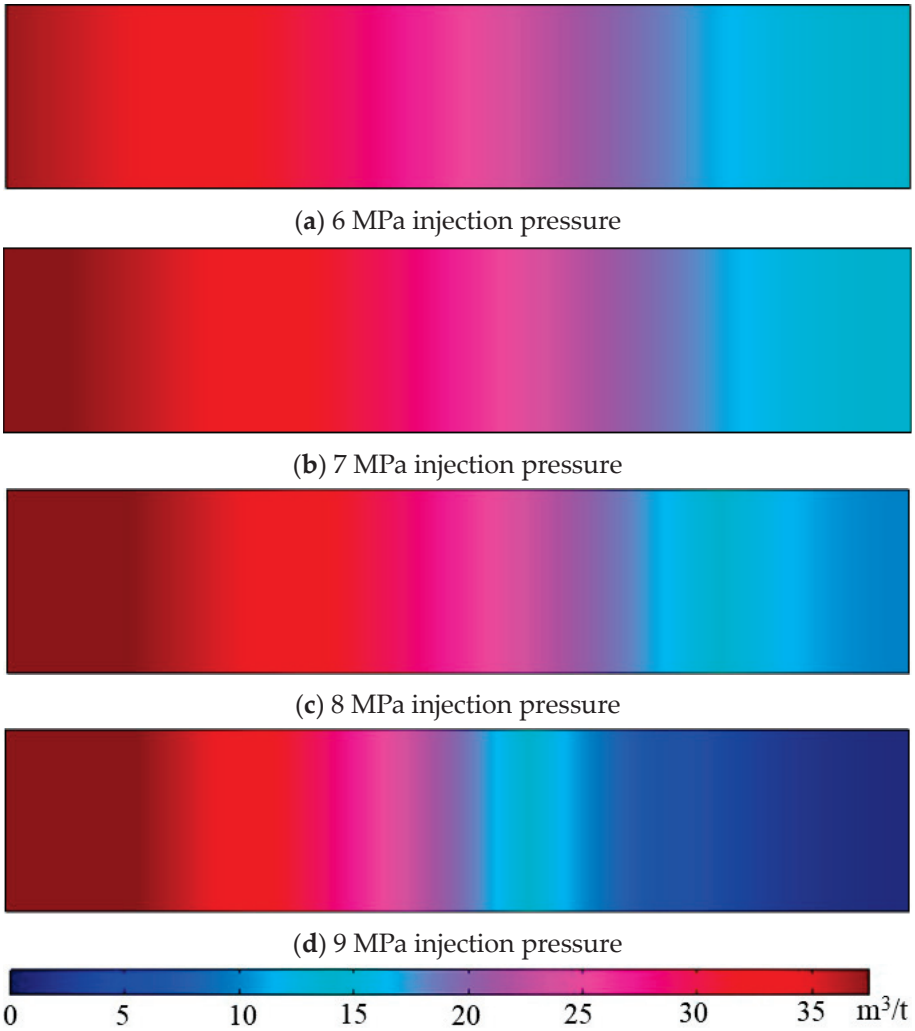

Figure 7. CO_2 concentration in coal at different injection pressures under 10 MPa axial stress after three-day injection.

4.3. Effect of Buried Depth on Gas Flow Behaviours in Coal

Deep coal seams are generally ideal target sinks for CO_2 sequestration, as there is less risk of the injected CO_2 back-migrating into the atmosphere [13,44]. However, the high-stress environment deep underground may create great obstacles for CO_2 to flow in the cleat system by closing fracture apertures, which generally require greater injection pressure to deliver CO_2 into coal seams. According to the previous discussion, higher CO_2 injection pressures, especially when in the super-critical state, may limit the flowability of CO_2, which complicates CO_2 migration patterns in coal. Therefore, this part of the study was dedicated to an investigation of the effect of stress conditions (buried depth) on CO_2 flow behavior in coal.

Figures 8 and 9 depict CO_2 pressure development in the sample under different axial stresses (from 10 MPa to 30 MPa) after a six-day injection of 6 MPa CO_2 and 9 MPa CO_2, respectively. As indicated in Figures 8 and 9, CO_2 pressure is less developed under higher stress conditions, which indicates that with the increase of axial stress (buried depth), CO_2 experiences greater difficulty migrating through the sample. This is in accordance with the

previous analysis that at greater depth, CO_2 movement is restricted because of the reduced flow paths due to the high-stress environment.

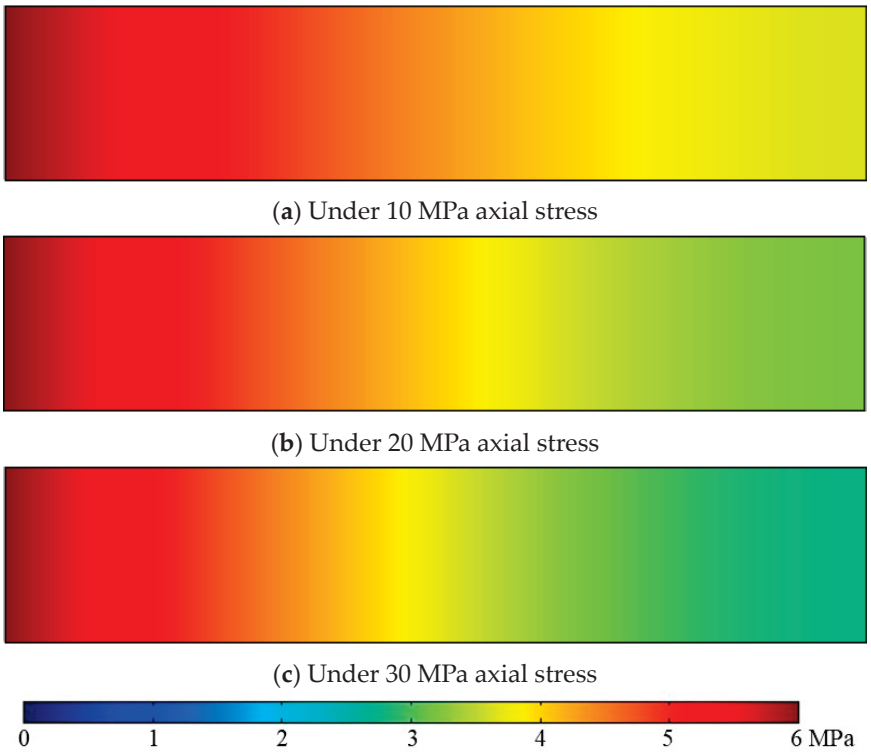

Figure 8. CO_2 pressure development in coal for different axial stresses at 6 MPa injection pressure after six-day injection.

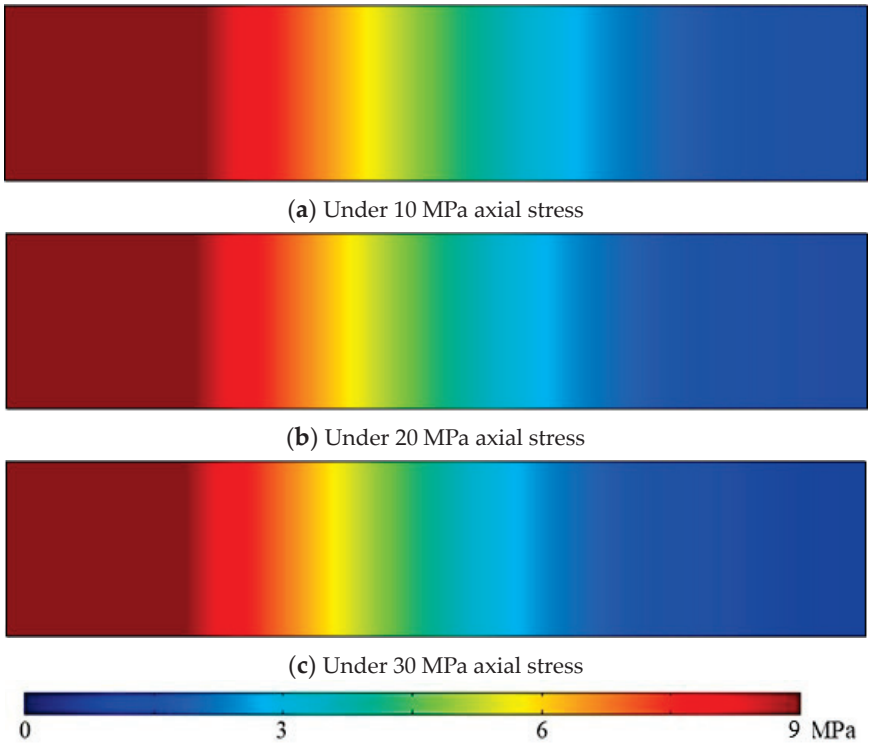

Figure 9. CO_2 pressure development in coal for different axial stresses at 9 MPa injection pressure after six-day injection.

A comparison of the results in Figures 8 and 9 reveals that greater alterations in CO_2 flow behaviors due to changes in effective stress are found for 6 MPa CO_2 injection compared with the associated changes for 9 MPa CO_2 injection. Figure 10a shows the time required for the downstream to reach the stable state (where downstream pressure is greater than 95% of the corresponding injection pressure) for each injection pressure under various stress conditions, and Figure 10b demonstrates the increment rate of injection time to achieve a stable state at downstream. As indicated in Figure 10a, it is evident that under high-stress conditions, a longer injection time is required for the CO_2 pressure to develop downstream for all the injection scenarios. The rate of increment of injection time to achieve a stable state downstream also increases with increasing axial stress, as shown in Figure 10b, and the gap between 6 MPa injection and 9 MPa injection increases with axial stress. This means that low injection pressures are more likely to be affected by changes in the stress condition, and this effect is enhanced in a high-stress environment. Therefore, it can be concluded that high CO_2 injection pressures are preferred for CO_2 sequestration projects with great buried depths. However, it should be mentioned that the CO_2 injection pressure needs to be well-managed to avoid the fracturing of the coal seam, which may lead to the early breakthrough of the injected CO_2.

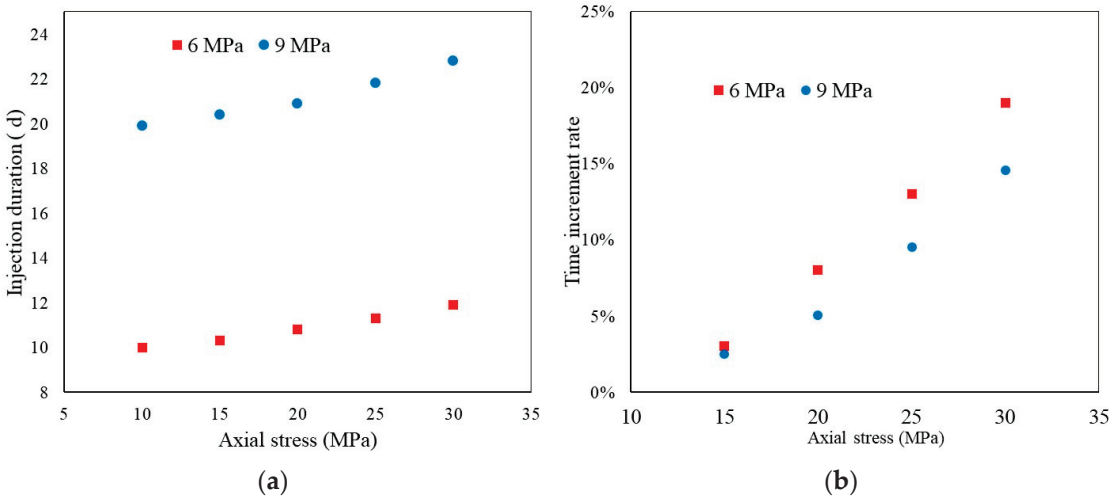

Figure 10. Relation between (**a**) time required for downstream to achieve stable and (**b**) rate of increment of injection time for downstream to achieve stable condition with stress.

Figures 11 and 12 depict the modeling results of the distribution of CO_2 concentration in the sample under different axial stresses after a three-day injection for 6 MPa CO_2 and 9 MPa CO_2 injection pressure, respectively. Similar to the effect of axial stress on the variation of pressure development, higher stress conditions restrict the adsorption of CO_2, and the amount of CO_2 injected into the sample decreases with increasing axial stress for both 6 MPa and 9 MPa CO_2 injection. A higher injection pressure (9 MPa in this case) appears to be less affected by the variation of stress conditions, which further demonstrates the effectiveness of high CO_2 injection pressures during CO_2 sequestration in deeply buried coal seams.

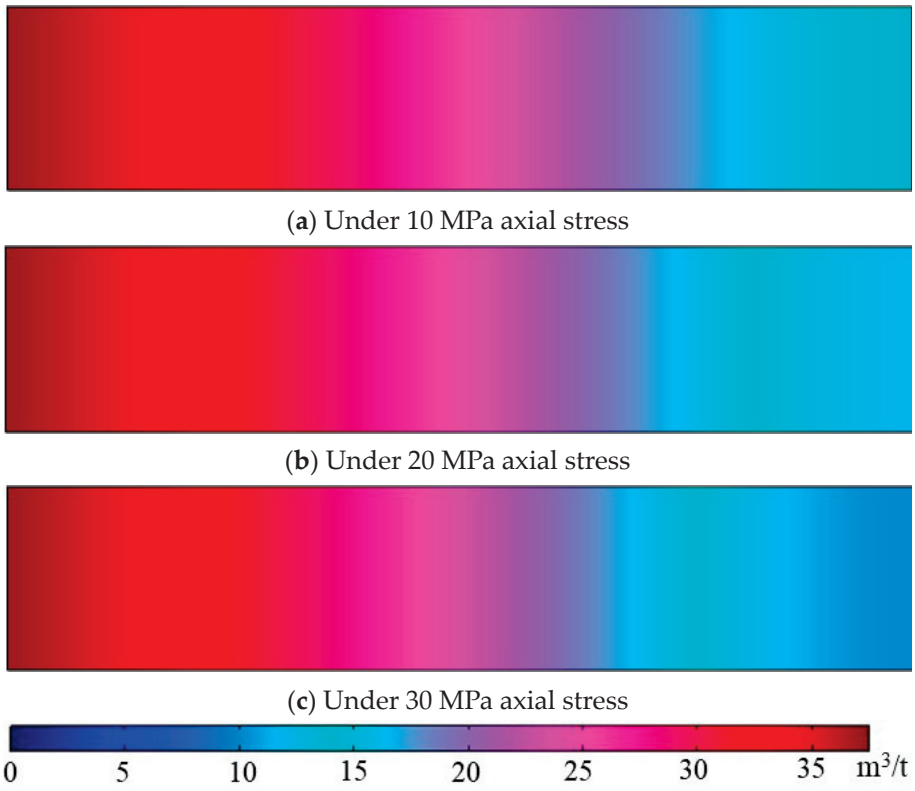

Figure 11. CO_2 concentrations in coal for different axial stresses under 6 MPa injection pressure after three-day injection.

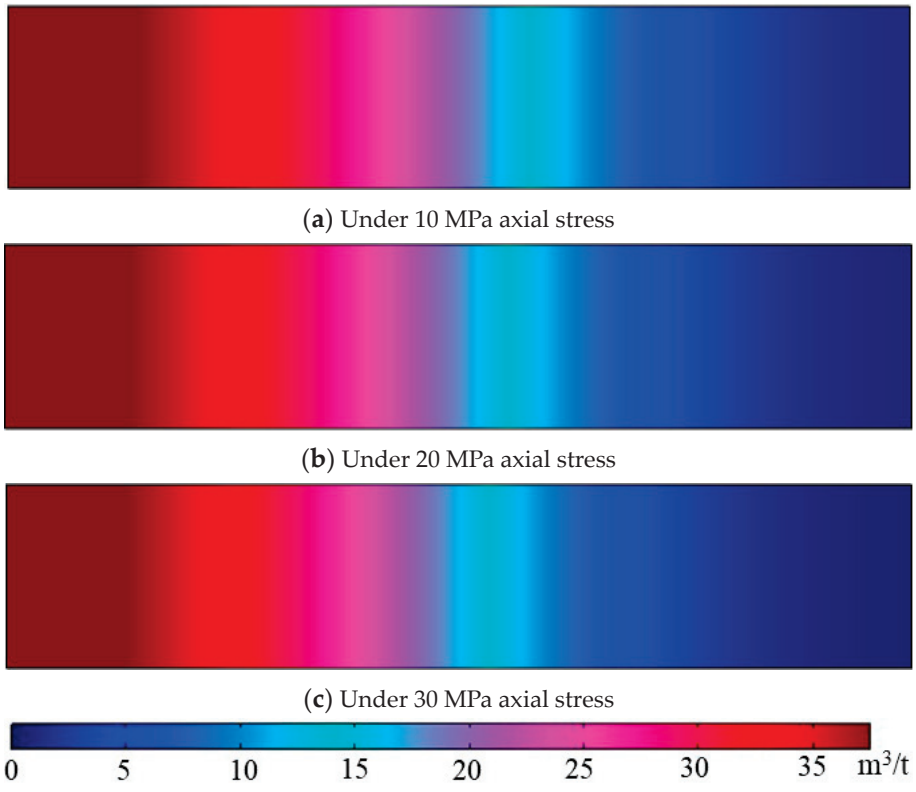

Figure 12. CO_2 concentrations in coal for different axial stresses under 9 MPa injection pressure after three-day injection.

5. Implications for CO_2 Sequestration in Deep Coal Seams

Deep coal seams are ideal sinks for CO_2 sequestration for their great storage potential and vast availability worldwide. High CO_2 injection pressures are required to overcome the high-stress condition deep underground, and CO_2 is, therefore, in its super-critical state along with the high-temperature condition. The findings of the present study suggest that migration of super-critical CO_2 in deep-buried coal seams is the main challenge for CO_2 sequestration projects since super-critical CO_2 injections face greater obstacles when flowing through a coal seam, but the ultimate storage of CO_2 can be achieved for higher injection pressures if sufficient injection time is given. Further, according to the result of pressure development for different axial stresses, high injection pressures are less affected by stress conditions compared with low injection pressures. Therefore, high injection pressures are preferred for economic and efficient CO_2 sequestration with great buried depths. However, the CO_2 injection pressure needs to be well-managed to avoid compromising the mechanical properties of the coal seam, which may lead to the early breakthrough of the injected CO_2. As the permeability reduction due to the adsorption of CO_2 is the major issue restricting the progress of field projects, permeability enhancement measures are therefore suggested. Injection of an inert gas such as N_2 has a stripping effect which can partly restore coal seam permeability. Other measures, such as thermal treatment and contained fracturing of the target coal seams, are also recommended; however, these operations need to be well-managed to minimize the disturbance to the coals and overlying strata. Since the associated macro-scale experimental studies were conducted using reconstructed coal samples, the samples are homogeneous in nature. Therefore, the model in the present study was also assumed to be homogeneous, the results of which cannot precisely mirror field conditions. Therefore, it is suggested to perform similar simulations on gas flow behaviors in heterogeneous coal models. Additionally, as discussed in the introduction, temperature has an intricate effect on CO_2 flow behaviors in coal. It is therefore suggested to study the effect of temperature, especially high temperature, on the hydro-mechanical performance of coal with the adsorption of CO_2.

6. Conclusions

Few studies to date have attempted to conduct CO_2 flow experiments on macro-scale coal samples as extensive time and labor are required to complete the associated tests. Numerical modeling can remove these barriers. In this study, a coupled gas flow, mechanical deformation, and sorption-induced deformation finite element model are developed to investigate CO_2 flow behavior in a laboratory-scale model under various test conditions. A general porosity model considering mechanical deformation-induced changes in pore volume and adsorption-induced changes in pore volume was adopted to describe the variation of model porosity. The mechanical deformation was modeled with the consideration of in situ stress and pore pressure changes. The coupling between gas flow behavior and variation of porosity was achieved through the cubic law, and the developed model was written in COMSOL Multiphysics to simulate CO_2 flow behavior during CO_2 sequestration in coal seams under various conditions. The following conclusions can be drawn from the results.

The sample is more permeable with pressure development at low injection pressure, which indicates that the effect of the reduction of effective stress on the enhancement of sample permeability is greater than the negative effect of permeability reduction due to CO_2 adsorption. Similarly, CO_2 concentration in coal increases with injection duration, especially at a later stage, due to the greater enhancement of sample permeability.

In the lower CO_2 injection pressure range (less than 8 MPa), CO_2 pressure development in coal increases with increasing injection pressure due to enhanced advection flux, while super-critical CO_2 injection faces greater obstacles in migrating within the coal sample compared to sub-critical CO_2 injections because of its significantly higher viscosity and density as well as the reduction in permeability due to adsorption-induced strain. However,

the ultimate pressure development or adsorption capacity increases with injection pressure regardless of the CO_2 phase.

CO_2 pressure and concentration development decrease with increasing axial stress (buried depth), which is related to the increased effective stress-induced reduction in gas flow paths.

The effect of axial stress on CO_2 migration in coal is more influential on lower injection pressures than higher super-critical CO_2 injection pressures, which demonstrates the effectiveness of using high injection pressures during CO_2 sequestration in high-stress deep coal seams. However, injection pressure needs to be well-managed to avoid compromising the mechanical properties of the coal seam and cap rock, rendering less effective storage of CO_2.

Author Contributions: Conceptualization, H.W. and Z.W.; methodology, H.W., Z.W. and H.Y.; software, C.J. and X.Z.; writing, H.W.; reviewing and editing, C.J., X.Z. and L.L.; All authors have read and agreed to the published version of the manuscript.

Funding: This research was funded by the National Natural Science Foundation of China (Grant No. 42005133, 92162105); the Hebei Natural Science Foundation (Grant No. D2022402005); the Key Program of Science and Technology Research Project of the Colleges and Universities of Hebei Province (Grant No. ZD2022130).

Institutional Review Board Statement: Not applicable.

Informed Consent Statement: Not applicable.

Data Availability Statement: The data used to support the findings of this study are available from the corresponding author upon reasonable request.

Conflicts of Interest: The authors declare no conflict of interest.

References

1. Mavrodieva, A.V.; Shaw, R. Disaster and Climate Change Issues in Japan's Society 5.0—A Discussion. *Sustainability* **2020**, *12*, 1893. [CrossRef]
2. Summers, J.K.; Lamper, A.; McMillion, C.; Harwell, L.C. Observed Changes in the Frequency, Intensity, and Spatial Patterns of Nine Natural Hazards in the United States from 2000 to 2019. *Sustainability* **2022**, *14*, 4158. [CrossRef] [PubMed]
3. Li, X.; Long, D.; Scanlon, B.R.; Mann, M.E.; Li, X.; Tian, F.; Sun, Z.; Wang, G. Climate Change Threatens Terrestrial Water Storage over the Tibetan Plateau. *Nat. Clim. Chang.* **2022**, *12*, 801–807. [CrossRef]
4. Hossain, B.; Sohel, M.S.; Ryakitimbo, C.M. Climate Change Induced Extreme Flood Disaster in Bangladesh: Implications on People's Livelihoods in the Char Village and Their Coping Mechanisms. *Prog. Disaster Sci.* **2020**, *6*, 100079. [CrossRef]
5. Al-Ghussain, L. Global Warming: Review on Driving Forces and Mitigation. *Environ. Prog. Sustain. Energy* **2019**, *38*, 13–21. [CrossRef]
6. Statistical Review of World Energy Energy Economics Home. Available online: https://www.bp.com/en/global/corporate/energy-economics/statistical-review-of-world-energy.html (accessed on 31 March 2023).
7. Climate Action—United Nations Sustainable Development. Available online: https://www.un.org/sustainabledevelopment/climate-action/ (accessed on 31 March 2023).
8. The Paris Agreement UNFCCC. Available online: https://unfccc.int/process-and-meetings/the-paris-agreement (accessed on 31 March 2023).
9. Zhang, X.G.; Ranjith, P.G.; Perera, M.S.A.; Ranathunga, A.S.; Haque, A. Gas Transportation and Enhanced Coalbed Methane Recovery Processes in Deep Coal Seams: A Review. *Energy Fuels* **2016**, *30*, 8832–8849. [CrossRef]
10. Zhu, W.; Liu, S.; Zhang, X.; Wei, C. Coupled coal–gas interaction during CBM and CO_2-ECBM recovery in coal seams: A critical review. *Geomech. Geophys. Geo-Energy Geo-Resour.* **2022**, *8*, 1–32. [CrossRef]
11. Tyne, R.L.; Barry, P.H.; Lawson, M.; Byrne, D.J.; Warr, O.; Xie, H.; Hillegonds, D.J.; Formolo, M.; Summers, Z.M.; Skinner, B.; et al. Rapid Microbial Methanogenesis during CO_2 Storage in Hydrocarbon Reservoirs. *Nature* **2021**, *600*, 670–674. [CrossRef]
12. Gunter, W.D.; Gentzis, T.; Rottenfusser, B.A.; Richardson, R.J.H. Deep Coalbed Methane in Alberta, Canada: A Fuel Resource with the Potential of Zero Greenhouse Gas Emissions. *Energy Convers. Manag.* **1997**, *38*, S217–S222. [CrossRef]
13. Pan, Z.; Ye, J.; Zhou, F.; Tan, Y.; Connell, L.D.; Fan, J. CO_2 Storage in Coal to Enhance Coalbed Methane Recovery: A Review of Field Experiments in China. *Int. Geol. Rev.* **2017**, *60*, 754–776. [CrossRef]
14. Zhang, X.; Ranjith, P.G.; Ranathunga, A.S. Sub- and Super-Critical Carbon Dioxide Flow Variations in Large High-Rank Coal Specimen: An Experimental Study. *Energy* **2019**, *181*, 148–161. [CrossRef]

15. Cui, X.; Bustin, R.M.; Chikatamarla, L. Adsorption-Induced Coal Swelling and Stress: Implications for Methane Production and Acid Gas Sequestration into Coal Seams. *J. Geophys. Res. Solid. Earth* **2007**, *112*, 10202. [CrossRef]
16. Qu, H.; Liu, J.; Pan, Z.; Connell, L. Impact of Matrix Swelling Area Propagation on the Evolution of Coal Permeability under Coupled Multiple Processes. *J. Nat. Gas. Sci. Eng.* **2014**, *18*, 451–466. [CrossRef]
17. Zhang, X.; Ranjith, P.G. Experimental Investigation of Effects of CO2 Injection on Enhanced Methane Recovery in Coal Seam Reservoirs. *J. CO2 Util.* **2019**, *33*, 394–404. [CrossRef]
18. Zhang, X.; Gamage, R.P.; Perera, M.S.A.; Ranathunga, A.S. Effects of Water and Brine Saturation on Mechanical Property Alterations of Brown Coal. *Energies* **2018**, *11*, 1116. [CrossRef]
19. Yao, H.; Chen, Y.; Liang, W.; Li, Z.; Song, X. Experimental Study on the Permeability Evolution of Coal with CO_2 Phase Transition. *Energy* **2023**, *266*, 126531. [CrossRef]
20. Wang, R.; Wang, Q.; Niu, Q.; Pan, J.; Wang, H.; Wang, Z. CO_2 Adsorption and Swelling of Coal under Constrained Conditions and Their Stage-Change Relationship. *J. Nat. Gas. Sci. Eng.* **2020**, *76*, 103205. [CrossRef]
21. Vishal, V. In-Situ Disposal of CO_2: Liquid and Supercritical CO_2 Permeability in Coal at Multiple down-Hole Stress Conditions. *J. CO2 Util.* **2017**, *17*, 235–242. [CrossRef]
22. Chen, L.; Zhao, M.; Li, X.; Liu, Y. Impact Research of CH4 Replacement with CO2 in Hydrous Coal under High Pressure Injection. *Min. Mineral. Depos.* **2022**, *16*, 121–126. [CrossRef]
23. Perera, M.S.A.; Ranjith, P.G.; Choi, S.K.; Airey, D. Investigation of Temperature Effect on Permeability of Naturally Fractured Black Coal for Carbon Dioxide Movement: An Experimental and Numerical Study. *Fuel* **2012**, *94*, 596–605. [CrossRef]
24. Jasinge, D.; Ranjith, P.G.; Choi, S.K. Effects of Effective Stress Changes on Permeability of Latrobe Valley Brown Coal. *Fuel* **2011**, *90*, 1292–1300. [CrossRef]
25. Connell, L.D. A New Interpretation of the Response of Coal Permeability to Changes in Pore Pressure, Stress and Matrix Shrinkage. *Int. J. Coal Geol.* **2016**, *162*, 169–182. [CrossRef]
26. Ren, J.; Niu, Q.; Wang, Z.; Wang, W.; Yuan, W.; Weng, H.; Sun, H.; Li, Y.; Du, Z. CO_2 Adsorption/Desorption, Induced Deformation Behavior, and Permeability Characteristics of Different Rank Coals: Application for CO_2-Enhanced Coalbed Methane Recovery. *Energy Fuels* **2022**, *36*, 5709–5722. [CrossRef]
27. De Silva, P.N.K.; Ranjith, P.G. Advanced Core Flooding Apparatus to Estimate Permeability and Storage Dynamics of CO2 in Large Coal Specimens. *Fuel* **2013**, *104*, 417–425. [CrossRef]
28. Ranathunga, A.S.; Perera, M.S.A.; Ranjith, P.G.; De Silva, G.P.D. A Macro-Scale View of the Influence of Effective Stress on Carbon Dioxide Flow Behaviour in Coal: An Experimental Study. *Geomech. Geophys. Geo-Energy Geo-Resour.* **2016**, *3*, 13–28. [CrossRef]
29. Zhang, X.; Jin, C.; Zhang, D.; Zhang, C.; Ranjith, P.G.; Yuan, Y. Carbon Dioxide Flow Behaviour in Macro-Scale Bituminous Coal: An Experimental Determination of the Influence of Effective Stress. *Energy* **2023**, *268*, 126754. [CrossRef]
30. Li, Z.; Yu, H.; Bai, Y. Numerical Simulation of CO_2-ECBM Based on Multi-Physical Field Coupling Model. *Sustainability* **2022**, *14*, 11789. [CrossRef]
31. Cun, Z.; Bo, L.; Ziyu, S.; Jinbao, L.; Jinlong, Z. Breakage Mechanism and Pore Evolution Characteristics of Gangue Materials under Compression. *Acta Geotech.* **2022**, *17*, 4823–4835. [CrossRef]
32. Connell, L.D.; Lu, M.; Pan, Z. An Analytical Coal Permeability Model for Tri-Axial Strain and Stress Conditions. *Int. J. Coal Geol.* **2010**, *84*, 103–114. [CrossRef]
33. Chen, Z.; Liu, J.; Elsworth, D.; Connell, L.D.; Pan, Z. Impact of CO_2 Injection and Differential Deformation on CO_2 Injectivity under In-Situ Stress Conditions. *Int. J. Coal Geol.* **2010**, *81*, 97–108. [CrossRef]
34. Xue, Y.; Ranjith, P.G.; Chen, Y.; Cai, C.; Gao, F.; Liu, X. Nonlinear Mechanical Characteristics and Damage Constitutive Model of Coal under CO_2 Adsorption during Geological Sequestration. *Fuel* **2023**, *331*, 125690. [CrossRef]
35. Zhu, W.C.; Wei, C.H.; Liu, J.; Qu, H.Y.; Elsworth, D. A Model of Coal–Gas Interaction under Variable Temperatures. *Int. J. Coal Geol.* **2011**, *86*, 213–221. [CrossRef]
36. Langmuir, I. The Constitution and Fundamental Properties of Solids and Liquids Part I. Solids. *J. Am. Chem. Soc.* **1916**, *38*, 2221–2295. [CrossRef]
37. Lemmon, E.W.; Huber, M.L.; McLinden, M.O. *NIST Standard Reference Database 23: Reference Fluid Thermodynamic and Transport Properties-REFPROP, Version 9.1*; National Institute of Standards and Technology: Gaithersburg, MD, USA, 2013.
38. Czerw, K. Methane and Carbon Dioxide Sorption/Desorption on Bituminous Coal—Experiments on Cubicoid Sample Cut from the Primal Coal Lump. *Int. J. Coal Geol.* **2011**, *85*, 72–77. [CrossRef]
39. Dutta, P.; Bhowmik, S.; Das, S. Methane and Carbon Dioxide Sorption on a Set of Coals from India. *Int. J. Coal Geol.* **2011**, *85*, 289–299. [CrossRef]
40. Bae, J.S.; Bhatia, S.K. High-Pressure Adsorption of Methane and Carbon Dioxide on Coal. *Energy Fuels* **2006**, *20*, 2599–2607. [CrossRef]
41. Vandamme, M.; Brochard, L.; Lecampion, B.; Coussy, O. Adsorption and Strain: The CO_2-Induced Swelling of Coal. *J. Mech. Phys. Solids* **2010**, *58*, 1489–1505. [CrossRef]
42. Hol, S.; Spiers, C.J. Competition between Adsorption-Induced Swelling and Elastic Compression of Coal at CO_2 Pressures up to 100 MPa. *J. Mech. Phys. Solids* **2012**, *60*, 1862–1882. [CrossRef]

43. Day, S.; Fry, R.; Sakurovs, R. Swelling of Australian Coals in Supercritical CO_2. *Int. J. Coal Geol.* **2008**, *74*, 41–52. [CrossRef]
44. Ge, Z.; Zeng, M.; Cheng, Y.; Wang, H.; Liu, X. Effects of Supercritical CO_2 Treatment Temperature on Functional Groups and Pore Structure of Coals. *Sustainability* **2019**, *11*, 7180. [CrossRef]

sustainability

MDPI

Article

Research on the Distribution Characteristics of the Bulking Coefficient in the Strike Direction of the Longwall Goaf Filled with Slurry

Wenyu Lv [1,2,3], Tianqi Song [1,4,*], Wenzhe Gu [4], Fengqi Qiu [1], Panshi Xie [1] and Kai Guo [1]

[1] School of Energy Engineering, Xi'an University of Science and Technology, Xi'an 710054, China
[2] Henan Key Laboratory for Green and Efficient Mining & Comprehensive Utilization of Mineral Resources, Henan Polytechnic University, Jiaozuo 454000, China
[3] Shaanxi Province Key Laboratory of Coal Mine Water Disaster Prevention and Control Technology, Xi'an 710077, China
[4] China Coal Energy Research Institute Co., Ltd., Xi'an 710054, China
* Correspondence: stq344359844@163.com

Abstract: Coal gangue slurry filling is an important technical means for harmless and large-scale disposal of gangue under low-interference conditions, and is one of the most important ways to achieve green mining, which is in line with the national concept of green development. This paper systematically expounds the technical background and scientific connotations of the birth of slurry filling, clarifies the key technology and process principles of slurry filling, and constructs the lag distance and optimization method of slurry filling based on the bulking coefficient. In order to explore the distribution law of the bulking coefficient of the overburden broken zone in the mining process, UDEC numerical simulation and similar simulations were used to analyze the movement law of a coal seam roof and the distribution characteristics of the bulking coefficient. The results show that with the evolution of the spatial structure of the overlying strata of the goaf, the subsidence of the coal seam roof decreases from the bottom to the top, and finally becomes stable. In the advancing direction of the working face, the bulking coefficient decreases continuously, and shows certain zoning characteristics. With the mining, it moves forward periodically with dynamic changes. In the strike direction, it can be divided into three areas: the natural accumulation area, the load-affected area and the gradual compaction area. Finally, the lag distance of slurry filling is determined to be 60 m, and the effect of adjacent grouting filling is good in the field test.

Keywords: overburden broken area; slurry filling; gap; lag distance; bulking coefficient

1. Introduction

In the process of coal resource development and utilization, a large number of solid wastes of coal gangue are produced. According to the statistics of the 13th Five-Year Plan of Coal Industry Development, the annual discharge of coal gangue in China has reached 759 million tons [1–3]. There are a series of eco-environmental problems, such as air pollution, groundwater pollution and soil pollution, produced during the process of waste rock discharge [4–6]. In order to realize the sustainable development of coal mining, slurry filling technology, as an effective technical approach for the green disposal of waste rock, has little impact on the original production system of the mine and can realize parallel mining and filling operations, and has been applied in many large mines in China [7]. The distance between slurry filling and coal face lag is the key parameter of this technology, and different lag distances will directly affect the filling effect and filling quantity [8,9]. However, the spatial distribution characteristics of mining overburden voids are the key factor to determine the lag distance of slurry filling, playing a decisive role in slurry filling quantity, and so the spatial distribution is an important parameter of

slurry filling design [10–13]. At present, domestic and foreign scholars have conducted a lot of research on mining overburden void space. Wang Yutao [14–18] built a three-dimensional spatial dynamic distribution model of voids and permeability in the goaf based on the theory of the conservation of mining space, and obtained the distribution maps of voids and permeability in different spatial positions and different mining end times; Liang Bing [19–24], etc., studied the distribution law of stress change and bulking coefficient of caving rock mass in the goaf of Shendong mining area, analyzed the structural characteristics of overburden "two zones", and divided the stress and bulking coefficient of caving rock mass in the goaf. Liu Yiyang [25–28] and others put forward a chain arch structure inclined to compound force, analyzed the characteristics of the chain arch under the influence of area length effect, and obtained the distribution characteristics of the crack field and void ratio of an "O"-shaped ring. The above research mainly focuses on the spatial distribution of the void space and permeability under the condition of goaf water storage. The research area in these studies is mainly the whole area of the fractured zone and caving zone, and the research object is mostly the old goaf after mining. There is little research on the trend distribution characteristics of void space in the caving zone in the mining face.

Based on this, this paper takes the lag distance of slurry filling as the research object, analyzes the roof movement and the variation law of the bulking coefficient in the mining process of the working face by using the method of numerical simulation and similar simulation, and establishes the lag distance optimization method based on the bulking coefficient, which provides a theoretical basis for the determination of the lag distance of slurry filling.

2. Principle of Slurry Filling Technology

2.1. Technical Background of the Birth of Slurry Filling

Coal gangue underground filling has been developed for decades in China, and in different periods, different underground filling methods [29–31] have been used according to different requirements, such as solid filling in the working face, paste filling in the working face, grouting filling in the overburdened separation layer and slurry filling in the goaf.

Before the 1980s, coal gangue in China was mostly disposed in the form of on-site stacking. Underground filling theories and technical systems of coal gangue had not yet been established, and only some mines tried to stack coal gangue in abandoned roadways to reduce the transportation volume.

From the 1980s to the end of the 1990s, aiming at addressing the problem of surface subsidence after coal seam mining, China carried out the experiment of separated layer grouting filling in Laohutai Coal Mine, Fushun, followed by the application of "three-under" mining in eastern mining areas such as Datun, Xinwen, Yanzhou and Zaozhuang, and gradually established the basic theory and technical system of separated layer grouting filling in overlying strata [32].

At the beginning of the 21st century, aiming to solve the "three-under" mining problem of coal seams in the central mining area, China began to study the underground treatment technology of solid filling, formulating a solid filling technology system, which was applied in the central and eastern mining areas such as Hebei, Kailuan, Shandong and Shanxi. In view of the layered mining problem of thick coal seams, paste filling technology was introduced in Taiping Coal Mine in 2006, and it was gradually applied in "three-under" mining, taking into account the disposal of coal gangue [32,33].

After 2010, in order to meet the demand for the green and low-interference disposal of coal gangue in high-yield and high-efficiency mines in the western Mengshan area, China started the research into and exploration of goaf slurry filling technology, and gradually carried out industrial tests in Huangling No. 2 coal mine and Dahaize coal mine [7,31]. The development process of coal gangue underground filling is shown in Figure 1.

Stacked on the ground	Demand for surface subsidence reduction ⇩ Overburden bed separation area filling	"Three under" mining ⇩ Solid backfill mining	Layered mining demand of thick coal seam ⇩ Paste filling	Green low-interference disposal requirements ⇩ slurry filling technology
Advantages	It will not affect the mine production. It can not only dispose gangue, but also reduce surface settlement.	The system has large processing capacity and good rock control effect.	The rock stratum control effect is good. The rock stratum control effect is good.	It will not affect the mine production. The filling process is simple.
Fault	It is not applicable to shallow coal seams and is greatly affected by the separation space.	There is a matching relationship between mining and filling in the new mining face.	The new mining face has large investment, complex process and high cost.	The treatment scale is affected by factors such as coal seam mining height and lithology.
Adaptability	It is applicable to the mining face with large burial depth and separation space.	It is applicable to coal seams with mining height of 2.5~5.0m.	It is mainly used for "three under" coal mining and layered mining.	It is applicable to various mining heights.

Figure 1. Development process of underground filling with coal gangue.

2.2. Principles and Methods of Slurry Filling Technology

Slurry pipeline filling technology refers to making coal-based solid waste produced in the production process of coal mines or power plants into powder with a certain particle size by crushing, grinding and other technical means, and mixing it with water according to a specific proportion to prepare slurry. The slurry is transported to the filling position through long-distance pipeline transportation, and the residual space after stope collapse is used for filling. The main technical means of filling include high grouting filling, adjacent grouting filling and low grouting filling, and the technical schematic diagram of these processes is shown in Figure 2.

High grouting filling refers to the construction of a vertical space slurry filling channel in the lower area of the mining overburden fracture zone. The means of realization can be divided into a ground high-level grouting borehole, an underground high-level grouting roadway, a kilometer borehole, an upper coal seam grouting borehole, etc.

Adjacent grouting filling refers to the arrangement of adjacent grouting and filling holes in the upper area of the collapse zone to build a slurry filling channel at the same level in the inclined space. The main means of implementation involves drilling upward from the adjacent working face roadway or the adjacent main roadway to the upper area of the collapse zone.

Low grouting filling refers to arranging grouting pipes at the lower part of the collapse zone to build a filling channel. The main means of implementation involves hanging pipes and filling the roadway in the working face.

Each technical means has its own applicable conditions and technical advantages. In practical engineering, the above technical means can be combined and matched according to specific conditions to form the optimal filling mode. This technology has little impact on the original production system, and can realize parallel mining and filling. The transportation mode of filling materials is efficient and fast, and the filling process can realize intelligent control. It is an effective technical method for the green disposal of waste rock.

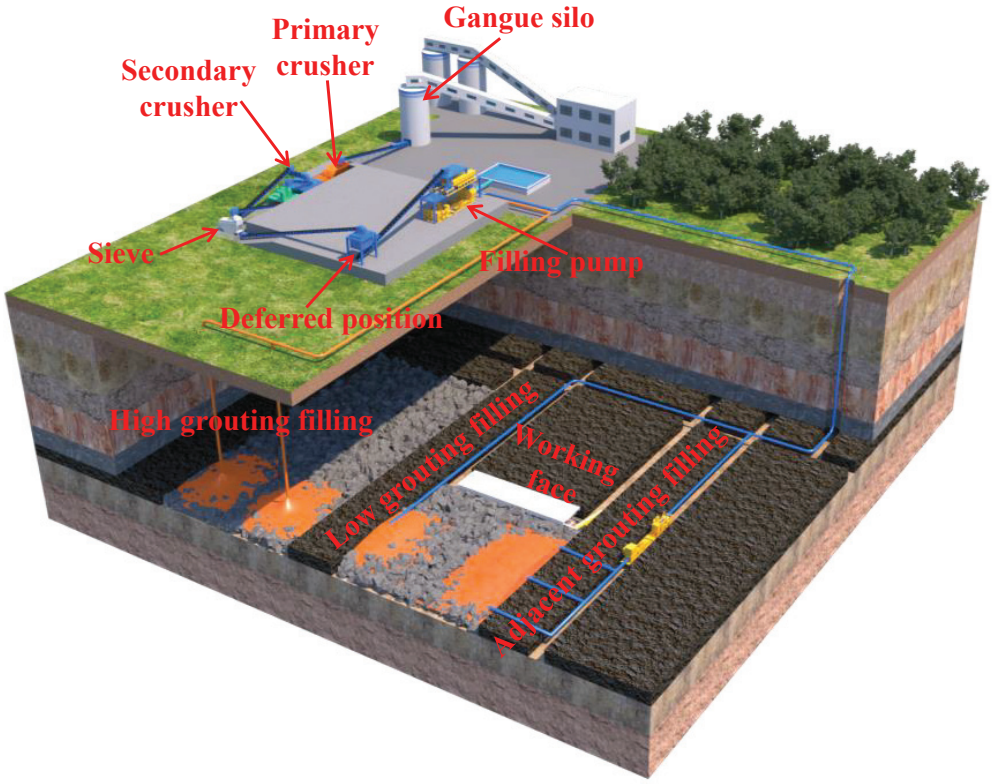

Figure 2. Schematic diagram of slurry filling technology.

2.3. Slurry Filling Lag Distance and Optimization Method

Different slurry filling methods, such as high-level grouting filling, adjacent grouting filling and low-level grouting filling, are used to fill the coal mining face with lag. The distance between the filling position and the coal mining face at the beginning of filling is called the lag distance. Its purpose is to ensure the relative independence of coal mining and filling, realize real parallel mining and filling, and improve the mining efficiency of the filling face. Different lag distances will directly affect the filling effect and filling quantity. A larger lag distance is more beneficial to the spatial independence of filling and coal mining operations, and will not influence cross operations. However, with the increase in lag distance, the compression degree of the gangue in the goaf also increased, and the difficulty of grouting rises, which will affect the grouting filling effect. However, the spatial distribution characteristics of the mining overburden void are the key factors determining the lag distance of slurry filling. Therefore, a method to determine the lag distance of gangue slurry filling based on the bulking coefficient of the goaf is proposed, as shown in Figure 3.

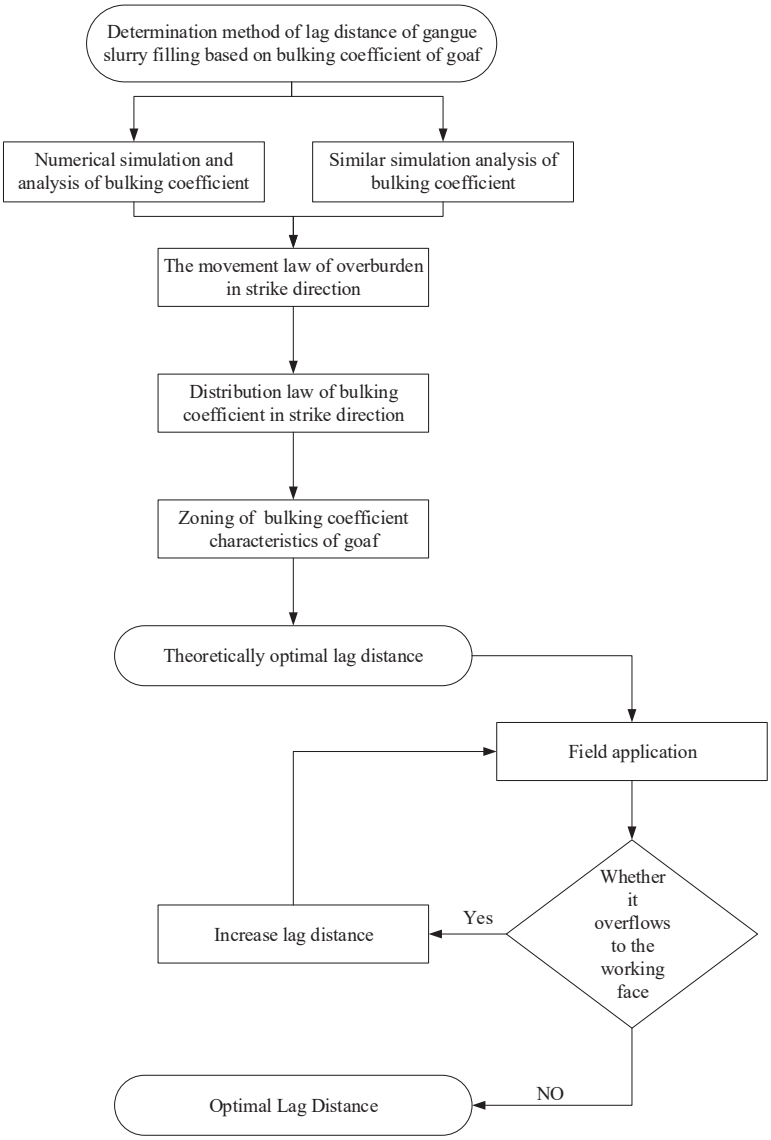

Figure 3. Determination method of lag distance of gangue slurry filling.

3. General Situation of the Project

The raw coal production capacity of a coal mine in Shaanxi province is 10 Mt/a, and the total amount of waste rock is about 0.85 Mt/a every year, among which the amount of pure waste rock generated from the bottom of the underground working face and tunneling in the cavern is about 200,000 t/a. In order to promote the ecological protection and high-quality development of the Yellow River Basin, and to avoid the environmental pollution caused by the ground discharge of gangue, the coal washing plant of the mine is equipped with a gangue power plant. The washed gangue can be directly utilized by the gangue power plant with low calorific value, and the underground-excavated gangue is mainly treated by slurry filling. The capacity of the industrial experimental system in the early stage of panel 3 is designed to be 118,000 t/a, and the capacity of the filling system in the later stage of panel 2 is designed to be 200,000 t/a, which is popularized and applied in the mode of panel replication.

Based on the specific mining geological conditions of the coal mine, the filling method is adjacent grouting filling, and the slurry filling of the goaf in the lagging mining face is realized by drilling upward from the roadway construction in the adjacent working face to the upper area of the caving zone, as shown in Figure 4.

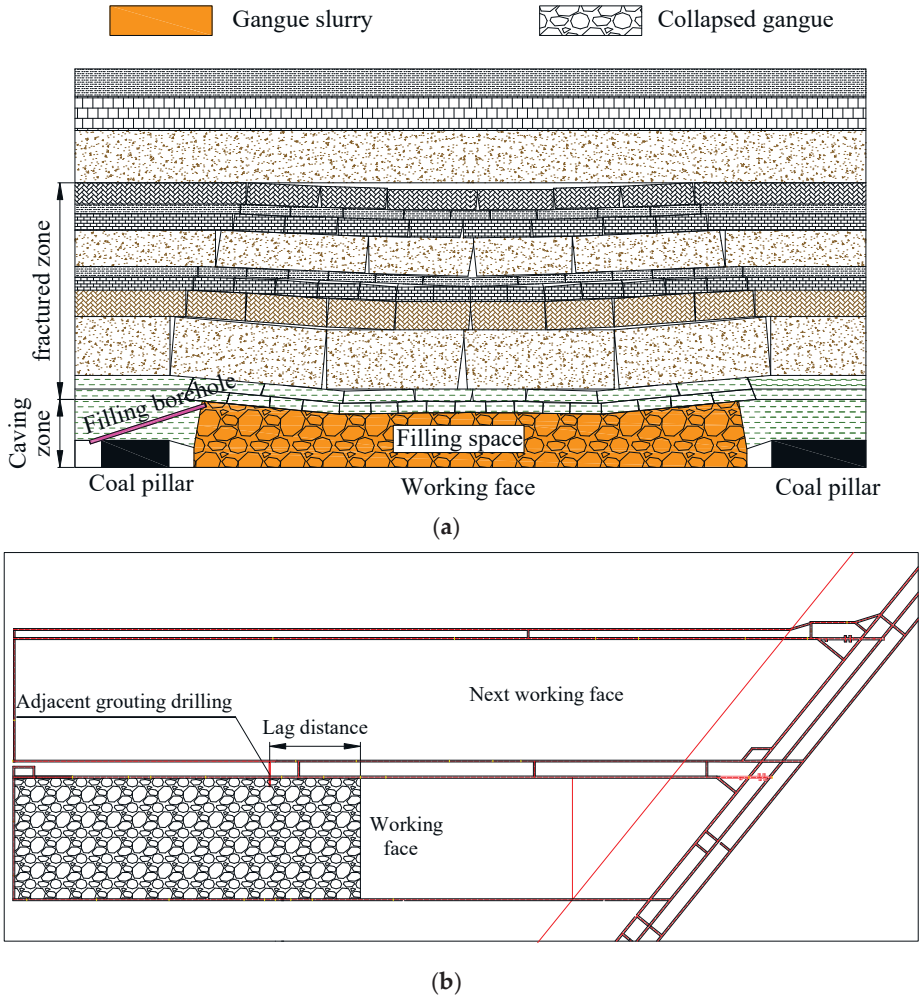

Figure 4. Schematic diagram of adjacent grouting filling technology: (**a**) profile; (**b**) plan.

In the process of mining the face, the overburden of the stope is constantly deformed and destroyed, which leads to the continuous compaction of waste rock in the goaf and the continuous change in the filling space. Reasonable determination of the filling hole position becomes one of the key factors to determine the filling amount of a single hole. Therefore, it is an effective means of reasonably determining the lag distance of adjacent grouting holes and increasing the filling amount of single hole by making clear the distribution characteristics of overburden failure and void space in the stope.

4. Numerical Simulation Analysis of Bulking Coefficient Characteristics of Overburden in Stope

4.1. Model Establishment

Combined with the geological conditions of the No. 301 working face in a coal mine in Shaanxi, the numerical model of overburden failure in the stope was established. To eliminate the stress boundary effect, the model size was determined to be 450 m × 200 m (length × height). A uniform load of 7.5 MPa was applied to the upper boundary of the model as the self-weight stress of the overlying strata, while horizontal constraints were applied to the left and right boundaries, and the vertical displacement was not constrained. The vertical displacement and horizontal displacement at the bottom of the model were both limited to 0. An elastic–plastic constitutive model was adopted for numerical calculation, and the yield criterion was the Moore–Coulomb yield criterion. Physical and mechanical parameters of coal strata in the numerical calculation model are shown in Table 1.

Table 1. Physical and mechanical parameters of coal and rock strata in the numerical calculation model.

Rock Stratum	Bulk Modulus/GPa	Shear Modulus/GPa	Density/g/cm^3	Cohesive Strength/MPa	Tensile Strength/MPa	Internal Friction Angle/°
Medium grained sandstone	5.91	5.81	2.66	3.15	1.68	37.2
Fine grained sandstone 1	7.87	3.63	2.55	3.89	1.75	36.9
siltstone	6.46	5.89	2.51	4.87	2.17	37.5
Fine grained sandstone 2	6.89	4.75	2.63	3.65	2.19	37.1
coal	2.35	1.42	1.33	2.99	1.10	36.2
Mudstone 1	3.64	2.10	2.36	3.20	1.50	34.8
Mudstone 2	2.23	1.19	2.45	2.81	1.32	33.1
Fine grained sandstone 3	5.35	4.89	2.55	4.76	2.18	37.5

4.2. Analysis of Caving Characteristics

Figure 5 presents overburden caving and fissure development in the stope when the working face advances over different distances.

As can be seen from the figure:

1. After the coal seam is mined, the basic roof and overlying strata move, which further leads to the collapse of the strata and forms the collapse zone. The overlying strata move upward and continue to transmit to form the delamination cracks and vertical fracture cracks, and the delamination cracks occur between the strata. With the advancing of the working face, the height of the caving zone is basically stable at about 15~18 m. The height of the fracture zone increases first and then stabilizes, and the broken fracture is formed by the fracture of the rock stratum. With the advancing of the working face, it continues to increase in the extension direction, and the height increases first and then stabilizes.
2. The location of the working face and the location of the open cut are affected by the hinge function and load transfer function of the roof rock, and the roof rock below is not completely compacted, showing a natural accumulation state, with a large amount of void space, which can be used as the space for slurry filling, and it is about one periodic weighting step away from the working face. However, with the advancing of the working face periodically, the hinge characteristics of overlying rock and the load transfer characteristics change, and the rock blocks below are constantly compacted, resulting in the phenomenon of decreasing void space. The length period from the area to the working face is about two to three periodic weighting steps.

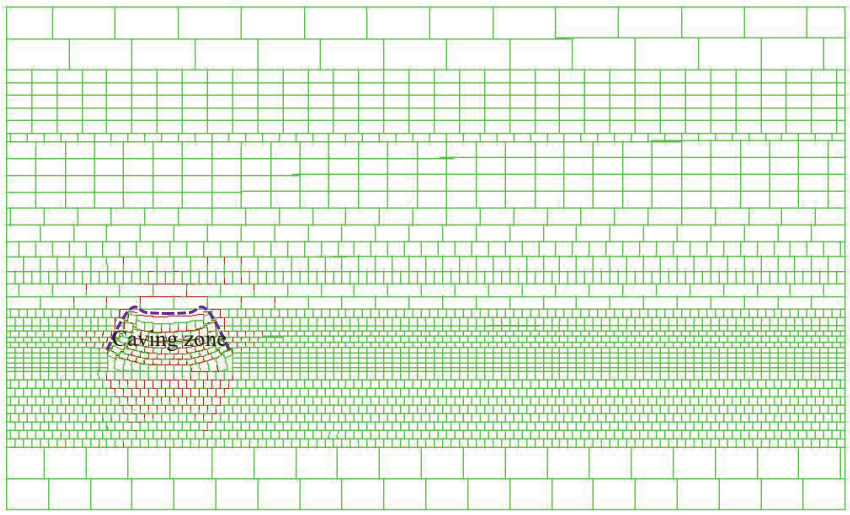

(**a**)

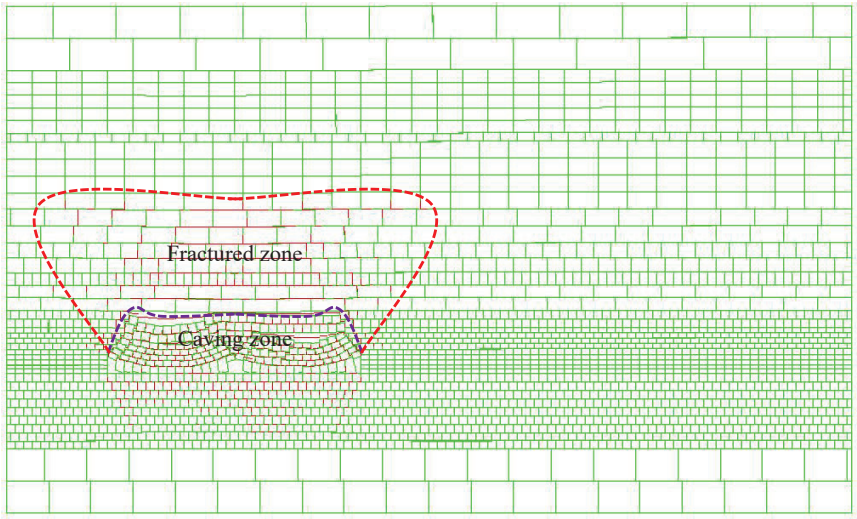

(**b**)

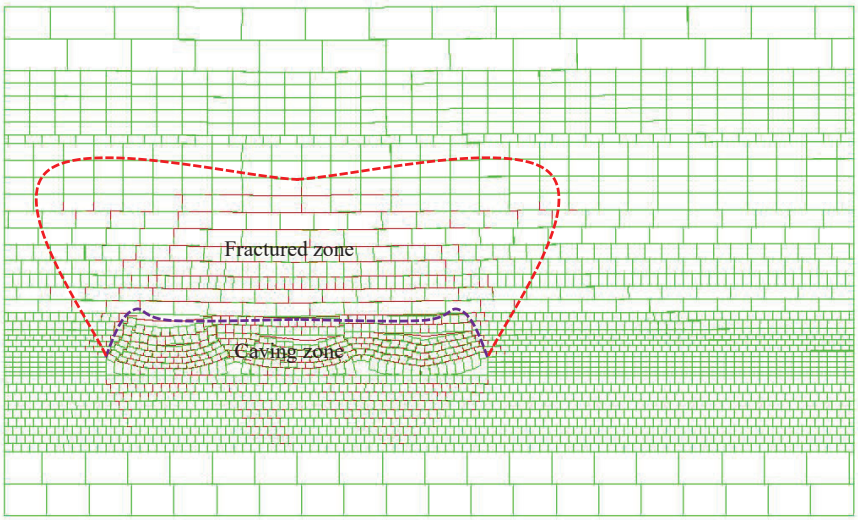

(**c**)

Figure 5. *Cont*.

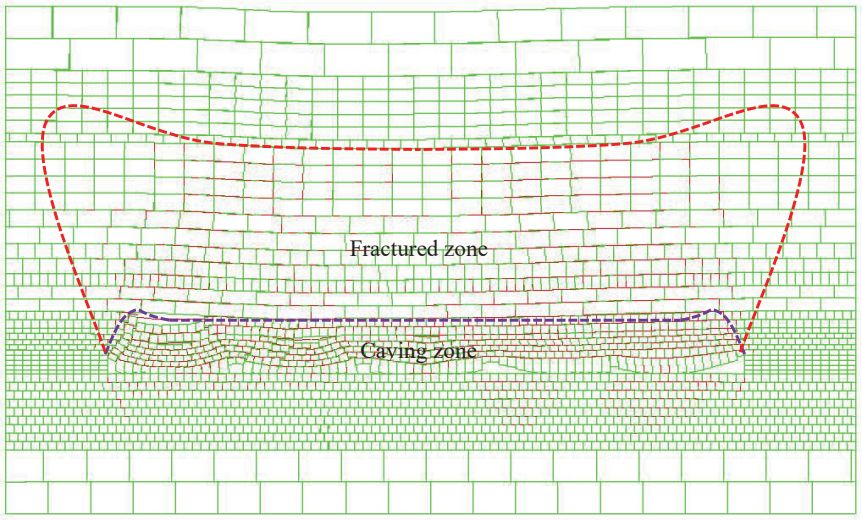

(**d**)

Figure 5. Failure characteristics of stope overburden during the advancing of the working face; (**a**) working face advancing 60 m; (**b**) working face advancing 120 m; (**c**) working face advancing 180 m; (**d**) working face advancing 300 m.

4.3. Analysis of Roof Displacement and Bulking Coefficient Characteristics

In order to further analyze the distribution of roof displacement and the characteristics of the goaf bulking coefficient, the roof displacement data of different strata when the working face advances 300 m are derived, as shown in Figure 6.

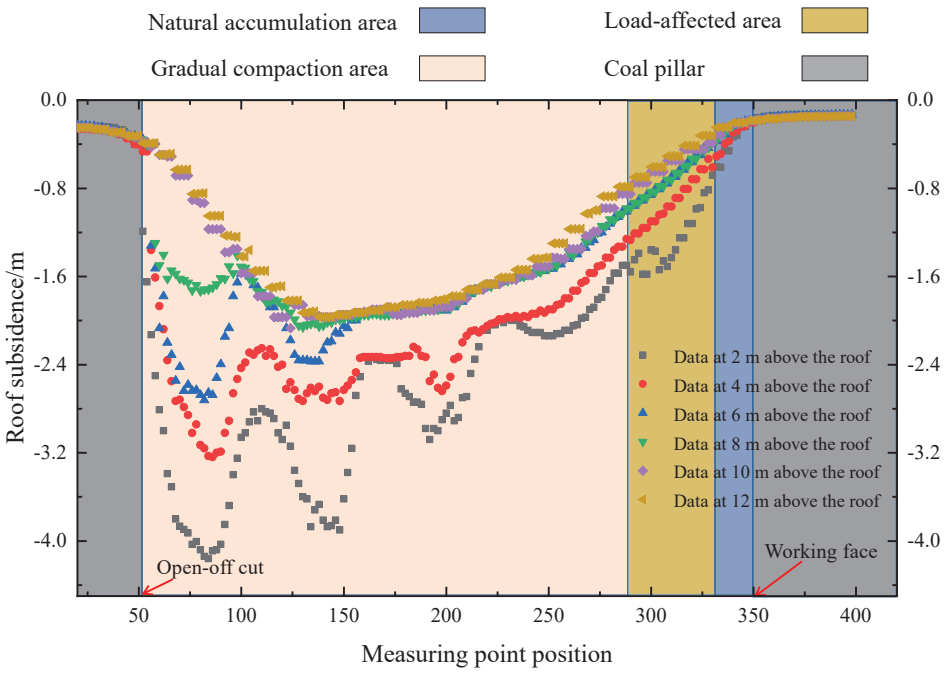

Figure 6. Displacement curve of the roof in different layers.

The state in which the caved rock mass volume in the goaf is significantly larger than that before caving is called dilatability, which is usually expressed by the bulking coefficient

$$k = \frac{V'}{V} \tag{1}$$

where k is the bulking coefficient of caved rock, V' is the volume of caved rock mass, and V is the volume of pre-caving rock mass.

It can be seen from the working face mining simulation test results that the displacement of overlying rock is mainly in the form of vertical subsidence, and the volume change is mainly along the vertical direction. Therefore, the bulking coefficient of caved rock mass in the goaf can be approximately replaced by the vertical bulking coefficient of rock mass—that is, the distance ratio before and after mining between two adjacent measuring points in the vertical direction of the model:

$$k \approx k_c = \frac{h_{n\sim n+1}}{h'_{n\sim n+1}} \tag{2}$$

where k_c is the vertical bulking coefficient of caving rock mass, $h'_{n\sim n+1}$ is the distance between two adjacent measuring points before mining, and $h_{n\sim n+1}$ is the distance between two adjacent measuring points after mining.

According to the displacement data of each stratum, the bulking coefficient from different heights to the coal floor can be obtained, as shown in Figure 7.

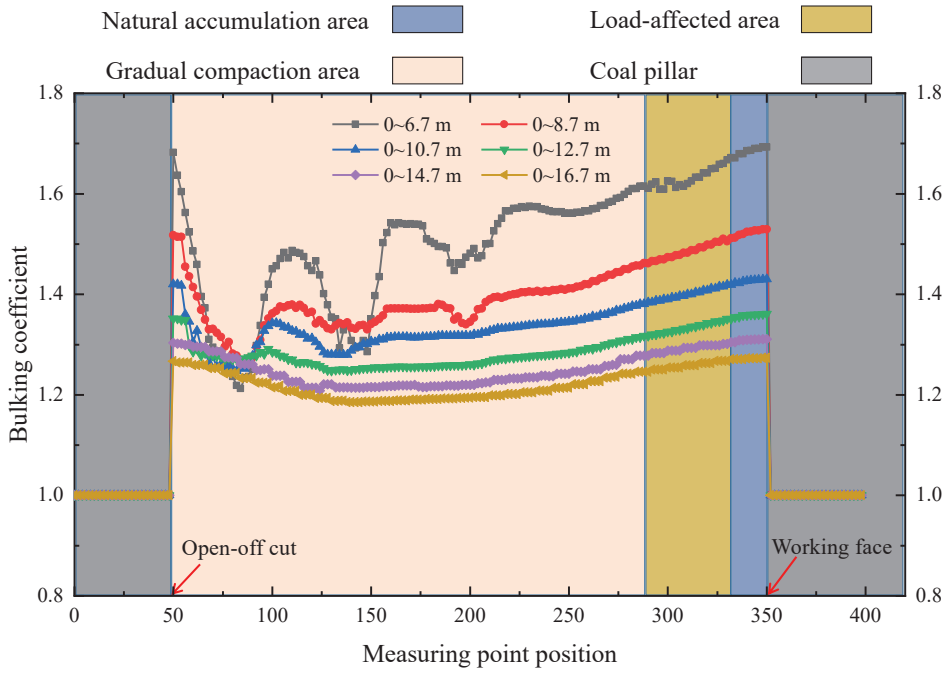

Figure 7. Bulking coefficient at different heights.

As can be seen from the figure:

1. The subsidence of the roof above the coal seam is 2.0 m > 4.0 m > 6.0 m > 8.0 m > 10.0 m > 12.0 m. This is because after the coal seam is mined, the roof strata collapse from bottom to top, and gradually weaken during the upward transmission of overlying strata. Layers and gaps will appear between the strata and between rock blocks. This phenomenon is also the realization feature of rock fragmentation, which further leads to the gradual decrease in the subsidence of the upper strata, which becomes stable.
2. In the advancing direction of the working face, the displacement of the roof near the working face is significantly smaller than that far from the working face. This is due to the change in the load transmission and hinge relation of the rear rock stratum during the periodic advancing process of the working face, which leads to the continuous compaction of the gangue in the rear goaf, the continuous reduction in the crushing bulking coefficient, and further leads to the increase in the roof displacement.

3. In the vertical direction of the same area of the stope, with the increase in the height range, the value of the bulking coefficient decreases continuously, and the decreasing range decreases continuously. This is because, in the vertical direction, the rock stratum near the coal floor breaks most violently, and the pores between the rocks are the largest, which leads to a higher bulking coefficient. Therefore, the average bulking coefficient in the vertical direction will decrease continuously.
4. In the advancing direction of the working face, with the increase in the length from the working face, the bulking coefficient decreases continuously, and presents certain zoning characteristics, especially in the range of 0~6.7 m in the height direction. It can be divided into three areas, namely the natural accumulation area, the load-affected area and the gradually compacted area. According to the distribution characteristics of the crushing bulking coefficient, the natural accumulation area moves forward periodically with the advancing of the working face, and its length is about one weighting step, while the crushing bulking coefficient within the caving zone is about 1.3. The length of the affected zone is about two to three weighting steps, and the bulking coefficient in the caving zone is about 1.25. The rear area is the compacted area, and the bulking coefficient is about 1.2, and the residual bulking coefficient is 1.15 as the working face continues to advance.

5. Similarity Simulation Analysis of Overburden Breaking and Bulking Coefficient Characteristics in Stope

5.1. Experimental Design

5.1.1. Similarity Criterion

The similarity conditions include geometric similarity, constitutive similarity of the deformation and failure process of mining rock and soil mass, the similarity of single-value conditions, and similarity criteria determined by dimensionless parameters [34].

These similarity conditions are determined by the physical and mechanical parameters, geometric size, unit weight, movement time, movement speed, gravity acceleration, properties of rock and soil layer (strength, elastic modulus E, cohesion c, internal friction angle φ, etc.) and force, which are related to the deformation and failure process of rock mass.

According to the occurrence conditions of the overburden in the area and the size parameters of the laboratory model frame, the plane stress model is determined for this physical simulation experiment. The geometric similarity ratio of the model is 1:120, and therefore:

Geometric similarity condition:

$$\alpha_1 = \frac{l_m}{l_p} = \frac{1}{120}$$

Gravity similarity condition:

$$\alpha_\gamma = \frac{\gamma_m}{\gamma_p} = \frac{2}{3}$$

Similarity conditions for gravitational acceleration:

$$\alpha_g = \frac{g_m}{g_p} = \frac{1}{1}$$

Time similarity condition:

$$\alpha_t = \frac{t_m}{t_p} = \sqrt{\alpha_1} = \frac{1}{11.4}$$

Velocity similarity condition:

$$\alpha_v = \frac{v_m}{v_p} = \sqrt{\alpha_l} = 0.0913$$

Displacement similarity condition:

$$\alpha_s = \alpha_1 = \frac{1}{120}$$

Similarity conditions for strength, elastic modulus and bond force:

$$\alpha_R = \alpha_E = \alpha_C = \alpha_1 \alpha_\gamma = \frac{1}{195}$$

Internal friction angle similarity conditions:

$$\alpha_\phi = \frac{R_m}{R_p} = \frac{1}{1}$$

Force similarity condition:

$$\alpha_f = \frac{f_m}{f_p} = \alpha_g \alpha_\gamma {\alpha_l}^3 = 0.385 \times 10^{-6}$$

According to the occurrence conditions of overburdened rock in this area and the size parameters of the laboratory model frame, the plane stress model is adopted in this physical simulation experiment, and the geometric size of the model is 3.0 m × 1.5 m, as shown in Figure 8. The geometric similarity ratio of the model is 1:120; the gravity similarity ratio is 1:1.5; the time similarity ratio is 1:11.4; and the speed similarity ratio is 1:10.95.

(**a**) (**b**)

Figure 8. Similar simulation experiment equipment: (**a**) physical model; (**b**) XTDIC three-dimensional strain measurement system.

5.1.2. Scheme of Similar Materials

The physical and mechanical parameters of similar materials were calculated according to the physical and mechanical properties and strength similarity ratio of each rock layer in the geological column chart.

The calculation method is:

$$[R_C]_m = \alpha_R \cdot [R_C]_P;\ [R_t]_m = \alpha_R \cdot [R_t]_P$$

According to the calculated physical and mechanical parameters of similar materials, the material that is close to them is found in the ratio table as similar material to this rock

formation. At the same time, similar materials are established according to the determined proportion, and a strength test is conducted for strength verification [35,36].

The proportioning experiment is the basis of similar material simulation, which needs to be repeated. Because of the different sources of raw materials, there are differences in performance, and the actual strength of the selected similar materials may be different from the value in the ratio table. If there is any error, it is necessary to adjust the ratio of material composition to ensure that similar materials meet the requirements of mechanical similarity.

The similar materials selected for the model mainly include river sand, gypsum, white powder, etc. Mica powder is evenly sprinkled as the weak surface of the layer during the laying of the model. The proportion of each rock stratum is determined according to the similarity theory and strength test results.

The specific matching scheme of similar materials is shown in Table 2.

Table 2. Proportioning scheme of similar materials at 1:120.

Number	Lithology	Thickness	Buried Depth	Model Thickness	Paving Thickness	Material Number	Material/kg			
							Total Weight	River Sand	Gypsum	White Powder
16	mudstone	13.5	460.85	11.25	1.5 (7)/0.5	846	108.00	86.40	8.64	12.96
15	Fine sandstone	10.2	471.05	8.5	1.5 (5)	746	81.60	57.12	9.79	14.69
14	Sandy mudstone	11.75	482.8	9.79	1.5 (6)	855	93.98	75.19	9.40	9.40
13	Medium grained sandstone	53.1	535.9	44.25	1.5 (29)	937	424.80	382.32	12.74	29.74
12	mudstone	16.7	552.6	13.91	1.5 (9)	846	133.54	106.83	10.68	16.02
11	Fine sandstone	6.2	558.8	5.16	1.6 (3)	746	49.54	34.68	5.94	8.92
10	Siltstone	4.2	563	3.5	1.6 (2)	828	33.60	26.88	1.34	5.38
9	Fine sandstone	8	571	6.67	1.5 (4)	746	64.03	44.82	7.68	11.53
8	mudstone	10.5	581.5	8.75	1.6 (5)	846	84.00	67.20	6.72	10.08
7	Fine sandstone	4.4	585.9	3.67	1.6 (2)	746	35.23	24.66	4.23	6.34
6	Siltstone	2.3	588.2	1.9	1.9 (1)	828	18.24	14.59	0.73	2.92
5	Fine sandstone	7.2	595.4	6	1.4 (4)	737	57.60	40.32	5.18	12.10
4	Siltstone	16.8	612.2	14	1.5 (9)	828	134.40	107.52	5.38	21.50
3	Fine sandstone	2.7	614.9	2.25	1.0 (2)	746	21.60	15.12	2.59	3.89
2	coal seam	4.7	619.6	3.9	1.5 (2)/0.5	20:1:5	37.44	28.80	1.44	7.20
1	Carbonaceous mudstone	2.4	622	2	2	846	19.20	15.36	1.54	2.30

Remarks: (1) The density of river sand is 1.6 g/cm^3, and the density of coal is 1.5 g/cm^3;.

5.1.3. Experimental Process

1. A physical simulation experiment simulated the overlying strata thickness of the coal seam (175 m), the total depth of the coal seam (622 m), and the remaining 447 m. After stress conversion, the uniform applied force was loaded at the top of the model through the top loading device. The loading system was divided into: a cylinder loading system, a tilt adjustment system, a hydraulic control system and an intelligent operating system.
2. Considering the influence of the model boundary effect, a boundary protection coal pillar of at least 25 cm was set on the left and right sides of the model.
3. The excavation was carried out from the left side of the model to the right side, with each excavation of 2 cm and the length of the model being 250 cm (with the actual working face length being 300 m).

4. After the excavation was completed, we analyzed the monitoring data.

5.2. Analysis of Failure Characteristics of Mining Overburden

Five typical stages in the excavation process of similar model were selected to analyze the failure characteristics of mining overburden, as shown in Figure 9.

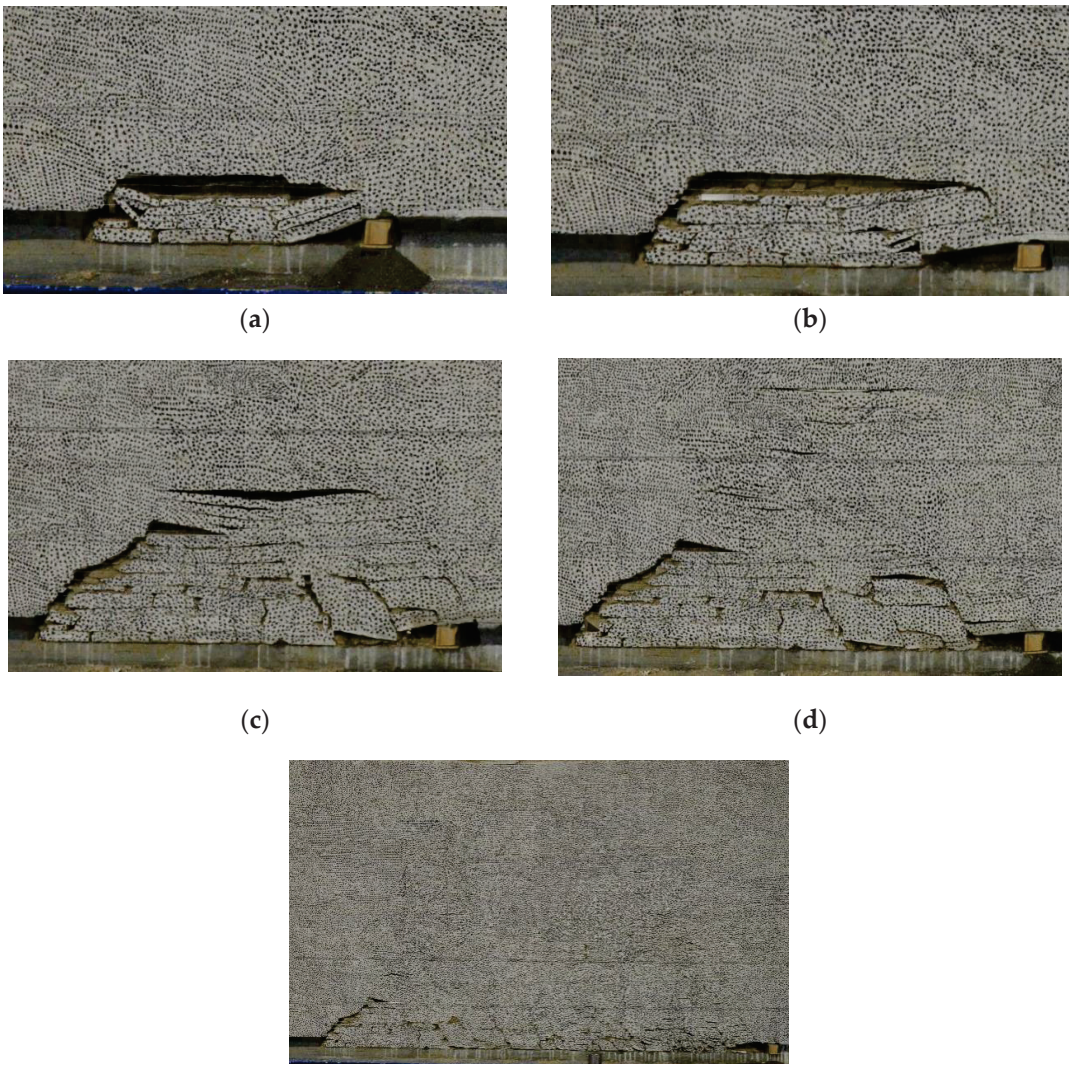

Figure 9. Excavation process of similar model. (**a**) Large area collapse of direct roof; (**b**) first periodic pressure; (**c**) the second periodic pressure; (**d**) the third periodic pressure; (**e**) mining is completed.

It can be seen from the figure that the failure characteristics of mining overburden are as follows:

1. When the working face advances 30 cm (36.0 m), the basic roof collapses in a large area, and the collapsed rock mass does not form a regular hinged structure, which is the first weighting of the basic roof. The caving height is 12.6 cm (10.5 m), the fracture zone height is 19 cm (22.8 m), the first weighting step is 36.0 m, the caving angle at the main roof cut is 65, and the caving angle at the coal wall is 55.
2. When the working face advances 46 cm (55.2 m), the basic roof collapses for the first time, with a caving step of 16 cm (19.2 m), a caving height of 11.4 cm (13.66 m), and a maximum separation distance of 2.6 cm (3.12 m). Micro-cracks appear in the upper strata, and obvious articulated structures are formed in the roof strata.

3. When the working face advances 62 cm (74.4 m), the basic roof collapses in the second cycle, with a caving step of 16 cm (19.2 m), a caving height of 16.5 cm (19.8 m) and a maximum separation distance of 2.6 cm (3.12 m).
4. When the working face is pushed 80 cm, it basically collapses in the third cycle, with the caving step distance of 18 cm (21.6 m) and the maximum caving height of 15.83 cm (19.0 m), and the maximum caving position is located obliquely above the working face. As the working face keeps pushing the rock strata to move, some separation layers close again, and the caving height is basically stable at 15 cm (18.0 m).
5. As the working face continues to advance, the overlying strata in the mining face are more clearly divided, and the rock mass under the fracture zone is highly broken and articulated, which has the basic conditions for slurry filling.

5.3. Analysis of Roof Displacement and Bulking Coefficient Characteristics

According to the above analysis, with the continuous advancement of the working face, the rock stratum moves continuously, and some separated layers are re closed, and the caving height is basically stable at 15 cm (18.0 m). The siltstone with a thickness of 16.8 m at 18.0 m above the coal seam is taken as the monitoring object. When the working face is mined to 88 cm, 108 cm, 132 cm, 156 cm, 180 cm, 216 cm and 240 cm, respectively, the corresponding subsidence curves of roof rock are shown in Figure 10, and the bulking coefficient curves are shown in Figure 11.

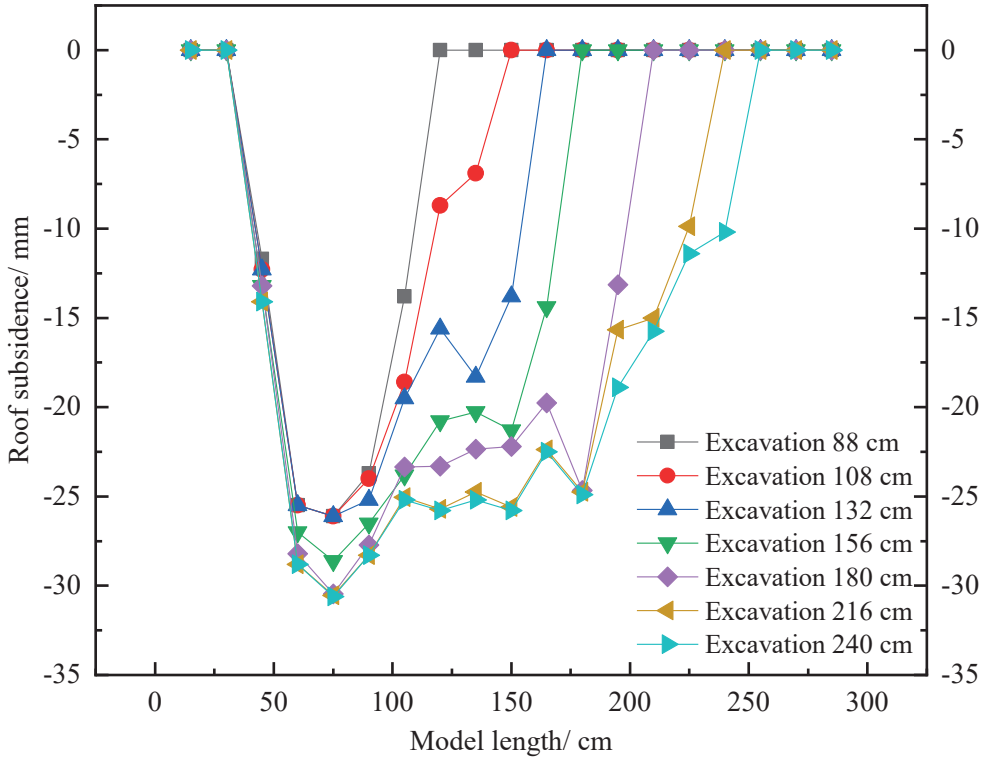

Figure 10. Displacement curve of coal seam roof.

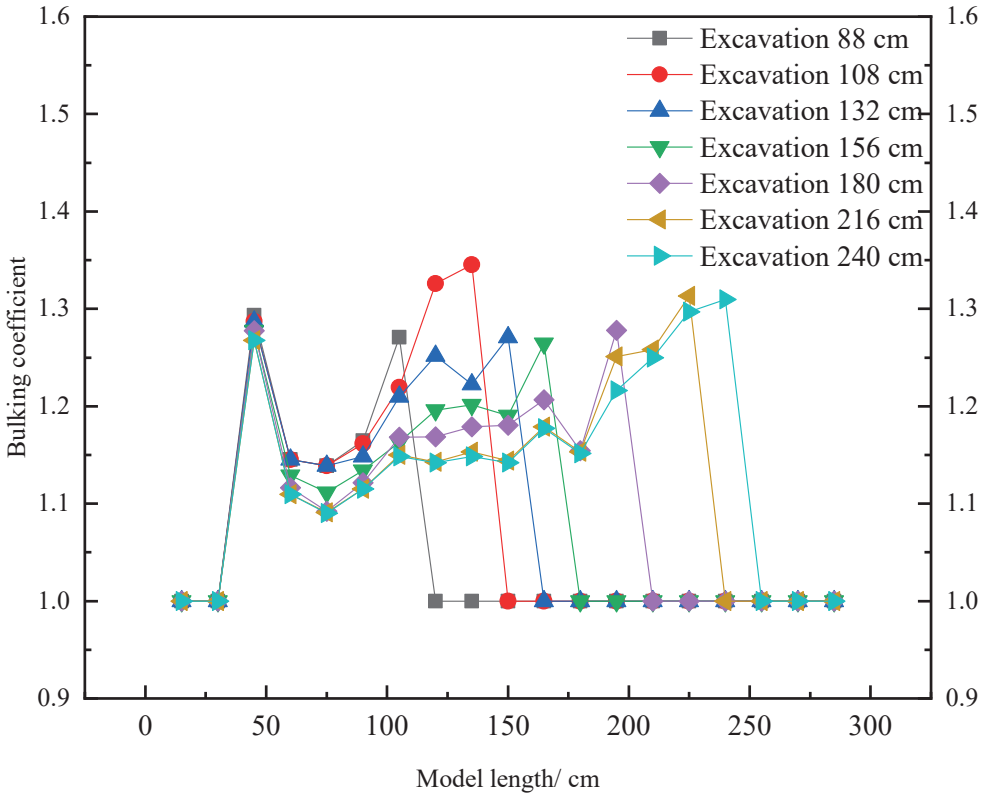

Figure 11. Bulking coefficient of different excavation times.

It can be seen from the figure that, according to the test data of the crushing bulking coefficient of different excavation times, it can be found that with the evolution of the spatial structure of the overlying strata in the goaf, the three zones of the caving zone show dynamic changes, and the natural accumulation zone moves forward periodically with the advancing of the working face. Because of the differential compaction degree of the goaf, the gangue forms three transverse zones in the caving zone space of the goaf, which can be divided into the natural accumulation zone, the load-affected zone and the gradually compacted zone according to the distance from the working face.

According to the distribution law of the crushing bulking coefficient, the natural accumulation area is distributed near the mining face, and its length is about one weighting step, with the largest crushing bulking coefficient. The load area is located behind the natural accumulation area, which changes with the evolution of the large spatial structure, and its length is about two to three weighting steps. The gradually compacted area is located behind the load-affected area, and in the gradually compacted area, the bulking coefficient decreases with the distance from the working face.

6. Strike Zoning of Goaf and Optimization Effect of Lag Distance

6.1. Goaf Strike Zoning Based on Bulking Coefficient

The caving zone of goaf is the key area of slurry filling research, and the space between rocks in this area is large, which can be used as then slurry filling space. By analyzing the results of numerical simulation and similar simulation tests, the division of the working face in the strike direction is obtained, as shown in Figure 12.

Among them, Area I (natural accumulation area) is 0~20 m behind the working face, Area II (load-affected area) is 20~70 m behind the working face, and Area III (gradual compaction area) is 70 m behind the working face. According to the previous analysis results, the bulking coefficient in area I and area II is about 1.25~1.4, and it gradually decreases after entering area III.

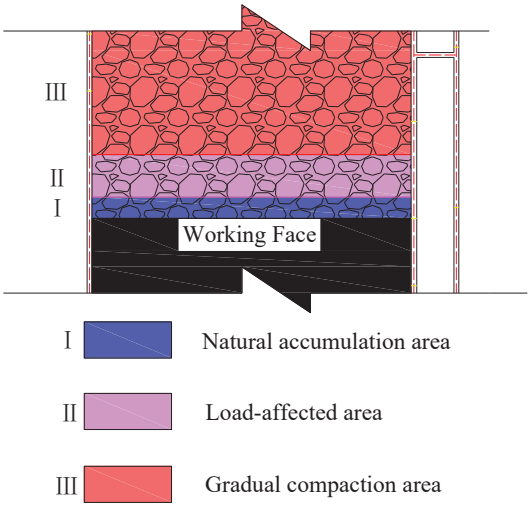

Figure 12. Zoning of slurry filling space in strike direction.

6.2. Lag Distance Optimization Effect

According to the distribution law of the bulking coefficient, the grouting difficulty in Area I (natural accumulation area) is the lowest, but it is only 0~20 m away from the working face. According to the previous construction experience, it is easy for slurry to overflow to the working face. Therefore, in order to ensure the single-hole filling amount of adjacent grouting holes and reduce the amount of drilling construction, grouting should be started when adjacent grouting holes are located in area II as far as possible, and the void space in goaf should be fully utilized. Therefore, a lag distance of 40 m was determined at first, and the field application was carried out according to this parameter. However, the slurry overflowed during the filling process, and continuous grouting could not be realized.

Therefore, according to the lag distance optimization method, we increased the lag distance to 60 m, and then carried out field application. There was no slurry overflow in the filling process, and the flow rate in the filling process was stable. The overall effect of adjacent grouting filling is good, as shown in Figure 13.

(**a**) (**b**) (**c**)

Figure 13. Adjacent grouting filling site. (**a**) Underground filling station; (**b**) filling pipeline pressure; (**c**) filling drilling hole.

7. Conclusions

1. This paper systematically examines various gangue filling technologies and their development history, and expounds the technical background and scientific connotations of slurry filling. The definition of the lag distance of slurry filling and the importance of reasonably determining this parameter for ensuring the filling effect are clarified, and the determination method of the lag distance of gangue slurry based on the dilapidation of goaf is established.

2. After the coal seam is mined out, the roof subsidence gradually decreases from bottom to top, and finally becomes stable. Because the roof rock stratum collapses, and the overburden movement gradually weakens in the process of upward transmission, there will be separation layers and gaps between rock strata and between rock blocks, and the bulking coefficient of rock strata will lead to the continuous reduction in the subsidence of the upper rock strata.
3. The distribution law of the crushing bulking coefficient is in the advancing direction of the working face. With the increase in the distance from the working face, the bulking coefficient decreases continuously, and presents certain zoning characteristics, especially in the range of 0~6.7 m in the height direction. It can be divided into three areas, namely the natural accumulation area, the load-affected area and the gradual compaction area.
4. Based on the comprehensive numerical simulation and similar simulation results, the natural accumulation area is 0~20 m behind the working face, the load-affected area is 20~70 m behind the working face, and the gradual compaction area is 70 m behind the working face. Combined with the field application, the lagging distance is determined to be 60 m, and the grouting and filling effect at the adjacent site is good.

Author Contributions: Conceptualization, W.G. and K.G.; Methodology, T.S.; Software, F.Q.; Validation, W.G. and K.G.; Formal analysis, T.S.; Investigation, W.L. and P.X.; Resources, W.L.; Data curation, W.L.; Writing—original draft preparation, T.S.; Writing—review and editing, T.S.; Visualization, physical similarity simulation experiment, W.G. and K.G. All authors have read and agreed to the published version of the manuscript.

Funding: This research was funded by the National Natural Science Foundation of China (No. 52174127, 51974226), the Key Research and Development Program of Shaanxi (No. 2023-YBGY-318), the Youth Innovation Team of Shaanxi University, the Research Fund of Henan Key Laboratory for Green and Efficient Mining & Comprehensive Utilization of Mineral Resources (Henan Polytechnic University, No. KCF202001) and the Research Fund of Shaanxi Key Laboratory of Coal Mine Water Disaster Prevention and Control Technology (No. 2020SKMS02).

Data Availability Statement: Relevant data are listed in the paper.

Conflicts of Interest: The authors declare no conflict of interest.

References

1. Zhang, J.; Ju, Y.; Zhang, Q.; Ju, F.; Xiao, X.; Zhang, W.; Zhou, N.; Li, M. Low ecological environment damage technology and method in coal mines. *J. Min. Strata Contr. Eng.* **2019**, *1*, 13515.
2. Fan, Y.; Lu, Z.; Cheng, J.; Zhou, Z. Major ecological and environmental problems and the ecological reconstruction technologies of the coal mining areas in China. *Acta Ecol. Sin.* **2003**, *23*, 2144–2152.
3. He, Y.; Ye, X.; Wang, Z. Consideration on the 13th Five Year Plan of Coal Industry. *Coal Econ. Res.* **2015**, *35*, 6–8.
4. SONG, T. *Study on Geochemical Characteristics and Heavy Metal Element Migration of Coal Gangue Backfilling Material*; China University of Mining and Technology: Beijing, China, 2019.
5. Song, T.; Huang, Y.; Zhang, J.; Li, J. Numerical simulation on migration effects of heavy metal elements in coal gangue backfilling body caused by the lithology of coal seam floor. *J. China Coal Soc.* **2018**, *43*, 1983–1989.
6. Yang, D.L.; Li, J.M.; Huang, Y.L.; Gao, H.; Qiao, M. Research on Migration Law of Mn in Mudstone Floor in the Goaf under Coupling Conditions of Seepage and Stress. *Pol. J. Environ. Stud.* **2019**, *29*, 939–950. [CrossRef]
7. Zhu, L.; Song, T.; Gu, W. Research and Application on Pipeline Backfill Technology of SlurryComprsing Coal-based Solid Waste. *Coal Technol.* **2021**, *40*, 47–51.
8. Cun, Z.; Bo, L.; Ziyu, S. Breakage mechanism and pore evolution characteristics of gangue materials under compression. *Acta Geotech.* **2022**, *17*, 4823–4835. [CrossRef]
9. Zhang, C.; Zhao, Y.; Bai, Q. 3D DEM method for compaction and breakage characteristics simulation of broken rock mass in goaf. *Acta Geotech.* **2022**, *17*, 2765–2781. [CrossRef]
10. Hao, L.; Zhang, B.; Bai, H.; Wu, J.; Meng, Q.; Ning, X. Surface Water Resource Protection in a Mining Process under Varying Strata Thickness—A Case Study of Buliangou Coal Mine, China. *Sustainability* **2018**, *10*, 4634.
11. Teng, H.; Xu, J.; Xuan, D.; Wang, B. Surface subsidence characteristics of grout injection into overburden: Case study of Yuandian No. 2 coalmine, China. *Environ. Earth Sci.* **2016**, *75*, 530. [CrossRef]

12. Xuan, D.; Xu, J. Longwall surface subsidence control by technology of isolated overburden grout injection. *Int. J. Min. Sci. Technol.* **2017**, *27*, 813–818. [CrossRef]
13. Zhu, L.; Xu, J.; Ju, J.; Zhu, W.; Xu, J. The effects of the rotational speed of voussoir beam structures formed by key strata on the ground pressure of stopes. *Int. J. Rock Mech. Min.* **2018**, *108*, 67–79.
14. Wang, Y. Three-dimensional spatial dynamic distribution model on porosity and permeability characteristics of porous media in goaf. *J. Safety Sci. Technol.* **2020**, *16*, 40–46.
15. Wang, S.; Wang, D.; Cao, K.; Pi, Z. Distribution law of 3D fracture field of goaf and overlying strata. *J. Cent. South. Univ.* **2014**, *45*, 833–839.
16. Wojtecki, U.; Goda, I.; Mendecki, M.J. The influence of distant coal seam edges on seismic hazard during longwall mining. *J. Seismol.* **2021**, *25*, 283–299. [CrossRef]
17. Deng, Q.W.; Liu, X.H.; Lu, C.; Lin, Q.Z.; Yu, M.G. Numerical Simulation of Spontaneous Oxidation Zone Distribution in Goaf under Gas Stereo Drainage. *Procedia Eng.* **2013**, *52*, 72–78. [CrossRef]
18. Zhang, C.; Bai, Q.; Zhu, C. A methodology for determining the size distribution of broken rock masses in longwall mining goaf. *Geomech. Geophys. Geo.* **2022**, *8*, 1–14. [CrossRef]
19. Liang, B.; Wang, B.; Jiang, L.; Li, G.; Li, C. Broken expand properties of caving rock in shallow buried goaf. *J. China Univ. Min. Technol.* **2016**, *45*, 475–482.
20. Jiao, Y.; Zhu, J.; Geng, Y.; Liang, Q.; Sun, X. Study on 3D distribution of porosity of overburden"horizontal three-zones"in goaf. *Saf. Coal Mines* **2021**, *52*, 159–165.
21. Sun, J. Effect of Mining Pore Thickness in Longwall Goaf. *Saf. Coal Mines* **2019**, *50*, 49–53.
22. Zheng, D.F.; Wang, B.D. Evaluation method for regulation and storage capacity of underground reservoir. *J. Hydraul. Eng.* **2004**, *35*, 56–62.
23. Wang, B.F.; Liang, B.; Wang, J.G.; Sun, K.; Sun, W.; Chi, H. Experiment study on rock bulking of coal mine underground reservoir. *Rock Soil Mech.* **2018**, *39*, 4086–4092.
24. Zhang, C.; Jia, S.; Bai, Q.; Zhang, H.; Chen, Y.; Jiao, Y. CFD-DEM Coupled Simulation of Broken Rock Mass Movement During Water Seepage in an Underground Goaf Reservoir. *Mine Water Environ.* **2021**, *40*, 1048–1060. [CrossRef]
25. Liu, Y.; Shi, G.; Zhang, G.; Li, Z.; Song, X. Study on effect of working face length on overburden caving form and force chain arch characteristics. *Saf. Coal Mines* **2021**, *52*, 242–249.
26. Pang, Y.; Li, Q.; Cao, G.; Zhou, B. Analysis and calculation method of underground reservoir water storage space composition. *J. China Coal Soc.* **2019**, *44*, 557–566.
27. Bai, D.Y.; Ju, J.F.; Xu, J.L.; Li, J. Stability analysis of mine underground reservoir artificial dam in Lijiahao Mine. *J. China Coal Soc.* **2017**, *42*, 1839–1845.
28. Xia, X.; Huang, Q. Study on the dynamic height of caved zone based on porosity. *J. Min. Saf. Eng.* **2014**, *31*, 102–107.
29. Xu, J. Research and progress of coal mine green mining in 20 years. *Coal. Sci. Technol.* **2020**, *48*, 1–15.
30. Yang, S.; Bai, Y.; Li, J. Comprehensive analysis onpresent status of mine backfill mining and prospects. *Coal Eng.* **2013**, *45*, 4–6.
31. Zhu, L.; Pan, H.; Gu, W.; Zhao, M.; Zhang, X.; Xu, K. Experimental study on flow and diffusion law of gangue filling slurryin caving zone. *J. China Coal Soc.* **2021**, *46*, 629–638.
32. Zhu, W.; Xu, J.; Lai, W.; Wang, Z. Research of isolated section-grouting technology for overburden bed separation space to reduce subsidence. *J. China Coal Soc.* **2007**, 458–462.
33. Zhou, H.; Hou, C.; Sun, X. Solid Waste Paste Filling for None-Village-Relocation Coal Mining. *J. China Univ. Min. Technol.* **2004**, *05*, 30–34+53.
34. Yan, L. Study on mine pressure with similar physical model. *Min. Saf. Environ. Prot.* **2009**, *36*, 20–22+34+91.
35. Lin, Y. *Experimental Rock Mechanics—Simulation Study*; Coal Industry Press: Beijing, China, 1984.
36. Hai-Feng, L.; Kai, Z.; Jin-Long, Y.; Wnga, A. A study on the optimal selection of similar materials for the physical simulation experiment based on rock mineral components. *Eng. Fail. Anal.* **2022**, *140*, 106607. [CrossRef]

sustainability

MDPI

Article

Mechanical Properties and Damage Characteristics of Coal-Based Solid Waste Paste Filling Materials with Different Moisture Content

Meng Wang [1,2], Xiang He [2,3,*] and Ke Yang [1,2,3]

[1] School of Mining Engineering, Anhui University of Science and Technology, Huainan 232001, China
[2] Institute of Energy, Hefei Comprehensive National Science Center, Hefei 230031, China
[3] State Key Laboratory of Mining Response and Disaster Prevention and Control in Deep Coal Mine, Anhui University of Science and Technology, Huainan 232001, China
* Correspondence: xianghe_cumtb@126.com

Abstract: It has been proven that it is a feasible treatment method to prepare paste filling material from coal-based solid waste to fill underground goaf. Based on the complexity of the goaf environment, especially the influence of humidity on paste filling materials, this paper prepared paste filling materials with a mass concentration of 80% by using coal gangue and fly ash, and carried out a uniaxial compression test of coal-based solid waste paste filling materials under four different water-bearing states. The experimental results show that: (1) The binary primary equation fits well the variation trend of paste filling strength with water content. With the increase of moisture content, the compressive strength of paste filling material gradually decreases, and the higher the moisture content, the more obvious the influence on the strength of paste filling. (2) The damage evolution equation and constitutive equation of paste filling materials with different moisture content were established. With the increase of strain, the influence of moisture content on the damage of paste filling material decreases gradually, and the moisture content can promote the damage development of paste filling material to a certain extent. (3) The influence mechanism of moisture content on coal based-solid waste paste filling material is discussed from the three aspects of physical effect, structural effect and chemical effect, which provides a direction for further research on the influence mechanism of moisture content on filling strength. The research on the failure mechanism of coal-based solid waste paste filling and the safety production of the mine can be used as a theoretical support.

Keywords: coal-based solid waste; paste filling; moisture content; stress-strain curve; characteristics of damage; mechanism of failure

1. Introduction

The accumulation of solid wastes such as coal gangue and fly ash generated by coal mining on the ground not only occupies a large amount of land surface but also seriously pollutes the ecological environment [1,2]. It is a feasible method to backfill underground under the premise of ensuring no pollution of solid waste [3]. Since the 21st century, with the increasing problem of "three under" coal pressure and the continuous proposal of national environmental protection policies, solid filling [4,5], paste filling [6,7], separation grouting [8,9] and other technologies have become the trend of green mining in coal mines. Using coal-based solid wastes to prepare paste filling materials for paste filling mining has become an important development direction of "green mine" construction [10–12]. However, due to the depletion of shallow coal resources, coal mining began to move deeper. The complex geological conditions of deep coal mining and the great changes in goaf humidity and temperature have become the restricting factors for paste filling mining [13]. There have been many studies on multi-field coupling such as rock mass [14,15], and paste filling materials are also subject to multi-field interaction in goaf. Therefore, the effect of

humidity on the strength and damage of the paste filling in goaf was of great significance to study.

Under laboratory conditions, the transportation and emergency stop of backfill mixture prepared based on water soluble ore-concentrated waste under different water solid ratios were simulated [16]. References [17–19] carried out uniaxial compression tests of cemented tailings filling under different curing ages, loading rates and mixed aggregates, analyzed pre-peak and post-peak damage and energy consumption characteristics of cemented tailings filling under different curing ages, loading rates and mixed aggregates, and expounded its evolution process. References [20–22] carried out uniaxial compression tests for gangue cemented filling with different sizes, early load and width-to-height ratio, analyzed the impact of size effect, early load and width-to-height ratio on filling strength, acoustic emission characteristics, resistivity and damage, and characterized the damage evolution process of filling based on the changes of acoustic emission ringing number and resistivity. Reference [23] used five kinds of coal-based solid wastes, such as coal gangue, fly ash, desulfurized gypsum, furnace bottom slag and gasification slag to prepare filling materials, carried out research on the strength and acoustic emission characteristics of filling specimens in different phases, and revealed the evolution law of filling strength based on the microstructure of specimens. Reference [24], based on acoustic emission, studied the damage mechanical characteristics and cooperative deformation mechanism of tailings cemented filling and different lime sand ratio combinations under uniaxial compression. Based on the statistical damage theory, strain equivalent hypothesis and maximum tensile stress criterion, reference [25] introduced the damage constitutive model of cemented tailing filling under uniaxial compression, and established the damage constitutive model modified by compaction process. Reference [26] studied the influence of curing temperature on shear failure of the cementing surface between filling and surrounding rock, and analyzed the internal mechanism of the influence of curing temperature on mechanical properties of the cementing surface between filling and surrounding rock. Based on DIC technology, reference [27] obtained the main strain nebulae of filling specimen when it was damaged, and analyzed the snatch characteristics and damage failure characteristics of tailings filling with different particle size distributions. Reference [28] analyzed the strength evolution mechanism of tailings filling under different curing pressures by binarization treatment of electron microscope scanning images and application of fractal theory. In terms of the influence of humidity on filling in complex geological environment, reference [29] carried out uniaxial compressive tests of full tailings cemented filling with different water content, and analyzed the relationship between its strength and damage with water content. Reference [30] studied the mechanical properties of cemented filling under different water saturations, and built the damage constitutive model of cemented filling under different water saturations based on Lemaitre strain equivalence principle and Weibull distribution. Reference [31] carried out uniaxial compression tests for two kinds of tailings paste filling materials with different cement contents, and analyzed the influence law of water content on the strength, elastic modulus and peak strain point of the filling materials. Reference [32] carried out triaxial creep tests of gangue cemented filling materials under different moisture content, analyzed the influence of moisture content on the creep rate, long-term deformation and strength of the filling body, and established a fractional creep model to describe the whole creep process.

To sum up, although many researchers have studied the strength and damage of paste filling, the research on the damage mechanism of coal-based solid waste paste filling caused by moisture content is still not perfect. Based on this, the paper takes coal gangue as aggregate, fly ash and cement as cementitious materials, prepares paste filling specimens with a concentration of 80%, carries out research on the strength characteristics of paste filling under different water content, establishes a damage constitutive model based on water content, and the influence mechanism of water content on filling body strength and failure form is further discussed from the physical, structural and chemical perspectives.

This study provides a theoretical reference for further discussing the damage mechanism of water content to coal-based solid waste paste filling and the safety production of the mine.

2. Experimental Methods

2.1. Physical and Chemical Property Analysis

The cement was ordinary Portland cement, the fly ash was Grade II fly ash from Yuanyanghu Power Plant in Ningdong Coal Power Base, and the coal gangue was from Renjiazhuang Coal Mine of Ningxia Coal Industry Co., Ltd. of National Energy Group, Ningxia Autonomous Region, China. SEM and XRD analysis can be used to analyze the existence of new formations and the presence of strong bonds in the new composite materials formed [33]. FlexSEM 1000 (Hitachi, Tokyo, Japan) and SmartLab SE (Rigaku, Tokyo, Japan) instruments were used for SEM and XRD analysis, respectively. The scanning speed of XRD is 4°/min, the range is 5~70°, and the continuous scanning mode is adopted. Physical and chemical properties of coal gangue and fly ash are shown in Figure 1.

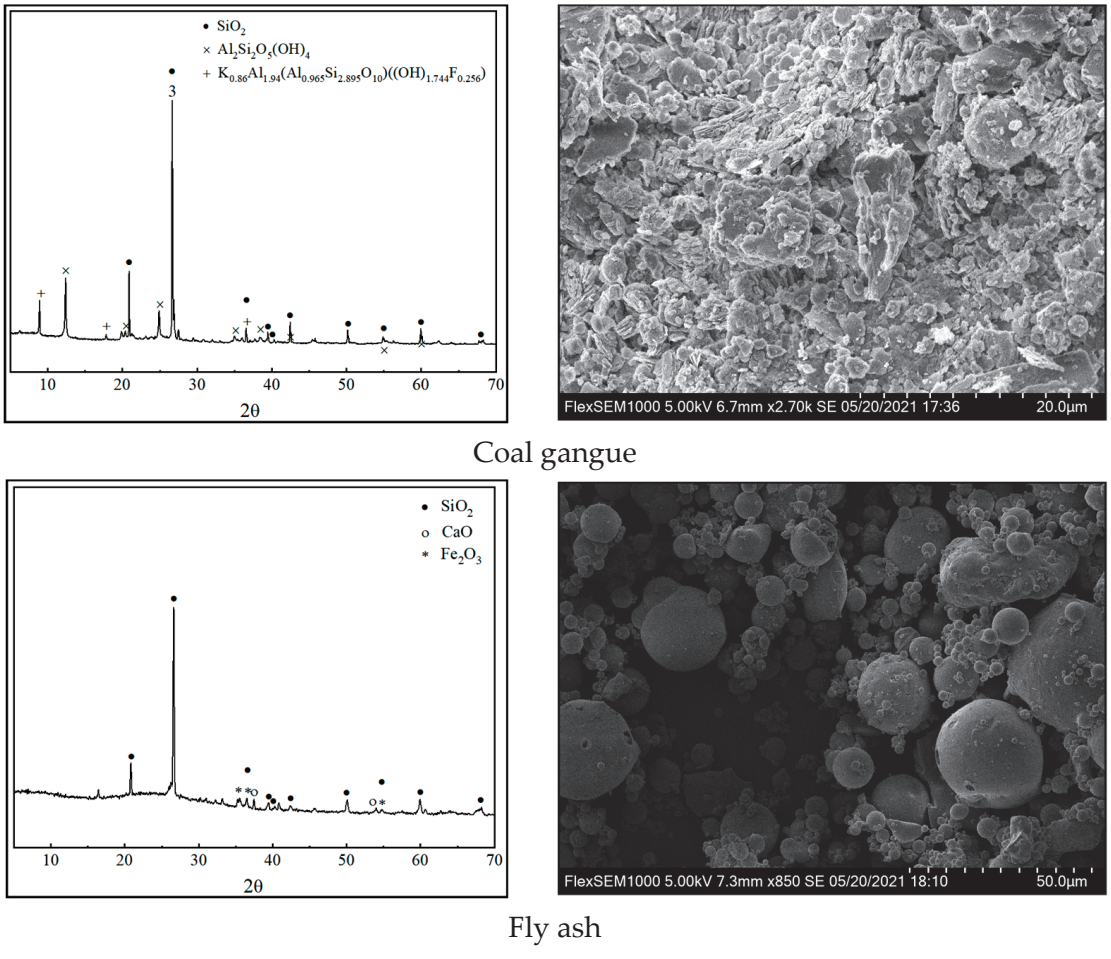

Figure 1. SEM and XRD analysis of coal gangue and fly ash.

Coal gangue comes from solid waste discharged during coal mining or coal washing. It is a black gray rock with lower carbon content and harder than coal in the process of coal forming. According to SEM and XRD in Figure 1, the micro morphology of coal gangue is irregular, such as block or sheet, which is not easy to flow on the static plane. The largest diffraction peak appears in the diffraction pattern of coal gangue samples between 20°~30°, indicating that the crystalline mineral composition in coal gangue is mainly SiO_2, and the content of other crystalline minerals such as CaO and Fe_2O_3 is less.

Fly ash is formed by the absorption and cooling of the heating surface of pulverized coal during suspension combustion in a furnace at 1300~1500 °C and its particle size is

generally between 1~100 μm. According to SEM and XRD in Figure 1, the microstructure of fly ash is relatively regular, showing spherical particles of different sizes, which increases the migration and flow of fly ash and is convenient to pass through the pores between large particles. The largest diffraction peak appears in the diffraction pattern of fly ash samples between 20°~30°, indicating that the crystalline mineral composition in fly ash is mainly SiO_2, and the content of other crystalline minerals is less.

2.2. Preparation of Filling Specimen

By changing the ratio and mass concentration, the activation characteristics of the composite can be conditioned, and then the strength characteristics of the backfill can be affected [34]. Coal-based solid waste was used to prepare paste filling materials, and coal gangue was selected as aggregate, fly ash and cement as cementing materials. Ordinary Portland cement is used as the cement, which has fast hydration reaction and high early and late strength. Paste filling specimens with a mass concentration of 80% were prepared according to the ratio of coal gangue: fly ash:cement:water = 5:2:1:2 [35,36]. The coal gangue was crushed and screened (particle size was 0~15 mm). During preparation, add coal gangue, fly ash and cement in the mixing tank according to the set proportion, and stir them fully, so that the coal gangue, fly ash and cement are fully mixed. After complete mixing, add a set proportion of water into the mixing tank and stir thoroughly for 15 min. Then poured into a cylindrical abrasive with a diameter of 50 mm and a height of 100 mm, demoulded 24 h later, and then immediately placed in an HBY-60B standard constant temperature and humidity curing box for 28 d, curing humidity was 95%, curing temperature was 20 ± 1 °C. A total of 12 paste specimens were prepared. Each moisture content was tested three times, and the average value of the three results was used as the experimental value to ensure the accuracy of the experimental results. The sample preparation process was shown in Figure 2.

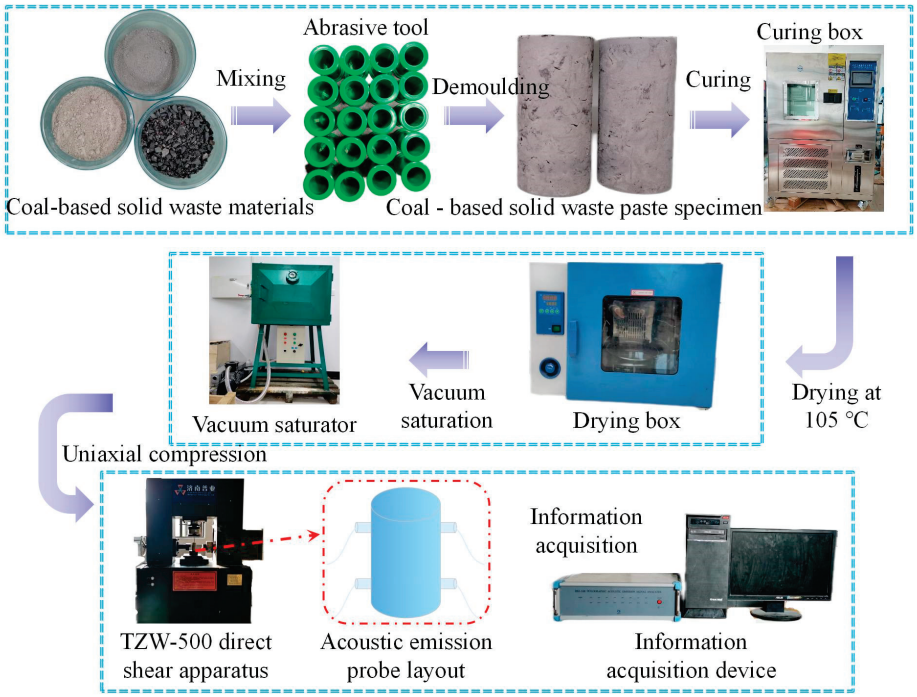

Figure 2. Experimental setup and procedure.

The curing filling specimen was put into the drying box, dried at 105 °C for 24 h, and weighed and recorded. Then, the dried filling specimens were divided into four groups: A, B, C, and D. Group A was the dried specimen, and group B, C, and D were saturated with water for 1 h, 2 h, and 4 h, respectively (the water content did not change and the filling

reached the state of full water). After saturation, each group of test pieces were weighed and recorded. Each group prepared 3 filling body test pieces. The average water content of 4 groups of filling body test pieces was shown in Table 1. The moisture content of different filling body specimens can be calculated with the following equation:

$$\omega_c = \frac{m_c - m_d}{m_d} \times 100\% \quad (1)$$

where: ω_c was the water content of the filling body, %; m_c was the mass of filling body after different saturation degrees, g; m_d was the mass of the filled body after drying, g.

Table 1. Average moisture content of the four groups of coal-based solid waste paste filling.

Classification	Group A	Group B	Group C	Group D
Before saturation	312.56 g	304.73 g	305.41 g	302.81 g
After saturation	-	332.03 g	367.00 g	377.70 g
Moisture content	0	8.96%	20.17%	24.73%
Uniaxial compressive strength	2.999 MPa	2.521 MPa	0.903 MPa	0.545 MPa

2.3. Experimental Instruments and Procedures

The test system consists of loading equipment and acoustic emission monitoring equipment. The loading equipment adopted a TZW-500 microcomputer controlled electro-hydraulic servo rock direct shear apparatus. Its normal load was 0~300 kN, the normal overload protection was 2% of the overload, the normal working stroke was 0~100 mm, and the loading mode was two-way electro-hydraulic servo coincidence loading, fully automatic closed-loop control. The test system was shown in Figure 2.

After the specimen reached the curing age, the loading test was started. The test conditions and steps were carried out in accordance with the Standard for Test Methods of Mechanical Properties of Ordinary Concrete (GB/T500801-2002). The stress loading mode was used to slowly load to 0.1 kN, and then the displacement loading mode was used to load until the specimen was damaged. The loading rate was 0.05 mm/min. Four acoustic emission sensors were arranged at an interval of 90° from top to bottom on the sample surface of the filling body, the sampling frequency is 2.5 MHz, and the threshold value of acoustic emission signal acquisition was 40 dB. During the loading process, load and deformation parameters were recorded and collected.

3. Experimental Results and Analysis

3.1. Influence of Water Content on the Strength of Paste Filling

Uniaxial compressive strength was an important parameter to measure the quality of filling. Figure 3 shows the stress-strain curves of four different water content fillings during uniaxial compression.

As can be seen from Figure 3, with the increase of water content, the compressive strength of filling specimen gradually decreases. The strength of filling specimens 1 h, 2 h and 3 h with saturated water decreased by 15.97%, 69.90% and 81.83%, respectively, compared with that of dry specimens. The stress-strain curves of filling with different water contents were divided into compaction stage (I), elastic deformation stage (II), plastic deformation stage (III) and post-peak failure stage (IV). With the increase of water content, filling specimens gradually changed from brittleness to ductility.

In the compaction stage (I), the filling body in the dry state and the filling body in different water-containing states show similar stress-strain phenomena, and the stress-strain curves were basically coincident, which indicates that the filling body has experienced the same structural change in this stage, because there were many large "closed" pore structures in it, which prevent the invasion of water. These "closed" pores were almost not affected by the water-containing state when they were closed under pressure, it shows that the filling sample was not affected by moisture during compaction.

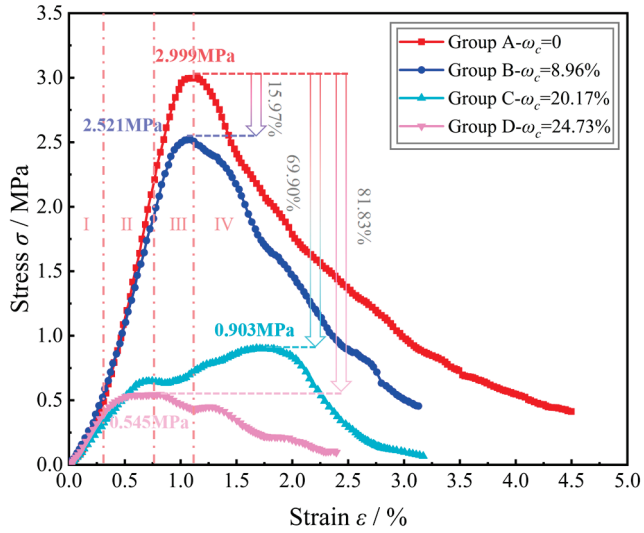

Figure 3. Stress-strain curves of filling body of coal-based solid waste paste with different moisture content.

In the elastic deformation stage (II), the curves of the filling body samples in the dry state and saturated for 1 h were basically consistent, indicating that the difference between their elastic moduli was small. However, with the increase of saturated time, the slope of the curve gradually decreases, and the elastic modulus decreases, indicating that the elastic modulus generally decreases with the increase of water content.

In the plastic deformation stage (III), the internal "closed" pores of the filling body specimen were further compressed and damaged, and the water gradually invades. It shows that the larger the water content was, the stronger the water invasion to the damaged pores was. It shows on the stress-strain curve that the filling body begins to change from brittleness to ductility with the increase of the water content.

In the post-peak failure stage (IV), after the filling body reaches the peak stress, its internal pores and fractures continue to expand, connect, and fuse, accompanied by the generation of new fractures, which ultimately leads to the failure of the filling body.

In the dry state, the stress-strain curve was smooth before and after the peak, no significant sudden drop was observed, and its elastic modulus was large. When the water content increased to 8.96%, there was no obvious fluctuation in the curve before the peak, and there were three irregular inflection points in the curve after the peak, indicating that the internal cracks of the filling body in this state continue to develop and connect after the peak, and large macro cracks were produced. When the water content was 20.17%, an inflection point appeared in the middle section of the curve before the peak, indicating that the original internal structure has been partially destroyed; new cracks appeared and recompacted, which showed that the stress-strain curve rises after the inflection point until the peak stress was reached. When the water content reached 24.73%, there were several irregular inflection points in the back-peak curve, indicating that the internal structure had multiple cracks developing and connecting, and producing macroscopic cracks. It can be inferred that the higher the water content, the greater the impact on the strength of filling specimen.

To more intuitively describe the change rule of filling body strength with water content, Figure 4 shows the change trend of filling body peak strength with water content. The quadratic function was used to fit the relationship between the peak strength of the filling body and the water content. The fitting correlation coefficient was 0.9498. The fitting result can better reflect the influence of the water content on the peak strength of the filling body. The fitting equation was:

$$\sigma_p = -20.78465\omega_c^2 - 5.43766\omega_c + 3.04507 \quad (2)$$

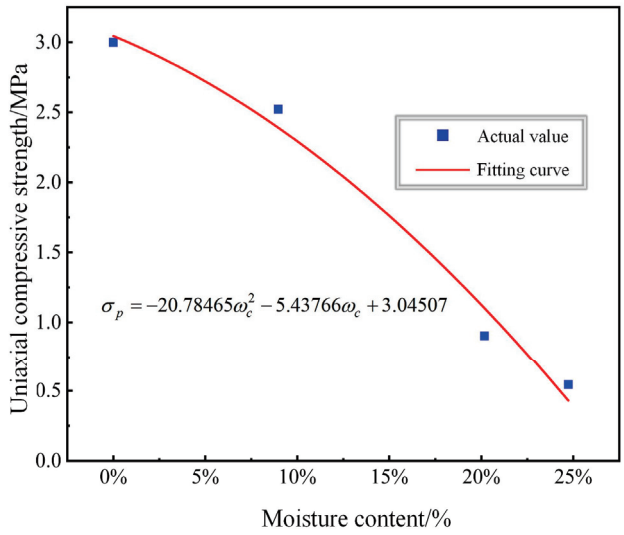

Figure 4. Relation curve between moisture content and uniaxial compressive strength of paste filling body.

3.2. Damage Constitutive Model of Paste Filling with Different Water Content

According to the strain equivalence principle proposed by Lemaitre (1971), it can be seen that the strain caused by the stress acting on the damaged filling was equivalent to the strain caused by the actual stress (effective stress) acting on the non-destructive filling [37]. If the filling body was regarded as an isotropic continuous medium, then:

$$\sigma = E\varepsilon(1 - D) \tag{3}$$

where: σ was the effective stress borne by the filling body; ε was the strain of the filling body; E was the elastic modulus of the filling body; D was the damage value of the filling body.

The stress-strain curve of the filling body obeys Weibull statistical distribution density function [38], which can establish a relationship between the damage and the defects contained in each micro element. Then, the damage value of the paste filling body under uniaxial compression was:

$$D = 1 - \exp\left[\frac{-(\varepsilon/\varepsilon_p)^{\lambda}}{\lambda}\right] \tag{4}$$

λ was the shape parameter of Weibull statistical distribution, which can be expressed as:

$$\lambda = 1/\ln(E\varepsilon_p/\sigma_p)$$

where σ_p was the peak stress of the filling body, ε_p was the peak strain of the filling body.

By introducing Equation (4) into Equation (3), the damage constitutive equation of filling under uniaxial compression can be obtained:

$$\sigma = E\varepsilon \exp\left[\frac{-(\varepsilon/\varepsilon_p)^{\lambda}}{\lambda}\right] \tag{5}$$

According to Equation (2), the relationship between the peak stress of the filling body and the water content was a quadratic function, so the Equation (2) was introduced to obtain the Weibull statistical distribution shape parameters of the filling body under different water content: $\lambda_c = 1/\ln\left[E\varepsilon_p/\left(A\omega_c^2 + B\omega_c + C\right)\right]$.

Taking λ_c into Equations (4) and (5), the damage evolution equation and damage constitutive equation of filling body with different water contents can be obtained. In combination with the stress-strain curves of four filling bodies with different water contents (Figure 3); the calculation results were shown in Table 2. According to

the damage evolution equation and damage constitutive equation of coal-based solid waste paste filling with different water content as shown in Table 2, the strain damage curve and stress strain curve of filling with different water contents can be drawn, as shown in Figures 5 and 6, respectively.

Table 2. Damage evolution equation and constitutive equation of filling with different moisture content.

Specimen	*E*/MPa	σ_{pc}/MPa	λ_c	Damage Evolution Equation	Damage Constitutive Equation
Group A	262.18	3.0451	4.4203	$D = 1 - \exp\left[\frac{-(\varepsilon/0.0115)^{4.4203}}{4.4203}\right]$	$\sigma = E\varepsilon \exp\left[\frac{-(\varepsilon/0.0115)^{4.4203}}{4.4203}\right]$
Group B	280.25	2.3910	1.5706	$D = 1 - \exp\left[\frac{-(\varepsilon/0.0109)^{1.5706}}{1.5706}\right]$	$\sigma = E\varepsilon \exp\left[\frac{-(\varepsilon/0.0109)^{1.5706}}{1.5706}\right]$
Group C	104.54	1.1027	2.1362	$D = 1 - \exp\left[\frac{-(\varepsilon/0.0168)^{2.1362}}{2.1362}\right]$	$\sigma = E\varepsilon \exp\left[\frac{-(\varepsilon/0.0168)^{2.1362}}{2.1362}\right]$
Group D	127.59	0.4292	1.1174	$D = 1 - \exp\left[\frac{-(\varepsilon/0.0082)^{1.1174}}{1.1174}\right]$	$\sigma = E\varepsilon \exp\left[\frac{-(\varepsilon/0.0082)^{1.1174}}{1.1174}\right]$

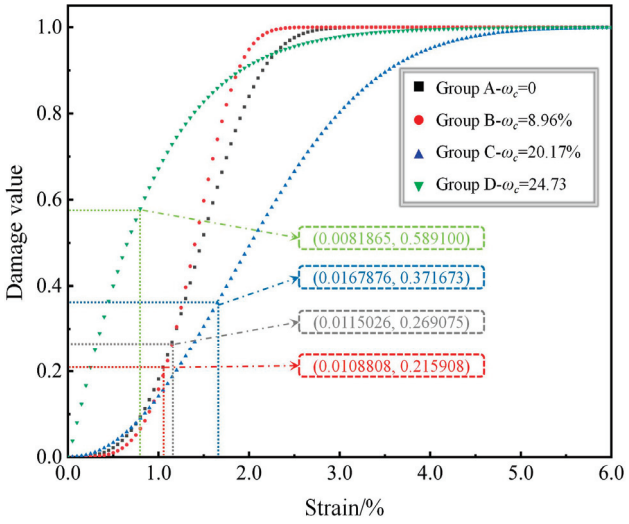

Figure 5. Variation curve of damage value of paste filling body.

The peak damage was defined as the damage value corresponding to the peak stress of the filling specimen. Figure 5 showed the coordinates of the peak strain and peak damage value corresponding to the peak strength of the filling body in each water-bearing state. It can be seen from Figure 5 that the filling body in all states reaches the peak strength when the strain is small. When the peak strength was reached, the peak damage value changes between 0.21 and 0.59. With the increase of water content, the peak damage value decreases first and then increases, indicating that the water content has a certain role in promoting the damage development of the filling body. At the initial stage of strain, the damage values of Group A, B and C fillings under the same deformation conditions show the phenomenon of Group C > Group A > Group B. By comparing the stress-strain curve, it can be seen that in the elastic stage, the curves of Group A and Group B were relatively close, but the elastic modulus of Group B was slightly higher than that of Group A. Therefore, at the initial stage of strain, it showed that the damage growth rate of Group A was greater than that of Group B. The stress-strain curve of Group C has an obvious inflection point before the peak, and the internal structure was partially damaged, resulting in its damage value at the initial strain stage being slightly greater than that of Group A and Group B. With the increase of strain, the damage value of filling in Group A, B and C began to show the phenomenon of Group B > Group A > Group C under the same deformation condition. This was because after the filling in Group B reached the peak stress, three

irregular inflection points appeared in its post-peak curve, and the internal fissure further developed and coalesced and formed a large crack, leading to greater damage. However, due to the increase of water content, the stress-strain curve of Group C shows obvious ductility, which slows down the development rate of damage. For Group D filling body, due to its small compaction stage and elastic stage, it reaches the peak stress under very little strain. There were two irregular inflection points on its post-peak curve, and the internal cracks further develop and connect, making its damage value slightly larger than that of Group A, Group B and Group C. It can be seen that with the increase of strain, the influence of water content on the damage of filling was gradually smaller.

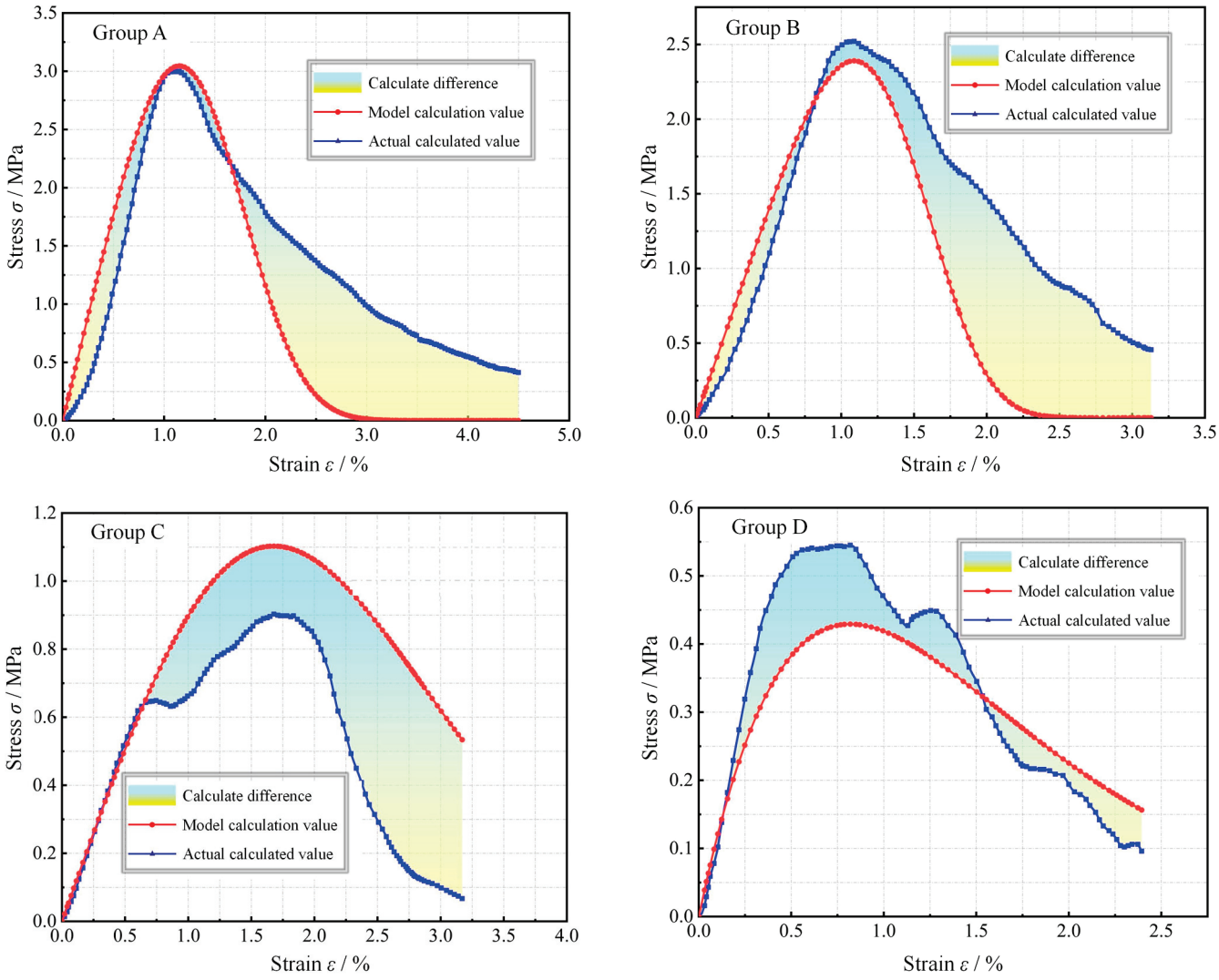

Figure 6. Comparison between experimental values and model values of stress-strain curves of paste filling body with different moisture content.

It can be seen from Figure 5 that the strain damage curve was "concave" before the damage reached peak damage, indicating that the growth rate of the damage value increases with the increase of strain; but after reaching peak damage, the strain damage curve starts to be "convex", and the growth rate of the damage value slows down with the increase of strain at this stage.

According to Figure 6, before the peak stress, the actual value of the filling sample basically coincides with the model value. After the peak stress, with the increase of water content, the model curve was closer to the test curve. When the water content was 18% (saturation was 100%), the model curve and the test curve basically coincide. Compared

with the completely dry filling sample, the calculated results have a higher agreement with the test results, and the higher the water content, the higher the agreement. It shows that this damage-constitutive model was more suitable for the filling body with water. In the underground mining environment of a coal mine, due to the action of the humidity of the mining environment and groundwater, the filling body was always in a state of water, and the water content was generally large, close to the saturated state. Therefore, this damage-constitutive model has important practical engineering significance.

4. Discussion

To further analyze the mechanism of the influence of water content on the strength of filling, the author makes the following assumptions from the three aspects of physical effect, structural effect and chemical effect, based on the existing research results:

(1) Physical effect: Water will reduce the friction between coal gangue, fly ash and cement cementation products in the filling body, resulting in the reduction of the force required for sliding between particles, which will lead to the failure of the filling body under low pressure (Figure 7).

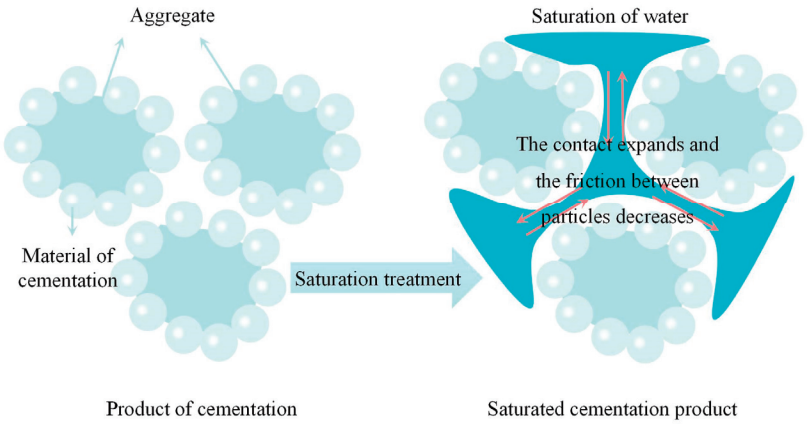

Figure 7. Physical effect of water saturation degree on strength of paste filling material.

(2) Structural effect: There were microcracks in the filling body. When water entered the microcracks in the object, the microcracks accelerated to expand and develop into cracks when it was compressed, resulting in a decrease in structural strength (Figure 8).

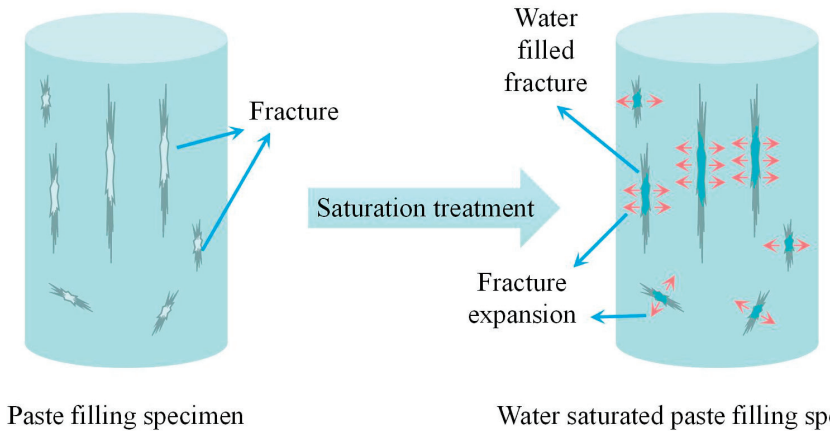

Figure 8. Structural effect of water saturation degree on strength of paste filling material.

(3) Chemical effect: Chemical reaction between high content of water and materials in the filling body will lead to dissolution and destruction of some materials in the filling body, thus reducing the structural strength of the filling body (Figure 9).

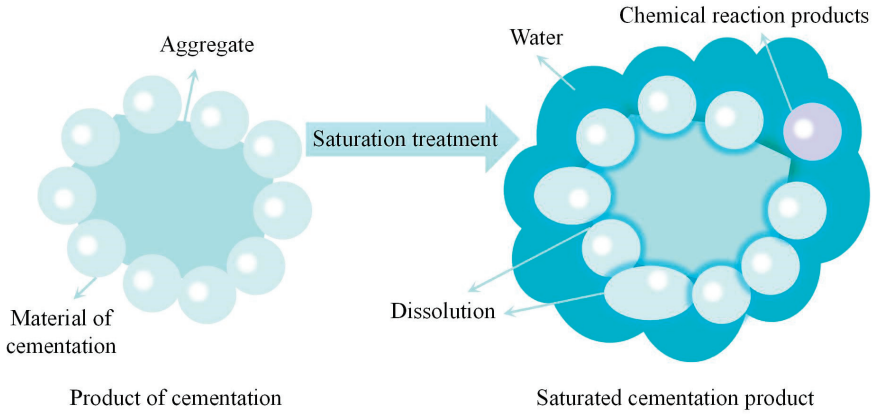

Figure 9. Chemical effect of water saturation degree on strength of paste filling material.

5. Conclusions

Through the analysis of strength characteristics and damage characteristics of coal-based solid waste paste filling materials with different water contents, the main conclusions were as follows:

(1) With the increase of water content, the compressive strength of the filling specimen decreases gradually. And the higher the moisture content, the greater the impact on the strength of the filling sample.
(2) The stress-strain curves of fillings with different water contents were divided into compaction stage (I), elastic deformation stage (II), plastic deformation stage (III) and post-peak failure stage (IV). With the increase of water content, the fillings gradually changed from brittle to ductile. The relationship between the water content and the peak strength was fitted by the binary linear equation, and the fitting results can better reflect the influence of the water content on the peak strength of the filling.
(3) With the increase of strain, the influence of water content on the damage of the filling was gradually reduced. The evolution equation and constitutive equation of filling damage under different water content were established, and the reliability of the constitutive equation was verified by comparing the experiment with the model.
(4) By discussing the water-bearing failure mechanism of paste backfill from the aspects of physics, chemistry and structure, it is clear that the water-bearing failure of backfill may be caused by the influence of water on the friction between particles, the expansion of micro-cracks and the generation of new hydration products. This study provides the direction for further research on the influence of water content on the strength and failure form of filling body.

Author Contributions: Methodology, X.H.; Formal analysis, M.W.; Writing—original draft, M.W.; Writing—review & editing, M.W. and K.Y.; Supervision, X.H.; Funding acquisition, X.H. All authors have read and agreed to the published version of the manuscript.

Funding: This research was funded by Scientific Research Foundation for High-level Talents of Anhui University of Science and Technology (2021yjrc11), Key Basic Research Project of China (2019YFC1904304), Institute of Energy, Hefei Comprehensive National Science Center (No.21KZS217), National Natural Science Foundation of China (52130402).

Institutional Review Board Statement: Not applicable.

Informed Consent Statement: Not applicable.

Data Availability Statement: Not applicable.

Acknowledgments: This paper was supported by the National Program on Scientific Research Foundation for High-level Talents of Anhui University of Science and Technology (2021yjrc11), Key Basic Research Project of China (2019YFC1904304), Institute of Energy, Hefei Comprehensive National Science Center under Grant No.21KZS217, National Natural Science Foundation of China (52130402).

Conflicts of Interest: The authors declare no conflict of interest.

References

1. Feng, G.R.; Du, X.J.; Guo, Y.X.; Qi, T.Y.; Wang, Z.H.; Li, Q.D.; Li, H.Y.; Kang, L.X. Basic theory of constructional backfill mining and the underground space utilization concept. *J. China Coal Soc.* **2019**, *44*, 74–84.
2. Chugh, Y.P.; Behum, P.T. Coal waste management practices in the USA: An overview. *Int. J. Coal. Sci. Technol.* **2014**, *1*, 163–176. [CrossRef]
3. Rybak, J.; Adigamov, A.; Kongar-Syuryun, C.; Khayrutdinov, M.; Tyulyaeva, Y. Renewable-Resource Technologies in Mining and Metallurgical Enterprises Providing Environmental Safety. *Minerals* **2021**, *11*, 1145. [CrossRef]
4. Zhang, C.; Li, B.; Song, Z.Y.; Liu, J.B.; Zhou, J.L. Breakage mechanism and pore evolution characteristics of gangue materials under compression. *Acta Geotech.* **2022**, *17*, 4823–4835.
5. Zhang, C.; Zhao, Y.X.; Bai, Q.S. 3D DEM method for compaction and breakage characteristics simulation of broken rock mass in goaf. *Acta Geotech.* **2022**, *17*, 2765–2781. [CrossRef]
6. Li, Y.L.; Lu, B.; Yang, R.S.; Lin, H.; Xu, B.; Wang, S.S.; Liu, C.H. Cemented backfilling mining technology with continuous mining and continuous backfilling method for underground coal mine and typical engineering cases. *J. China Coal Soc.* **2022**, *47*, 1055–1071.
7. Lin, H.; Yang, R.S.; Li, Y.L.; Lu, B.; Xu, B.; Fan, Z.Y.; Li, J.N. Application of short-wall continuous mining and continuous backfilling cemented-fill mining technology. *Chin. J. Eng.* **2022**, *44*, 981–992.
8. Xuan, D.Y.; Xu, J.L.; Wang, B.L. Green mining technology of overburden isolated grout injection. *J. China Coal Soc.* **2022**, *12*, 4265–4277. Available online: http://kns.cnki.net/kcms/detail/11.2190.TD.20221128.1838.002.html (accessed on 28 November 2022).
9. Wang, Z.Q.; Guo, X.F.; Gao, Y.; Chen, C.F.; Li, P.F.; Wang, L.; Zhao, J.L. Study of grouting technology of overburden-separation to reduce ground subsidence in Huafeng coal mine. *Chin. J. Rock Mech. Eng.* **2014**, *33*, 3249–3255.
10. Liu, J.G.; Li, X.W.; He, T. Application status and prospect of backfill mining in Chinese coal mines. *J. China Coal Soc.* **2020**, *45*, 141–150.
11. Yang, K.; Wei, Z.; Zhao, X.Y.; He, X.; Zhang, J.Q.; Ji, J.S. Theory and technology of green filling of solid waste in underground mine at coal power base of Yellow River Basin. *J. China Coal Soc.* **2021**, *46*, 925–935.
12. Wu, A.X.; Yang, Y.; Cheng, H.Y.; Chen, S.M.; Han, Y. Status and prospects of paste technology in China. *Chin. J. Eng.* **2018**, *40*, 517–525.
13. Yang, K.; Zhao, X.Y.; Wei, Z.; Zhang, J.Q. Development overview of paste backfill technology in China's coal mines: A review. *Environ. Sci. Pollut. Res.* **2021**, *28*, 67957–97969. [CrossRef]
14. Zhao, Y.L.; Liu, Q.; Zhang, C.S.; Liao, J.; Lin, H.; Wang, Y.X. Coupled seepage-damage effect in fractured rock masses: Model development and a case study. *Int. J. Rock Mech. Min. Sci.* **2021**, *144*, 104822. [CrossRef]
15. Liu, Q.; Zhao, Y.L.; Tang, L.M.; Liao, J.; Wang, X.G.; Tan, T.; Chang, L.; Luo, S.L.; Wang, M. Mechanical characteristics of single cracked limestone in compression-shear fracture under hydro-mechanical coupling. *Theor. Appl. Fract. Mech.* **2022**, *119*, 103371. [CrossRef]
16. Kongar-Syuryun, C.; Aleksakhin, A.; Khayrutdinov, A.; Tyulyaeva, Y. Research of rheological characteristics of the mixture as a way to create a new backfill material with specified characteristics. *Mater. Today Proc.* **2021**, *38*, 2052–2054. [CrossRef]
17. Yin, S.H.; Hou, Y.Q.; Yang, S.X.; Zhang, M.Z.; Cao, Y. Analysis of deformation failure and energy dissipation of mixed aggregate cemented backfill during uniaxial compression. *J. Cent. South. Univ.* **2021**, *52*, 936–947.
18. Hou, Y.Q.; Yin, S.H.; Cao, Y.; Dai, C.Q. Research on Damage and Energy Dissipation Characteristics of Cemented Backfill under Different Loading Rates. *J. Hunan Univ.* **2020**, *47*, 108–117.
19. Hou, Y.Q.; Yin, S.H.; Cao, Y.; Dai, C.Q. Analysis of damage characteristics and energy dissipation of cemented tailings backfill with different curing ages under uniaxial compression. *J. Cent. South. Univ.* **2020**, *51*, 1955–1965.
20. Feng, G.R.; Xie, W.S.; Guo, Y.X.; Guo, J.; Ran, H.Y.; Zhao, Y.H. Effect of early load on mechanical properties and damage of cemented gangue backfill. *Chin. J. Rock Mech. Eng.* **2022**, *41*, 775–784.
21. Guo, Y.X.; Zhao, Y.H.; Feng, G.R.; Ran, H.Y.; Zhang, Y.J. Study on damage size effect of cemented gangue backfill body under uniaxial compression. *Chin. J. Rock Mech. Eng.* **2021**, *40*, 2434–2444.
22. Zhao, Y.H.; Ran, H.Y.; Feng, G.R.; Guo, Y.X.; Fan, Y.J. Damage evolution and failure characteristics of cemented gangue backfill body with different height-width ratios under uniaxial compression. *J. Min. Saf. Eng.* **2022**, *39*, 674–682.
23. Hua, X.Z.; Chang, G.F.; Liu, X.; Yang, K.; Chen, D.H.; Li, C.; Wang, E.Q. Strength evolution law and acoustic-emission characteristics of multi-source coal-based filling body of solid wastes. *Chin. J. Rock Mech. Eng.* **2022**, *41*, 1536–1551.
24. Zhao, K.; Huang, M.; Yan, Y.J.; Wan, W.L.; Ning, F.J.; Zhou, Y.; He, Z.W. Mechanical properties and synergistic deformation characteristics of tailings cemented filling assembled material body with different cement-tailings ratios. *Chin. J. Rock Mech. Eng.* **2021**, *40*, 2781–2789.

25. Jin, S.B.; Liu, K.W.; Huang, J.; Jin, S.H. Study on Damage Constitutive Model of Backfill Under Uniaxial Compression Loading. *Gold Sci. Technol.* **2021**, *29*, 555–563.
26. Yang, X.L.; Wang, W.J. Shear failure characteristics of cemented interface between filling material and surrounding rock at different curing temperatures. *China Civil Eng. J.* **2022**, *55*, 76–87.
27. Jin, A.B.; Wang, J.; Chen, S.J.; Li, H. Strength and damage characteristics of tailings filling body with different particle size distributions. *Rock Soil Mech.* **2022**, *43*, 3083–3093.
28. Chen, S.M.; Wang, W.; Wu, A.X.; Wang, Y.M. Influence rules of curing stress on strength of cemented paste backfill materials and its mechanism analysis. *Chin. J. Nonferrous Met.* **2021**, *31*, 3740–3749.
29. Nie, Y.L.; Wang, X.J.; Huang, G.L.; Li, S.C.; Feng, X.; Cao, S.R. Strength and Damage Model Analysis of Pure Tailings Cemented Filling Body with Different Water Content. *Bull. Chin. Ceram. Soc.* **2018**, *37*, 2008–2013.
30. Li, Z.F.; Zhang, C.; Zhang, J.; Jin, Q.; Wang, Y.S.; Yan, N. Mechanical properties and damage mechanism of backfill with different water saturation. *J. Min. Saf. Eng.* **2021**, *38*, 1063–1069 + 107.
31. Wang, Y.Y.; Yu, Z.Q.; Cui, L.Z. Experimental study on compressive behavior of cemented paste backfill material with different water contents. *Coal Sci. Technol.* **2022**, *50*, 219–224.
32. Liu, D.; Xu, J.C.; Pu, H. Experimental study on creep characteristics of gangue cemented fillers with different water content. *J. Min. Saf. Eng.* **2021**, *38*, 1055–1062.
33. Ermolovich, E.A.; Ivannikov, A.L.; Khayrutdinov, M.M.; Kongar-Syuryun, C.B.; Tyulyaeva, Y.S. Creation of a Nanomodified Backfill Based on the Waste from Enrichment of Water-Soluble Ores. *Materials* **2022**, *15*, 3689. [CrossRef]
34. Kongar-Syuryun, C.; Tyulyaeva, Y.; Khairutdinov, A.M.; Kowalik, T. Industrial waste in concrete mixtures for construction of underground structures and minerals extraction. *Conf. Ser. Mater. Sci. Eng.* **2020**, *869*, 032004. [CrossRef]
35. Liu, W.Z.; Chen, J.T.; Guo, Z.P.; Yang, H.Z.; Xie, W.W.; Zhang, Y.D. Mechanical properties and damage evolution of cemented coal gangue-fly ash backfill under uniaxial compression: Effects of different. *Constr. Build. Mater.* **2021**, *305*, 124820. [CrossRef]
36. Liu, W.Z.; Guo, Z.P.; Wang, C.; Niu, S.W. Physico-mechanical and microstructure properties of cemented coal Gangue-Fly ash backfill: Effects of curing temperature. *Constr. Build. Mater.* **2021**, *299*, 124011. [CrossRef]
37. Lemaitre, J. How to use damage mechanics. *Nucl. Eng. Des.* **1984**, *80*, 233–245. [CrossRef]
38. Zhao, K.; Zhu, S.T.; Zhou, K.P.; Yan, Y.J.; Zhao, K.; Li, Q.; Gu, S.J. Research on mechanical properties and damage law of tantalum-niobium ore cemented tailings backfill. *J. Min. Saf. Eng.* **2019**, *36*, 7.

sustainability

MDPI

Article

Evaluation of the Coordination Degree of Coal and Gas Co-Mining System Based on System Dynamics

Shuheng Zhong * and Dan Lin

School of Energy and Mining Engineering, China University of Mining and Technology (Beijing), Beijing 100083, China
* Correspondence: zhsh@cumtb.edu.cn

Abstract: Coal and gas co-mining is one of the green mining technologies in coal mines. Coal and gas co-mining can reduce environmental pollution and supply-side carbon emissions from the coal industry. It has an important role to play in achieving the goal of carbon peaking and carbon neutrality. The perfect state of safety production and economic efficiency is a "win-win" situation. Therefore, it is of great theoretical and practical importance to evaluate the safety and economic coordination of coal and gas co-mining systems. This study used a system dynamics approach to analyze and evaluate the coordination of coal and gas co-mining systems in a dynamic simulation. A case study was conducted using the Zhuxianzhuang coal mine as an example. The results showed that the coordination degree of the coal and gas co-mining system exhibited dynamic changes. The average value of the system coordination degree is 0.790, which is a good coordination degree. This demonstrates that the system dynamics method is feasible for evaluating the coordination degree of the coal and gas co-mining system. The system dynamics evaluation model can effectively simulate the dynamic changes of different variable factors in the co-mining system. Therefore, these research results can provide corresponding optimization recommendations for practical production needs.

Keywords: system dynamic model; simulation analysis; co-mining of coal and gas; coordination degree evaluation

1. Introduction

To address global warming and accelerate global greenhouse gas emission reduction, China proposed the goal of "carbon capping and carbon neutrality" at the 75th session of the United Nations General Assembly in September 2020 [1]. In the context of the "carbon peaking and carbon neutrality" goal, coal extraction is both an important source of energy supply and a major source of greenhouse gas emissions [2–4]. In addition to carbon dioxide, greenhouse gases include methane, nitrous oxide, and sulfur hexafluoride, which are collectively referred to as non-carbon dioxide greenhouse gases by the international community. Methane (CH_4) is the second most important greenhouse gas after carbon dioxide. The greenhouse effect of a methane molecule is more than 20 times that of a carbon dioxide molecule. The *6th Assessment Report of the Intergovernmental Panel on Climate Change (IPCC)* has proposed global medium- and long-term coal and gas emission reduction goals around achieving different temperature control goals [5]. This increases the pressure on the global mining industry to decarbonize coal mining and consumption for minimizing coal mine methane emissions, which is an actual scientific and technical problem [6].

The main source of energy in China is coal, which is extremely rich in energy reserves [7]. However, the discovered coal resources account for a relatively small proportion of the coal reserves. With China's rapid economic development, coal demand is gradually increasing. According to statistics, coal consumption in 2021 accounts for 56.0% of total energy consumption [8]. It leads to a gradual increase in the depth of coal mining in China as well. AS the depth of mining increases, coal bed methane pressure and gas gushing

are increasing, and the danger is significantly increasing. Gas, as an associated product of coal, is mainly composed of methane (CH_4). While it is a source of disaster and air pollution in coal mines, it is also a valuable, clean, and efficient non-renewable energy source from the carbon footprint perspective [9]. The extraction of gas can improve the safety of mining production and protect the environment. It can also improve the coordination of resource, economic, safety, and environmental factors, ensuring that the coal industry can maximize its benefits and also the sustainable development of society within the corresponding constraints.

Coal and gas co-mining is a method of mining both coal and gas as resources. Compared to traditional coal mining, coal and gas co-mining has the characteristics of reducing greenhouse gas emissions in the atmosphere, improving economic benefits, reducing gas hazards, and lowering ventilation costs. The premise of the coal production system is safe production, and it aims to ensure maximum economic benefits in a safe state. Therefore, in the background of the "double carbon" goal, a coordinated degree evaluation of the safety and economy of coal and gas co-mining can be a good contribution to mine production.

Dzhioeva, A.K. et al. [10] describe the non-linear variation of methane concentrations in subsurface boreholes and the specific characteristics of their implementation. Brigida, V.S. et al. [11] studied the characteristics of local minimum methane concentrations in drainage holes. Bing Qin et al. [12] pointed out that the stress redistribution caused by coal and gas co-mining mining affects the permeability and thus the gas co-mining. At present, many scholars' research on coal and gas co-mining is mostly focused on the research co-mining theory, the influence of pressure relief for outgassing dynamics, technological processes, and related questions [13–17], while the research on the evaluation of coal and gas co-mining remains insufficiently studied. Zhiheng Cheng et al. [18] constructed a co-mining technology system and dynamic evaluation model for determining the effect of extraction-mining-extraction on coal seam clusters near the mine area. Bing Liang et al. [19] established a fuzzy comprehensive evaluation model with three parts: economic pre-evaluation, safety evaluation, and co-mining effect. On this basis, it quantified the degree of coordination between coal mining and gas extraction systems using the coordination degree function. The evaluation of coal and gas co-mining has mainly focused on the evaluation of co-mining effectiveness. The dynamic assessment of the coordination degree of the co-mining system is a less studied area.

In this paper, the possibility of application is being considered the System Dynamics method to co-production system coordination assessments. The co-mining system is divided into economic benefits and safety levels according to production and operational objectives. Then the system dynamics method is used to establish the corresponding coordination evaluation model of the co-mining system. Finally, it is simulated and evaluated, and rationalization recommendations are given.

2. Materials and Methods

2.1. Dynamic Evaluation Methods

System Dynamics (SD) is a method for studying the structure of systems created by Forrester [20]. It is a dynamic evaluation method. System dynamics uses the theory and method of information feedback to study complex systems. It is argued that its behavior patterns and properties depend mainly on its internal dynamic structure and feedback mechanisms. System dynamics can solve highly nonlinear, high-order, multivariate, multi-feedback, and complex system problems. It can grasp the trend of development of things at the macroscopic level as well as analyze the interactions of microscopic factors within the system. Currently, system dynamics methods have been successfully applied to risk assessment [21], efficiency evaluation [22], resource contribution evaluation [23], policy evaluation [24], and economic benefits evaluation [25].

This paper adopts a system dynamics-based method for evaluating the coordination of coal and gas co-mining systems. The coal and gas co-mining system is dynamic, and its structure as well as the economic benefits and safety level in the production process can

be seen as a complex system. The dynamic evaluation of the coordination degree of coal and gas co-mining systems first requires consideration of the system as a whole. Secondly, the influence constraints between the indicators of the system and between the indicators and other relevant factor variables are summarized, taking into the characteristics of coal and gas co-mining into account. Finally, a system dynamics model is established for the evaluation of the coordination degree of the co-mining system. The level of coordination of the coal and gas co-mining system and the trend behavior of the results of other variables over time is obtained through simulation analysis. Based on this, key factors are selected to study the degree of influence of different influencing factors on the coordinated development of the co-mining system, and then optimization suggestions for mine production are provided.

2.2. Construction of System Dynamics Indexes

The system dynamics cause-effect diagram is a reflection of the cause-effect relationship between various factors of the system, which is the basis of the final simulation flow diagram of the system. The coal and gas co-mining system is a multi-level and multi-factor complex system. The maximization of efficiency and safe production are important goals pursued by the enterprise. The system coordination evaluation in this paper will focus on these two goals and divide them into the economic benefits subsystem and the safety level subsystem. Through a literature research and data collation, factors affecting the coordination of the coal and gas co-mining system were distilled [19,26–29]. We then distributed questionnaires on the influencing factors to people working in coal-related industries to filter the indicators and obtain the final subsystem factors and influencing factors. Finally, combining the characteristics of the coal and gas co-mining system, the relationship between the influencing factors in the system is analyzed, and the cause-and-effect diagrams of its economic efficiency sub-system, safety level sub-system, and coal and gas co-mining system are constructed.

2.2.1. Economic Benefits Subsystem

The economic benefits of the coal and gas co-mining systems are influenced by the level of geology, technology, economy, and environment. The feedback relationship of the economic benefit subsystem is shown in Figure 1. In the figure, "+" indicates a positive correlation, and "−" indicates a negative correlation. The main feedback relationships include:

(1) Depth of coal seam buried → (−) Geological level of coal seam → (+) Geological level → (+) Economic benefits
(2) Coal seam thickness → (+) Geological level of coal seam → (+) Geological level → (+) Economic benefits
(3) Top and bottom slab lithology → (+) Basic geological level → (+) Geological level → (+) Economic benefits
(4) Hydrogeological situation → (−) Basic geological level → (+) Geological level → (+) Economic benefits
(5) Complexity of geological structure → (−) Basic geological level → (+) Geological level → (+) Economic benefits
(6) The degree of difficulty of gas extraction → (−) Gas geological level → (+) Geological level → (+) Economic benefits
(7) Gas content → (+) Gas geological level → (+) Geological level → (+) Economic benefits
(8) Gas pressure → (+) Gas geological level → (+) Geological level → (+) Economic benefits
(9) Coal mining rate → (+) Technical level → (+) Economic benefits
(10) Gas mining rate → (+) Technical level → (+) Economic benefits
(11) Coal price → (+) Economic level → (+) Economic benefits
(12) Production cost → (−) Economic level → (+) Economic benefits
(13) Total investment → (−) Economic level → (−) Economic benefits
(14) Land reclamation rate → (+) Environmental level → (+) Economic benefits

(15) Wastewater utilization rate → (+) Environmental level → (+) Economic benefits
(16) Gas emission utilization rate → (+) Environmental level → (+) Economic benefits

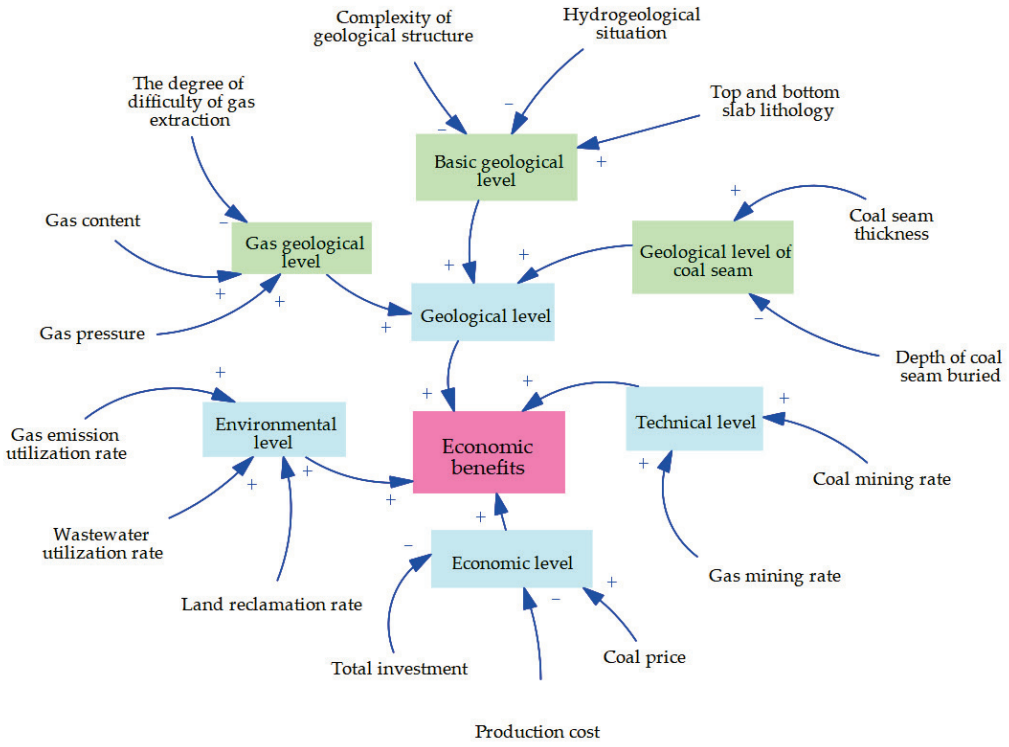

Figure 1. Cause and effect analysis of economic benefits.

2.2.2. Safety Level Subsystem

The safety level of the coal and gas co-mining systems is influenced by the level of gas geology, the level of basic geology, the level of inputs, and the level of production. The feedback relationship of the safety level subsystem is shown in Figure 2. In the figure, "+" indicates a positive correlation, and "−" indicates a negative correlation. The main feedback relationships include:

(1) Hydrogeological situation → (−) Basic geological level → (+) Safety level
(2) Complexity of geological structure → (−) Basic geological level → (+) Safety level
(3) Top and bottom slab lithology → (+) Basic geological level → (+) Safety level
(4) Gas pressure → (+) Gas geological level → (−) Safety level
(5) Gas content → (+) Gas geological level → (−) Safety level
(6) The degree of difficulty of gas extraction → (−) Gas geological level → (−) Safety level
(7) Electrical and mechanical equipment integrity rate → (+) Production level → (+) Safety level
(8) Education level of personnel → (+) Production level → (+) Safety level
(9) Number of extraction roadway layout → (+) Input level → (+) Safety level
(10) Number of drill holes arranged in the mining site → (+) Input level → (+) Safety level
(11) Production cost → (+) Input level → (+) Safety level
(12) Relative gas emergence volume → (+) Gas level → (−) Safety level
(13) Return airflow gas concentration → (+) Gas level → (−) Safety level

The cause-and-effect diagram of the coal and gas co-mining system is built based on the analysis of the relationship between the variables of the economic benefits and safety level subsystems. The cause-effect relationship of the coal and gas co-mining system is shown in Figure 3.

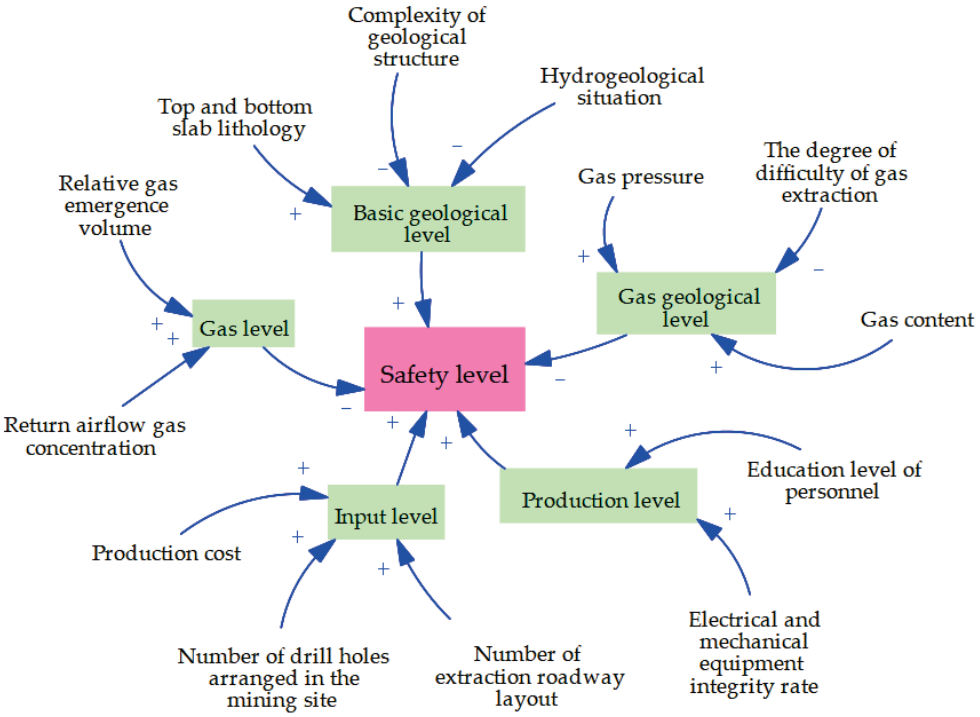

Figure 2. Cause and effect analysis of safety level.

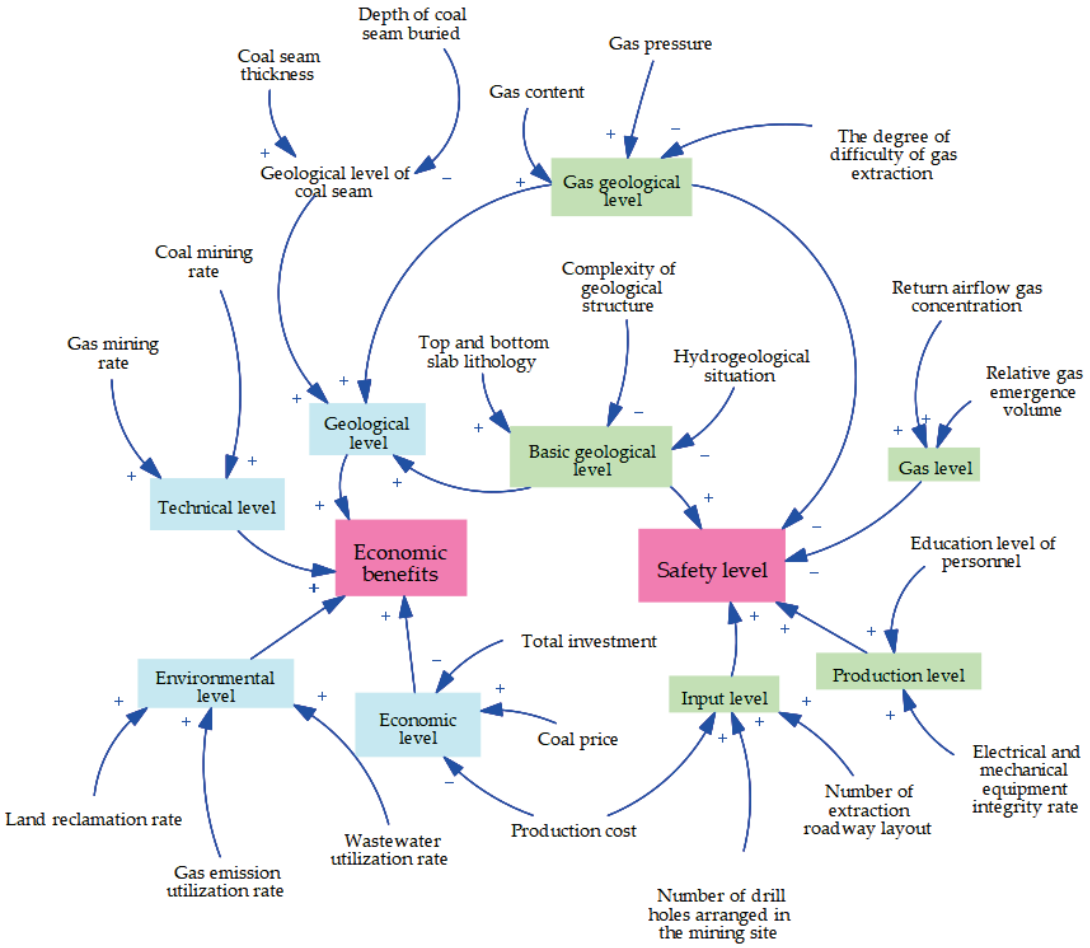

Figure 3. Cause and effect analysis of coal and gas co-mining system.

2.3. System Dynamics Model

By analyzing the relationship between the variables of the economic benefits and safety level subsystems, and combining the variable relationships between the subsystems, a coal and gas co-mining system dynamics model was constructed using Vensim PLE 9.2.4 software, as shown in Figure 4.

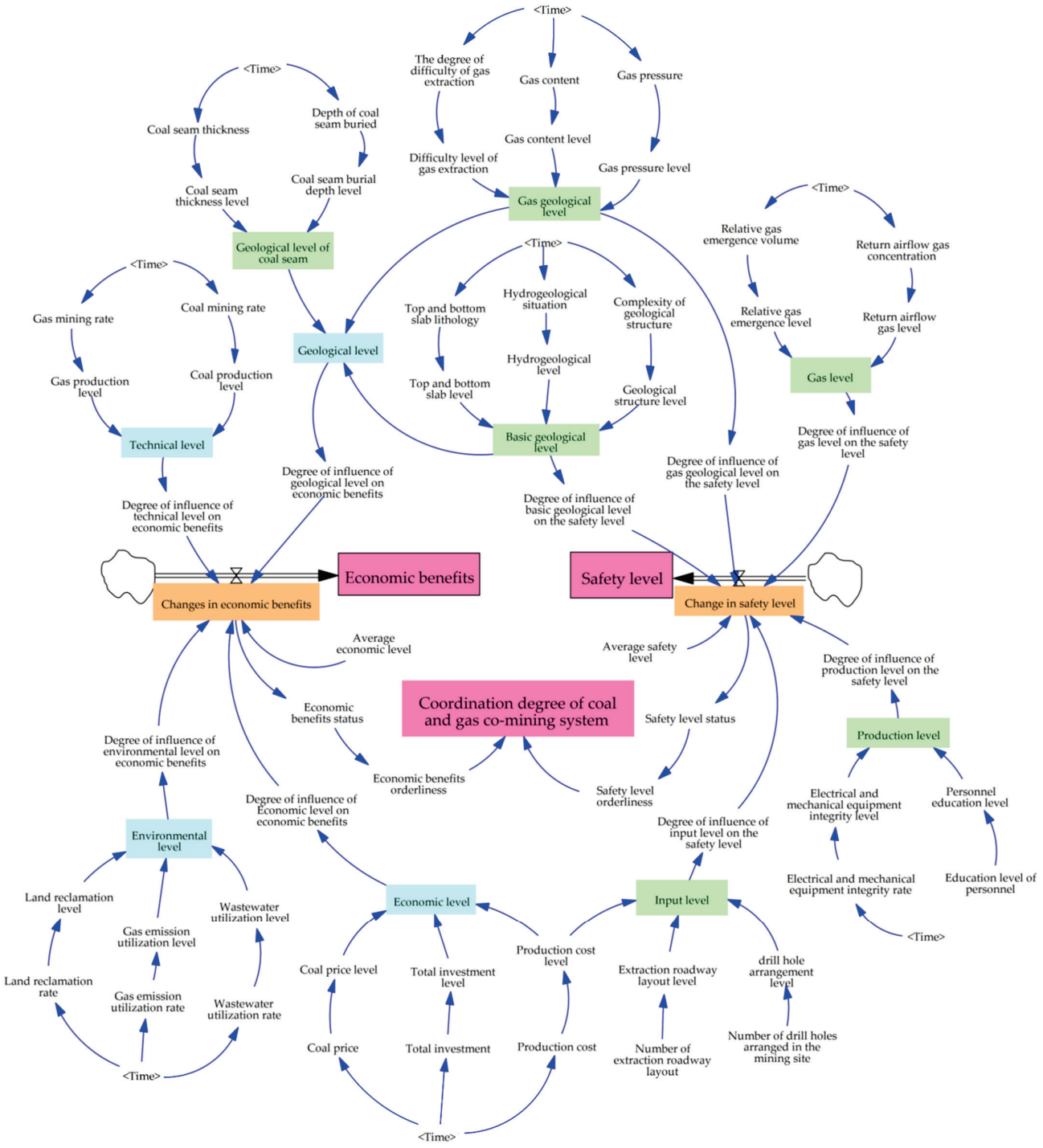

Figure 4. System dynamics model of the coordination degree of the coal and gas co-mining system.

3. Case Study

The Zhuxianzhuang coal mine is mainly for fully mechanized top coal caving, and the degree of mechanization is 100%.

It adopts the method of coal mining with strike longwall and all trap roofs.

It uses an advanced mining sequence in the mining area and a backward mining sequence in the section. For gas protruding working faces, high-level boreholes and upper-corner buried pipes are mainly used to extract gas from the mining area during the recovery period.

Taking the II851 working face as an example, its coal seam original gas pressure is 1.55 MPa and its original coal seam gas content is 9.71 m^3/t. The working face was located in the protrusion risk area. It adopted the measures of protection layer mining combined with a hole drilled along seam-enhanced gas drainage and the coal mining method of strike longwall full seam cutting.

3.1. Parameters

3.1.1. Determination of Parameters

In this study, we used the coal and gas co-mining system at the Zhuxianzhuang coal mine as a case study. The simulation was carried out using Vensim PLE 9.2.4 software to establish the coordination degree dynamic model of the coal and gas co-mining system. The simulation time was set at 12 months to accommodate the effects of different climates on coal mining and gas extraction. The data for the model comes from the 2020 statistics for the Zhuxianzhuang Mine. The model data includes some constants and variables, and the model data values are taken based on monthly average data. The variables are coal seam thickness, coal seam burial depth, coal production rate, gas production rate, coal price, etc. The principles of influence level and influence degree of each variable in the model are as follows.

(1) Influence level assignment

The degree of influence of each variable in the system dynamics model varies with its value. By using the table function of the Vensim PLE 9.2.4 simulation software, the change in the value of the influence factor corresponds to its level of influence. Finally, the level of influence is then quantified in a range of scores from 40 to 100.

(2) Influence degree assignment

The degree of influence is the degree of influence of the influence factor on the corresponding influence object in the system. The greater the degree of influence means that the greater the promotion of the influence object. Conversely, the greater the weakening effect. The influence degree is taken as a value between 0.5 and 1.5.

3.1.2. Coordination Degree Function

$U_{i(sj)}$ indicates the degree of ordering of the variable x_j on the system. ω_j indicates indicator weighting. In this paper, the geometric average method is integrated with the linear weighted sum method. The integrated function is called the coordination degree function.

(1) Geometric average method

$$D = \sqrt[n]{U_{i(s1)}U_{i(s2)}\dots U_{i(sj)}} = \sqrt[n]{\prod_{j=1}^{n} U_{i(sj)}} \tag{1}$$

(2) Linear weighting method

$$F = \sum_{j=1}^{n} \omega_j U_{i(sj)} \tag{2}$$

Finally, the coordination degree function is constructed as follows.

$$C = \sqrt{D \times F} \tag{3}$$

3.1.3. Equations

The equation in the model flow diagram is:

(1) Coordination degree of coal and gas co-mining system = ((safety level orderliness × economic benefits orderliness)^(1/2) × (economic benefits orderliness × W1 + safety level orderliness × W2))^(1/2)
(2) Changes in economic benefits = average economic level × (degree of influence of geological level on economic benefits × W3 + degree of influence of technical level on economic benefits × W4 + degree of influence of environmental level on economic benefits × W5 + degree of influence of economic level on economic benefits × W6)
(3) Geological level = basic geological level × W7 + geological level of coal seam × W8 + gas geological level × W9
(4) Geological level of coal seam = coal seam thickness level × W10 + coal seam burial depth level × W11
(5) Gas geological level = gas pressure level × W12+gas content level × W13 + difficulty level of gas extraction × W14
(6) Basic geological level = geological structure level × W15 + hydrological level × W16 + top and bottom slab level × W17
(7) Technical level = coal production level × W18 + gas production level × W19
(8) Environmental level = land reclamation level × W20 + wastewater utilization level × W21 + gas emission utilization level × W22
(9) Economic level = total investment level × W23 + coal price level × W24 + production cost level × W25
(10) Change in safety level = average safety level × (degree of influence of basic geological level on safety level × W26 + degree of influence of input level on safety level × W27 + degree of influence of gas geological level on safety level × W28 + degree of influence of gas level on safety level × W29 + degree of influence of production level on safety level × W30)
(11) Gas level = return airflow gas level × W31 + relative gas emergence level × W32
(12) Production level = personnel education level × W33 + electrical and mechanical equipment integrity level × W34
(13) Input level = extraction roadway layout level × W35 + production cost level × W36 + drill hole arrangement level × W37

3.1.4. Determination of Weights

In this paper, we chose the hierarchical analysis method to determine the weights, and they are shown in Table 1.

Table 1. Simulation indicator weights.

Indicators	Indicates a Function	Weights
Economic benefits orderliness	W_1	0.35
Safety level orderliness	W_2	0.65
Degree of influence of geological level on economic benefits	W_3	0.2347
Degree of influence of technical level on economic benefits	W_4	0.4148
Degree of influence of environmental level on economic benefits	W_5	0.0662
Degree of influence of Economic level on economic benefits	W_6	0.2802
Basic geological level	W_7	0.1893
Geological level of coal seam	W_8	0.4163
Gas geological level	W_9	0.3944
Coal seam thickness level	W_{10}	0.3056
Coal seam burial level	W_{11}	0.6944
Gas pressure level	W_{12}	0.3366
Gas content level	W_{13}	0.3978

Table 1. *Cont.*

Indicators	Indicates a Function	Weights
The difficulty level of gas extraction	W_{14}	0.2656
Geological structure level	W_{15}	0.1219
Hydrogeological level	W_{16}	0.1124
Top and bottom slab level	W_{17}	0.7657
Coal production level	W_{18}	0.491
Gas production level	W_{19}	0.509
Land reclamation level	W_{20}	0.5193
Wastewater utilization level	W_{21}	0.1358
The gas emission utilization level	W_{22}	0.3449
Total investment level	W_{23}	0.277
Coal price level	W_{24}	0.2814
Production cost level	W_{25}	0.4416
Degree of influence of basic geological level on safety level	W_{26}	0.1086
Degree of influence of input level on safety level	W_{27}	0.2395
Degree of influence of gas geological level on safety level	W_{28}	0.227
Degree of influence of gas level on safety level	W_{29}	0.2718
Degree of influence of production level on safety level	W_{30}	0.1531
Return airflow gas level	W_{31}	0.4288
Relative gas emergence level	W_{32}	0.5712
Personnel education level	W_{33}	0.0839
Electrical and mechanical equipment integrity level	W_{34}	0.9161

3.2. Dynamic Simulation and Analysis of Results

3.2.1. Model Validation

According to the established system dynamics model, initial settings were made for the data of the Zhuxianzhuang coal mine. The simulation of the degree of coordination of the co-mining system in the Zhuxianzhuang coal mine was carried out. To make the final model simulation results more objective and accurate, economic benefits are used in the model simulation to test the validity of the model. In the simulation result after the operation, the economic benefits were 1.0399 billion yuan. Compared with its actual economic benefits of 1.008 billion yuan, the difference was 0.0319 billion yuan. The deviation rate was +3.165%. The error was within $\pm$10%, and the relative error was small. The simulation results of the model are relatively consistent with the actual situation. The model test results were good. The model can be used to evaluate the coordination degree of the coal and gas co-mining system.

3.2.2. Results

The specific simulation results are shown below.

The relationship between the economic benefits and safety level and the coordination degree of the coal and gas co-mining system is shown in Figure 5.

From Figure 5, it can be seen that the coordination degree of the coal and gas co-mining system shows dynamic changes. Both economic benefits and safety levels have an impact on the coordination degree of coal and gas co-mining systems, and the overall change trend is the same. Analyzing the simulation data, we can get that the average value of the coordination degree of the coal and gas co-mining system is 0.790, the evaluation of economic benefit is good, and the safety level is evaluated as average.

An analysis of the dynamic change simulation data produces the following results. The coordination degree of February and August is relatively good, and its economic benefits and safety level evaluation is relatively good, which is in the peak position in 12 months. The coordination degree of May and December is relatively poor. May has a lower evaluation of economic benefits and is in a trough position during the 12 months. December has a low level of safety and is at the lowest level in the 12 months. Therefore, economic benefits and safety levels can be improved by taking corresponding measures to ensure the production of coordinated coal and gas co-mining.

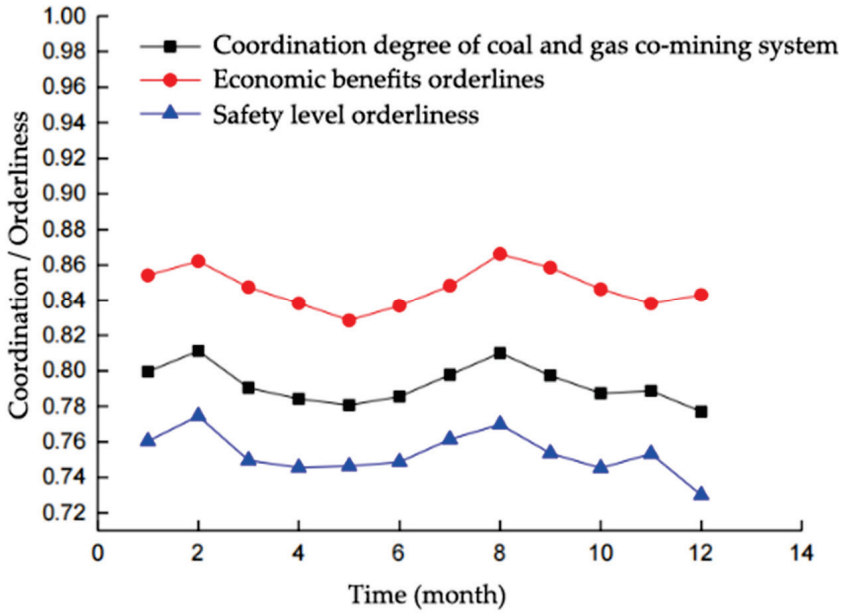

Figure 5. Relationship between economic benefits and safety level and coordination of the co-mining system.

The relationship between the level of each influencing factor and the level of economic benefits is shown in Figure 6.

As seen in Figure 6e, the level of each influencing factor and the level of economic benefits show dynamic changes. The relationship between the level of each influencing factor and the level of economic benefits can be seen in that the factors that mainly affect the economic benefits are technology and the economy, and the geological and environmental factors have less influence on the economic benefits. As seen in Figure 6b, the dynamic trend in the coal production level and gas production level are the same as the trend in the technology levels. It shows that both the coal production level and the gas production level are the main factors affecting the technology level. As seen in Figure 6c, the coal price and production level are the main factors affecting the economy. The higher the coal price, the better the financial economics. The higher the production cost level and the lower the production cost, the better the financial economics. The coal price is influenced by the market and policy. It cannot be subjectively controlled. Therefore, while ensuring safe production, appropriately reducing production costs and increasing the coal extraction and gas extraction rates can help to improve the level of economic benefits.

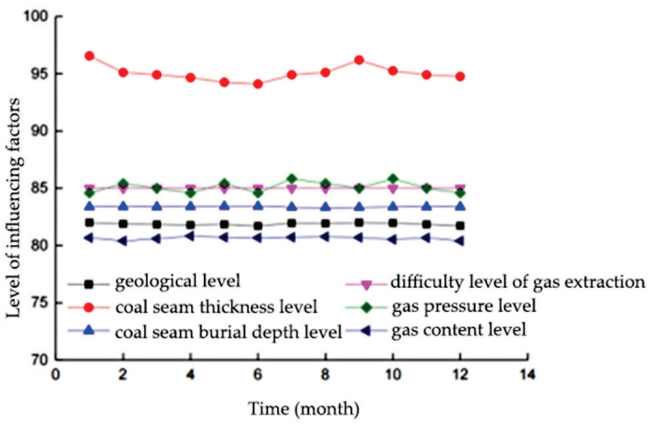

(**a**)

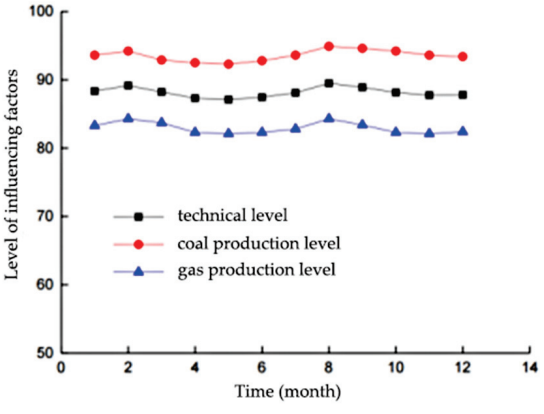

(**b**)

Figure 6. *Cont.*

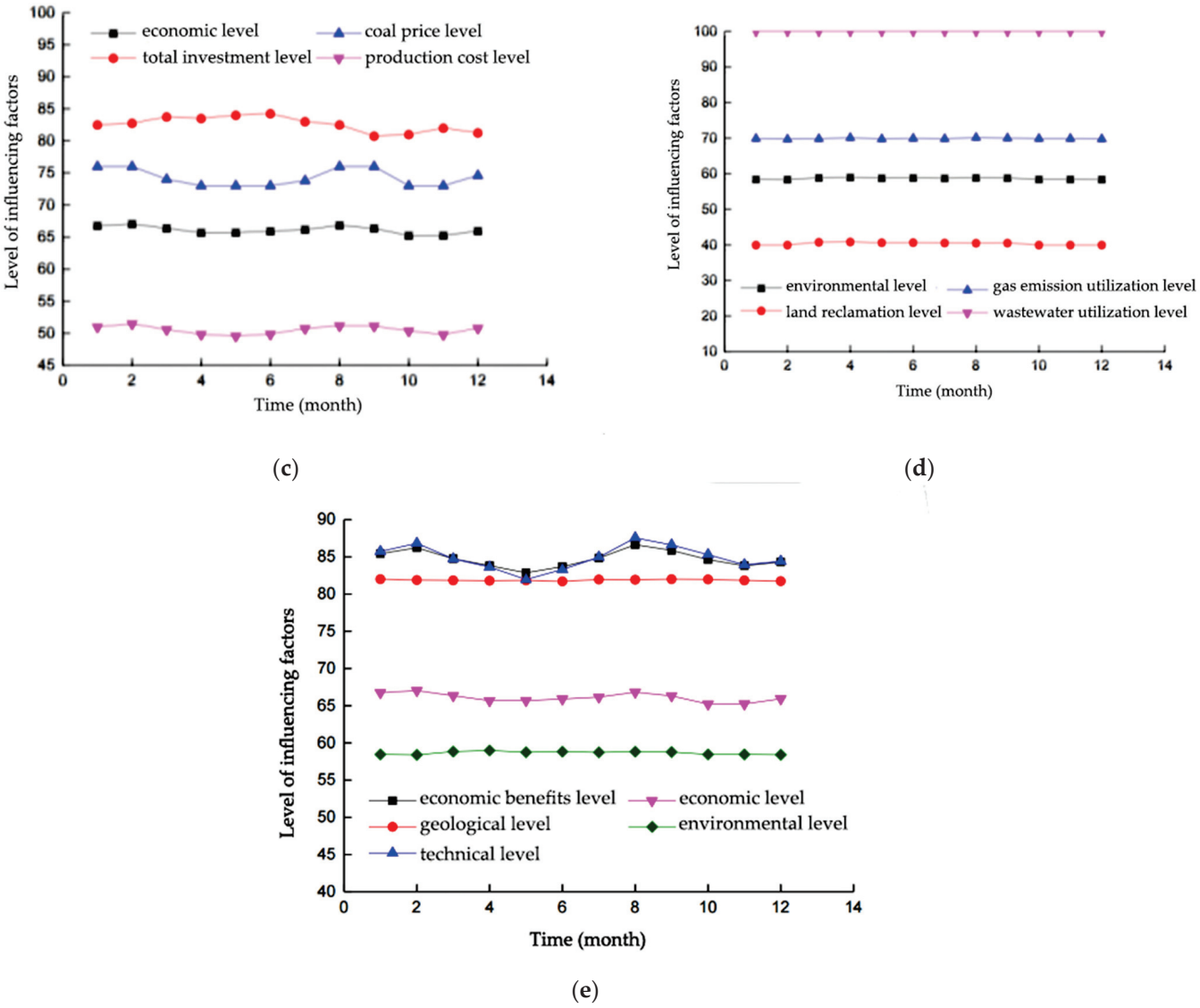

Figure 6. (**a**) Geological factors; (**b**) Technical factors; (**c**) Economic factors; (**d**) Environmental factors; (**e**) Relationship between the level of each influencing factor and the level of economic benefits.

From the analysis of its simulation data in Figure 6e, it can be obtained that the level of economic benefits in May is lower compared to other months. The technical level of May is at the lowest level among the 12 months. In conclusion, the mining techniques such as coal extraction rate and gas extraction rate can be used to improve the technology level to achieve better economic benefits.

The relationship between the influencing factors related to the safety level and its relationship is shown in Figure 7.

From Figure 7, it can be seen that the level of each influencing factor and the safety level show dynamic changes. All influencing factors have an impact on safety levels. Of these, the integrity of the electrical and mechanical equipment and the return airflow gas concentration has a greater degree of influence on the safety level. The higher the integrity rate of the electrical and mechanical equipment, the higher the safety during the mining process, which will ensure the safety of the coal and gas co-mining production process. The higher the level of return airflow gas, the lower the concentration of return airflow gas and the higher the safety level. Therefore, the following measures are taken to ensure the safe production of coal and gas co-mining. First, the performance of electromechanical equipment by strengthening capital investment is guaranteed. The second point involves

the strengthening of the frequency of personnel maintenance to improve the intact rate of electromechanical equipment. Thirdly, reduce the concentration of gas in the return stream during the mining process through ventilation and extraction.

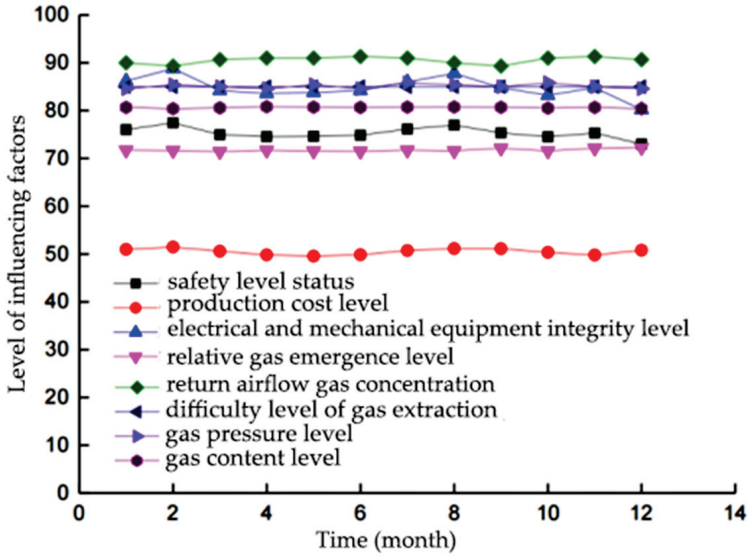

Figure 7. Relationship between the level of each influencing factor and the state of the safety level.

From the analysis of its simulation data in Figure 7, the safety level in December is lower compared with other months, in which the mechanical and electrical equipment completeness rate is at the lowest level of the 12 months. In summary, we can improve the integrity of electrical and mechanical equipment by strengthening the financial investment and frequency of personnel maintenance. Ultimately, the safe production of coal and gas co-mining is ensured.

3.2.3. Discussion

At present, the commonly used evaluation methods mainly include the hierarchical analysis method, fuzzy comprehensive evaluation method, grey comprehensive analysis method, etc. [29–31] The common feature of these methods is that they can only reflect the overall level of the evaluated object at a certain point in time but cannot reflect the influence relationship between the index and related factors within a certain time range, as well as the evolution trend of the index over time. The coal production process is always changing and dynamic evaluation is more in line with the needs of actual production. System dynamics, as a research method that integrates systems theory, cybernetics, and information theory, provides insight into current non-linear and time-varying phenomena and offers the possibility of evaluating complex systems. Therefore, the evaluation of coal and gas co-mining by introducing system dynamics is a topic worthy of further study.

4. Conclusions

In this paper, the coordination degree of the coal and gas co-mining system in the Zhuxianzhuang coal mine was simulated and evaluated. The main findings are as follows:

(1) Taking the Zhuxianzhuang coal mine as an example, the dynamic model of the coordination degree of the coal and gas co-mining system was established. The average co-mining coordination degree of the Zhuxianzhuang coal mine is 0.790. The coordination degree of this co-mining system is on the good side of coordination.

(2) The economic benefits and safety levels of the coal and gas co-mining system were analyzed based on the results of the simulation analysis subsystem. We compared the dynamic trend graphs of the two subsystems and their influencing factors and screened the main influencing factors that affect the degree of coordination of coal and

gas co-mining. We then suggested relevant opinions for the coordinated operation of the coal and gas co-mining system in the mine area.

(3) The reasonableness and practicality of the system dynamics model for the coordination degree of the coal and gas co-mining system were verified. The results show that the system dynamics model can effectively simulate the dynamic changes of different variable factors in the co-mining system.

Author Contributions: S.Z. contributed to the conception of the study; D.L. analyzed the data; S.Z. and D.L. interpreted the results; D.L. wrote the paper; all authors discussed the results and revised the manuscript. All authors have read and agreed to the published version of the manuscript.

Funding: This research was funded by the National Key Research and Development Plan (Grant no. 2017YFC1503103).

Institutional Review Board Statement: Not applicable.

Informed Consent Statement: Not applicable.

Data Availability Statement: Not applicable.

Acknowledgments: The authors wish to acknowledge financial support from the National Key Research and Development Plan (Grant no. 2017YFC1503103).

Conflicts of Interest: The authors declare no conflict of interest.

References

1. Hu, Z.J.; Liu, R.; Chen, Z. Strategic Thinking on the Ecological Development of Technology Under China's "Carbon Neutrality" Commitment. *Forum Sci. Technol. China* **2021**, *5*, 14–20. [CrossRef]
2. Liu, W.G.; Xu, X.; Han, J.Y.; Wang, W.; Li, Z.; Yan, Y. Trend model and key technologies of coal mine methane emission reduction aiming for the carbon neutrality. *J. China Coal Soc.* **2022**, *47*, 470–479. [CrossRef]
3. Ren, S.H.; Xie, Y.C.; Jiao, X.M.; Xie, H.P. Characteristics of Carbon Emissions During Coal Development and Technical Approaches for Carbon Neutral Development. *Adv. Eng. Sci.* **2022**, *54*, 60–68. [CrossRef]
4. Xie, H.P.; Wu, L.X.; Zheng, D.Z. Prediction on the energy consumption and coal demand of China in 2025. *J. China Coal Soc.* **2019**, *44*, 1949–1960. [CrossRef]
5. Liang, M.C.; Qin, Y.Y.; Fan, X.; Gao, X. Interpretation of the Main Conclusions and Suggestions of IPCC AR6 Working Group III Report. *Environ. Prot.* **2022**, *50*, 72–76. [CrossRef]
6. Markevych, K.; Maistro, S.; Koval, V.; Paliukh, V. Mining sustainability and circular economy in the context of economic security in Ukraine. *Min. Miner. Depos.* **2022**, *16*, 101–113. [CrossRef]
7. Yuan, L.; Zhang, N.; Kan, J.G.; Wang, Y. The concept, model and reserve forecast of green coal resources in China. *J. China Univ. Min. Technol.* **2018**, *47*, 1–8. [CrossRef]
8. National Bureau of Statistics of China. Statistical Communiqué of the People's Republic of China on the 2021 National Economic and Social Development. *China Stat.* **2022**, *3*, 9–26. Available online: https://kns.cnki.net/kcms/detail/detail.aspx?FileName=ZGTJ202203003&DbName=DKFX2022 (accessed on 20 September 2022).
9. Xie, H.P.; Zhou, H.W.; Xue, D.J.; Gao, F. Theory, technology and engineering of simultaneous exploitation of coal and gas in China. *J. China Coal Soc.* **2014**, *39*, 1391–1397. [CrossRef]
10. Dzhioeva, A.K.; Brigida, V.S. Spatial non-linearity of methane release dynamics in underground boreholes for sustainable mining. *J. Min. Inst.* **2020**, *245*, 522–530. [CrossRef]
11. Brigida, V.S.; Zinchenko, N.N. Methane release in drainage holes ahead of coal face. *J. Min. Sci.* **2014**, *50*, 60–64. [CrossRef]
12. Qin, B.; Shi, Z.S.; Hao, J.F.; Ye, D.L.; Liang, B.; Sun, W.J. Analysis of the Space–Time Synergy of Coal and Gas Co-mining. *ACS Omega* **2022**, *7*, 13737–13749. [CrossRef]
13. Yuan, L.; Guo, H.; Shen, B.T.; Qu, Q.D.; Xue, J.H. Circular overlying zone at longwall panel for efficient methane capture of multiple coal seams with low permeability. *J. China Coal Soc.* **2011**, *36*, 357–365. [CrossRef]
14. Yuan, L. Theory of pressure-relieved gas extraction and technique system of integrated coal production and gas extraction. *J. China Coal Soc.* **2009**, *34*, 1–8.
15. Li, X.S.; Peng, J.; Xie, Y.L.; Li, Q.H.; Zhou, T.; Wang, J.W.; Zheng, W.B. Influence of High-Temperature Treatment on Strength and Failure Behaviors of a Quartz-Rich Sandstone under True Triaxial Condition. *Lithosphere* **2022**, *2022*, 3086647. [CrossRef]
16. Wang, F.; Zhang, C.; Liang, N. Gas Permeability Evolution Mechanism and Comprehensive Gas Drainage Technology for Thin Coal Seam Mining. *Energies* **2017**, *10*, 1382. [CrossRef]
17. Xie, H.P.; Gao, F.; Zhou, H.W.; Cheng, H.M.; Zhou, F.B. On theoretical and modeling approach to mining-enhanced permeability for simultaneous exploitation of coal and gas. *J. China Coal Soc.* **2013**, *38*, 1101–1108. [CrossRef]

18. Cheng, Z.H.; Chen, L.; Zou, Q.L.; Wang, H.B.; Pu, S.J.; Qi, Q.X.; Liang, C.H.; Fan, S.W.; Su, S.L.; Yan, D.H. Study on high-efficiency co-mining technology system of coal and gas in contiguous seams: A case study of Shaqu Mining Area in Lüliang, Shanxi Province. *Coal Sci. Technol.* **2021**, *49*, 122–137. [CrossRef]
19. Liang, B.; Qin, B.; Sun, F.Y.; Wang, Y.; Sun, Y.N.; KHUONG, P. Application of evaluation index system of coal and gas co-extraction and evaluation model. *J. China Coal Soc.* **2015**, *40*, 728–735. [CrossRef]
20. Forrester, J.W. Industrial Dynamics. *J. Oper. Res. Soc.* **1997**, *48*, 1037–1041. [CrossRef]
21. Jiang, Q.X.; Zhao, Y.Z.; Wang, Z.L.; Fu, Q.; Zhou, Z.M.; Wang, T. Predicting and Evaluating the Water and Soil Resources Security Risk Based on System Dynamics and Variable Fuzzy. *J. Basic Sci. Eng.* **2018**, *26*, 780–792. [CrossRef]
22. Zhou, Z.L.; Cheng, Y.; Kou, T.; Guo, P.C. Air penetration combat forces plan evaluation method based on two-stage DEA model. *Syst. Eng. Electron.* **2018**, *40*, 797–804. Available online: https://kns.cnki.net/kcms/detail/detail.aspx?FileName=XTYD201804013&DbName=CJFQ2018 (accessed on 2 September 2022).
23. Sun, S.P.; Liu, F.L.; Xue, S. Comprehensive evaluation system for contribution degree of demand-side resources to renewable energy source integration. *Electr. Power Autom. Equip.* **2015**, *35*, 77–83. [CrossRef]
24. Yafei, W. Evaluation system construction of health policy based on system dynamics and complex network. *Clust. Comput.* **2019**, *22*, 4589–4596. [CrossRef]
25. Nguyen, T.; Cook, S.; Ireland, V. Application of System Dynamics to Evaluate the Social and Economic Benefits of Infrastructure Projects. *Systems* **2017**, *5*, 29. [CrossRef]
26. Lu, W.D.; Cheng, G.; Liu, J.; Li, X.C. Based on GAHP-BOCR Coal and Gas Simultaneous Extraction Decision Analysis. *Coal Technol.* **2017**, *36*, 146–149. [CrossRef]
27. Sherin, S.; Rehman, Z.; Hussain, S.; Mohammad, N.; Raza, S. Hazards identification and risk analysis in surface mines of Pakistan using fault tree analysis technique. *Min. Miner. Depos.* **2021**, *15*, 119–126. [CrossRef]
28. Kobylianskyi, B.; Mykhalchenko, H. Improvement of safety management system at the mining enterprises of Ukraine. *Min. Miner. Depos.* **2020**, *14*, 34–42. [CrossRef]
29. Zhong, S.H.; Jiang, X.D. Mining Mode Selection of Coal and Gas Simultaneous Mining Based on FAHP. *Coal Eng.* **2015**, *47*, 87–89. Available online: https://kns.cnki.net/kcms/detail/11.4658.TD.20151020.0948.056.html (accessed on 3 August 2022).
30. Liu, X.L.; Zhang, Z.Y. Risk analysis of coal and gas outburst using gray comprehensive evaluation. *J. Liaoning Tech. Univ. Nat. Sci.* **2012**, *31*, 609–612. Available online: https://kns.cnki.net/kcms/detail/detail.aspx?FileName=FXKY201205009&DbName=CJFQ2012 (accessed on 3 August 2022).
31. Xu, E.Y.; Li, X.J.; Xue, F. Assessment of coal and gas outburst by AHP-GT combined model. *Saf. Coal Mines* **2022**, *53*, 172–177. [CrossRef]

sustainability

MDPI

Article

Overlying Strata Movement and Mine-Pressure Weakening Law of High-Efficiency Longwall Paste Backfilling of Thick Coal

Qi Ma, Yidong Zhang *, Yu Zheng, Zexin Li, Guangyuan Song and Lei Hu

State Key Laboratory of Coal Resources and Safe Mining, School of Mines, China University of Mining and Technology, Xuzhou 221116, China

* Correspondence: ydzhang@cumt.edu.cn; Tel.: +86-139-5211-8118

Abstract: This work focused on the serious coal compression under buildings, railways, and water bodies in central and eastern China; the wide range of rock formation damage during the collapse mining process; the high pressure of mines; and difficulties in controlling surface subsidence after mining. The E1302 working face of Shanxi Gaohe Energy was taken as the engineering background in the work. The mechanical properties of gangue paste-filling materials were studied through laboratory tests, and the critical conditions for bending and fracture of the coal seam roof were analyzed. Discrete-element numerical simulation software was used to study the fracturing process of the roof, and the reasonable filling rate to ensure roof stability was determined to be 95%. Meanwhile, overlying stratum movement and mine-pressure weakening law were studied through numerical simulations and field measurement. The results showed that fracture development during the mining process of thick-coal paste filling was divided into the advanced development, re-compaction, and steady-state maintenance of fractures. Fractures advanced in a "sail shape" and developed only in the main-roof rock strata after recompaction. The maximum subsidence angle of the working face was 87.13° after mining, with a subsidence factor of 0.034 and a maximum horizontal movement coefficient of 0.71. The advanced stress value was weakened by 40%, and the influenced area was reduced by 13%. Overlying stratum movement was controlled, and mine pressures were significantly weakened. The work can provide a scientific basis for green backfill mining, roadway support design, and backfill mining equipment selection.

Keywords: green mining; paste filling; overlying stratum movement; fracture development; mine pressure weakening

1. Introduction

Concepts such as green mining and ecological mining have been put forward one after another recently. They aim toward a coal-resource mining model with optimal socio-economic benefits and minimal ecological environmental impact; the environmental disturbance caused by mines should be less than the environmental capacity. The model has been widely recognized by the international mining community [1–3]. The recoverable resources in the central and eastern regions are increasingly exhausted by long-term high-intensity coal mining. Resources are being exploited under buildings, railways, and water bodies in western China with a burial depth greater than 1000 m for energy succession as soon as possible [4,5].

The traditional caving method of coal pressing from floor to roof under buildings, railways, and water bodies can easily induce rock pressure shocks, water resource losses, surface subsidence, damage to building and transportation facilities, and prominent negative environmental effects (see Figure 1a). Traditional caving methods will face huge social and economic problems [6–8]. In contrast, paste backfill mining is used [9–13] (see Figure 1b) after coal resources are mined, and backfill bodies replace mined coal resources in time to carry the bulk density of overlying strata. Overlying stratum movement and

mine pressures under the bearing system are inevitably different from those of traditional caving mining.

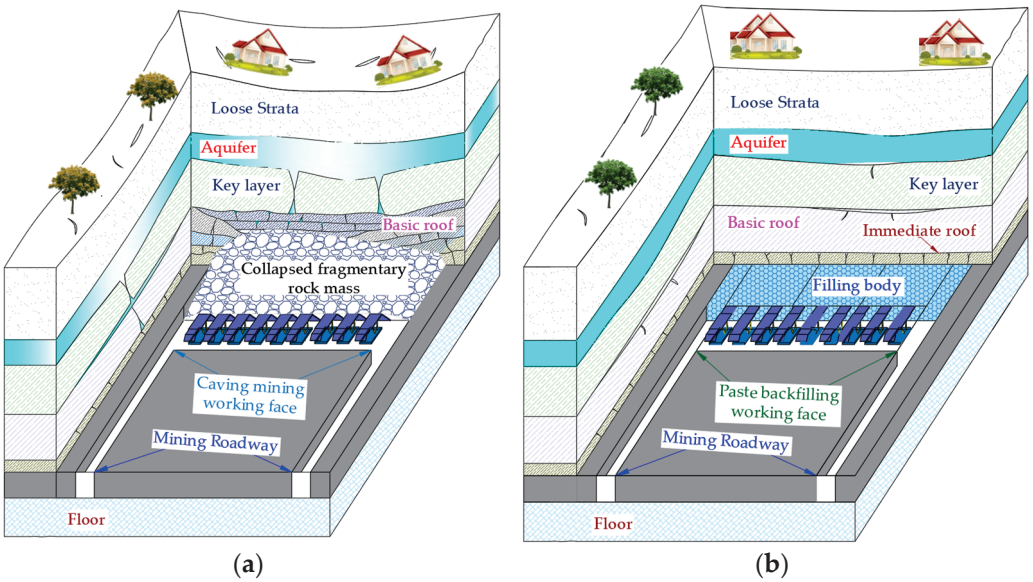

Figure 1. Mining ratios of filling and caving methods. (**a**) Caving mining, (**b**) Filling mining.

Therefore, overlying stratum movement and mine pressure weakening in paste backfill mining should be studied to understand the fractures of the backfill mining roofs, crack development in overlying strata, and the characteristics of surface subsidence and deformations after backfilling. This will all provide a theoretical basis and technical support for designing green paste backfill mining, selecting key backfill equipment, and promoting support parameters and ecological mining.

Researchers have studied the movement law of overlying strata and the appearance of mine pressures in backfill mining. Wang et al. [14,15] studied overlying stratum movement and the law of surface subsidence in deep wells and ultra-high water filling mining by combining various methods. The failure characteristics of overlying strata and the occurrence law of mine pressures were studied in the context of when the ultra-high water backfilling working face passes through the fault. Zhang et al. [16–19] combined the mining conditions to study the energy accumulation and stress concentration of coal seams under different filling methods and filling rates. The critical conditions for the occurrence of dynamic disasters in mines were determined, and the anti-scour mechanism of backfilling and mining was proved, which ensured the safe and efficient production of impacted mines. Xie et al. [20,21] established a mechanical model of the main-roof elastic-foundation sheet for backfill mining. The difference theory and the breaking criterion of the main bending moment were used to study the influences of elastic foundation coefficients of the filling body, the thickness of the main roof, elastic moduli, and boundary elastic foundation coefficients on the main bending moment and the rupture regularity of the main roof. The control mechanism of the immediate-roof state of solid-filling mining was revealed, and the precise control method was proposed to ensure roof stability.

Jia et al. [22–25] used the inclined borehole detection method to conduct long-term and multiple fixed-point detections at goaf roof according to the working face conditions of gangue filling in a mine in Tangshan. The distribution law of mining fractures in the roof was quantitatively described by the fracture density. A similar model test method was used for auxiliary analysis, which revealed the development process of roof fractures in gangue backfill mining. It provides a research basis for roof failures in backfill mining. Petlovanyi et al. [26–30] studied the characteristics of surface subsidence with different filling mining methods, filling rates, and coal seam thicknesses to establish a numerical simulation model. Simulation results were verified by field measurements. The influence of mine gangue

filling mining on surface buildings was evaluated with relevant deformation indices, which laid a foundation for studying surface subsidence in solid-filling mining. Sun et al. [31–34] used numerical simulation software and combined on-site industrial practice to study stress concentration and energy accumulation in the stope under different filling methods and filling rates. When the filling rate was increased, stress, energy accumulation, and mine pressures were weakened. Both the filling-to-collapse ratio (with a certain coal pillar) and the collapse-column ratio (with a certain length of the filling section) affected mine-pressure weakening, and the collapse-column ratio had a greater impact.

Researchers have studied the weakening law of rock pressures of overlying stratum movement in backfill mining. Most of the studies focused on thin and medium-thick coal seams instead of overlying stratum movement and the law of mine pressure weakening in backfill mining of thick coal. Combining the engineering geological conditions of the first working surface that Shanxi Gaohe Energy filled, the work studied the law of overlying stratum movement and mine-pressure weakening in thick-coal-seam filling and mining. It provides a theoretical basis for designing backfill mining roadway support, controlling mine pressures, selecting backfill support, and promoting the green mine concept.

2. General Situation of Filling in Lu'an and the Properties of Related Equipment and Materials

Lu'an Group is located in Changzhi City, Shanxi Province, China, and there is a serious problem of mine pressures under buildings, railways, and water bodies. The 12 coal mines in the headquarters have the mine pressure of 3.31 billion tons, which accounts for 37.7% of industrial reserves. Mine pressures seriously restrict the long-term sustainable development of Lu'an Group. Lu'an Group's Gaohe Coalmine Field is 13.4 km long from north to south and 4.9 km wide from east to west. Coal seam $3^{\#}$ is the most extensively mined. It has an approved production capacity of 7.5 million t/a and a service life of 40 years. The mine is connected to Changzi County in the west, Wuzhen Road in the north, Taiyuan-Jiaozuo Railway, National Highway 208, Zhuozhang River, and Changjin Expressway running through the north and south. There are 38 coal-pressing villages, and the total amount of coal-pressing in the whole mine is as high as 372 million t. If the problem of coal mining under buildings, railways, and water bodies cannot be solved, the mine will face the dilemma of resource depletion.

To this end, Gaohe Energy adopted "high-efficiency paste-filling mining" to solve coal pressing under buildings, railways, and water bodies; and the E1302 working face was first selected for filling. The coal seam buried depth of the E1302 working face was 404–425 m. The average buried depth was 415 m, the average coal seam thickness was 6.38 m, the uniaxial compressive strength of the coal mass was 9.49 MPa, and the average inclination angle of the coal seam was 2°. Above the coal seam had a 1.82 m thick mudstone immediate roof and 5.25 m sandy mudstone main roof. The east of the working face was the mine boundary; the west was the goaf of the E1303 working face; the south was the goaf of the E1302 top coal caving working face; the north was the +450 m horizontal east-wing roadway.

The roof of the working face was stable, and the isolation process of the filling area behind the working face could quickly achieve high-efficiency paste filling and mining. Secondly, the filling material has good fluidity and stability after setting and could carry the bulk density of overlying strata. Finally, the long-distance pumping of gangue gypsum filling materials should be stable and smooth. ZC8500/22/40 paste-filling hydraulic support was developed (see Figure 2a for filling support) to ensure the roof stability of the filling surface and the quick and safe completion of the filling and isolation work. Support was designed with a rear-hinged tail beam without descending, which could ensure the safety of operators in the area to be filled. The isolation structure was optimized, and the dedicated isolation structure could realize the rapid isolation and sealing of coal-seam roof and floor, which doubled the filling efficiency.

A large-displacement, high-pressure (19 MPa) paste-filling pump (see Figure 2b) was developed to ensure the stable and smooth long-distance pumping of gangue gypsum filling materials. The pumping capacity reached 250 m^3/h, and the output pressure exceeded 19 MPa. The impact pressure was low during reversing, and the failure rate was low after working for a long time. Self-flow could be realized in the self-standing pipe in the filling pipeline. The filling pump mainly provided power for paste flow in the horizontal pipeline, and the normal pumping pressure was 1–2 MPa. When the filling pipe reached full pipe flow (300 m^3), the pumping capacity was increased to nearly 4 MPa. At this time, the oil pressure of the filling pump reached 8–10 MPa, which was far from designed power. The large displacement filling pump could ensure the stable and smooth pumping of filling slurries.

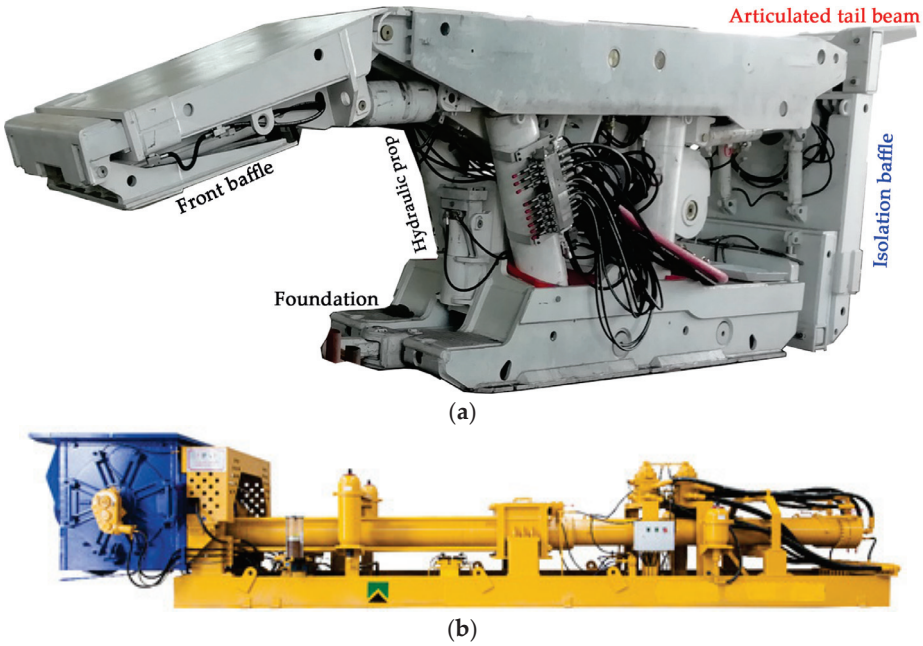

Figure 2. Filling equipment. (**a**) Filling hydraulic support, (**b**) Large-discharge-capacity filling pump.

According to the *Standard for the Test Method of Mechanical Properties of Ordinary Concrete* (GB/T 50081-2002) and *Methods for Determination of Physical and Mechanical Properties of Coal and Rocks* (GB/T 23561.1-2009) [35–41], multiple proportioning tests were carried out after sampling at Gaohe Energy Filling Station to ensure that the filling materials had good fluidity and could bear the bulk density of overlying strata after setting. Slump and expansion tests were performed on paste-filling slurries before preparing specimens, and uniaxial compression tests were performed on specimens of different ages after preparing specimens (see Figure 3 for the test process).

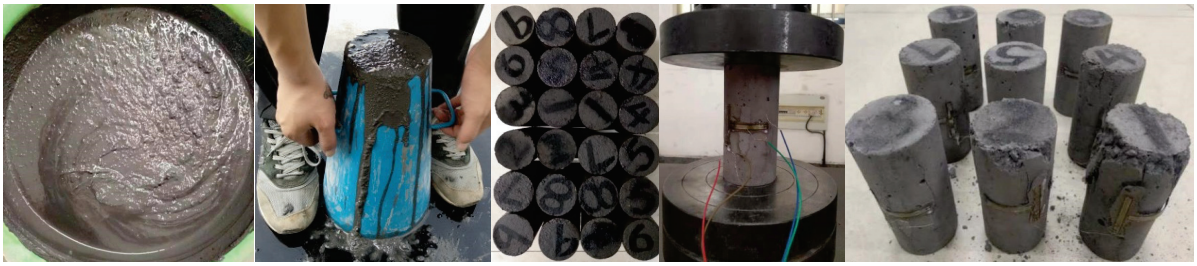

Figure 3. Gangue gypsum bodies.

Mass concentrations tested for the gangue fluidity test were 83, 84, and 85% (see Figure 4). The slumps of filling material slurries was 255–265 mm, and the expansion

of filling material slurries was 510–620 mm. When the slumps of gangue gypsum body materials were greater than 240 mm, they could be pumped and transported through pipelines. The mass concentration of gangue gypsum used by Gaohe Energy was about 81%, so the flow performance of Gaohe gypsum filling materials could meet the requirements of engineering practice.

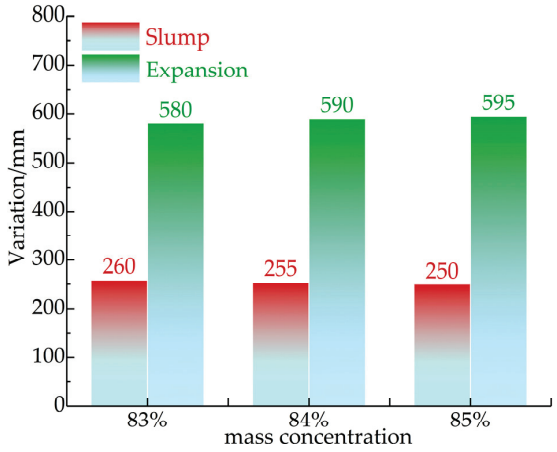

Figure 4. Statistics of the paste fluidity test.

Specimens were prepared and tested at the ages of 1, 3, 7, 14, 21, and 28 d, and the total stress–strain curve of the gangue gypsum body material was drawn (see Figure 5). The stage characteristics of the stress–strain curve at each age had high consistency, and the stress–strain curve could be divided into four stages of OA, AB, BC, and CD. The OA section was the initial compaction stage; the AB section was the elastic stage; the BC section was the yield stage; the CD section was the failure stage. The peak value of the curve gradually increased with age, and the slope of the AB section increased gradually. The uniaxial compressive strength and elastic modulus of the gangue gypsum body increased gradually with age. The ages of 21 d and 28 d were nearly coincident, indicating that the elastic modulus of the gangue gypsum body increased very little after 21 d. The uniaxial compression test curve was similar to that of rocks, and uniaxial compressive strength was 5.45 MPa, which could bear the bulk density of overlying strata.

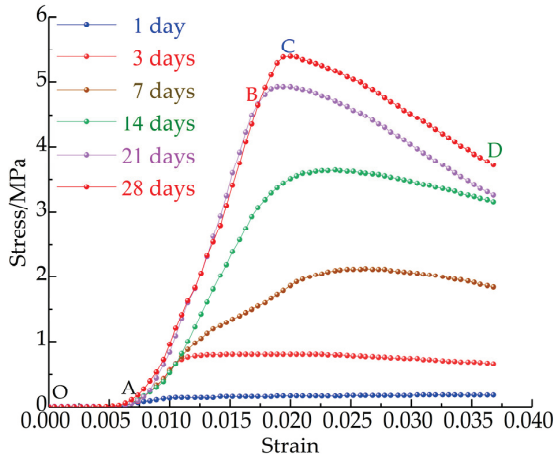

Figure 5. Mechanical properties of gangue gypsum bodies.

The coal mass mined in Lu'an Mining Area is coal 3#, and the thickness of the coal seam is relatively large. If full-thickness backfill mining is used at one time, the height of the backfill area is large, and the stability of backfill materials before the initial setting is difficult to control. In addition, the stability of the coal walls of the working face with large

mining height is not easy to control. Therefore, layered filling mining can be selected—according to the thickness of the coal seam of coal 3#, the coal mass can be mined in two layers, that is, upper-layered and lower-layered mining.

If upper-layered mining is adopted, the lower-layered coal mass shall be mined first. Mining causes a large disturbance to upper-layered coal, and broken coal falls after the disturbance. When the upper layer is mined again, the coal mass is broken, and the control of coal walls and roadway retention is relatively difficult. If lower-layered mining is adopted, the upper-layered coal mass is mined, and the disturbance to the lower-layered coal mass is relatively small. Backfill is condensed into a whole after mining, and the coal wall and paste false roof are relatively stable during mining lower layers, which is conducive to safe and efficient mining. Figure 6a shows the layout of the working face during downward layered mining.

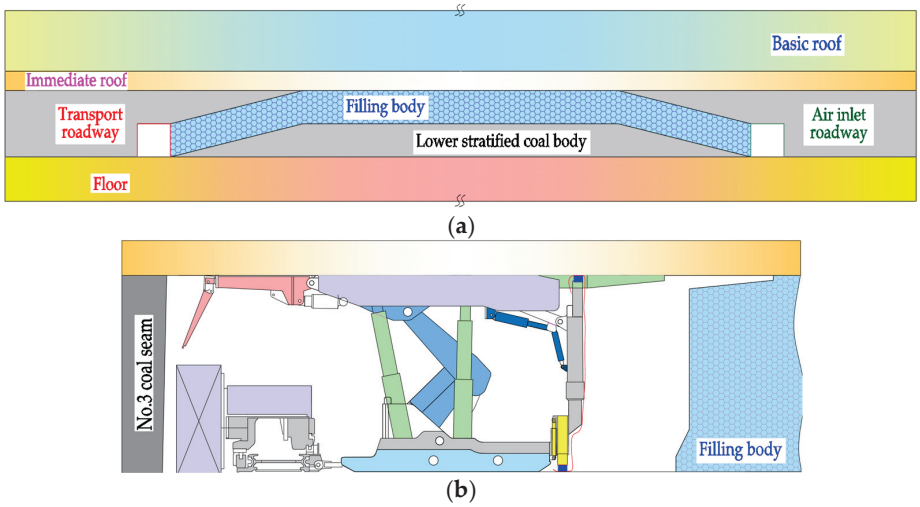

Figure 6. Filling workingface layout and recovery process. (**a**) Layout of the filling working face, (**b**) Backfilling process.

The upper and lower working faces share a set of mining tunnels in layered filling mining. When the upper layered working face is mined, there is a 30 m climbing area at both ends of the working face. Two mining tunnels are reserved for lower-layer mining (see Figure 6b for the mining process of the backfilling working face). The coal mining team carries out processes such as coal cutting, coal loading, coal transportation, and rack shifting with the shearer cutting coal as the main line. When there is enough area behind the working face for filling, the filling shift first completes roof isolation. Meanwhile, the ground filling station uses mortar to push water and gangue slurries to push mortar. The mortar along the filling pipe reaches the front of the work, and roof isolation has been completed. It enters the normal filling stage from the initial filling stage after the gangue slurries appear in the working face.

3. Roof Stability Analysis of Backfill Mining

Roof stability control is the key to whether the paste-filled working face can be recovered safely and efficiently. Roof stability also directly affects the overlying stratum movement and surface subsidence. The key to roof stability control is the breaking step distance of the roof and the bending deflection during breaking. There is a lot of free space in the area where the original coal mass is located after mining, and stope stress is redistributed. The load borne by mining overlying strata generally includes the self-weight and the load generated by overlying strata. It is generally assumed that the rock load is uniformly distributed for the convenience of analysis. Overlying strata interact with evenly distributed loads, and upper and lower strata deform synchronously to form a composite beam structure [42]. The roof of the coal seam forms a fixed beam structure under the

support of the coal mass behind incision and the coal mass in front of the working face. The fixed beam bends and sinks under overlying strata and their self-weights (see Figure 7 for the stress situation).

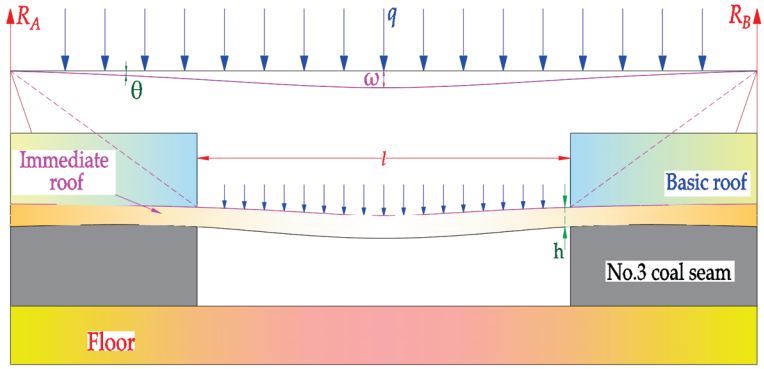

Figure 7. Mechanical model of roof fracture caving.

It is necessary to ensure roof stability during the mining process of the working face (see Figure 7) for safe and efficient mining. Bending subsidence ω of the working-face roof should be less than the equivalent mining height, and roof stress q can be calculated according to the composite beam theory. Opposite force R_A and R_B are formed at both ends of the clamped beam in the process of bending and sinking the clamped beam. The symmetry of the clamped beam is used to obtain Equation (1) [43,44].

$$R_A = R_B = \frac{ql}{2} \tag{1}$$

Shear force Q_x in the section at position x from the left end of the beam is

$$Q_x = R_A - \frac{q}{2}x = \frac{ql}{2} - \frac{q}{2}x \tag{2}$$

Bending moment M_x of this section is

$$M_x = R_A x - \frac{ql}{2}x + M_A \tag{3}$$

where M_A is the bending moment at the left end. $M_A = -\frac{ql^2}{12}$, which is substituted into Equation (3) to obtain

$$M_x = \frac{q}{12}(6lx - 6x^2 - l^2) \tag{4}$$

When $x = 0$ and l, $M_{max} = -\frac{ql^2}{12}$. When $x = \frac{l}{2}$, $M_{\frac{l}{2}} = \frac{ql^2}{24}$.

The deflection curve of a clamped beam is approximated by differential equation $\omega'' = -\frac{M(x)}{EI}$. ω is solved to obtain

$$EI\omega' = -\int M(x)dx + C_1 \tag{5}$$

where E is the elasticity modulus, GPa; I the section inertia, m^4; I the sectional inertial distance, m^4; l the beam width, m; h the beam height, m.

$$EI\omega = -\int \left[\int M(x)dx\right]dx + C_1x + C_2 \tag{6}$$

Equation (4) is substituted into Equation (6) to obtain

$$EI\omega = -\frac{q}{12}(lx^3 - \frac{x^4}{2} - \frac{l^2x^2}{2}) + C_1x + C_2 \tag{7}$$

When $x = 0$ and l, $\omega = 0$. $C_1 = 0$ and $C_2 = 0$, so

$$\omega = -\frac{q}{24EI}(x^4 + l^2x^2 - 2lx^3) \tag{8}$$

When the maximum deflections is $x = \frac{l}{2}$, $\omega_{max} = \frac{ql^4}{384EI}$.

According to the maximum tensile stress intensity criterion of material mechanics, the ultimate span of the beam without fractures is

$$l \leq 2h\sqrt{\frac{\sigma}{nq} - \frac{1}{5}} \tag{9}$$

where l is the safe span of the basic roof, m; h the roof thickness, m; σ the tensile strength of the roof, MPa; n the safety factor; q the load of the basic roof, MPa.

According to the theoretical calculation of composite beams, the load on the immediate roof is 0.042 MPa. Laboratory tests show that tensile strength σ of the immediate mudstone roof is 1.50 MPa; the elastic modulus E is 5.78 GPa; thickness h of the mudstone immediate roof is 1.82 m. Considering the safety of backfilling mining, the safety factor n is 1. The initial breaking step distance of the immediate roof is 19.8 m, and the maximum bending deflection is 0.29 m. Gaohe Energy adopts layered mining, and the thickness of the upper layer is 3.2 m. If the stability of the direct roof is guaranteed without breaking, theoretically, the layered filling rate should be greater than 91%, and the overall filling rate should be greater than 95.4%. In the following, it is proposed to further study the bending fractures of roof under caving mining and different filling rates utilizing UDEC discrete element numerical simulation software. The law of overburden migration, fracture development, and mine pressure weakening in thick-coal backfill mining should be explored.

4. Simulation of Overlying Strata Movement and Mine-Pressure Weakening in Thick-Coal Backfill Mining

According to the engineering geological overview of the first E1302 working face that Gaohe Energy filled, a numerical simulation model with a width of 350 m and a height of 120 m was established using discrete-element numerical simulation software (UDEC 6.0 version). Seventy-five meter boundary coal pillars were left on the left and right sides of the model to eliminate the boundary effect. The stress of 7.6 MPa was applied to the model roof to simulate the bulk density of overlying strata, which constrained the movement of both sides and floor. The 200 m wide area in the middle of the model was the mining area. Figures 8 and 9 show the specific simulation model and the parameters of rock strata, respectively.

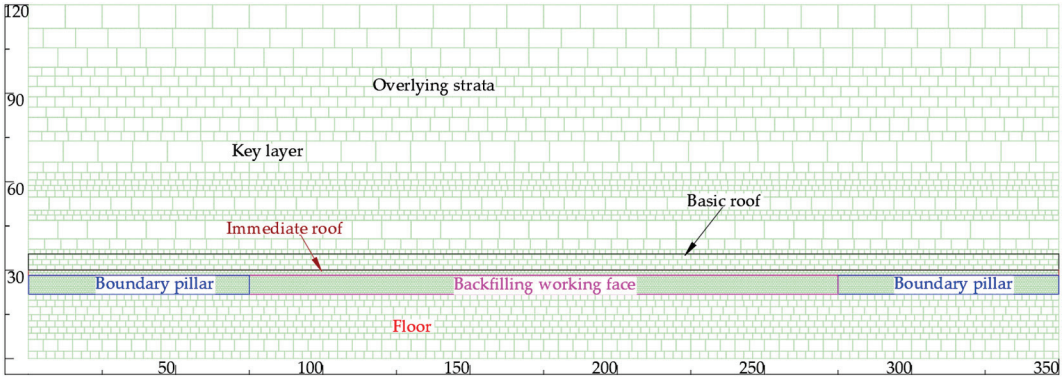

Figure 8. Numerical simulation model.

Histogram	L	B	Th	V	Ts	C	E
	Fine grained sandstone	388.51	4.52	2527	8.73	68.35	38.4
	Sandy mudstone	393.03	1.55	2489	4.42	33.14	15.2
	Siltstone	394.58	1.85	2602	7.31	56.27	21.3
	Sandy mudstone	396.43	6.32	2493	3.66	29.03	13.8
	Sandy mudstone	402.75	3.50	2501	3.52	28.75	14.1
	Fine grained sandstone	406.25	1.62	2531	7.84	58.32	38.6
	Sandy mudstone	407.87	5.25	2431	4.33	31.21	12.9
	Mudstone	413.12	1.82	2463	4.58	25.36	16.2
	Coal	414.94	6.38	1487	1.12	11.69	4.7
	Mudstone	421.32	2.00	2465	3.64	23.94	14.5
	Siltstone	423.32	2.23	2621	7.44	55.32	20.6
	Fine grained sandstone	425.55	2.67	2574	8.32	58.46	35.7
	Sandy mudstone	428.22	8.41	2498	3.26	31.08	13.6

Figure 9. Mechanical parameters and histogram of rock strata. Note: L: rock stratum name; B: Burial depth; Th: depth of stratum; V: density; Ts: tensile strength; C:compressive strength; E: elastic modulus.

The mechanical parameters of rock strata were assigned after the modeling was completed. The working face consistent with the site was excavated step by step after the model reached the equilibrium state again, and the support unit was used to simulate the support. The support units of the previous step were removed during the excavation of the next step. Simulation content concluded the bending failure process of the working face roof under caving mining and filling rates of 90 and 95%. The fracture development of overlying strata and the characteristics of layered-filling mine-pressure weakening were simulated by filling and caving methods after a reasonable filling rate was determined.

4.1. Simulation Analysis of Roof-Fracture Failure in Backfill Mining

Figures 10a and 11a show the bending, subsidence, and damage of the roof during the advancing process of the working face under the caving method. Figures 10b–c and 11b–c show the bending, subsidence, and failure process of the roof during the advancement of the working face when the filling rates are 90 and 95%, respectively.

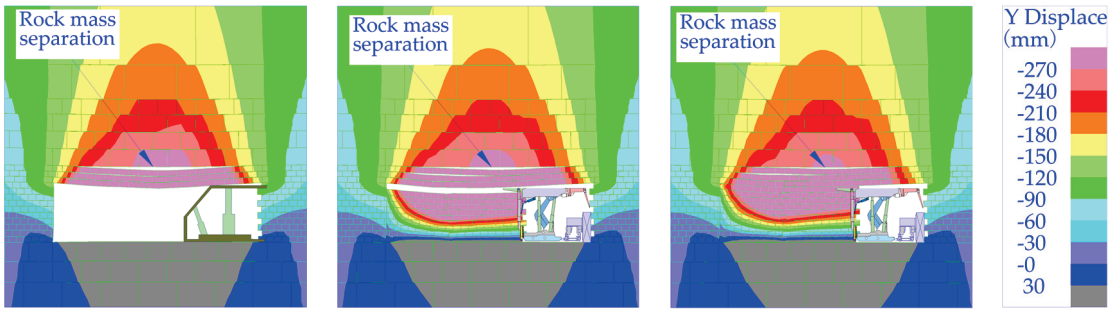

Figure 10. Immediate-roof bending and sinking. (**a**) Caving mining. (**b**) Filling rate of 90%. (**c**) Filling rate of 95%.

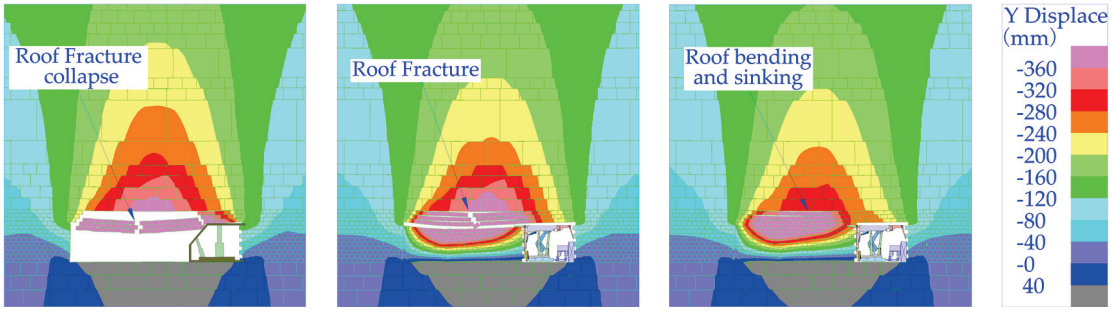

Figure 11. Immediate-roof sinking and caving. (**a**) Caving mining. (**b**) Filling rate of 90%. (**c**) Filling rate of 95%.

The immediate-roof thickness of the working face is 1.82 m, and the thickness of the main roof is 5.25 m. The immediate roof bends and sinks in both caving mining and filling mining during the advancing of the working face. The immediate roof is bent and separated from the main roof due to the large thickness of the main roof and the relatively small amounts of bending and sinking. There is a lot of free space under roof after coal masses are mined in the case of caving mining. The immediate roof breaks and collapses during moving forward.

When the filling rate is 90%, the equivalent mining height below the working face is 0.64 m, and fractures and caving can also occur during the advancement of the working face. When the filling rate is 95%, the equivalent mining height is 0.32 m, which exceeds the limit breaking bending deflection of the immediate roof of 0.29 m. However, the filling body is contacted in time after roof bends and sinks, and there is no room for breaking. Therefore, the immediate roof will not break and slump, which can ensure roof integrity. The filling rate should be greater than 95% to ensure the stability of backfill-mining roof. When the filling rate is 95%, although the roof does not break down, fractures still develop. Figure 12 shows fracture development in caving mining and filling mining.

Fractures in overlying strata are divided into open and slip ones during the mining process of the working face. Opening fractures are caused by the separation and fracturing of overlying strata; slip fractures are caused by slip dislocations in strata. Rock masses above the working face produce a large number of open fractures during the slewing and subsidence process (see Figure 12a). However, a large number of slip fractures are generated during overlying stratum movement above the rear side of the working face. A large number of open fractures above the middle area of the goaf are gradually compacted during the subsidence of overlying strata, and the total amount of fractures is small. Both open and slip fractures are develop above the incision. Fractures have developed to 17.37 m behind the working face in a "saddle shape" as a whole. There are mainly open fractures above the working face developing in a "sail shape" during the advancing process of the working face in the case of backfill mining. The advanced working face developed at 11.89 m, and the fracture height above the coal seam is 30.5 m.

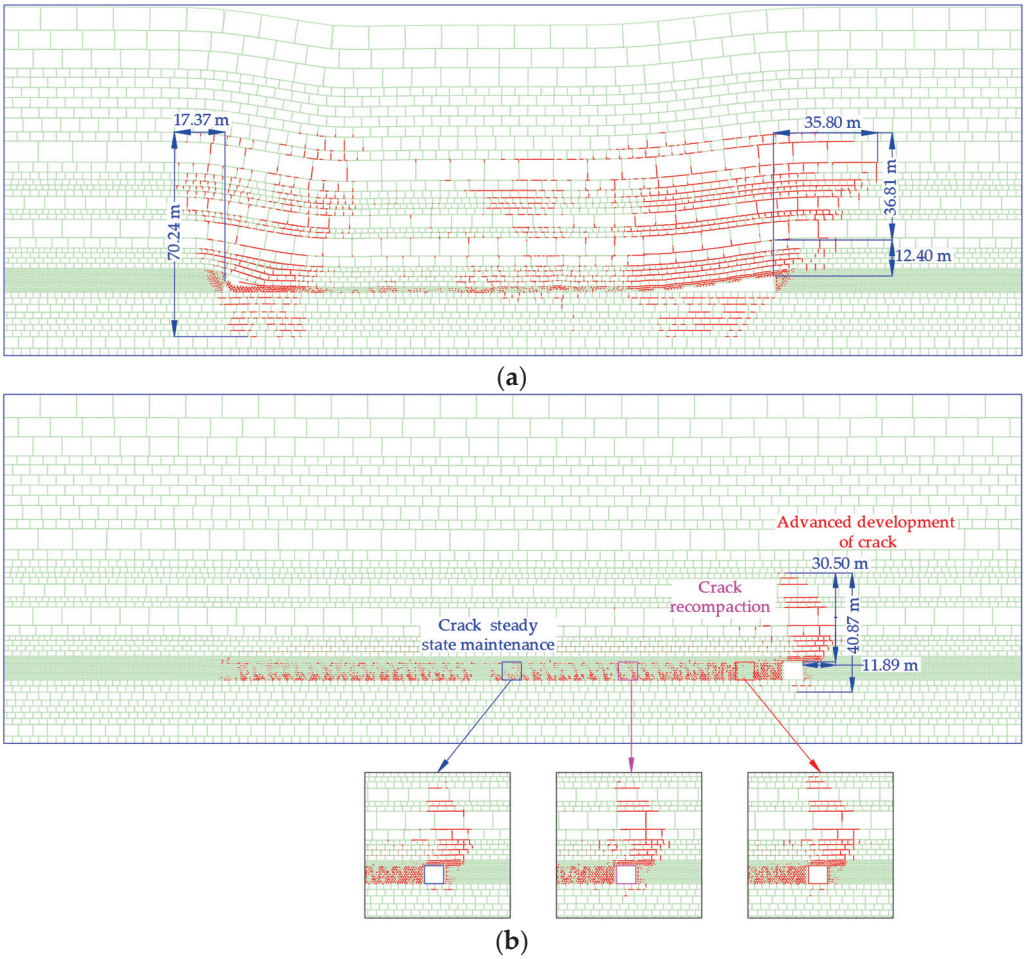

Figure 12. Fracture development in different mining methods. (**a**) Caving mining, (**b**) Backfill mining.

The backfill body replaces the mined coal mass in time and directly contacts the backfill body after bending and sinking without breaking. The movement of overlying rocks is restricted after contacting backfill, and fractures generated by overlying strata at the working face are re-compacted. Therefore, fracture development in filling and mining can be divided into the following stages: advanced fracture development, re-compaction of fissures, and steady maintenance of fractures. Advanced fracture development presents a "sail-shaped" progression. The fracture-recompacting area is above the rear side of incision, and the rear fractures only appear in main-roof strata. Figure 13 shows the movement curves of overlying strata after mining with different mining methods.

Entire immediate roof cave-in occurred after the caving mining working face was recovered, and the maximum displacement is 6335 mm. Immediate roof has a certain crushing effect after the collapse, and crushed rock masses of immediate roof after crushing and swelling can reduce the falling space of main-roof rock masses. Therefore, the maximum subsidence of main roof is 5914 mm, and the maximum displacements of the key layer and overlying strata are 5046 and 4407 mm, respectively. When backfill mining is used, the equivalent mining height is 320 mm, and the maximum subsidence of the immediate roof is 315 mm. The curved and subsided immediate roof controls the overlying stratum movement of the main roof. The immediate roof only sinks without distending, and the maximum subsidence of the main roof is 282 mm. The maximum subsidence degrees of the key layer and overlying strata are 243 and 226 mm, respectively. Above overlying strata is the quaternary unconsolidated formation, and the unconsolidated formation sinks synchronously with the subsidence of overlying strata. The subsidence coefficient of simulated caving mining is 0.688, and it is 0.035 when the filling rate is 95%.

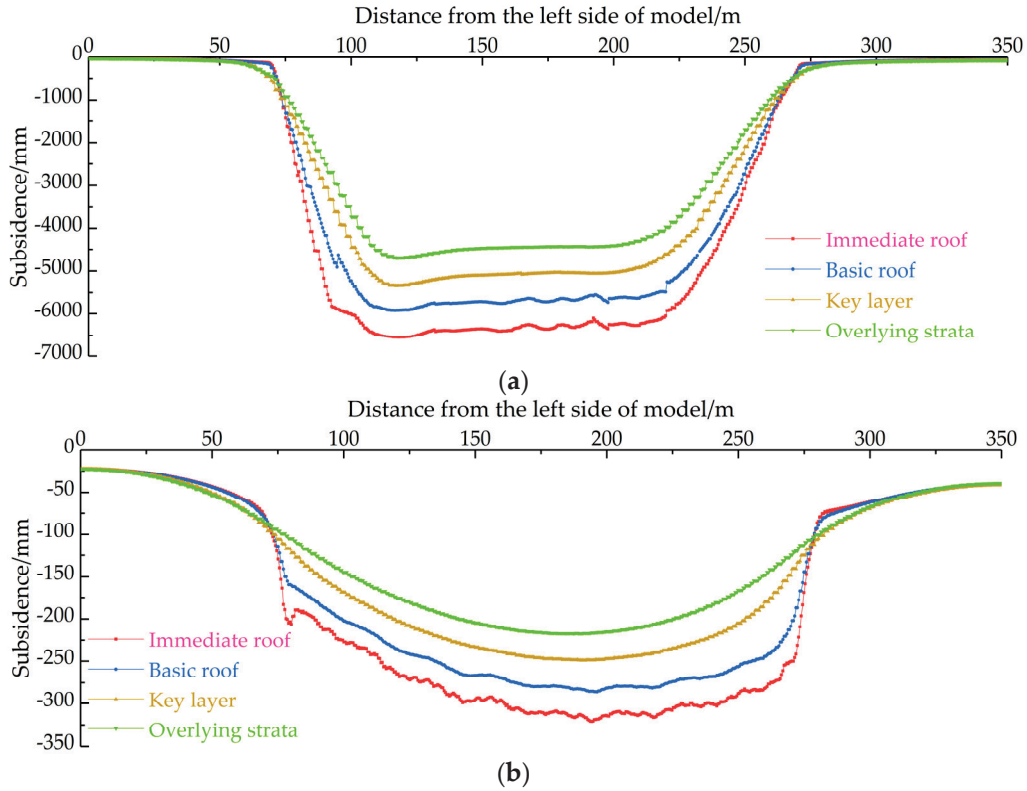

Figure 13. Curves of overlying stratum movement with different mining methods. (**a**) Caving mining, (**b**) Backfill mining.

4.2. Simulation of Advanced Stress Distribution and Weakening Law

Overlying strata above the working face form a cantilever beam structure which showed rotary sinking after the working face was mined. Coal masses in front of the working face were squeezed during the process of overburden slewing and subsidence, which resulted in stress redistribution in front of the coal walls of the working face—that is, the leading bearing pressure appeared. As the working face moves forward, the advanced support pressure moves forward. The stress of the coal wall in front of the working face increases, and coal masses are prone to deformations and failure under high support pressures. Therefore, the influences of advanced bearing pressures should be considered in the roof management of the working face and the support of the mining roadway. The section derives the stress data of the coal seam when the roof is managed by the caving method and the stress data of different layers in the case of layered mining. In addition, the distribution law of the advance support pressure in backfill mining has been studied. The caving method was used to manage the advanced roof stress (see Figure 14a), and Figure 14b,c show the advanced stress distributions of upper and lower layers, respectively.

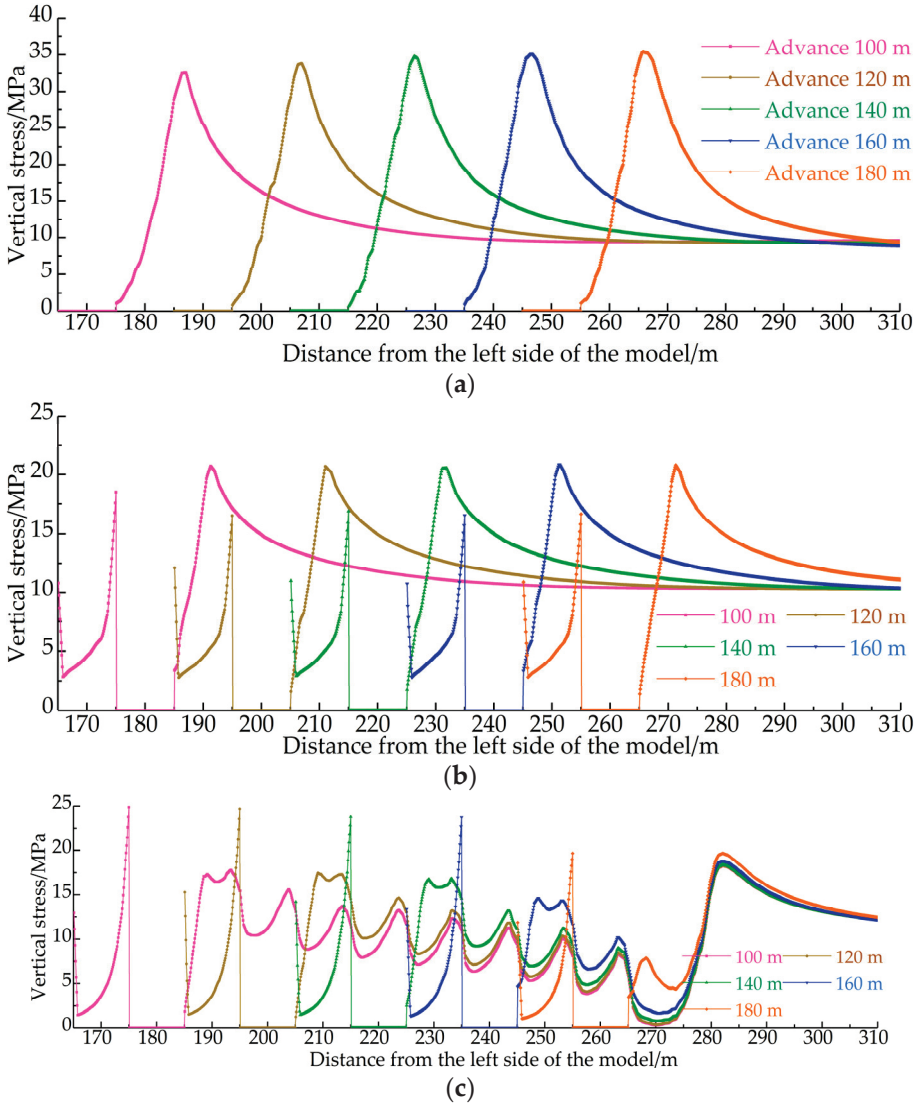

Figure 14. Distribution law of advanced stress during the advancing process of the working face. (**a**) Caving mining, (**b**) Upper-layered mining, (**c**) Lower-layered mining.

Figure 14a shows the advanced stress distribution curve of 100, 120, 140, 160, and 180 m in the caving mining face. When the working face advances by 100 m, the leading stress peak is 33.2 MPa in the simulation, and the peak position is 11.2 m away from the coal wall of the working face. The peak value of the advanced stress of the working face increases to 33.8 MPa after advancing to 120 m from incision, and the peak position is 11.6 m from the coal wall of the working face. When it continues to advance to 140 m from the cut, the peak value of leading stress increases to 34.5 MPa, and the peak position is 11.7 m from the coal wall of the working face. When the working face continues to advance to 160 and 180 m from the cut, the advanced stress peak value rises to 34.8 MPa, and the peak position is 11.8 m away from the coal wall of the working face. Peak stress always remains around 34.8 MPa after moving forward, and its concentration factor is 3.48. The distance from the peak point to the coal wall is unchanged at 11.8 m, and the influence range of the leading stress is about 55.4 m.

The average coal thickness of the E1302 working face is 6.4 m, and the coal mining is carried out by layered filling mining. The upper and lower layers are both 3.2 m deep at an average filling rate of about 95% and a simulated filling rate of 95%. Figure 14b shows the leading stress distribution during the advancing process of the upper layer working face. When the backfilling face is advanced by 100 m, the advanced stress peak is 20.6 MPa,

which is 7.2 m away from the coal wall of the working face. The advanced stress peak is 20.7 MPa after advancing 120 m to incision. The advanced stress peak is 20.8 MPa after advancing 140 m away from incision. When the distance between the working face and incision is greater than 160 m, advanced stress distribution in front of the working face reaches a stable state. The peak value of advanced stress is 20.9 MPa, with a peak value of the stress concentration factor of 2.09 and an influence range of advanced stress of about 48.2 m.

When the lower layered working face advances by 100 m, the advanced stress peak is 17.9 MPa. Advanced stress decreases slightly after advancing to 120 and 140 m. The advanced stress peak value drops below 15 MPa after the working face advances to 160 m. Advanced stress shows a waveform decrease as a whole during the mining process of lower-layered filling. The peak value of advanced stress are smaller than those of the upper-layered working face. When the upper-layered working face is mined and filled, the backfill body is not fully compacted after overlying strata subsidence, which causes the failure of overburden stress to be completely transferred to the lower-layered working face. Meanwhile, parts of the roof have been damaged during the upper layer mining process, and the overhang distance of the cantilever beam is limited. Therefore, the advanced stress is smaller than that of the upper-layered filling. Compared with caving mining, the mining pressure of backfill mining is significantly weakened. The stress concentration factor is weakened by 40%, and the influence range of advanced stress is reduced by 13%.

5. Discussion and Analysis of Research Results

We used on-site research on the geological profile of coal seams in the Lu'an Mining Area to grasp the geological profiles of coal seams in the mining area. The mechanical properties of the paste-filling body were obtained through laboratory tests. A mechanical analysis model was established to analyze the bending and breaking characteristics of the roof. The movement of the overlying strata, failure of filling mining, and leading stress distribution were studied through numerical simulation and comparison. These research results provide a theoretical basis for selecting filling materials for filling mining and determining filling rates. The control of rock formation movement and surface subsidence can be ensured with efficient and economical mining. However, the model established in the research process is under conventional geological conditions and does not consider overburden stratum movement and ore-pressure weakening under special geological conditions such as faults and collapse columns. More in-depth research will be performed. The distribution of ore pressures and the actual measurement of surface subsidence were carried out in Gaohe Coal Mine in Lu'an Mining Area to verify the reliability and authenticity of the research results. Overburdened stratum movement and the weakening law of mine pressures were further studied.

6. Field Measurement and Analysis

Test points were set up on the surface corresponding to the first test surface of Gaohe backfilling to explore the law of overlying stratum movement and mine pressure weakening in thick-coal, longwall, high-efficiency paste backfill mining. The subsidence and deformation of the working face of the backfill mining were used to study overlying stratum movement in the backfill mining. A borehole stress gauge was installed in the coal mass in front of the working face to monitor the change characteristics of advanced stress during the advancing process of the working face, which could study the law of mining pressure weakening in backfilling. Figure 15 shows the layout of the station.

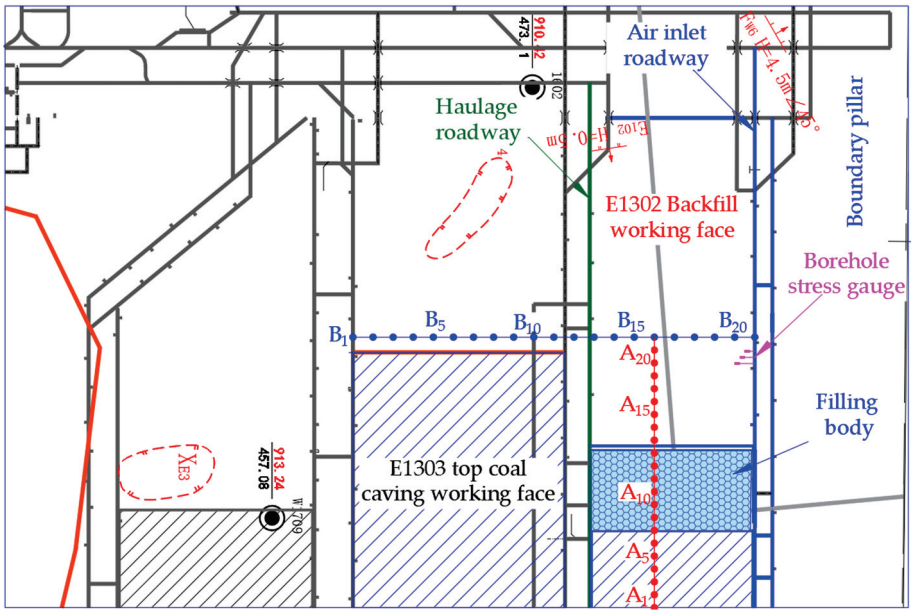

Figure 15. Monitoring locations.

A total of two survey lines were arranged for the surface subsidence monitoring of the filling surface (see Figure 15). Survey line A is the trend with a length of 600 m. There are a total of 24 measuring points, of which three are control points and 21 are deformation monitoring points. Survey line B is the inclination one with a length of 510 m and a total of 21 deformation monitoring points. There were a total of 11 monitoring iterations from the station's deployment in December 2019 to the completion of monitoring in June 2022 (see Figure 16 for deformation monitoring results). The advanced stress monitoring station is arranged in the air inlet roadway to eliminate the influence of the adjacent goaf on stope stress. A total of three borehole stress gauges are present, and the hole depths are 15, 10, and 5 m, respectively; the borehole stress gauge with a hole depth of 5 m failed to leak during the monitoring process. Figure 17 shows specific monitoring results.

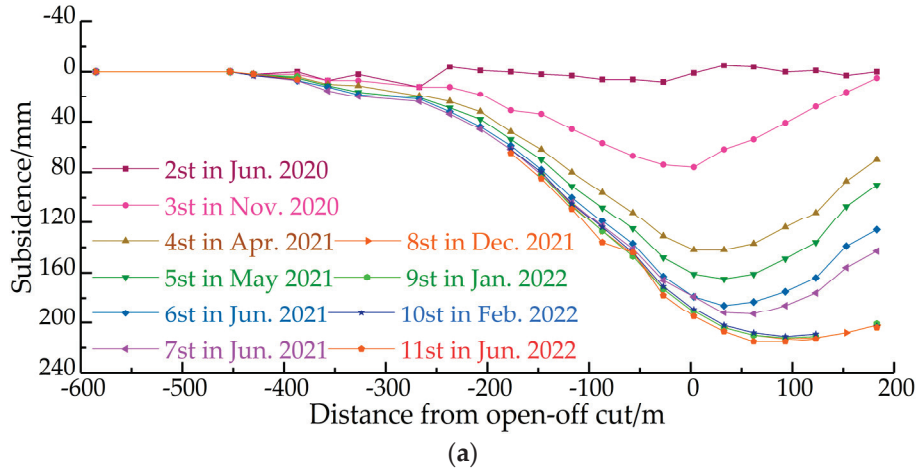

(**a**)

Figure 16. *Cont.*

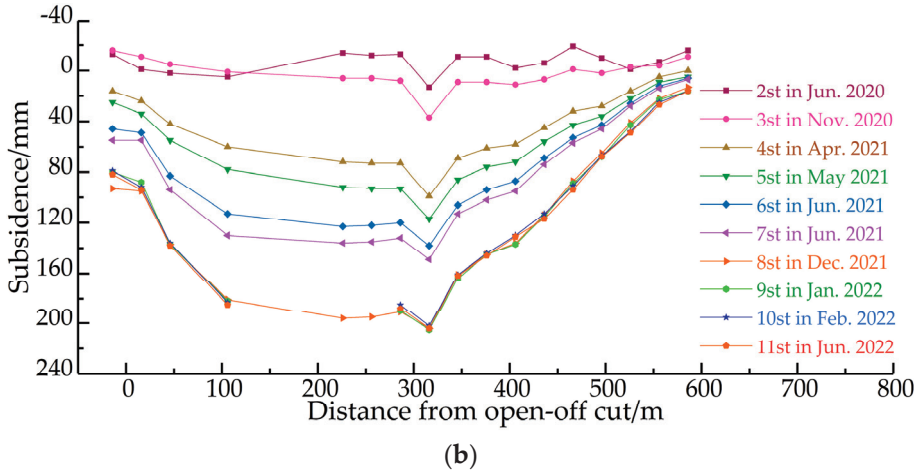

Figure 16. Lines of surface subsidence monitoring. (**a**) Deformations of line A, (**b**) Deformations of line B.

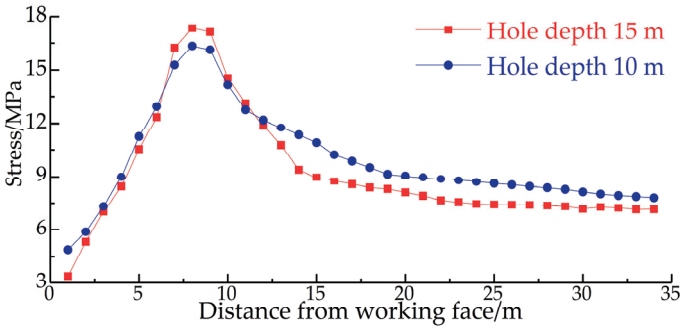

Figure 17. Lines of advanced stress monitoring.

Affected by geological factors, the maximum subsidence point of the surface subsidence basin is measuring point B16, and the middle distance from the goaf is 20.75 m. According to the average burial depth of the coal seam of 415 m, the maximum subsidence angle is calculated as $\theta_1 = \arctan(\frac{415}{20.75}) = 87.13°$. The maximum sinking position of survey line A occurred at measuring point A17, and the maximum sinking amount is 214 mm. The maximum horizontal movement position occurred at measuring point A13, coinciding with a subsidence coefficient of 0.035, the maximum horizontal movement of 80 mm, and a horizontal movement coefficient of 0.37. The maximum sinking position of survey line B occurred at measuring point B16, coinciding with the maximum sinking of 204 mm and a sinking coefficient of 0.032. Maximal horizontal movement occurred at measuring point B21, coinciding with the maximum movement of 144 mm and a horizontal movement coefficient of 0.71. The maximum subsidence of the survey line at the top of numerical simulation's overlying rocks was 226 mm, and the model roof was a quaternary unconsolidated formation, which sank with the subsidence of the rock stratum. Therefore, simulations were in agreement with the measured data.

The injection of hydraulic oils results in initial stress of about 8 MPa during the layout of the borehole stress gauge. When the layout is completed, the measuring station is about 75 m away from the working face. Combined with the online monitoring of borehole stress and daily mining and charging data, a broken line between borehole stress and working face distance changes is drawn (see Figure 17). The drilling stress peak is 8 m away from the working surface. The stress gauge of the 10 m-deep borehole is affected by the stress concentration of surrounding rocks of the mining roadway, coinciding with a stress peak value of 17.35 MPa and a stress concentration factor of 2.42. The 15 m depth borehole stress

gauge has a stress peak value of 16.34 MPa and a stress concentration factor of 2.08 m. These values are consistent with the simulation results.

7. Conclusions

The overlying stratum movement of a thick-coal, long-wall, paste-filling mine and the weakening law of mine pressures were studied based on the surface engineering overview of Gaohe Energy backfilling through laboratory tests, theoretical analysis, numerical simulation, on-site measurement, and other research methods. The following conclusions were obtained.

(1) The initial breaking-step distance of the immediate roof of the first test face filled by Gaohe Energy was 19.8 m, and the maximum bending deflection at the time of breaking was 0.29 m. When the filling rate reached 95% and above, the equivalent mining height was 0.32 m. Although the roof reached the maximum bending deflection after bending and sinking, there was no breaking space to ensure roof stability without breaking. A reasonable filling rate can be calculated in this way for similar projects.

(2) Overlying fractures developed in "saddle-shaped" distribution during caving mining. The development of overlying fractures in the advancing process of the working face presented three stages of advanced fracture development, re-compacting fractures, and steady-state maintenance of fractures in the case of backfill mining. Fracture development showed a "sail-shaped" migration during the advance process, and fractures behind the working face remained stable in main-roof rock strata.

(3) The stress concentration coefficient and influence range of filling mining were significantly reduced compared with the caving method for mining. The surface subsidence coefficient of thick-coal filling mining was 0.034, and the horizontal movement coefficient was 0.71. Rock stratum movement was controlled, and the mine pressure was significantly weakened. Research results provide a theoretical basis for determining a reasonable filling rate and a scientific basis for designing filling mining support and selecting equipment.

Author Contributions: Conceptualization, Q.M. and Y.Z. (Yidong Zhang); methodology, L.H.; software, Z.L. and Y.Z. (Yu Zheng); validation, G.S.; formal analysis, Q.M.; writing—original draft preparation, Q.M.; writing—review and editing, Y.Z. (Yidong Zhang) and Q.M.; project administration, Y.Z. (Yu Zheng). All authors have read and agreed to the published version of the manuscript.

Funding: The work was funded by the Key Project of Joint Funds of the National Natural Science Foundation of China (grant number U1903209); the Key Coal Based Scientific and Technological Research Projects in Shanxi Province in 2014 (grant number MJ2014-12).

Institutional Review Board Statement: Not applicable.

Informed Consent Statement: Not applicable.

Acknowledgments: The authors would like to thank the engineering technicians in Shaping Coal Mine for their enthusiastic assistance and suggestions.

Conflicts of Interest: The authors declare no conflict of interest.

References

1. Qian, M.G. Resources and Environment Harmonics (Green) Mining and Its Technological System. *J. Min. Saf. Eng.* **2006**, *1*, 1–5.
2. Yang, K.; Wei, Z.; Zhao, X.Y. Theory and technology of green filling of solid waste in underground mine at coal power base of Yellow River Basin. *J. China Coal Soc.* **2021**, *46*, 925–935.
3. Huang, Y.F.; Zhu, T. Application and prospect of green filling mining technology in coal mine in China. *China Min. Mag.* **2021**, *30*, 5–8.
4. Guo, W.B.; Ma, Z.B.; Bai, E.H. Current status and prospect of coal mining technology under buildings, water bodies and railways, and above confined water in China. *Coal Sci. Technol.* **2020**, *48*, 16–26.
5. Li, S.Z. Present Status and Outlook on Land Damage and Reclamation Technology of Mining Subsidence Area in China. *Coal Sci. Technol.* **2014**, *42*, 93–97. [CrossRef]

6. Chen, D.D. *Research and Application of the Fracture and Turbulence Law of the Main Roof Plate Structure of the Stope*; China University of Mining & Technology: Beijing, China, 2018.
7. Dou, L.T. *Mechanism and Control Technology of Strong Rock Pressure Induced by Structural Instability of Hard Roof in Thick Coal Seam*; Anhui University of Science and Technology: Huainan, China, 2021.
8. Bai, E.H.; Guo, W.B.; Tan, Y. Analysis on Strip-filling in Water Preserved Mining under Shallow Buried Thick Coal Seam. *Chin. J. Under Space. Eng.* **2019**, *15*, 1225–1231.
9. Zhang, Z.W. Research and application of water conservation mining technology based on partial filling green coal mining. *Coal Eng.* **2018**, *50*, 105–107.
10. Li, M.; Zhang, J.X.; Deng, X.J. Method of water protection based on solid backfill mining under water bearing strata and its application. *J. China Coal Soc.* **2017**, *42*, 127–133.
11. Qin, H.Y.; Wang, H.D.; Zhang, F. Development law of fractured zone of overburden strata in backfill mining based on plate and shell theory. *Saf. Coal Mines* **2021**, *52*, 64–70.
12. Chang, X.K.; Wang, G.M.; Wang, Z.Q. Application of green filling mining with solid waste under villages in an ecologically fragile area of western China. *Coal Eng.* **2022**, *54*, 1–6.
13. Hu, B.N.; Liu, P.L.; Cui, F. Review and development status of backfill coal mining technology in China. *Coal Sci. Technol.* **2020**, *48*, 39–47.
14. Wang, F.T.; Ma, Q.; Li, G. Overlying Strata Movement Laws Induced by Longwall Mining of Deep Buried Coal Seam with Superhigh-Water Material Backfilling Technology. *Adv. Civ. Eng. Mater.* **2018**, *2018*, 4306239. [CrossRef]
15. Wang, F.T.; Ma, Q.; Zhang, C. Overlying strata movement and stress evolution laws triggered by fault structures in backfilling longwall face with deep depth. *Geomat. Nat. Hazards Risk* **2020**, *11*, 949–966. [CrossRef]
16. Zhang, J.X.; Li, B.Y.; Zhou, N. Application of solid backfilling to reduce hard-roof caving and longwall coal face burst potential. *Int. J. Rock Mech. Min. Sci.* **2016**, *88*, 197–205. [CrossRef]
17. Ren, S.; Yu, G.F. Study on Prevention and Control Effect of Rockburst in Super-High Water Backfilling Mining. *Min. Res. Dev.* **2022**, *42*, 74–78.
18. Chen, Y.; Li, D.; Jiang, F.X. Prevention mechanism of rock burst in backfill mining in extra-thick coal seam with deep shaft. *J. Min. Saf. Eng.* **2020**, *37*, 969–976.
19. Chen, Y. *Rockburst Occurrence and Control in Deep Longwall Coal Panels with Backfill Skipping Mining*; University of Science and Technology: Beijing, China, 2021.
20. Xie, S.R.; Chen, D.D.; Gao, M.M. Fracture regularity of thin plate model of main roof with elastic foundation boundary for backfill mining. *J. China Coal Soc.* **2017**, *42*, 2270–2279.
21. Zhang, Q.; Yang, K.; Zhang, J.X. Immediate roof control mechanism in solid backfill mining method and its engineering case. *J. China Univ. Min. Technol.* **2022**, *51*, 35–45.
22. Jia, L.G. Experimental study on failure characteristics of strata with different filling rates in longwall filling mining. *Coal Sci. Technol.* **2019**, *47*, 197–202.
23. Zhang, T.F.; Zhao, T.B.; Ma, X.Y. Analysis on crack distribution and evolution characteristics of gangue backfilled working face roof. *Chin. J. Rock Mech. Eng.* **2022**, *41*, 969–978.
24. Chang, Q.L.; Zhou, H.Q.; Bai, J.B. Stability Study and Practice of Overlying Strata with Paste Backfilling. *J. Min. Saf. Eng.* **2011**, *28*, 279–282.
25. Zhao, T.B.; Fu, Z.Y.; Li, G. In situ investigation into fracture and subsidence of overburden strata for solid backfill mining. *Arab. J. Geosci.* **2018**, *11*, 398. [CrossRef]
26. Petlovanyi, M.; Malashkevych, D.; Sai, K.; Bulat, I.; Popovych, V. Granulometric composition research of mine rocks as a material for backfilling the mined-out area in coal mines. *J. Min. Depos.* **2021**, *15*, 122–129. [CrossRef]
27. Petlovanyi, M.; Malashkevych, D.; Sai, K.; Zubko, S. Research into balance of rocks and underground cavities formation in the coal mine flowsheet when mining thin seams. *J. Min. Depos.* **2020**, *14*, 66–81. [CrossRef]
28. Guo, G.L.; Feng, W.K.; Zha, J.F. Subsidence control and farmland conservation by solid backfilling mining technology. *Trans. Nonferrous Met. Soc. China* **2012**, *21*, 665–669. [CrossRef]
29. Xu, H.G. Characteristics of gangue filling mining and surface subsidence deformation. *Coal Eng.* **2022**, *54*, 131–135.
30. Chang, Q.L. *Research on Theory and Practice of Mining Induced Overlying Strata Deformation and Surface Subsidence with Paste Backfilling*; China University of Mining & Technology: Xuzhou, China, 2009.
31. Xia, K.Q. *The Law of Weakening Strata Behavior in Backfilling Mining and Engineering Practice*; China University of Mining & Technology: Xuzhou, China, 2020.
32. Sun, X.K.; Li, X.S.; Shi, X.Y. Study on mine strata behavior with full backfill effect of paste backfill in coal mine. *Coal Sci. Technol.* **2017**, *45*, 48–53.
33. Zhang, Q.; Yang, K.; Zhang, H. Research on weakening law and quantitative characterization of strata behavior in solid filling mining. *J. China Univ. Min. Technol.* **2021**, *50*, 479–488.
34. Zhang, Q.; Zhang, J.X.; Kang, T. Mining pressure monitoring and analysis in fully mechanized backfilling coal mining face-A case study in Zhai Zhen Coal Mine. *J. Cent. South Univ.* **2015**, *22*, 1965–1972. [CrossRef]
35. Qi, Q.X.; Li, J.Q.; Mao, D.B. *Methods for Determining the Physical and Mechanical Properties of Coal and Rock*; Standards Press of China: Beijing, China, 2009.

36. Li, Y.W.; Jia, D.; Rui, Z.H.; Peng, J.Y.; Fu, C.K.; Zhang, J. Evaluation method of rock brittleness based on statistical constitutive relations for rock damage. *J. Pet. Sci. Eng.* **2017**, *153*, 123–132. [CrossRef]
37. Li, Y.W.; Long, M.; Zuo, L.H.; Li, W.; Zhao, W.C. Brittleness evaluation of coal based on statistical damage and energy evolution theory. *J. Pet. Sci. Eng.* **2019**, *172*, 753–763. [CrossRef]
38. Zhang, C.; Li, B.; Song, Z.Y.; Liu, J.B.; Zhou, J.L. Breakage mechanism and pore evolution characteristics of gangue materials under compression. *J. Acta Geotech.* **2022**, *17*, 4823–4835.
39. Rong, J.M.; Lu, J.W.; Yao, Y. *Standard for Test Method of Mechanical Properties on Ordinary Concrete*; China Architecture & Building Press: Beijing, China, 2003.
40. Iordanov, I.; Novikova Yu Simonova Yu Yefremov, O.; Podkopayev, Y.e.; Korol, A. Experimental characteristics for deformation properties of backfill mass. *J. Min. Depos.* **2020**, *14*, 119–127. [CrossRef]
41. Liu, J.M. *Study and Application of Mechanical Properties of Gangue Paste Material*; China University of Mining & Technology: Xuzhou, China, 2020.
42. Qian, M.G.; Shi, P.W.; Xu, J.L. *Ground Pressure and Strata Control*; China University of Mining and Technology Press: Xuzhou, China, 2010.
43. Zhang, C.; Zhao, Y.X.; Han, P.H.; Bai, Q.S. Coal pillar failure analysis and instability evaluation methods: A short review and prospect. *Eng. Fail. Anal.* **2022**, *138*, 106344. [CrossRef]
44. Yang, G.T. *A Concise Course in Elasticity*; Tsinghua University Press: Beijing, China, 2013.

sustainability

MDPI

Article

Study on the Optimization of Proportion of Fly Ash-Based Solid Waste Filling Material with Low Cost and High Reliability

Denghong Chen [1,2,*], Tianwei Cao [1], Ke Yang [3,*], Ran Chen [1], Chao Li [1] and Ruxiang Qin [4]

[1] School of Mining Engineering, Anhui University of Science and Technology, Huainan 232001, China; twahlgdx@163.com (T.C.); cr3066141768@163.com (R.C.); lichao17793477139@163.com (C.L.)
[2] Institute of Special Mining, Anhui University of Science and Technology, Huainan 232001, China
[3] Institute of Energy, Hefei Comprehensive National Science Center, Hefei 230031, China
[4] Joint National-Local Engineering Research Centre for Safe and Precise Coal Mining, Huainan 232001, China; rxqin@aust.edu.cn
* Correspondence: dhchen@aust.edu.cn (D.C.); yksp2003@163.com (K.Y.); Tel.: +86-181-5546-5228 (D.C.); +86-182-5540-1572 (K.Y.)

Abstract: In order to solve the problem of the high cost of coal-based solid waste bulk stacking and paste filling in the large-scale coal electrification base in East NingXia, in this study, fly ash is skillfully used to replace the broken coal gangue as the mixed filling material. As using a jaw crusher for crushing large coal gangue is expensive, and its energy consumption is relatively high, paste filler using fly ash as aggregate is studied through micro and macro test analyses. Using response surface methodology design software, 29 groups of mix proportion schemes are designed to obtain the best mix proportion. In addition, the radar results of slump, slump flow, and comprehensive strength are obtained by the normalization method. According to the radar chart results of the three normalized indexes, the optimal ratio parameters are as follows: the fly ash in solid phase is 79%, the mass of fly ash to the mass of cement (FA/C) is 6:1, the solid mass concentration is 78%, the fly ash to gasification slag is 1:1, and the results show that σ_{3d} = 2.20 MPa, slump = 205 mm, and flow = 199 mm. Taking the solid mass concentration, FA/C, the fly ash content in solid phase, and the coal gangue-to-gasification slag ratio as independent variables, the influence of single-factor and multi-factor interactions of the independent variables are analyzed based on the response surface model. It is found that the solid mass concentration and FA/C have a very significant effect on the early strength. Replacing coal gangue base with fly ash base can effectively reduce the crushing cost and energy consumption and provide low-cost and highly reliable technical reserves for large-scale filling.

Keywords: solid waste filling materials; fly ash base; low cost and high reliability; response surface methodology; early strength

1. Introduction

As a major coal producer and consumer, China's coal-based energy system will not change for a long time [1]. In addition, with the rapid development of China's coal, chemical, and other industries, more than 3.3 billion tons of industrial solid waste are produced per year. The cumulative stock is more than 60 billion tons, and this number is accelerating [2]. The East NingXia coal and electricity base is one of the 1400 million-ton coal bases. From the perspective of the East NingXia coal and electricity base, with the rapid development of the modern coal chemical industry, the ecological risk level of the coal industry base in East NingXia urgently needs to be effectively controlled [3]. Industrial solid waste—mainly fly ash, gasification slag, coal gangue, desulfation gypsum, and bottom slag—has increased rapidly. Since 2016, the annual increase in solid waste at the East NingXia base has exceeded 10 million tons. In NingXia's modern coal chemical industry, the solid waste treatment methods are mainly landfill and outbound transportation [4]. Furthermore, the coal-fired thermal power and chemical industry bases in East NingXia

(Figure 1), Yulin (Shaanxi), and Ordos (Inner Mongolia) together form the "Golden Triangle" of the national energy and chemical industry [5]. The geographical location is far from the eastern coastal market and more than 100 km away from the surrounding large cities, including Xi'an and Beijing, as shown in Figure 1. In addition, the original storage and new displacement volumes are large, and the market capacity is small [6]. The transportation of coal-based solid waste, such as fly ash, increases costs invisibly. According to the data, transportation around the East NingXia mining area is convenient, so automobile and coal railway transportation can be considered the transportation scheme. On the basis of the comprehensive quota of the auxiliary cost of coal mine shaft construction and roadway engineering in 2015, the cost of automobile waste discharge is 2.5 CNY/(kilometer × ton). The railway construction cost was calculated to be 25 million CNY/kilometer, the railway maintenance cost was calculated to be 2.5% of the initial cost, and the shared cost per ton of solid waste is 0.1 CNY/ton. The material unloading cost was calculated to be 4.3 CNY/ton, and the annual filling material transporting and unloading cost is very high too. According to statistics from the East NingXia base, solid waste production increased from 4.4 million tons in 2010 to 24 million tons in 2020, of which gasification slag production exceeded 7 million tons. Due to the high cost of treatment, the utilization of solid waste such as gasification slag, and technical difficulties, the comprehensive utilization rate of solid waste at the East NingXia base in 2020 was only 43%. The accumulation of a large amount of coal slag not only takes up a lot of land resources but also causes serious environmental problems, such as soil pollution, air pollution, and geological disasters [7]. On the basis of the East NingXia coal and electricity base, traditionally, paste filling can be the first choice because of a lower investment at the early stage, less ground solid stacking, and less surface ecological damage after filling. However, the first option for the coal mine filling gelling agent is cement. The high cement cost not only affects the operation of the coal mine but also restricts the popularization of filling mining technology [8]. Many scholars have conducted research using coal gangue as a filling material. A three-dimensional simulation method for the compaction fracture of crushed rock and coal particles was proposed, and the effects of the strength and size of crushed samples on the fracture characteristics and stress evolution of the crushing model during loading were further discussed [9]. Coal gangue smaller than 20 mm was used as aggregate to prepare downhole filling materials, and the particle gradation, fluidity, and strength of the filling materials were studied. The influence of coal gangue gradation and different raw material content on the fluidity and compressive strength of the filling material by response surface methodology was studied [10]. This study focused on the method of estimating the load and strength of the pillar system, pointed out the main factors for evaluating the stability of the coal pillar, and concluded that the failure criterion of the coal pillar is an important factor for calculating the strength of the coal pillar. According to the statistics, the power consumption of crushing operations accounts for more than 50% of the total power consumption of the concentrator. The total power consumption for crushing operations in the country is more than 2×10^9 kW·h [11]. With increases in the crushing cost of coal gangue, the energy consumption becomes larger, and the particle size requirement becomes higher, which is no longer conducive to emission reductions and economic benefits.

The microstructure and physicochemical properties of the filler were analyzed by various research methods by examining the proportion of coal-based solid waste filler with fly ash as the aggregate and gasification slag combined with coal gangue. The particle size of fly ash was obtained using a laser particle size analyzer, and the particle size of cement was calculated. The phase and composition of raw materials were analyzed using an X-ray diffractometer. The filler was designed using the response surface methodology with fly ash as the main material and gasification slag and coal gangue as the auxiliary material. Through comparison, the influence of single-factor and multi-factor interaction on the early strength and fluidity of the filler was analyzed considering the influence of solid mass concentration, fly ash content, and other factors on the early strength and other mechanical properties of the filler. The best ratio of fly-ash-based solid waste filler with

good fluidity, low cost, and high-strength reliability provides basic parameters for the large-scale utilization of coal-based solid waste in the Eastern NingXia mining area.

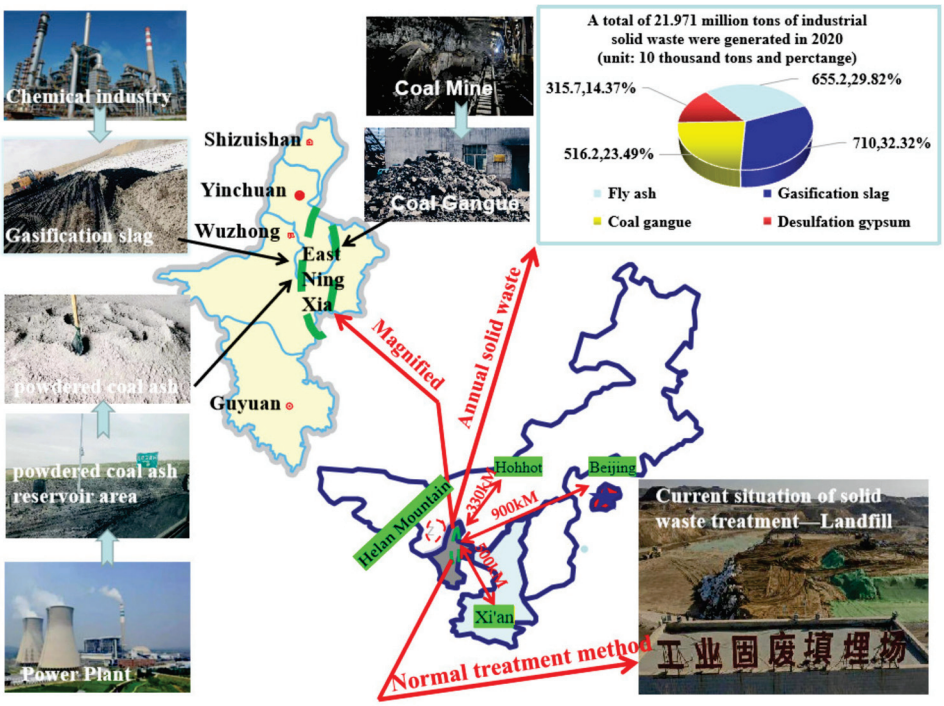

Figure 1. Generation, Stockpiling and geographical location of solid waste in coal–thermal power–chemical industry base in East NingXia.

2. Analysis on Physical Properties of Solid Waste Filling Material and Experiment Plan Design

2.1. Raw Materials and Their Physical Properties

The gasification slag, fly ash, and coal gangue used in this study were, respectively, taken from East NingXia Base No.1 Waste Slag Reservoir, the coal-to-liquid branch of the National Energy Group NingXia Coal Industry Co., Ltd. (Yinchuan, China), and Renjiazhuang coal mine, a subsidiary of NingXia Coal Industry Group Co., Ltd.

The instrument used for the test was procured from the Analysis and Test Center of the Anhui University of Science and technology, as shown in Figure 2. The parameters of the BT-2003 laser particle size analyzer were as follows: the test range was 0.04–1000 μm, the reproducibility was <1%, and the sampling speed was 3500 times/s. The parameters of the Smartlab X-ray diffractometer were as follows: power was 3 kW, minimum step diameter was 0.0001°, and goniometer radius was 300 mm. The parameters of the FlexSEM 1000 scanning electron microscope (SEM) were as follows: the acceleration voltage was 0.3–20 kV, the resolution was 4 nm, and the magnification was 6–300,000×. The main mineral phase of the cement was calcium silicate, followed by tricalcium silicate, which determined its early strength. In addition, the particle size distribution was measured using a laser particle size analyzer, and the result is shown in Figure 3a. The main particle size of the cement used was less than 100 μm. The particles with a particle size of 10–40 μm accounted for the majority, and the particles were relatively fine.

2.1.1. Fly Ash

As a coal-based solid waste, fly ash is high-quality external ash with small particle size. Its particle size distribution was measured using a laser particle size analyzer. The fly ash particle size distribution curve is shown in Figure 3. The main microscopic morphology of fly ash is shown in Figure 4a. The fly ash mainly comprised particles with a particle size of less than 200 μm. The majority of particles were of size 10–80 μm. The use of aggregates was beneficial to improve the early strength of the filling body. The analysis of fly ash using

X-ray diffraction (XRD) is shown in Figure 5a. It was mainly composed of spherical states with different particle sizes, but the difference in particle size was small. Adjacent spherical particles overlapped and had a better encapsulation effect on large-size aggregates.

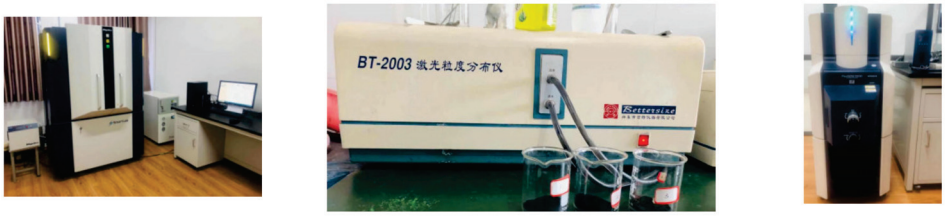

(**a**) (**b**) (**c**)

Figure 2. Micro testing instrument for multi-source coal based solid waste. (**a**) SmartLab X-ray diffractometer; (**b**) laser particle size analyzer; (**c**) SEM instrument.

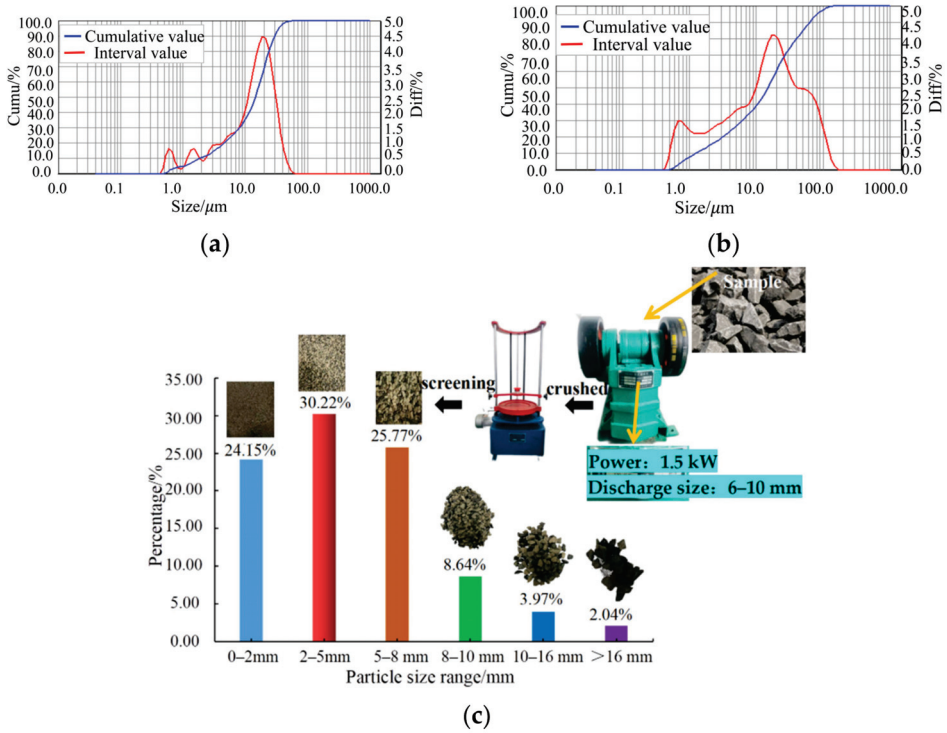

Figure 3. The particle size test results and process of proportioning raw materials. (**a**) Distribution curve of cement particle size; (**b**) distribution curve of fly ash particle size; (**c**) statistical diagram of coal gangue crushing and particle size distribution.

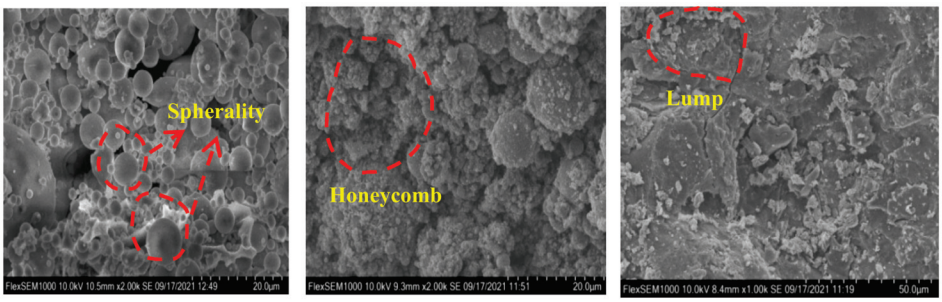

(**a**) (**b**) (**c**)

Figure 4. SEM scanning of solid wastes in the coal–electricity–chemical process. (**a**) Fly ash; (**b**) gasification slag; (**c**) coal gangue.

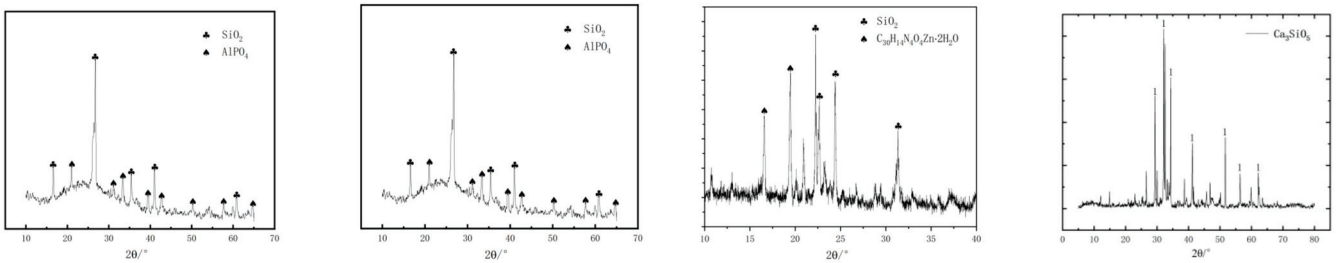

(**a**) (**b**) (**c**) (**d**)

Figure 5. X-ray diffraction (XRD) patterns of filling materials. (**a**) Fly ash; (**b**) coal gangue; (**c**) gasification slag; (**d**) cement.

2.1.2. Gasification Slag

As a product of coal chemical utilization, gasification slag is the waste residue produced by coal gasification reaction at high temperatures. The microstructure of lead was observed using an SEM (Figure 4b). Using XRD analysis (Figure 5c), it was concluded that the main chemical composition of the gasification slag was quartz, besides lead arsenate. The particles mainly existed in an irregular honeycomb state, with large differences in particle size. Therefore, it was concluded that as the content of gasification slag increases. When other factors were the same, the strength of the consolidated product decreased.

2.1.3. Coal Gangue

The coal gangue used in this study was taken from the Renjiazhuang coal mine. It was in the form of a gray-black block. The experiment used a two-stage jaw crusher (Figure 3c) to crush the coal gangue to a maximum particle size of 16 mm. Then, 5 kg of the randomly collected gangue was crushed by the sieve analysis method and screened using a standard vibrator. The particle size distribution of coal gangue after crushing was obtained. The statistical distribution is shown in Figure 3c [12]. Scanning using an SEM (Figure 4c) showed that the microscopic morphology comprised blocks of different sizes, and the pores between adjacent blocks were relatively large. Meanwhile, the method specified in the standard for test methods of Geotechnical Engineering (GB/T50123-2019) was used as the benchmark. The main chemical component was kaolinite, accompanied by quartz. The XRD analysis findings are shown in Figure 5b.

The cement used was ordinary 42.5 Portland cement. Figure 5d shows the XRD analysis of the cement [13].

The optimization idea of using fly-ash-based filler instead of crushed coal gangue-based filler was put forward. The energy consumption of coal gangue in the laboratory was estimated. For this, 15 kg crushed coal gangue was selected, and the experiment was completed in 30 min. On the basis of the crusher nameplate information in Figure 3, the power of the two-stage jaw crusher was 1.5 kW; thus, the total energy consumption this time was 0.45 kW·h. According to the industrial electricity price of RMB 1 per day, the laboratory needed to consume RMB 0.75 to crush 15 kg coal gangue. It was estimated that the crushing cost of coal gangue was increased by at least RMB 50 per ton.

2.2. Proportion Optimization Experiment Plan

The results of the optimized filling test scheme were deeply analyzed by microanalysis, probability analysis, and response surface methodology to obtain a low-cost and highly reliable coal-based solid waste filling material ratio scheme, referring to the requirements of the concrete strength test standard [14]. In the experiment, a triple mold with a length $\times$ width $\times$ height of 70.7 $\times$ 70.7 $\times$ 70.7 mm^3 (Figure 6a) was used. The fly ash was used as the aggregate, gasification slag was added, and two kinds of solid waste coal gangue were mixed and stirred evenly for 180 s to form a specimen of 70.7 $\times$ 70.7 $\times$ 70.7 mm^3 (Figure 6b). The test blocks were placed in a box with constant temperature and humidity

(temperature of 20 °C and humidity of 95%) (Figure 6c) [15]. The blocks were taken out after reaching the age of 3 and 7 days. The early compressive strength test of the specimens was completed on an automatic compression test machine (Figure 6d–f).

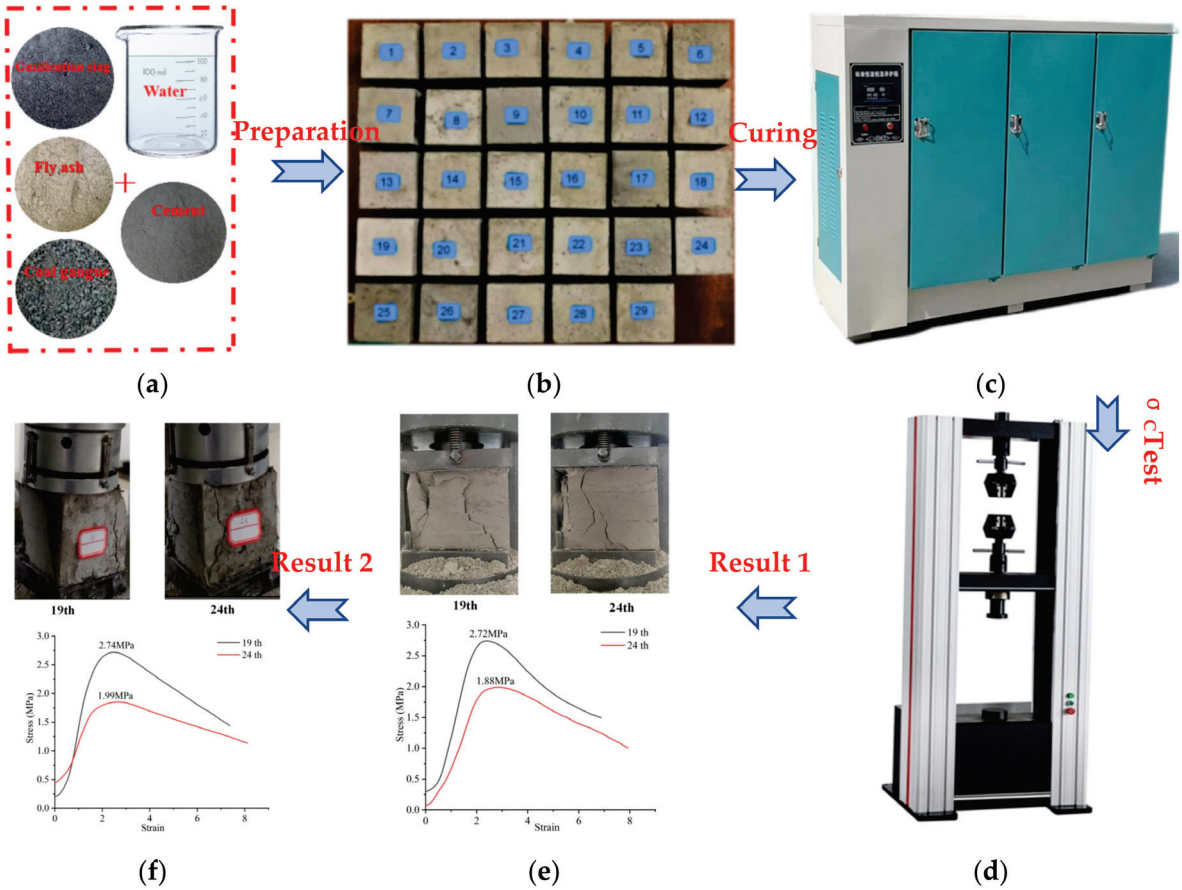

Figure 6. Making and uniaxial compression test of paste filling material specimens. (**a**) Triple mold; (**b**) test block; (**c**) curing box; (**d**) pressure machine; (**e**) σ_c of 3 d age; (**f**) σ_c of 7 d age.

By reading relevant documents, combined with the characteristics of large coal-based solid waste storage yards in the mining area of the eastern base of NingXia [16]. These characteristics mainly included fly ash, gasification slag, and coal gangue. Considering the cost of the bulk crushing of coal gangue and the performance requirements of coal-based solid waste fillers, coal gangue with particle size less than or equal to 16 mm after crushing was adopted [17]. Using fly ash as the aggregate, the experimental factors and levels were obtained, as shown in Table 1.

Table 1. Factors and gradients based on response surface design.

Factor	Gradient		
	−1	0	1
X_1 (The amount of fly ash in the solid)/%	70	75	80
X_2 (FA:C, Mass of Fly ash:Mass of Cement)	6:1	7:1	8:1
X_3 (Solid mass fraction)/%	75	79	83
X_4 (Coal Gangue:Gasification slag)	0.7:1	0.85:1	1:1

A design based on the Box–Behnken design (BBD) method of response surface methodology (RSM) was used for the factors affecting the performance of the filling body, as shown in Table 1. Different gradient-based numerical arrangements were made for the four design factors to get a more in-depth and rigorous experimental scheme. By designing the

influencing factors and gradients of filling material performance, the quality of fly ash and cement was simplified to FA:C.

3. Analysis of Experimental Results Based on Response Surface Methodology

3.1. Early Strength Analysis of Filling Material

It was necessary to study the proportioning scheme, such as parameters of paste filling materials for rapid filling and solidification, to realize the parallel operation of coal mining and filling in the working face. Therefore, 3-day early strength was more effective than 7-day strength. Using the BBD method, 29 groups of four-factor and three-level filler proportioning test schemes were designed. The 3-day and 7-day uniaxial compressive strength of the response surface experimental design scheme is shown in Figure 7.

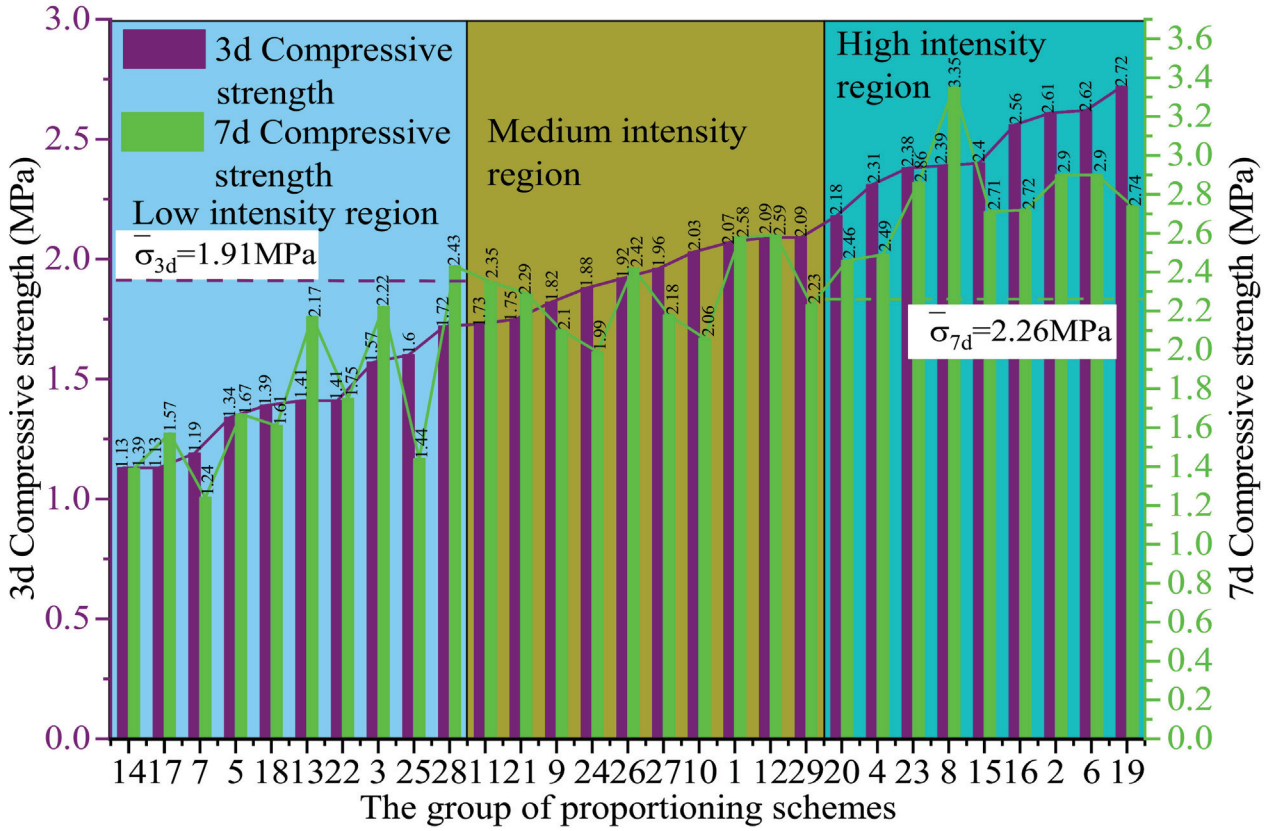

Figure 7. Statistical histogram of compressive strength at different ages.

According to the three levels of low, medium, and high, 29 groups of proportioning schemes were divided into 10 groups, 10 groups, and 9 groups, respectively. The 3-day and 7-day compressive strengths in the filling material scheme were sorted from small to large. The uniaxial compressive strength of all schemes was calculated for 3 and 7 days, which was 1.91 MPa and 2.26 MPa, respectively. Using this uniaxial compressive strength, the early compressive strength at 3 days was selected. The strength of most groups of filling schemes was greater than the average value, and the same was true under the age of 7 days. Furthermore, the crack growth diagrams of filling materials in the five high-strength groups at the age of 3 days were randomly selected. The filling body under this strength followed two-way vertical crack growth. It provided an optimized coal-based solid waste filling material scheme with the intersection of fluidity and uniaxial compressive strength for subsequent analysis.

According to the calculation of the mean value of the 3-day compressive strength of the filling body, this study divided the compressive strength data of 29 groups of 3-day design schemes into four gradients, as shown in Figure 8. The reliability of the optimized pro-

portioning scheme was further improved by comparing the divided compressive strength range with the strength of the optimized proportioning scheme. According to the failure characteristics of the test block at the age of 3 days, the brittleness of the test block was large, the surface block fell off greatly during fracture failure, and the development of cracks after failure was chaotic [18].

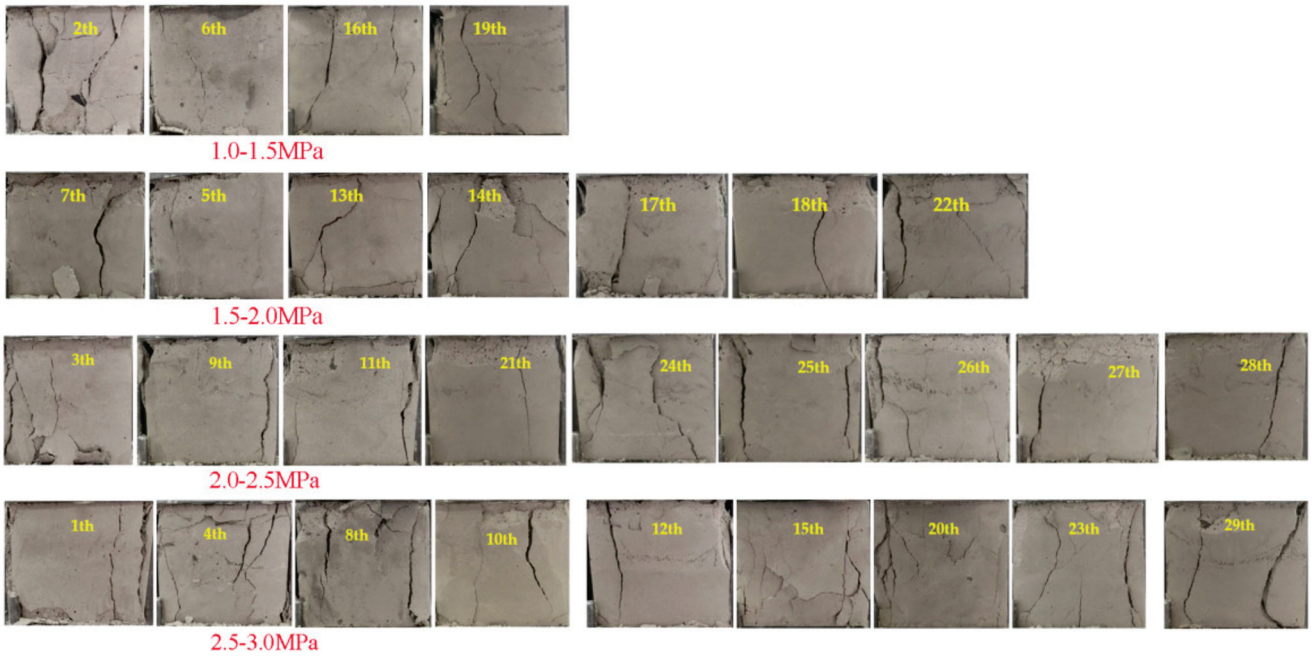

Figure 8. Fracture morphology of mix proportion test block at three days of age under different schemes.

The analysis of early compressive strength and propagation crack of the test block (Table 2), combined with the SEM analysis of fly ash, revealed that the spherical structure of fly ash increased with the increase in the filler ratio [19]. The coating effect for coarse-grained auxiliary materials was better; therefore, the early compressive strength of the filling body also increased slowly. In the meantime, when the solid mass concentration of the filling material paste increased, the compressive strength of the filling body was also positive. With the gradual increase in the mass concentration of the test block, it was concluded that the compressive strength basically tended to increase, while the content of fly ash in the test block decreased. The SEM analysis of the selected test block showed that the internal hydration products of the high-strength test block were rich, as shown in Figure 9. The SEM image in Figure 9 shows that the concentration of needle-like hydration products in the two groups of test blocks was obvious. As shown in Figure 9a, the spherical structure of powdered coal ash with different particle sizes had more hydration products in the place where fly ash accumulated, but with more pores. However, as shown in Figure 9b, the hydration products of each material were dense. As the solid mass concentration increased, cement and powdered coal ash packed more coarse particles, and the compressive strength increased. The compressive strength of the test block of the filling material ratio significantly reduced with the increase in the content of the gasification slag. The gasification slag had a porous honeycomb structure, and hence the wrapping effect for each admixture was poor. In addition, the amount of cement was relatively small to control the cost of the filling paste. It was also seen that the early compressive strength increased significantly with the increase in cement content.

Referring to Figure 9, the distribution trend of early compressive strength at the age of 3 days under the ratio test scheme of 29 groups of filling materials was analyzed. The compressive strength was mostly distributed in 1.5–2.5 MPa, and the early compressive strength at the age of 7 days was mostly distributed in 2.0–3.0 MPa. It was seen that the

distribution law of the early compressive strength under each plan is more obvious. After establishing the Weibull model of early compressive strength at the age of 3 and 7 days, the fitting variance of model Equations (1) and (2) was $R^2 = 0.9671$ and $R^2 = 1$, respectively. The fitting variances were close to 1, which was more accurate.

$$y = -0.0421x^2 + 0.1879x + 0.1 \quad (1)$$

$$y = 0.0333x^4 - 0.4233x^3 + 1.7917x^2 - 2.8417 + 1.54 \quad (2)$$

Table 2. Code and level of response surface design factors.

No.	The Content of Fly Ash in the Solid/%	FA:C	Solid Mass Concentration/%	Coal Gangue: Gasification Slag/%	3 d Compressive Strength (MPa)	7 d Compressive Strength (MPa)
1	79	6:1	79	1:1	2.22	2.67
2	78	6:1	79	1:1	2.21	2.65
3	79	6:1	78	1:1	2.20	2.64

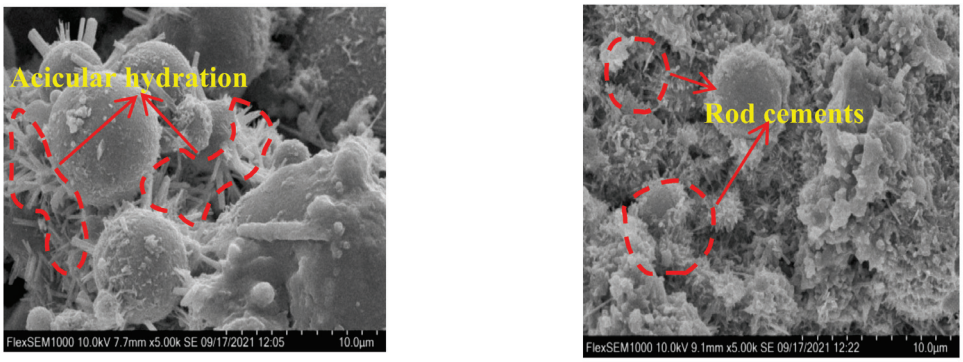

(**a**) (**b**)

Figure 9. SEM image of the hydration products in 3 d. (**a**) The 12th set of proportioning test block; (**b**) the 19th set of proportioning test block.

The strength curve fitting of different ages showed that with the increase in strength, the early compressive strength of multi-component mix containing gasified slag and fly ash gradually decreased. In general, the strength of fly-ash-based filler slurry was relatively low, and its early compressive strength was mainly distributed in 2.0–2.5 MPa. The analysis of the statistical results of strength distribution showed that the experimental results of the proportioning scheme had low discreteness. The reliability was guaranteed in terms of strength.

3.2. Analysis of Optimal Mix Proportion of Filling Materials Based on Low Cost and High Reliability

The paste mass concentration was generally 75–85% to adapt to the low-cost and high-reliability filling material ratio of a Renjiazhuang coal mine in the eastern mining area of NingXia [20]. Combined with the mass concentration level, the mass concentration of the final selected filling material was 75–79% [21]. Then, the best parameter combination of the filler slurry mix proportion was finally obtained using RSM and fitting module analysis, as shown in Table 2 [22].

In this study, the optimized mix proportion was based on the early strength reliability of the backfill. Meanwhile, combined with the current situation of coal-based solid waste disposal in the eastern mining area of NingXia, the slump in the three groups of filling materials in the RSM optimization fitting module was obtained. The partial fluidity experiment of the expansion degree was performed, as shown in Figure 10. In this study, the micro-slump test was performed to characterize the flow properties of the filling material, and the test was conducted in accordance with the National Standardization

Committee GB/T50080 standard. According to the conclusion drawn by Ouattara et al. [23], the coefficient of proportionality between the micro-slump value and the corresponding value of the standard slump cone was 2.28 [24]. The specific size of the slump is shown in Figure 10. The slump value indicated the initial flow capacity of the filling material and could reflect the cohesion and friction resistance of the slurry.

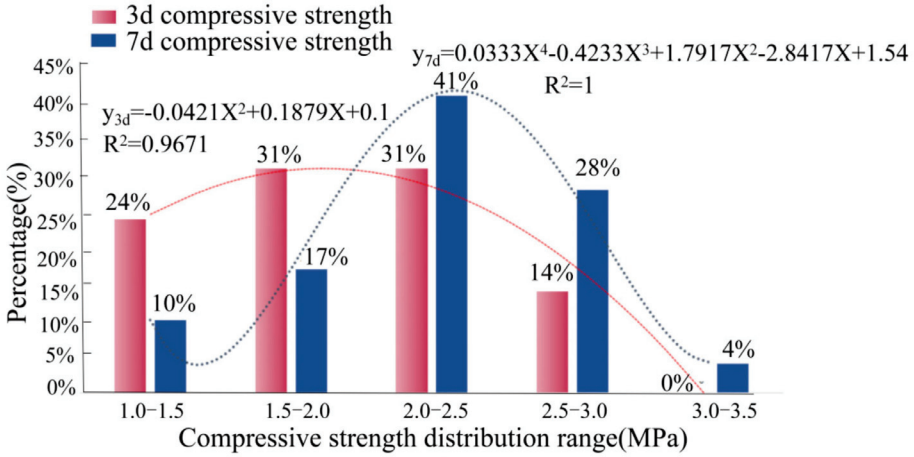

Figure 10. Distribution trend of compressive strength range at different ages.

The test results of each group of schemes were obtained based on the aforementioned experiment and analysis [25]. The slump of the filling paste in the first group was 200 mm, and the slump flow was 197 mm, as shown in Figure 11a (No. 1). The slump of the filling paste in the second group was 202 mm, and the slump flow was 198 mm, as shown in Figure 11a (No. 2). The slump of the third group of the filling paste was 205 mm, and the slump flow was 199 mm, as shown in Figure 11a (No. 3) [26].

To ensure that the three columns of data were of the same order of magnitude, No. 1 was selected as 1, and the other numbers in the same column were divided by it; No. 2 was selected as 1 for the slump, and the other numbers in the same column were divided by it; and No. 9 was selected as 1 for 3-day compressive strength, and the other numbers in the same column were divided by it. The typical mix proportion of filling materials at low, medium, and high levels was obtained through the correlation analysis of the uniaxial compressive strength of multiple groups of schemes in Section 2 of Part III. Based on this, the compressive strength and fluidity indexes of nine groups of filling materials were selected. The radar diagram was analyzed with the optimized mix proportion of three groups of filling materials obtained based on RSM. As shown in Figure 11b, among the 12 groups of batching schemes including low, medium, and high strength and optimization, optimization group 3 presented a stable equilateral triangle. Under the restriction of three factors, the correlation performance of proportioning number was consistent. This was consistent with the mix proportion obtained by RSM analysis and optimization, which had high reliability. The reliability of the regression model was verified from the theoretical and on-site perspectives. The optimal mix ratio for the bulk coal-based solid waste disposal in the East NingXia mining area was obtained. The fly ash content in solids was 79%, the solid mass concentration was 78%, the FA:C was 6:1, and the coal gangue:gasification slag was 1:1, which had a certain guiding significance and reference value for the optimization of low-cost and high-reliability filling materials [27].

(**a**)

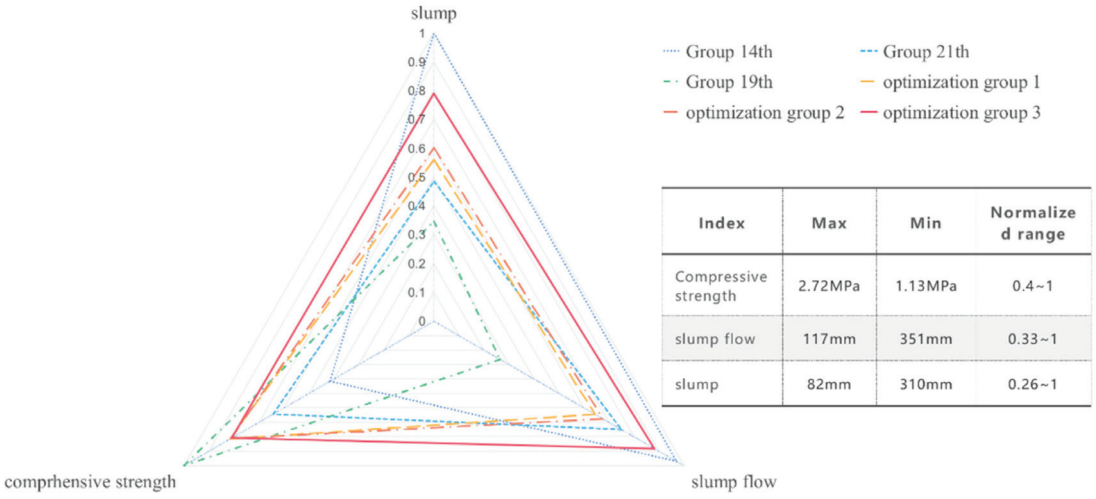

Index	Max	Min	Normalized range
Compressive strength	2.72MPa	1.13MPa	0.4~1
slump flow	117mm	351mm	0.33~1
slump	82mm	310mm	0.26~1

(**b**)

Figure 11. Test and analysis of fluidity and compressive strength of experimental group and optimization group. (**a**) Simple mobility test process and results; (**b**) radar analysis of fluidity and compressive strength data.

4. Multiple Factors Affect the Results and Discussion

4.1. Discussion

For the aforementioned multivariate linear equation with early compressive strength as the dependent variable obtained using RSM, the optimal model equation was obtained by analyzing the correlation coefficients of multiple models [28]. The prediction correlation coefficient R^2_{pred} was 0.6399, which confirmed that the model was highly accurate and the modified model had multiple regressions, as shown in Table 3. Furthermore, as shown in Table 4, the optimal model R^2 ranked fourth among the multiple models. However, its complex correlation coefficient R^2_{pred} ranked second in the model. The comprehensive coefficient should be close to 1, which was called a significant model. The multiple correlation coefficient R^2 was 0.8208 and the corrected correlation coefficient R^2_{Adj} was 0.7611, which were very close. Therefore, the aforementioned discussion showed that the modified model was the best; see Formula (1) for the linear equation obtained from the model.

Table 3. Response surface methodology R^2 analysis of the fit degree of each model.

Model Source	R^2 Correction Value	R^2 Predictive Value	Remark
Linea model	0.7872	0.6798	
2FI model	0.8243	0.4770	
Modified model	0.8208	0.6399	Recommended
Quadratic model	0.8484	0.2298	
Cubic model	0.9583	−1.4975	

Table 4. Analysis of variance of response surface regression model.

Source	Sum of Squares	Mean Square	F Value	*p*-Value
Model	5.13	0.73	13.74	<0.0001
X_1	0.21	0.21	3.85	0.0631
X_2	0.26	0.26	4.84	0.0391
X_3	4.42	4.42	82.81	<0.0001
X_4	0.04	0.04	0.74	0.3981
X_1X_3	0.16	0.16	3	0.0979
X_2X_3	0.048	0.048	0.91	0.3516
X_3X_4	1.60×10^{-3}	1.60×10^{-3}	0.03	0.8641
Residual	1.12	0.053		
Lack of Fit	0.97	0.057	1.48	0.3822
Pure Error	0.15	0.038		
Cor Total	6.25			

In addition, the significance of the model was determined using the F value and the P value. The larger the F value, the smaller the P value and the more significant the impact. The F value of the established regression model was 13.74; the P value was < 0.0001, which showed that the regression effect of the model was significant. The first term, quadratic term, and cross terms were all statistically significant. The model fit the experimental values well. The single factor resulted in the significance ranking as $X_1 > X_2 > X_3 > X_4$, and the factor interaction affected the significance ranking $X_1X_3 > X_2X_3 > X_3X_4$. The model was used to determine the correlation coefficient to evaluate the accuracy and reliability of the regression model. Meanwhile, the model for determining the correlation coefficient explained the difference between the response surface and the real value. The fit degree of each model was analyzed using RSM. The evaluation results are shown in Table 4. The closer the correlation coefficient was to 1, the higher the credibility of the model. The contour line of the equation and the 3-day response surface represented the interactive result of each factor, which could not only predict and optimize the response value but also analyzed the interaction of any two factors to obtain the interaction law.

After discussing and analyzing the fitting degree and model value of the aforementioned models, the response mass concentration, fly ash content, coal gangue:gasification slag, and FA:C were obtained through multiple linear regression fitting of the data according to the experimental results and software design-export10:

$$Y = 1.91 + 0.13X_1 - 0.15X_2 + 0.61X_3 + 0.057X_4 - 0.20X_1X_3 + 0.11X_2X_3 - 0.02X_3X_4 \quad (3)$$

4.2. Analysis of Influencing Factors under Response Surface Methodology

The study next aimed to obtain the correlation law of the content of fly ash, gasification slag, coal gangue, and cement on the early compressive strength of filling materials. According to the regression model, the contour plots (Figure 12a–c) and response surface plots (Figure 12d–f) of the early compressive strength varying with the factor level were drawn.

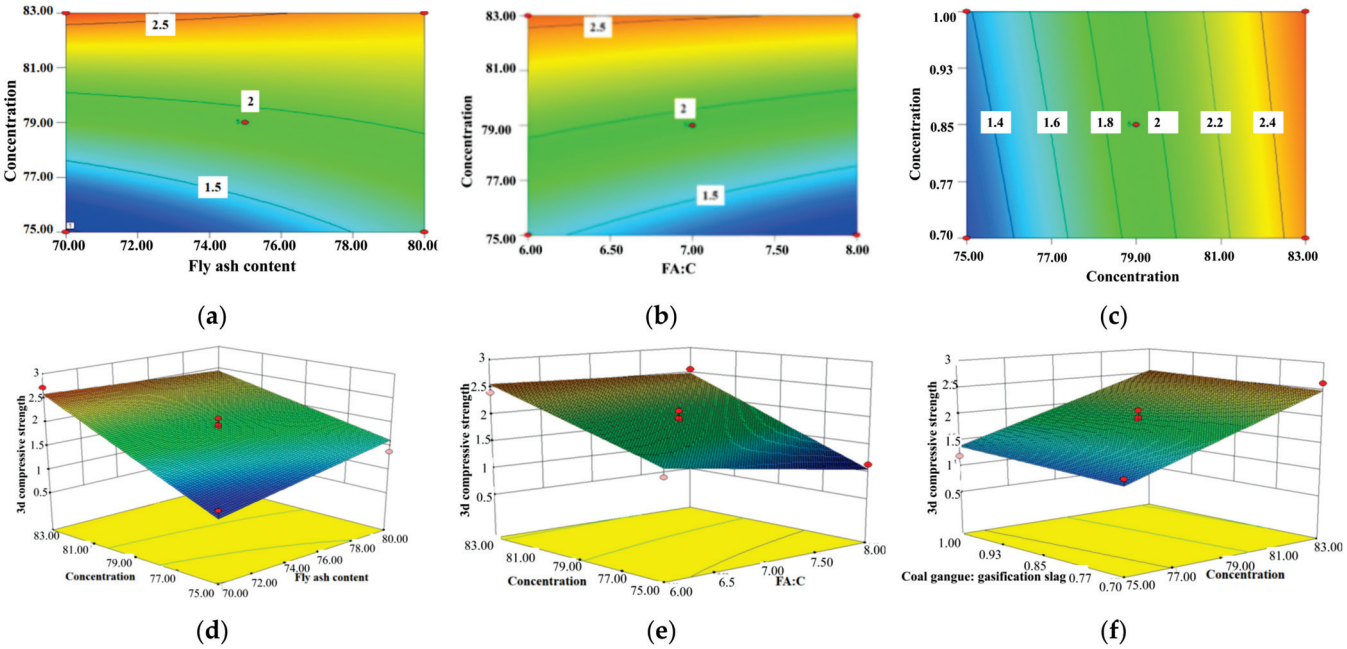

Figure 12. Influence analysis of strength response surface factor interaction on 3 d. (**a**) A relationship contour map between strength and X_1X_3; (**b**) relationship contour map between strength and X_2X_3; (**c**) relationship contour map between strength and X_3X_4; (**d**) relationship response surface plot between strength and X_1X_3; (**e**) relationship response surface plot between strength and X_2X_3; (**f**) relationship response surface plot between strength and X_3X_4.

Meanwhile, we also analyzed the 7-day two-factor interaction regression model to demonstrate the two-factor interaction model under 3-day early compressive strength. The 7-day regression model was consistent with the 3-day regression model. As shown in Figure 13a–c, the solid mass fraction had a significant effect on the compressive strength.

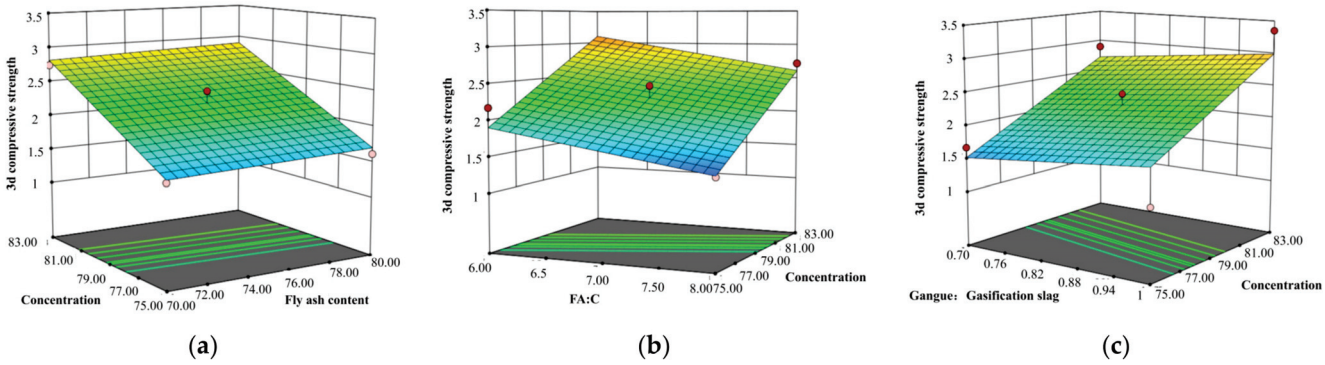

Figure 13. Influence analysis of strength response surface factor interaction on 7 d. (**a**) A relationship response surface plot between strength and X_1X_3; (**b**) relationship response surface plot between strength and X_2X_3; (**c**) relationship response surface plot between strength and X_3X_4.

The results of the analysis of variance and factor interaction showed that the three-dimensional compressive strength of the backfill was sensitive to the response of the single factor. Meanwhile, the interaction among various factors also showed strong significance, as shown in Table 4. A single factor affected the order of significance: solid mass concentration ($F = 82.81$, $p < 0.0001$) > FA:C ($F = 4.84$, $p = 0.0391$) > the amount of fly ash in the solid ($F = 3.85$, $p < 0.0631$) > coal gangue:gasification coarse slag ($F = 0.74$, $p < 0.3981$). The interaction between solid mass concentration and FA:C ($F = 3$, $p < 0.0979$) was the decisive factor affecting the early strength of the backfill. The second was the interaction between

solid mass concentration and fly ash content ($F = 0.91, p < 0.3516$). The interaction between solid mass concentration and coal gangue:gasification slag ($F = 0.03, p < 0.8641$) had the least effect. The analysis results of single-factor and double-factor interaction showed that the factors of filling materials with different fluidity and compressive strength requirements were also different. High-strength and low-fluidity filling materials could be controlled to have high concentration and high FA:C. Low-strength and high-fluidity materials could be controlled to have low concentration and low FA:C. High-strength and high-fluidity materials could be controlled to have medium concentration.

5. Conclusions

In this study, the BBD method was used to carry out the experiment, and the response surface regression model of fly ash content, mass concentration, coal gangue:gasification slag, and FA:C was established. Then, the normalization method was used to optimize the coal-based solid waste mix proportion. Finally, the optimal solution was obtained. A low-cost and high-reliability filling material was proposed, which provided important support for large-scale utilization and low-risk mining of solid waste. The main conclusions of this study were as follows:

(1) The particle size distribution of the main components was studied. The particle size distribution of fly ash and cement was below 100 μm, accounting for 79% of the crushed coal gangue below 8 mm. The application showed that the coal gangue was massive. The main component of fly ash was quartz, which was spherical. The gasification residue contained toxic lead arsenate in the form of honeycomb. The economic value was estimated. The crushing cost of coal gangue was increased by at least RMB 50 per ton.

(2) Further, 29 groups of experimental schemes were designed, and the filling proportion scheme and parameters with low cost and high reliability were optimized. Using the normalization method and radar visualization, the mix proportion was further analyzed to verify the reliability of the optimization results. The optimal proportioning parameters were obtained. The fly ash content in solids was 79%, the solid mass concentration was 78%, FA:C was 6:1, and coal gangue:gasification slag was 1:1.

(3) The influence laws of strength and various factors were analyzed, and the significance ranking of various factors was obtained. The effect of mass concentration on compressive strength and fluidity was significant. High-strength and low-fluidity filling materials were controlled to have high concentration and high FA:C. Low-strength and high-fluidity filling materials were controlled to have low concentration and low FA:C. High-strength and high-fluidity materials were controlled to have medium concentration.

Author Contributions: Conceptualization, D.C. and K.Y.; methodology, T.C.; software, C.L. and R.C.; validation, D.C., K.Y., and C.L.; resources, K.Y.; data curation, D.C. and R.Q.; writing—original draft preparation, T.C.; writing—review and editing, T.C. All authors have read and agreed to the published version of the manuscript.

Funding: This work is supported by National Key Research and Development Program of China: (2019YFC1904300), the institute of Energy, Hefei Comprehensive National Science center under Grant No.21kzs217, the University of Synergy Innovation Program of Anhui Province No.GXXT-2021-017, No.GXXT-2020-008, and the National Natural Science Foundation of China (Grant No. 51974008).

Data Availability Statement: Not applicable.

Conflicts of Interest: The authors declare no conflict of interest.

References

1. Qian, M.G.; Xu, J.L.; Miao, X.X. Coal mine green mining technology. *J. China Univ. Min. Technol.* **2003**, *32*, 343–348.
2. Wang, L.; Yu, Y.; Ren, H.B.; Liang, X.F. How to Get out of the Embarrassment of "Buried and Buried" with the Accumulation of over 60 Billion Tons of Industrial Solid Waste. *Resour. Regen.* **2020**, 40–42. Available online: https://www.sohu.com/a/477984877_121123735 (accessed on 4 May 2022).
3. Wang, J.S.; Li, J.; Chen, B.X.; Fu, Z.Q.; Zhang, Z.L. Ecological Risk Assessment of Coal Industry in the Energy and Chemical Base of Eastern NingXia. *Resour. Sci.* **2013**, *35*, 2011–2016.
4. Wei, T.; Wu, L.X. Restrictive Factors and Development Suggestions for the Development of Modern Coal Chemical Industry in NingXia. *Coal Econ. Res.* **2021**, *41*, 65–69.
5. Li, J. "The Development of the Golden Triangle" of Energy and Chemical Industry Have Been Upgraded to a National Strategy. NingXia Dly. 2019. Available online: http://www.ocn.com.cn/free/201009/huagong150940.htm (accessed on 4 May 2022).
6. Han, X.Y.; Liu, R.A. Research on Comprehensive Utilization, Storage and Disposal Countermeasures of Industrial Solid Waste in East NingXia Base. *Resour. Conserv. Environ. Prot.* **2015**, *2015*, 66–67.
7. Li, J.; Wang, J. Comprehensive utilization and environmental risks of coal gangue: A review. *J. Clean. Prod.* **2019**, *239*, 117946. [CrossRef]
8. Zhang, C.; Wang, X.L.; Li, S.G.; Liu, C.; Xue, J.H. Proportion optimization of modified lye for treating hydrogen sulfide in the coal mine based on response surface method. *J. China Coal Soc.* **2020**, *45*, 2926–2932.
9. Zhu, D.F.; Tu, S.H.; Yuan, Y. 3D DEM Method for Compaction and Breakage Characteristics Simulation of Broken Rock Mass in Goaf. *Acta Geotech.* **2021**. Available online: https://www.cnki.com.cn/Article/CJFDTotal-YTLX201803034.htm (accessed on 4 May 2022).
10. Tang, Y.; Zhang, L.; Lu, H. Experimental study on optimization of coal-based solid waste preparation filling material ratio. *J. Min. Sci.* **2019**, *4*, 327–336.
11. Li, L. *Research on Energy Consumption and Tooth Plate Structure Parameters of Jaw Crusher*; Central South University: Changsha, China, 2009.
12. *GB/T 50123—2019*; Geotechnical Test Method Standard. Chinese Standard: Beijing, China, 2019.
13. Huo, X.; Lu, C. Influence of Portland Cement Mineral Composition and Fineness on Concrete Durability. *People's Yangtze River* **2020**, *51*, 294–296.
14. *JGJ/T 70-2009*; Standard for Basic Performance Test Method of Building Mortar. Chinese Standard: Beijing, China, 2009.
15. Cui, Z.T.; Sun, H.H. Preparation and performance of coal gangue conglomerate-like filling material. *J. China Coal Soc.* **2010**, *35*, 896–899.
16. Yan, P. The Mechanism of Fly Ash in the Hydration Process of Composite Cementitious Materials. *J. Chin. Ceram. Soc.* **2007**, 167–171. Available online: https://kns.cnki.net/kcms/detail/detail.aspx?dbcode=CJFD&dbname=CJFD2007&filename=GXYB2007S1025&uniplatform=NZKPT&v=KwyYkQjFzYwbMxuNE-DcwYaIPCqQk4z9GgkWX0l3d4WEgPTrccAVbdT4_OoOZjV8 (accessed on 4 May 2022).
17. Sun, Q.W.; Zhu, H.; Cui, Z.L. Study on Preparation and Performance of fly ash-Coal Gangue Based Cemented Filling Material. *China Saf. Sci. J.* **2012**, *22*, 74–80.
18. Zhang, C.; Zhao, Y.; Han, P.; Bai, Q. Coal pillar failure analysis and instability evaluation methods: A short review and prospect. *Eng. Fail. Anal.* **2022**, *138*, 106344. [CrossRef]
19. Liu, S.; Li, G.; Liu, G.; Wang, F.; Wang, J.; Qi, Z.; Yang, J. Optimization of slag-based solid waste cementitious material ratio based on response surface methodology. *Silic. Bull.* **2021**, *40*, 187–193.
20. Hu, B.N. My country's coal mine filling mining technology and its development trend. *Coal Sci. Technol.* **2012**, *40*, 1–5, 18.
21. Wu, A.X.; Wang, Y.; Wang, H.J. Current Status and Trend of Paste Filling Technology. *Met. Mine* **2016**, 1–9. Available online: https://kns.cnki.net/kcms/detail/detail.aspx?dbcode=CJFD&dbname=CJFDLAST2016&filename=JSKS201607002&uniplatform=NZKPT&v=WZAV0-oV9UAmGGpVjXyDEFfCTur-iuXGED_lrh-DhKDKRh7ElgEhuvAOIdt6Tfc7 (accessed on 4 May 2022).
22. Li, L.; Zhang, S.; He, Q.; Hu, X.B. Application of Response Surface Method in Experimental Design and Optimization. *Lab. Res. Explor.* **2015**, *34*, 41–45.
23. Ouattara, D.; Belem, T.; Mbonimpa, M.; Yahia, A. Effect of superplasticizers on the consistency and unconfined compressive strength of cemented paste backfills. *Constr. Build. Mater.* **2018**, *181*, 59–72. [CrossRef]
24. Qiu, J.; Guo, Z.; Yang, L.; Jiang, H.; Zhao, Y. Effect of tailing fineness on flow, strength, ultrasonic and microstructure characteristics of cemented paste backfill. *Constr. Build. Mater.* **2020**, *263*, 120645. [CrossRef]
25. Zhang, X.G.; Jiang, N.; Zhang, Y.H.; Jiang, X.Y.; Zhang, B.L. Experimental study on fly ash used as underground filling material. *Met. Mine* **2012**, *135*, 127–131.
26. Wang, Y.Z. Experimental study on coal gangue fly ash used as underground filling material. *Non-Ferr. Met. Eng.* **2019**, *10*, 108–113.
27. Hu, H.; Sun, H. Development of Mine Filling Technology and New Paste-like Filling Technology. *China Min.* **2001**, *10*, 49–52.
28. Dou, Y.; Liu, F.; Zhang, W. Comparative analysis of response surface modeling methods. *J. Eng. Des.* **2007**, *14*, 359–363.

sustainability

MDPI

Article

Research on the Impact of the Digital Economy on Carbon Pollution Based on the National Big Data Comprehensive Pilot Zone in China

Mingguang Liu [1] and Gaoyang Li [2,*]

[1] School of Politics and Public Administration, South China Normal University, Guangzhou 510006, China; 20071077@m.scnu.edu.cn
[2] College of Water Conservancy and Civil Engineering, South China Agricultural University, Guangzhou 510642, China
* Correspondence: ligaoyang@scau.edu.cn

Abstract: The digital economy (DE) is increasingly recognized as a principal driver of high-quality economic development. With the dual carbon goals of carbon peak and carbon neutrality, it is essential to urgently discuss whether the DE can also provide an aid to restrain carbon pollution. For this reason, the purpose of this paper is to examine the influence of the DE on urban carbon pollution and its underlying mechanism, utilizing balance panel data for Chinese cities from 2012 to 2021. Additionally, this study adopts the quasi-natural experiment in the National Big Data Comprehensive Pilot Zone to empirically analyze this relationship using the Difference-in-Differences (DID) and mediating effect models. The findings indicate that the DE can significantly decrease carbon pollution, exhibiting a clear carbon pollution reduction effect. These conclusions remain valid even after implementing various robustness tests. This examination of the action mechanism reveals that it is effective for the DE to mitigate urban carbon pollution by enhancing energy efficiency and attracting foreign investment. Further analysis of heterogeneity reveals that it is more effective for the DE to reduce carbon pollution in the non-resource-based cities, large cities, eastern regions, and cities with high urbanization levels as compared to the resource-based cities, small or mega cities, central and western regions, and cities with a low level of urbanization. These findings not only offer robust objective evidence for the positive influence of the DE on carbon pollution reduction, but also present valuable policy implications for minimizing carbon pollution and enhancing environmental quality.

Keywords: DE; carbon pollution; action mechanism; heterogeneity

1. Introduction

After more than 40 years of reform and opening up, the Chinese economy has achieved remarkable success, with its GDP (gross domestic product) surpassing CNY 100 trillion in 2020 and reaching CNY 114 trillion in 2021 [1]. However, along with this rapid development, China's carbon emissions have increased almost 14 times from 1959 to 2020, making it the largest carbon generator. During the United Nations General Assembly on 22 September 2020, President Xi Jinping declared China would strengthen its national independent contributions by implementing stronger policies and strategies and endeavoring to reach the zenith of CO_2 emissions before 2030 and carbon neutrality by 2060 [2,3]. Concurrently, China's DE has experienced incredible growth. In accordance with the White Paper on Global DE (2023), which is released by the China Academy of Information and Communications Technology, DE in China has undergone expeditious development from 2016 to 2022. During this period, the size of the DE has grown by USD 4.1 trillion, with a mean annual growth rate of 14.2% [4]. The incessant development of modern information technology, including big data, blockchain, cloud computing, and artificial intelligence, has played a momentous role in driving China's economic development [5,6]. The DE has actualized an

increasingly crucial strength in stimulating consumption, boosting investments, creating job opportunities, and upgrading industrial structures.

With the increasing influence of the DE on various aspects of society, including economic growth, industrial development, and social life, there has been a growing interest in researching how the DE can empower the environment and contribute to sustainable development. Initially, scholars primarily investigated the influence of the DE on various pollutants, such as industrial sulfide gas, industrial sewer water, and industrial smut [7,8]. Subsequently, attention has shifted towards detecting the connection between the DE and factors such as carbon efficiency, carbon dioxide emissions, air quality, and PM2.5. Of particular interest is the carbon reduction effects of the DE, which has emerged as a prominent focus of research. For instance, Dong F, Hu M, Gao Y et al. (2022) conducted a study using national panel data from 2008 to 2018 and found that the DE significantly mitigated carbon pollution vehemence but concurrently played a part in an increase in per capita carbon emissions. The study further identified that economic growth, financial development, and industrial structure upgrading played a critical intermediary role between the DE and carbon pollution [9]. Wang J., Dong K., Dong X. et al. (2022) implemented a study employing panel data from 30 provinces in China from 2006 to 2017. Their findings implied that the DE had a negative impact on carbon pollution. This negative impact principally occurred through several channels, including the expansion of the tertiary industry, the reduction in the proportion of coal consumption, and the booster of green technology innovation. These factors indirectly contribute to a reduction in carbon dioxide emissions [10]. Cheng Y., Zhang Y., Wang J. et al. (2023) analyzed data from 278 prefecture-level cities in China from 2011 to 2019. Their research indicated that industrial structure and technological innovation are important mechanisms of DE affecting carbon pollution [11]. However, upon reviewing the existing research literature, it becomes evident that there are three main limitations. Firstly, most studies utilize an index system to measure the DE, but there is currently no generally recognized index system available. Consequently, there is a substantial discrepancy in the measurement results of the DE, making it challenging to accurately evaluate the carbon pollution reduction effect of the DE. Secondly, while numerous studies have explored the mechanisms by which the DE impacts carbon pollution through economic growth, industrial structure supererogation, financial development, and green innovation, there has been limited investigation into the ways in which the DE influences carbon pollution in terms of energy efficiency and foreign investment. Lastly, existing research has not adequately addressed the diverseness of the impact of the DE on carbon pollution from various perspectives, such as regions, city sizes, city resource endowment, and urbanization level. These limitations highlight the need for future research to address these gaps in knowledge and provide a more comprehensive understanding of the relationship between the DE and carbon pollution.

The purpose of this paper is to examine the impact of the DE on carbon pollution from both theoretical and empirical perspectives. The focus is on investigating the impact effect, action mechanism, and heterogeneity of the DE on carbon pollution. To achieve these research objectives, several steps are taken, as follows. First, the relationship and mechanism between the DE and carbon pollution are explored from a theoretical level. Second, the DID model is utilized to measure the policy effect of the DE on urban carbon pollution, and a series of robustness testing methods are conducted to validate the robustness of the research conclusions of the benchmark regression model. Third, in order to examine the mediating action mechanism of the impact of the DE on carbon pollution, the study employs the mediating effect model, taking into account two mechanism variables: energy efficiency and foreign investment. Finally, the study investigates the heterogeneity of the impact of the DE on carbon pollution by grouping regression analysis from various perspectives, including regions, city sizes, city resource endowments, and levels of urbanization.

The research presented holds significant implications, as it can offer crucial support for accurately assessing the carbon pollution reduction effects of the DE and informing relevant policy designs.

2. Theoretical Analysis of the Relationship between the DE and Carbon Pollution

2.1. The DE and Carbon Pollution

Sustainable development refers to the simultaneous consideration of economic, social, and ecological development. True sustainable development can only be achieved by simultaneously meeting economic sustainable development, social sustainable development, and ecological sustainable development. The DE utilizes digitized, networked, intelligent, and innovative technologies to impact the real economy and social development [12]. By integrating the DE into the real economy, it contributes to high-quality economic and social development while also improving environmental pollution and urban air quality. Therefore, the DE serves as a crucial driver for both sustainable economic and social development, as well as ecological sustainability. In terms of the borderless organization theory, the growth of the DE empowers the expeditious crossing of information, resources, creativity, and energy between corporations, permitting managers to respond blazingly to environmental variations [13]. This not only optimizes processing technology to achieve emission reduction from enterprises but also realizes a more energy-efficient production process to reduce carbon pollution [14]. From the perspective of environmental supervision, the digital economy can utilize information technology to achieve real-time monitoring of various pollutants and pollution sources. In particular, smart monitoring systems play a crucial role in encouraging polluting firms and industries to effectively control and eliminate excessive pollutant emissions, thereby achieving environmentally friendly production and reducing carbon pollution [15]. From the perspective of macro-governance, the government can leverage digital technology to acquire a better comprehension of energy trade direction and price oscillations. By regulating energy prices and employing cross-subsidies, the government can constrain the total energy provision and conduct the provision of clean energy. This enables the optimization of the energy supply system and reduces carbon pollution [16]. Additionally, the DE has revolutionized the way in which people work and live, especially during the pandemic. It has reduced the need for daily travel and transportation, promoted the adoption of home online offices, and efficiently decreased carbon pollution in work and life. As such, the following hypothesis is put forward.

Hypothesis 1. *The DE can have a significant influence on reducing carbon pollution.*

2.2. The Underlying Mechanism of the DE Acting on Carbon Pollution

Among the various factors contributing to the continuous rise in total carbon pollution, excessive reliance on fossil fuels is considered a significant cause. It is widely acknowledged that adopting a reasonable energy structure and improving energy efficiency are crucial strategies for reducing CO_2 emissions. The emergence of the DE has introduced fresh tools for managers to monitor the dynamics among producers, suppliers, and consumers, thereby facilitating the adaptation of production plans and achieving effective resource distribution. Simultaneously, the DE also disrupts conventional models of resource utilization. Various businesses have different preferences when it comes to implementing digital technologies, which can enhance resource allocation and boost energy efficiency [17]. Advancements in emerging digital technologies have led to increased automation, interconnectivity, and flexibility in the processes of production, manufacturing, and consumption [18,19]. These technologies also enable intelligent administration and monitoring of energy systems and data, which can be beneficial for improving energy efficacy. The DE heavily relies on information technology, which involves the input of knowledge, technology, and other elements. This approach presents superiorities such as low cost of diffusion, high marginal revenue, and scale efficiency. The integration of these novel elements with traditional industries can accelerate the optimization of product mix, improve energy efficacy, and facilitate the transformation towards low energy consumption and low carbon pollution. Ultimately, these initiatives will contribute to reducing pollution emissions. Additionally, the development of the DE facilitates the transformation from high-energy and high-pollution industries to low-energy, low-pollution, and knowledge-intensive industries [20]. This transition

towards industries with lower energy consumption and pollution levels is primarily attributed to the optimization and upgrading of the industrial structure enabled by the DE. Consequently, the growth of these low-energy-consumption and low-pollution industries has bolstered energy efficiency and indirectly mitigated carbon pollution. Therefore, the following hypothesis is proposed:

Hypothesis 2. *The DE can enhance energy efficiency, thereby reducing carbon pollution.*

The growth of the DE has the potential to enhance the market economy system, ameliorate information symmetry among market participants, eliminate information barriers between regions, ameliorate the efficiency of information transmission, decrease transaction expenditure for foreign investment, and ultimately attract more foreign investment [21]. While some scholars argue that developed countries have been transferring traditional industries with low added value and high pollution to China, which has contributed to the industrialization in China to some extent [22], this practice is not beneficial for the high-level development of the service industry or carbon pollution reduction. However, the Chinese economy has now reached a state of high-quality development. Emerging technologies, including blockchain, big data, artificial intelligence, and cloud computing, have played a remarkable part in making these information mechanisms in the economy and society more transparent [23]. These technologies have also alleviated the problem of information asymmetry to a great extent, reducing the flow barriers of factors in the market and decreasing the additional cost associated with foreign investment. Consequently, the DE has been successful in attracting foreign investment. Additionally, the DE has ameliorated the efficacy of foreign investment supervision and made it easier to guide foreign investors towards investing in the fields of energy conservation and environmental protection. This positive influence has facilitated the transformation of polluting industries, ultimately resulting in a significant diminution of carbon pollution. Therefore, it is hypothesized that the DE has the potential to attenuate carbon pollution with its ability to attract foreign investment.

Hypothesis 3. *The DE can contribute to the reduction of carbon pollution by attracting foreign investment.*

3. Research Design

3.1. Model Setting

To assess whether the DE can contribute to reducing urban carbon pollution in China, we use the pilot of the National Big Data Comprehensive Pilot Zone as a case study to test the research hypothesis by evaluating the effectiveness of its policies. To achieve this, a two-way fixed-effect Difference-in-Differences (DID) model is constructed, taking advantage of the quasi-natural experiment provided by the pilot zone. The baseline regression model is specified as follows:

$$\ln CE_{it} = \beta_0 + \beta_1 did_{it} + \beta_2 Control_{it} + \eta_i + \delta_t + \varepsilon_{it} \quad (1)$$

In the formula provided, the subscripts i and t severally denote a city and a year. The $\ln CE_{it}$ represents the logarithm of city i's per capita carbon dioxide pollution in year t, did_{it} indicates if city i implemented the National Big Data Comprehensive Pilot Zone pilot policy in year t. $Control_{it}$ denotes a set of control variables that influence urban carbon pollution and vary across cities and time. η_i represents the individual fixed effect of the city that does not change over time. δ_t denotes the year fixed effect, which controls time-related factors that affect all cities that change over time. ε_{it} is a residual term. The estimation coefficient β_1 is a policy effect concerned in this paper. Assuming that β_1 is significantly negative, this indicates that this policy is effective, meaning that the DE has a considerable inhibition effect on carbon pollution.

Based on the baseline regression about the identification of policy effects, we aim to probe if the DE impacts carbon pollution through two pathways: energy efficiency and foreign investment. To achieve this, we employ the mediating effect test approach put forward by Wen Zhonglin et al. (2014) and Lin Feng et al. (2022) to construct the following test equation [24,25]:

$$M_{it} = \alpha_0 + \alpha_1 \mathrm{did}_{it} + \alpha_2 \mathrm{Control}_{it} + \eta_i + \delta_t + \varepsilon_{it} \quad (2)$$

$$\ln CE_{it} = \varphi_0 + \varphi_1 \mathrm{did}_{it} + \varphi_2 M_{it} + \varphi_3 \mathrm{Control}_{it} + \eta_i + \delta_t + \varepsilon_{it} \quad (3)$$

wherein M_{it} is a mechanism variable, representing energy efficiency (lnene) and foreign investment (lnfdi), and other variables have been explained earlier. The validity of the mediating effect will be determined by whether both coefficients α_1 and φ_2 are significant. The Bootstrap method will be used to directly test the hypothesis $\alpha_1 \times \varphi_2 = 0$ if at least one of the coefficients is not significant. If $\alpha_1 \times \varphi_2$ significantly deviates from 0, it confirms the existence of a mediating effect. Conversely, if it does not significantly deviate from 0, the mediating effect is considered invalid. In the case of a mediating effect, it suggests that the direct effect is not significant, indicating the existence of only the mediating effect when the coefficient φ_1 is not significant. Conversely, if the coefficient φ_1 is significant, the direct effect is deemed significant, and it is necessary to compare the symbols of $\alpha_1 \times \varphi_2$ and φ_1. If the symbols are the same, it is considered a partial mediating effect, but if they are different, it's referred to as a masking effect.

3.2. Various Variable Settings

3.2.1. The Explained Variables

The explained variable in this study is carbon pollution, measured by per capita carbon dioxide emissions (lnCE). According to Cong et al. (2014), total carbon dioxide emissions can be measured across various sectors, including urban transport, construction, industrial production processes, land-use changes in agriculture and forestry, and greenhouse gas emissions from waste treatment activities. Furthermore, these measurements also take into account emissions from electricity, heating, or refrigeration required for urban consumption, as well as greenhouse gas emissions from the production, transport, use, and waste treatment of all goods purchased by cities from outside their jurisdiction [26]. The total carbon dioxide emissions of a city are calculated as the aggregate carbon pollution within the above scope. Meanwhile, the per capita carbon dioxide emissions are determined by dividing the total carbon dioxide emissions of the city by its permanent population.

3.2.2. Core Explanatory Variables

The National Big Data Comprehensive Pilot Zone is considered the core explanatory variable, denoted by the variable did. The calculation for did is $\mathrm{did}_{it} = \mathrm{treat}_i \times \mathrm{post}_t$, where treat_i denotes a dummy variable indicating whether city i is attached to the treatment group, and post_t also denotes a dummy variable representing the time of policy implementation. In 2016, 10 provinces and cities in China were authorized to establish National Big Data Comprehensive Experimental Zones. Hence, if the time $t \geq 2016$, $\mathrm{post}_t = 1$, otherwise $\mathrm{post}_t = 0$. If the city i builds a National Big Data Comprehensive Pilot Zone, $\mathrm{treat}_i = 1$, and if not, $\mathrm{treat}_i = 0$.

3.2.3. Control Variables

Urban carbon pollution is also affected by many other factors. It is necessary to include the following control variables that have been identified in existing studies:

- The economic development (lngdp). This variable is gauged by per capita GDP, which is a crucial factor to consider. However, it is also important to take into account the theory of the environmental Kuznets curve [27], which suggests that an inverted U-shaped connection exists between economic development level and environmental

pollution. Therefore, the regression model includes the square term (lngdp2) of per capita GDP.

- Population density (lnpop). This variable is included in the study due to its significance in the IPAT model's understanding of urban carbon pollution [28,29]. On the one hand, higher population density usually leads to increased resource consumption, resulting in higher carbon pollution. On the other hand, the concentration of the population can also promote energy efficiency and the sharing of infrastructure, which in turn reduces carbon pollution [30]. Therefore, this paper incorporates population density as a control variable, measured by the ratio of the total population to the administrative area.
- Trade openness (lntrd). This variable plays a significant role in influencing carbon pollution through its impact on domestic technological progress and the transformation and upgrading of industrial structures. This is achieved through cross-border technological exchanges and the enforcement of stricter environmental access standards. As a result, trade openness is included as a control variable in this study, utilizing the total import and export volume of the city as a measure.
- Urbanization (lnurc). Existing studies have shown a strong relationship between urban carbon pollution and urbanization. On the one hand, the rapid advancement of urbanization leads to a substantial increase in energy consumption and, subsequently, carbon pollution. On the other hand, the progress made in urbanization facilitates the more concentrated use of urban energy, the optimization of energy structures, and the upgrading of industrial structures, all of which contribute to decreasing urban carbon pollution. Consequently, urbanization is considered a control variable in this study, measured by the ratio of the urban population to the total city population.
- Investment in fixed assets (lnfai). Investment in fixed assets plays a crucial role in influencing urban carbon pollution. Increased investment in urban fixed assets, particularly in environmental protection, not only promotes the development of environmental protection technologies but also facilitates the upgrading of industrial structures. Consequently, this ultimately helps to decrease urban carbon pollution. Thus, fixed asset investment is included as a control variable in this study, measured by the total amount of urban fixed asset investment.
- Social consumption (lnsoc). This variable is closely connected to urban carbon pollution. Social consumption, which is one of the three major drivers of economic growth, has significant implications for resource consumption and environmental issues. Traditional social consumption tends to increase resource consumption and contribute to environmental problems [31]. However, with an increased awareness among residents about environmental conservation, green consumption that promotes nature preservation and ecological protection can incentivize enterprises to produce more environmentally friendly products. As a result, urban carbon pollution can be reduced. Given the importance of this variable, social consumption is also considered a control variable in this study, measured by the ratio of total retail sales of urban social consumer goods to GDP.

3.2.4. Mechanism Variables

In light of the theoretical analysis of the action mechanism, this study selects two mechanism variables. One variable is energy efficiency (lnene), which denotes the output value per unit of energy consumption. It is denoted as the ratio of the city's GDP to its total energy consumption. Considering the possible lack of various energy consumption data for cities, the total energy consumption is converted into standard coal instead of the electricity consumption of the entire city. The other variable is foreign investment (lnfdi), which serves as a proxy variable for the real utilization of foreign investment.

3.3. Data Origins and Processing

Considering data accessibility, the balance panel data of 282 prefecture-level cities in China spanning from 2012 to 2021 were selected as a research sample. The data used primarily comes from sources such as statistical yearbooks of different levels in China, the Strawberry Scientific Research Service Network, Prospective Database, etc. In cases where data was missing, it was supplemented through linear interpolation. To reduce data discretization and mitigate the adverse effects of heteroscedasticity on equation estimation, logarithmic processing was applied to variables other than the core explanatory variables. The descriptive statistics of the variables are presented in Table 1.

Table 1. Descriptive statistics of the variables.

Variable Class	Name	Sign	N	Mean	SD	Min	Max
Explained variables	Carbon pollution	lnCE	2820	2.198	0.707	0.105	5.037
Explanatory variables	DE	did	2820	0.121	0.327	0.000	1.000
	Economic development	lngdp	2820	10.790	0.530	8.783	12.320
	The square of economic development	$lngdp^2$	2820	116.800	11.470	77.150	151.900
	Population density	lnpop	2820	5.759	0.921	1.628	8.058
	Trade openness	lntrd	2820	14.020	2.110	3.211	21.330
	Urbanization	lnurc	2820	3.997	0.267	3.105	4.605
	Investment in fixed assets	lnfai	2820	7.192	0.915	4.086	9.992
	Social consumption	lnsoc	2820	3.614	0.359	−5.773	4.618
Mechanism variables	Energy efficiency	lnene	2820	2.774	0.774	−0.567	5.596
	Foreign investment	lnfdi	2820	11.78	2.105	−5.015	16.83

Note: It should be noted that the variables, except for did, were logarithmically transformed for statistical analysis.

4. Empirical Results and Analysis

4.1. Baseline Regression

On the basis of the panel data from 282 of China's prefecture-level cities spanning from 2012 to 2021, we utilized a two-way fixed effect regression model to test Hypothesis 1 as specified in Equation (1). To avoid potential autocorrelation problems associated with the panel data, cluster-robust standard errors were used to estimate the standard errors. Table 2 presents the baseline regression consequences for the impact of the DE on carbon pollution. Column (1) displays the regression consequences without control variables, while columns (2) to (7) progressively include different control variables. The baseline regression consequences indicate that did has a consistently significant negative effect on urban carbon pollution, regardless of the inclusion of control variables. This suggests that the growth of the DE can effectively decrease carbon pollution in urban areas, thus providing support for research Hypothesis 1.

Considering the regression consequences of control variables in column (7), the primary coefficient of per capita GDP is significantly positive, while the secondary coefficient is significantly negative. This suggests that there are inverted "U"-type connections between economic development level and carbon pollution, which proves the existence of the environmental Kuznets curve. Additionally, population density has a considerable inhibitory impact on carbon pollution, indicating that the agglomeration effect of population density is dominant. The positive externality of this effect can reduce carbon pollution through cost-saving measures and technology spillover [32]. Furthermore, foreign trade has a noticeable inhibitory effect on carbon pollution, indicating that transnational technological exchanges and cooperation facilitated by foreign trade can promote technological progress and industrial structure upgrading in cities, which in turn can slow down urban carbon pollution. The coefficient of urbanization is significantly positive, indicating that the increase in urbanization level will lead to a rise in carbon pollution because of the expanded energy consumption demand. The coefficient between fixed asset investment

and carbon pollution is significantly negative. This finding is in accordance with the research consequences of Chen (2022) [33]. This suggests that fixed asset investment activities can result in production-scale effects and reduce carbon pollution. Social consumption has a significant positive influence on carbon pollution, demonstrating that an increase in social consumption will stimulate the supply level of enterprises, resulting in higher energy consumption and increased carbon pollution.

Table 2. Test results of the DE on carbon pollution.

Variables	(1)	(2)	(3)	(4)	(5)	(6)	(7)
did	−0.043 ***	−0.038 ***	−0.022 **	−0.022 *	−0.026 **	−0.021 *	−0.021 *
	(0.012)	(0.012)	(0.011)	(0.011)	(0.011)	(0.012)	(0.012)
lngdp		2.335 ***	2.059 ***	2.098 ***	1.935 ***	1.924 ***	1.871 ***
		(0.573)	(0.579)	(0.572)	(0.634)	(0.576)	(0.568)
$lngdp^2$		−0.104 ***	−0.090 ***	−0.091 ***	−0.084 ***	−0.080 ***	−0.078 ***
		(0.026)	(0.026)	(0.025)	(0.028)	(0.025)	(0.025)
lnpop			−0.464 ***	−0.455 ***	−0.453 ***	−0.399 ***	−0.400 ***
			(0.117)	(0.114)	(0.112)	(0.112)	(0.112)
lntrd				−0.019 **	−0.020 **	−0.015 **	−0.016 **
				(0.008)	(0.008)	(0.008)	(0.008)
lnurc					0.103 *	0.088	0.096 *
					(0.058)	(0.055)	(0.055)
lnfai						−0.065 ***	−0.065 ***
						(0.018)	(0.018)
lnsoc							0.027 *
							(0.016)
Constant	2.203 ***	−10.857 ***	−6.835 **	−6.892 **	−6.424 *	−6.575 **	−6.419 **
	(0.002)	(3.222)	(3.434)	(3.371)	(3.574)	(3.292)	(3.255)
Urban fixed effect	*Yes*	*Yes*	*Yes*	*Yes*	*Yes*	*Yes*	*Yes*
Year fixed effect	*Yes*	*Yes*	*Yes*	*Yes*	*Yes*	*Yes*	*Yes*
Sample size	2820	2820	2820	2820	2820	2820	2820
Adj. R^2	0.976	0.978	0.978	0.979	0.979	0.979	0.979

Note: "***", "**", and "*" express significance levels at 1%, 5%, and 10%, respectively. The numbers in brackets are cluster-robust standard errors.

4.2. Parallel Trend Test

The primary premise of implementing the DID model is that both the treatment group and the control group should exhibit parallel trend hypotheses. In other words, when the experimental group is not subject to policy intervention, its time trend effect should theoretically be consistent with that of the control group [34]. Currently, there are two methods for testing parallel trend tests: the time trend chart and the event research method. The time trend chart, illustrated in Figure 1, demonstrates that the carbon pollution (lnCE) of the pilot in the treatment group and the control group is not systematically different over the time before 2015, indicating a parallel trend. Therefore, Figure 1 clearly illustrates that this study satisfies the prerequisite for utilizing the DID model.

Compared to the time trend chart, the event research method is considered to be more accurate because the time trend chart relies on only subjective determination to identify whether there exists a pronounced divide. Within the study, this event research method is employed to conduct a parallel trend test using 2012 as the reference period. The results of this method are presented in Figure 2, wherein the horizontal axis denotes the year, the vertical axis denotes the estimated effect value of the processing effect, the dots in the figure represent the policy effect of the treatment group established in the National Big Data Comprehensive Pilot Zone in the year, and the dashed line represents the 10% confidence interval. It is evident from the figure that there was no statistically significant difference in the carbon pollution reduction effect between the treatment group and the control group before the establishment of the National Big Data Comprehensive Pilot Zone.

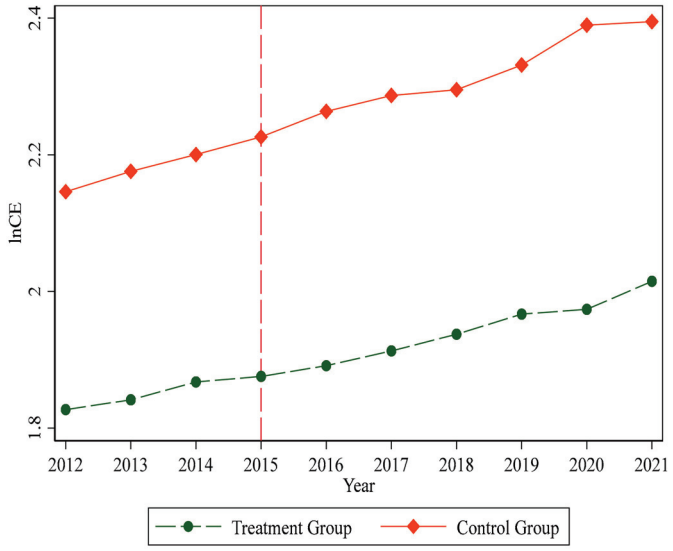

Figure 1. Time trend chart for lnCE change.

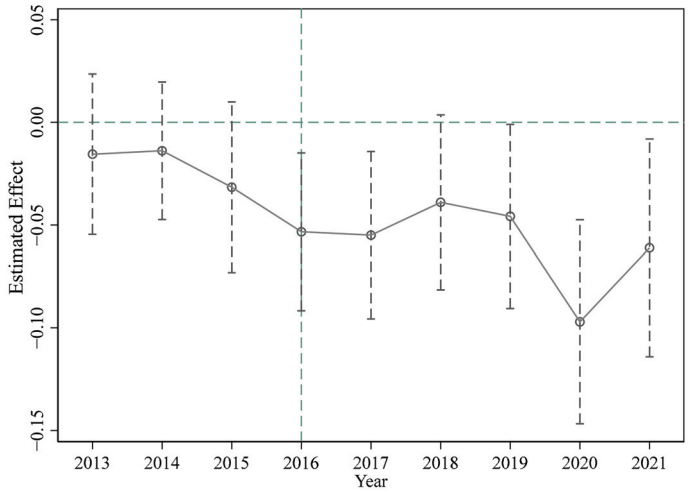

Figure 2. The event research method for parallel trends.

In the year following the establishment of the National Big Data Comprehensive Pilot Zone, the carbon pollution reduction effect of the treatment group, with the exception of 2018, is significantly reduced compared to the control group. This suggests that the DID model adopted in this research meets the parallel trend assumption.

4.3. Placebo Test

To examine whether the regression results in Table 2 are influenced by missing variables and random factors, a permutation test is employed to conduct a placebo test [35]. This involves randomly sampling all cities and policy time, selecting 57 cities each time, and generating a random time. The 57 cities selected each time are considered the dummy treatment group, while the remaining cities serve as the dummy control group. This process is repeated 500 times to obtain the regression coefficients of the interaction terms of the 500 dummy treatment groups and their policy time. The coefficient distribution graph presented in Figure 3 indicates that the coefficients of the spurious did terms are centered around zero, and the majority of the corresponding *p*-values are bigger than 0.1. These results are consistent with the normal distribution. Moreover, in column (7) of Table 2, the coefficient did for the interaction term is −0.021, which is located at the low end of the distribution of the coefficient obtained through the permutation test. The placebo test indicates that there are no significant problems with missing variables or random factors

interfering in the model setting. As a result, the conclusions of the previous study are considered to be relatively robust.

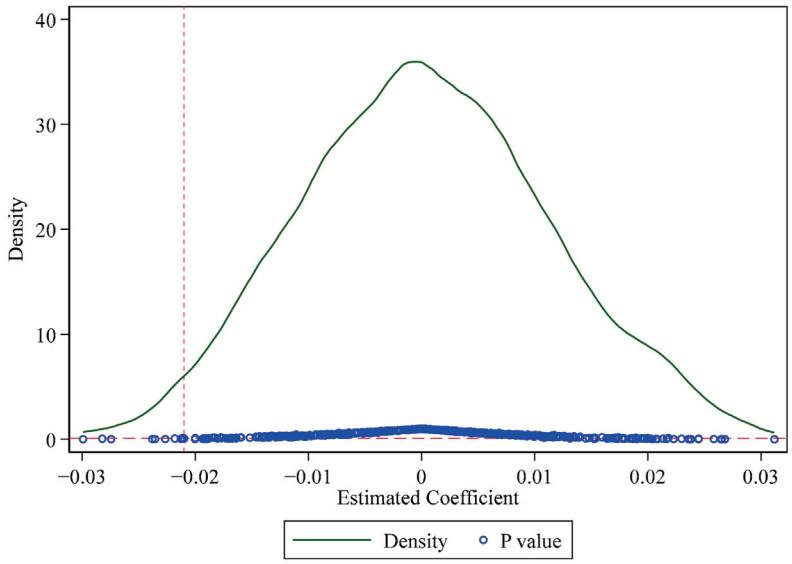

Figure 3. Placebo tests.

4.4. Other Robustness Tests

4.4.1. PSM–DID Estimation

In order to avoid the endogeneity issue due to the potential non-random selection of policies, we refer to the methods employed by Xu Si et al. (2019) and Wang et al. (2023) [36,37]. We further utilize a combination of propensity score matching (PSM) and the DID model to regress the model again. Firstly, the dummy variable of whether the city is a National Big Data Comprehensive Pilot Zone is taken as the explained variable, and all control variables in the baseline regression model are taken as the explanatory variables. The logit regression is carried out, and the corresponding propensity score value for each sample is calculated. Secondly, according to the propensity score, the nearest neighbor matching is carried out among the cities that are not yet in the National Big Data Comprehensive Pilot Zone, and a group of cities with a similar propensity score to the cities in the National Big Data Comprehensive Pilot Zone is picked out as the control group.

Table 3 illustrates that after matching, the deviation between pilot cities and non-pilot cities is significantly reduced, the mean value of covariates is not significantly different, and the standard deviation absolute value is controlled below 10%, suggesting that the matching effect is ideal. The effectiveness of the matching can also be observed in Figure 4, which displays the kernel density maps of propensity scores both before and after matching. From the figure, the deviation of the former two kernel density curves is relatively large when matched, but the latter two curves are close to each other, and the distance between the mean lines is shortened after matching. Therefore, it further indicates that PSM has a good matching effect by reducing sample selectivity bias. Lastly, the regression analysis is conducted again using the matched samples described above, and the specific results are presented in column (1) of Table 4. It is found that the research conclusion of this paper remains valid even after applying PSM in the regression analysis. Additionally, other matching methods such as kernel matching, radius calipers matching, and Mahalanobis distance matching are also employed, and the regression results are consistently aligned with the aforementioned conclusions.

Table 3. Balance testing results.

Variables	Unmatched	Mean Value		Bias (%)	Reduct	*t*-Test	
	Matched	Treated	Control		|Bias| (%)	t	$p > \|t\|$
lngdp	U	10.890	10.768	23.000	77.800	4.930	0.000
	M	10.890	10.917	−5.100		−0.860	0.388
$lngdp^2$	U	118.870	116.220	23.000	78.000	4.950	0.000
	M	118.870	119.460	−5.100		−0.850	0.396
lnpop	U	5.999	5.698	30.000	85.500	7.010	0.000
	M	5.999	5.955	4.300		0.750	0.452
lntrd	U	14.550	13.891	30.300	98.900	6.720	0.000
	M	14.550	14.543	0.300		0.060	0.954
lnurc	U	4.044	3.985	20.800	90.100	4.720	0.000
	M	4.044	4.050	−2.100		−0.360	0.718
lnfai	U	7.620	7.084	62.200	93.500	12.850	0.000
	M	7.620	7.585	4.000		0.710	0.480
lnsoc	U	3.581	3.623	−12.800	29.400	−2.510	0.012
	M	3.581	3.551	9.000		1.400	0.161

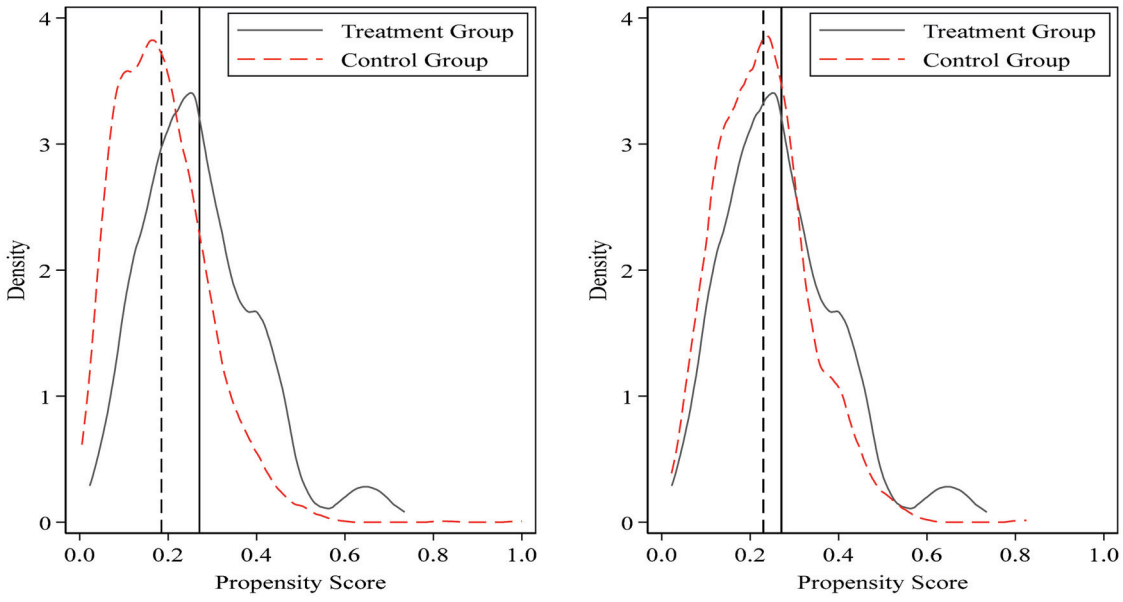

Figure 4. Propensity score probability distribution density function. (**a**) Propensity score before matching; (**b**) propensity score after matching.

4.4.2. Excluding the Influence of Contemporaneous Relevant Policies

Policies related to the DE implemented during the sample period may also influence the carbon pollution of the pilot cities, which might potentially interfere with the estimation of the carbon pollution reduction effects of pilot policies in the National Big Data Comprehensive Pilot Zone. Besides the pilot cities in the National Big Data Comprehensive Pilot Zone, two other initiatives, the "Smart City" pilot launched from 2012 to 2014 and the "Broadband China" initiative implemented from 2014 to 2016, are closely linked to this study [38,39]. Inspired by the methodologies employed by Bai Junhong et al. (2022) [16] and Zhi Yupeng et al. (2023) [40], this paper incorporates dummy variables for the "Smart City" and "Broadband China" pilot policies into the baseline regression model in a consec-

utive manner, aiming to isolate the impacts of relevant policies. The values presented in columns (2) and (3) of Table 4 indicate that the did coefficient remains significantly negative. Furthermore, when considering the policy coupling factor, both the pilot policies of "Smart City" and "Broadband China" are included in the model simultaneously, as shown in column (4) in Table 4. In this case, the coefficient of the pilot policy variables in the National Big Data Comprehensive Pilot Zone remains significantly negative at the 10% significance level. These findings suggest that the pilot policies of "Smart city" and "Broadband China" have only a limited influence on the carbon pollution reduction effect of the pilot policies in the National Big Data Pilot Zone.

Table 4. Results of other robustness tests.

Variables	(1)	(2)	(3)	(4)	(5)	(6)	(7)	(8)	(9)
	PSM-DID	Policies Excluded Related to the Same Period			Transforming the Explained Variable		Excluding Samples	Winsorize	Transformation Explanatory Variable
did	−0.027 **	−0.020 *	−0.021 *	−0.020 *	−0.016 **	−0.021 *	−0.024 *	−0.026	
	(0.013)	(0.012)	(0.012)	(0.012)	(0.008)	(0.012)	(0.013)	**(0.012)	
did_1		−0.017		−0.016					
		(0.013)		(0.012)					
did_2			−0.014	−0.013					
			(0.011)	(0.011)					
dig									−0.028 *
									(0.016)
Constant	−6.489 ***	−6.333 *	−6.218 *	−6.145 *	7.649 ***	2.791	−5.517	−5.490 **	−6.748 ***
	(2.384)	(3.248)	(3.331)	(3.322)	(0.994)	(3.255)	(3.647)	(2.402)	(1.152)
Control variables	Yes	Yes	Yes	Yes	Yes	Yes	Yes	Yes	Yes
Urban fixed effect	Yes	Yes	Yes	Yes	Yes	Yes	Yes	Yes	Yes
Year fixed effect	Yes	Yes	Yes	Yes	Yes	Yes	Yes	Yes	Yes
Sample size	1510	2820	2820	2820	2820	2820	2470	2820	2820
Adj. R^2	0.978	0.979	0.979	0.979	0.977	0.986	0.977	0.979	0.979

Note: Symbols did_1 and did_2 are policy dummy variables for "smart city" and "Broadband China", respectively. Others are the same as before. "***", "**", and "*" express significance levels at 1%, 5%, and 10%, respectively. The numbers in brackets are cluster-robust standard errors.

4.4.3. Transforming the Explained Variable

The baseline regression model employs per capita carbon dioxide emissions as a measure of carbon pollution levels in cities. To strengthen the robustness of the research findings, two alternative indicators, namely total carbon emission and carbon emission intensity (the ratio of the total carbon emission of the city to the city's gross domestic product), are employed as measurement indicators for the explained variables. The regression results for the explained variables of total carbon emission and carbon intensity are presented in columns (5) and (6) of Table 4, respectively. It can be observed that even after substituting the measurement indicators for the explained variables, the coefficient of the did coefficient remains significantly negative, consistent with the results of the baseline regression.

4.4.4. Sample Elimination and Variable Winsorize

To eliminate the possible intervention of urban development imbalance on the research conclusion, it is acknowledged that there may be significant differences between municipalities, provincial capitals, sub-provincial cities, and general prefecture-level cities in carbon pollution, the DE, and economic development. Hence, samples from municipalities, provincial capitals, and sub-provincial cities are excluded, and only samples from general cities are retained. The regression consequences are presented in column (7) of Table 4. The evaluated coefficient of the did remains significantly negative. This indicates that even after removing samples of cities with high administrative ranks, the research

conclusion of this paper remains stable. Furthermore, to mitigate the effect of outliers on the consequences, both the explained variables and all control variables were subjected to 1% winsorization. The regression results after winsorization for each tail are presented in column (8) of Table 4. The evaluated coefficient for the pilot policy variables in the National Big Data Comprehensive Pilot Zone remains significantly negative. This highlights the robustness of the baseline regression results even after eliminating those variable outliers.

4.4.5. Transformation Variables

In order to obtain a more comprehensive understanding of the relationship between the level of DE development and urban carbon pollution, the core explanatory variable of this paper, which is a dummy variable indicating whether a city has established a National Big Data Comprehensive Pilot Zone, needs to be transformed. The regression results, based solely on this dummy variable, may not fully capture the relationship between DE development and urban carbon pollution. To address this limitation, a measurement index system for the DE is adopted, following the approach of Zhao Tao, Zhang Zhi, and Liang Shangkun (2020) [12].

The measurement index system includes variables such as the Internet penetration rate, Internet-related output, the number of mobile Internet users, the inclusive finance index, and the number of employees in the Internet-related sector. These variables are used to construct the DE Development Index (dig) using the entropy method. In the regression analysis, the dummy variable (did) is replaced with the DE Development Index (dig), and the results are presented in column (9) of Table 4. The coefficient of the dig variable is -0.028, and it passes the significance test at the 10% level. This finding further strengthens the research conclusion of this paper.

4.5. Analysis of Action Mechanism

The above baseline regression results indicate the DE has a significant influence on reducing the carbon pollution of pilot cities, and the research findings are robust. However, the specific mechanism of this impact is not yet clear. The theoretical analysis indicates that the DE may decrease carbon pollution through two channels: ameliorating energy efficacy and attracting foreign investment. The test results of the action mechanism, as given in Table 5, are derived from Equations (2) and (3). Columns (1) and (2) in Table 5 display the test results for energy efficiency as the action mechanism variable. In column (1), the coefficient of the did is significantly positive, indicating that the pilot policy has a substantial positive effect on energy efficiency. In column (2), the coefficient of the did is significantly negative. The coefficient of energy efficiency, denoted as lnene, is significantly negative. The product of the coefficient did in column (1) and the coefficient lnene in column (2) has the same negative sign as the coefficient did in column (2). This suggests the presence of a relatively significant partial mediating effect. The mediating effect of energy efficiency accounts for nearly 13.47% of the gross reduction in carbon pollution attributed to the DE. This indicates that improving energy efficiency can help reduce carbon pollution in the DE. Therefore, research Hypothesis 2 has been verified, asserting that the DE can decrease carbon pollution through the enhancement of energy efficiency.

The test results for the action mechanism of foreign investment (lnfdi) are presented in columns (3) and (4) of Table 5. In column (3), the regression results show a significantly positive coefficient for the dummy variable did, indicating that the pilot policy of the National Big Data Comprehensive Pilot Zone has a significant impact on attracting foreign investment. Meanwhile, in column (4), the regression results reveal a significantly negative coefficient for the variable did. Moreover, the coefficient for foreign investment (lnfdi) is also significantly negative. The symbol of the product of the coefficients for did in column (3) and lnfdi in column (4) aligns with that of the coefficient for did in column (3). Both of them are negative, indicating that there is a significant partial intermediary effect. The analysis suggests that the intermediary effect of foreign investment accounts for approximately 11.54% of the total carbon pollution reduction effect of the DE. This finding

shows that the DE, through enhancing energy efficiency, can reduce carbon pollution by attracting foreign investment. It is important to note potential conflicts between the mechanism variable foreign investment (lnfdi) and the control variable trade openness (lntrd) in testing the intermediary action mechanism of foreign investment, which will affect the test results. However, the variance inflation factor (VIF) test for multicollinearity reveals that both of the VIF values for foreign investment (lnfdi) and trade openness (lntrd) are 2.40 and 2.97, respectively. They are below 5, indicating no issues of multicollinearity that could affect the test results for the action mechanism of foreign investment. Thus, the verification results for Hypothesis 3 of this study can be considered reliable.

Table 5. Test results of the action mechanism.

Variables	(1)	(2)	(3)	(4)
	lnene	**lnCE**	**lnfdi**	**lnCE**
did	0.123 ***	−0.018 *	0.303 ***	−0.018 *
	(0.037)	(0.010)	(0.106)	(0.010)
lnene		−0.023 ***		
		(0.005)		
lnfdi				−0.008 ***
				(0.002)
Constant	51.741 ***	−5.255 ***	7.822	−6.355 ***
	(4.171)	(1.155)	(17.006)	(1.122)
Control variables	Yes	Yes	Yes	Yes
Urban fixed effect	Yes	Yes	Yes	Yes
Year fixed effect	Yes	Yes	Yes	Yes
Sample size	2820	2820	2820	2820
Adj. R^2	0.763	0.979	0.780	0.979

Note: "***", and "*" express significance levels at 1%, and 10%, respectively. The numbers in brackets are cluster-robust standard errors.

4.6. Further Analysis

This paper aims to investigate the influence of the DE on carbon pollution and the underlying mechanism. It acknowledges that the impact of the DE on carbon pollution might vary across different regions, city sizes, resource endowments, and levels of urbanization.

4.6.1. Regional Heterogeneity

Regional heterogeneity refers to the variations or differences in certain aspects or characteristics among different regions. In this paper, it refers to the distinctions in economic development, industrialization stage, and resource endowment among cities, and how these differences may impact the connection between the DE and carbon pollution. To investigate this heterogeneity, the study divides the 282 prefecture-level cities in China into two categories: eastern cities and central and western cities [41]. This division allows for an exploration of how the DE affects carbon pollution in different regions. The regression results for regional heterogeneity are presented in columns (1) and (2) of Table 6. The findings indicate the coefficient for did in eastern cities is significantly negative, suggesting the DE has a significant negative effect on carbon pollution in the eastern districts. However, the coefficient for did in central and western cities is negative but not statistically significant, implying that the DE does not have a considerable effect on carbon pollution in the central and western regions. Due to the advanced economic growth in the eastern regions and the early establishment of digital infrastructure and industries, the level of DE growth is higher in comparison to the central and western regions. This has enabled the full realization of the carbon pollution reduction benefits associated with the DE. Conversely, the development of the DE in the central and western regions is still in its initial stages. These regions have relatively underdeveloped digital infrastructure and have taken over polluting industries in the east. Consequently, the DE in the central and western regions

has not been able to significantly reduce carbon pollution [42]. It is important to note that the regional heterogeneity analysis in this paper is similar to that of Li Y, Yang X, Ran Q et al. (2021) [43], but there are also significant differences. Li Y, Yang X, Ran Q et al. (2021) primarily focused on examining the regional heterogeneity in the regulatory effect of the DE on the relationship between energy structure and carbon pollution. In contrast, this paper concentrates on exploring the regional heterogeneity impact of the DE on carbon pollution.

Table 6. Results of heterogeneity tests.

Variables	(1) East Cities	(2) Midwest Cities	(3) Mega Cities	(4) Big Cities	(5) Small and Medium Cities	(6) Resource-Based Cities	(7) Non-Resource-Based Cities	(8) High Urbanization Cities	(9) Low Urbanization Cities
did	−0.020 *	−0.027	−0.001	−0.037 **	0.153	−0.013	−0.023 *	−0.032 *	−0.010
	(0.012)	(0.019)	(0.016)	(0.016)	(0.132)	(0.023)	(0.013)	(0.018)	(0.015)
Constant	−5.218 **	−6.921	−6.022 ***	−1.242	−21.294 *	−8.494	−4.287 **	−12.084 *	−2.418
	(2.498)	(4.384)	(2.121)	(2.422)	(11.822)	(6.027)	(2.049)	(6.331)	(1.972)
Control variables	Yes	Yes	Yes	Yes	Yes	Yes	Yes	Yes	Yes
Urban fixed effect	Yes	Yes	Yes	Yes	Yes	Yes	Yes	Yes	Yes
Year fixed effect	Yes	Yes	Yes	Yes	Yes	Yes	Yes	Yes	Yes
Sample size	1000	1820	899	1830	84	1120	1700	1331	1489
Adj. R^2	0.990	0.976	0.979	0.966	0.964	0.974	0.982	0.355	0.507

Note: "***", "**", and "*" express significance levels at 1%, 5%, and 10%, respectively. The numbers in brackets are cluster-robust standard errors.

4.6.2. Urban Size Heterogeneity

On the one hand, in comparison to small cities, large cities have higher resource allocation and utilization efficiency advantages [44]. These factors contribute to a diminution in environmental pollution. On the other hand, overcrowded cities tend to experience congestion effects, exacerbating urban diseases and environmental pollution problems [45]. Hence, it is essential to investigate whether the carbon pollution reduction effect of the DE is influenced by the heterogeneity of city sizes. In terms of the 2014 Notice on the Adjustment of Urban Size Division Standards released by the State Council, cities with a permanent population of over 5 million are classified as megacities, those with a population between 1 million and 5 million are classified as large cities, and those with a population below 1 million are classified as small and medium-sized cities [46]. The heterogeneity regression results for city size are presented in columns (3) to (5) of Table 6. The coefficient did for small and medium-sized cities is positive, while that for megacities is negative. However, both coefficients are not statistically significant. In addition, the coefficient for large cities is significantly negative. This indicates that the DE plays a significant role in reducing carbon pollution in large cities, but its impact is not significant in small and medium-sized cities, as well as megacities. One possible explanation is that larger cities, in comparison to small and medium-sized cities, possess superior digital infrastructure, DE-related technologies, capital, and a pool of high-quality talent. These advantages enable larger cities to foster technological advancements in the energy field through knowledge sharing and technology spillover [47]. As a result, larger cities experience a significant reduction in carbon pollution. However, too extensive a scale of cities also leads to increased energy consumption and congestion effects. Although the DE can curb carbon pollution, the effect is not obvious.

4.6.3. Heterogeneity in Urban Resource Endowment

Resource endowment has a significant impact on various aspects of urban technological progress and development patterns, including the DE. As a result, the effects of carbon reduction in DE may vary due to variations in resource endowments [48]. In terms of the National Sustainable Development Plan for Resource-Based Cities in China

(2013–2020) released by the State Council [49], the sample cities are divided into two categories: resource-based cities and non-resource-based cities. Columns (6) and (7) of Table 6 present the regression results for the impact of urban resource endowment heterogeneity on carbon pollution. The results demonstrate the DE has a considerable reduction effect on the carbon pollution of non-resource-based cities. However, it has a negative but statistically insignificant effect on the carbon pollution of resource-based cities. This suggests the DE has a greater potential for carbon pollution diminution in non-resource-based cities. The discrepancy can likely be attributed to the fact that resource-based cities have abundant fossil energy and mineral resources. Historically, these cities have relied heavily on these resources to develop resource-intensive industries, neglecting the development of environmental protection technologies. Consequently, carbon pollution has increased in these cities. Moreover, the level of digital industrialization in resource-intensive industries has been relatively low, which limits the extent to which the DE can be helpful to carbon pollution diminution in these cities.

4.6.4. Urbanization Heterogeneity

Due to the late start of China's urbanization and the rapid pace of development, the initial phase was primarily characterized by extensive expansion. Consequently, the industrial structure has developed in an unbalanced manner, hindering the realization of the carbon pollution diminution benefits of the DE. When urbanization reaches the middle and late stages, there are several benefits to reducing CO_2 emissions. First, the centralized utilization of resources, coupled with the spillover of information and technological progress brought about by urbanization, can enhance resource efficiency. This alternately leads to a reduction in carbon pollution. Second, as urbanization progresses, the growth of digital services reaches a new level. This can greatly facilitate the efficient flow of resources, minimizing resource consumption loss and ultimately mitigating urban carbon pollution [50]. Therefore, the impact of the DE on carbon pollution reduction may vary depending on the level of urbanization. Based on the median value of urbanization, urbanization values in the sample cities above the median are categorized as high-urbanization cities, while cities with urbanization values below the median are classified as low-urbanization cities. To evaluate the heterogeneity concerning the effect of urbanization on carbon pollution reduction, we present the regression results in columns (8) and (9) of Table 6. The findings indicate that, when compared to areas with low levels of urbanization, the DE significantly improves carbon pollution in highly urbanized regions.

5. Comparison with Existing Studies

Current literature studies primarily explore the DE's impact on economic development. For instance, Lu and Zhu (2022) found a significant spatial correlation between the DE and high-quality economic development, with the DE directly driving the latter through notable spillover effects [51]. Jiang and Deng (2022) similarly concluded that the DE has a substantial positive impact on high-quality economic development, displaying distinct non-linear characteristics [52]. However, beyond its influence on economic development, it is also crucial to explore whether the DE can offer novel solutions for carbon pollution reduction. Considering the correlation between high-quality economic development and environmental pollution, this paper aims to further investigate the impact of the DE on carbon pollution, thus expanding the scope of research on the DE in the environmental domain. The findings of this research align with the studies conducted by Li and Wang (2022) [53] and Yan et al. (2023) [54], both supporting the notion that the DE serves as an effective means of mitigating carbon pollution. In comparison to previous literature that employed index systems to measure the DE, this paper employs the National Big Data Comprehensive Pilot Zone. By utilizing the DID model, it comprehensively evaluates the net effect of the DE on carbon pollution, effectively addressing endogeneity concerns and testing the robustness of the analysis results, thus contributing to more reliable research conclusions.

6. Research Conclusions and Policy Recommendations

There is no doubt that the DE has become increasingly significant for high-quality economic development. With the dual goals, it is crucial to determine whether the thriving DE can effectively reduce carbon pollution while promoting economic growth. This paper aims to empirically investigate the connection between the DE and carbon pollution utilizing 282 of China's cities, spanning from 2012 to 2021. The findings of this study are outlined below:

- After conducting various robustness tests, including the parallel trend test, placebo test, PSM–DID estimation, exclusion of the influence of relevant policies, transformation of explained variables, removal of samples, and variable winsorize, it can be concluded that the DE has a considerable effect on reducing urban carbon pollution.
- The DE achieves this by enhancing energy efficiency and attracting foreign investment, which helps reduce carbon pollution effectively.
- The diminution in carbon pollution is more noticeable in the eastern regions compared with the central and western regions. Moreover, cities with excessively large or small scales do not experience a considerable diminution in carbon pollution through the DE. Instead, moderate-sized cities benefit the most from the carbon reduction effect. Additionally, non-resource-based cities and highly urbanized cities demonstrate a notable decrease in carbon pollution through the DE.

Based on the research findings mentioned above, this study proposes the following policy recommendations:

Firstly, on the basis of the establishment of the National Big Data Comprehensive Pilot Zone, a key initiative is to develop the DE, which can effectively contribute to reducing carbon pollution, thus playing a significant role in achieving environmental sustainability. The construction of the National Big Data Comprehensive Pilot Zone should be continued at a national level due to the significant reduction in carbon pollution resulting from the DE. It is important to consistently analyze the experience gained from the initial pilot zone and progressively develop a replicable and scalable construction approach. This pilot scope should be expanded based on the functional layout, geographical region, and urban characteristics of the pilot zone. This expansion should include a broader scope of application scenarios for the DE, with an emphasis on accelerating the development of emerging digital industrial clusters. It is crucial to ensure that the DE promotes economic development while effectively curbing carbon pollution. This can be achieved by simultaneously advancing economic growth and reducing carbon pollution, thus realizing a win-win situation. Overall, by implementing these policy recommendations, we can maximize the potential of the DE to spur economic growth while contributing to carbon pollution reduction.

Secondly, it is crucial to give due consideration to the mediating role of energy efficiency and foreign investment in reducing carbon pollution within the DE. On the one hand, efforts should be made to enhance connectivity in energy-related sectors, utilize more energy-efficient production equipment, foster the development of low-energy consumption products, and minimize energy consumption and losses throughout the usage process. On the other hand, seizing the opportunities presented by foreign investment in the DE era is essential. It is crucial to reform the traditional approach to attracting foreign investment and instead focus on strengthening investment in areas such as the Internet of Things, artificial intelligence, cybersecurity, blockchain, and global digital business.

Thirdly, it is imperative for cities to adopt tailored strategies for the development of the DE, considering the heterogeneity of regional, city size, urban resource endowments, and levels of urbanization.

- In the eastern region, it is important to not only focus on enhancing the application and innovation of digital technology but also take the lead in addressing the key technological challenges associated with reducing carbon pollution through the DE. Meanwhile, the central and western regions, as well as resource-based cities, should

accelerate the development of sustainable infrastructure projects. They can leverage their resource advantages to attract capital and talent in order to promote sustainable growth and reduce carbon pollution.

- It is necessary to rigorously control the scale of development in megacities, steer the development of large cities in a rational manner, and actively encourage the growth of small and medium-sized cities into larger ones. This will enable cities to fully capitalize on the advantages of economies of scale and agglomeration while reducing urban carbon pollution.
- It is important to promote a new form of urbanization. The current level of urbanization is generally not conducive to reducing carbon pollution; however, high-level urbanization can facilitate the carbon reduction potential of the DE. This suggests that urbanization has moved beyond the phase of extensive expansion. Therefore, it is crucial to promote the growth of new urbanization and strive for the construction of green, low-carbon, cyclic, ecological, and livable cities.

Of course, this paper also has some limitations. The analysis only focuses on the action mechanism of the DE on carbon pollution through the lenses of energy efficiency and foreign investment. It is worthwhile to explore additional mechanisms from other perspectives. Additionally, the regression analysis mainly relies on the classic DID model, which ignores the spatial correlation between individuals. Therefore, the research conclusions may not be fully comprehensive. Future studies should consider spatial correlation and investigate the effects of the DE on carbon pollution.

Author Contributions: Conceptualization, G.L.; Data curation, G.L.; Formal analysis, M.L.; Writing—original draft, M.L. and G.L.; Writing—review and editing, G.L. All authors have read and agreed to the published version of the manuscript.

Funding: This research was funded by the Social Science Planning Office, Foshan City, Guangdong Province (2023-GJ039).

Institutional Review Board Statement: Not applicable.

Informed Consent Statement: Not applicable.

Data Availability Statement: The data in this paper are from the statistical yearbook of Chinese cities and the statistical yearbook of prefecture-level cities.

Conflicts of Interest: The authors declare no conflict of interest.

References

1. Wang, X.Y.; Li, J.Y. Did the digital economy effectively promote energy conservation and CO_2 reduction? *China Popul. Res. Environ.* **2022**, *32*, 83–95.
2. Xue, F.; Zhou, M.L. Research on emission reduction effect of carbon trading market size in China. *East China Econ. Manag.* **2021**, *35*, 11–21.
3. Chen, F.; Peng, K.N. Practical ethics of emerging technology: Dilemma and countermeasures. *Stud. Sci. Sci.* **2023**, *41*, 11–17.
4. Chen, G.; Han, J.; Yuan, H. Urban digital economy development, enterprise innovation, and ESG performance in China. *Front Environ. Sci.* **2022**, *10*, 955055. [CrossRef]
5. Yang, H.T.; Hu, Y.M. Uncertainty, Information Production and the Development of Digital Economy. *China Ind. Econ.* **2023**, *4*, 24–41.
6. Zhou, S.B.; Zhang, Y.Y.; Zhang, Y.Y. Impact Path of Digital Finance Development on Regional Innovation: From the Perspective of "Dual Circulation". *Sci. Technol. Manag. Res.* **2022**, *42*, 31–37.
7. Shun, Y.H.Z. Digital economy, industrial upgrading and urban environmental quality improvement. *Stat. Decis.* **2021**, *37*, 91–95.
8. Sun, X.; Chen, Z.; Shi, T.; Yang, G.; Yang, X. Influence of digital economy on industrial wastewater discharge: Evidence from 281 Chinese prefecture–level cities. *J. Water Clim. Chang.* **2022**, *13*, 593–606. [CrossRef]
9. Dong, F.; Hu, M.; Gao, Y.; Liu, Y.; Zhu, J.; Pan, Y. How does digital economy affect carbon emissions? Evidence from global 60 countries. *Sci. Total Environ.* **2022**, *852*, 158401. [CrossRef] [PubMed]
10. Wang, J.; Dong, K.; Dong, X.; Taghizadeh-Hesary, F. Assessing the digital economy and its carbon-mitigation effects: The case of China. *Energ. Econ.* **2022**, *113*, 106198. [CrossRef]
11. Cheng, Y.; Zhang, Y.; Wang, J.; Jiang, J. The impact of the urban digital economy on china's carbon intensity: Spatial spillover and mediating effect. *Res. Conserv. Recy.* **2023**, *189*, 106762. [CrossRef]

12. Zhao, T.; Zhang, Z.; Liang, S.K. Digital Economy, Entrepreneurship, and High-Quality Economic Development: Empirical Evidence from Urban China. *J. Manag. World* **2020**, *36*, 65–76.
13. Li, Z.; Pang, C. Does Digital Economy Contribute to Regional Carbon Productivity? Evidence of China. *Math. Probl. Eng.* **2022**, *2022*, 1–13. [CrossRef]
14. Hu, J. Synergistic effect of pollution reduction and carbon emission mitigation in the digital economy. *J. Environ. Manag.* **2023**, *337*, 117755. [CrossRef]
15. Sun, X.; Chen, Z.; Loh, L. Exploring the Effect of Digital Economy on PM2.5 Pollution: The Role of Technological Innovation in China. *Front. Environ. Sci.* **2022**, *10*, 1–10. [CrossRef]
16. Bai, F.P.; Huang, Y.J.; Shang, M.T.; Ahmad, M. Modeling the impact of digital economy on urban environmental pollution: Empirical evidence from 277 prefecture-level cities in China. *Front. Environ. Sci.* **2022**, *10*, 1–19. [CrossRef]
17. Chen, P. Relationship between the digital economy, resource allocation and corporate carbon emission intensity: New evidence from listed Chinese companies. *Environ. Res. Commun.* **2022**, *4*, 75005. [CrossRef]
18. Zhang, L.; Mu, R.; Zhan, Y.; Yu, J.; Liu, L.; Yu, Y.; Zhang, J. Digital economy, energy efficiency, and carbon emissions: Evidence from provincial panel data in China. *Sci. Total Environ.* **2022**, *852*, 158403. [CrossRef] [PubMed]
19. Borowski, P. Digitization, Digital Twins, Blockchain, and Industry 4.0 as Elements of Management Process in Enterprises in the Energy Sector. *Energies* **2021**, *14*, 1885. [CrossRef]
20. Yi, M.; Liu, Y.; Sheng, M.S.; Wen, L. Effects of digital economy on carbon emission reduction: New evidence from China. *Energ. Policy* **2022**, *171*, 113271. [CrossRef]
21. Jin, F.X.C. Research on the nonlinear effects of the digital economy development on carbon emission. *Mod. Econ. Res.* **2022**, *11*, 14–23.
22. Bai, X.; Song, P.; Li, L. The development of the digital economy promotes the transformation of industrial structure. *Shanghai Econ. Res.* **2022**, *5*, 77–91.
23. Peng, W.; Han, D.; Yin, Y. Spatial effects of the digital economy in Beijing–Tianjin–Hebei region. *Econ. Geogr.* **2022**, *42*, 136–143.
24. Wen, Z.L.; Ye, B.J. Analyses of Mediating Effects: The Development of Methods and Models. *Adv. Psychol. Sci.* **2014**, *22*, 731–745. [CrossRef]
25. Lin Feng, Q.J. Digital economy, technological innovation and high–quality export of Chinese enterprises. *Acad. Res.* **2022**, *11*, 110–116.
26. Cong, J.H.; Liu, X.M.; Zhao, X.R. Demarcation Problems and the Corresponding Measurement Methods of the Urban Carbon Accounting. *China Popul. Resour. Environ.* **2014**, *24*, 19–26.
27. Shun, P.; Wu, Y.M.; Bao, S.M.; Zhong, Y.J. A Study on Economic Growth and Smog Pollution: Testing Spatial Environmental Kuznets Curve Hypothesis in China. *South China J. Econ.* **2019**, *12*, 100–117.
28. York, R.; Rosa, E.A.; Dietz, T. STIRPAT, IPAT and ImPACT: Analytic tools for unpacking the driving forces of environmental impacts. *Ecol. Econ.* **2003**, *46*, 351–365. [CrossRef]
29. Liu, L.; Zhang, Y.; Gong, X.; Li, M.; Li, X.; Ren, D.; Jiang, P. Impact of Digital Economy Development on Carbon Emission Efficiency: A Spatial Econometric Analysis Based on Chinese Provinces and Cities. *Int. J. Environ. Res. Public Health* **2022**, *19*, 14838. [CrossRef]
30. Wan, Q.; Shi, D. Smarter and Cleaner: The Digital Economy and Environmental Pollution. *China World Econ.* **2022**, *30*, 59–85. [CrossRef]
31. Noda, H.; Kano, S. Environmental economic modeling of sustainable growth and consumption in a zero-emission society. *J. Clean Prod.* **2021**, *299*, 126691. [CrossRef]
32. Deng, R.Z. A Study on the impact and mechanism of urban digital economy development on environmental pollution in China. *South. Econ.* **2022**, *2*, 18–37.
33. Chen, S.; Ding, D.; Shi, G.; Chen, G. Digital economy, industrial structure, and carbon emissions: An empirical study based on a provincial panel data set from China. *China Popul. Resour. Environ.* **2022**, *20*, 316–323. [CrossRef]
34. Hua, Y.; Ye, Y. Carbon Reduction Effect of Green Place-based Policy: Evidence from the National Eco-Industrial Exemplary Park. *J. Quant. Technol. Econ.* **2023**, *40*, 94–112.
35. Wang, Y.X.; Zhang, H.F.; He, X.; Li, R. Can Urban Agglomeration Policy Promote Enterprise Specialization? Evidence from Chinese Listed Companies. *J. Fin. Econ.* **2023**, *49*, 19–33.
36. Xu, S.; He, X.Y.; Zhong, K. The Belt and Road Initiative and Chinese Firms' Financial Constraints. *China Ind. Econ.* **2019**, *7*, 155–173.
37. Wang, L.; Liu, L.Y.; Jiang, Y.Z. Spatial spillover effects of digital economy on carbon productivity. *Fin. Econ.* **2023**, *1*, 61–73.
38. Shi, D.Q.; Ding, H.; Wei, P.; Liu, J.J. Can Smart City Construction Reduce Environmental Pollution. *China Ind. Econ.* **2018**, *6*, 117–135.
39. Xuan, Y.; Peng, J. The digital economy, green innovation and new urbanization. *Ind. Technol. Econ.* **2022**, *41*, 3–12.
40. Zhi, Y.; Lu, X. Establishment of National Big Data Comprehensive Pilot Zone and Urban Entrepreneurship Activity—Based on Empirical Evidence from 284 Cities. *J. China Bus. Mark.* **2023**, *37*, 84–96.
41. Yu Shan, F.X.J.H. Study on the impact of the digital economy development on carbon productivity improvement. *Stat. Inf. Forum* **2022**, *37*, 26–35.

42. Guo, F.; Yang, S.; Ren, Y. The digital economy, green technology innovation and carbon emissions: Empirical evidence from Chinese cities. *J. Shanxi Norm. Univ. Philos. Soc. Sci. Ed.* **2022**, *51*, 45–60.
43. Li, Y.; Yang, X.; Ran, Q.; Wu, H.; Irfan, M.; Ahmad, M. Energy structure, digital economy, and carbon emissions: Evidence from China. *Environ. Sci. Pollut. R.* **2021**, *28*, 64606–64629. [CrossRef]
44. Chen, X.; Zhang, L.; Zhang, S. Polycentric spatial structure and haze pollution: An empirical study based on Chinese urban data. *J. Chongqing Univ. Soc. Sci. Ed.* **2021**, *27*, 30–44.
45. Li, J.J. The Relationship of Institutional Arrangement, Urbanization and Environmental Pollution. *Econ. Surv.* **2020**, *37*, 29–36.
46. Guo, B.; Wang, Y.; Zhang, H. Does the development of digital economy improve urban air quality?—A quasi–natural experiment based on the national Big Data Comprehensive Pilot Zone. *J. Guangdong Univ. Fin. Econ.* **2022**, *37*, 58–74.
47. Gao, W.; Peng, Y. Energy saving and emission reduction effects of urban digital economy: Technology dividends or structural dividends? *Environ. Sci. Pollut. R.* **2023**, *30*, 36851–36871. [CrossRef] [PubMed]
48. Che, S.; Wang, J. Digital economy development and haze pollution: Evidence from China. *Environ. Sci. Pollut. Res.* **2022**, *29*, 73210–73226. [CrossRef]
49. Zhang, W.; Liu, X.; Wang, D.; Zhou, J. Digital economy and carbon emission performance: Evidence at China's city level. *Energ. Policy* **2022**, *165*, 112927. [CrossRef]
50. Kong, L.; Dong, Y.; Zhao, X. The impact of digital economy development on carbon emission: Based on the test of intermediary effect and threshold effect. *Urban Dev. Res.* **2022**, *29*, 42–49.
51. Lu, Y.; Zhu, S. Digital economy, scientific and technological innovation, and high-quality economSic development: A mediating effect model based on the spatial perspective. *PLoS ONE* **2022**, *17*, 277245. [CrossRef]
52. Jiang, Y.; Deng, F. Multi-dimensional threshold effects of the digital economy on green economic growth?—New evidence from china. *Sustainability* **2022**, *14*, 12888. [CrossRef]
53. Li, Z.; Wang, J. The dynamic impact of digital economy on carbon emission reduction: Evidence city-level empirical data in china. *J. Clean. Prod.* **2022**, *351*, 131570. [CrossRef]
54. Yan, X.; Deng, Y.; Peng, L. Study on the impact of digital economy development on carbon emission intensity of urban agglomerations and its mechanism. *Environ. Sci. Pollut. Res.* **2023**, *30*, 33142–33159. [CrossRef] [PubMed]

sustainability

MDPI

Article

Impact of Changes in Membership on Prices of a Unified Carbon Market: Case Study of the European Union Emissions Trading System

Yue Xu [1] and Dayu Zhai [2,*]

[1] School of Management, China University of Mining and Technology-Beijing, Beijing 100083, China
[2] School of International Development and Cooperation, University of International Business and Economics, Beijing 100029, China
* Correspondence: zhaidy@uibe.edu.cn

Abstract: Using the event study methodology, the paper studies the effects of 22 key events in countries' process of entering and exiting the European Union on returns of European Union Allowance (EUA) future prices in the EU Emissions Trading System (EU ETS). The events include 17 entry events concerning the signing of relevant agreements, becoming a candidate or potential candidate country, the process of a negotiation and formally entering the EU, and five exit events including the process of Brexit and the suspension of Iceland. The results show that two entry events involving Albania and Ukraine, respectively, have a significant positive impact, and five entry events have a significant negative impact. Among the exit events, the announcement of the Brexit referendum results causes significant negative market reaction. Most events regarding small carbon emitters entering the EU lead to negative cumulative abnormal returns (CAR) of EUA prices, and a significant negative correlation between the countries' annual average carbon emissions and CAR is found, while the change of national allocation plans does not affect the market reaction notably. In the process of establishing a unified carbon market, regulators should carry out appropriate policy arrangements of emission allowances allocation when new members join, in order to guide market expectations and enhance market stability.

Keywords: unified carbon market; carbon price; EU member states; EU ETS; event study

1. Introduction

Climate change has become an important global ecological and environmental concern to the international community. The signing of framework agreements such as the United Nations Framework Convention on Climate Change (UNFCCC) and the Kyoto protocol has contributed to the establishment of a trading market with greenhouse gas emission rights as commodities, so that countries can achieve certain emission reduction targets through market-oriented means at a lower total cost. The 2022 International Carbon Action Partnership (ICAP) Status Report demonstrates how emission trading system (ETS) developments are proliferating and picking up pace across the globe, with an increasing number of systems. There are now 25 such systems in force, covering 17% of global GHG emissions. A total of 22 ETSs are currently under development or under consideration, mainly in South America and South-East Asia. Today, almost one third of the global population lives under an active ETS [1].

As the largest carbon emitter, China aims to reach its peak in CO_2 emissions before 2030 and achieve carbon neutrality before 2060. The construction and stable operation of a national unified carbon market is one of the effective means for China to achieve this goal. On a global scale, big differences exist among countries and regions regarding the coverage and trading mechanism of carbon trading markets. Difficulties and challenges will remain in the future regarding how to expand the scope of national and regional carbon markets

and how to explore the establishment of a global unified carbon trading system. Europe is the most successful region in the development of regional integration and is the leader and promoter in the field of ecological environment. The European Union Emissions Trading System (EU ETS) is the most mature carbon market in the world, which is worth using for reference.

The success of the European unified carbon market benefits from the development of European integration, which is nevertheless a dynamic process. While the European Union (EU) continues to expand eastward, Brexit has brought great uncertainty to the future of the EU. Continuous changes in the process of European integration are alongside changes of EU ETS members. In the first stage of the EU ETS from 2005 to January 2021, six countries joined successively, and the UK also left the EU ETS due to its withdrawal from the EU. The entry and exit of a country will have an impact on both the supply and demand of emission allowances, therefore, affecting carbon prices. In addition, since all new member states that accede to the EU become members of the EU ETS as they adopt and implement EU legislation [2], apart from formally joining or withdrawing from the EU ETS, entering or exiting the EU process may also affect traders' expectations of supply and demand in the carbon market, thus, also affecting carbon prices. The Paris agreement has set the control target of long-term global warming, which promotes the establishment of a unified global carbon market. The two UN climate conferences in 2018 and 2019 also negotiated the establishment of a unified global carbon trading system. The establishment of a worldwide unified carbon market has become a future development trend and the carbon markets of various countries and regions will also face expansion and integration. In the case of China, nine regional carbon markets with national records were established by the end of 2021, and the construction of a national carbon emissions trading market began in December 2017. The market was officially launched in July 2021 and more industry and regional members will become involved in the future. Therefore, exploring the impact of the process of entering and leaving the EU on carbon prices can provide reference not only for EU ETS traders and regulators, but also for the construction of China and even the world unified carbon market in aspects of market risk management and allowances allocation.

Based on the perspective of supply and demand, the factors affecting the operation of carbon markets mainly include macroeconomic conditions, policies and systems, energy prices and weather. Studies mainly focus on the relationship between macro-economic conditions [3–5] or energy prices [6–12] and carbon price fluctuations. Few studies explore the impact of policy factors on the operation of carbon markets. The interdisciplinary research methods of economics and political science are utilized in this paper to form a useful supplement to this research perspective.

Using the event study methodology, the paper examines the effects of 22 key events in countries' process of entering and exiting the EU on the returns of European Union Allowance (EUA) future prices in the EU ETS. The events include 17 entry events concerning the signing of relevant agreements, becoming a candidate or potential candidate country, the process of a negotiation and formally entering the EU, and five exit events including the process of Brexit and the suspension of Iceland. The results show that two entry events involving Albania and Ukraine, respectively, have a significant positive impact, and five entry events have a significant negative impact. Among the exit events, the announcement of the Brexit referendum results causes a significant negative impact. It indicates that for most small carbon emitters, the promotion of their EU accession process tends to generate market expectation that the allocation of the EU ETS to the country's emission allowances will be greater than its demand. The situation for large emitters is the opposite. Most events regarding small carbon emitters entering the EU cause a negative market reaction and a significant negative correlation between the countries' annual average carbon emissions, and cumulative abnormal returns of EUA prices are found. It is likely that the greater the country's carbon emission, the stronger the expectation of this oversupply. Therefore, carbon market regulators should pay attention to the policy arrangement of allowances allocation. For the EU ETS, the allowances allocation for small economies should be

appropriately reduced and the allocation for large economies should be increased. The change of the EU ETS national allocation scheme from National Allocation Plan (NAP) to National Implementation Measure (NIM) has no significant impact on reversing the market expectations of allowances allocation, indicating that the EU ETS should further improve the rationality of allowances allocation, especially to appropriately reduce the allocation of small economies and expand the market transparency. Regulators in China and other countries can also adjust their allocation policies accordingly to guide market expectations and strengthen the stability of carbon markets in the case of market expansion, merger, member withdrawal and other changes. For market traders, membership change is also one of key factors that causes market risk, which needs management through corresponding hedging strategies.

The rest of the paper is organized as follows. Section 2 presents the literature review. Section 3 demonstrates the methodology and data. Section 4 analyzes the study results. Section 5 illustrates a further study on the influencing factors of the market reaction. Section 6 provides the conclusions and implications.

2. Literature Review

As the carbon market is based on law, its operation is highly dependent on institution and supervision. The literature concentrates on the impact of relevant policies and political events on the carbon market, most of which take the EU ETS as the research object. Based on the event study method, some studies analyzed the impact of EU ETS NAP and verified emissions announcements on carbon prices. Mansanet-Bataller and Pardo [13] and Lepone et al. [14] found that NAP announcements and verifications announcements in Phase 1 and Phase 2 of the EU ETS had an impact on carbon returns but no significant impact on their volatilities. Hitzemann et al. [15] found absolute abnormal returns of carbon price on the day of the release of annual realized emissions announcements in the European carbon market, as well as an increase in trading volumes and intraday volatilities on the event day. Jia et al. [16] used the method of the econometric model with bilaterally modified dummy variables and suggested that verified emission announcements have a significant impact on the expected returns of EU carbon price. Guo et al. [17] argued that verified emissions announcements increase the compliance trading volumes of the EU ETS, especially in Phase 1. The study also showed that the over-allocation of carbon allowances disturbs the carbon market to a greater extent than verification events.

Some research focuses on the impact of high-frequency information on carbon markets. Conrad et al. [18] modeled the EUA price-adjustment process with the release of high-frequency information and found that the release of NAP in Phase 2 and the news that the future economy is better than expected have an obvious impact on EUA prices. Chen et al. [19] studied the impact of high-frequency information related to macro-economic and verified emission announcements on prices, volatility, trading volumes and illiquidity in the European carbon futures market, defending the belief that some announcements can affect carbon prices within five minutes.

Other literature argued that restrictions on the banking of emission allowances in the EU ETS cause a significant impact on carbon futures prices [20,21]. Regarding other policy events, Koch et al. [22] examined how the evolution of emission cap stringency affects the carbon market and found that the EU ETS backloading policy of the auction would significantly reduce carbon prices. In addition, 2020 and 2030 policy packages would lead to positive price reactions. Deeney et al. [23] used the event study method and GARCH model, suggesting that decisions made by the European Parliament can influence both the prices and volatilities of EUA, and the impact is related to "party political", market sentiment and market attention. Fan et al. [24] comprehensively selected 50 events concerning the release of six types of policies, including aviation emission and cap regulations, and assessed their impact on EUA returns, analyzing the impact mechanism of various events, respectively.

Recent literature found that correlations also exist between economic policy uncertainty or climate policy uncertainty and carbon markets. Ye et al. [25] found that cross-

correlation exists between the returns of EU carbon market futures and economic policy uncertainty, and the cross-correlation behavior structure is different across trading phases. By constructing the GARCH-MIDAS-EUEPU and GARCH-MIDAS-GEPU models, Dai et al. [26] illustrated that both European and global economic policy uncertainty aggravate the long-term fluctuation of European carbon spot returns, with the latter having a stronger impact. Dou et al. [27] found a significant negative impact of economic policy uncertainty shock on the volatility of carbon futures price returns in the long run, and the COVID-19 epidemic pandemic also affects the spillover between them. Wu et al. [28] argued that climate policy uncertainty negatively affects the volatility of EUA futures.

Relations between trading policies and carbon price are also found in China carbon markets. Song et al. [29] found that the release of carbon trading policy can improve Shanghai Emission Allowance (SHEA) price. Song et al. [30] further developed a fuzzy stochastic model to predict the impact of demand-related policies on China's carbon price and applied it to analyze the second developing phase of the Shanghai Environment and Energy. Through the jump test and Logit regression, Song et al. [31] also suggested that the release of the new policy can lead to substantial fluctuations in China's carbon price in the short term, but it can also reduce the abnormal fluctuations caused by the dissemination of price information. They also argued that demand-stimulus policy can promote the positive fluctuation of carbon price and will lead to the excessive correction of carbon price in the long run.

Abundant literature has proved that carbon prices are likely to be affected by a variety of policy information such as allowances allocation policy, banking restrictions, emission cap regulations and policy uncertainty. As an obvious policy-oriented market, there are few studies on the impact of relevant information involving the change of participating members on the carbon market. Referring to previous research methods, the paper focus on the influence of relevant information regarding the change of EU ETS membership of different economic scales on carbon prices and explores its impact mechanism. The contributions of this paper are two-fold. First, the paper employs a new cross-level perspective and tries to bridge the macro-political factors with the micro-carbon market operation, which expands the analytical scope of carbon market research. Second, the study is significant for allowances allocation and market management for both traders and regulators in the case of scope changes in the carbon markets of the EU, other countries and regions, and even a world unified carbon market in the future.

3. Methodology and Data

3.1. Research Hypothesis

According to the EU, the process of a country's accession to the EU is generally a complex procedure requiring several stages, including the signing of relevant agreements, applying for membership, becoming a candidate or potential candidate country, undergoing the process of negotiations, and formally entering the EU. A country's withdrawal from the EU also requires working through the stages of its exit plan proposal, the EU's adoption of the exit agreement, and the formal exit. According to the regulations of the EU and EU ETS, all new member states that accede to the European Union become members of the EU ETS as they adopt and implement EU legislation [2]. The process of a country's withdrawal from the EU will also be accompanied by the process of withdrawal from the EU ETS. Therefore, the promotion of each stage of EU entry and exit will affect the market expectation of its accession or withdrawal from the EU ETS. It will further affect the market expectation of the allocation of emission allowances, and then disturb carbon prices.

To summarize, the paper tests the hypothesis that the carbon prices of the EU ETS could react to countries' process of entering and exiting the EU, and there are three possible explanations of such impact:

1. The event of entering the EU has a positive impact on carbon prices or the event of leaving the EU has a negative impact on carbon prices, indicating that the market expects that the allocation of emission allowances is less than the country's demand;

2. The event of entering the EU has a negative impact on carbon prices or the event of leaving the EU has a positive impact on carbon prices, indicating that the market expects that the allocation of emission allowances is greater than the country's demand;
3. The event of entering or leaving EU does not have a significant impact on carbon prices, indicating that the market expects that the country's allowances can balance supply and demand, or the country does not play an important role in the EU ETS, which cannot significantly affect the market expectation.

If the procedure of a country's entry into or exit from the EU significantly influences carbon prices, it suggests that traders should pay attention to the market risk caused by the change of market participants. On the other hand, it can prompt regulators to improve the rationality of allowances allocation, so as to enhance the stable operation of the carbon market.

3.2. Methodology

Referring to the event research method used by Brown et al. [32,33], the paper assesses the impact of the key events of the EU entry and exit process on carbon prices. Specifically, referring to the method of Fan et al. [24], the paper sets $t = 0$ as the event day and [−5, +5] as the event window of 11 trading days, which can take into account the possibility of information leakage in advance to study the overall impact before and after the event. The paper also sets [0, +5] as the second event window of six trading days to study the impact after the event and enhance the robustness of the results. [−65, −6] is selected as the estimation window of 60 trading days to calculate the normal return of carbon prices.

In the event window, the abnormal returns of carbon prices are calculated as the difference between daily returns and expected returns, as shown in Equations (1) and (2):

$$AR_t = R_t - E(R_t) \tag{1}$$

$$R_t = \ln(\frac{P_t}{P_{t-1}}) \tag{2}$$

where AR_t, R_t and $E(R_t)$ denote the abnormal returns, rate of returns and expected returns of carbon prices on day t, respectively, and P_t is the EUA price on day t.

Due to the particularity of EUA price series, which can only be used once for compliance [24], traditional pricing models such as the market model and the multi-factor model cannot be used to calculate expected returns. Following the mean-adjusted model developed by Brown et al. [33], the paper calculates the expected returns $E(R_t)$ of carbon prices based on the truncated mean model adopted by Mansanet-Bataller and Pardo [13], Lepone et al. [14] and Fan et al. [24]. That is, $E(R_t)$ is calculated as the average of carbon price returns between the 5% and 95% percentiles in the estimation window. Although the mean-adjusted model is rather simple, it has similar power to the market model [33]. Specifically, $E(R_t)$ can be obtained as:

$$E(R_t) = \frac{1}{54}\sum_{4}^{57}(R_i) \tag{3}$$

where R_i is the ith return of the estimation period after they have been organized in ascending order. This method can exclude the impact of other events in the estimation window to make more accurate expected returns. The cumulative abnormal returns (CAR) in the event window are calculated as follows:

$$CAR_{[\tau_1,\tau_2]} = \sum_{t=\tau_1}^{\tau_2} AR_t \tag{4}$$

For the 11-day event window, $\tau_1 = 5$, $\tau_2 = -5, -4, \ldots, 4, 5$; for the 6-day event window, $\tau_1 = 0$, $\tau_2 = 0, 1, \ldots, 4, 5$. The variance of CAR can be obtained by Equation (5):

$$\mathrm{var}(CAR_{[\tau_1,\tau_2]}) = (\tau_2 - \tau_1 + 1)\sigma^2 \tag{5}$$

where σ^2 is the variance of abnormal returns in the event window. The t statistic is used to determine whether the CAR of each day in the event window is significant. The t statistic is calculated as follows:

$$t_{[\tau_1,\tau_2]} = \frac{CAR_{[\tau_1,\tau_2]}}{\sqrt{\mathrm{var}(CAR_{[\tau_1,\tau_2]})} \cdot \sqrt{(L-2)/(L-4)}} \sim N(0,1) \tag{6}$$

where L denotes the length of the estimation period.

3.3. Data of EUA Prices

Compared to spot prices, futures prices can better reflect market expectations and represent the trend of market supply and demand more accurately. Therefore, carbon prices in the paper are selected as the settlement prices of EUA futures (continuous) of the European Climate Exchange (ECX) in the EU ETS, and the data source is Intercontinental Exchange (ICE) and Wind. Since the EUA futures trading data of ECX began on 22 April 2005, the time span of data is from 22 April 2005 to 30 June 2022. Figure 1 illustrates the EUA futures prices used in the paper. It can be seen that the series declined sharply from April 2006 in Phase 1 but became relatively stable in Phases 2 and 3. After the approval of the reform of Phase 4 in February 2018, EUA prices began to rise continuously.

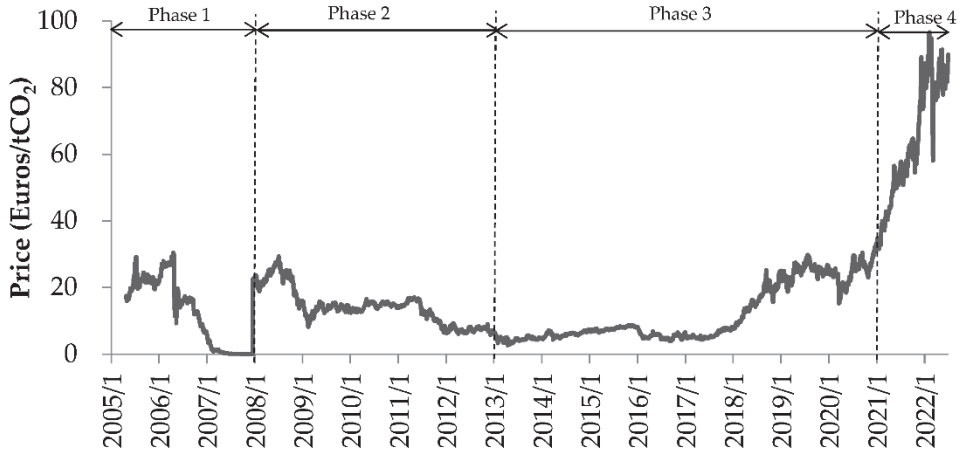

Figure 1. Settlement prices of EUA futures (continuous). Source: Intercontinental Exchange (ICE) and Wind.

The EU ETS stipulates that the EUA in Phase 1 cannot be used in Phase 2, while the EUA in Phases 2 to 4 can be used universally. Therefore, the descriptive statistics of the EUA futures returns series of the two time intervals are illustrated separately in Table 1.

Table 1. The descriptive statistics of EUA futures returns series.

	Sample Period	Mean	Std. Dev.	Maximum	Minimum	Skewness	Kurtosis	Observations
Phase 1	22 April 2005–31 December 2007	−0.0109	0.1072	1.0986	−1.3863	−3.1656	73.3346	684
Phases 2, 3 and 4	2 January 2008–30 June 2022	0.0004	0.0316	0.2405	−0.4347	−0.7815	14.4729	3734

3.4. Event Selection

The paper selects key events in the process of entering and leaving the EU from 22 April 2005 to 30 June 2022, in order to study their impact on carbon prices. Since the

European Council and the Council of the European Union are the decision-making bodies of the EU, they can release the strongest information to the market. The selection of events is essentially based on the decisions of the two bodies.

The following five categories of EU entry events are selected:

1. The Stabilisation and Association Agreement (SAA) between the EU and a country was signed.
2. The EU confirmed granting a country EU candidate or potential candidate status.
3. The EU proposed a negotiation plan for a country to join the EU. (Since the proposal of a negotiation plan has provided the market with an expectation of opening negotiations, the proposal rather than the formal opening is selected here. If a country joined the EU ETS before the proposal of negotiation (e.g., Iceland), the event of negotiation is not selected).
4. The EU agreed to end its accession negotiations with a country.
5. A country formally joined the EU or EU ETS. (If a country joined the EU ETS before joining the EU (e.g., Croatia), the event of joining the EU ETS is selected.)

The exit events only involve two countries, namely the UK and Iceland. The following four types of events are selected:

1. The country requested that it no longer be regarded as a candidate country.
2. The results of the Brexit referendum were announced.
3. The European Council adopted the Withdrawal Agreement.
4. The country formally left the EU and EU ETS.

If the event day is not a trading day, the first trading day after the event day is taken as day 0. The events with an estimation window or event window that span Phases 1 and 2 are eliminated since the change of EUA universality. Finally, 22 events are selected in the event study, as shown in Table 2.

Table 2. Selected events regarding entering and leaving the EU.

EU ETS Phase	No.	Date	Event	Type
Phase 1 (2005–2007)	1	16 December 2005	The European Council decided to grant candidate country status to the former Yugoslav Republic of Macedonia. (Macedonia was renamed as the "the Republic of North Macedonia" in February 2019. Since the events related to this country in the paper were before its re-name, it is still called "the former Yugoslav Republic of Macedonia" or “Macedonia” in the paper.)	Entry
	2	12 June 2006	The SAA and Interim Agreement between the EU and Albania were signed.	Entry
	3	1 January 2007	Romania and Bulgaria formally joined the EU.	Entry
	4	15 October 2007	The SAA between the EU and Montenegro was signed.	Entry
Phase 2 (2008–2012)	5	29 April 2008	The SAA and Interim Agreement between the EU and Serbia were signed.	Entry
	6	16 June 2008	The SAA and Interim Agreement between the EU and Bosnia and Herzegovina were signed.	Entry
	7	17 December 2010	The European Council confirmed Montenegro as a candidate country.	Entry
	8	10 June 2011	The European Commission proposed to the EU Council of Ministers to close the last four chapters in the accession negotiations with Croatia. (The European Commission made a recommendation before the decision of the European Council, which is also included in events, considering that the incident may also affect market expectations.)	Entry
	9	24 June 2011	The European Council agreed that the accession negotiations with Croatia should be concluded by the end of June 2011, paving the way for the country to become the 28th EU member in 2013.	Entry
	10	9 December 2011	The European Council launched the accession process with Montenegro in a view to open negotiations in June 2012.	Entry
	11	1 March 2012	The European Council confirmed Serbia as a candidate country.	Entry
Phase 3 (2013–2020)	12	1 January 2013	Croatia joined the EU ETS.	Entry
	13	28 June 2013	The European Council agreed to open accession negotiations with Serbia.	Entry
	14	27 June 2014	The European Council granted candidate status to Albania.	Entry
	15	25 July 2014	The SAA between the EU and Kosovo was initialed. (According to the official website of the EU (see https://europa.eu), this designation is without prejudice to positions on status, and is in line with UNSCR 1244/1999 and the ICJ Opinion on the Kosovo declaration of independence. The paper holds no position on the status of Kosovo.)	Entry

Table 2. *Cont.*

EU ETS Phase	No.	Date	Event	Type
	16	12 March 2015	Iceland requested that it no longer be regarded as a candidate country.	Exit
	17	24 June 2016	The UK held a referendum on its membership of the EU, with the majority of voters choosing to leave the EU (51.9% of the vote versus 48.1% voting to remain).	Exit
	18	26 June 2018	The European Council agreed to set out the path towards opening accession negotiations with the former Yugoslav Republic of Macedonia and Albania in June 2019.	Entry
	19	25 November 2018	At a special meeting of the European Council, EU27 leaders endorsed the Withdrawal Agreement and approved the political declaration on future EU–UK relations.	Exit
	20	31 January 2020	The UK formally left the EU.	Exit
	21	1 January 2021	The UK formally left the EU ETS.	Exit
Phase 4 (2021–2030)	22	23 June 2022	Ukraine and Moldova were granted candidate status by unanimous agreement between the leaders of all 27 EU member states. Georgia was identified as a potential candidate.	Entry

Note: According to the official website of the EU, see https://europa.eu (accessed on 7 October 2022); European Commission [2]; Walker [34].

4. Results

Figure 2 shows the events with significant CAR at the 5% level. The CAR of all 22 events are shown in Table 3. It can be seen that eight events have significant impacts on the fluctuation of EUA futures prices. Events 3, 4, 6, 8, 9 and 17 have negative impacts and Events 2 and 22 show positive impacts. Events 3 and 22 have significant impacts of 3 days and Events 4 and 17 have significant impacts of 2 and 5 days, respectively. Other significant events indicate one significant day. The rest of the events have no significant impact on CAR. It is likely that the promotion of the EU entry or exit process can indeed lead to significant reactions of carbon price in some cases. Changes in membership or expected membership will lead unified carbon market traders to expect changes in the supply and demand of emission allowances, which will generate certain market risk. The risk caused by such policy events is necessary to gain the attention of carbon market traders and regulators.

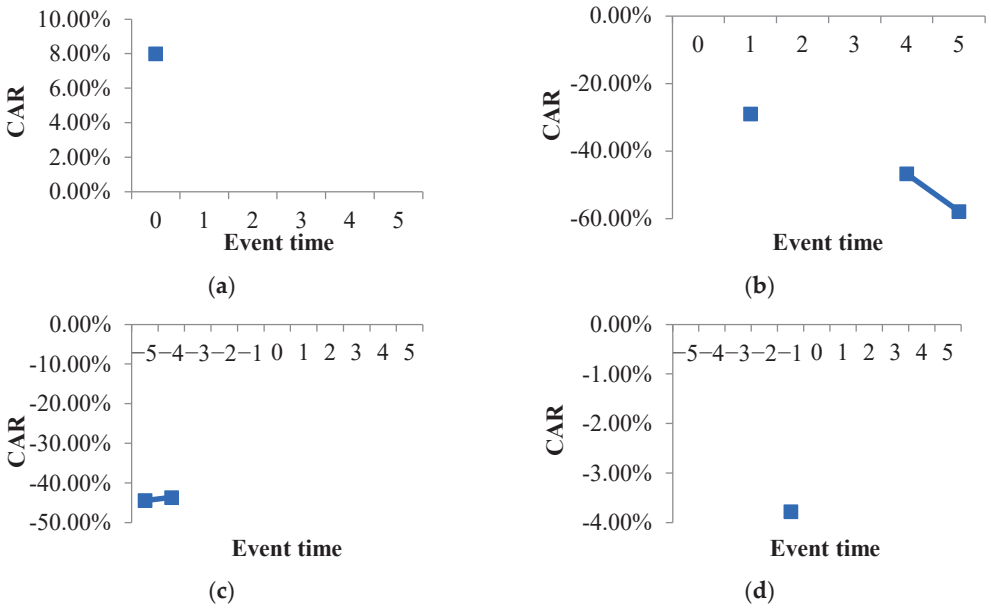

Figure 2. *Cont.*

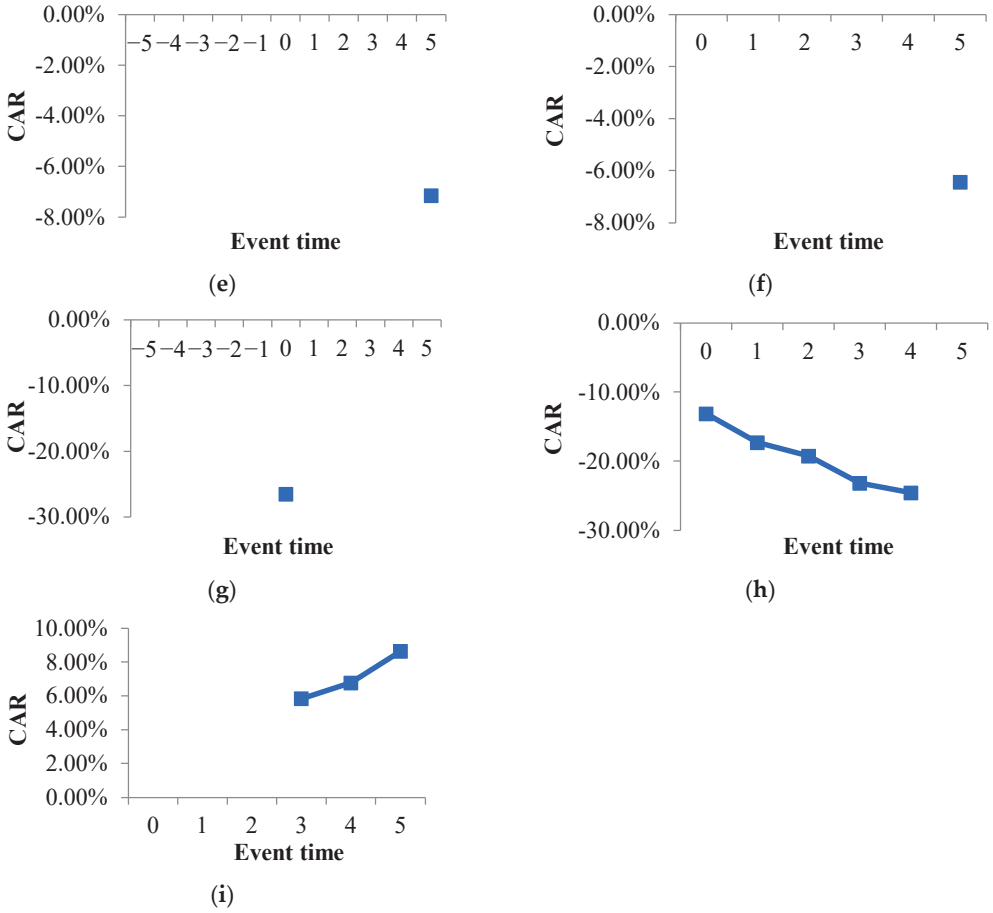

Figure 2. Significant impact of events on EUA futures price returns. (**a**) 6-day event window of Event 2, (**b**) 6-day event window of Event 3, (**c**) 11-day event window of Event 4, (**d**) 11-day event window of Event 6, (**e**) 11-day event window of Event 8, (**f**) 6-day event window of Event 8, (**g**) 11-day event window of Event 9, (**h**) 6-day event window of Event 17, (**i**) 6-day event window of Event 22. Note: The dots in the figures are the cumulative abnormal returns (CAR) that are significant under the 5% level.

Table 3. Impact of each event on EUA futures price returns (in %).

Event Window	[−5, +5]	[0, +5]	[−5, +5]	[0, +5]	[−5, +5]	[0, +5]	[−5, +5]	[0, +5]
	Event 1 (16 December 2005)		Event 2 (12 June 2006)		Event 3 (1 January 2007)		Event 4 (15 October 2007)	
CAR-5	−1.14		−1.4		3.92		−44.39 ***	
CAR-4	1.29		−2.21		7.04		−43.59 **	
CAR-3	2.98		−6		4.32		−42.79 *	
CAR-2	1.64		−12.13 *		5.26		−41.98	
CAR-1	1.92		−11.36		4.69		−41.18	
CAR0	1.04	−0.88	−3.36	8.00 ***	−10.8	−15.49 *	−40.37	0.8
CAR+1	0.39	−1.54	−3.59	7.77 *	−24.24	−28.93 **	−39.57	1.61
CAR+2	2.56	0.63	−3.16	8.2	−23.3	−27.99 *	−38.77	2.41
CAR+3	2.38	0.45	−2.73	8.63	−23.4	−28.09 *	−37.96	3.22
CAR+4	1.73	−0.19	−0.62	10.75	−41.95	−46.64 **	−37.16	4.02
CAR+5	0.37	−1.56	2.13	13.50 *	−53.11 *	−57.80 ***	−36.36	4.82
	Event 5 (29 April 2008)		Event 6 (16 June 2008)		Event 7 (17 December 2010)		Event 8 (10 June 2011)	
CAR-5	0.06		−0.54		0.49		0.38	
CAR-4	−1.66		−1.96 *		0.16		−0.52	
CAR-3	−4.01		−1.88		−0.24		−0.8	
CAR-2	−3.45		−2.83 *		−1		−1.71	
CAR-1	−4.26		−3.77 **		−1.48		−0.71	

Table 3. *Cont.*

Event Window	[−5, +5]	[0, +5]	[−5, +5]	[0, +5]	[−5, +5]	[0, +5]	[−5, +5]	[0, +5]
CAR0	−6.44	−2.17	−3.65 *	0.12	−3.38	−1.9	−0.82	−0.11
CAR+1	−8.1	−3.83	−3.61 *	0.17	−3.88	−2.4	−0.68	0.03
CAR+2	−9.82 *	−5.55	−3.02	0.76	−3.37	−1.89	−1.89	−1.18
CAR+3	−6.28	−2.01	−2.87	0.91	−2.29	−0.81	−3.36	−2.65
CAR+4	−3.39	0.87	−4.06	−0.29	−3.93	−2.45	−4.41	−3.7
CAR+5	−4.88	−0.62	−3.12	0.66	−3.78	−2.3	−7.15 **	−6.44 **
	Event 9 (24 June 2011)		Event 10 (9 December 2011)		Event 11 (1 March 2012)		Event 12 (1 January 2013)	
CAR-5	−2.6		−0.71		−3.66		−0.96	
CAR-4	−5		−6.77		2.62		−0.78	
CAR-3	−8.08		−5.95		3.47		−1.75	
CAR-2	−8.05		−6.78		−1.97		−6.66	
CAR-1	−18.01		−0.3		−7.46		−7.25	
CAR0	−26.48 **	−8.47	2.97	3.27	−3.94	3.52	−8.31	−1.06
CAR+1	−20.83	−2.82	−0.25	0.05	−2	5.46	−10.83	−3.58
CAR+2	−16.43	1.57	−6.57	−6.27	−4.53	2.93	−11.62	−4.37
CAR+3	−20.09	−2.08	−14.49	−14.19	−7.84	−0.38	−6.35	0.9
CAR+4	−15.94	2.06	−8.96	−8.66	−7.37	0.09	−9.15	−1.9
CAR+5	−17.74	0.27	−8.58	−8.28	−9.3	−1.84	−13.03	−5.78
	Event 13 (28 June 2013)		Event 14 (27 June 2014)		Event 15 (25 July 2014)		Event 16 (12 March 2015)	
CAR-5	−1.43		1.68		−2.79		−3.99	
CAR-4	−7.87		3.84		−2.1		−3.32	
CAR-3	−4.32		2.68		−0.6		−5.16	
CAR-2	−1.36		1.87		−0.91		−3.16	
CAR-1	−1.41		1.41		−3.19		−4.11	
CAR0	−6.82	−5.41	2.17	0.76	−2.18	1.01	−9.49	−5.38 *
CAR+1	−6.39	−4.98	2.75	1.34	−1.51	1.68	−8.78	−4.67
CAR+2	−5.49	−4.08	5.84	4.43	−4.28	−1.09	−8.38	−4.28
CAR+3	3.2	4.61	6.55	5.14	−3.1	0.09	−4.82	−0.71
CAR+4	−0.13	1.28	4.93	3.52	−2.11	1.08	−4.73	−0.63
CAR+5	−6.34	−4.93	−1.2	−2.61	−1.29	1.89	−5.85	−1.74
	Event 17 (24 June 2016)		Event 18 (26 June 2018)		Event 19 (25 November 2018)		Event 20 (31 January 2020)	
CAR-5	−0.96		−2.74 *		−1.04		−1.31	
CAR-4	1.92		−1.16		1.63		−0.5	
CAR-3	−3.61		0.72		6.7		−0.21	
CAR-2	−1.55		2.56		8.68		−2.94	
CAR-1	−2.51		1.66		5.14		−4.08	
CAR0	−15.64	−13.13 **	1.43	−0.24	3.15	−1.99	−3.41	0.67
CAR+1	−19.81	−17.30 **	2.65	0.98	1.89	−3.25	−6.22	−2.14
CAR+2	−21.76	−19.25 **	0.75	−0.91	0.2	−4.93	−5.58	−1.5
CAR+3	−25.71 *	−23.20 **	0.45	−1.21	3.83	−1.31	−3.84	0.24
CAR+4	−27.08 *	−24.57 **	0.75	−0.91	6.1	0.97	−4.73	−0.65
CAR+5	−24.03	−21.52	0.71	−0.95	6.64	1.51	−5.76	−1.68
	Event 21 (1 January 2021)		Event 22 (23 June 2022)					
CAR-5	0.52		−3.97 *					
CAR-4	4.03		−4.87					
CAR-3	2.44		−3.1					
CAR-2	−0.41		−2.39					
CAR-1	0.88		−5.98					
CAR0	3.55	2.67	−3.43	2.55 *				
CAR+1	1.06	0.18	−4.43	1.55				
CAR+2	2.76	1.88	−2.66	3.32				
CAR+3	5.75	4.88	−0.14	5.84 **				
CAR+4	5.89	5.01	0.79	6.77 **				
CAR+5	4.47	3.59	2.66	8.64 ***				

Note: *, **, *** indicate that *t* statistic is significant at 10%, 5% and 1% level, respectively.

Among the significant entry events, only Events 2 and 22 have positive impacts and Event 22 shows a longer impact. Event 2 involves the accession of Albania. Event 22 involves three countries, of which Ukraine has the largest average carbon emissions among the countries involved in the entry events. The five entry events with negative significant impacts involve countries including Romania, Bulgaria, Montenegro, Bosnia and Herzegovina and Croatia. Among these events, Event 3 has the longest and greatest degree of impact, and it also involves two relatively large carbon emitters, namely Romania

and Bulgaria. Figure 3 shows the average CO_2 emissions of the countries involved in the events selected. Combined with the figure, it can be seen that the impact of certain events on carbon prices may be related to the emissions of corresponding countries. It indicates that for most small carbon emitters, the promotion of their EU accession process tends to generate the market expectation that the allocation of the EU ETS to the country's emission allowances will be greater than its demand. However, the situation for large emitters is likely to be just the opposite, which means that the market would expect a greater demand than supply of its emission allowances when it joins the EU ETS. The rest of the EU entry events do not have a significant impact on the carbon price, which may be due to the small carbon emissions of the countries involved. The small allowances allocation of related countries does not produce a big shock of market expectation.

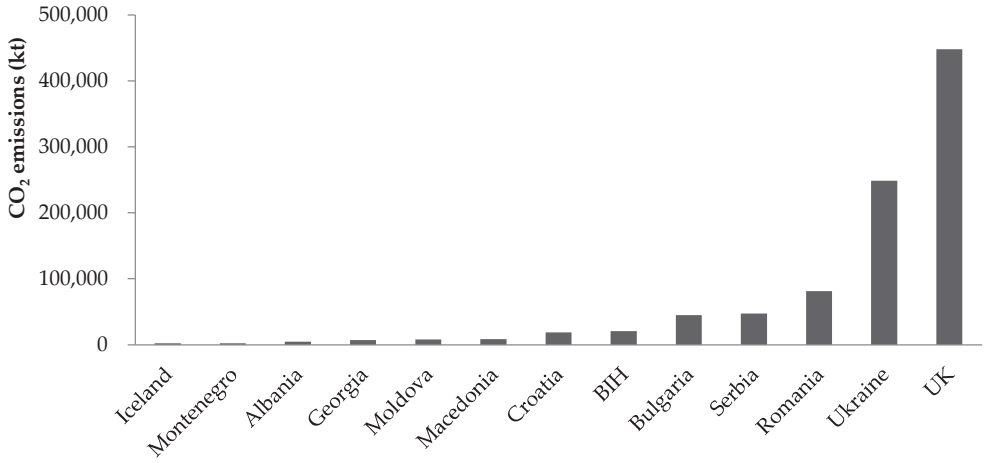

Figure 3. Average annual CO_2 emissions of related countries. Note: Due to the data availability, the emission of each country is on average from 2005 to 2019 and there are no data available on the emission of Kosovo. Source: World Development Indicators (WDI) of the World Bank.

Among the exit events, the announcement of the Brexit referendum results (Event 17) has a significant negative impact on carbon prices for five consecutive days in the post event window, indicating that Brexit negatively influences market expectations. The UK, which is the country with the highest degree of economic development involved in the events, also has much higher carbon emissions than other countries, as shown in Figure 3. As one of the pioneer countries to mitigate climate change, the UK established the UK Emissions Trading System (UK ETS) in 2002, which provides much reference for the operation of the EU ETS. Moreover, the UK has a sound carbon market supervision system and has promulgated the world's first law and other relevant regulations to deal with climate change [35,36], which improves the international prestige of the UK carbon market and its influence on global carbon markets. Higher carbon emissions and strict requirements for its own emission allowances grant the UK a special position compared with other countries, leading the market to believe that the UK's demand for allowances is higher than the allowances allocation by the EU ETS. Therefore, the market expectation of Brexit causes significant negative abnormal returns of EUA prices. In addition, the UK was a major participant in the EU ETS, and London was also the EU's emission allowances trading center. With Brexit, the operation of the EU ETS also entails many uncertainties, causing market participants to form a certain pessimistic expectation, which is likely to be one of reasons for the negative abnormal returns. Since the UK remained in the EU ETS in 2020 and the Brexit referendum has sent sufficient information to the market, Events 19, 20 and 21 do not show significant impacts on the market expectations of the EU ETS. The exit event re-grading Iceland (Event 16) does not lead to significant market reaction. This may be due to the small carbon allowance of the country which cannot affect the market expectation, and the market may also believe that Iceland will remain in the EU ETS.

5. Further Analysis

From previous results, it is likely that the market reaction of each event may be related to the emission of each country, and the influential mechanism seems to be different for large and small carbon emitters. Since there are only two large emitters involved in the events (i.e., UK and Ukraine), the relationship between the CAR of the entry events of small emitters and emissions of corresponding countries is worth further discussion.

In addition, the national allocation scheme of the EU ETS might also impact the supply and demand of emission allowances. The free allocation scheme for EU ETS member states in Phases 1 and 2 (2005–2012) is the National Allocation Plan (NAP), allowing member states to form their own allocation scheme "from the bottom up", according to their national conditions, which can then be approved by the European Commission. During the implementation process of NAPs, problems were found to be complex, including a lack of transparency and insufficient uniformity of assessing methodology in various countries [2]. Moreover, it has also led to the excessive allocation of national allowances, and member states maximize their allowances for their own interests. From 2005 to 2007, the annual allocation of 10 member states, including the UK and Germany, was 917.6 million metric tons of CO_2, while the annual verified emissions were only 868.68 [37]. The allowances submitted by countries were still large when submitting the second NAP, which was approximately 5% more than the verified emissions in 2005 [38]. To a certain extent, this may also cause the market to expect that the supply of allowances would exceed the demand when new member states enter, causing negative abnormal returns on carbon prices.

During Phase 3 in 2013, the EU ETS replaced NAP with National Implementation Measure (NIM), raising the decision-making position of allowances allocation to the EU level. When member states submit NIM, they use unified methods and standards, which are verified and approved by the European Commission and require necessary modifications. This has also promoted the transparency of implementing the allowances allocation scheme and the consistency of all participants [2]. After a country's entry into Europe, it is also worth discussing whether the change of the national allocation scheme will change the market expectation of the supply and demand of its emission allowances, and then change the impact of the event on carbon prices.

In the paper, the 11-day event window CAR and the 6-day event window CAR (*CAR11* and *CAR6*, respectively) of each entry event regarding small carbon emitters (i.e., excluding Event 22) are taken as dependent variables. The natural logarithm of annual average carbon emissions (The emission of each country is on average from 2005 to 2019 and there are no data available on the emission of Kosovo. If an event involves multiple countries, the sum of average carbon emissions of the countries is taken) of corresponding countries (*Emission*) and the national allocation scheme of corresponding years, which is taken as a dummy variable *NAP_NIM* (0 for NAP, 1 for NIM), are used as independent variables for regression analysis. The results are shown in Table 4.

Table 4. Regression results of CAR of entry events and related variables.

Variable	*CAR11*			*CAR6*		
Constant	−12.8655 ** (−2.9030)	23.1454 (0.7638)	23.0694 (0.7607)	−5.4173 (−1.1557)	57.2720 * (2.0769)	57.2438 * (2.0071)
NAP_NIM	8.6355 (1.0893)		8.6884 (0.9908)	2.9413 (0.3508)		3.2238 (0.3909)
Emission		−3.5794 (−1.1280)	−3.8160 (−1.1983)		−6.5663 ** (−2.2740)	−6.6541 ** (−2.2218)

Note: ** $p < 0.05$, * $p < 0.1$; t statistics are listed in parentheses.

A significant negative correlation can be seen between *CAR6* and *Emission* at the 5% level, whether *NAP_NIM* is added or not. Among the 16 European entry events involving

small emitters, 13 of *CAR11* and 11 of *CAR6* are negative, which indicates that certain EU entry events are more likely to cause a negative market reaction on carbon prices. Moreover, the absolute value of the negative abnormal returns increases along with the emissions of countries. The amount of carbon emissions is generally in proportion to the economic scale of a country. This suggests that for countries with a low level of economic scale, the promotion of a country's accession process will lead the market to expect a greater allowances allocation to the country than its demand. In addition, the greater the country's carbon emission, the stronger the expectation of this oversupply, thus, increasing the range of negative abnormal returns on carbon prices and aggravating market risk.

The change of national allocation scheme in the EU ETS has a positive impact on CAR, but the impact is not significant, indicating that this change does not play a significant role in reversing the market expectation of the oversupply of carbon allowances.

6. Conclusions and Implications

Using the event study methodology, the paper examines the effects of 22 key events in countries' process of entering and exiting the EU on the returns of EUA future prices in the EU ETS. The events include 17 entry events concerning the signing of SAA, becoming a candidate or potential candidate country, the process of a negotiation and formally entering the EU, and five exit events including the process of Brexit and the suspension of Iceland. The results show that eight events have a significant impact on EUA returns. Among them, two entry events involving Albania and Ukraine, respectively, have a positive impact, and five entry events have a negative impact. Regarding the exit events, the announcement of the Brexit referendum results causes a significant negative impact. It indicates that for most small carbon emitters, the promotion of their EU accession process tends to generate the market expectation that the allocation of the EU ETS to the country's emission allowances will be greater than its demand. However, the situation for large emitters is the opposite. Most events regarding small carbon emitters entering the EU lead to a negative market reaction, and a significant negative correlation between the countries' annual average carbon emissions and the cumulative abnormal returns of EUA prices is found. It is likely that the greater the country's carbon emission, the stronger the expectation of this oversupply, while the change of national allocation plans does not affect the market reaction notably.

As the region with the highest degree of integration in the world, the EU ETS is by far the most successful transnational regional unified emission trading mechanism. The impact of the entry of Eastern European countries and Brexit on the EU ETS can be used as a reference for other emission trading markets. With the increasing attention to climate change, the establishment of a unified carbon market in China and even the world will become the future development trend. In the process of building a unified carbon market, market regulators and traders should be concerned with the market risk caused by the change of participants. The paper shows that when the participation process of members with a lower economic development level is promoted, the market will tend to produce the expectation that the supply of carbon allowances will exceed the demand, which has a negative impact on the carbon price, and the impact will increase with the amount of carbon emissions of the participants. However, the participation of members with a higher degree of economic development leads to a tendency of the market to produce the expectation that the supply of carbon allowances is less than the demand, which has a positive impact on the carbon price. In short, the process of entering or exiting the existing carbon trading market as a buyer or a seller will have different impacts on the operation of the market. Therefore, carbon market regulators should pay attention to the policy arrangement of carbon allowance allocation. For the EU ETS, the allowances allocation for small economies should be appropriately reduced and the allocation for large economies should be increased. The change of the EU ETS national allocation scheme from NAP to NIM has no significant impact on reversing the market expectations of allowances allocation, indicating that the EU ETS should further improve the rationality of

allowances allocation, especially appropriately reducing the allocation of small economies and expanding the market transparency.

In the future, as the international community makes more efforts to mitigate climate change, governments will likely rely more on market-based means to reduce greenhouse gas emissions. The continuous expansion of the scope of emission trading markets will be a long-term trend in climate governance. During the operation of existing carbon markets, new regions may gradually join in. Taking China as an example, in order to achieve the goals of carbon peak and carbon neutralization, the national carbon market was launched in July 2021 and is still under construction. The national carbon market only covers the power generation industry at present, and high energy consumption industries such as steel, nonferrous metals and petrochemicals may also become involved in the future. The regional carbon markets that are in operation may also be merged and integrated. In this process, regulators and traders should pay attention to the impact of the change of membership on carbon price fluctuation. Referring to the experience of the EU, in the process of expanding the coverage of membership, regulators should appropriately control the allocation of emission allowances for industries with low emissions and regions with a low degree of economic development and increase the allocation of allowances for industries with high carbon emissions and regions with a high degree of economic development. Corresponding policies should also be gradually introduced to stabilize market expectations. Regulators in China and other countries can also adjust their allocation policies accordingly to guide market expectations and strengthen the stability of carbon markets in the case of market expansion, merger, member withdrawal and other changes. In addition, market traders should also regard the process of membership change as one of the factors that causes market risk and take corresponding hedging strategies in trading.

The paper tries to employ a new cross-level perspective and illustrate the relationship between political events and carbon prices. However, since the entry and exit events occurred at different points, the methodology applied in the paper may lead to an upward bias in the results. Other methods, such as a Difference-in-Differences setting with staggered adoption, can be considered for further studies to achieve more robust results. Moreover, further research can contribute to demonstrate a clearer causal mechanism between political factors and the operation of carbon markets.

Author Contributions: Conceptualization, D.Z. and Y.X.; methodology, Y.X.; software, Y.X.; validation, Y.X. and D.Z.; formal analysis, Y.X. and D.Z.; investigation, Y.X. and D.Z.; resources, Y.X. and D.Z.; writing—original draft preparation, Y.X. and D.Z.; writing—review and editing, Y.X. and D.Z.; supervision, Y.X. and D.Z. All authors have read and agreed to the published version of the manuscript.

Funding: This research was supported by "the Fundamental Research Funds for the Central Universities" (2021YQGL01) and "the Fundamental Research Funds for the Central Universities" in UIBE (21QD37).

Institutional Review Board Statement: Not applicable.

Informed Consent Statement: Not applicable.

Data Availability Statement: The data used in this study are publicly available and the data sources have been described in this article.

Conflicts of Interest: The authors declare no conflict of interest.

References

1. International Carbon Action Partnership. Emissions Trading Worldwide: Status Report 2022. 2022. Available online: https://icapcarbonaction.com/system/files/document/220408_icap_report_rz_web.pdf (accessed on 13 July 2022).
2. European Commission. EU ETS Handbook. 2015. Available online: https://ec.europa.eu/clima/sites/clima/files/docs/ets_handbook_en.pdf (accessed on 14 February 2020).
3. Lutz, B.J.; Pigorsch, U.; Rotfuß, W. Nonlinearity in cap-and-trade systems: The EUA price and its fundamentals. *Energy Econ.* **2013**, *40*, 222–232. [CrossRef]

4. Koch, N.; Fuss, S.; Grosjean, G.; Edenhofer, O. Causes of the EU ETS price drop: Recession, CDM, renewable policies or a bit of everything?—New evidence. *Energy Policy* **2014**, *73*, 676–685. [CrossRef]
5. Bel, G.; Joseph, S. Emission abatement: Untangling the impacts of the EU ETS and the economic crisis. *Energy Econ.* **2015**, *49*, 531–539. [CrossRef]
6. Alberola, E.; Chevallier, J.; Chèze, B. Price drivers and structural breaks in European carbon prices 2005–2007. *Energy Policy* **2008**, *36*, 787–797. [CrossRef]
7. Creti, A.; Jouvet, P.-A.; Mignon, V. Carbon price drivers: Phase I versus Phase II equilibrium? *Energy Econ.* **2012**, *34*, 327–334. [CrossRef]
8. Byun, S.J.; Cho, H. Forecasting carbon futures volatility using GARCH models with energy volatilities. *Energy Econ.* **2013**, *40*, 207–221. [CrossRef]
9. Boersen, A.; Scholtens, B. The relationship between European electricity markets and emission allowance futures prices in phase II of the EU (European Union) emission trading scheme. *Energy* **2014**, *74*, 585–594. [CrossRef]
10. Balcılar, M.; Demirer, R.; Hammoudeh, S.; Nguyen, D.K. Risk spillovers across the energy and carbon markets and hedging strategies for carbon risk. *Energy Econ.* **2016**, *54*, 159–172. [CrossRef]
11. Ji, Q.; Zhang, D.; Geng, J. Information linkage, dynamic spillovers in prices and volatility between the carbon and energy markets. *J. Clean. Prod.* **2018**, *198*, 972–978. [CrossRef]
12. Zhu, B.; Ye, S.; Han, D.; Wang, P.; He, K.; Wei, Y.-M.; Xie, R. A multiscale analysis for carbon price drivers. *Energy Econ.* **2019**, *78*, 202–216. [CrossRef]
13. Mansanet-Bataller, M.; Pardo, A. Impacts of regulatory announcements on CO2 prices. *J. Energy Mark.* **2009**, *2*, 75–107. [CrossRef]
14. Lepone, A.; Rahman, R.; Yang, J.-Y. The impact of European Union Emissions Trading Scheme (EU ETS) National Allocation Plans (NAP) on carbon markets. *Low Carbon Econ.* **2011**, *2*, 71–90. [CrossRef]
15. Hitzemann, S.; Uhrig-Homburg, M.; Ehrhart, K.-M. Emission permits and the announcement of realized emissions: Price impact, trading volume, and volatilities. *Energy Econ.* **2015**, *51*, 560–569. [CrossRef]
16. Jia, J.-J.; Xu, J.-H.; Fan, Y. The impact of verified emissions announcements on the European Union emissions trading scheme: A bilaterally modified dummy variable modelling analysis. *Appl. Energy* **2016**, *173*, 567–577. [CrossRef]
17. Guo, J.; Su, B.; Yang, G.; Feng, L.; Liu, Y.; Gu, F. How Do Verified Emissions Announcements Affect the Comoves between Trading Behaviors and Carbon Prices? *Evidence from EU ETS. Sustainability* **2018**, *10*, 3255. [CrossRef]
18. Conrad, C.; Rittler, D.; Rotfuß, W. Modeling and explaining the dynamics of European Union Allowance prices at high-frequency. *Energy Econ.* **2012**, *34*, 316–326. [CrossRef]
19. Chen, J.; Muckley, C.B.; Bredin, D. Is information assimilated at announcements in the European carbon market? *Energy Econ.* **2017**, *63*, 234–247. [CrossRef]
20. Alberola, E.; Chevallier, J. European Carbon Prices and Banking Restrictions: Evidence from Phase I (2005–2007). *Energy J.* **2009**, *30*, 51–79. [CrossRef]
21. Daskalakis, G.; Psychoyios, D.; Markellos, R.N. Modeling CO2 emission allowance prices and derivatives: Evidence from the European trading scheme. *J. Bank. Financ.* **2009**, *33*, 1230–1241. [CrossRef]
22. Koch, N.; Grosjean, G.; Fuss, S.; Edenhofer, O. Politics matters: Regulatory events as catalysts for price formation under cap-and-trade. *J. Environ. Econ. Manag.* **2016**, *78*, 121–139. [CrossRef]
23. Deeney, P.; Cummins, M.; Dowling, M.; Smeaton, A.F. Influences from the European Parliament on EU emissions prices. *Energy Policy* **2016**, *88*, 561–572. [CrossRef]
24. Fan, Y.; Jia, J.-J.; Wang, X.; Xu, J.-H. What policy adjustments in the EU ETS truly affected the carbon prices? *Energy Policy* **2017**, *103*, 145–164. [CrossRef]
25. Ye, S.; Dai, P.-F.; Nguyen, H.T.; Huynh, N.Q.A. Is the cross-correlation of EU carbon market price with policy uncertainty really being? A multiscale multifractal perspective. *J. Environ. Manag.* **2021**, *298*, 113490. [CrossRef] [PubMed]
26. Dai, P.-F.; Xiong, X.; Duc Huynh, T.L.; Wang, J. The impact of economic policy uncertainties on the volatility of European carbon market. *J. Commod. Mark.* **2022**, *26*, 100208. [CrossRef]
27. Dou, Y.; Li, Y.; Dong, K.; Ren, X. Dynamic linkages between economic policy uncertainty and the carbon futures market: Does Covid-19 pandemic matter? *Resour. Policy* **2022**, *75*, 102455. [CrossRef]
28. Wu, X.; Yin, X.; Mei, X. Forecasting the Volatility of European Union Allowance Futures with Climate Policy Uncertainty Using the EGARCH-MIDAS Model. *Sustainability* **2022**, *14*, 4306. [CrossRef]
29. Song, Y.; Liang, D.; Liu, T.; Song, X. How China's current carbon trading policy affects carbon price? *An investigation of the Shanghai Emission Trading Scheme pilot. J. Clean. Prod.* **2018**, *181*, 374–384. [CrossRef]
30. Song, Y.; Liu, T.; Liang, D.; Li, Y.; Song, X. A Fuzzy Stochastic Model for Carbon Price Prediction Under the Effect of Demand-related Policy in China's Carbon Market. *Ecol. Econ.* **2019**, *157*, 253–265. [CrossRef]
31. Song, Y.; Liu, T.; Ye, B.; Zhu, Y.; Li, Y.; Song, X. Improving the liquidity of China's carbon market: Insight from the effect of carbon price transmission under the policy release. *J. Clean. Prod.* **2019**, *239*, 118049. [CrossRef]
32. Brown, S.J.; Warner, J.B. Measuring security price performance. *J. Financ. Econ.* **1980**, *8*, 205–258. [CrossRef]
33. Brown, S.J.; Warner, J.B. Using daily stock returns: The case of event studies. *J. Financ. Econ.* **1985**, *14*, 3–31. [CrossRef]

34. Walker, N. Brexit Timeline: Events Leading to the UK's Exit from the European Union. House of Commons Library Briefing Paper Number 7960. 2020. Available online: https://researchbriefings.files.parliament.uk/documents/CBP-7960/CBP-7960.pdf (accessed on 13 July 2022).
35. de Aguiar, T.R.S.; Bebbington, J. Disclosure on climate change: Analysing the UK ETS effects. *Account. Forum* **2014**, *38*, 227–240. [CrossRef]
36. Lorenzoni, I.; Benson, D. Radical institutional change in environmental governance: Explaining the origins of the UK Climate Change Act 2008 through discursive and streams perspectives. *Glob. Environ. Chang.* **2014**, *29*, 10–21. [CrossRef]
37. Ellerman, A.D.; Buchner, B.K. The European Union Emissions Trading Scheme: Origins, Allocation, and Early Results. *Rev. Environ. Econ. Policy* **2007**, *1*, 66–87. [CrossRef]
38. Carbon Trust. EU ETS Phase II Allocation: Implications and Lessons. 2007. Available online: https://prod-drupal-files.storage.googleapis.com/documents/resource/public/EU%20Emissions%20Trading%20Scheme%20%28EU%20ETS%29%20-%20EU%20ETS%20Phase%20II%20Allocation_Implications%20And%20Lessons%20-%20REPORT.pdf (accessed on 13 July 2022).

MDPI AG
Grosspeteranlage 5
4052 Basel
Switzerland
Tel.: +41 61 683 77 34

Sustainability Editorial Office
E-mail: sustainability@mdpi.com
www.mdpi.com/journal/sustainability

Academic Open
Access Publishing

mdpi.com

ISBN 978-3-7258-6495-9